Relaxation Processes in Electronically Excited States: Blue-Light Receptors and Related Compounds

Inaugural-Dissertation

zur
Erlangung des Doktorgrades der
Mathematisch-Naturwissenschaftlichen Fakultät
der Heinreich-Heine-Universität Düsseldorf

vorgelegt von
Susanne Salzmann
aus München

Düsseldorf 2009

Aus dem Institut für Theoretische Chemie und Computerchemie
der Heinrich-Heine-Universität Düsseldorf

Gedruckt mit Genehmigung der

Referent:	Prof. Dr. Christel M. Marian
Korreferent:	Prof. Dr. Walter Thiel

Tag der mündlichen Prüfung: 24.07.2009

Dans la vie rien n'est á craindre, tout est á comprendre.
Marie Curie

Hiermit versichere ich, die hier vorgelegte Arbeit eigenständig und ohne unerlaubte Hilfe angefertigt zu haben. Die Dissertation wurde in der vorgelegten oder in ähnlicher Form noch bei keiner Institution eingereicht. Ich habe keine erfolglosen Promotionsversuche unternommen.

Düsseldorf, den

(Susanne Salzmann)

List of papers included in the thesis

- **Paper I**
  The photophysics of flavins: What makes the difference between gas phase and aqueous solution?
  Susanne Salzmann, Jörg Tatchen, and Christel M. Marian, *J. Photochem. Photobiol. A*, **198** (2008) 221-231.
  After an initial introduction to the calculations of the ISC rate constants by J. Tatchen, I contributed all calculations and major parts of the discussion and conclusion.

- **Paper II**
  Effects of protonation and deprotonation on the excitation energies of lumiflavin
  Susanne Salzmann and Christel M. Marian, *Chem. Phys. Lett.*, **463**, (2008) 400-404.
  All calculations and most of the discussion and conclusion were provided by me.

- **Paper III**
  Photophysical properties of structurally and electronically modified flavin derivatives determined by spectroscopy and theoretical calculations
  Susanne Salzmann, Víctor Martinez-Junza, Björn Zorn, Silvia Braslavsky, Madina Mansurova, Christel M. Marian, and Wolfgang Gärtner, *J. Phys. Chem.*, *submitted.*
  For this combined experimental and theoretical work, I contributed all calculations as well as major parts of the discussion and conclusion.

- **Paper IV**
  The photophysics of alloxazines: A quantum chemical investigation in vacuum and solution
  Susanne Salzmann and Christel M. Marian, *Photochem. Photobiol. Sci. submitted.*
  For this paper, I provided all calculations and most of the discussion and conclusion.

- **Paper V**
  Influence of the LOV domain on low-lying excited states of flavin: A combined quantum-mechanics / molecular-mechanics investigation
  Susanne Salzmann, Mario R. Silva-Junior, Walter Thiel, and Christel M. Marian, *unpublished manuscript.*
  The setup of YtvA-LOV was taken from M. Silva-Junior, who also contributed an initial introduction to and further supervision of the QM/MM calculations. My contribution comprises conception and performance of the calculations, as well as major parts of the discussion and conclusion.

- **Paper VI**
  Excited states of thiophene: Ring opening as deactivation mechanism
  Susanne Salzmann, Martin Kleinschmidt, Jörg Tatchen, Rainer Weinkauf, and Christel M. Marian, *Phys. Chem. Chem. Phys.*, **10** (2008) 380-392.
  The majority of the calculations for this publication have been carried out within the

framework of my diploma thesis. During my time as a PhD student I continued with additional calculations (i.e. CASPT2 results) and contributed parts to the paper text.

- **Paper VII**
  Ultrafast dynamics in thiophene investigated by femtosecond pump probe photoelectron spectroscopy and theory
  Rainer Weinkauf, Leo Lehr, Edward W. Schlag, **Susanne Salzmann**, and Christel M. Marian, *Phys. Chem. Chem. Phys.*, **10** (2008) 393-404.
  The focus of this paper clearly lies on the experimental work. My contribution comprises the calculation and evaluation of the vertical ionization energies at different geometries in order to support the interpretation of the fs pump-probe experiment.

- **Paper VIII**
  Deactivation via ring opening: A quantum chemical study of the excited states of furan and comparison to thiophene
  Nemanja Gavrilov, **Susanne Salzmann**, and Christel M. Marian, *Chem. Phys.*, **349** (2008) 269-277.
  This publication was done together with Nemanja Gavrilov a summer intern from Belgrade, who performed the calculations under my supervision. In addition I contributed all presented calculations on thiophene as well as a good part of the text.

- **Paper IX**
  UV excitation and radiationless deactivation of imidazole
  Mario Barbatti, Hans Lischka, **Susanne Salzmann**, and Christel M. Marian *J. Chem. Phys.*, **130** (2009) 034305 (8 pages).
  In this paper, my contribution comprises the calculation and analysis of the DFT/MRCI energy profiles of the four reaction paths.

List of related papers not included in the thesis

- **Paper X**
  Electronically excited states of tryptamine and its microhydrated complex
  Michael Schmitt, Robert Brause, Christel M. Marian, **Susanne Salzmann**, and W. Leo Meerts, *J. Chem. Phys.* **125** (2006) 124309 (10 pages).

- **Paper XI**
  Photophysics of phenalenone: Quantum-mechanical investigation of singlet-triplet intersystem crossing
  Martha C. Daza, Markus Doerr, **Susanne Salzmann**, Christel M. Marian, and Walter Thiel *Phys. Chem. Chem. Phys.*, **11** (2009) 1688-1696.

Zusammenfassung

Die vorliegende Arbeit beschäftigt sich mit der quantenchemischen Modellierung von Relaxationsprozessen elektronisch angeregter Flavine, welche als Pigment/Kofaktor natürlicher Blaulichtsensoren vorkommen. Im Zuge dieser Doktorarbeit wurde hierbei besonderes Augenmerk auf den ersten Schritt des blaulichtinduzierten Reaktionszyklus sogenannter LOV (light, oxygen, and voltage sensitive) Domänen des Phototropins gelegt, einer Interkombination (intersystem crossing, ISC) vom ursprünglich angeregten Singulettzustand des Kofaktors in die Triplettmannigfaltigkeit desselben.

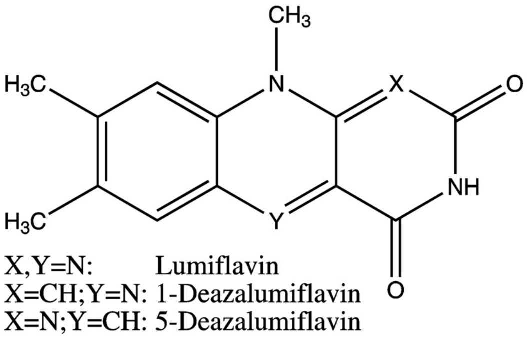

Abbildung Strukturformel von Flavin und zwei untersuchter Derivate

Um die photophysikalischen Vorgänge, welche direkt nach Absorption eines Photons des blauen Spektralbereichs in der LOV Domäne auftreten, zu verstehen, wurden in einer ersten Studie der optisch aktive Teil des freien Kofaktors (siehe Abbildung) im Vakuum und, mit Hilfe einer Kombination aus Mikrohydrierung und Kontinuumsmodell, in wässriger Lösung untersucht. Es stellte sich heraus, dass nicht nur die Form der Absorptionsspektren, sondern auch der Bildungsmechanismus der Triplettspezies in diesen beiden Medien unterschiedlich ist. Im Vakuum wird ein effizienter, nach El Sayed erlaubter, direkter ISC-Mechanismus gefunden. In wässriger Lösung ist dieser Kanal durch Lösungsmittelverschiebung jedoch nicht mehr zugänglich. Stattdessen wird durch diese Verschiebung ein anderer ISC-Kanal erreichbar, der hingegen nach El Sayeds Regel verboten ist. Erst durch die Berücksichtigung vibronischer Spin-Bahn-Kopplung, einem Mechanismus, der in heterozyklischen Systemen weit verbreitet zu sein scheint, wird das ISC erheblich beschleunigt, wodurch die experimentellen Befunde erklärt werden können. Desweiteren wurden in Kooperation mit Experimentatoren mehrere Flavinderivate, welche als künstliche Pigmente in natürlichen Blaulichtsensoren Anwendung finden könnten, in Vakuum und wässriger Lösung untersucht. Hierbei weisen insbesondere die zwei Deazaverbindungen (siehe Abbildung) veränderte spektroskopische Eigenschaften auf. Für das 1-Deazaflavin konnte kein effizienter ISC-Kanal identifiziert werden, während die Population der Triplettmannigfaltigkeit von

5-Deazaflavin in wässriger Lösung dem Mechanismus der Mutterverbindung folgt.

In einem zweiten Schritt wurde das Flavin mit Hilfe einer Kombination aus Quantenmechanik und Molekülmechanik in der LOV Domäne des Photosensors YtvA aus Bacillus subtilis untersucht. Schwerpunkt dieser Untersuchung war es, zum Einen, den Einfluss von vier polaren Aminosäuren in der unmittelbaren Umgebung des Flavins, und zum Anderen, den Einfluss der Konformation des für den Reaktionszyklus essentiellen Cysteins auf die Photophysik des Kofaktors zu untersuchen. Hierbei zeigte sich, dass der Einfluss der Proteinumgebung zustandsabhängig ist. Während die energetische Lage der optisch aktiven Zustände den Verhältnissen in Wasser sehr ähnlich ist, zeigt sich, dass die energetische Position relevanter, optisch inaktiver Zustände der Situation im Vakuum sehr nahe kommt. Als Resultat zeichnet sich ab, dass sowohl der direkte ISC-Kanal als auch der durch vibronische Spin-Bahn-Kopplung beschleunigte Kanal erreichbar sind. Zudem zeigt die Untersuchung eindeutige Indizien für einen externen Schweratomeffekt, welcher durch das Schwefelatom des Cysteins verursacht wird und für den experimentelle Anhaltspunkte gegeben sind.

In dieser Arbeit wird nicht nur die energetische Lage optisch aktiver Zustände von Flavinen in den verschiedenen Umgebungen in sehr guter Übereinstimmung mit experimentellen Daten beschrieben, sondern auch die Position dunkler, experimentell schwer zugänglicher Zustände wird vorausgesagt, welche ebenfalls eine Rolle für die Photophysik dieser Verbindungen spielen.

Summary

The present work is concerned with the quantum chemical modeling of relaxation processes in electronically excited flavins, which are found as chromophores/cofactors in natural blue-light sensors. In the course of this dissertation the focus was put on the first step of the blue-light induced reaction cycle of so-called LOV (light, oxygen and voltage sensitive) domains of phototropin: an intersystem crossing (ISC) of the initially excited singlet state to the triplet manifold of the cofactor.

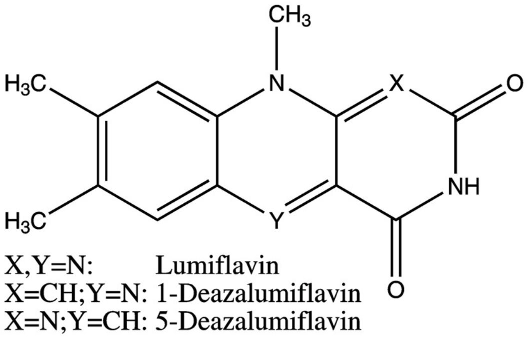

Figure Structure of flavin and two investigated derivatives

In order to understand the photophysical events that take place immediately after absorption of a photon from the blue spectral region, the optically active part of the free chromophore (see Figure) was investigated in a first study in vacuum and, by means of a combination of microhydration and continuum model, in aqueous solution. As it turned out, not only the form of the absorption spectra, but also the mechanism for the generation of the triplet species is different in these environments. In vacuum an efficient El Sayed allowed direct ISC mechanism is found. In aqueous solution this channel is not available due to solvent shifts. Instead, this shift causes another ISC channel to be accessible. As this channel is, however, forbidden according to El Sayeds rule, vibronic spin-orbit coupling, a mechanism that seems to be widely common in heterocyclic systems, has to be taken into account in order to find ISC rates comparable to experiment. In addition, several flavin derivatives that are anticipated to serve as artificial pigments in natural blue-light sensors, have been investigated in close cooperation with experiment. At this, the two deaza compounds (see Figure) in particular show altered spectroscopical properties. For 1-deazaflavin, no efficient ISC channel was found, while in 5-deazaflavin in aqueous solution the population of the triplet manifold follows the respective mechanism of the parent compound.

In a second step, the flavin has been investigated in the LOV domain of the photosensor YtvA of Bacillus subtilis by means of a combination of quantum mechanics and

molecular mechanics. The focus of this investigation was to determine the influence on the photophysics of the cofactor of a) the four polar amino acids in the vicinity of the flavin and b) conformational effects of the cysteine that is essential for the photocycle essential. In this connection it could be shown that the influence of the protein environment is state dependent. While the energetic position of the optically active states is very similar to the circumstances in water, it turns out that in relevant optically inactive states the situation in vacuum is closely resembled. As a result it emerges that the direct ISC channel as well as the channel enhanced by vibronic spin-orbit coupling are available in LOV domains. In addition, clear evidence for an external heavy-atom effect, caused by the sulfur center of the reactive cysteine, are found.

In the present work not only the energetic position of the optically active states of flavins in different environments are reproduced in very good agreement to experiment, but also the position of dark states is predicted, which are difficult to capture by means of experimental techniques, but nevertheless participate in the photophysics of these compounds.

Contents

III. Results and discussion 41

Motivation

The sun is the source of energy for a vast majority of biomass on this planet. Autotrophic creatures like plants use that energy directly and are able to transform it into a form that can be used by heterotrophic creatures, like us. Apart from the beneficial effects, sunlight holds danger. On a molecular basis, the interaction of light and matter results in electronically excited molecules. Hereby, electronic excitation triggers a manifold of mechanisms that participate in the dissipation of the excess energy. Those dissipation mechanisms range from physical processes to chemical reactions. While the photophysical processes preserve the chemical identity of the molecule and do not pose an immediate threat, photochemical reactions possess the danger of permanent alteration to the molecule.

One of the largest biomolecules in organisms is DNA. In plants, but also in other living creatures, DNA is exposed to sun light on a daily basis. This exposure contains the risk of various photochemical reactions. Although ultrafast decay of the UV-induced excited-state population to the electronic ground state is an intrinsic photophysical property of all nucleobases (see Ref. [1]), sites with two or more pyrimidine bases are mutational hotspots. [2] These photo lesions alter the genetic information and possibly render the same useless. Over the eons, nature developed elaborate detection and repair mechanisms for the various photo damages. These mechanisms are able to identify such a mutation and, in the ideal case, repair the DNA or at least initiate programmed cell death (apoptosis). Otherwise, the mutated cell bears the risk of unfavorable biological responses, e.g. cancer.

An even better strategy than detection and elimination, is to prevent photo damage in the first place. There are various examples for photophobic reactions of bacteria (mostly unicellular organisms) upon exposure to (intense) blue light, presumably in

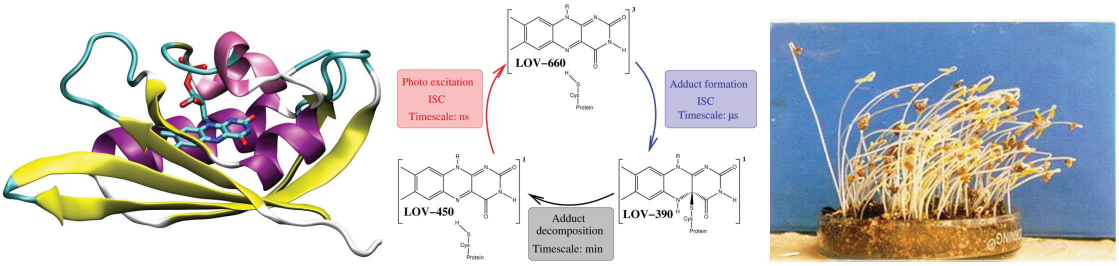

Figure Left: X-ray structure of the light, oxygen, and voltage sensitive (LOV) domain of the photosensor YtvA in *Bacillus subtilis*. [3] Middle: Schematic illustration of the blue-light triggered photocycle in the LOV domains of photopropin and related photosensors. Right: Phototropism, the ordered movement in response to light, one of the processes triggered by blue light and mediated by phototropin.

order to avoid the damaging effects of UV light. [4] While this and other responses have been known for many years, they have been widely anticipated to be a reaction to photosynthetic electron flow or reactive oxygen species. It took some time to realize that most of these responses are actually mediated by a variety of photosensors, even though this concept has emerged quite early in evolution, as the discovery of a photosensor in cyanobacteria demonstrates. [5, 6]

The sensing of quality, quantity, duration and direction of light is, of course, also vital with regard to the optimization of photosynthesis. Higher plants possess various photoreceptors and are able to respond to blue-light radiation with a multitude of processes. [7] The most commonly observed in everyday life is the ordered movement towards light (phototropism, see Figure). This photophysiological process is mediated by the protein phototropin. [8] As genome sequencing and annotation projects have shown, similar structures are also found in some prokaryotes (e.g. *Bacillus subtilis* [9]). [7] The process of light sensing hereby utilizes fully oxidized flavins, vitamin B2 related molecules, as cofactors in so-called light, oxygen, and voltage (LOV) domains. (See Figure (left) for an X-ray structure of such a LOV domain.) Blue-light absorption triggers a series of fully reversible photophysical and photochemical reactions of the chromophore schematically shown in Figure (middle).

Until the start of this thesis, the processes that lead to signalling were not completely understood. Apart from some exceptions little was known about intermediate transient states or the influence of the LOV domain on the low-lying electronically excited states of the cofactor. This is where the contribution of this work lies. As modern quantum chemical methods nowadays are able to predict the structure and energetic position of relevant electronic states in a satisfying manner, I have added to the understanding of the blue-light induced photophysical processes from a quantum chemists point of view.

Part I.

Introduction

1. Flavins - Sensing the blue

' There was no moon, and although the night was perfectly clear and the stars shone brightly, the lustre of the heavens was fairly eclipsed by that of the sea. The unbroken part of the surface appeared pitch black, but wherever there was the least ripple the whole line broke into a brilliant crest of clear white light. Near the ship the black interspaces predominated, but as the distance increased the glittering ridges looked closer, until toward the horizon, as far as the eye could reach, they seemed to run together and melt into one continuous sea of light.'
C. W. Thompson (1877)[a]

Since their first description in the year 1879 by the English chemist A. W. Blyth, [11] who isolated the bright yellow pigment (riboflavin) from cow milk, flavins have been the object of many investigations. This interest is well founded due to the chemical versatility of flavins. Next to their role as a constituent of the vitamin B complex (riboflavin is vitamin B_2), flavin-binding proteins are involved in a variety of biological processes mostly in the context of redox reactions. (For a detailed review see Ref [10].)

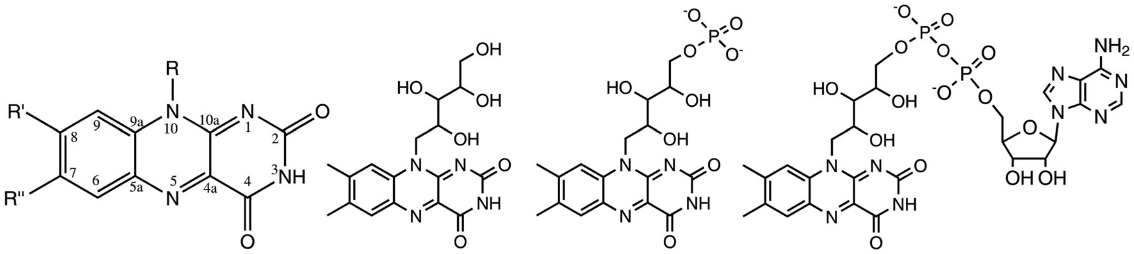

Figure 1.1.: Left: Structure and IUPAC labeling of flavins.(R=R'=R"=H: Isoalloxazine (IA); R=Me, R'=R"=H: 10-Methylisoalloxazine (MIA,DMLF); R=R'=R"=Me: Lumiflavin (LF)) Right: Three biologically relevant flavins, riboflavin (RF, vitamin B_2), flavin mononucleotide (FMN), and flavin adenine dinucleotide (FAD).

1.1. Flavins in solution

The photophysical and photochemical behavior of flavins is dominated by the isoalloxazine (benzol[g]pteridine-2,4,(3H10H)-dione) core ring, shown in Figure 1.1. The experimental absorption and emission properties of the 7,8-dimethylisoalloxazines lumiflavin (LF), RF and flavin mononucleotide (FMN) are very similar. [12–14] Flavins absorb in

---

[a] Excerpt from the Voyage of the Challenger, vol. 2, p 85, Macmillan & Co., London. Described was the bioluminescence of marine bacteria originating from the enzyme luciferase, acting on reduced flavin and oxygen. [10]

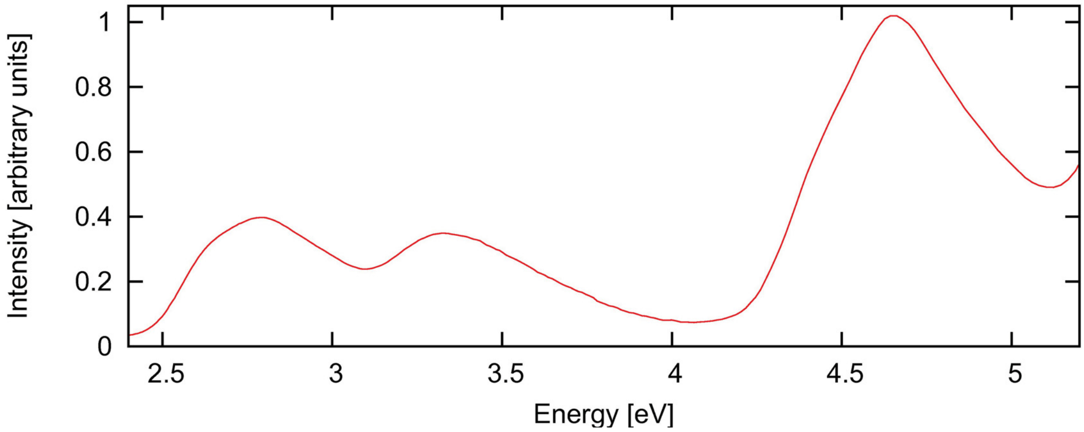

Figure 1.2.: Absorption spectrum of riboflavin in neutral aqueous solution in the energy range below 5 eV. Given is the energy [eV] against the intensity of the absorption.

the visible and ultraviolet regions (200 - 800 nm) of the spectrum. In the energy regime up to 5 eV (500 - 250 nm) the absorption spectrum of neutral, oxidized isoalloxazines is dominated by three bands as can be seen in Figure 1.2, which shows the absorption spectrum of RF in aqueous solution. [12, 14–17] The first band is located around 2.8 eV (446 nm, blue light). In water this band is structureless, but in less polar solvents such as ethanol, (EtOH) acetonitrile (*AcCN*) and 2-methyltetrahydrofuran (MTHF) vibronic structure with peaks at 2.63 eV, 2.79 eV and 2.99 eV (LF in EtOH; [14] 2.72 eV, 2.87 eV and 3.03 eV for MIA in MTHF, [18]) can be observed. Apart from this lack of vibrational structure, the position of this band is hardly affected by the environment. In variance to that, the second absorption band shows a pronounced solvatochromism. [15, 17, 19] Whereas in nonpolar solvents like dioxane (DX) [15] and MTHF [18] it is located around 3.7-3.8 eV (330 nm), a noticeable red shift of that band to 3.3 eV (375 nm) [15, 17, 20] is found in water. Experiments hereby have shown that the influence of the polarity on the position of the second band is rather low and that the ability of the solvent to form hydrogen bonds plays a more decisive role. [15, 19] The third band, which is found to be the most intense band in the absorption spectrum below 5 eV, is located around 4.6 - 4.7 eV (270 - 260 nm). As for the first absorption band the influence of the environment on its position is weak. [17] Previous CASPT2, [21] SAC-CI, [22] and TDDFT [12, 23–26] studies assign the three absorption bands to ($\pi \rightarrow \pi^*$) transitions.

In aqueous solution flavins exhibit a bright yellow fluorescence from which their name is derived (Latin *flavus*=yellow). In LF the emission band is centered around 2.33 eV (530 nm) and its position is mostly unaffected by the surrounding solvent. The quantum yield of flavin fluorescence, however, is dependent on the solvent and rises in nonpolar, aprotic solvents. [15, 17] In water the experimentally determined quantum yield of LF fluorescence ranges between 0.14 and 0.29 depending on the pH. (Bowd *et al.* Φ_F=0.16 and pH 2.2, [13] Sikorska *et al.* Φ_F=0.14 and pH ≈6, [15], Visser *et al.* Φ_F=0.25 and pH 7, [17], Bowd *et al.* Φ_F=0.29 and pH 7, [13]. For RF and

FMN similar fluorescence properties are found. [13]) For LF, RF and FMN in neutral aqueous solution, the strongest competition for the spin-allowed radiative deactivation is triplet formation. Experimentally the triplet quantum yield Φ_T is found to range between 0.4 [27, 28] and 0.6 [29, 30]. The quantum yield of photosensitized formation of singlet oxygen is found to be around 0.5. [31, 32] Although $O_2(^1\Delta)$ can be formed from a singlet excited state, too, this hints for $\Phi_T < 0.5$. [7]

1.2. Flavins in blue-light photosensors

In the last 15 years flavins, in the form of FMN and flavin adenine dinucleotide (FAD), have gained further interest due to their role as chromophores in blue-light photosensors. In connection with their discovery it became evident that a change in configuration of the chromophore, via an E/Z isomerization as it occurs in all photoreceptor protein families known so far (rhodopsins, phytochromes and xanthopsins), does not cover the full richness of nature.

Until today, three different kinds of flavin-based photoreceptor families are known, namely, cryptochromes (cry), BLUF (Blue Light sensing Using FAD) containing proteins and phototropins (phot). (On this see Ref. [7].) Those blue-light photosensors show a great variety of functions in lower and higher eukaryotes (including mammals, insects, plants, fungi, and algae) and prokaryotes (bacteria). [33]

1.2.1. Cryptochrome

Cryptochromes, which received their name from the long-hidden nature of their chromophore, are the oldest family of flavin-containing photoreceptors. They are involved in a variety of processes triggered by blue light, but the most prominent application is the synchronization of the circadian clock in animals including mammals. [33–35] It it worth mentioning that the amino acid sequence of cryptochromes is highly homologous to DNA photolyases, although the two flavoproteins accomplish completely different tasks in the cell. [36, 37]

Cryptochromes are two-chromophore proteins, containing either a pterin or a deazaflavin and a FAD. Hereby, the pterin/deazaflavin merely acts as an antenna for the reduced flavin. For the signaling, electron transfer mechanisms are under discussion. [7, 33, 38] However, cryptochromes exhibit significant mechanistic and functional differences in comparison to the other two flavin-binding blue-light photosensors.

1.2.2. Flavin in the BLUF domain

In BLUF proteins, the flavin photosensor last being identified, the signaling state, commonly denoted BLUF_{Red}, is formed from the excited singlet state of the FAD chromophore. [40, 41] In comparison to the dark-adapted absorption spectrum, the two spectral features undergo a red shift in BLUF_{Red} of about 0.1 eV and 0.05 eV, respectively. [7] The formation of the BLUF_{Red} state happens within 1 ns, whereas the amount of triplet state formed is insignificant (Φ_T=0.09). [40] In the dark, the signaling

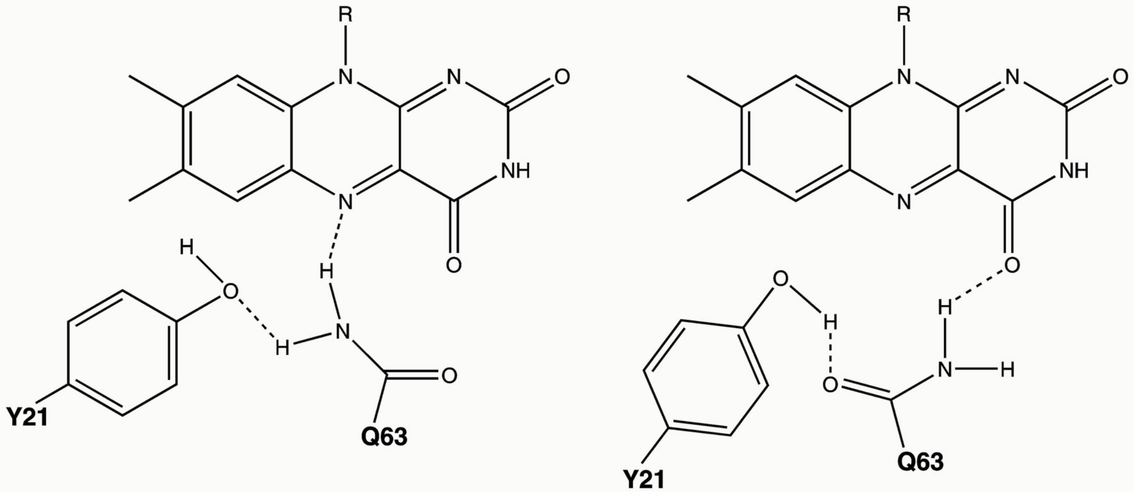

Figure 1.3.: Scheme for the possible orientations of glutamine (Q63) and its hydrogen-bonding interactions with the flavin chromophore and the nearby tyrosine (Y21) residue in the BLUF domain (AppA-BLUF, 1YRX [39]). Reproduced from Ref. [7].

state decays within minutes. Two amino acids (tyrosine (Y) and glutamine (Q), see Figure 1.3) are known to be crucial for the BLUF photocycle. Even with the exact orientation of the glutamine under question, the mechanistic details of signaling are a matter of discussion. However, it is widely accepted that the light-induced red shift in the absorption spectrum is caused by hydrogen-bond rearrangement. (See [7, 42] and references within.)

1.2.3. Flavin in the LOV domain

Phototropin is a plasma membrane-associated protein. In plants, it mediates phototropism, chloroplast relocation, stomata opening and leaf expansion (see Figure 1.4). [43] It comprises of two LOV (light, oxygen, and voltage sensitive) domains, LOV1 and LOV2, each binding FMN as a chromophore and a serine/threonine kinase. In the dark, the FMN is bound non-covalently. Upon illumination with blue light, a photocycle (see Figure 1.5) is triggered that leads to photobleaching. Schematically this photocycle is shown in Figure 1.5.

Figure 1.4.: Four processes in plants triggered by blue light and regulated by phototropin: Stomata and leaf opening, chloroplast relocation and phototropism (left to right).

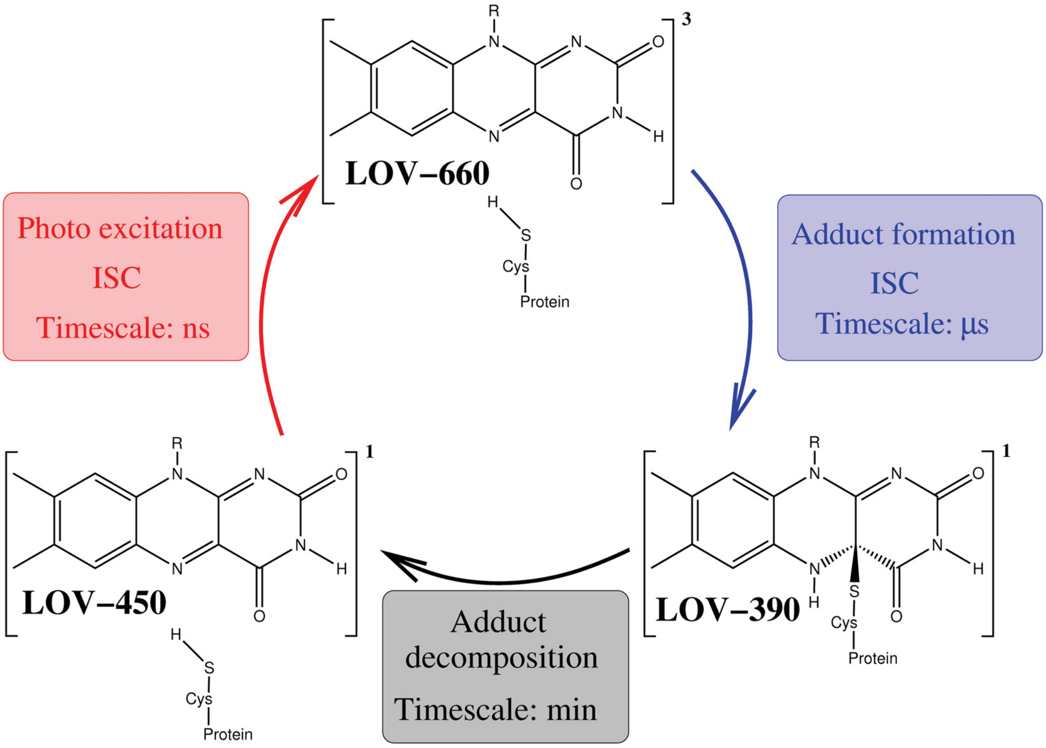

Figure 1.5.: Photocycle of the LOV domains. In the darkness the chromophore FMN is bound noncovalently in the LOV domain. (LOV-447) Upon photoexcitation the lowest-lying triplet state (LOV-660) is formed via intersystem crossing (ISC). Accompanied by a second ISC an adduct (LOV-390) between the chromophore and a nearby cysteine is formed. For possible reaction pathways see Figure 1.6. LOV-390 usually decomposes on the timescale of minutes and the photocycle can start again.

The primary step after blue-light absorption hereby involves a rapid decay of the excited singlet state population to the lowest excited triplet state on the nanosecond timescale. In the second step an adduct is formed between the C(4a) atom of the isoalloxazine ring and the sulfur atom of a nearby cysteine residue. This metastable adduct usually decomposes on the timescale of minutes and the photocycle can start again. Experimentally the quantum yields for formation of triplet state Φ_T and formation of adduct Φ_{Ad} are found to depend on the respective LOV domain (for a detailed compilation of spectroscopic data see [7] and citations therein). As I will present results of flavin in the LOV domain of the photosensor YtvA from *B. subtilis* in section 2, I will limit my description to quantum yields of this system. In YtvA the formation of triplet state is measured to be 0.62 and the quantum yield of adduct formation is found to be 0.49. [9] Although time and effort have been directed into the elucidation of the adduct formation, the mechanistic details are still a matter of debate. [43] It has been shown that in the dark the cysteine is protonated. [44] This gives rise to the four possible reaction pathways shown in Figure 1.6.

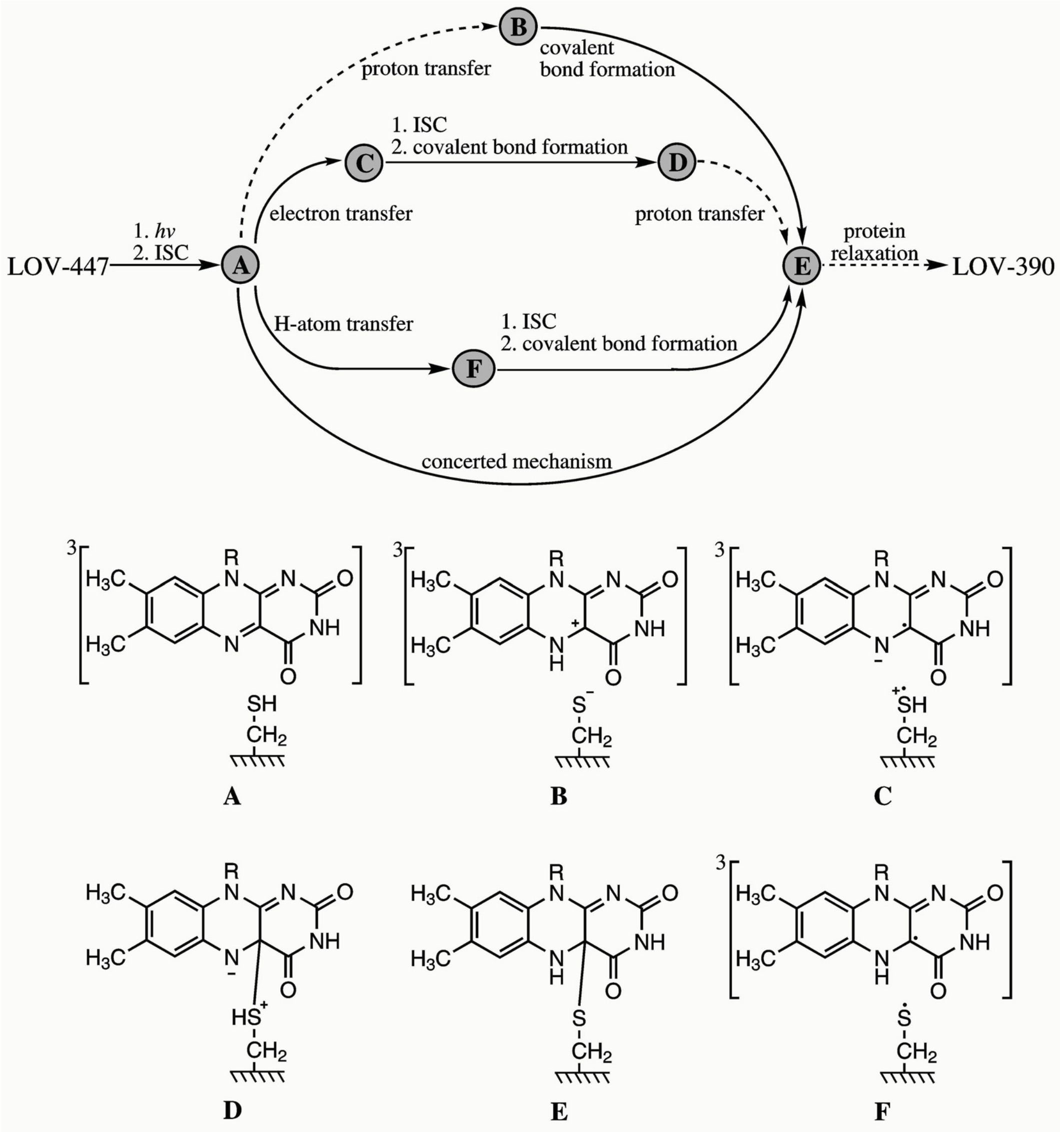

Figure 1.6.: Suggested reaction pathways (top) and intermediates (bottom) of the photoadduct (LOV-390) formation in wild-type LOV domains. **A** (bottom) is the reactive triplet state LOV-660. Reaction steps that are inhibited at $T \leq 80$ K are shown with dashed arrows. Reproduced from Schleicher et *al.*. [45]

1. As a possible reaction mechanism an initial proton transfer from the cysteine to the N(5) atom of the chromophore converts the S-H to the S^- in LOV-660 (Figure 1.6, **B**). In a second step, the thiolate attacks at the C(4a) atom of FMN and after an ISC the covalent bond is formed. [30]

2. As second reaction mechanism an initial electron transfer from the cysteine to the FMN produces a radical pair consisting of the anionic FMN and the cationic cysteine radicals (Figure 1.6, **C**). After ISC radical recombination leads to covalent bond formation (Figure 1.6, **D**) and in a final step the proton is transferred to the N(5) atom. [45]

3. In an alternative reaction pathway hydrogen transfer yields a neutral radical (Figure 1.6, **F**) After ISC radical recombination leads to the formation of the covalent bond. [46]

4. Finally, a concerted mechanism remains as a fourth possibility.

Transient EPR experiments, however, show that at a temperature of 77 K proton transfer to the ^{3}FMN does not occur. [45, 47] Therefore, at a temperature of 77 K reaction pathway 1 can be ruled out which, of course, is different at room temperature. In addition, FTIR investigations find the designated proton-donor cysteine protonated in the transient triplet state, which rules out pathway 1 and 3. [48, 49] However, the latter reaction mechanism is favored by recent quantum chemical [25, 50] and combined quantum mechanics / molecular mechanics (QM/MM) [51] studies. This reflects that, as to date, the protonation state of the transient triplet and its immediate influence on the adduct formation is under discussion.

The absorption spectra of the initial, dark-adapted state of FMN in the LOV domain are very similar for the LOV domains. Besides, absorption spectra of the dark-adapted state of FMN in LOV are almost identical to those of free FMN in water. The first absorption band is centered around 2.76 eV (450 nm), showing a well resolved vibronic structure with peaks at 2.62-2.63 eV (474-471 nm), 2.77-2.79 eV (447-445 nm), and 2.94-2.95 eV (422-420 nm). The second absorption band is centered around 3.31-3.44 eV (375-360 nm), reflecting the proximity of polar amino acids to the heteroatom moiety of the flavin core ring. [9, 30, 52, 53]

2. Project definition and embedding into SFB 663

2.1. Open questions concering LOV domains

In the previous chapter I outlined open questions with regard to the signaling mechanism of two flavin conatining photosensors. At the beginning of my work (September 2005) relatively little was known about the blue-light triggered processes in BLUF domains, while the photo-cycle of LOV domains (see Figure 1.5) was quite established. Therefore, the present work focuses on light-induced processes in LOV domains. The following list contains the main questions that were still open at the time:

1. How does the triplet formation occur in flavins and what is the influence of the environment on this process?
2. According to which mechanism does the adduct form?
3. How can cofactor and protein be modified in order to manipulate the photocycle with respect to possible applications?

2.2. Contributions within the framework of SFB 663

Thematically, this work is embedded into the Sonderforschungsbereich (SFB, Collaborative research center) 663 “Molekulare Antwort nach elektronischer Anregung (Molecular response to electronic excitation)”. Within this collaborative research center three further research groups are working on flavins, namely the groups of Prof. W. Gärtner, Prof. Heberle, and Prof. W. Thiel (see below). Additionally, the Deutsche Forschungsgemeinschaft (DFG, German research foundation) funds a Forschergruppe (FOR, Research unit) 526 “Blaulicht-sensitive Photorezeptoren (Blue-light Sensitive Photoreceptors)”, concerned with the understanding of the primary processes of three principle blue-light sensitive photoreceptor domains LOV, Cryptochrome and BLUF. Since 2002 this research unit has been contributing results in various fields, including structural determination, spectroscopic characterization, site-directed mutagenesis and elucidation of biophysical processes (For a complete list of publications see `http://www.bluelightphotoreceptors.de`). Since it would go beyond the scope of this work to completely summarize the studies of FOR 526, I restrict myself to including only those findings directly related to my work.

2.2.1. Modified flavins in biomimetric environment

The emphasis of project B3 (Gärtner and Heberle) lies on the synthesis and spectroscopical characterization of structurally and electronically modified flavins (corresponding to item 3 in the list above). During the time of my PhD (September 2005 to Mai 2009) the workgroup synthesized the four modified flavins shown in Figure 2.1: 1-deaza-RF (1DRF), 5-deaza-RF (5DRF), 7,8-didemethyl-RF (DMRF) and 8-isopropyl-RF (*ipr*RF). The photochemistry of these compounds was investigated by spectroscopical means (absorption and fluorescence spectra, fluorescence lifetimes, fluorescence quantum yields, transient triplet-triplet absorption spectra, transient triplet lifetimes and quantum yields of triplet generation) in aqueous solution. In addition, the incooperation of a modified flavin (5DRF) into a recombinant, flavin binding protein (LOV domain of the bacterial photosensor YvtA) was started and yielded promising results. [54] As reported by Hecht *et al.*, [55] with 5DRF as cofactor the LOV photocycle stopped after the adduct was formed. During the experiment the 5DRF-LOV adduct remaind stable for several days and was transferred to the initial state by means of light exposure. The impact of this finding lies in the identification of a dual photo switch with a broad range of potential biological and biotechnological applications.

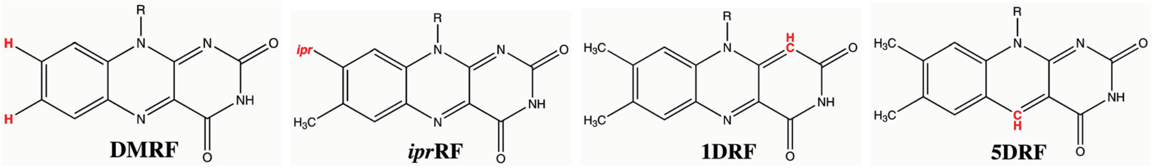

Figure 2.1.: Chemical structure of the four modified riboflavins synthesized by Mansurova et. *al.* [56]

2.2.2. Photochemical reactions of FMN in LOV domains

The goal of project C4 (Thiel) is to determine the mechanism of adduct formation (and adduct decomposition) by means of a combined quantum mechanics / molecular mechanics (QM/MM) treatment. In this connection, the relative stability of occuring transition states and the thioadduct, the influence of nearby residues on the mechanism, plus the spectroscopical properties of intermediate species are of interest. The QM/MM investigations have been carried out for phot1-LOV1 of the wild-type protein (PBD codes 1N9L and 1N9N) and the two mutants C57S and C57M, where the reactive cysteine residue is replaced with serine (replacement of SH against OH) and methionine (replacement of SH against CH_2-S-CH_3), respectively.

2.3. Own contributions

This work is concerned with understanding the first step in the photocycle of LOV domains, the formation of the reactive flavin triplet species. In order to understand the ISC mechanism in the protein, it is important to obtain a comprehensive knowledge about the relaxation processes that are triggered by blue-light absorption in flavins. As a starting point the following issues were investigated for free flavins (see Chapter 1, Paper I, Paper II and Paper III):

A What is the nature of low-lying excited states in flavins?

B What is the ISC mechanism?

C Which other relaxation processes compete?

D How are **A**-**C** affected when solvent (water) is taken into account?

E How does (de)protonation influence spectroscopical properties?

With this background the investigation was expanded to flavin in the LOV domain. This was done by means of QM/MM calculations with help from Prof. Thiel and his coworker M. R. Silva-Junior, who provided the setup of the protein, force-field parameters for the FMN and technial support. With respect to the work of Prof. Gärtner the LOV domain of the bacterial photosensor YvtA was chosen as working system. This investigation laid its main focus on the influence of the LOV domain on the low-lying excited states in flavins and discussed the ISC mechanism of FMN in YtvA-LOV in a qualitative manner (see Chapter 2 and Paper IX).

Along with flavins, I investigated photophysical relaxation processes in various flavin related compounds. The experimental investigation of the electronically modified flavin compounds 1DRF and 5DRF (Prof. Gärtner see 2.2.1) was accompanied by quantum chemical calculations. Additionally, alloxazines which differ from flavins in the ordering of the low-lying excited states, have been studied.

Part II.

Theory and methods

1. Theoretical background

1.1. The Born-Oppenheimer approximation and the Franck-Condon principle [a]

Born-Oppenheimer approximation When a molecule absorbs light, the transition of the electron from the initial state to the final state occurs on an ultrafast timescale ($\approx 10^{-15} - 10^{-16}$ s^{-1}). In comparison to the timescale of nuclear motions ($\approx 10^{-12} - 10^{-13}$ s^{-1}), an electronic transition can be considered to take place *instantaneously.* Hence, in a simple picture, when electrons move the nuclei can be seen as stationary and, on the other hand, when the nuclei rearrange the motion of the electrons can be regarded as simultaneous. This is the basic thought behind the Born-Oppenheimer (BO) approximation, which separates the Schrödinger equation of the electrons and the nuclei. With the neglect of nonadiabatic coupling terms, the dependence of the electronic problem on the position of the nuclei is reduced to parametric. This approximation introduces the potent paradigm of potential energy hypersurfaces (PEH). However, as we shall see later, when two PEHs come very close this approximation breaks down.

Franck-Condon principle The Franck-Condon (FC) principle is based on the separation of nuclear and electronic degrees of freedom as introduced by the BO approximation. In this case, electronic transition between the initial state and the final state is vertical. The probability of a transition between the two states is proportional to the square of the corresponding electronic transition moment matrix element [b]. The latter is given as:

$$\mathbf{R} = \langle i|\mathbf{M}|f\rangle \tag{1.1}$$

where **M** is a vector, here given in the dipole approximation, which can be resolved into one part depending on the electrons and one depending on the nuclei.

$$\mathbf{M} = \mathbf{M}_e + \mathbf{M}_n \tag{1.2}$$

The total eigenfunctions of the initial and final state, $\langle i|$ and $|f\rangle$, respectively, can be put (neglecting rotations)

$$\langle i| = \langle i_e i_n|, \qquad |f\rangle = |f_e f_n\rangle. \tag{1.3}$$

Substituting expressions 1.2 and 1.3 into 1.1 leads to:

---

[a] This chapter keeps close to Ref. [57–59].

[b] The following formulation keeps very close to the explanations in '*Molecular Spectra and Molecular Structure*' from G. Herzberg. [57]

$$\mathbf{R} = \langle i_e i_n | \mathbf{M_e} | f_e f_n \rangle + \langle i_e i_n | \mathbf{M_n} | f_e f_n \rangle \tag{1.4}$$

$\mathbf{M_n}$ does not depend on the coordinates of the electrons and the second term in this expression can be written as:

$$\langle i_n | \mathbf{M_n} | f_n \rangle \langle i_e | f_e \rangle. \tag{1.5}$$

However, as the electronic eigenfunctions, which belong to different electronic states, are orthogonal to one another, $\mathbf{R_n}$ is trivially zero due to the following relation:

$$\langle i_e | f_e \rangle = \delta_{if}. \tag{1.6}$$

Therefore, expression 1.4 is reduced to the first term which, taking the implications of the BO approximation into account, can be obtained to:

$$\mathbf{R} = \langle i_e | \mathbf{M_e} | f_e \rangle \langle i_n | f_n \rangle. \tag{1.7}$$

The first term in this expression is the electronic transition moment (also denoted $\mu_{el}(i,f)$ in section 1.2.1). Due to the BO approximation, the electronic eigenfunction and, as a result, this matrix element do not depend directly on the position of the nuclei. However, a parametric dependence of the electronic eigenfunctions on the nuclear coordinates remains. If the electronic transition takes place *instantaneously*, i.e. the nuclei do not move during the time of the transition and, if only one nuclear arrangement is considered, this matrix element will not change and can be treated as constant. (In section 1.2.2 we shall see that for intersystem crossing in some cases the description of the transition matrix element has to be extended beyond this zeroth-order term.)
With the transition probability and therefore the intensity being proportional to the square of expression 1.7 and in the end to the square of the integral over the product of the vibrational eigenfunctions of the initial and the final state, the so-called Franck-Condon factor (FCF).

$$I \approx R^2 \approx c \cdot |\langle i_n | f_n \rangle|^2 \tag{1.8}$$

Observed intensity distributions in absorption bands The FC principle is a powerful means in order to understand the shape and intensity distributions of an absorption (emission) band. A schematic illustration of this principle is shown in Figure 1.1. In a simple picture, the transition occurs vertically between the zeroth vibrational level of the initial state ($\Psi_i, \mathbf{v} = 0$) and the vibrational levels of the final state ($\Psi_f, \mathbf{v}' = \{0, 1, 2, ...\}$). (See dashed line in Figure 1.1.) In the lowest vibrational level of a given electronic state the probability density distribution for r is large only at the equilibrium nuclear arrangement of this state. In excited vibrational levels this probability distribution becomes larger near the classical turning points until, for high-lying vibrational states, a quasi-classical situation is reached. For the low-lying vibrational states of the final state this situation is illustrated schematically in Figure 1.1.
The shape of the absorption band not only depends on the form of PEHs of initial and final state and the vibrational wave functions, but also on the displacement between

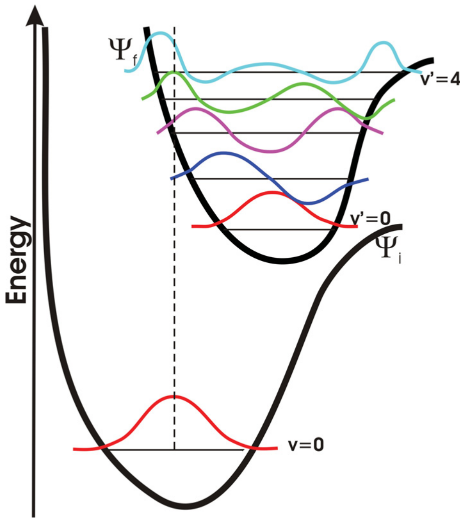

Figure 1.1: Schematic illustration of the Franck-Condon (FC) principle for the absorption of light. The electronic transition is represented by the dashed vertical line. The absorption intensity is proportional to the square of the overlap of the two vibrational wave functions (Franck-Condon factors, see text).

the geometries of the two states. The latter is illustrated in Figure 1.2, where three cases are distinguished.

- **A**:Equilibrium nuclear arrangements of initial and final state are (almost) identical
  In this case the by far largest FCF is obtained for the 0-0 transition and transitions to higher-lying vibrational levels are nearly forbidden. In an ideal system, where the nuclear coordinates of initial and final state are exactly identical no other transitions are observable, due to the orthogonality of the vibrational eigenfunctions.
- **B**: Equilibrium nuclear arrangements of initial and final state are similar
  In this case the 0-0 transition is not longer the most probable, but still possesses a sizable FCF. Instead, the highest overlap for the eigenfunctions occurs between v = 0 and a low-lying vibrational level (v′ = 2 in Figure 1.2). In addition, it can be seen that in this case the largest probability distribution does not coincide with the classical turning point.
- **C**: Equilibrium nuclear arrangements of initial and final state are (very) different
  In this case the FCF of the 0-0 transition is very small and the most probable transition occurs between v = 0 and a high-lying vibrational level (v′ = 6 in Figure 1.2). The shape of the resulting absorption band is wide.

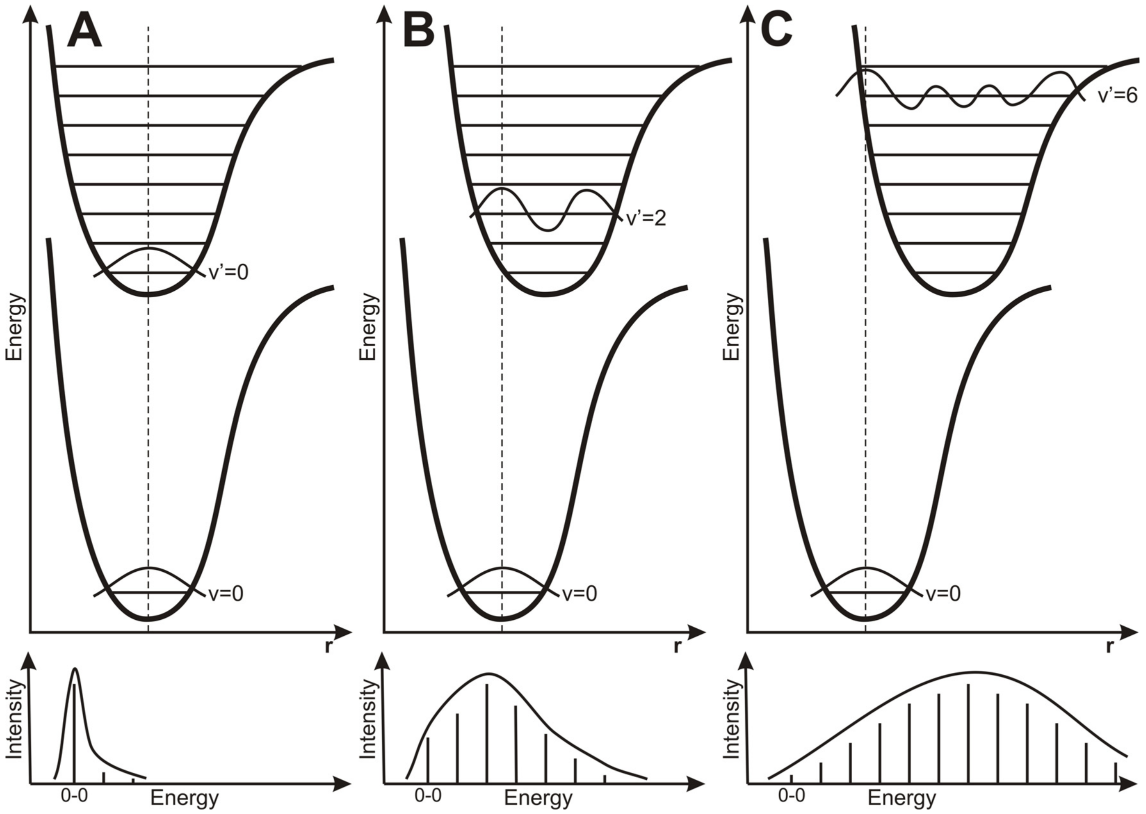

Figure 1.2.: Potential curves explaining the intensity distribution in absorption spectra according to the FC principle for three different cases. (The electronic transition is represented by the dashed vertical line.) In addition, the intensity distributions and resulting shape of the absorption band are given. In case **A** the equilibrium geometries of initial and final states are the same. For case **B** the geometry difference between the two states is small and for case **C** it is large. (See text for further details.)

1.2. Photophysical relaxation processes: Molecular response to electronic excitation

In comparison to the electronic ground state, the lifetime of electronically excited states is rather short. In general, the absorption of light triggers a multitude of processes that compete for the dissipation of the excess energy in the excited states. One generally distinguishes between photochemical processes, where the electronically excited molecule undergoes a chemical reaction in order to form a new species, and photophysical processes, which lead to alternative states of the same species, although it is not always straight forward to make such a distinction. As will be seen later, the major part of my work is concerned with photophysical deactivation processes. Therefore, this section outlines the most important photophysical processes and gives an overview over the dominance and relevance of these processes.

It is common practice to outline the competing photophysical processes that occur after light absorption in a so-called Jablonski diagram (also: state energy diagram) as it is depicted in Figure 1.3. In principle, there are three different ways for a molecule to get rid of the excess energy: (1) emission of light, (2) conversion of electronic energy into heat, and (3) dispension of energy to the environment. While in condensed phase all three possibilities are available, isolated molecules in the gas phase, of course, cannot decay via the last process. In the following, processes that belong to 1 and 2 are discussed in more detail.

1.2.1. Luminescence

One way for a molecule to get rid of the excess excitation energy is the emission of light (luminescence). In the Jablonski diagram (Figure 1.3) these processes are indicated as straight arrows. Depending on the initial state, luminescence may correspond to spin-allowed (fluorescence) and spin-forbidden (phosphorescence) transitions, respectively. Originally the distinction between the two processes was defined on the basis of the

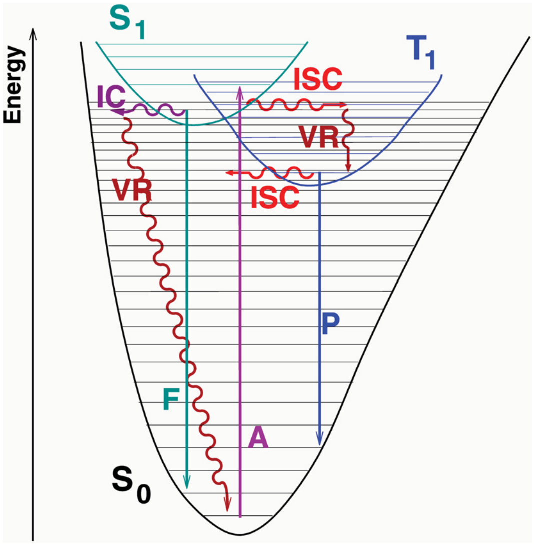

Figure 1.3: Jablonski diagram: Absorption (A) and emission processes are indicated by straight arrows (F: fluorescence, P: phosphorescence). Radiationless processes are symbolized by wavy arrows (IC: internal conversion, ISC: intersystem crossing, VR: vibrational relaxation, IVR: intramolecular vibrational energy relaxation (not shown)).

lifetime of the radiation. In fluorescence, the radiation ceased as soon as the exciting radiation was removed. In phosphorescence, however, the luminescence continues for a short time. [60] Although this paradigm is out-dated, it throws some light on the long lifetime and the associated reactivity of the first excited triplet state.
The radiative rate constant depends on the transition dipole moment $\mu_{el}(i,f)$ between the initial state i and the final state f and the vertical energy gap $\Delta E_{i,f}$ between the two states. It can be estimated with the following expression [61] [c]

$$k_{rad}(i \rightarrow f) = \frac{4e^2}{3c^3\hbar^4} \cdot \Delta E_{i,f}^3 \cdot \mu_{el}(i,f)^2 \tag{1.9}$$

For fluorescence, the determination of the transition dipole moment is accessible in the framework of non-relativistic theory. For phosphorescence this is different. In a non-relativistic treatment, these transitions are spin-forbidden. In a relativistic treatment, however, it is not so. In a simple picture, spin-orbit coupling mixes singlet and triplet states, which in turn results in non-vanishing transition dipole moment between singlet and triplet states.

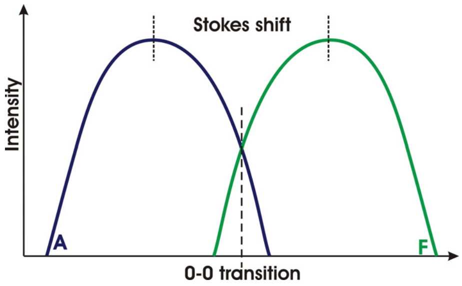

Figure 1.4: Schematic illustration of the Stokes shift. If the 0-0 transition of absorption (A) and emission (F, fluorescence) do not coincide, this is referred to as anomalous Stokes' shift. (See text)

The shape of the emission bands are determined in the same way as those of the absorption bands. For most molecules the equilibrium geometry of the ground state and the excited state are different. This results in a red shift of the emission maximum with respect to the absorption maximum, which in case of fluorescence, is denoted as Stokes' shift. Schematically this is shown in Figure 1.4. In condensed phase, various intermolecular interactions in the ground and excited states cause a separation of the 0-0 transitions of absorption and emission. This phenomenon is referred to as *anomalous* Stokes' shift and can be seen as a measure of the interaction of solvent and molecule.

1.2.2. Non-radiative processes

In the Jablonski diagram (Figure 1.3) the radiationless processes are symbolized by wavy arrows. In processes, such as internal conversion (IC) and intersystem crossing (ISC), the transition between the two states occurs isoenergetically, resulting in a vibrationally excited (hot) final state. While IC is a transition between states of the same multiplicity, ISC occurs between states of different multiplicity.
The rate of radiationless transitions between different states is particularly large, when the adiabatic energy separation between the two involved states is rather small. This

---

[c] Expressing the rate constants in s^{-1}, $\Delta E_{i,f}$ in cm^{-1}, and $\mu_{el}(i,f)$ in atomic units (ea_0) the numerical value of the prefactor becomes 2.0261×10^{-6}.

finding holds importance especially for the rate of IC processes. Usually, $S_n \rightsquigarrow S_1$ and $T_n \rightsquigarrow T_1$ ICs are substantially faster than $S_1 \rightsquigarrow S_0$ IC, since the adiabatic energy differences among the electronically excited states are much smaller than between the S_1 and the S_0 state. Experimental observations show an exponential dependence of the $S_1 \rightsquigarrow S_0$ IC rate constant on the energy gap between the two states. Commonly, this relation is referred to as the energy-gap law. [62] One consequence of the fast $S_n \rightsquigarrow S_1$ and $T_n \rightsquigarrow T_1$ ICs in the vast majority of molecules is that luminescence is observed only from the lowest excited-state PEH. (Kasha's rule)

Within the framework of the Born-Oppenheimer approximation, radiationless transitions between two PEHs are impossible. In order to describe those transitions it is necessary to go beyond the Born-Oppenheimer approximation. The interaction between different electronic states of the molecule arises through vibrational motion and has to be included in order to be able to describe those transitions. Using time-dependent perturbation theory, the rate constant k_{NR} for a radiationless transition starting from an initial single level $|i\rangle$ toward a manifold of final levels $\{|f\rangle\}$ is given by the well-known Fermi Golden Rule expression [63]

$$k_{NR}(|i\rangle \rightsquigarrow \{|f\rangle\}) = \frac{2\pi}{\hbar} \sum_{\{|f\rangle\}} |\langle i|\hat{H}'|f\rangle|^2 \delta(E_i^0 - E_f^0). \tag{1.10}$$

$\hat{H}'$ is the perturbation operator. In case of internal conversion this operator is the kinetic energy operator of the nuclei. In case of intersystem crossing, spin-orbit interaction couples the two states.

The consequences of direct and vibronic spin-orbit coupling on intersystem crossing [d] In order to obtain an ISC rate constant from Fermi's Golden Rule approximation several modifications have to be done. According to Toniolo and Persico [65, 66], it is possible to approximate expression 1.10 by a summation over rates of transitions in an energy interval of width 2η around the energy of the zeroth level of the initial state ($E_{i,\mathbf{v}=\mathbf{0}}$). (Here, the vectors $\mathbf{v}$ and $\mathbf{v}'$ represent sets of vibrational quantum numbers in all normal modes of the initial (i) and final (f) electronic state, respectively.) If we denote the coupling matrix elements driving the radiationless transition by $H^{SO}_{\mathbf{v}=\mathbf{0},\mathbf{v}'}$, the rate constant is obtained as

$$k_{ISC}\left(i \rightsquigarrow f\right) = \frac{2\pi}{\hbar\eta} \sum_{\left|E_{f,v'} - E_{i,\mathbf{v}=\mathbf{0}}\right| < \eta} \left|H^{SO}_{\mathbf{v}=\mathbf{0},\mathbf{v}'}\right|^2 \quad . \tag{1.11}$$

$H^{SO}_{\mathbf{v}=\mathbf{0},\mathbf{v}'}$ can be expanded in a Taylor series in the variables $\{q_\kappa\}$, the normal coordinates, around some reference point $\mathbf{q}_0$ [67] which we have chosen to coincide with the minimum

---

[d] This brief overview is kept very close to the work of Tatchen *et al.* [64]

of the initial state.

$$\begin{aligned} H^{SO}_{\mathbf{v}=\mathbf{0},\mathbf{v}'} &= \left\langle i \left| \hat{\mathcal{H}}_{\mathrm{SO}} \right| f \right\rangle \Big|_{\mathbf{q}_0=\mathbf{0}} \langle \mathbf{v}=\mathbf{0} | \mathbf{v}' \rangle \\ &+ \sum_{\kappa} \left(\frac{\partial}{\partial q_\kappa} \langle i | \hat{\mathcal{H}}_{\mathrm{SO}} | f \rangle \right) \Big|_{\mathbf{q}_0=\mathbf{0}} \langle \mathbf{v}=\mathbf{0} | q_\kappa | \mathbf{v}' \rangle \\ &+ O\left(|\mathbf{q}|^2 \right) \end{aligned} \tag{1.12}$$

The first term on the right-hand side of equation (1.12) is a purely electronic matrix element and is denominated direct spin-orbit coupling or Condon approximation in the following, whereas the term in the second line of equation (1.12) represents the first-order derivative coupling and is named vibronic spin-orbit coupling or Herzberg-Teller type coupling. (For more background on this deviation see [64] and [68].) In section 1.1 we have approximated the transition matrix element $\langle i_e | \mathrm{M}_e | f_e \rangle$ to be constant, which is equivalent with the Condon approximation. However, this approximation is only justified, when the change of the matrix element is negligible with respect to the variation of the nuclear coordinates. In cases, where this prerequisite is not fulfilled the Condon approximation is not sufficient and the contribution of the first order term of expression 1.12 will be substantial.

The implications of direct spin-orbit coupling are also known as El-Sayed's rule. [69] According to this rule of thumb, spin-orbit coupling matrix elements (SOME) between $(\pi\pi^*)$ and $(n\pi^*)$ states are in general much larger than SOME between two $(\pi\pi^*)$ states. Thus, when only direct spin-orbit coupling is considered (Condon approximation), ISC rate constants are much slower for $(\pi\pi^*) \rightsquigarrow (\pi\pi^*)$ processes than for $(\pi\pi^*) \rightsquigarrow (n\pi^*)$ processes. In case of vibronic spin-orbit coupling, out-of-plane distortions along the vibrational normal modes yield an interaction and thus a mixing of $(\pi\pi^*)$ and $(n\pi^*)$ states. Qualitatively the resulting enhancement of the ISC rate constants between two $(\pi\pi^*)$ states can be seen as an intensity borrowing from the much faster $(\pi\pi^*) \rightsquigarrow (n\pi^*)/(n\pi^*) \rightsquigarrow (\pi\pi^*)$ processes. As recent studies have shown, this ISC mechanism is common in various chromophores, including flavins (See Paper I and Paper III for details). [e] [64, 70]

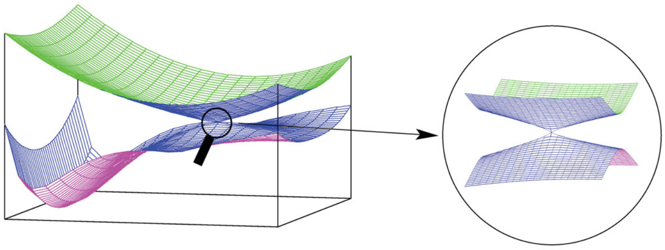

Figure 1.5: Conical intersection of two potential energy hypersurfaces. Left: The dependence of the two PEHs on two nuclear degrees of freedom. Right: Magnification of the conical intersection. (Source: Jörg Tatchen.)

---

[e] How the choice of the parameters, e.g. number of accepting and coupling modes, width of the search interval,... influences the ISC rate constants is explaind in Paper I, Paper III, and Paper IV and the respective Supplementary information.

Conical intersections In the last ten to twenty years, the so-called conical intersections (ConIn) have been accepted to be efficient funnels for the decay of electronically excited molecules. [f] At a ConIn, two PEHs are degenerate, which is illustrated in figure 1.5 for two reaction coordinates. In general, such a ConIn point is part of a subspace of ConIn points, usually denoted intersection space or seam of the dimension 3N-8 (N is the number of atoms of the system). In order to provide an ultrafast deexcitation of the excited state population, not only the presence, but also the energetic accessibility of a low-lying ConIn from the FC region is crucial.

IC, ISC and absorption of energy (i.e. a photon) create vibrationally hot states of a molecule. In condensed phase, the excess vibrational energy can be transferred to surrounding solvent molecules in order to reach the vibrational ground state. [g] This process is called vibrational relaxation (VR) and is, of course, not available in vacuum. A process that is able to relax a vibrationally hot state even in isolated molecules is intramolecular vibrational energy relaxation (IVR). This process redistributes the energy initially localized in a given vibrational mode of the molecule among the remaining vibrational modes. At least 5-10 atoms are required for IVR to occur. [72]

1.2.3. Which process prevails?

The question which process dominates the deexcitation of the molecules, depends predominantly on the electronic structure of the chromophore. A useful measure for the contribution of photophysical and photochemical processes to the depopulation of the excited state is the quantum yield Φ. The quantum yield of a process is defined as the ratio between the number of molecules that undergo this process and the number of light quanta absorbed. If the rate constants of all competing relaxation processes are known, the quantum yield of a process P can be calculated according to:

$$\Phi_P = \eta_{abs} \cdot \frac{k_P}{\sum k} \tag{1.13}$$

with η_{abs} being the efficiency of the absorption. In addition, when the quantum yield of a process is known it is possible to obtain the *natural* lifetime from the experimentally accessible *observed* lifetime of a process with the following relation.

$$\tau_{observed} = \Phi \cdot \tau_{natural} \tag{1.14}$$

In the absence of competing deactivation processes *natural* and *observed* lifetime are the same, of course. The rate constant of a given process P is the reciprocal of the *natural* lifetime and compares to theoretically determined rate constants. However, when a process is not the dominant deexcitation mechanism, the natural and the observed lifetime can differ by several orders of magnitude. A very prominent example for this variance is the fluorescence in the nucleobases. Although the natural fluorescence

---

[f] For an elaborate introduction to conical intersections see Ref. [71]. The part about conical intersection shown here is very close to this reference.

[g] Note: More accurately, thermal equilibrium is reached, since the occupation of the vibrational levels is temperature dependent according to Boltzmann's law.

lifetime in DNA and RNA bases is several nanoseconds, the low fluorescence quantum yield results in an observed fluorescence lifetime (often denoted as S_1 lifetime) ≤ 1 ps. [1]

2. Methods

2.1. Modeling electronic excited states

Flavin, like many other biologically relevant pigments, contains an extended π-system with a variety of low-lying electronic states. If one is interested in modeling the electronic structure of these states, dynamic and static electron correlation have to be accounted for. One of the established *ab-initio* treatments that includes both effects is the complete active space second order perturbation theory (CASPT2) [73]. However, with increasing molecule size, it becomes more and more demanding, if not impossible to include the necessary orbitals in the active space. As we shall see later, it is still possible to conduct CASPT2 calculations for the smallest flavin compound isoalloxazine, the exigency to keep the active space manageable, however, bears the risk of artifacts. (See section 1.1 for the implications of a too small active space on vertical absorption spectra of flavins.) In the last years, time-dependent density functional theory (TDDFT) [74] and, to some extent, time-dependent (resolution of identity) coupled-cluster with approximate treatment of the doubles ((RI)CC2)[a] have emerged as standard tools for the evaluation of electronically excited states of medium and large molecules. However, both treatments are bound to a single-reference configuration and have been shown to fail for states with strong multi-reference character. [76–78] Due to the use of linear response, these methods are also not suited for the description of double excitations.

2.1.1. Time-dependent DFT and charge-transfer states [b]

A note of caution regarding TDDFT in combination with standard functionals is in place when spatially extended Rydberg excitations and charge transfer (CT) states are concerned, since these functionals possess an incorrect asymptotical behavior, [79–81] which means that they decay faster than $1/R$, where R is the charge-separation coordinate. In addition, the excitation energies for such states are usually significantly underestimated.

As I will discuss the behavior of DFT/MRCI regarding CT states in the following, the failure of TDFFT with respect these states is visualized as presented in [79] and [82]. The TDDFT equation, a non-Hermitian eigenvalue equation, is obtained as

---

[a] The CC2 method is an approximation to the coupled-cluster singles and doubles (CCSD) method where the equations of the singles are retained in the original form and the doubles equations are truncated to the first order in the fluctuation potential. [75]

[b] This section is very close to the work of Dreuw *et al.* [79].

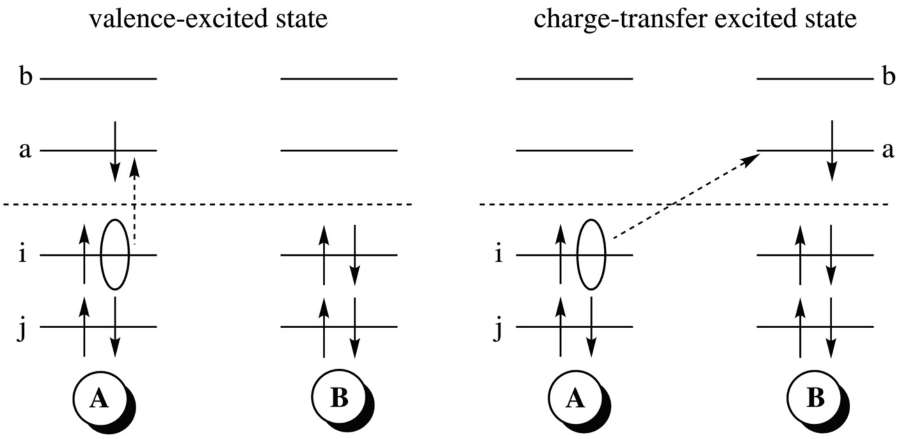

Figure 2.1.: Schematic sketch of a typical valence excited state (left) and a charge-transfer excited state (right). In the first, the transition occurs on one of the individual molecules, that is, the orbitals i, j and a, b are located on the same molecule. In contrast, in a CT excited state an electron is transferred from an occupied orbital i of molecule A into a virtual orbital a of another molecule B. When the molecules A and B are spatially separated from each other the orbitals i and j do not overlap with a and b. (Reproduced from Ref. [82].)

$$\begin{bmatrix} \mathbf{A} & \mathbf{B} \\ \mathbf{B}^* & \mathbf{A}^* \end{bmatrix} \begin{bmatrix} \mathbf{X} \\ \mathbf{Y} \end{bmatrix} = \omega \begin{bmatrix} 1 & 0 \\ 0 & -1 \end{bmatrix} \begin{bmatrix} \mathbf{X} \\ \mathbf{Y} \end{bmatrix} \tag{2.1}$$

with $\mathbf{A}$ and $\mathbf{B}$ as matrix representations of the Hamitonian, ω being the diagonal matrix of the excitation energies and $\mathbf{X}$, $\mathbf{Y}$ are expansion coefficients of the first-order frequency dependent response of the density matrix. Herein, the elements of the matrices $\mathbf{A}$ and $\mathbf{B}$ for hybrid functionals, i.e. functionals that contain parts of Hartree-Fock (HF) exchange, are given as

$$A_{ia,jb} = \delta_{ij}\delta_{ab}\left(\epsilon_a - \epsilon_i\right) + (ia|jb) - c_{\text{HF}}\,(ij|ab) + \left(1 - c_{\text{HF}}\right)(ia|f_{\text{xc}}|jb) \tag{2.2}$$

$$B_{ia,jb} = (ia|bj) - c_{\text{HF}}\,(ib|aj) + \left(1 - c_{\text{HF}}\right)(ia|f_{\text{xc}}|bj) \tag{2.3}$$

where i, j are used for ground-state occupied orbitals and a, b for the virtual orbitals. ϵ refers to the ground-state orbital energy and c_{HF} is the coefficient of the HF exchange part in the hybrid functionals. (For $c_{\text{HF}} = 1$ one arrives with TDHF, accordingly.) In contrast to a valence-excited state, in a long-range (intermolecular) charge-transfer state, an electron is transferred from an occupied orbital i of molecule A into a virtual orbital a of another molecule B (see Figure 2.1). If, for simplicity, the overlap between the two orbitals i and a is assumed to be zero, the second and fourth [c] terms in

---

[c] f_{xc} is the non-local xc-kernel. However, this functional is not known and generally approximated with the so-called *adiabatic local density approximation* (ALDA). In this approximation the originally non-local (in time) time-dependent xc-kernal is replaced with a time-independent local one based on the assumption that the density varies only slowly with time. This approximation allows the use of a standard local ground-state xc potential in the TDDFT framework.

expression 2.2 vanish. The first term of this expression yields the difference of the energies of the donor orbital i on A and the acceptor orbital a on B. The excitation energy of a CT state can also simply be estimated via

$$\omega_{\mathrm{CT}}(R) > IP_A + EA_B - 1/R \tag{2.4}$$

where R is the distance between the two subsystems and IP_A is the ionization potential of molecule A, EA_B is the electron affinity of molecule B, and $1/R$ is the electrostatic attraction between them. As compared to expression 2.4, within HF theory term 1 of expression 2.2 is, according to Koopman's theorem, already a rough estimate for the energy of the CT state. In DFT, however, this relation is not necessarily fulfilled, as the LUMO is generally more strongly bound in DFT than in HF theory and cannot be related to the EA. Hence, if only the energy difference between HOMO and LUMO gives rise to the excitation energy of the CT, the latter is underestimated. The third term of expression 2.2 originates from the non-local HF exchange part of the Kohn-Sham operator and contributes to the matrix elements of **A**. The **B** matrix vanishes for a CT state.

As a consequence, when a pure local xc-functional is employed, the excitation energy of a CT state is given within TDDFT by the difference of the orbital energies of the electron-accepting and the electron-donating molecular orbitals. Since the electrostatic interaction between the separated charges is a non-local property and is contained in the third term of expression 2.2, the shape of the long-range behavior depends on c_{HF} and a correct shape cannot be obtained with a local xc-functional. As a solution of this problem, non-local xc-kernels have to be introduced. Moreover, the excitation energies of CT states are underestimated in TDDFT, while for valence-excited states they can exhibit impressive accuracy. [78] For valence-excited states all terms of expressions 2.2 and 2.3, especially term 2 of 2.2 and term 1 of 2.3 which describe the coulomb repulsion between singly-excited configurations, contribute to the excitation energy, whereas CT states completely lack these corrections. Despite these artefacts, excited-state geometries have been shown to be predicted reliably using TDDFT. [83] (See Paper I, Paper IV, Paper VI, and Paper VIII and citations within for a discussion of an additional minor artefact of TDDFT with respect to excited-state nuclear arrangements.)

2.1.2. The combined density functional theory / multi-reference configuration interaction method[d]

The combined density functional theory / multi-reference configuration interaction method (DFT/MRCI) [80] by Stefan Grimme and Mirco Waletzke constitutes an efficient alternative to the above mentioned methods. The principle idea of this approach is to include major parts of dynamic electron correlation by DFT whereas static electron correlation effects are taken into account by a short MRCI expansion. In order to achieve this, the MRCI expansion is built up from Kohn-Sham (KS) orbitals employing the BHLYP functional. As basis functions configuration state functions (CSF)

---

[d] The description of the DFT/MRCI follows closely Ref. [80].

Figure 2.2: Structure of the two different C_{2v} symmetric ethylene-tetrafluoroethylene dimers used within the test calculations. The intermolecular distance is defined as the distance between the centers-of-mass of both molecules. The left structure is used in the test calculations from Dreuw *et al.*, see Ref. [79].

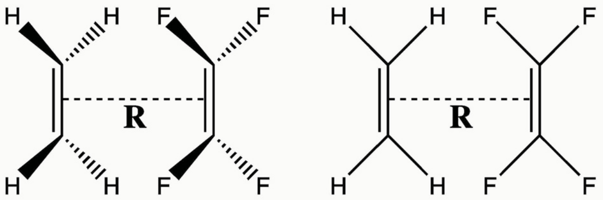

are used. [84, 85] The exact electronic Hamiltonian is replaced by an empirical operator where the exact matrix elements are replaced by KS orbital energies and scaled two-electron integrals. The Hamiltonian hereby differs for diagonal and off-diagonal matrix elements. Five global parameters, obtained from fits to experimental data, are used for this scaling. In difference to other semiempirical methods, these parameters are independent of the atom type and depend on the multiplicity and the number of open shells exclusively.

Diagonal elements of the effective DFT/MRCI Hamiltonian are constructed from the exact expression and a DFT specific correction term. In comparison to the conventional expression, the HF energies are replaced by their KS counterparts and the Coulomb and the exchange integral are scaled with a total of three parameters. For off-diagonal elements between equal configurations, the exact matrix element is used and for the evaluation of off-diagonal elements between different configurations, the exact matrix element is scaled by $p_1 e^{-p_2 \Delta E^4}$ in order to prevent double counting of dynamical electron correlation. [e] This damping factor depends on the energy difference between the CSFs (ΔE) and two parameters (p_1 and p_2). Due to the exponential damping, the influence of high lying CSFs is very small. With an attempt to decrease the calculation time with respect to a classical MRCI, only CSFs below a threshold are included in the DFT/MRCI expansion. This selection results in a compact CI expansion and allows the treatment of very large systems such as carotenes and chlorophylls. [f] Additionally, the resolution of the identity (RI) approximation is used for the two-electron integrals. The errors for relative energies with the DFT/MRCI method are in most cases below 0.2 eV [76, 78, 80] which is in the same range as those obtained from CASPT2 calculations. With respect to charge transfer states, the behavior of the DFT/MRCI is not clearly deductible. One has to keep in mind that the underlying Kohn-Sham potential had not been corrected for the right asymthotic behavior. [80]

Long-range and short-range behavior Following a study from Dreuw *et al.* [79] I tested the long-range behavior of the DFT/MRCI in comparison to the underlying BHLYP functional and RICC2 [86] for the low-lying CT states along the intermolecular

---

[e] This damping makes use of the fact that for MRCI dynamical electron correlation effects are represented by a huge number of energetically high-lying configurations, whereas the static correlation is accounted for by a smaller number of low-lying configurations.

[f] For large conjugated systems such as long polyenes and carotenes DFT/MRCI is the only available method that reproduces the ordering of the low-lying excited states correctly. [76]

distance coordinate R of two different ethylene-tetrafluoroethylene dimers (see Figure 2.2). As can be seen in figure 2.3 the long-range behavior of the DFT/MRCI method is almost identical to that of the BHLYP functional. Comparison to RICC2 shows that the long-range behavior of DFT/MRCI and BHLYP is far from being ideal, but Dreuw *et al.* have shown that, due to the high amount of HF exchange (50%), the BHLYP functional does not fail completely. With regard to my work, this finding raises the question, how far the DFT/MRCI can be trusted if CT states are concerned. Although, as we will see later, I only treat poly-molecular systems where the intermolecular distances are shorter than 5 Å. One has to keep in mind, however that for TDDFT not only the long-range behavior is described incorrectly, but also the excitation energy of the CT state is computed as too low. In my work, I did not test the short-range behavior of the DFT/MRCI method explicitly. However, it could be anticipated that the CI part is able to apply corrections to the short-range behavior. [80] An indication for a trustworthiness of the DFT/MRCI with respect to the short-range behavior is found in connections with the investigation of lumiflavin in the LOV domain (see chapter 2). There excitation energies are calculated not only for mere lumiflavin, but also for a complex of flavin with functional groups of 5 surrounding amino acids. When, for the latter system, the excitation energies for the five lowest-lying singlet states, obtained at the DFT/MRCI level and the TDDFT/B3LYP level, are compared, I find good qualitative agreement between the optically bright (valence-excited) states. However, when using TDDFT/B3LYP, one CT state (CYS → LF) is found below the first $^1(\pi\pi^*)$ state and more are found slightly above this state. In contrast, DFT/MRCI identifies only one CT state within the same number of low-lying excited states. In addition,

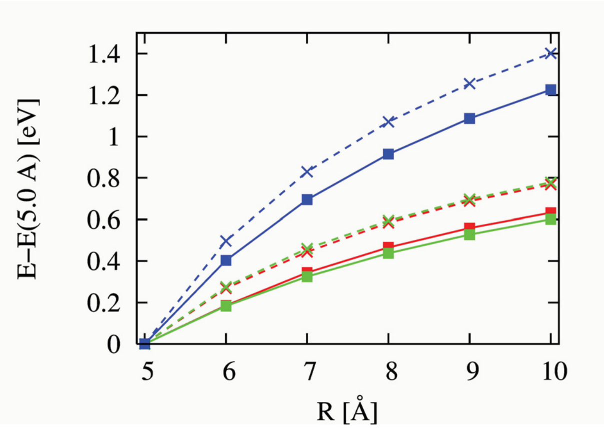

Figure 2.3: Comparison of the long-range behavior of two low-lying CT states of the ethylene-tetrafluoroethylene dimer (Figure 2.2, right) along the intermolecular distance coordinate computed at the level of DFT/MRCI, (red line) BHLYP, (green line) and RICC2 (blue line). The solid line corresponds to an electron transfer from the HOMO of tetrafluoroethylene to the LUMO of ethylene and the dashed line corresponds to a respective charge transfer from ethylene to tetrafluoroethylene. The excited-state energy of the respective CT state at 5 Å is set to zero for all methods. For the other ethylene-tetrafluoroethylene dimer configuration a qualitatively identical situation is found.

this CT state is located well (about 0.8 eV) above the first $^1(\pi\pi^*)$ state and more than 1.1 eV higher than the respective TDDFT/B3LYP excitation energy.

Excitations with four or more open shells Investigation of the long-range behavior of the DFT/MRCI method revealed another issue. For both dimers, the lowest-lying excited state is found to be a singlet state, situated around 2.8 eV. The electronic structure of this state is dominated by double excitations with four open shells (denoted as D4 in the following) corresponding to the transition of one electron from the HOMO of each monomer to the respective LUMO. The corresponding triplet state is found around 4.8 eV, while the respective singly excited triplet states are located at 4.3 eV and 4.8 eV. In a simple picture, the excitation energy of these doubly excited states should be around the sum of the two separate excitation energies, thus 4-6 eV higher than DFT/MRCI situates them. Unlike polyenes and carotenoids, the low-lying excited states of flavins and related compounds do not show any (major) intrinsic contribution of double excitations with four open shells. Although, in general, closer investigations and a solution to this problem is desirable, in this work no problem with such intruder states was encountered and therefore a correction was not necessary in order to perform the calculations.

2.2. Modeling of solvent effects

To my knowledge, for flavins and related compounds, there is no gas phase data available. As we will see later, certain features of the absorption spectrum of flavins (steady state and transient absorption) depend on the environment. Therefore it is not only reasonable but even necessary, to extend the investigation from vacuum to aqueous solution or protein in order to get the absorption properties and last but not least, the photophysical behavior in these media right.

2.2.1. Aqueous solution

Conductor like screening model The Conductor-like Screening Model (COSMO) [87, 88] belongs to the continuum solvation models. Here the solvent is not represented explicitly, but rather by a structureless continuous medium which is polarized by the solute. In order to achieve that, the solute molecule forms a cavity within the dielectric continuum of permittivity ε that represents the solvent. The charge distribution of the solute polarizes the dielectric medium and the response of the medium is described by the generation of screening charges on the cavity surface. In COSMO these screening charges are approximated and the deviations of this approximation from the exact solution are rather small. For strong dielectrics like water they are less than 1%, while for non-polar solvents with $\varepsilon \approx 2$ they may reach 10% of the total screening effects. [89] In my work, I used COSMO to model water ($\varepsilon \approx 78$) and acetonitrile ($\varepsilon \approx 36$). While for the latter solvent interaction is dominated by electrostatic interaction, for water the ability of the solvent to form a hydrogen-bonding network with the chromophore has to be accounted for, too. However, a description of hydrogen bonding is not included in COSMO and will be presented in the following.

Solvation with explicit water molecules A different approach to account for solvent-solute interaction are discrete models, where a (large) number of solvent molecules are treated explicitly together with the solute. Consequently, localized interactions, like hydrogen-bonding effects, can be accounted for. However, a realistic description of solvent needs a huge number of solvent molecules, which renders the calculations laborious, if not impossible, if sophisticated quantum chemical methods are applied. One workaround is to use different levels of theory for the solute and some important water molecules on one side and the rest on the other side, of course. This is the philosophy of QM/MM methods, which will be described in the next section.

Introduction and justification of the employed solvent model In this work, I combined the advantages of COSMO, for the description of electrostatic interaction, and microhydration with few explicit water molecules, in order to account for hydrogen-bonding effects. Figure 2.4 shows an optimized ground-state structure where four water molecules are arranged around the heteroatoms of the isoalloxazine ring. In section 1.1.2 I will compare and discuss the results of COSMO, microhydration and combination of both. As we shall see, the latter model outperforms mere COSMO or microhydration. Hence, if possible, this model was used for the determination of excitation energies in aqueous solution.

When COSMO was applied, the DFT/MRCI expansion was built up from the one-particle basis of COSMO optimized Kohn-Sham orbitals. As DFT/MRCI calculations for singl*et and* triplet states always employ the orbitals of the electronic singlet ground state, the charge distribution of the molecule that polarizes the surrounding solvent is considered correctly only for the vertical absorption energies at the FC point. For excited-state absorption spectra (singlet-singlet or triplet-triplet) or adiabatic excitation energies this is different, as for a correct description the charge distribution of the excited state has to be considered. In the case of flavins, however, spectroscopic investigations by Weigel *et al.* find the anomalous Stokes shift to be around 500 cm^{-1}, [19] much smaller than the error of the DFT/MRCI method (around 0.2 eV [76, 78, 80]).

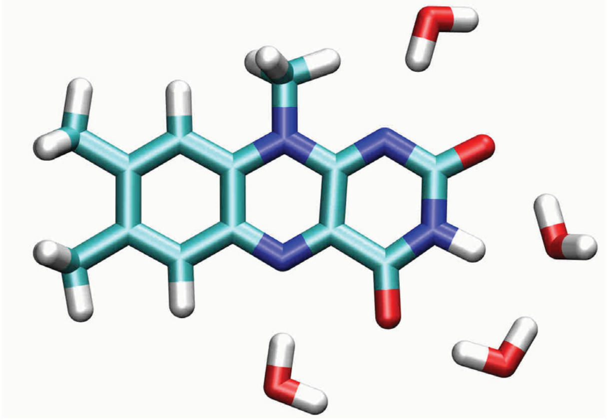

Figure 2.4: Microhydrated cluster of lumiflavin and four explicit water molecules. For flavin derivatives a similar assembly is found. For alloxazine, up to six water molecules were used (see Paper IV).

As we shall see later, many states that are relevant for the blue-light induced photophysical relaxation processes show significant solvent shifts (0.3-0.7 eV). The following list comprises information about the employed solvent model as well as a justification for them for various problems that go beyond the calculation of vertical absorption energies at the FC point.

- **Triplet-triplet absorption** As we shall see in section 1.1.1, the transient triplet-triplet absorption spectra show significant solvent dependence. As compared to experimental data of flavins in water the calculated spectra for flavin in vacuum (see Figure 1.4) give a wrong qualitative answer, while the results obtained with the best solvent model, COSMO and microhydration, show excellent agreement with experiment (see Figure 1.7). Therefore, employment of the COSMO approach is justified as the error due to the missing solvent interaction can be anticipated to be by far larger than the error due to the slightly wrong polarization of the COSMO screening charges.
- **Adiabatic excitation energies and solvent shifts along relaxation pathways** In addition to the solvent shift of vertical excitation energies, the influence of the environment on the adiabatic excitation energies or other points of the excited state PEHs is of interest. In variance to the COSMO model, for microhydration alone no issues arise with respect to a correct description of the charge distribution of electronically excited states. In various cases the TDDFT/B3LYP geometry optimizations resulted in the nuclear minimum arrangements of CT states instead of those of the desired valence-excited states. This failure is an artifact of the TDDFT/B3LYP method, which systematically underestimates the energy of a CT state whereas DFT/MRCI finds this state at much higher excitation energies. However, as an analytic DFT/MRCI gradient is not available, the minimum nuclear arrangements of the valence excited state are out of reach. (See section 2.1.1 for an explanation about TDDFT and CT states and section 2.1.2 on an explanation about the improved short-range behavior of the DFT/MRCI method.) As a workaround the solvent shift of a particular state was taken to be constant and applied as a correction on the adiabatic excitation energy of this state. Even though this approach introduces some errors (e.g. neglect of anomalous Stokes shift), it is more appropriate than the complete neglect of solvent shift. In order to model the solvent shifts along relaxation pathways either this approach or mere COSMO was employed.
- **Spin-orbit coupling matrix elements** In order to obtain ISC rate constants in aqueous solution, direct and vibronic spin-orbit coupling has to be determined. As the spin-orbit coupling depends on the electronic structure of the excited states and the latter, among others, depends on the environmental influences, solvent shifts have to be included in the calculation of the SOMEs and their derivatives. However, as these calculations are typically done for the minimum nuclear arrangement of the initial singlet excited state it is not possible to employ the full solvent model, COSMO and microhydration (see above). As a workaround mere COSMO was used. (See Paper I, Paper III, and Paper IV.)

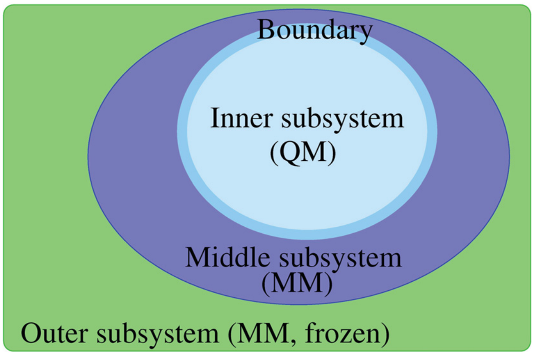

Figure 2.5: Partitioning of the entire system into inner, middle and outer subsystems. For the QM/MM optimizations presented in chapter 2, the core LOV domain (PDB code 2PR5, [3]) consisting of 101 amino acids, 240 crystallographic water molecules, and the FMN cofactor was solvated in a 35 Å water sphere. Six different QM-regions (see Figure 2.2) were employed and the middle system was made up of all residues with a distance of less than 9 Å from FMN. (See Paper IX and its Supplementary Information for further details.)

2.2.2. LOV domains: The combined quantum-mechanics/ molecular-mechanics approach[g]

In the last years the combined quantum-mechanics/ molecular-mechanics (QM/MM) approach has emerged as the method of choice for the modeling of reactions in biomolecular systems. While the majority of atoms are described well by molecular-mechanics (MM) force fields (FFs), the description of the, in most cases much smaller, active center which undergoes chemical reactions or other changes in its chemical structure requires quantum-mechanical (QM) methods. The combined or hybrid QM/MM method tries to merge the benefits of these two worlds.

In a QM/MM calculation all atoms have to be assigned to one of the three subsystems illustrated in Figure 2.5. The main difference between middle and outer subsystem is that the atoms of the outer subsystem are frozen during the QM/MM geometry optimization, while the middle system is allowed to relax. For the purpose of calculating the total QM/MM energy, middle and outer subsystem are considered as one. In the following the inner subsystem will be referred to as QM region, while middle and outer subsystem will be denoted MM region. The boundary region designates the region, where QM and MM atoms come close. As the QM and MM regions interact, various approaches exist to take this dependence into account. (For a detailed reviews on this see [90, 91].)

In the QM/MM study for flavin in the LOV domain, presented in chapter 2, the electrostatic interaction between QM and MM atoms was taken into account by electrostatic embedding. In this embedding scheme, the MM-atom partial charges are taken from the applied biomolecular force field (CHARMM/TIP3P [92, 93]) and included as point charges in the one-electron part of the QM Hamiltonian. [90] In cases, where the border between QM and MM region cuts through a covalent bond, as it is the case here, special care is required at the QM-MM boundary. In this study, the boundary region

---

[g] This introduction is kept close to [90].

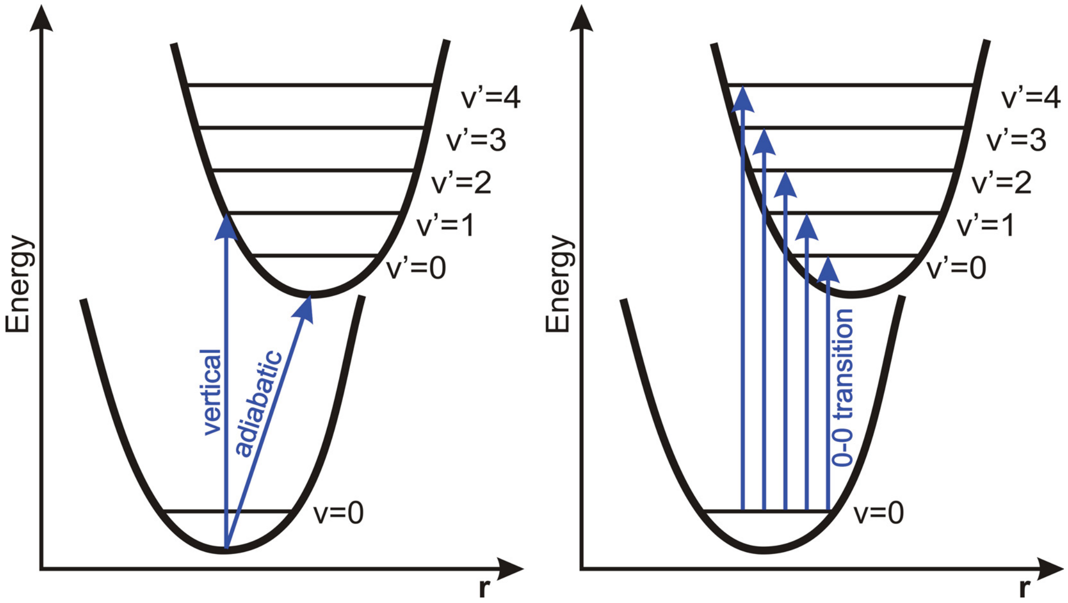

Figure 2.6.: Comparison between theoretical vertical and adiabatic excitation energies and vibrational absorption spectra (theoretical and experimental). In order to obtain the energy of the 0-0 transition from the theoretical adiabatic excitation energy, zero-point vibrational energy corrections have to be applied. (See Figure 1.2, case B and text in section 1.1.)

was treated via a link-atom approach with the charge-shift scheme. [94, 95] The link atom is treated by quantum mechanics explicitly and, in the present study, comprised hydrogen atoms.

2.3. Vibrational absorption spectra

It is a common practice to identify the experimental band maxima with vertical excitation energies. Nevertheless, it has been shown that this presumption does not always hold. [96–98] In cases, where the geometry shift is small the vibrational wave functions do not necessarily have their maxima at the classical turning points, [98] and a displacement of the absorption maximum from the vertical excitation energy can occur. (See Figure 1.2, case B and text in section 1.1.) Therefore, it is more meaningful to compare calculated adiabatic excitation energies with experimental 0-0 transitions, if the latter are available. As illustrated in Figure 2.6, the adiabatic excitation energy and the 0-0 transition differ by zero-point vibrational energy (ZPVE) corrections. In case of flavins and related compounds, these ZPVE corrections are quite substantial (about 1000 cm^{-1} for the $(gs) \rightarrow {}^1(\pi\pi^*)$ absorption) and, of course, also contribute to the differences between band maximum and vertical excitation energy. An even better strategy is to compare theoretical and experimental vibrational spectra.
In order to obtain vibrational absorption or emission spectra, vibrational intensity distributions of the respective transition have to be computed. (Harmonic vibrational normal modes were acquired numerically with the program packages SNF [99] and the

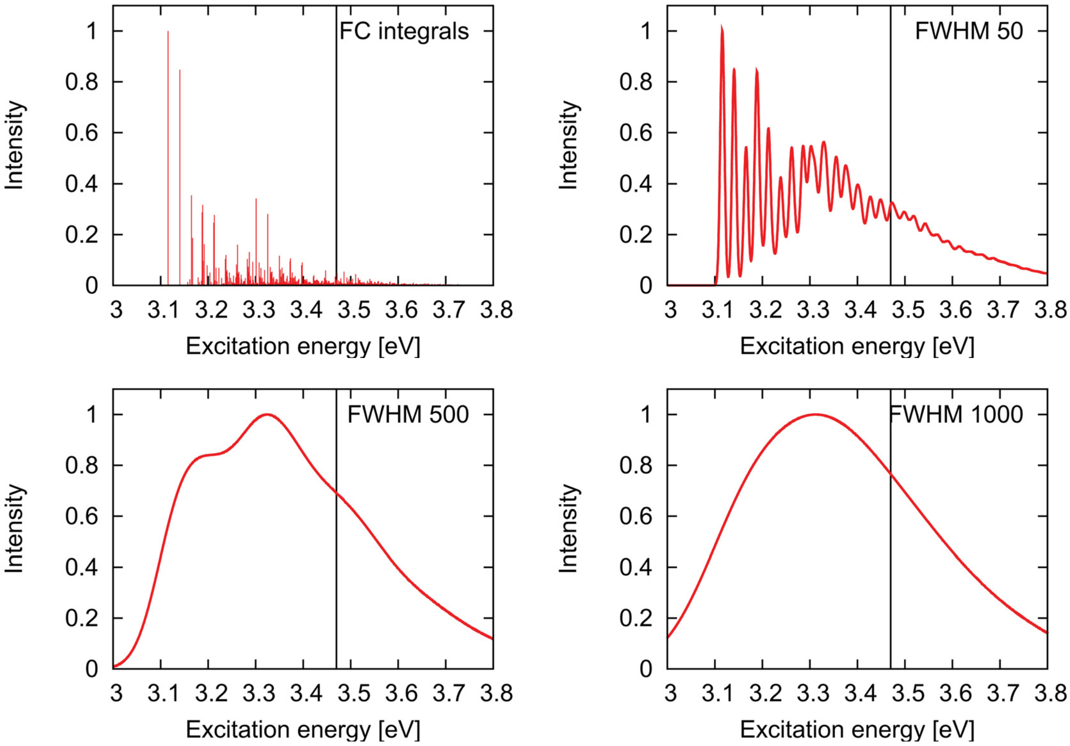

Figure 2.7.: Illustration of how the shape of the vibrational $(gs) \rightarrow {}^1(\pi\pi^*)$ absorption spectra (for AL in vacuum) depend on the full width half maximum (FWHM) of the employed Gaussian functions. The vertical line represents the vertical excitation energy.

numforce script of the TURBOMOLE 5.10 [100] package.) In this work, these intensity distributions were determined in the FC approximation using the VIBES program. [101] (See section 1.1 on a short introduction of the FC principle.) As all investigated molecules meet the requirements of Cs-symmetry, only symmetric A' modes (ranging from 41 to 58 depending on the respective molecule) had to be included into the calculation of the FC spectra, which reduces the computational cost noticeably. The FC distributions of the spectra were obtained by computing transitions between the lowest vibrational level in the initial state and vibrational levels in a chosen energy range ($\approx$ 4000-6000 cm^{-1}, depending on the molecule) in the final state. Therefore, hot bands do not occur in the simulated absorption spectra. To keep the calculations practicable, a limit of 10 quanta per mode was set for the excitation of the final state modes. For the generation of the line spectra, all FC factors were gathered into bins on a grid with interval width $d = 2$ cm^{-1}. Such a resulting line spectrum is shown in Figure 2.7 (top left). [h]

For better comparison with the experimental spectra in the condensed phase, the line spectra were broadened by Gaussian functions with full width at half maximum (FWHM) of 50 cm^{-1}, 500 cm^{-1}, or 1000 cm^{-1} with the program PLOTTER. [102] Fig-

---

[h] The absorption spectra presented in Figure 2.7 are for isolated alloxazine. For flavins qualitative similar results are obtained.

ure 2.7 shows, how this choice influences the shape of the obtained band. The origin transition and the second transition are by far the strongest single lines in the spectrum (FC integrals 0.028 and 0.024 in case of isolated alloxazine). As soon as the line spectrum is convoluted with Gaussian functions, the intensities of the enormous number of states with tiny FC integrals at higher energies accumulate. With growing FWHM of the Gaussian functions this effect is intensified and the relative intensity of the origin transition and the second transition decrease. With a FWHM of 500 cm^{-1} the obtained band appears very similar to that of alloxazine in acetonitrile and with a FWHM of 1000 cm^{-1} all vibronic structure has disappeared. The shape of the latter band is used for my comparison to experimental bands in water, which are observed to be structureless. (See section 1.1.3, Figure 1.6 and Paper IV, Figure 3 for a comparison of the shape of the simulated absorption bands of various flavin compounds with experimentally obtained absorption bands in water.) For none of the investigated compounds (IA, AL, MIA/DMLF, LF, 1DLF, and 5DLF) the estimated band maximum and the vertical excitation energy were found to coincide.

Part III.

Results and discussion

1. Free flavins

Before a problem like the triplet formation in phototropin can be addressed, it is necessary to obtain a deeper understanding of the energy dissipation mechanisms in isolated flavins. In any case, a detailed knowledge of the low-lying singlet and triplet PEHs is indispensable, and is accomplished by optimizing the nuclear arrangements of the electronic ground and excited states. I present and discuss results for free flavins in the following sections. However, the determination of the energy of electronically excited states in medium sized and large organic molecules is to date no trivial undertaking. Although, nowadays, different approaches are available, there is no ultimate choice for a reliable quantum chemical description of electronically excited states. In section 2.1.2 I already explained my motivation in choosing the DFT/MRCI method and pointed out the resulting advantages and disadvantages.

1.1. Absorption spectra

A first step towards the elucidation of the intricate photophysical relaxation mechanisms flavins undergo after electronic excitation, is to understand the electronic structure in the FC region. Comparison to experimentally observable states as well as to earlier quantum chemical work can be used to validate the computed spectra. Herein the focus is not restricted to steady-state singlet-singlet absorption spectra alone, but also excited-state absorption spectra of transient states contribute to the understanding of the low-lying PEHs and to validate the optimized geometries. However, the quantum chemical calculations are done for isolated molecules. While comparison of these results to experimental gas phase measurements is justified, a comparison to ex-

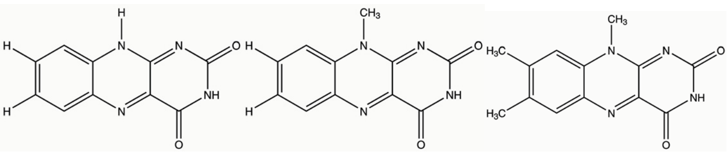

(a) IA *(b)* MIA *(c)* LF

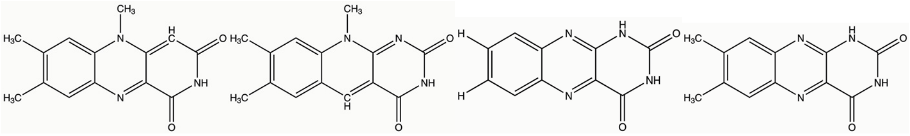

(d) 1DLF *(e)* 5DLF *(f)* AL *(g)* LC

Figure 1.1.: Structure of all molecules investigated here.

State		electr.	ΔE				
		struct.	**MIA**	**LF**	**1DLF**	**5DLF**	**LC**
S_1	2^1A'	$\pi\pi^*$	3.00	2.94	2.62	3.12	3.41
S_2	1^1A"	$n\pi^*$	3.18	3.21	3.23	3.66	3.44
S_3	2^1A"	$n\pi^*$	3.33	3.35	3.58	4.02	3.89
S_5	3^1A'	$\pi\pi^*$	3.93	3.84	3.80	4.08	3.91
T_1	1^3A'	$\pi\pi^*$	2.30	2.24	1.88	2.54	2.76
T_2	1^3A"	$n\pi^*$	2.87	2.90	3.10	3.58	3.02
T_3	2^3A'	$\pi\pi^*$	3.08	3.05	3.11	3.19	3.07

Table 1.1: Selected vertical singlet and triplet excitation energies ΔE [eV] (DFT/MRCI, TZVP) at the ground state geometry.

periments in condensed phase has to be met with some reservation. Unfortunately, to my knowledge, there is no experimental gas phase data available for the molecules discussed in this chapter. As will be seen, environmental effects play a key role in the photophysics of flavins. Subsection 1.1.1 will compare the absorption spectra of flavins *in vacuo* with the results of other quantum chemical treatments and point out the issues that arise when those results are compared with measurements in polar and protic solvents. In subsection 1.1.2 I will show how the solvent effects are incorporated into the calculations and how they alter the absorption properties. Additionally, the problems are discussed that occur if the description of the solvent shell has to be extended beyond the FC region. In the last subsection (1.1.3) it will be shown that the approach of comparing the calculated vertical excitation energy with the experimental band maximum is not always correct.
Although RF, FMN, and FAD[a] are the species with the largest biological relevance, their optically active part is restricted to the isoalloxazine ring. Experimental work has shown that the absorption and emission properties as well as the photophysical behavior of lumiflavin (LF), RF and FMN are very similar. For this reason the sterically flexible ribityl chain is neglected in all calculations and modeled as a methyl group. Figure 1.1 shows the compounds that have been investigated in this work.

1.1.1. Vacuum

The vertical absorption properties of the three flavins isoalloxazine (IA), 10-methylisoalloxazine (MIA) and LF are found to be very similar. Comparison with earlier quantum chemical investigations [b] shows that all methods consistently assign the experimentally observed bands of the absorption spectrum of flavins to ($\pi \rightarrow \pi^*$) transitions. Selected vertical excitation energies of my DFT/MRCI results for MIA and LF can be found in Table 1.1. To aid the discussion, the shape and ordering of decisive molecular frontier orbitals of MIA are depicted in Figure 1.2.

---

[a] In variance with LF and FMN, FAD has a second chromophore unit, which has some implications on the photophysical behavior. However, this goes beyond the scope of the present work.

[b] Earlier theoretical investigations comprise CASPT2, [21] SAC-CI, [22] DFT/MRCI, [24] TDDFT(B3LYP), [12,23–25,103] investigations.

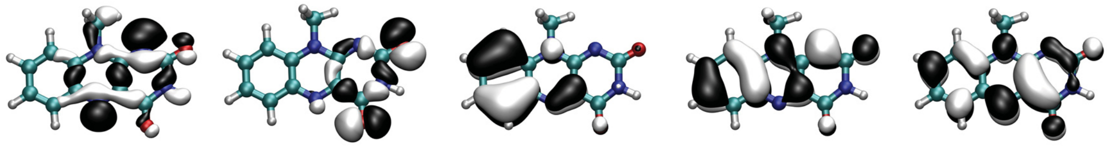
(a) n_{N2} (b) n_{O2} (c) π_{H-1} (d) π_H (e) π_{L^*}

Figure 1.2.: Decisive frontier orbitals (BHLYP/TZVP) at the optimized ground-state (S0) geometry of MIA. (Isovalue=0.3) For IA and LF the shape and energetic ordering is almost identical.

In the singlet manifold, the lowest-lying, optically bright excited state (2^1A' state, S_1) is dominated by the HOMO-LUMO ($\pi_H \rightarrow \pi_L^*$) transition and can be assigned to the lowest energy band in the experimental spectrum. The second optically bright state (3^1A' state, S_5) is dominated by the ($\pi_{H-1} \rightarrow \pi_L^*$) transition. (For details and comparison to earlier quantum chemical investigations see Paper I.) Whereas these low-lying $^1(\pi\pi^*)$ A' states have been discussed quite homogeneously in the literature, the description of the $^1(n\pi^*)$ states differs significantly in the different quantum chemical treatments. Due to possible participation of these optically dark states in the deexcitation of the lowest-lying $^1(\pi\pi^*)$ state, the energetic position of the low-lying $^1(n\pi^*)$ states is of significant interest. In the DFT/MRCI calculations, the two lowest-lying ^{1}A" states are represented by linear combinations of the two excitations ($n_{O2} \rightarrow \pi_L^*$) and ($n_{N2} \rightarrow \pi_L^*$) and are located more than 0.1 eV above the optically active $2^1A'$ state, with the gap increasing from IA to LF. A close proximity or even a state flip of the $1^1A''$ state with the $2^1A''$ state, as predicted in earlier TDDFT(B3LYP) treatments, is not observed for those compounds. As mentioned before, for the smallest flavin CASCSF/CASPT2 calculations have been performed. In order to keep the calculations manageable, Climent *et al.*, [21] included only one n-orbital per state into the active space for the calculation of the ($n\pi^*$) states. By this particular choice of the active space, a mixing of the ($n_N \rightarrow \pi_L^*$) and ($n_O \rightarrow \pi_L^*$) excitations is excluded. Hence, the electronic structure and the vertical excitation energies of these states differ significantly from my DFT/MRCI results. (See Paper I for details.) With respect to ISC processes originating from the lowest vibrational level of the S_1 state, the energetic position of the low-lying excited triplet states is of interest. In IA, MIA and LF, two triplet states are located below the S_1 state in the FC region, corresponding to ($\pi \rightarrow \pi^*$) and ($n \rightarrow \pi^*$) electronic structures. In addition, a third triplet state with ($\pi \rightarrow \pi^*$) structure is found slightly above the S_1 state. As we will see later, when solvent effects are taken into account, this state will gain increased importance.

The vertical excitation energies of the electronically altered flavin derivatives, 1DLF and 5DLF, differ with respect to the parent compound LF, whereas the electronic structure of the low-lying optically bright states is retained. (See Paper III for details.) For 1DLF, the first optically bright state (2^1A' state, S_1) exhibits a strong bathochromic shift. This shift results in an increased energy gap between the optically bright state and the ($n\pi^*$) states. In addition, only one excited triplet state is found below the S_1 state at the FC point, corresponding to ($\pi \rightarrow \pi^*$) electronic structure. As we will see later, this changed order of states results not only in altered absorption properties but also significantly different photophysical relaxation processes. In 5DLF, on the other hand, the low-lying excited states are hypsochromically shifted. While for the first optically bright state (2^1A' state, S_1) the excitation energy is increased by about 0.2 eV, the blue shift is more pronounced for the $(n\pi^*)$ states. As a result, only one excited triplet state is found below the S_1 state in the FC region, corresponding to $(\pi \rightarrow \pi^*)$ electronic structure. In addition, a second $^3(\pi\pi^*)$ state is found almost degenerate to the S_1 state. While in vacuum this state will play no role for the relaxation processes out of the S_1 state, this situation will change in water.

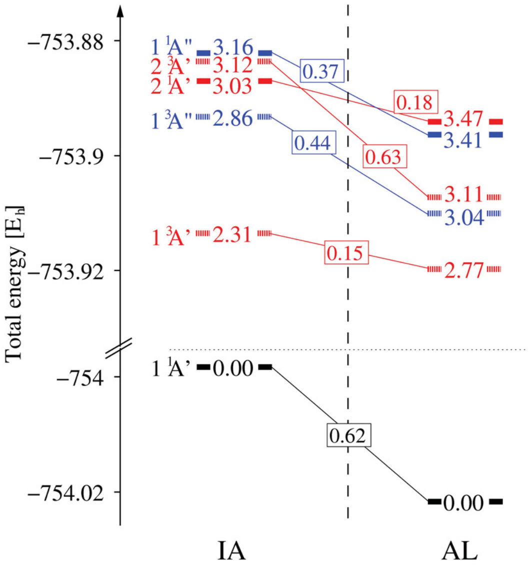

Figure 1.3: Comparison of the total energies [E$_h$] of AL and IA at the ground state geometry. Electronic excitation energies (DFT/MRCI, [eV] are given with respect to the ground state of each molecule. The energetic difference [eV] between corresponding states in the two isomers is given in boxes. Singlet energy profiles are presented by solid lines, triplet profiles by dashed lines. $(\pi\pi^*)$ states are colored red and $(n\pi^*)$ states are colored blue.

As compared to flavins, alloxazines and lumichromes (7,8-dimethyl-alloxazines) exhibit the first and second absorption band in the ultra violet A (UVA) region. A comparison of the total energies of alloxazine (AL) and its isomer IA (see Figure 1.3) shows that in vacuum alloxazine is about 0.6 eV more stable. For the low-lying excited states the stabilization of AL with respect to IA depends on the electronic character. For the $(\pi\pi^*)$ states the stabilization is much less pronounced than for the $(n\pi^*)$ states. With respect to the vertical absorption energies of isolated alloxazines this means that the energy gap between the lowest-lying $^1(\pi\pi^*)$ and $^1(n\pi^*)$ state decreases. In case of lumichrome (LC) those two states are found to be nearly degenerate at an excitation energy of roughly 3.4 eV. As we will see later, this has a significant impact on the photophysical behavior of this class of molecules.

That a comparison of theoretical results, obtained for vacuum, with experimental data in aqueous solution is problematic is reflected nicely for the transient triplet-triplet absorption spectra of RF. As Figure 1.4 illustrates, the calculated and measured absorption spectra do not correlate. At an excitation energy of about 1.8 eV the experimental spectrum of RF in water shows a strong absorption band, typical for neutral, oxidized flavins in the triplet state. At higher excitation energies, two further absorption bands with significantly lower intensity are found, partially overlaid by the bleach peak. It is obvious that the calculated spectra of isolated LF give a wrong qualitative answer,

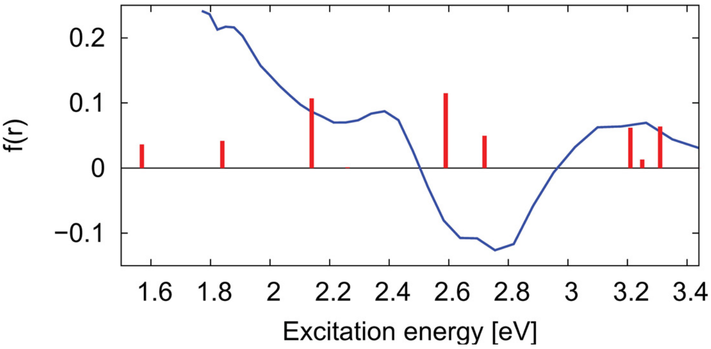

Figure 1.4: Comparison of the experimental (RF, water) and calculated (LF, vacuum) triplet-triplet absorption spectra of the parent flavin. (See Paper IV for details.)

especially in the region of the intense peak at low excitation energies. This failure has been observed before in earlier DFT/MRCI calculations. [24] As we will see in the next section, this behavior is due to the absence of solvent interaction.

1.1.2. Changes in solution

In section 2.2 I introduced two concepts for the modeling of solvent effects, COSMO and microhydration. In the following, these two models are compared with each other and a combination of both as well as results for vacuum (see Figure 1.5). In principle, QM/MM methods are another alternative for the description of solvent-solute interaction and have shown convincing results e.g. for guanine. [104] However, inclusion of the QM/MM approach for the determination of solvent effects in water is beyond the scope of the present work.

In agreement with experimental trends and earlier quantum chemical investigations, the excitation energy of the first visible transition ($^1(\pi_H\pi_L^*)$ state) is hardly affected by solvent effects, while the second visible transition ($^1(\pi_{H-1}\pi_L^*)$ state) is red shifted by up to 0.3 eV. [15, 17, 19, 22, 25] It is seen that COSMO (model II) and microhydration (model III) alone underestimate the solvent shift of that state. A comparison of these two models with vacuum shows that a major part of the solvatochromism originates from hydrogen bonding. This finding is in accordance to the experimental observation that the proticity of the solvents plays a more important role for the solvatochromism

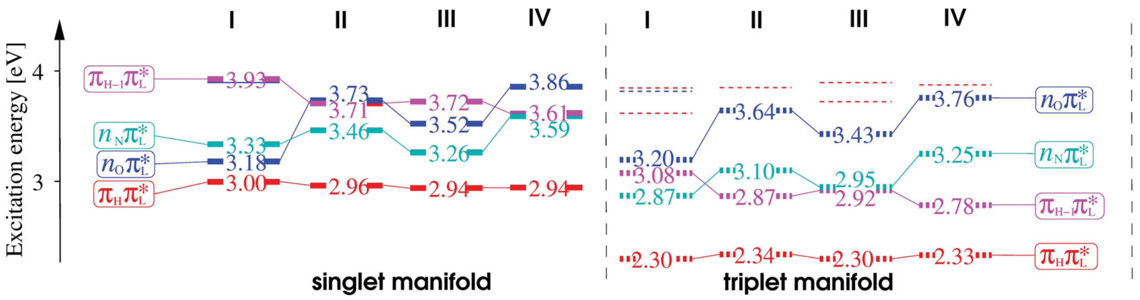

Figure 1.5.: Comparison of vertical excitation energies for vacuum (I), solvation with COSMO (II), microhydration with four explicit water molecules (III), and a combination of the latter (IV) for MIA. For LF comparable results are obtained.

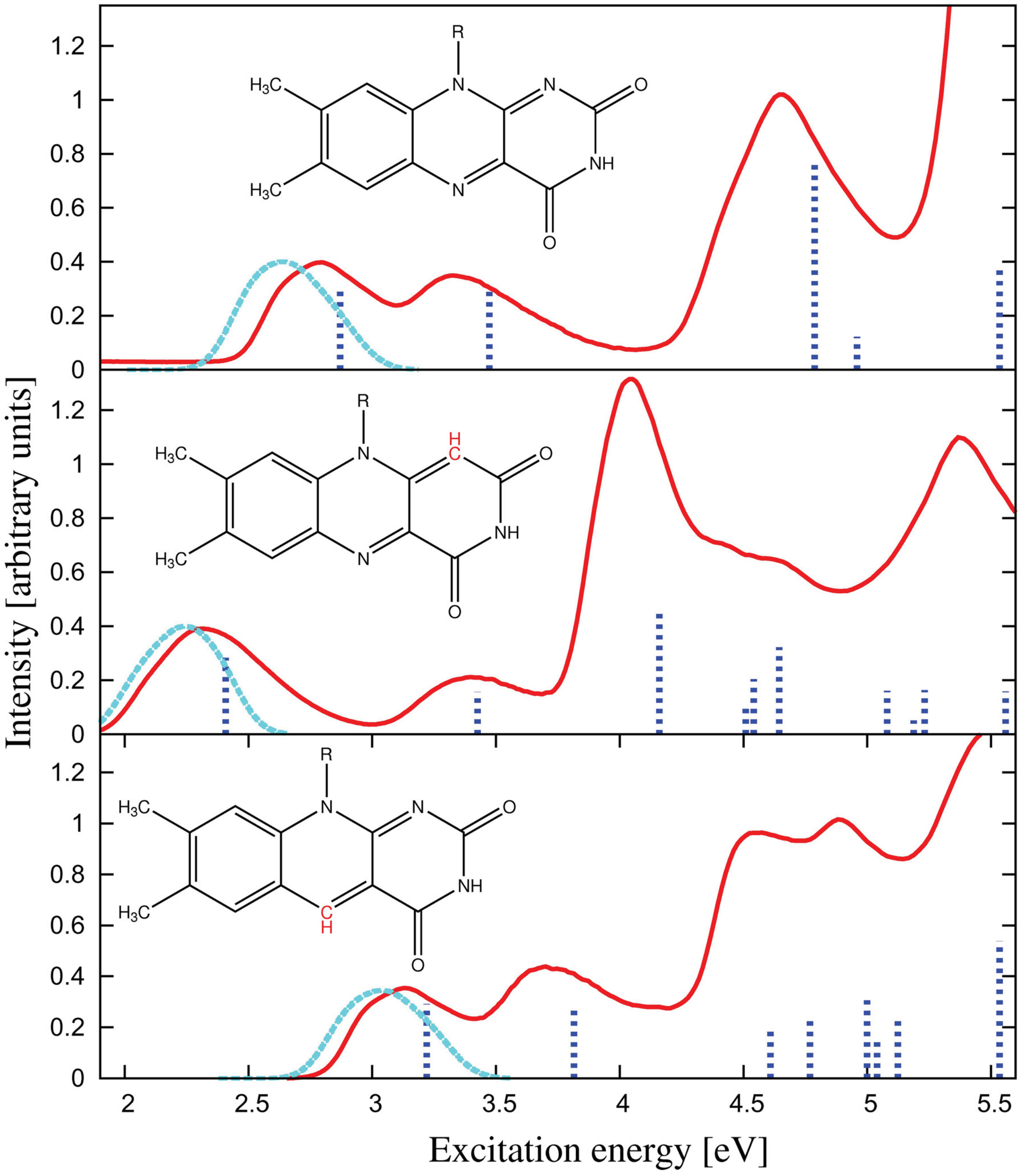

Figure 1.6.: Comparison of calculated vertical excitation energies and oscillator strengths (blue linespectra) of LF, 1DLF and 5DLF in water in comparison to experimental absorption spectra (red profiles) of RF, 1DRF and 5DRF. In addition, simulated $S_0 \rightarrow S_1$ absorption bands (FWHM=1000 cm^{-1}, cyan profiles) are shown. (See Paper IV, Figure 3 for details.)

of this state than the polarity. [12, 19] Within the manifold of $(n\pi^*)$ states, the solvent shifts are more pronounced for the $(n_O\pi_L^*)$ states than for the $(n_N\pi_L^*)$ states. In addition, comparison of model II and III shows that most of the solvent shift of the $(n_N\pi_L^*)$ states originates from electrostatic interaction, whereas for the $(n_O\pi_L^*)$ states hydrogen-bonding effects show significant influence. Qualitatively this is easily understood as the water molecules form strong hydrogen bonds with the oxygen acceptors. (See Figure 2.4 and explanation in Paper I.) However, both states are blue shifted and a participation of these in the radiationless decay of the first excited singlet state is therefore hindered with respect to the vacuum.
The sensitivity of the second absorption band with respect to the surrounding environment is a feature all flavin related compounds have in common. For the first absorption band the various flavin derivatives and isomers, however, show diverse solvent shifts. As compared to experimental absorption spectra in condensed phase, the respective solvent-corrected results for all investigated compounds[c] show excellent agreement. For LF, 1DLF, and 5DLF in water this is explicitly shown in Figure 1.6. (See Paper IV for a detailed discussion.)

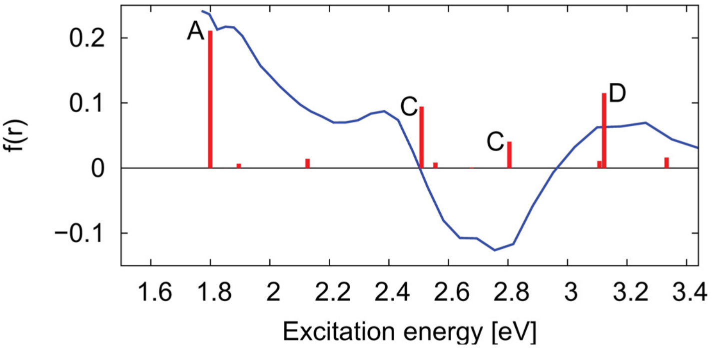

Figure 1.7: Comparison of the experimental (RF in water) and calculated (LF, water) triplet-triplet absorption spectra of the parent flavin. (For more details and an assignment of states see Paper III.)

For the transient triplet-triplet absorption spectra the inclusion of solvent effects have an even larger impact. The agreement of experimental and calculated spectra for LF/RF (see Figure 1.7), MIA/DMRF, and 5DLF/5DRF is excellent when the effects of aqueous solution are taken into account. (See section 2.2 and Paper I and IV for introduction and justification of the solvent model.) On the basis of these calculation the assignment of the transient absorption spectra is possible. For all investigated flavins three different electronic transitions that contribute with significant intensity to the transient spectra could be identified. (For further information see Paper III.)

1.1.3. Vertical excitation energies versus band maxima

For IA, MIA, and LF it is evident that most quantum chemical investigations find the vertical absorption energy approximately 0.2 eV above the experimental band maximum. [12, 21, 23–25, 103] As we have seen in 1.1.2, solvent effects can be excluded as a reason for this deviation. In order to shed light on this finding and to validate the theoretically determined excited state geometries, vibrational intensity distributions of

---

[c] Due to isomerization, no experimental data of IA is available.

the $S_0 \rightarrow S_1$ transition were computed and broadened with Gaussian functions in order to compare with the experimental spectra in solution. (See section 2.3 and Paper III for details.)

It turns out that, as compared to the DFT/MRCI vertical excitation energies of isolated IA, MIA and LF, the absorption band maximum is red shifted by about 0.2 eV. For other flavin related compounds the band maximum is found 0.1 eV - 0.2 eV below the vertical excitation energy. Although it is a common practice to identify the measured absorption maxima with vertical excitation energies, it has been shown before that this approach is not always correct. [96–98] (See section 1.1 for more details.) The solvent-corrected (see section 2.3) absorption bands for flavin and two of its derivatives in water (cyan profiles in Figure 1.6) shows satisfactory agreement with respective experimental results.

1.2. Triplet generation

1.2.1. ISC in flavins: What makes the difference between vacuum and aqueous solution

As Figure 1.8 shows, a crossing between the S_1 and T_2 PEH along a reaction path is found in flavins. In agreement with earlier theoretical work by Climent *et al.* [21] SOME between the $^1(\pi\pi^*)$ and $^3(n\pi^*)$ PEHs are substantial in that region. While these two facts are a good indication for efficient ISC, it is also important that the minimum of the $^3(n\pi^*)$ state is situated energetically below that of the $^1(\pi\pi^*)$ state, which is the case here. Hence, in isolated flavins the ISC rate constant k_{ISC} between these two states is obtained to at be least $\sim 10^9$ s^{-1}.

As aqueous solution yields a significant blue shift of the $(n\pi^*)$ states, this ISC channel is not available in aqueous solution. Inspection of Figure 1.9 shows, however that due to a strong red shift, the $^3(\pi_{H-1} \rightarrow \pi^*_L)$ electronic structure represents the second excited triplet state (T_2) in aqueous solution and a crossing with the $^1(\pi\pi^*)$ state takes place. Between the two $(\pi\pi^*)$ states the SOME are much smaller. If only direct spin-orbit

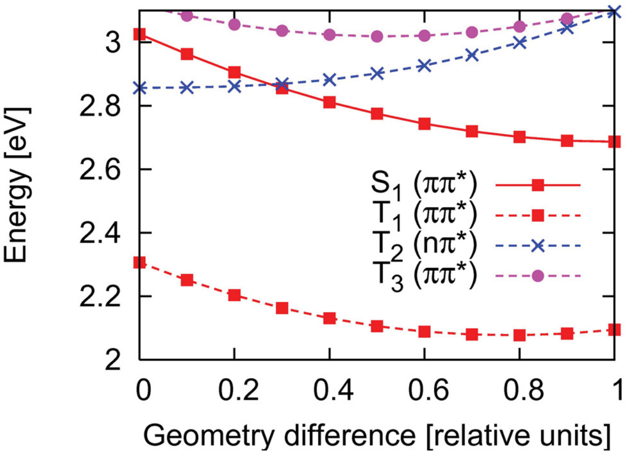

Figure 1.8: DFT/MRCI energies of low-lying excited states of IA in the vacuum along a linearly interpolated path constructed between the Franck-Condon (FC) region (0) and the minimum geometry of the first excited $^1(\pi\pi^*)$ state (1). For MIA and LF almost identical results are found.

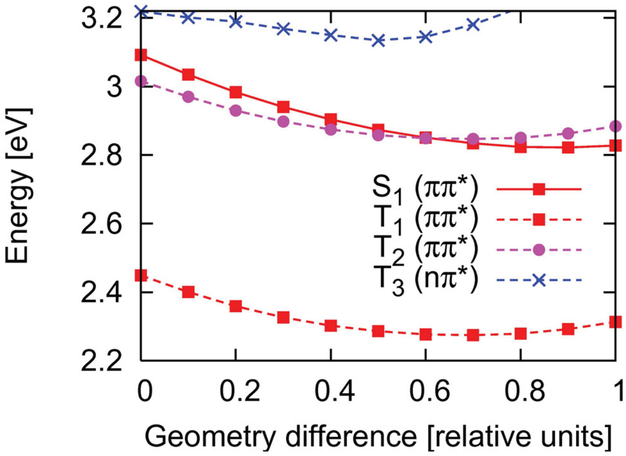

Figure 1.9: DFT/MRCI energies of low-lying excited states of IA in aqueous solution (COSMO) along the linearly interpolated path from Figure 1.8. For MIA and LF almost identical results are found.

coupling is taken into account, a significantly smaller ISC rate constant is obtained, which cannot explain the high triplet quantum yields observed in experiment. [29, 30] However, vibronic spin-orbit coupling increases the latter to $k_{ISC} \sim 10^7 - 10^8$ s^{-1} in good agreement with experimental results. [30]

1.2.2. ISC in flavin related compounds

In the two electronically modified flavins, 1DLF and 5DLF, the energy gap between the $(n\pi^*)$ states and the S_1 states is increased with respect to the parent compound. An additional blue shift of these states is observed in aqueous solution. Therefore, as Figure 1.10 illustrates, the $(n\pi^*)$ states do not yield direct contribution to ISC processes initiating from the $^1(\pi\pi^*)$ (S_1) state. Hence, only $^3(\pi\pi^*)$ states (T_1 in 1DLF and T_1/T_2 in 5DLF) can be populated. However, the extent of mixing between the $(\pi\pi^*)$ and $(n\pi^*)$ states that enhances the ISC rate constants in the vibronic spin-orbit

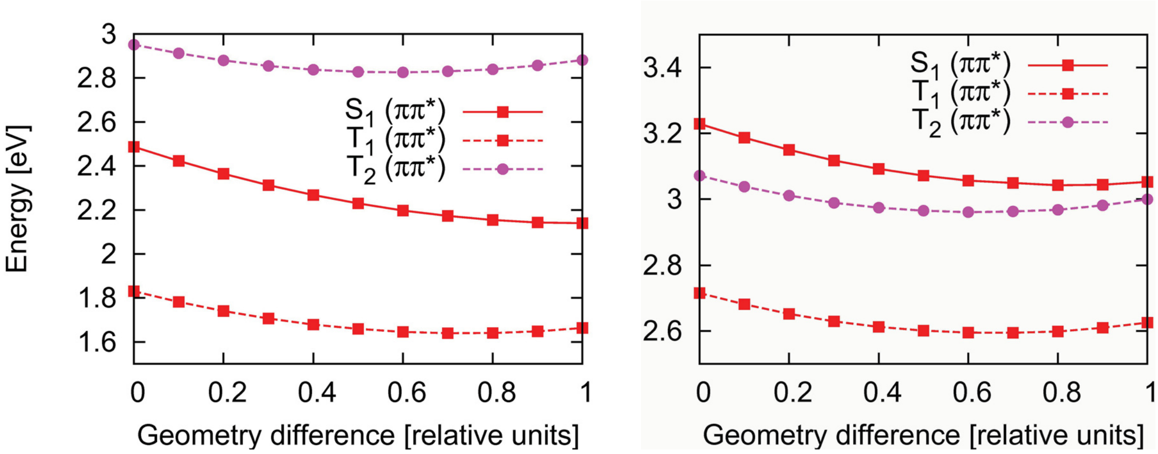

Figure 1.10.: DFT/MRCI energies of low-lying excited states of 1DLF (left) and 5DLF (right) in aqueous solution (COSMO) along the linearly interpolated path between the FC region (0) and the $^1(\pi\pi^*)$ minimum (1).

coupling mechanism depends on the energy gap between those states. In other words, the smaller the gap between ($\pi\pi^*$) and ($n\pi^*$) states, the larger the enhancement of the ISC process. In parent flavins in water the gap is determined to be 0.6-0.7 eV. With 0.8-1.2 eV and 1.2-1.4 eV these energy gaps are found to be larger for 5DLF and 1DLF, respectively. As can be seen in Table 1.2 this situation is reflected in the calculated ISC rate constants.

1.3. Competing relaxation mechanisms for the depopulation of the $^1\pi\pi^*$ state

1.3.1. Relaxation processes in LF, MIA and 5DLF

In Table 1.2 the calculated rate constants for fluorescence and ISC are compared with experimental data. For 1DLF we find the radiative deactivation via fluorescence one order of magnitude faster than ISC. Hence, triplet generation in 1DLF should be negligible and radiative decay via fluorescence should be substantial in vacuum and aqueous solution. However, no steady state fluorescence is detectable for this compound. Experiments using sub-ns pulses revealed a clearly detectable fluorescence for this compound in the short ps time range. [105] (For more details see 1.3.3.)

Water Summarizing, the calculations yield fluorescence rates and ISC rates of comparable magnitude for LF. These findings are in qualitative agreement with the experimental quantum yields as well as the experimental rate constants of RF (see Table 1.2). However, for a quantitative comparison nonradiative depopulation of the S_1 state by internal conversion needs to be taken into account. In a recent work of Weigel *et al.* [19] evidence for the participation of a $^1(n\pi^*)$-like state in the photophysics of RF in water at elevated temperatures on an ultrafast timescale was found by means of femtosecond pump-supercontinuum probe spectroscopy. This finding raises the question

	vacuum			water
	k_F	k_{ISC}		k_{ISC}
MIA	$5{\cdot}10^7$	$\sim 10^{10}$		$\sim 10^7 - 10^8$
LF	$6{\cdot}10^7$	$\sim 10^9$		$\sim 10^8$
1DLF	$2{\cdot}10^7$	$\sim 10^6$		$\sim 10^6$
5DLF	$7{\cdot}10^7$	$\sim 10^6$		$\sim 10^7 - 10^8$
	experiment (water)			
	k_F	k_{ISC}	Φ_F	Φ_T
DMRF	$3.8{\cdot}10^7$		0.27	0.23
RF	$5.6{\cdot}10^7$	$1{\cdot}10^8$	0.27	0.60
5DRF	$10{\cdot}10^7$		0.52	0.62

Table 1.2: Fluorescence rate constants k_F [s^{-1}] and ISC rate constants k_{ISC} [s^{-1}] for singlet-triplet ISC MIA, LF, 1DLF and 5DLF in comparison to experimental fluorescence rates k_F, fluorescence quantum yields Φ_F, and triplet quantum yields Φ_T (see Paper IV for details). The experimental k_{ISC} is taken from Ref. [30]). For 1DRF fluorescence decays on the short ps timescale and no triplet is formed. [105]

about the influence of temperature on the photophysics which, in my work, has not been addressed yet. For the demethylated compounds (MIA and DMRF, respectively) similar fluorescence rates as for the parent compound are found. However, my calculations cannot explain the significantly lower triplet quantum yield Φ_T (0.23) observed for DMRF. For 5DLF the fluorescence decay is found to be somewhat faster than in the parent compound. In addition, again compared to LF, the ISC rate is found to be slightly smaller. Therefore, for 5-deazaflavin, fluorescence should gain importance with respect to the ISC process. This prediction is qualitatively well reflected in the experimental data, when the ratios of fluorescence and triplet quantum yield (Φ_F:Φ_T) of RF (∼1:2) and 5DRF (∼1:1) are compared with each other.

Vacuum As inspection of Table 1.2 reveals, for LF and MIA my calculations find the nonradiative depletion of the $^1(\pi\pi^*)$ state more than one order of magnitude faster than the spin-allowed radiative transition to the electronic ground state. In addition, two minima with $(n\pi^*)$ electronic structure have been located on the lowest excited singlet PEH, corresponding to the 1^1A" (S$_2$) and 2^1A" (S$_3$) states in the vertical spectrum. This finding suggests internal conversion to the ground state enhanced by the energetic proximity of the $^1(n\pi^*)$ state as a competing channel. On this basis it can be predicted that for isolated LF (RF) and MIA (DMRF) fluorescence should not be observable. On the contrary, fluorescence should prevail for 5DLF (5DRF) in the gas phase, due to the lack of an efficient ISC channel and the higher energy gap to the $^1(n\pi^*)$ state.

1.3.2. Internal conversion in alloxazines

So far, fluorescence and singlet-triplet ISC have been presented as leading deexcitation channels for flavins in polar protic solvents. As compared to these molecules, alloxazines show a significantly lower fluorescence quantum yield ($\Phi_F < 0.1$) in various solvents, while the triplet quantum yield is very similar. [12, 14, 15, 106–108] In section 1.1.1 I pointed out that in isolated alloxazines the lowest-lying $^1(n\pi^*)$ and $^1(\pi\pi^*)$ states are almost degenerate at the FC point. As further investigations (see Paper IV for details) have revealed, both electronic structures constitute minima on the S$_1$ PEH, even when solvent shifts are taken into account. Figure 1.11 schematically represents various competing relaxation processes for vacuum (left) and aqueous solution (right). In vacuum the minimum of the $^1(n\pi^*)$ structure is located 0.1 eV below the minimum of the $^1(\pi\pi^*)$ structure. Although only the latter state is connected to the electronic ground state by a considerable dipole transition probability, population of the dark $^1(n\pi^*)$ state from the optically bright $^1(\pi\pi^*)$ state is found to occur along an almost barrierless pathway. Hence, the ($S_2 \rightsquigarrow S_1$) IC rate is anticipated to be ultrafast. Along with the presence of various efficient ($S \rightsquigarrow T$) ISC channels nonradiative depletion is predicted to quench fluorescence from the $^1(\pi\pi^*)$ to the electronic ground state in isolated alloxazines.

In aqueous solution the energetic order of the $^1(n\pi^*)$ and $^1(\pi\pi^*)$ states reverses as a result of the blue shift of the former state and the red shift of the latter state. Hence, the minimum of the $^1(\pi\pi^*)$ electronic structure is found to be 0.3 eV below the minimum of the $^1(n\pi^*)$ structure. At the relaxed $^1(\pi\pi^*)$ state, fluorescence rates and ISC rates of

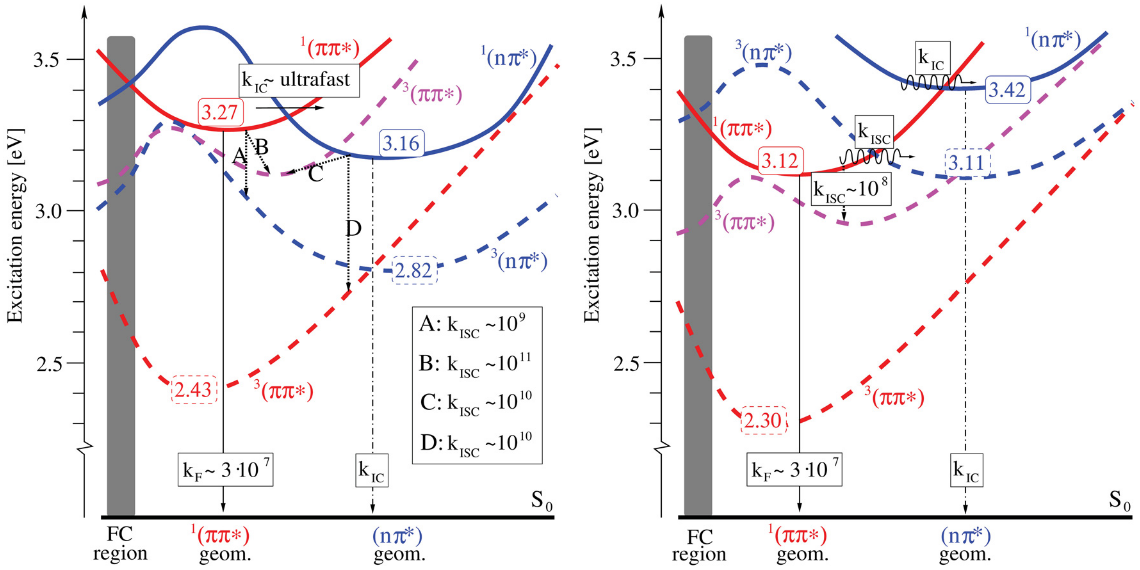

Figure 1.11.: Schematic representation of the relaxation channels in alloxazine in vacuum (left) and aqueous solution (right). In the latter, a constant solvent shift has been assumed. (See Paper IV for details.) Only relevant processes are depicted. All rates are given in [s^{-1}]. Curly arrows represent processes that are activated by temperature. Note that non-radiative transitions are isoenergetic, leading from the initial state to vibrational hot levels of the final state. For the sake of clarity, this fact has been neglected and is represented by dashed and dotted lines. For lumichrome a qualitatively similar picture is expected.

comparable order of magnitude are found by my calculations. As a result, fluorescence should be observable for excitations with a laser wavelength corresponding roughly to the adiabatic transition. However, at elevated temperatures or high excess energy of the pump laser additional ISC channels and IC to the $^1(n\pi^*)$ state are expected to weaken the spin-allowed radiative transition to the electronic ground state, which is in good qualitative agreement with the experimental results.

1.3.3. Nonradiative decay of 1DRF: What causes the difference?

Early spectroscopic investigations on 1DRF report the absence of fluorescence as well as no detectable generation of a transient triplet state. [109] In variance to this, recent sub-ps time-resolved fluorescence spectroscopy studies have found significant fluorescence in water and acetonitrile, while triplet generation was found to be insignificant. [105] However, fluorescence decay has been observed in the ps time domain with a low quantum yield. In addition, the fluorescence kinetics are quite complex, as they are built up of two parts: (1) two connected states (state 1 and state 2) and (2) a single state (state A) (see Figure 1.12). While state 1 and state 2 have been assigned to the initially excited, hot state and the relaxed state, respectively, the nature of state A has been tentatively related to a tautomerization. As the results presented so far cannot explain these experimental findings, additional calculations have been performed in

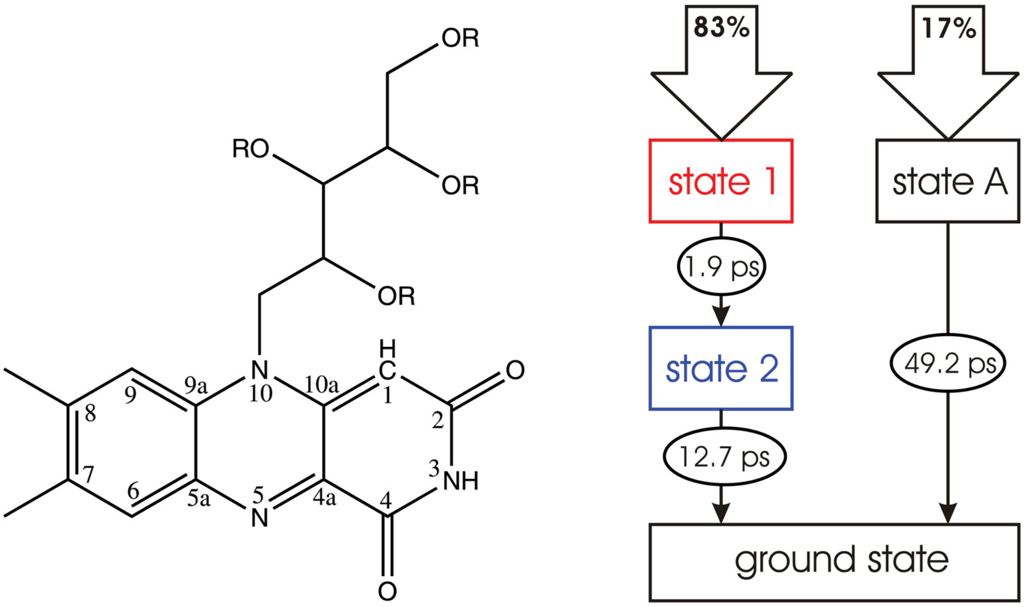

Figure 1.12.: Left: Structural formula and labeling of 1-deazariboflavin (R=H) and its tetraacetyl derivative (R=Ac). The latter was used for the spectroscopic investigation in acetonitrile by Slavov et *al.* [105] Right: Reaction scheme for the decay processes of 1DRF in water as proposed in Ref. [105]. (For the tetraacetyl derivative a similar behavior is found.)

order to elucidate this phenomenon.

In case of the DNA bases, maybe the most prominent heterocycles, UV excitation is followed by a decay on the sub-ps time scale to vibrationally hot levels of the electronic ground state. [1] For these systems, several energetically accessible points on the S_1/S_0 conical intersection seam have been located, which can be summarized in three different deecxitation channels. (1) In the biologically relevant purine bases, 9H-adenine and 9H-guanine, conical intersections between the optically bright $^1(\pi\pi^*)$ state and the electronic ground state have been found along puckering modes, which serve as a funnel for deexcitation. [110,111] (2) Additionally, a second mechanism for rapid decay is found along a N(9)-H stretch coordinate. In variance to the before-mentioned deactivation channel, this ConIn happens between the ground state and the optically dark $^1(n\pi^*)$ state. [112] (3) The third deexcitation channel is observed in the pyrimidine bases, uracil, thymine, and cytosine. In these systems the optically bright $^1(\pi\pi^*)$ state and the electronic ground state are found degenerate for an out-of-plane distortion of the C-C double bond. [113–116]

For 1DLF the energy gap between the optically bright S_1 state and the electronic ground state is decreased as compared to the parent compound. For polar solvents, such as water or acetonitrile, an additional red shift of this state is observed. At the minimum of the $^1(\pi\pi^*)$ state the gap is reduced even more (vertical emission energies: 1.89 eV in vacuum and 1.70 eV in water, microhydration only). Hence, the assumption that an energetically accessible conical intersection between the $^1(\pi\pi^*)$ state and the ground state exists, which drives the fast fluorescence decay, seems plausible.

For this reason constrained minimum energy path (CMEP) optimizations of the S_1 state in vacuum have been performed along various possible reaction coordinates. These comprise elongation of the C(1)-C(10a), C(1)-H(1), C(1)-C(2), C(2)-N(3), N(3)-H(3), N(3)-C(4), and C(4a)-N(5) bonds as well as out-of-plane distortions of the H(1), O(2), O(4), C(4a), and N(5) centers. The latter type of distortion, e.g. leads to nuclear arrangements which resemble those of the $^1(\pi\pi^*)$/ground state conical intersections of pyrimidine nucleobases, as the N(5)-C(4a)-C(10a)-C(10) dihedral angle is gradually increased. [113–116] Unfortunately, all these reaction coordinates do not yield a low-lying conical intersection of the $^1(\pi\pi^*)$ state and the electronic ground state.
In addition to the ultrafast decay mechanism, the nature of state A is unknown. Based on the tentative assignment of this state as a tautomer by the authors of the experimental paper, [105] I investigated the influence of tautomerization on the vertical excitation energies of three tautomers, 2-ol-3-imin-1DLF, 4-ol-3-imin-1DLF, and 5-amin-3-imin-1-deaza-1DLF. As it turns out, the tautomers are 0.7-1.6 eV less stable than 1DLF and the optically bright states $^1(\pi\pi^*)$ states are located 0.5-1 eV above the S_1 state of 1DLF. On the basis of these results, the nature of state A cannot be explained.
In the end, I do not have a conclusive explanation for the origin of the ultra-fast deexcitation channel in 1DRF. However, there are also open questions from the experimental side. The most important being: *Do the complex fluorescence kinetics on the picosecond timescale appear in the parent compound as well?* This leaves the door open for future investigations, both theoretical and spectroscopical.

2. Flavin in the LOV domain of YtvA

2.1. Initial considerations

As we have seen so far, the photophysical behavior of free flavins significantly depends on the environment. This finding, of course, raises the question about the influence of the LOV domain on this behavior. As a result, one has to deal with the issue of how to include the protein environment of YtvA-LOV into the calculation. This section will point out how the flavin cofactor is coordinated in the different LOV domains, present results of earlier theoretical investigations, discuss their relevance for this work and motivate the usage of the QM/MM method.

2.1.1. The binding pocket of LOV

In its dark-adapted state, the FMN cofactor is bound non-covalently to the LOV binding pocket, which is mainly achieved by electrostatic interaction of the sugar/ phosphate chain with polar amino acids (AA). Experimental data shows that the FMN binding pocket of LOV domains is highly conserved in the wild type AA sequence of different organisms. [3, 7, 117] Figure 2.1 (left) depicts the X-ray structure of the FMN binding site of YtvA-LOV, a bacterial blue-light photosensor. YtvA from *Bacillus subtilis* is a flavo-protein strictly related to the plant blue-light receptors in pho-

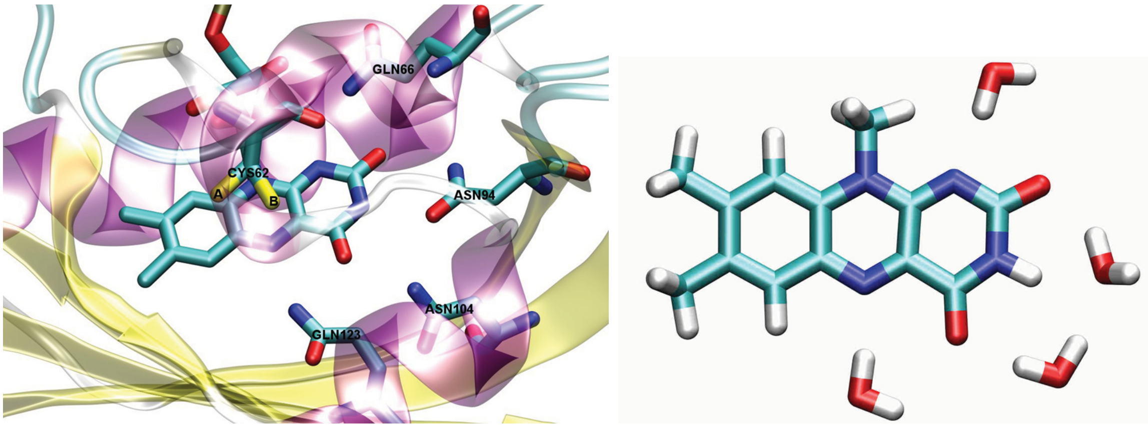

Figure 2.1.: Left: View into the binding pocket of FMN in the LOV domain of the photosensor YtvA of *Bacillus subtilis* (Experimental X-ray structure, PDB code 2PR5, position of the hydrogen atoms is not resolved). [3] Shown are the two conformers of the cysteine residue (confA and confB) and the four polar AAs that coordinate the pteridine moiety. Right: Coordination of the heteroatoms of LF with four explicit water molecules.

totropins, [9] which positively regulates the general stress transcription factor $\sigma\mathbf{B}$ and is activated by blue-light absorption. [118–120] In accordance to the polar and nonpolar moieties of the isoalloxazine core ring, the binding pocket can be divided into polar and nonpolar regions. The benzene part of the cofactor is embedded in a nonpolar region, mainly build up of LEU, ILE and VAL.

The heteroatoms of the pteridine moiety are coordinated by four highly conserved polar AAs, GLN66, ASN94, ASN104, and GLN123, respectively. In the last chapter, I have pointed out that a major part of the solvent shift of flavins in aqueous solutions results from the ability of water to build up a hydrogen bonding network around the heteroatoms of the flavin. As an inspection of Figure 2.1 shows, the four polar AAs in LOV domains and the four water molecules in the solvent model coordinate the cofactor in a similar manner. Therefore, the treatment of the protein has to take this inequality of charges in the binding pocket into account.

Due to its essentiality for the photocycle, the reactive cysteine residue CYS62 is conserved in all WT LOV domains. [3, 7, 117] In the X-ray experiments of YtvA-LOV and the phot1-LOV1 of the algae *Chlamydomonas reinhardtii (Cr)* (PDB codes 2PR5 and 1N9L, respectively), two positions are found for the sulfur atom of the reactive residue CYS62 (see Figure 2.1, left), with a probability of 70% for conformation A (confA) and 30% for conformation B (confB), respectively. [3, 121] With regard to the ISC mechanism, this finding arises the question as to how the sulfur center of CYS62 and in particular the two cysteine conformations affect the photophysics after blue-light absorption.

2.1.2. Earlier theoretical investigations

Until May 2009, to my knowledge, only three quantum chemical investigations of flavin in the LOV domain existed. [25, 50, 51] All these studies employ the crystal structure of the phot1 LOV1 domain of the algae *Chlamydomonas reinhardtii* (1N9L/1N9N) [121] and the main focus lies on the adduct formation mechanism. In the following a brief summary is given for each work:

- Dittrich *et al.* [51] performed QM/MM ((RO)HF/(U)B3LYP/AMBER94) calculations that focus on the elucidation of the adduct formation, which is found to proceed via a neutral radical state generated by hydrogen atom transfer from the reactive CYS residue to the cofactor.

- Domratcheva *et al.* [50] modeled the light-triggered reactions between the cofactor and the CYS residue for a system consisting of LF and thiomethanol by means of CASSCF(2,2/4,4)/MCQDPT2 calculations. Except for the explicit description of the mandatory cysteine residue, the protein environment was not accounted for in this study. This, however, poses the question as to what extent the energy profiles obtained for the adduct formation are meaningful, especially since the adduct is found to be 12.8 kcal/mol more stable than the dark-adapted ground state. As in the first study, adduct formation via a radical pair mechanism is reported.

- In their work Zenichowski *et al.* [25] conducted calculations on the absorption properties of LF in various environments (B3LYP, vacuum, chloroform, and LOV) and the adduct formation mechanism for a LF and thiomethanol model system (B3LYP/MCQDPT2, energies and spin-orbit coupling). For the determination of absorption properties phot1-LOV1 was modeled as LF with seven additional AA side chains, reduced to their functional groups with geometries taken from the X-ray structure. The rest of the LOV domain is accounted for by enclosing the whole system in a polarizable continuum model (PCM) field with ϵ=4.9. In the resulting vertical excitation spectrum a number of low-energy states corresponding to charge-transfer excitations are found below the first optically bright state. For the determination of the adduct formation energy profiles a similar approach was chosen as in the work from Domratcheva et *al.* [50] In addition, these calculations locate the thiomethanol group above the middle ring of the cofactor, as it is found for LOV domains (see Figure 2.1, left for a WT crystal structure). In spite of the deficiencies oft the model system adduct formation is found, as in the two other theoretical investigations, to proceed via an hydrogen transfer biradical pair mechanism.

2.1.3. Interlude: How to account for the protein?

As we have seen in section 2.1.1, hydrogen-bonding interaction is crucial for the appropriate description of the FMN binding pocket of LOV domains. These condition exceeds the capability of continuum solvent models, like COSMO (see section 2.2.1), as these models do not account for hydrogen bonding or external heavy-atom effect. Therefore, it would be highly desirable to include CYS62, GLN66, ASN94, ASN104, and GLN123 explicitly in the calculations. This was done by me in a first attempt (very similar to the approach of Zenichowski *et al.* [25]) in order to investigate the spectroscopic properties of flavin in the LOV domains. The model system comprised LF (or MIA) and the side chains of the above mentioned AAs reduced to their functional groups. However, several problems were encountered during the initial test calculations. Due to the lack of an available DFT/MRCI gradient, geometry optimizations were performed at the (TD)DFT/B3LYP level of theory. As we have seen in chapter 2, section 2.1.1 TDDFT underestimates the excitation energy of charge-transfer states. As a result, there are (several) CT states below the first valence-excited states when this model was applied. While this failure is, at best, inconvenient for the calculation of vertical excitation energies, it renders the optimization of the nuclear arrangements of the valence-excited states nearly impossible. But even for the electronic ground state, geometry optimization with this model has proven problematic. Although parts of LF and the five AAs were frozen to constrain the system to a *LOV-type* geometry, the various molecules started to drift apart during the optimization process yielding an aphysiological structure.

The combined QM/MM approach, as shortly introduced in chapter 2 section 2.2.2, provides an adequate solution for these problems. With this approach, the flavin and the surrounding AAs are constrained to their positions by the AA backbone of the protein itself, preventing unphysiological structures, as they were obtained with the

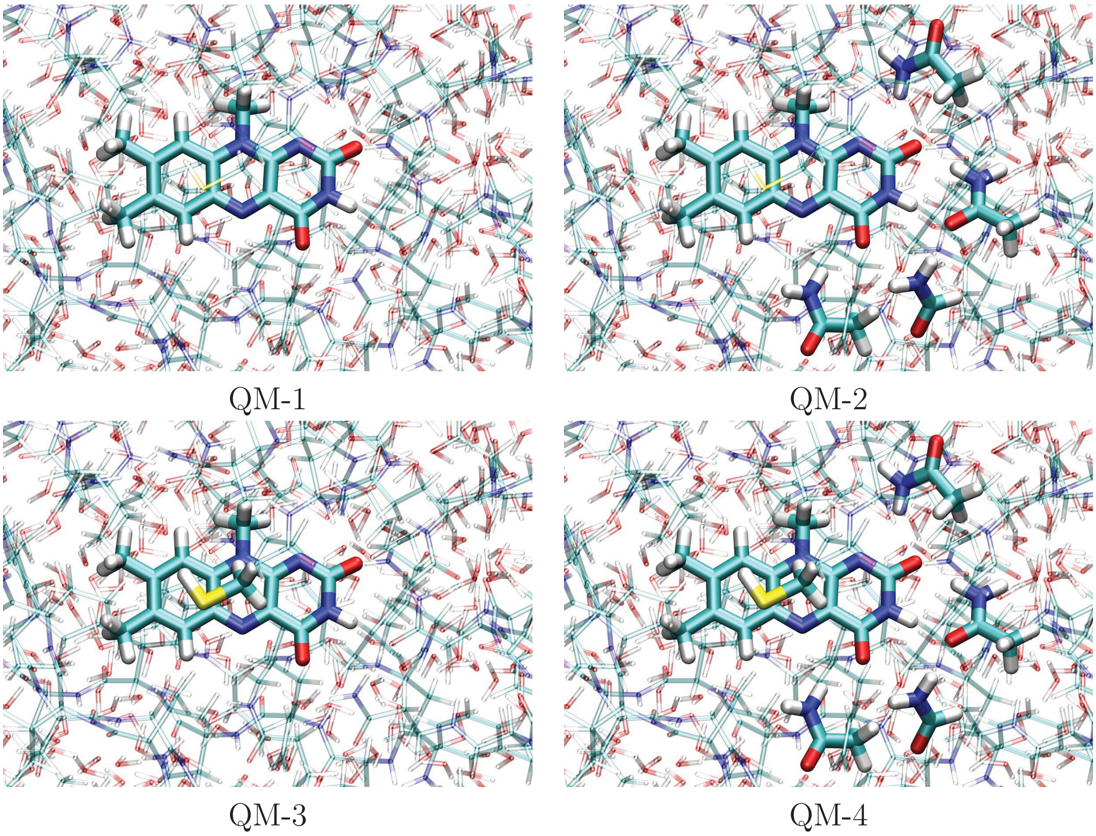

QM-1

QM-2

QM-3

QM-4

Figure 2.2.: Illustration of various QM-regions employed in the ground state QM/MM geometry optimizations and the evaluation of the vertical excitation state energies. The atoms and bonds of the QM region are depicted solid and the MM region is shown transparent. (See paper IX for further details.)

initial test model. In addition, the selective choice of molecules in the QM-region allows for a systematic investigation of the influence of the LOV domain on the spectroscopic properties of its cofactor. Figure 2.2 shows the different QM-regions applied in this work. For the smallest QM-region (QM-1, mere LF), another advantage of the QM/MM approach in comparison to the initial test model is revealed. Although the protein environment influences the quantum mechanical wave function (see section 2.2.2 for details), the QM-region comprises only one molecule. Hence, no intermolecular CT states can interfere with the TDDFT/B3LYP calculation and a optimization of valence-excited state nuclear arrangements is manageable. (See Paper V for more details.)

2.2. How YtvA-LOV influences low-lying excited states of its flavin cofactor

As it turns out, YtvA-LOV resembles an environment significantly more like aqueous solution than vacuum. This can be seen for the ground-state nuclear arrangements (see Table 1 of Paper V) as well as for the solvent shifts of the vertical excitation energies (see Table 2.1 and Table 2 of Paper V). Taking the carbonyl bond as an example, the introduction of solvent, be it water or protein, widens the bonds around 2 pm as the lone-pair orbitals of the O(2) and O(4) centers form strong hydrogen bonds with the surrounding AA residues or water molecules. Correspondingly, the elongation of these bonds is more pronounced, when the 4 polar AAs of YtvA-LOV are described by quantum mechanics. (See Paper V for a closer description.)

Table 2.1 compiles the change of the vertical excitation energies of LF in YtvA-LOV with respect to the four QM regions. (For the adiabatic excitation energies see Table 3 of Paper V.) As the energetic position of the low-lying excited states is decisive for the photophysical relaxation mechanism out of the blue-light excited $^1(\pi\pi^*)$ state, the influence of YtvA-LOV on those state is listed in the following with respect to the electronic structure. For an elaborate discussion as well as detailed comparison of the obtained vertical and adiabatic excitation energies to experimental data see Paper V.

- **$\pi_H\pi^*_L$ electronic structure**
  In compliance with my findings for vacuum and aqueous solution, these states are found to be the first excited state of each multiplicity, respectively, independent of a particular combination of QM region and conformation. Their vertical excitation energies 2.77-2.86 eV (S_1) and 2.15-2.19 eV (T_1) and the adiabatic

Table 2.1.: Vertical singlet and triplet excitation energies ΔE [eV] for all QM regions of confA in comparison to experimental absorption maxima and the results of LF in vacuum and aqueous solution. Optically bright transitions are marked in bold numbers. The shape of the MOs is very similar to Figure 1.1 and can be found in Figure 5 of Paper V.

		$\Delta\mathbf{E}(f(r))$						
		confA				**LF**		**YtvA**
	electronic structure	**QM-1**	**QM-2**	**QM-3**	**QM-4**	**vac.**	**H$_2$O**	**Exp.**[a]
S_1	$\pi_H \rightarrow \pi^*_L$	**2.84**	**2.79**	**2.82**	**2.77**	**2.94**	**2.87**	2.76
S_2	$\pi_{H-1} \rightarrow \pi^*_L$	**3.40**	**3.31**	**3.21**	**3.14**	**3.84**	**3.47**	3.31
S_3	$n_N \rightarrow \pi^*_L$	3.46	3.35	3.45	3.34	3.35	3.64	
CT	$p_S \rightarrow \pi^*_L$	-	-	3.65	3.57	-	-	
S_4	$n_O \rightarrow \pi^*_L$	3.87	3.71	3.89	3.71	3.18	3.86	
T_1	$\pi_H \rightarrow \pi^*_L$	2.19	2.16	2.19	2.15	2.24	2.23	-
T_2	$\pi_{H-1} \rightarrow \pi^*_L$	2.68	2.63	2.59	2.53	3.05	2.73	-
T_3	$n_N \rightarrow \pi^*_L$	3.08	2.99	3.07	2.99	2.90	3.29	-

[a] Absorption maxima of FMN in the LOV domain of YtvA, Ref. [9].

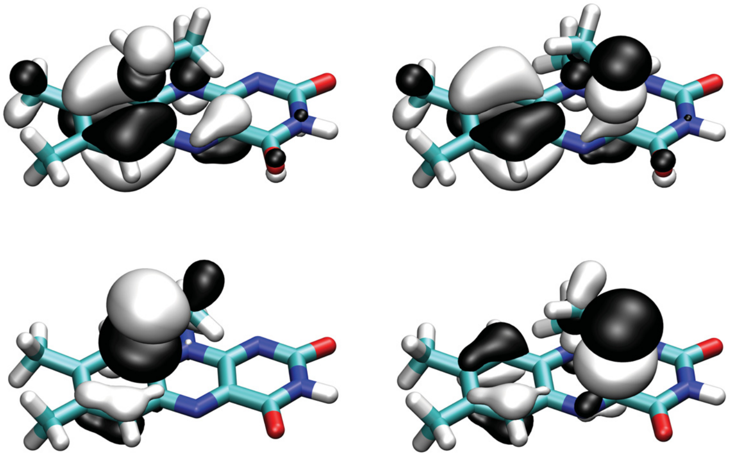

Figure 2.3.: Admixture between the π_S and π_{H-1} MOs for QM-3 of confA (left) and confB (right).

excitation energies (see Paper V for more details) of these two states are comparable to my results of LF in vacuum, which is in line with the observed solvent independence of the first absorption band.

- $\pi_{H-1}\pi_L^*$ **electronic structure**
  Comparison with DFT/MRCI results for the $^1(\pi_{H-1}\pi_L^*)$ and $^3(\pi_{H-1}\pi_L^*)$ states of LF in vacuum and water shows that the environmental influence of the binding pocket of YtvA-LOV closely resembles the situation in aqueous solution, with a pronounced red shift in both media (see 2.1). This finding is in line with experimental studies which locate the maximum of the second absorption band around 3.3 eV in YtvA and water. [9,15,17,20]. The same trend is found for the adiabatic excitation energy of the $^3(\pi_{H-1}\pi_L^*)$ state. As compared to the corresponding vacuum result, the minimum of this state is found clearly below that of the $\pi_H\pi_L^*$ state in protein and water and is anticipated to participate in the photophysical relaxation of the latter state (see section 1.2.1 and Paper I).
  In addition, the $(\pi_{H-1}\pi_L^*)$ states show high sensitivity towards the applied QM region. In confA extension of the QM region such that the cysteine is included (QM-3, QM-4) yields a preferential red shift of the $(\pi_{H-1}\pi_L^*)$ excited states, which is by far more pronounced in confA than in confB. As 2.3 illustrates for QM-3, a lone-pair orbital (π_S) at the sulfur center of CYS62 mixes with the π_{H-1} MO of the cofactor. Since in the latter MO the electron density is mainly located at the benzene moiety of LF, the pronounced red shift of the $(\pi_{H-1}\pi_L^*)$ states in QM-3 and QM-4 of confA can be attributed to the interaction between the π_S and π_{H-1} orbitals. This finding is in line with recent fluorescence line narrowing experiments that identify a weak electronic interaction between the flavin and the thiol group of the conserved cysteine. [122]

- **CT states**
  Contrary to an earlier TDDFT study of phot1-LOV1 by Zenichowski *et al.*, [25] I do not find low-energy CT excitations below or slightly above the optically bright S_1 state at the DFT/MRCI level. However, one CT state which corresponds to the excitation of one electron from a sulfur lone-pair (see 2.3) into the LUMO of LF an be identified. In the singlet and triplet manifold this state is situated well above the S_1 state (by 0.8 eV in confA and 1 eV in confB), and thus it does not contribute to the S_1 photophysics studied here.

- $n_O\pi_L^*$ **electronic structure**
  In YtvA-LOV, these states show a similar solvent shift (by about 0.7 in QM-1 and 0.5 in QM-4 for the $^1(n_O\pi_L^*)$ state, as compared to vacuum) as in aqueous solution. I explained above that the four polar AA side chains of YtvA-LOV and the explicit water molecules of our solvent model coordinate the carbonyl groups of the pteridine moietey of flavin in a similar manner. As a substantial part of the solvent shift of the $(n_O \rightarrow \pi_L^*)$ state arises from this interaction (see section 1.1.2 and Paper I), comparable vertical excitation energies for this state are found in protein and water.

- $n_N\pi_L^*$ **electronic structure**
  Compared with the gas phase, this $(n\pi^*)$ state is blue shifted in water by about 0.3 eV. In YtvA-LOV, however, these states are less affected by the protein environment (almost no shift in QM-4). While a substantial part of the solvent shift of the $(n_O \rightarrow \pi_L^*)$ state arose from hydrogen-bonding interaction, the blue shift of these states has been shown to originate from the polarity of the solvent (see section 1.1.2 and Paper I). Hence, little solvent shift of this state is to be expected in protein which accords with the results of my best model (QM-4). Since I did not compute the minimum nuclear structure of the $^3(n_N\pi^*)$ state in YtvA-LOV, a participation of this state in the relaxation processes of S_1 via a direct spin-orbit coupling ISC mechanism (see section 1.2.1 and Paper I) cannot be ruled out. Even with the $^1(\pi\pi^*)$ minimum and the $^3(n_N\pi^*)$ minimum being degenerate, under physiological conditions, thermal population of excited vibrational levels of the initial state is assumed to preserve this ISC channel in YtvA-LOV.

2.3. ISC in YtvA-LOV

As explained in section 1.2.2, the calculation of the ISC rate constants requires a summation over FC factors. As these are the overlaps of the vibrational wave functions, the normal modes of initial and final state of the ISC process have to be known. However the calculation of the harmonic frequencies produced several (4-5) imaginary frequencies. [a] Some of these are due to the external constraints during QM/MM

---

[a] Harmonic vibrational frequencies of only the QM-1 region were calculated numerically at the QM/MM optimized geometries of the ground and excited states, using the NumForce script from the TURBOMOLE 5.10 [100] program package (with energies and gradients computed at the QM

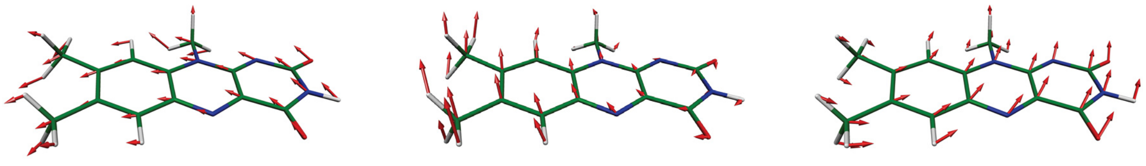

$\nu_3 = i47.47\text{cm}^{-1}$ $\nu_4 = i27.01\text{cm}^{-1}$ $\nu_6 = 33.05\text{cm}^{-1}$

Figure 2.4.: Low-energy vibrational normal modes.

geometry optimization which transform the translational and rotational motions of free LF to very low-frequency librations with respect to the protein cage; in the test calculations, these librations (see Figure 2.4 for three examples) may be found at small imaginary frequencies since the QM/MM interactions are only partly taken into account (electrostatics). (For more details see Paper V and supplementary information.) As the determination of vibrational overlaps between initial and final state depends on the separation of molecular translation and rotation from vibrational degrees of freedom, I refrained from calculating the ISC rate constants in YtvA-LOV explicitly. However, a qualitative discussion of the situation in YtvA-LOV shall be given in the following.

There is experimental evidence that the presence of the cysteine in the LOV domain is responsible for a shortening of the observed lifetime of the initially excited singlet state by a factor of 2-3 as compared to FMN in aqueous solution or cysteine-less mutants. [30, 53, 123] This enhancement of the ISC rate of LF in LOV domains has been attributed to a heavy-atom effect of the sulfur center of the cysteine residue near the isoalloxazine ring [30, 53, 121] and recent fluorescence line narrowing experiments identify a weak electronic interaction between the flavin and the thiol group of the conserved cysteine [122] for *wild type* LOV domains.

I calculated SOME for two different QM regions, QM-1 and QM-4, for the two cysteine conformations, respectively. (See Table 4 of Paper V for more details and SOME between the S_1 state and the T_1, T_2, and T_3 states.) In order to capture a possible heavy-atom effect the sulfur atom of CYS62 has to be included in the QM region. Hence, only model QM-4 can reproduce this effect. However, in a very crude approximation, model QM-1 can be seen as a model system for a cysteine-less mutant. In the following the occurrence and relevance of three different ISC mechanism is discussed. (See also Paper V.)

- **Direct spin-orbit coupling**
  Two excited triplet states, T_1 and T_2, are situated below the blue-light absorbing S_1 state in the vertical absorption spectrum. When these states are relaxed to their nuclear arrangements, the T_1 and T_2 states are found to lie about 0.6 eV and 0.2 eV below the S_1 state, which is a prerequisite for ISC. However, SOME between the S_1 and T_1 states and between the S_1 and T_2 states are calculated to be very small, as these states are all dominated by ($\pi \rightarrow \pi^*$) excitations. The lowest-lying $^3(n\pi^*)$ state, for which SOME with the S_1 state are found to be more substantial, is located slightly above S_1 in the vertical excitation spectrum. Since

---

level with inclusion of MM charges).

I did not compute the minimum nuclear structure of the $^3(n\pi^*)$ state in YtvA-LOV, I cannot rule out a participation of this state in the relaxation processes of S_1 via a direct spin-orbit coupling ISC mechanism (see above).

- **Vibronic spin-orbit coupling**
  For mere LF (QM-1) indications of a substantial increase of the SOME with regard to out-of-plane motion of the isoalloxazine ring can be seen. Due to the protein environment the chromophoric ring system does not retain planarity. In this context it should be noted that the slight out-of-plane distortion is more pronounced for confB than for confA, which increases the admixture of $(n\pi^*)$ character into the electronic structure of initial and final states. As a result, the SOME for QM-1 between the S_1 and the T_2 state are found noticeably increased for confB, as compared to the results for confA or *planar* LF in water (see Table 4 of Paper V for these SOME). Considering the rather small energy gap between the T_2 state and the $^3(n\pi^*)$ state this hints to a substantial enhancement of the ISC rate constants due to vibronic spin-orbit coupling.

- **External heavy-atom effect**
  When the sulfur atom of CYS62 is included in the QM region, SOME between the S_1 and T_1 states and between the S_1 and T_2 states are increased. Above, we pointed out that an explicit description of CYS62 in QM regions QM-3 and QM-4 shows the largest influences on states with $(\pi_{H-1} \rightarrow \pi_L^*)$ electronic structure. This effect is caused by the admixture of a lone-pair of sulfur to the π_{H-1} MO (see 2.3). As the T_2 state is dominated by the $(\pi_{H-1} \rightarrow \pi_L^*)$ excitation, SOME between the S_1 and the T_2 state show increased sensitivity towards the CYS62 conformation.

Even without the presence of the sulfur center of cysteine, be it in the QM region or the protein itself, two ISC mechanisms can be identified that are expected to yield an efficient population of the triplet manifold. In addition, when CYS62 is represented by quantum mechanics, evidence for an external heavy-atom effect is found which is in line with experimental findings mentioned above. Even without explicitly calculating ISC rate constants, it can be proposed that $(\pi\pi^*) \rightsquigarrow (\pi\pi^*)$ processes play an important role for the ISC mechanism in YtvA-LOV, as vibronic spin-orbit coupling and external heavy-atom effect are observed. In addition, variations in the isoalloxazine sulfur distance, as induced by thermal vibrations, could increase the latter effect. A proper description of the thermal fluctuations would necessitate dynamics simulations, which are clearly beyond the scope of the present work.

3. (De)Protonated flavins

3.1. Motivation

In the first two chapters the focus was on the energy dissipation mechanisms in neutral flavin compounds. In this section initial studies on the ground state and low-lying excited states of charged lumiflavin species are in the main focus. With respect to the BLUF and LOV domains, the implications of protonation at the N(5) position are of particular interest since that atom is involved in the reactions after blue-light absorption. Therefore, the next section shows the implications of (de)protonation on the absorption spectra for two protonated (N(1) and N(5) positions) and a deprotonated (N(3) position) lumiflavin. Moreover, in a second section, protonation energies for the ground state and the first excited singlet and triplet states are presented. Finally, future prospects for those protonated flavin species are discussed.

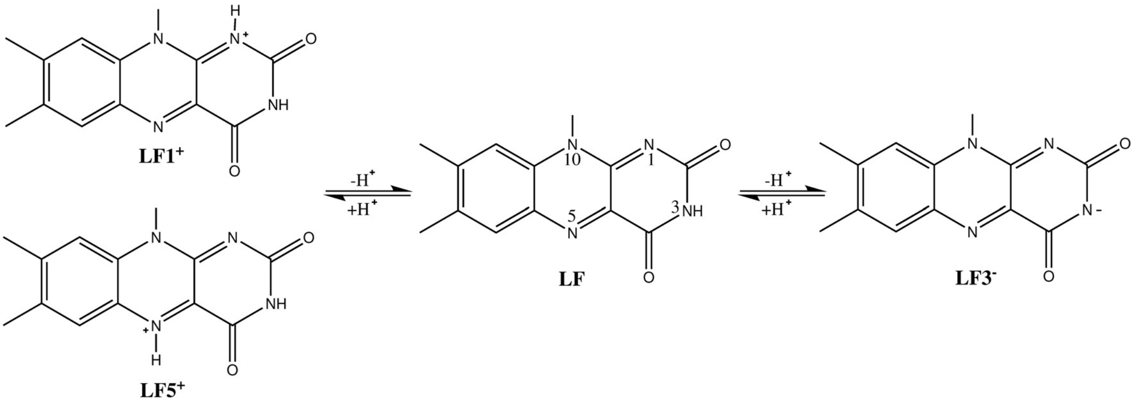

Figure 3.1.: (De)Protonated and neutral species of LF

3.2. Vertical excitation energies

The low-lying and optically bright excited states of neutral and ionic lumiflavin are compared to experimental band maxima in Table 3.1. As in chapter 1, the calculations had to be compared with experimental data in aqueous solution. Since this was meant to serve as an initial investigation, aqueous solution was simulated with a conductor-like screening model (COSMO). As described in section 2.2.1, COSMO alone does not capture the full solvent-interaction. For neutral flavins (see section 1.1.2) it has been shown that this model underestimates the solvent shifts. In a qualitative picture, however, the shift of the states follows the right trend. It is obvious that protonation has significant influence on the vertical absorption properties (see Paper II, Tables 2-4 for details). Therefore, the vertical excitation energies of flavins in water obtained with mere COSMO should be representative as I am interrested in a qualitative description of the system, exclusively.

Table 3.1.: Selected vertical DFT/MRCI excitation energies *[eV]* in comparison to experimental excitation energies *[eV]* in the energy range below 5 eV for protonated and deprotonated lumiflavin species and the neutral compound. The absorption maxima in water are taken from Ref. [124]. In the calculations the aqueous solution has been modeled with COSMO.

	DFT/MRCI				Experiment		
band	**LF**	**LF1**$^+$	**LF5**$^+$	**LF3**$^-$	**LF**^{a}	**LF1**$^{+b}$	**LF3**$^{-c}$
1	2.90	3.12	2.29	2.91	2.78	3.18	2.79
2	3.58	3.36	2.95	3.67/3.87	3.35		3.54
3	4.80/4.97	4.84	4.59/4.90	4.77/4.96	4.59	4.70	4.59

^{a}Phosphate-buffer, pH=7.0 ^{b}6N HCl, pH=0 ^{c}2N NaOH, pH=13

Experimental investigations have shown that the available absorption spectra arise from LF1$^+$. [124] This is supported by the vertical DFT/MRCI results. It appears plausible that the experimentally observed band around 3.18 eV can be assigned to both, the S_1 and the S_3 states of LF1$^+$, whereas the S_7 state can be attributed to the higher lying band of that species. (See Paper II, Table 2 and paper text for more details.) In LF5$^+$ two lowest-lying optically bright transitions are found with a considerable gap between the two states, situated below the experimental band maxima. As pointed out in section 1.2.2, the signaling state of BLUF proteins (AppA), BLUF$_{Red}$, exhibits a slight red shift of the first (0.09 eV) and second (0.05 eV) absorption band. [7] Even with the small errors arising from the incomplete treatment of the solution, the two species LF1$^+$ and LF5$^+$, can be excluded from being BLUF$_{Red}$. This finding supports the interpretation that the observed red shifts in BLUF$_{Red}$ are not due to a protonated flavin but rather to a reorganization in the protein. [7,42,125,126] In variance with the protonated flavin species, the vertical excitation energies of the deprotonated lumiflavin depend heavily on the environment. For the calculations in vacuum (not shown, see Paper II, Table 4), no agreement with experiment can be found. As soon as solvent effects are taken into account a substantial change in the ordering as well as in the electronic structure of the excited states is found, which comes along with a reordering of the occupied π orbitals. With respect to the constrained treatment of the solvent the agreement can be considered satisfactory.

3.3. Protonation energies

As mentioned above, experimental investigations [124] have determined that in the ground state protonation takes place at N(1) position. As Figure 3.2 shows our DFT/MRCI calculations reproduce this. In LF1$^+$ the ground state is 43.6 kJ/mol lower in energy than in LF5$^+$. The electronic structures of the S_1 and the T_1 state of lumiflavin are very similar. Both are dominated by the $(\pi_H \rightarrow \pi_L^*)$ transition. Therefore, in both transient states protonation at N(5) position is favored over that at N(1) position by 60-76 kJ/mol. [a]

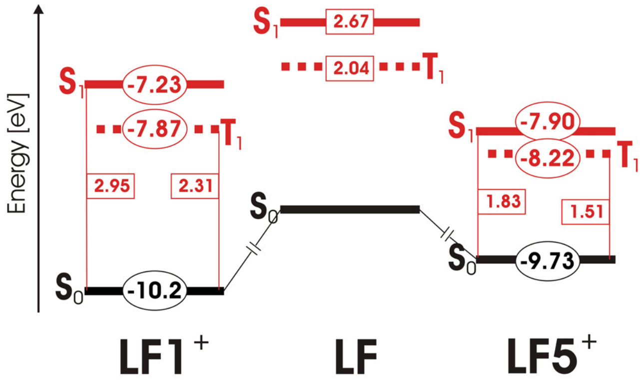

Figure 3.2: Comparison of the excitation energies [eV] (rectangular boxes and respective protonation energies [eV] (ovals) for the two protonated species in vacuum.

In LOV domains one of the possible adduct formation mechanisms comprises an initial proton transfer from cysteine to the N(5) atom of LOV-660. As to the present, the protonation state of the transient triplet and its immediate influence on the adduct formation are under discussion. Whereas experimental findings seem to rule out mechanisms that occur with a proton or hydrogen transfer as initial step of the adduct formation pathway, theoretical investigations favor the latter. [25, 45, 47–51] Although, in vacuum, protonation of the N(5) atom appears to be an energetically favorable reaction, the present results do not allow the preference or exlusion of any one of the postulated adduct formation mechanisms.

3.4. Future prospects

The results of this initial study can be seen as a starting point for several further investigations. On the basis of time-resolved transient spectroscopy, the fine structure of the LOV-660[b] spectrum was interpreted to originate mainly from a protonated triplet excited state by nanosecond proton transfer from the cysteine. [30] Since the protonation state of LOV-660 is the subject of recent discussion, [49] a quantum chemical treatment would be of interest. As laid out in chapter 1, the transient triplet-triplet absorption spectra are very sensitive to the environment. In order to give a qualitatively correct answer as to whether the fine structure of the LOV-660 is due to a protonation of the flavin or due to influences of the protein, the treatment of the environment has to be pursued beyond COSMO. In addition to electronic excitation spectra, vibrational spectra, zero-field splitting parameter, and, possibly, g-tensors of the transient triplet state are of interest. Although work on a mixed experimental and theoretical investigation

---

[a] Earlier (U)DFT(B3LYP/6-31G**) [47] calculations show the same trends, predicting similar energy differences for the ground states (34.5 kJ/mol) and the first excited triplet states (79.6 kJ/mol) of LF1$^+$ and LF5$^+$.

[b] In addition to LOV-660, the transient triplet state is also referred to as LOV-715 in the Literature.

on the vibrational properties of flavins in different environments is in progress, this is clearly beyond the scope of this work.

4. Deactivation in aromatic fivemembered heterocycles

4.1. Foreword

Although small heterocyclic molecules such as furan, thiophene, pyrrole, and imidazole (see Figure 4.1) cannot be regarded as flavin related compounds, they, nevertheless, show a wide spectrum of applications in nature as well as industry. Thiophene for example, is the monomer unit of α-oligothiophene polymers which possess a high photostability and high photoconductivity and promise to bridge the properties of plastics and semiconductors. [127, 128] Imidazole, on the other hand, is a chromophore in important biological compounds such as histidine and histamine. Furthermore, it is a constituent of purine, a chromophore of species like adenine, guanine, caffeine, and theobromine.

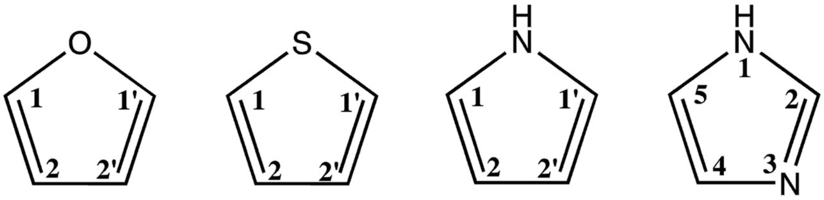

Figure 4.1.: Structures of furan, thiophene, pyrrole, and imidazole (left to right)

The work in this chapter started with my diploma thesis on the relaxation pathways of electronically excited thiophene. Although the main part of my PhD studies were occupied with the investigation of flavins and related compounds, I continued working on those small heterocycles and extended the investigation to furan and imidazole.

4.2. Ultrafast relaxation in photo-excited thiophene

4.2.1. Experimental findings and related theoretical investigations

In his PhD thesis, L. Lehr presented time-resolved pump-probe femtosecond multiphoton ionization spectra of thiophene. [129] In these experiments, the zeroth vibrational level of the optically bright S_1 state was populated by one-photon absorption and the time-evolution of the excited state was probed by ionizing the molecule with a second laser and measuring the energy of the resulting photoelectrons. A decay time for this state was found to be 80 fs ± 10 fs, in agreement with the previous observation of broad $A - X$ absorption bands and the lack of fluorescence. [130–132] Since two triplet states are known to be situated energetically below the S_1 state [133–135] and in α-oligothiophenes, inter-system crossing (ISC) rates increase with decreasing chain length n, [136–139] the femtosecond decay of the S_1 population in thiophene was tentatively attributed to a fast ISC by then. [129]

However, it has not been possible to unravel the identity of the fast deactivation mechanism by experimental means alone. A first quantum chemical investigation including spin-orbit interaction between the S_1 state and closeby triplet states, which has been carried out by Kleinschmidt *et al.*, [140] was rather disappointing in this respect.

Spin-orbit coupling between the S_1 and T_2 states is symmetry forbidden at the (C_{2v} symmetric) S_0 equilibrium geometry and it remains small (< 1 cm^{-1}) even for sizeable out-of-plane distortions of the sulfur atom. Spin-orbit interaction between the S_1 and T_1 states is symmetry allowed but is too small to explain an ISC on the femtosecond time scale. Large spin-orbit coupling matrix elements (SOMEs) were observed for states involving a $\pi \rightarrow \sigma^*$ excitation but these states are situated significantly above the S_1 state in the vertical absorption region. [140] These findings demanded a quantum chemical investigation that goes beyond the FC region and explores the characteristics of electronically excited PEHs.

4.2.2. Electronic structure of excited states in thiophene

The assignment of the spectral features of low-lying absorption bands in thiophene and the other heterocycles has been a topic of lively discussion in the last decades. This situation is due to the fact that these compounds possess several close-lying excited states, both optically dark and bright, in the UVA regime. As compared to experimental findings, the present work illustrates that the DFT/MRCI method describes these

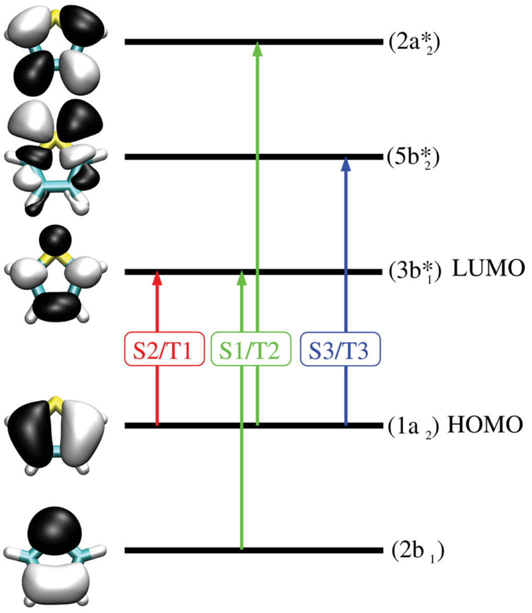

Figure 4.2: Schematic overview over, and labeling of the electronic structure of low-lying excited states. In the FC region, the first excited singlet state does not correspond to the HOMO-LUMO transition (red), which in fact is found to be the second excited singlet state, but comprises a linear combination of two A_1 symmetric excitations (green). (For a detailed description of the vertical excitation properties see Table 2 in Paper VI.)

states in a reliable manner. (For more details and references see Paper VI - VIII.)
To aid the discussion of the ultrafast relaxation mechanism, a brief description of the electronic structures of low-lying excited states of thiophene is given in Figure 4.2. Multiple minima are found on the S$_1$ PEH with S1 ($2b_1 \rightarrow 3b_1^* + 1a_2 \rightarrow 2a_2^*$), S2 ($1a_2 \rightarrow 3b_1^*$), and S3 ($1a_2 \rightarrow 5b_2^*$) electronic structure, corresponding to the first three states in the vertical absorption spectrum. As seen in Figure 4.3, the S1 and S2 minimum are characterized by out-of-plane distortions of the ring, while the nuclear arrangement of the S3 electronic structure, which yields the global minimum on the S$_1$ PEH, is planar, but asymmetrically distorted with one elongated CS bond. In fact, this bond can be considered broken. While in the FC region a Rydberg state mixes into the electronic structure, at the ring-opened nuclear arrangements $\pi\sigma_{CS}^*$ character prevails. In the triplet manifold, the T1 ($2b_1 \rightarrow 3b_1^* + 1a_2 \rightarrow 2a_2^*$) and T3 ($1a_2 \rightarrow 5b_2^*$) electronic structures are found to possess minima on the T$_1$ PEH, with the T1 minimum being the lowest point on that PEH. The minimum of the T3 electronic structure resembles the S3 geometry. At these ring-opened geometries the S$_1$, T$_1$ and S$_0$ PEHs come very close. In order to rule out artifacts of the (TD/U)DFT / DFT/MRCI methods, the validity of the S3 electronic structure was probed with a few high-level CASPT2 calculations, which reproduced the small energy gap between the S$_1$ and S$_0$ PEHs as well as the CS bond dissociation.

4.2.3. Relaxation pathways

The fact that thiophene shows no fluorescence and the ultrafast depletion of the S$_1$ state population indicate the presence of effective nonradiative relaxation processes. Multiple minima on the S$_1$ PEHs suggest the existence of several intersections between the electronically (excited) singlet surfaces in addition to ISC processes with triplet states. Two deactivation mechanisms have been detected in the present study and are schematically shown in Figure 4.3. (An elaborate discussion of relaxation pathways are found in Paper VI.)

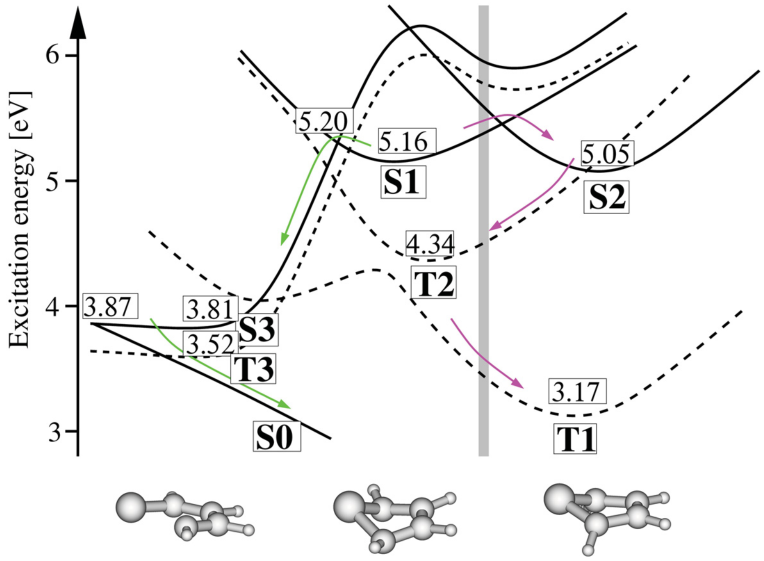

Figure 4.3: Schematic overview over the two nonradiative relaxation pathways of electronically excited thiophene. Magenta arrows indicate the relaxation according to path **1** and green arrows indicate the decay via path **2**. The gray bar symbolizes the vertical absorption region. For the electronic structure of S1, T1, etc. see Figure 4.2.

1. *Coupling between S_1 and S_2 PEHs*
   The nuclear arrangements of the S1 and S2 electronic structures have comparable minimum energies. Therefore, strong vibronic coupling between the vibrational levels of the S1 and S2 potential wells of the S_1 surface is expected. Close to the S2 minimum an intersection between the S_1 and T_2 PEHs is found, where an efficient ISC and subsequent IC within the triplet manifold can take place. At low temperatures, the population of the T_1 PEH should decay via detectable phosphorescence.

2. *Ring opening*
   This mechanism involves the intermediate opening of the thiophene ring for one CS bond. The reaction proceeds from the S1 minimum almost barrierless to the global $^1(\pi\sigma^*_{CS})$ (S3) minimum of the S_1 PEH. In close proximity to the saddle point, the reaction path is intersected by the T_2 and T_3 PEHs. SOC is strong here and could lead to an efficient ISC. From the S3 (T3) minimum a conical intersection between the S_1 (T_1) and S_0 PEHs is accessible without significant barrier. (The spin-allowed transitions are assumed to prevail, however.) Nonradiative decay of the excited state population to the electronic ground state and subsequent vibrational relaxation restores the cyclic structure of thiophene.

From the present theoretical data it is very difficult to discriminate between the two pathways. From the lack of strong phosphorescence in experimental emission spectra of thiophene it appears unlikely that the ISC between S_1 and T_2 in path **1** can compete with the ring opening mechanism. Extended multistate dynamical studies would be highly desirable in order to determine rate constants and branching ratios of these processes. Earlier multidimensional quantum dynamics performed by Köppel *et al.* [141], find an ultrafast bidirectional internal conversion, i.e., the population fluctuates back and forth between the 2^1A_1 (S1) and 1^1B_2 (S2) states at the femtosecond time scale ($\approx 10fs$). Such an ultrafast oscillation could not be resolved at the time resolution of the experiment, even though it would lead to an average population in the S1 and S2 potential wells. Ionization of the S2 electronic structure, however, would yield a different ionic state than observed in the pump-probe experiment. Therefore, the experimental and theoretical findings were interpreted as following. The pump experiment excites to the S1 state and fast wave packet dynamics in that state (80 ± 10 fs) relax thiophene from the S0 geometry to the S1 minimum. From there, an ultrafast (25 ± 10 fs) decay via the ring opening channel is predicted. Opening of the thiophene ring hereby reduces the ionization intensity, due to an increased ionization energy. Earlier photo-dissociation experiments in the gas phase have postulated the linear thiophene structure as reactive intermediate. [142] (For detailed discussion see Paper VII.)

4.3. Relevance to other five membered heterocycles

4.3.1. Furan

With the results for the ultrafast deactivation of electronically excited thiophene via ring opening outlined above, the question arises whether a similar mechanism plays a key role in photo-excited furan, as well. The results of the purely theoretical investigation are available in Paper VIII. Summarising, the deactivation mechanism of photo-excited furan is found to be qualitatively similar to the ring opening mechanism in the heavier homologue thiophene and only subtle differences between these two molecules, with regard to the ordering of electronic states in the FC region and their minimum nuclear arrangements, exist. Earlier multidimensional quantum dynamical studies of photo-excited furan, performed by Köppel and coworkers, [141, 143, 144] did not take the dissociative S3 state into account, which in the light of the present results appears to be mandatory.

4.3.2. Pyrrole and imidazole

In 2000, Domcke et al. [145] detected a relaxation pathway of photo-excited pyrrole that involves a repulsive, N-H bond breaking $^1(\pi \rightarrow \sigma^*_{NH})$ state. The authors point out that this state undergoes conical intersections with the primarily excited $^1(\pi \rightarrow \pi^*)$ state and the electronic ground state and thus leads to an ultrafast decay of the excited state population. An inspection of Figure 4.1 shows that such a deactivation pathway is not available in photoexcited furan or thiophene, whereas it can play a role for electronically excited imidazole.

MRCI calculations performed by Barbatti *et al.* [146] show a second deactivation channel for photo-excited pyrrole. The presented mechanism is based on out-of-plane deformation of the ring. At the respective conical intersection, significant elongation of one NC bond is observed. This finding gave rise to a collaborative investigation of radiative deactivation in imidazole. At the level of CASSCF, four geometries located on the S_1/S_0 conical intersection seam were obtained (See Figure 4.4). As CASSCF excitation energies are typically too high, due to an underestimation of electron correlation, I contributed to this work by calculating the energy profiles of the reaction paths between the ground state geometry and the CoIns at the level of DFT/MRCI. The lowest energy conical intersection is due to the NC dissociation. As for furan and thiophene, the reaction path is almost without barrier. The second-lowest CoIn is the NH dissociation, while the two puckered conical intersections are found at higher energies. As their nuclear structure is shaped like an envelope, they are denoted E_1 and E_3, with the subscript denoting the label of the atom at the tip of the envelope (see Paper IX for details). Although the electronic structure of the NC-dissociated and E_1-puckered conical intersections are different, they are connected on a branch of crossing seam (Figure 4.5), with the two nuclear arrangements probably being minimum and maximum of that seam, respectively. Therefore, deactivation of electronically excited imidazole is expected to happen at all points of this branch of crossing seam. (For more details see Paper IX.)

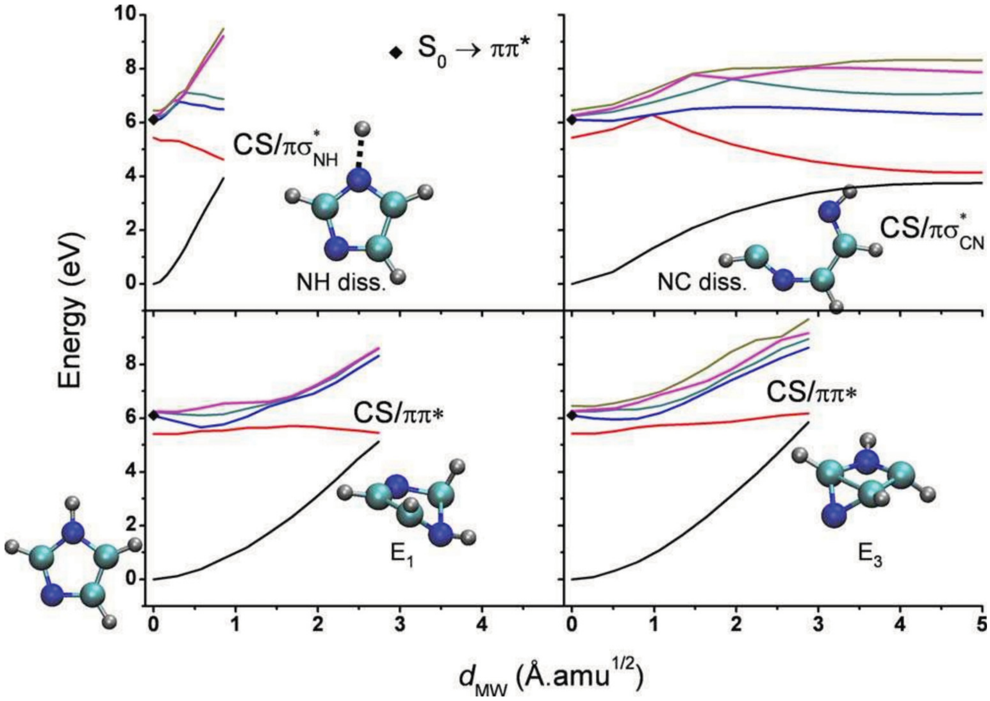

Figure 4.4.: DFT/MRCI energy profiles of linearly interpolated reaction paths connecting the FC region with the four S_1/S_0 conical intersections located by means of CASSCF optimizations. The paths are plotted as a function of the mass-weighted distance to the ground state minimum. Top, left: NH dissociation as first described by Domcke and Sobolweski. [145]. Top, right: NC dissociation similar to the asymmetric ring-opening of furan and thiophene (see above). Bottom, left: E_1-puckered structure with a strong elongation of a CN bond similar to the findings in pyrrole. [146] Bottom, right: E_3 puckering with additional CC bond formation.

Recent non-adiabatic on-the-fly-dynamics simulations of the photo-dynamics of pyrrole by Vazdar *et al*, [147] reveal that after excitation into the optically bright state 80% of the trajectories follow the NH-stretching mechanism. A fraction of 13% of trajectories follow ring-deformation channels involving either ring-puckering (10%) or planar ring-opening (3%). Although, for pyrrole, the ring-puckering/ring-opening seam was not mapped explicitly, as it was for imidazole, the results, however, quite clearly show that

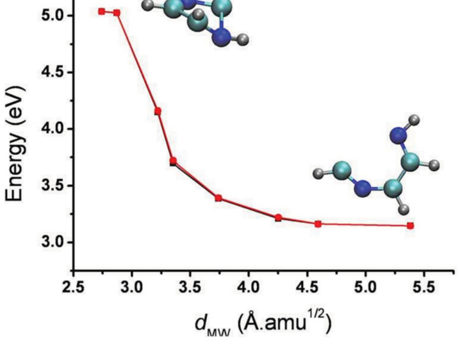

Figure 4.5: S_1 and S_0 energies (CASSCF) along the branch of crossing seam connecting the planar, NC-dissociated and the E_1-puckered conical intersections, obtained by restricted conical intersection optimizations.

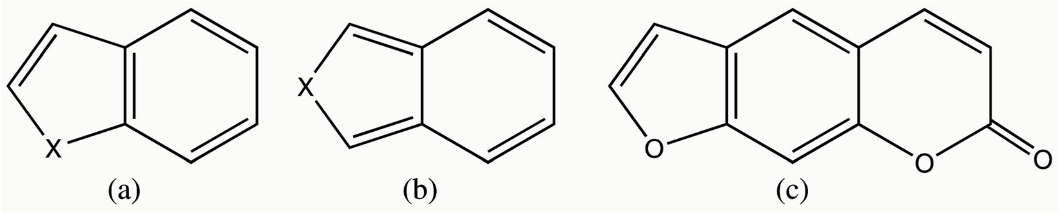

Figure 4.6.: Chemical structure of (a) indole (X=N), benzofuran (X=O) and benzothiophene (X=S), (b) isoindole (X=N), isobenzofuran (X=O) and isobenzothiophene (X=S), and (c) psoralen, a prominent benzofuran derivative.

the conical intersections may appear for various degrees of puckering. [147, 148] Within the above mentioned collaboration, investigations in furan and thiophene have shown that both molecules possess the E_1 puckered type conical intersection, too. With the presence of the ring-dissociative conical intersection it suggests itself that both molecules exhibit a similar intersection seam, as obtained for imidazole. As compared to pyrrole, the absence of the NH dissociation channel should yield increased significance for the puckering-dissociation seam and therefore the ring-dissociation channel in the nonradiative decay mechanisms of these molecules.

4.3.3. More complex systems

In Nature many compounds are found where a five membered heteroaromat is condensed with one or more benzene ring. Initial test calculations suggest that the ring dissociative conical intersection is also present in (iso)benzofuran. In a quantum chemical investigation of psoralen, a benzofuran derivative (see Figure 4.6), Tatchen and Marian showed that ring-opening of the furan side of the molecule yields a S_1/S_0 conical intersection. [149] However, the obtained results indicate that the associated reaction path possesses a substantial barrier. [a] In another quantum chemical investigation a planar ring opening mechanism was found for the imidazole group of adenine. [150] In dynamics simulations this process was observed to occur in a minor fraction of trajectories. [151]

---

[a] Instead, the molecule deactivates via an opening of a lactone OC bond.

Part IV.

Conclusion and outlook

1. Concluding remarks

The results presented in this thesis are aimed at the understanding of the photophysical relaxation processes that take place in flavins and related compounds immediately after (blue-)light absorption. As the first step in the photocycle of the light, oxygen, and voltage sensitive (LOV) domains is the formation of the reactive transient triplet species (LOV-660), particular emphasis of this work lies in the identification of the intersystem crossing (ISC) mechanism and its dependance on the environment. In order to compete with other dissipation mechanisms that depopulate the first excited singlet state the ISC channel(s) have to be efficient. Chapter 1 hereby paves the way to the understanding of triplet formation in flavins by elucidating the different ISC mechanisms of the free compound in vacuum and aqueous solution and in chapter 2 the influence of a LOV domain on the low-lying excited states of the flavin cofactor is investigated by means of combined quantum mechanics / molecular mechans (QM/MM) calculations.

Free flavins In the vacuum a crossing between the primarily excited $^1(\pi\pi^*)$ state (S_1) and a $^3(n\pi^*)$ state (T_2) serves as a funnel for the population of the triplet manifold. Spin-orbit coupling matrix elements (SOME) between the potential energy hypersurfaces (PEHs) are substantial in that region and in combination with favorable Franck-Condon factors between the two states and a small energy gap, the calculations predict the transition to occur at the nanosecond time scale via a direct spin-orbit coupling mechanism (see Figure 1.1, left). In aqueous solution, however, the $(n\pi^*)$ states are significantly blue shifted so that the ISC channel described above for the isolated chro-

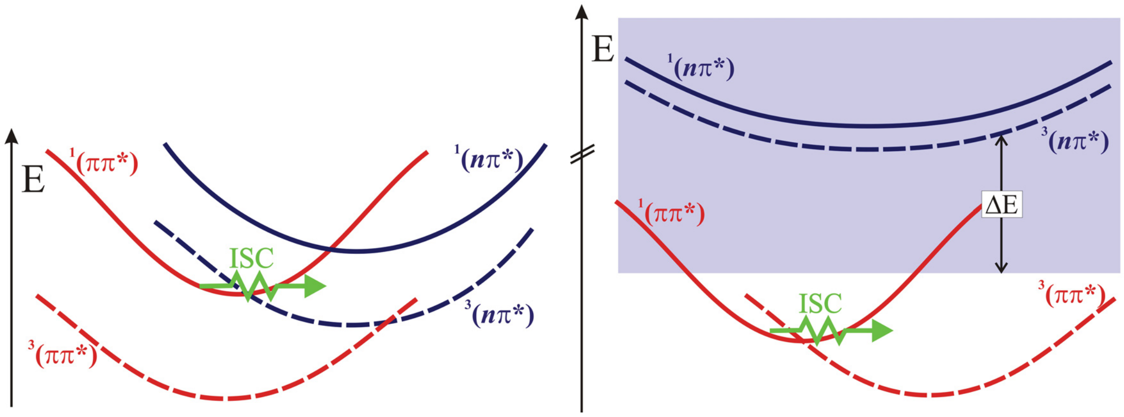

Figure 1.1.: Schematic representation for efficient ISC channels in flavins and related compounds. On the left, the ISC mechanism in vacuum is shown (direct spin-orbit coupling / El'Sayed allowed) and on the right, the ISC mechanism in aqueous solution is depicted (vibronic spin-orbit coupling / El'Sayed forbidden).

mophore is no longer available. Instead, a crossing between the $^1(\pi\pi^*)$ (S_1) and $^3(\pi\pi^*)$ (T_2) takes place. With SOME several orders of magnitude smaller than those for the gas phase, a much smaller ISC rate constant is obtained. So far, this coincides with El-Sayed's rule that predicts fast ISC for transitions between $(\pi\pi^*)$ and $(n\pi^*)$ states and slow ISC for transitions between states with identical character. If, on the other hand, the influence of out-of-plane distortions of the chromophore framework on the SOME is taken into account, the ISC rate constants are increased by several orders of magnitude to $k_{ISC} \approx 10^8 s^{-1}$, which is in good agreement with experiment [30] and therefore shows that El-Sayed's rule does not hold here. This phenomenon, denoted vibronic spin-orbit coupling (see Figure 1.1, right), has been encountered before [64, 70] and can qualitatively be seen as an intensity borrowing from the much faster $(\pi\pi^*) \rightsquigarrow (n\pi^*)$ process. In the two electronically modified flavin derivatives, 1-deaza-flavin (1DF) and 5-deaza-flavin (5DF), which show promising properties and cofactors in LOV domains (5DF), the energy gap between the $^1(\pi\pi^*)$ and the $(n\pi^*)$ states are found to be increased in my calculations. As a result, no direct ISC channel should be observed, independent of the environment. However, in 5DF ISC is anticipated to take place by a vibronic spin-orbit couling mechanism with rates similar to the flavins, whereas for 1DF ISC is predicted to be slow.

LOV domain of the photosensor YtvA For many of the properties investigated, the polar hydrogen-bonding environments in YtvA-LOV and in aqueous solution induce similar changes as compared to the gas phase. One example is the considerable red shift of the second absorption band in the experimental spectra of FMN in LOV domains and water, which can be reproduced by my QM/MM calculations. However, the energetic position of the dark $(n\pi^*)$ states, which is not as easily accessible by means of experimental techniques, depends on their electronic structure. In case of the above mentioned $^3(n\pi^*)$ state (T_2) that serves as a funnel for the population of the triplet manifold in vacuum, the protein environment of (YtvA-)LOV domains shows a negligible solvent shift and, thus, YtvA-LOV is more similar to vacuum in this case. This diversity is sustained in the available ISC channels. In YtvA-LOV the direct spin-orbit coupling mechanism, which has been encountered in isolated flavins in vacuum, and the vibronic spin-orbit coupling mechanism, which was found for free flavins in aqueous solution, are both anticipated to play a role in the generation of LOV-660. In addition, the highly conserved cysteine residue that is essential for the formation of the signaling state shows a substantial influence on spin-orbit coupling via an external heavy-atom effect due to its sulfur center, which is in line with experimental observations. [30, 53, 122, 123]

2. What is still missing?

Although this work answers some issues regarding the photophysical processes in flavins and its derivatives, various questions remain open, some of them also of experimental nature. Some are compiled in the following points:

- What can (QM/MM) dynamics simulations reveal about the energetic position of the low-lying excited states of flavins and derivatives in aqueous solution and LOV proteins (e.g. can the findings of Weigel *et al.* [19] for LF in water be reproduced)?
- According to which mechanism does the ultrafast decay of 1DRF in water/ acetonitrile occur and what is the nature of state A?
- In which way does protonation alter the transient triplet-triplet absorption spectra?
- What is the mechanism of the adduct formation in the LOV domains?
  (As mentioned bevor, this question was attended by means of QM/MM investigations by M. R. Silva-Junior (SFB 663, project C4 (Thiel)). [152]

List of Tables

List of Figures

Bibliography

[1] C. E. Crespo-Hernandez, B. Cohen, P. M. Hare and B. Kohler, *Chem. Rev.*, 2004, **104**, 1977.

[2] J. Cadet and P. Vigny, in *Bioorganic Photochemistry*, ed. H. Morrison, Wiley, 1990, vol. 1, p. 1.

[3] A. Möglich and K. Moffat, *J. Mol. Biol.*, 2007, **373**, 112.

[4] S. Braatsch and G. Klug, *Photosyn. Res.*, 2004, **79**, 45.

[5] J. Huges, T. Lamparter, F. Mittmann, E. Hartmann, W. Gärtner, A. Wilde and T. Börner, *Nature*, 1997, **386**, 663.

[6] K. C. Yeh, S. H. Wu, J. T. Murphy and J. C. Lagarias, *Science*, 1997, **277**, 1505.

[7] A. Losi, *Photochem. Photobiol.*, 2007, **83**, 1283.

[8] W. R. Briggs, C. F. Beck, A. R. Cashmore, J. M. Christie, J. Hughes, J. A. Jarillo, T. Kagawa, H. Kanegae, E. Liscum, A. Nagatani, K. Okada, M. Salomon, W. Rüdiger, T. Sakai, M. Takano, M. Wada and J. C. Watson, *Plant Cell*, 2001, **13**, 993.

[9] A. Losi, E. Polverini, B. Quest and W. Gärtner, *Biophys. J.*, 2002, **82**, 2627.

[10] V. Massey, *Biochem. Soc. Trans.*, 2000, **28**, 283.

[11] A. W. Blyth, *J. Chem. Soc.*, 1877, **35**, 530.

[12] E. Sikorska, I. V. Khmelinskii, D. R. Worrall, J. Koput and M. Sikorski, *J. Fluores.*, 2004, **14**, 57.

[13] A. Bowd, P. Byrom, J. B. Hudson and J. H. Turnbull, *Photochem. Photobiol.*, 1968, **8**, 1.

[14] M. Sung, T. A. Moore and P.-S. Song, *J. Am. Chem. Soc.*, 1972, **94**, 1730.

[15] E. Sikorska, I. V. Khmelinskii, W. Prukala, S. L. Williams, M. Patel, D. R. Worrall, J. L. Bourdelande, J. Koput and M. Sikorski, *J. Phys. Chem. A*, 2004, **108**, 1501.

[16] M. Sakai and H. Takahashi, *J. Mol. Struct.*, 1996, **379**, 9.

[17] A. J. W. G. Visser and F. Müller, *Helv. Chim. Acta*, 1979, **62**, 593.

[18] J. K. Eweg, F. Müller, A. J. W. G. Visser, C. Veeger, D. Bebelaar and J. D. W. van Voorst, *Photochem. Photobiol.*, 1979, **30**, 463.

[19] A. Weigel, A. L. Dobryakov, M. Veiga and J. L. P. Lustres, *J. Phys. Chem*, 2008, **112**, 4294.

[20] P. F. Heelis, *Chem. Soc. Rev.*, 1982, **11**, 15.

[21] T. Climent, R. González, M. Merchán and L. Serrano-Andrés, *J. Phys. Chem. A*, 2006, **110**, 13584.

[22] J. Hasegawa, S. Bureekaew and H. Nakatsuji, *J. Photochem. Photobiol. A*, 2007, **189**, 205.

[23] E. Sikorska, I. V. Khmelinskii, J. Koput, J. L. Bourdelande and M. Sikorski, *J. Mol. Struct.*, 2004, **697**, 137.

[24] C. Neiss, P. Saalfrank, M. Parac and S. Grimme, *J. Phys. Chem. A*, 2003, **107**, 140.

[25] K. Zenichowski, M. Gothe and P. Saalfrank, *J. Photochem. Photobiol. A*, 2007, **190**, 290.

[26] M. Kowalczyk, E. Sikorska, I. V. Khmelinskii, J. Komasa, M. Insińska-Rak and M. Sikorski, *J. Mol. Struct.: THEOCHEM*, 2005, **756**, 47.

[27] A. Penzkofer, L. Endres, T. Schiereis and P. Hegemann, *Chem. Phys.*, 2005, **316**, 185.

[28] S. D. M. Islam, A. Penzkofer and P. Hegemann, *Chem. Phys.*, 2003, **291**, 97.

[29] M. S. Grodowski, B. Veyret and K. Weiss, *Photochem. Photobiol.*, 1977, **26**, 341.

[30] J. T. M. Kennis, S. Crosson, M. Gauden, I. H. M. van Stokkum, K. Moffat and R. van Grondelle, *Biochem.*, 2003, **42**, 3387.

[31] J. Baier, T. Maisch, M. Maier, E. Engel, M. Landthaler and W. Bäumler, *Biophys. J.*, 2006, **91**, 1452.

[32] R. W. Chambers and D. R. Kearns, *Photochem. Photobiol.*, 1969, **10**, 215.

[33] M. A. van der Horst and K. J. Hellingwerf, *Acc. Chem. Res.*, 2004, **37**, 13.

[34] D. E. Somers, P. F. Devlin and S. A. Kay, *Science*, 1998, **282**, 1488.

[35] E. A. Griffin, D. Staknis and C. J. Weitz, *Science*, 1999, **286**, 768.

[36] A. Sancar, *Biochemistry*, 1994, **33**, 2.

[37] V. Balland, M. Byrdin, A. P. Eker, M. Ahmad and K. Brettel, *J. Am. Chem. Soc.*, 2009, **131**, 426.

[38] A. R. Cashmore, J. A. Jarillo, Y. J. Wu and D. Liu, *Science*, 1999, **286**, 760.

[39] S. Anderson, V. Dragnea, S. Masuda, J. Ybe, K. Moffat and C. Bauer, *Biochemistry*, 2005, **44**, 7998.

[40] M. Gauden, S. Yeremenko, W. Laan, I. H. M. van Stokkum, J. A. Ihalainen, R. van Grondelle, K. Hellingwerf and J. T. M. Kennis, *Biochemistry*, 2005, **44**, 3653.

[41] V. Dragnea, M. Waegele, S. Balascuta, C. Bauer and B. Dragnea, *Biochemistry*, 2005, **44**, 15978.

[42] J. Götze and P. Saalfrank, *J. Photochem. Photobiol. B: Biology*, 2009, **94**, 87.

[43] D. Matsuoka, T. Iwata, K. Zikihara, H. Kandori and S. Tokutomi, *Photochem. Photobiol.*, 2007, **83**, 122.

[44] K. Ataka, P. Hegemann and J. Heberle, *Biophys. J.*, 2003, **84**, 466.

[45] E. Schleicher, R. M. Kowalczky, C. W. M. Kay, P. Hegemann, A. Bacher, M. Fischer, R. Bittl, G. Richter and S. Weber, *J. Am. Chem. Soc.*, 2004, **126**, 11067.

[46] C. W. W. Kay, E. Schleicher, A. Kupping, H. Honer, W. Rüdiger, M. Schleicher, M. Fischer, A. Bacher, S. Weber and G. Richter, *J. Biol. Chem.*, 2003, **278**, 10973.

[47] R. M. Kowalczyk, E. Schleicher, R. Bittl and S. Weber, *J. Am. Chem. Soc.*, 2004, **126**, 11393.

[48] Y. Sato, T. Iwata, S. Tokutomi and H. Kandori, *J. Am. Chem. Soc.*, 2006, **127**, 1088.

[49] A. Pfeifer, T. Majerus, K. Zikihara, D. Matsuoka, S. Tokutomi, J. Heberle and T. Kottke, *Biophys. J.*, 2009, **96**, 1462.

[50] T. Domratcheva, R. Fedorov and I. Schlichting, *J. Chem. Theory Comput.*, 2006, **2**, 1565.

[51] M. Dittrich, P. L. Freddolino and K. Schulten, *J. Phys. Chem. B*, 2005, **109**, 13006.

[52] W. Holzer, A. Penzkofer and P. Hegemann, *Chem. Phys.*, 2005, **308**, 79.

[53] W. Holzer, A. Penzkofer, M. Fuhrmann and P. Hegemann, *Photochem. Photobiol.*, 2002, **75**, 479.

[54] W. Gärtner, *in preparation.*

[55] S. Hecht, G. Richter, A. Bacher, M. Joshi, W. Römisch, G. Greiner, R. Frank, S. Weber, W. Eisenreich and M. Fischer, in *Flavins and Flavoproteins*, ed. T. Nishino, R. Miura and M. T. und K. Fukui, ARchiTect Inc., 2005, p. 569.

[56] M. Mansurova, M. S. Koay and W. Gärtner, *Eur. J. Org. Chem.*, 2008, 5401.

[57] G. Herzberg, *Molecular Spectra and Molecular Structure*, Krieger Publishing Company, 1989.

[58] F. Jensen, *Introduction to Computational Chemistry*, Wiley, 2001.

[59] B. H. Bransden and C. J. Joachain, *Physics of atoms and molecules*, Longman Group Limited, 1983.

[60] P. Atkins and R. Friedmann, *Molecular quantum mechanics*, Oxford University Press, 2003.

[61] C. Marian, in *Reviews In Computational Chemistry*, ed. K. Lipkowitz and D. Boyd, Wiley-VCH, Weinheim, 2001, vol. 17, p. 99.

[62] W. Siebrand, *J. Chem. Phys.*, 1967, **46**, 2411.

[63] E. Fermi, *Nuclear Physics*, University of Chicago Press, 1950.

[64] J. Tatchen, N. Gilka and C. M. Marian, *Phys. Chem. Chem. Phys.*, 2007, **9**, 5209.

[65] A. Toniolo and M. Persico, *J. Chem. Phys.*, 2001, **115**, 1817.

[66] A. Toniolo and M. Persico, *J. Comput. Chem.*, 2001, **22**, 968.

[67] B. R. Henry and W. Siebrand, *Organic Molecular Photophysics*, John Wiley & Sons, London, 1973, vol. 1, p. 153.

[68] J. Tatchen, *Dissertation*, Heinrich Heine Universität Düsseldorf, 2006.

[69] M. A. El-Sayed, *J. Chem. Phys.*, 1962, **36**, 573.

[70] S. Perun, J. Tatchen and C. M. Marian, *ChemPhysChem*, 2008, **9**, 282.

[71] W. Domcke, D. R. Yarkony and H. Köppel, *Conical Intersections: Electronic Structure, Dynamics and Spectroscopy*, World Scientific, Singapore, 2004.

[72] K. Kay, *J. Chem. Phys*, 1976, **64**, 2112.

[73] K. Anderson, P. Å. Malmqvist, B. O. Roos, A. Sadley and K. Wolinski, *J. Phys. Chem.*, 1990, **94**, 5483.

[74] F. Furche and R. Ahlrichs, *J. Chem. Phys.*, 2002, **117**, 7433.

[75] O. Christiansen, H.Koch and P. Jørgensen, *Chem. Phys. Lett.*, 1995, **243**, 409.

[76] C. M. Marian and N. Gilka, *J. Chem. Theory Comput.*, 2008, **4**, 1501.

[77] M. Schreiber, M. R. Silva-Junior, S. P. A. Sauer and W. Thiel, *J. Chem. Phys.*, 2008, **128**, 346.

[78] M. R. Silva-Junior, M. Schreiber, S. P. A. Sauer and W. Thiel, *J. Chem. Phys.*, 2008, **128**, 104103.

[79] A. Dreuw, J. L. Weisman and M. Head-Gordon, *J. Chem. Phys.*, 2003, **119**, 2943.

[80] S. Grimme and M. Waletzke, *J. Chem. Phys.*, 1999, **111**, 5645.

[81] D. J. Tozer, R. D. Amos, N. C. Handy, B. O. Roos and L. Serrano-Andrés, *Mol. Phys.*, 1999, **97**, 859.

[82] A. Dreuw and M. Head-Gordon, *Chem. Rev.*, 2005, **105**, 4009.

[83] M. Schmitt, R. Brause, C. M. Marian, S. Salzmann and W. L. Meerts, *J. Chem. Phys.*, 2006, **125**, 124309.

[84] A. D. Becke, *J. Chem. Phys.*, 1993, **98**, 1372.

[85] C. Lee, W. Yang and R. G. Parr, *Phys. Rev.*, 1988, **B 37**, 785.

[86] M. Etinski, *unpublished results.*

[87] A. Klamt and G. Schüürmann, *J. Chem. Soc., Perkin Trans.*, 1993, **2**, 799.

[88] A. Schäfer, A. Klamt, D. Sattel, J. Lohrenz and F. Eckert, *Phys. Chem. Chem. Phys.*, 2000, **2**, 2187.

[89] *http://www.turbomole-gmbh.com/manuals/.*

[90] H. M. Senn and W. Thiel, *Top. Curr. Chem.*, 2007, **268**, 173.

[91] H. M. Senn and W. Thiel, *Angew. Chem. Int. Ed.*, 2009, **48**, 1198.

[92] L. W. Jorgensen, J. Chandrasekhar, J. D. Madura, R. W. Impey and M. L. Klein, *J. Chem. Phys.*, 1983, **79**, 926.

[93] B. R. Brooks, R. E. Bruccoleri, B. D. Olafson, D. J. States, S. Swaminathan and M. Karplus, *J. Comp. Chem.*, 1983, **4**, 187.

[94] P. Sherwood, A. H. de Vries, M. F. Guest, G. Schenckenbach, C. R. A. Catlow, S. A. French, A. A. Sokol, S. T. Bromley, W. Thiel, A. J. Turner, S. Billeter, F. Terstegen, S. Thiel, J. Kendrich, S. C. Rogers, J. Casci, M. Watson, F. King, E. Karlsen, M. Sjøvoll, A. Fahmi, A. Schäfer and C. Lennartz, *J. Mol. Struct. (THEOCHEM)*, 2003, **632**, 1.

[95] A. H. de Vries, P. Sherwood, S. J. Collins, A. M. Rigby, M. Rigutto and G. J. Kramer, *J. Phys. Chem. B*, 1999, **103**, 6133.

[96] Y. J. Bomble, K. W. Sattelmeyer, J. F. Stanton and J. Gauss, *J. Chem. Phys.*, 2004, **121**, 5236.

[97] E. R. Davidson and A. A. Jarzecki, *Chem. Phys. Lett*, 1998, **285**, 155.

[98] L. S. Cederbaum and W. Domcke, *J. Chem. Phys.*, 1976, **64**, 603.

[99] C. Kind, M. Reiher and J. Neugebauer, SNF *Version 2.2.1: A Program Package for Numerical Frequency Analyses*, Universität Erlangen, 1999-2002.

[100] R. Ahlrichs, M. Bär, H.-P. Baron, R. Bauernschmitt, S. Böcker, N. Crawford, P. Deglmann, M. Ehrig, K. Eichkorn, S. Elliott, F. Furche, F. Haase, M. Häser, C. Hättig, H. Horn, C. Huber, U. Huniar, M. Kattannek, A. Köhn, C. Kölmel, M. Kollwitz, K. May, P. Nava, C. Ochsenfeld, H. Öhm, H. Patzelt, D. Rappoport, O. Rubner, A. Schäfer, U. Schneider, M. Sierka, O. Treutler, B. Unterreiner, M. von Arnim, F. Weigend, P. Weis and H. Weiss, *TURBOMOLE (Vers. 5.10)*, Universität Karlsruhe, 2008.

[101] J. Tatchen, VIBES, Universität Düsseldorf, 2005.

[102] M. Dierksen, PLOTTER *Verison 0.3*, Westfälische Wilhelms-Universität Münster, 2002.

[103] Y.-K. Choe, S. Nagase and K. Nishimoto, *J. Comput. Chem.*, 2007, **28**, 727.

[104] M. Parac, M. Doerr, C. M. Marian and W. Thiel, *J. Comp. Chem. (accepted)*, 2009.

[105] C. Slavov, M. Mansurova, A. R. Holzwarth and W. Gärtner, *Photochem. Photobiol. (submitted).*

[106] M. Sikorski, D. Prukala, M. Insińska-Rak, I. Khmelinskii, D. R. Worrall, S. L. Williams, J. Hernando, J. L. Bourdelande, J. Koputa and E. Sikorska, *J. Photochem. Photobiol. A*, 2008, **783**, 184.

[107] M. Sikorski, E. Sikorska, D. R. Worrall and F. Wilkinson, *J. Chem. Soc. Faraday Trans.*, 1998, **94**, 2347.

[108] M. S. Grodowski, B. Veyret and K. Weiss, *Photochem. Photobiol.*, 1977, **26**, 341.

[109] R. Spencer, J. Fischer and C. Walsh, *Biochemistry*, 1977, **16**, 3586.

[110] C. M. Marian, *J. Chem. Phys*, 2005, **122**, 104314.

[111] C. M. Marian, *J. Phys. Chem. A*, 2007, **111**, 1545.

[112] A. L. Sobolewski and W. Domcke, *Eur. Phys. J. D*, 2002, **20**, 369.

[113] S. Matsika, *J. Phys. Chem. A*, 2005, **109**, 7538.

[114] S. Perun, A. L. Sobolewski and W. Domcke, *J. Phys. Chem. A*, 2006, **110**, 13238.

[115] M. Merchan, R. Gonzalez-Luque, T. Climent, L. Serrano-Andrés, E. Rodriguez, M. Reduero and D. Pelaez, *J. Phys. Chem. B*, 2006, **110**, 26471.

[116] Z. Lan, E. Fabiano and W. Thiel, *J. Phys. Chem. B*, 2009, **113**, 3548.

[117] M. Nakasako, K. Zikihara, D. Matsuoka, H. Katsura and S. Tokutomi, *J. Mol. Biol.*, 2008, **381**, 718.

[118] S. Akbar, T. A. Gaidenko, C. M. Kang, M. O'Reilly, M. K. Dervine and C. W. Price, *J. Bacteriol.*, 2001, **183**, 1329.

[119] T. A. Gaidenko, T. J. Kim, A. L. Weigel, M. S. Brody and C. M. Price, *J. Bacteriol.*, 2006, **188**, 6387.

[120] M. Avila-Perez, K. J. Hellingwerf and R. Kort, *J. Bacteriol.*, 2006, **188**, 6411.

[121] R. Fedorov, I. Schlichting, E. Hartmann, T. Domratcheva, M. Fuhrmann and P. Hegemann, *Biophys. J.*, 2003, **84**, 2474.

[122] M. T. A. Alexandre, R. van Grondelle, K. J. Hellingwerf, B. Robert and J. T. M. Kennis, *Phys. Chem. Chem. Phys.*, 2008, **10**, 6693.

[123] T. A. Schuttrigkeit, C. K. Kompa, S. Salomon, W. Rudiger and M. E. Michel-Beyerle, *Chem. Phys.*, 2003, **294**, 501.

[124] K. H. Dudley, A. Ehrenberg, P. Hemmerich and F. Müller, *Helv. Chim. Acta*, 1964, **47**, 1354.

[125] T. Domratcheva, B. L. Grigorenko, I. Schlichting and A. V. Nemukhin, *Biophys. J.*, 2008, **94**, 3872.

[126] A. L. Stelling, K. L. Ronayne, J. Nappa, P. J. Tonge and S. R. Meech, *J. Am. Chem. Soc.*, 2007, **129**, 15556.

[127] A. Weissberger, E. C. Taylor and S. Gronowitz, *One Dimentional Metals*, VCH Weinheim, 1995.

[128] T. A. Skotheim, *Handbook of conducting polymers*, Marcel Dekker New York, 1986, vol. 1 & 2.

[129] L. Lehr, *Dissertation*, Technische Universität München, 2000.

[130] G. Di Lonardo, G. Galloni, A. Trombetti and C. Zauli, *Chem. Soc. Faraday Trans. II*, 1972, **68**, 2009.

[131] M. H. Palmer, I. C. Walker and M. F. Guest, *Chem. Phys.*, 1999, **241**, 275.

[132] R. S. Becker, J. S. de Melo, A. L. Maçanita and F. Elisei, *J. Phys. Chem.*, 1996, **100**, 18683.

[133] S. Rentsch, J. P. Yang, W. Paa, E. Birckner, J. Schiedt and R. Weinkauf, *Phys. Chem. Chem. Phys.*, 1999, **1**, 1707.

[134] K. R. Asmis, *Dissertation*, Université de Fribourg (Switzerland), 1996.

[135] H. Haberkern, K. R. Asmis and P. Swiderek, *Phys. Chem. Chem. Phys.*, 2003, **5**, 827.

[136] H. G. Longuet-Higgins, *Trans. Faraday Soc.*, 1949, **45**, 173.

[137] R. P. T. Lun, L. Bouscasse, E. J. Vincent and J. Metzger, *Bull. Soc. Chim. Fr.*, 1969, 1149.

[138] W. Paa, J.-P. Yang and S. Rentsch, *Synthetic Metals*, 2001, **119**, 525.

[139] G. Buemi, F. Zuccarello and G. Romeo, *J. Mol. Struct. THEOCHEM*, 1983, **94**, 115.

[140] M. Kleinschmidt, J. Tatchen and C. M. Marian, *J. Comput. Chem.*, 2002, **23**, 824.

[141] H. Köppel, E. V. Gromov and A. B. Trofimov, *Chem. Phys.*, 2004, **304**, 35.

[142] H. A. Wiebe and J. Heicklen, *Can. J. Chem.*, 1969, **47**, 2965.

[143] E. V. Gromov, A. B. Trofimov, N. M. Vitkovskaya, H. Köppel, J. Schirmer, H.-D. Meyer and L. S. Cederbaum, *J. Chem. Phys.*, 2004, **121**, 4585.

[144] E. V. Gromov, A. B. Trofimov, N. M. Vitkovskaya, J. Schirmer and H. Köppel, *J. Chem. Phys.*, 2003, **119**, 737.

[145] A. L. Sobolewski and W. Domcke, *Chem. Phys.*, 2000, **295**, 181.

[146] M. Barbatti, M. Vazdar, A. J. A. Aquino, M. Eckert-Maksic and H. Lischka, *J. Chem. Phys.*, 2006, **125**, 164323.

[147] M. Vazdar, M. Eckert-Maksic, M. Barbatti and H. Lischka, *Mol. Phys.*, 2009.

[148] M. Barbatti, *private communication.*

[149] J. Tatchen and C. M. Marian, *Phys. Chem. Chem. Phys.*, 2006, **8**, 2133.

[150] S. Perun, A. L. Sobolewski and W. Domcke, *Chem. Phys.*, 2006, **313**, 107.

[151] M. Barbatti and H. Lischka, *J. Am. Chem. Soc.*, 2008, **130**, 6831.

[152] M. R. Silva-Junior, *Dissertation*, MPI Kohlenforschung, Mülheim, 2009.

Acknowledgement

My first thanks go to my advisor Christel M. Marian who entrusted me with this highly interesting project. Over the time, she has not only guided me, but has also given me the freedom to pursue my own interests and offered a valuable discussion partner. I cordially thank her for her confidence and her support, which goes beyond scientific matters.

Jörg Tatchen has helped me in the first two years. He answered many questions and introduced me into his and other programs, which I am very thankful for. The contribution from Martin Kleinschmidt was an ongoing one. He was there, when I needed technical help with the MRCI, SPOCK or whatnot. Thank you for this support. Another thank you goes to the rest of the theoretical chemistry group in Düsseldorf, as they all have contributed to the good atmosphere!

To Walter Thiel and Mario R. Silva Junior I owe thanks for various reasons, as they made the QM/MM investigations possible and offered valuable discussion partners. In addition, I want to thank Walter Thiel for accepting the laborious task of a second reviewer. Thanks are also due to Wolfgang Gärtner, whom I worked with on the flavin derivatives and who politely offered discussions about flavoproteins as well as corrections of parts of my thesis. With Mario Barbatti and Nemanja Gavrilov I worked together productively for some time on the small five-membered ring systems. I want to thank them for their cooperation.

For her excellent team work I want to thank Brigitte Bier, whom I organized the PhD conference 2008 in Papenburg with. Natalie Gilka I want to thank for her help with scripts and information at the start of my thesis. I hope to see you more often in the future! To Vidisha Rai-Constapel thanks are due, as she read through large parts of my thesis and tried to improve my English. A special thank you is addressed to Birgit Weitzel, who has not only proven to be a loyal friend, but who also tried to help me where she could!

To Lasse Kragh Sørensen I want to say thank you for a multitude of reasons. In the last years I could be sure of his unconditional support and advice. I wish him all the best and promise better food in the future. I also owe thanks to my parents for their continuous support (especially to my dad for help with the chaos car). Last but not least, I want to thank the DFG for funding via the collaborative research center 663.

Abbreviations

1DLF	1-deazalumiflavin
1DRF	1-deazariboflavin
5DLF	5-deazalumiflavin
5DRF	5-deazariboflavin
AA	amino acid
AcCN	acetonitrile
AL	alloxazine
ASN	asparagine
BO	Born-Oppenheimer
BLUF	sensor of blue light using flavin adenine dinucleotide
CASPT2	complete active space with second-order perturbation theory
ConIn	conical intersection
COSMO	conductor-like screening model
CT	charge transfer
CYS	cysteine
DFT	density functional theory
DFT/MRCI	combined density functional theory / multi-refernce configuration interaction method
DMLF	7,8-didemethyllumiflavin
DMRF	7,8-didemethylriboflavin
DX	1,4-dioxane
EtOH	ethanol
FAD	flavin adenine dinucleotide
FC	Franck-Condon
FCF	Franck-Condon factor
FMN	flavin mononucleotide
FTIR	fourier transform infrared spectroscopy
FWHM	full width half maximum
GLN	glutamine
HF	Hartree-Fock
HOMO	highest occupied molecular orbital
IA	isoalloxazine
IC	internal converion
ISC	intersystem crossing
IVR	intramoleculer vibrational energy relaxation
KS	Kohn-Sham
LC	lumichrome
LF	lumiflavin
LOV	light, oxygen, and voltage sensitive
LUMO	lowest unoccupied molecular orbital
MIA	10-methylisoalloxazine (also DMLF)
MO	molecular orbital

MTHF	2-methyltetrahydrofuran
PDB	protein data base
PEH	potential energy hypersurface
phot	phototropin
QM/MM	quantum mechanics / molecular mechanics
RF	riboflavin
SACCI	symmetry-adapted-cluster configuration interaction
SOME	spin-orbit coupling matrix elements
TDDFT	time dependant density functional theory
UV	ultra violet
VR	vibrational energy relaxation
WT	wild type

Paper I

The photophysics of flavins:
What makes the difference between gas phase and aqueous solution?

Susanne Salzmann, Jörg Tatchen, and Christel M. Marian

J. Photochem. Photobiol. A, **198** (2008) 221-231.

Journal of Photochemistry and Photobiology A: Chemistry 198 (2008) 221–231

Contents lists available at ScienceDirect

Journal of Photochemistry and Photobiology A: Chemistry

journal homepage: www.elsevier.com/locate/jphotochem

The photophysics of flavins: What makes the difference between gas phase and aqueous solution?

Susanne Salzmann[a], Jörg Tatchen[a,b], Christel M. Marian[a,*]

[a] *Institute of Theoretical and Computational Chemistry, Heinrich Heine University Düsseldorf, Universitätsstr. 1, D-40225 Düsseldorf, Germany*
[b] *Chemical Physics Department, Weizmann Institute of Science, 76100 Rehovot, Israel*

ARTICLE INFO

Article history:
Received 2 January 2008
Received in revised form 4 March 2008
Accepted 21 March 2008
Available online 1 April 2008

Keywords:
Flavins
Multi-reference configuration interaction
Excited states
Solvatochromism
Intersystem crossing rate constants

ABSTRACT

The ground and low-lying excited electronic states of isoalloxazine, 10-methylisoallox-azine and lumiflavin, three flavin-related compounds, were investigated by means of quantum chemical methods. Minimum structures were determined employing (time-dependent) Kohn–Sham density functional theory. Spectral properties were computed utilizing a combined density functional and multi-reference configuration interaction (DFT/MRCI) method. Solvent effects were mimicked by a conductor like screening model and micro-hydration with four explicit water molecules. At selected points along a linearly interpolated path connecting the Franck–Condon region and the S_1 minimum, spin–orbit interaction was computed employing a nonempirical mean-field Hamiltonian. For isoalloxazine, intersystem crossing (ISC) rate constants were computed, taking both direct and vibronic spin–orbit coupling into account.

On the basis of these calculations we suggest the following photo relaxation model. In the vacuum, efficient ISC ($k_{\mathrm{ISC}} \approx 10^9\,\mathrm{s}^{-1}$) takes place between the primarily excited $^1(\pi \rightarrow \pi^*)$ state (S_1) and the lowest $^3(n \rightarrow \pi^*)$ state (T_2). The energetic proximity of the $^1(n \rightarrow \pi^*)$ state (S_2) enhances the nonradiative relaxation of S_1 by internal conversion (IC). In aqueous solution these ISC and IC channels are energetically not accessible due to the blue shift of the $(n \rightarrow \pi^*)$ states. The high triplet quantum yield observed in experiment [J.T.M. Kennis, S. Crosson, M. Gauden, I.H.M. van Stokkum, K. Moffat, R. van Grondelle, Biochemistry 42 (2003) 3385–3392] is explained by the intersection between the $^1(\pi \rightarrow \pi^*)$ state (S_1) potential energy hypersurface (PEH) and the second $^3(\pi \rightarrow \pi^*)$ (T_2) PEH along the relaxation pathway and the strong enhancement of their spin–orbit coupling by vibronic interactions. The calculated ISC rate for this channel ($k_{\mathrm{ISC}} \approx 10^8\,\mathrm{s}^{-1}$) is in good agreement with experimental results. According to our model, lack of an efficient IC channel leads to an increased fluorescence quantum yield in aqueous solution.

1. Introduction

In recent years flavins have received growing attention especially due to their decisive role in blue light-mediated signal transduction in plants and bacteria [1–3]. They serve, for example, as cofactors in phototropins (phot), plasma membrane-associated proteins which are primary photoreceptors for the mediation of phototropic plant movement. Two light, oxygen and voltage-sensitive (LOV) domains are present in each phot protein which both bind one flavin mononucleotide (FMN) noncovalently. Upon absorption of blue light, the LOV domain undergoes a photocycle that leads to photobleaching. The primary step after light absorption hereby involves a rapid decay of the excited singlet state to the lowest excited triplet state via an intersystem crossing (ISC) mechanism. In a second step a metastable covalent adduct of a nearby cysteine residue and the isoalloxazine framework of the chromophor is generated resulting in a structural signal that affects autophosphorylation.

The environmental effects of the LOV domains on the photophysics of the FMN chromophore have been the topic of several experimental studies [4–8]. The experimental ISC rate constants for FMN are $k_{\mathrm{ISC}} = 10^8\,\mathrm{s}^{-1}$ in water (pH 7.0) and $k_{\mathrm{ISC}} = 3 \times 10^8\,\mathrm{s}^{-1}$ in the LOV2 domain at ambient temperatures [4]. In both cases the measured triplet quantum yield ϕ_{T} amounts to 0.60. In comparison to free FMN in water, the FMN in the LOV1 and LOV2 domains show a decrease of the fluorescence quantum yield Φ_{F} and the fluorescence lifetime τ_{F} by roughly a factor of two [4].

The chromophore of the LOV domain, FMN can be divided into two parts: (A) the isoalloxazine (benzol[*g*]pteridine-2,4(3H,10H)-dione) core ring and (B) the ribophosphyl chain. Since the photophysical and photochemical behavior of flavins is dominated by the isoalloxazine core, the experimental absorption and emission spectra of different flavins are very similar. In the energy

---

[*] Corresponding author. Tel.: +49 211 8113209; fax: +49 211 8113466.
E-mail address: Christel.Marian@uni-duesseldorf.de (C.M. Marian).
URL: http://www.theochem.uni-duesseldorf.de (C.M. Marian).

1010-6030/$ – see front matter © 2008 Elsevier B.V. All rights reserved.
doi:10.1016/j.jphotochem.2008.03.015

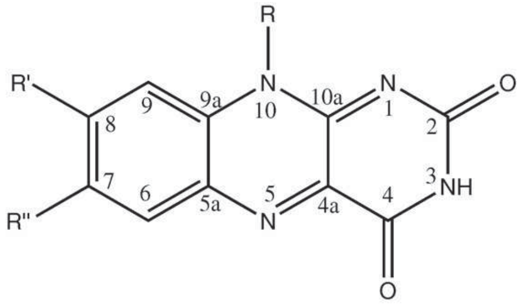

Fig. 1. Chemical structure and labeling of the isoalloxazine core ring of flavins (R=R′=R″=H: isoalloxazine (IA), R=Me,R′=R″=H: 10-methylisoalloxazine (MIA) and R=R′=R″=Me: lumiflavin (LF)).

regime up to 5.5 eV the absorption spectrum of isoalloxazines in solution as well as in the protein environment is dominated by three bands [9,4,6]. In ethanol (EtOH) and the LOV domain, the lowest energy band shows a well-resolved vibronic structure with peaks at 2.63 eV, 2.79 eV, and 2.99 eV (LF in EtOH [9]). In more polar solvents the absorption spectrum is smoothed out. However, the position of this band is hardly affected by the polarity or the proticity of the solvent. In difference to that, the position of the second absorption maximum depends heavily on the environment [10,11]. Experiments in solvents like 1,4-dioxane, 1,2-dichloroethane and acetonitrile confirm that the rising polarity has no major influence on the position of that band. The noticeable red shift of that transition band in solvents like methanol, ethanol, and water shows that the proticity of the solvent plays a more important role [10,9].

The photophysical behavior of different flavins has been the matter of several recent quantum chemical investigations [12–14,10,15,16]. Spin–orbit coupling has been taken into account for the primary step of the photocycle by Climent et al. [13] while Zenichowski et al. [16] have investigated spin–orbit coupling in connection with the adduct formation. In this work, the absorption spectra of the three flavin related compounds isoalloxazine (IA), 10-methylisoalloxazine (MIA), and lumiflavin (LF) (see Fig. 1) are investigated. For MIA, the impact of solvent effects (in water and acetonitrile) on the vertical singlet and the triplet excited energies is evaluated. For all compounds, relaxation pathways after electronic excitation in the vacuum and aqueous solution are studied, taking spin–orbit coupling into account. For IA, intersystem crossing rate constants have been computed, taking both direct and vibronic spin–orbit coupling into account. On this basis the accessibility of the above mentioned ISC channels in water and vacuum is discussed.

2. Methods and computational details

Geometry optimizations of the ground state and low-lying electronically excited states of three isoalloxazines were carried out at the level of density functional theory (DFT) using the TURBOMOLE 5.7[17] program package. For all calculations we employed the standard TZVP basis set from the TURBOMOLE library. The B3LYP functional [18,19] as implemented in TURBOMOLE 5.7 was used for optimizing the geometries. C_s symmetry constraints were imposed on the ground and excited state geometries of all molecules. The cartesian coordinate system was chosen in a way that the *xy* plane coincides with the molecular plane. For the optimization of the electronically excited singlet and triplet state geometries time-dependent DFT [20] (TDDFT) was employed. To ensure that the resulting geometries correspond to true minima of the potential energy hypersurface (PEH), harmonic vibrational frequencies were calculated numerically with the program SNF [21]. Zero-point vibrational energy corrections (ZPVE) were scaled by a factor of 0.9614 as recommended for the B3LYP functional [22].

Vertical electronic excitation energies and dipole moments were obtained from subsequent single-point calculations using the combined density functional theory/multi-reference configuration interaction (DFT/MRCI) method of Grimme and Waletzke [23]. This approach represents an effective means to obtain spin-restricted electronic spectra for organic systems with errors typically less than 0.2 eV. The principle idea is to include major parts of dynamic electron correlation by DFT whereas static electron correlation effects are taken into account by short MRCI expansions. This MRCI expansion is built up in a one-particle basis of Kohn–Sham orbitals employing the BHLYP functional [24,25]. For effectivity reasons and to avoid double-counting of the dynamic correlation, the MRCI expansion is kept short by extensive configuration selection. Furthermore, the 1s electrons of carbon, nitrogen, and oxygen constitute a frozen core. The remaining valence electrons were correlated. Virtual orbitals with energies above $2E_H$ were discarded in the DFT/MRCI calculations. For all geometries we calculated ten roots for each of the two irreducible representations A′ and A″ of the C_s symmetry, both for the singlet and triplet manifolds.

Dipole transition matrix elements and oscillator strength were evaluated at the DFT/MRCI level. From these values, fluorescence rates were obtained according to

$$k_F = \frac{4e^2}{3c^3\hbar^4}(E_i - E_f)^3 |\langle f|\vec{r}|i\rangle|^2 \tag{1}$$

Expressing k_F in units of s^{-1}, ΔE in cm^{-1} and $\langle f|\vec{r}|i\rangle$ in atomic units (ea_0) the numerical prefactor becomes 2.0261×10^{-6}.

For the computation of the spin–orbit matrix elements (SOMEs) between the correlated DFT/MRCI wavefunctions we used the spin–orbit coupling kit (SPOCK) [26,27] developed in our laboratory. For reasons of efficiency, the one-center mean-field approximation to the Breit–Pauli Hamiltonian is used for the description of the spin–orbit coupling. This nonempirical effective one-electron operator treats the expensive two-electron terms of the full Breit–Pauli Hamiltonian in a Fock-like manner [28,29]. It has been shown that the accuracy of this approximation lies within better than 5% of the full treatment [30,31].

According to Toniolo and Persico [32,33], it is possible to approximate the Fermi Golden Rule expression for the ISC rate constants k_{ISC} by a summation over rates of transition from the initial level $|i, \mathbf{v} = 0\rangle$ to individual final vibronic levels $|f, \mathbf{v}'\rangle$ in an energy interval of width 2η around the energy $E_{i,\mathbf{v}=0}$. Here, the vectors $\mathbf{v}$ and $\mathbf{v}'$ represent sets of vibrational quantum numbers in all normal modes of the initial (i) and final (f) electronic state, respectively. If we denote the coupling matrix elements driving the radiationless transition by $H^{SO}_{\mathbf{v}=0,\mathbf{v}'}$, the rate constant is obtained as

$$k_{ISC}(i \rightsquigarrow f) = \frac{2\pi}{\hbar\eta} \sum_{|E_{f,\mathbf{v}'} - E_{i,\mathbf{v}=0}| < \eta} |H^{SO}_{\mathbf{v}=0,\mathbf{v}'}|^2. \tag{2}$$

$H^{SO}_{\mathbf{v}=0,\mathbf{v}'}$ can be expanded in a Taylor series in the variables $\{q_\kappa\}$, the normal coordinates, around some reference point $\mathbf{q}_0$ [34] which we have chosen to coincide with the minimum of the S_1 state.

$$H^{SO}_{\mathbf{v}=0,\mathbf{v}'} = \langle i|\hat{\mathcal{H}}_{SO}|f\rangle\Big|_{\mathbf{q}_0=0} \langle \mathbf{v} = 0|\mathbf{v}'\rangle + \sum_\kappa \left(\frac{\partial}{\partial q_\kappa} \langle i|\hat{\mathcal{H}}_{SO}|f\rangle \right)\Bigg|_{\mathbf{q}_0=0}$$
$$\langle \mathbf{v} = 0|q_\kappa|\mathbf{v}'\rangle + O(|\mathbf{q}|^2) \tag{3}$$

The first term on the right-hand side of Eq. (3) is a purely electronic matrix element and is denominated direct spin–orbit coupling in the following, whereas the term in the second line of Eq. (3) represents the first-order derivative coupling and is named vibronic spin–orbit coupling.

Rate constants for inter-system crossing from the S_1 state to the three sublevels of the T_1 and T_2 state, respectively, were calculated taking both direct and vibronic spin–orbit coupling into account. According to El-Sayed's rule, SOME between $(\pi \rightarrow \pi^*)$ and $(n \rightarrow \pi^*)$ states are in general much larger than SOME between two $(\pi \rightarrow \pi^*)$ states. Thus, the Condon approximation will yield ISC rate constants that are much slower for $(\pi \rightarrow \pi^*) \rightsquigarrow (\pi \rightarrow \pi^*)$ processes than for $(\pi \rightarrow \pi^*) \rightsquigarrow (n \rightarrow \pi^*)$ processes. As recent studies by Tatchen et al. [35] have shown, vibronic spin–orbit coupling enhances the ISC rate constants between two $(\pi \rightarrow \pi^*)$ states in psoralen. Therefore, a Herzberg–Teller type expansion of spin–orbit coupling around the $^1(\pi \rightarrow \pi^*)$ state minimum (Eq. (3)) was carried out, taking the first-order derivatives of the spin–orbit interaction with respect to *out-of-plane* (*oop*) normal mode coordinates into account. When the molecular geometry is distorted in this way, $(\pi \rightarrow \pi^*)$ and $(n \rightarrow \pi^*)$ states are able to interact and become mixed. This can qualitatively be seen as an intensity borrowing from the much faster $(\pi \rightarrow \pi^*) \rightsquigarrow (n \rightarrow \pi^*)$ process.

The calculations of the ISC rate constants were performed using the VIBES program [36]. The first-order derivatives of the SOME were calculated numerically by finite difference techniques as described in Ref. [35]. The rate constants were calculated for the smallest flavin compound (isoalloxazine) only, for efficiency reasons. In isoalloxazine there are in total 60 vibrational degrees of freedom. Only totally symmetric vibrational modes can serve as accepting modes. In the calculations we allowed excitations into all 41 accepting modes. When vibronic spin–orbit coupling was taken into account, between 8 and 19 *oop* vibrational modes were used as coupling modes. (For further details on the choice of computational parameters see Electronic Supplementary Material (ESM).)

To estimate spectral shifts due to electrostatic interaction in polar solvents we employed the conductor-like screening model (COSMO) which is implemented in the TURBOMOLE package [37,38]. Dielectric constants of $\epsilon = 78$ and $\epsilon = 36$ were chosen, [39] corresponding to water and acetonitrile, respectively, at ambient temperatures. When COSMO was applied, the MRCI expansion was built up from the one-particle basis of COSMO optimized Kohn–Sham orbitals. Because of technical reasons, C_1 symmetry had to be used for all calculations involving COSMO. For both singlet and triplet multiplicity 20 roots were computed. Since COSMO cannot properly model hydrogen bonding, the effects of hydrogen bonding in aqueous solution were mimicked by micro-hydration. For this purpose, we placed four water molecules next to the hetero atoms of the isoalloxazine ring and optimized the ground state without symmetry constraints. In a last approach, the two previous models were combined.

3. Results and discussion

In this section the minimum nuclear arrangements of the ground state as well as the lowest-lying excited states of IA, MIA, and LF and the corresponding vertical electronic spectra are presented. The energetic order of the states is sensitive to the nuclear geometry and typically more than one minimum is found on a particular PEH. This situation is known for various molecules [40,41]. Here, the vertical order of the excited states does not correspond to their adiabatic order. To avoid confusion, we use two different nomenclatures to designate pure multiplicity states: S1, S2, ..., T1, T2, ... denominate *electronic structures* in their energetic order at the ground state minimum geometry. The nomenclature $S_1, S_2, \ldots, T_1, T_2, \ldots,$ refers to the actual order of *electronic states* at a given geometry. At the ground state equilibrium geometry, the two nomenclatures are identical, of course.

Table 1
IA, MIA, and LF: selected ground-state geometry bond lengths [pm] and experimental (X-ray) data of MIA [42]

	IA	MIA	LF	(Exp.)
N(1)—C(2)	138.4	138.1	138.0	136.0(5)
C(2)—N(3)	141.8	141.4	141.4	140.8(5)
N(3)—C(4)	138.1	137.9	137.9	135.4(5)
C(4)—C(4a)	150.1	150.2	150.0	148.5(5)
C(4a)—N(5)	129.2	129.0	129.3	129.5(5)
N(5)—C(5a)	137.3	136.9	136.6	136.6(5)
C(5a)—C(6)	140.6	140.5	140.5	141.8(5)
C(6)—C(7)	137.9	137.8	138.0	136.8(6)
C(7)—C(8)	140.4	140.1	142.1	139.5(6)
C(8)—C(9)	138.3	138.4	138.8	138.8(6)
C(9)—C(9a)	139.9	140.3	140.1	139.2(5)
C(9a)—N(10)	137.5	138.6	138.5	139.0(5)
N(10)—C(10a)	136.8	138.2	138.2	136.9(5)
C(10a)—N(1)	129.6	129.9	130.1	131.9(5)
C(5a)—C(9a)	141.6	141.9	141.5	141.8(5)
C(4a)—C(10a)	146.3	146.2	146.1	146.6(5)
C(10)—R	101.2	146.8	146.7	148.8(5)
C(2)—O	121.0	121.1	121.2	121.6(5)
C(4)—O	121.0	121.0	121.1	121.7(5)

Atomic labels are displayed in Fig. 1. Estimated experimental uncertainties are given in parentheses.

3.1. Gas phase

3.1.1. Ground state geometry and vertical excitation spectrum of IA, MIA, and LF

The DFT optimized ground state (S0) geometry of MIA is displayed in Fig. 2. An overview over the most important structural parameters of IA, MIA, and LF can be seen in Table 1. Experimental data for crystalline 10-methylisoalloxazine is available [42] and shows good agreement with the results of our calculations. A comparison of MIA with IA and LF shows that methylation has only minor influence on the geometry. As expected, the addition of a methyl group at N(10) position shows a widening of the C(9)—N(10) and the N(10)—C(10a) bonds. Methylation at C(7) and C(8) position shows a remarkable widening only of the C(7)—C(8) bond by about 2.0 pm which can mainly be explained by sterical effects.

An overview of the vertical DFT/MRCI excitation energies of IA, MIA, and LF in the vacuum can be seen in Table 2. To aid the discussion, the shape and ordering of relevant molecular frontier orbitals of MIA are depicted in Fig. 3. The highest occupied molecular orbital (HOMO) shows electron density mainly at the benzene part of the isoalloxazine ring and the N(1) atom. In contrast, the lowest unoccupied MO (LUMO) shows an increased electron density in the region of the C(4)—C(4a) and C(4a)—C(10a) bonds where the wave function exhibits binding character and in the region of the C(4a) —N(5) where the wave function amplitudes have opposite sign and thus are antibonding. The two MOs, n_{O1} and n_{O2}, are mainly the minus and plus linear combinations of the in-plane lone pairs belonging to the two oxygen atoms. The same principle applies for the two MOs, n_{N1} (not shown) and n_{N2}. The shape of the molecular orbitals of IA and LF hardly differs from the orbitals shown here. It is noticeable that the HOMO and LUMO are very similar for various quantum chemical treatments [15,16,13,12]. For the SAC-CI treatment [12] the ordering of the *n*-MOs changes mainly due to the usage of Hartree–Fock (HF) orbitals.

Unfortunately, there is no experimental gas phase spectrum available for comparison. The comparison with experimental absorption maxima will be postponed to Section 3.2 where results including a solvent model are presented.

In agreement with previous CASPT2, [13] SAC-CI, [12] and TDDFT [14,10,15,16] studies all three experimentally observed bands of the absorption spectrum of flavins can be assigned to $(\pi \rightarrow \pi^*)$ transitions. In the singlet manifold, the lowest-lying excited state is

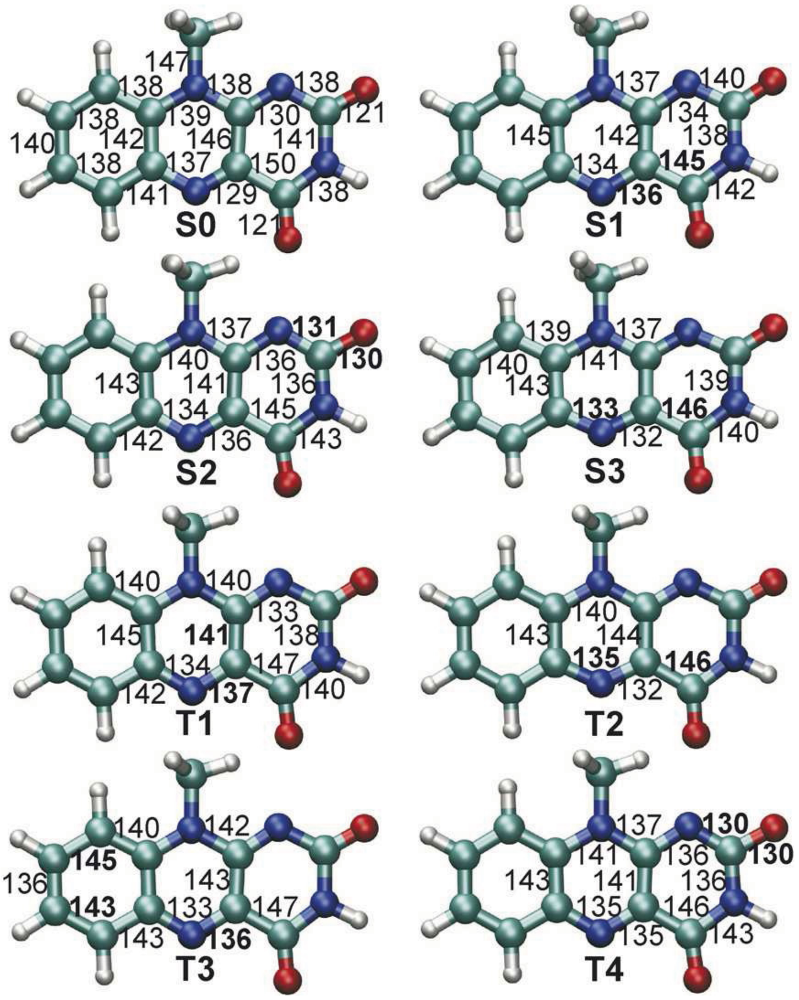

Fig. 2. MIA: TDDFT equilibrium structures of excited states in comparison with the ground-state geometry. (B3LYP,TZVP) All bond lengths in pm, only changes larger than 1 pm with respect to the S0 geometry are shown.

Table 2

IA, MIA, and LF: vertical singlet and triplet excitation energies ΔE [eV] in comparison with recent quantum chemical calculations

State		Electronic structure (MIA)	ΔE					$f(r)$ MIA	μ MIA
			IA [a]	MIA [a]	LF [a]	IA [b]	LF		
S_0	$1^1A'$	(0.95) Ground state	0.00					0.0000	8.20
S_1	$2^1 1A'$	(0.83) $\pi_H \rightarrow \pi^*_L$	3.03	3.00	2.94	3.09	2.46 [c], 3.04 [d]	0.2849	9.75
S_2	$1^1A''$	(0.44) $n_{O2} \rightarrow \pi^*_L - (0.33)n_{N2} \rightarrow \pi^*_L$	3.16	3.18	3.21	3.75	3.59 [c], 3.09 [d]	0.0025	4.17
S_3	$2^1A''$	(0.42) $n_{N2} \rightarrow \pi^*_L + (0.27)n_{O2} \rightarrow \pi^*_L$	3.34	3.33	3.35	3.34	3.18 [c], 3.30 [d]	0.0007	3.95
S_4	$3^1A''$	(0.59) $n_{O1} \rightarrow \pi^*_L$	3.90	3.90	3.93	4.43	3.84 [d]	0.0000	3.64
S_5	$3^1A'$	(0.74) $\pi_{H-1} \rightarrow \pi^*_L$	3.94	3.93	3.84	4.28	3.84 [c], 3.86 [d]	0.1811	12.97
S_6	$4^1A'$	(0.74) $\pi_{H-2} \rightarrow \pi^*_L$	4.05	4.07		4.69	–	0.0350	1.07
⋮	⋮	⋮	⋮	⋮	⋮	⋮	⋮	⋮	⋮
S_9	$6^1A'$	(0.56) $\pi_H \rightarrow \pi^*_{L+1} - (0.10)\pi_H \rightarrow \pi^*_{L+2}$	4.86	4.84	4.77	5.00	4.55 [c], 4.91 [d]	0.6275	7.76
S_{10}	$7^1A'$	(0.37) $\pi_H \rightarrow \pi^*_{L+2} + (0.17)\pi_H \rightarrow \pi^*_{L+1}$	5.01	5.00	4.91	5.37	4.86 [c]	0.1753	7.41
T_1	$1^3A'$	(0.85) $\pi_H \rightarrow \pi^*_L$	2.31	2.30	2.24	2.51	–	–	8.19
T_2	$1^3A''$	(0.59) $n_{N2} \rightarrow \pi^*_L - (0.14)n_{O2} \rightarrow \pi^*_L$	2.85	2.87	2.90	2.97	–	–	7.03
T_3	$2^3A'$	(0.76) $\pi_{H-1} \rightarrow \pi^*_L$	3.12	3.08	3.05	–	–	–	12.38
T_4	$2^3A''$	(0.55) $n_{O2} \rightarrow \pi^*_L$	3.18	3.20	3.21	3.70	–	–	1.65

In addition the dominant excitations, c^2-values, oscillator strengths $f(r)$ and dipole moments μ [Debye] of MIA are given.

[a] DFT/MRCI(TZVP), this work.

[b] CASPT2(6-31G(d)), Ref. [13].

[c] SAC-CI(D95V(d)), Ref. [12].

[d] TDDFT(B3LYP/6-31G(d)), Ref. [16].

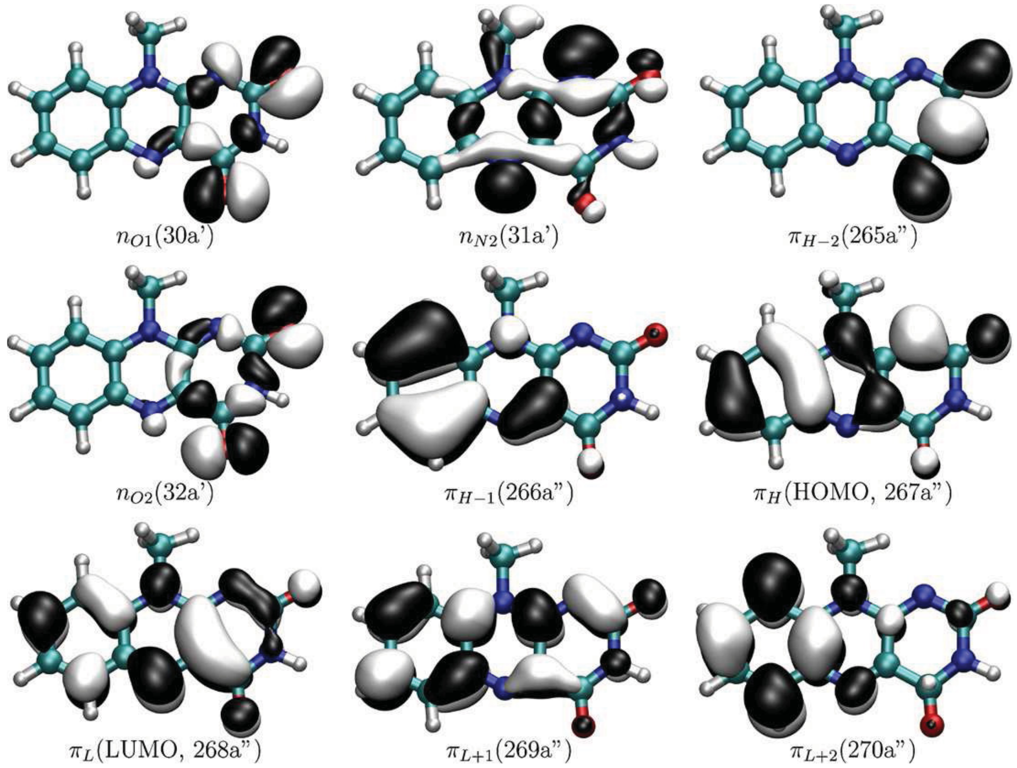

n_{O1}(30a') n_{N2}(31a') π_{H-2}(265a")

n_{O2}(32a') π_{H-1}(266a") π_H(HOMO, 267a")

π_L(LUMO, 268a") π_{L+1}(269a") π_{L+2}(270a")

Fig. 3. MIA: Frontier orbitals at the optimized ground-state (S0) geometry (isovalue = 0.3).

dominated by the ($\pi_H \rightarrow \pi^*_L$) (HOMO–LUMO) transition. With an oscillator strength of 0.287 this transition can be assigned to the lowest energy band in the experimental spectrum. For IA, Climent et al. [13] find a CASPT2 energy of 3.09 eV which is very similar to our finding of 3.03 eV. In case of LF the most recent TDDFT treatment [16] has found an energy of 3.04 eV which is in good agreement with the DFT/MRCI and experimental energies. In contrast, the vertical SAC-CI energies for this transition are lower by 0.33 eV. The second excited $^1A'$ state (S_5) can be assigned to the second visible band in the spectrum. This state is mainly dominated by the ($\pi_{H-1} \rightarrow \pi^*_L$) transition. Its oscillator strength of 0.181 is somewhat smaller than for the first optically bright transition. The vertical CASPT2 excitation energy for IA is much higher (4.28 eV) than our value of 3.94 eV. For LF our DFT/MRCI, the SAC-CI and the TDFFT results all show similar values. The third experimentally observed band of the absorption spectrum can be assigned to the sixth excited $^1A'$ state (S_9) state. This state is represented by a minus linear combination of the two excitations ($\pi_H \rightarrow \pi^*_{L+1}$) and ($\pi_H \rightarrow \pi^*_{L+2}$), with approximately 56% contribution from the first excitation and only 11% from the second excitation. With an oscillator strength of 0.628 it is the strongest transition in the energy regime up to 5.5 eV. The following excited state is the corresponding plus linear combination with only 17% contribution from the ($\pi_H \rightarrow \pi^*_{L+1}$) excitation and 37% from the ($\pi_H \rightarrow \pi^*_{L+2}$) excitation. With 0.175 the oscillator strength of this $7^1A'$ state is much weaker than for the $6^1A'$ state, hinting that it is the ($\pi_H \rightarrow \pi^*_{L+1}$) excitation that is optically bright. For LF the multi-reference character of these two states is more pronounced ($6^1A'$ state with 42% and 25%, $7^1A'$ state with 32% and 29%), thus the oscillator strengths of the two states becomes more even ($6^1A'$ state with 0.491 and $7^1A'$ state with 0.346). The vertical CASPT2 excitation energies for IA are (much) higher (5.00 eV and 5.37 eV) than our values of 4.86 eV and 5.01 eV. For LF the SAC-CI of the $6^1A'$ state is by 0.22 eV lower than our value of 4.77 eV, while the TDDFT result is 0.14 eV higher. For the $7^1A'$ state our DFT/MRCI and the SAC-CI results show similar values.

Contrary to the low-lying (partly) visible $^1(\pi \rightarrow \pi^*)A'$ states which have been discussed quite homogeneously in the literature, the description of the $^1(n \rightarrow \pi^*)$ states differs significantly in the different quantum chemical treatments. Between the first and second visible band we find three $^1(n \rightarrow \pi^*)$ states with small or evanescent oscillator strength. The first $^1A''$ state is represented by a minus linear combination of the two excitations ($n_{O2} \rightarrow \pi^*_L$) and ($n_{N2} \rightarrow \pi^*_L$), where both c^2-values are quite similar. With an excitation energy ranging between 3.16 eV and 3.21 eV in the three isoalloxazines IA, MIA,and LF this state lies up to 0.25 eV above the first visible $2^1A'$ state. A close proximity or even a state flip, as observed for TDDFT treatments, [14,10,15,16] is not found with DFT/MRCI, supporting a similar conclusion drawn by Neiss et al. [15] on the basis of DFT/MRCI calculations employing a smaller basis set. The second $^1A''$ state is the corresponding plus linear combination with approximately 42% contribution from the ($n_{N2} \rightarrow \pi^*_L$) excitation and only 27% from the ($n_{O2} \rightarrow \pi^*_L$) excitation. The vertical DFT/MRCI excitation energies of 3.33–3.35 eV for the three isoalloxazines agree with the TDDFT value for LF. A comparison of the energies and dominant contributions of these two states with those of CASPT2 and SAC-CI calculations shows that in the latter treatments no multi-reference character is reported. Furthermore, the order of states is flipped with respect to our results, with the ($n_{N2} \rightarrow \pi^*_L$) excitation as the first $^1A''$ state and the ($n_{O2} \rightarrow \pi^*_L$) excitation heavily blue-shifted. Reasons for this behavior can be seen in the different energetic order of the MOs (SAC-CI, [12] see above) and in an insufficiently large CAS space. According to Climent et al. [13] only one n-orbital per state was included into the active space for the calculation of the ($n \rightarrow \pi^*$) states. By that particular choice of the active space a mixing of the ($n_N \rightarrow \pi^*_L$) and ($n_O \rightarrow \pi^*_L$) excitations as found here is excluded. The third $^1A''$ state is dominated by the single excitation ($n_{O1} \rightarrow \pi^*_L$). With an excitation energy of 3.84–3.94 eV it lies in close proximity to the second visible state ($3^1A'$).

As in the singlet case, the lowest-lying triplet excited state is dominated by the ($\pi_H \rightarrow \pi^*_L$) (HOMO–LUMO) transition. The excitation energy of the $1^3A'$ state ranges between 2.24 eV and 2.31 eV, clearly below the corresponding singlet state. The second excited triplet (T_2) state is the minus linear combination of the two excitations ($n_{O2} \rightarrow \pi^*_L$) and ($n_{N2} \rightarrow \pi^*_L$). In contrast to the corresponding singlet state the latter excitation dominates with a c^2-value of 58.7. For all investigated isoalloxazines this $1^3A''$ state also lies below the S_1 states in the vertical excitation spectrum. The T_3 state exhibits ($\pi \rightarrow \pi^*$) character with the ($\pi_{H-1} \rightarrow \pi^*_L$) excitation as the leading conformation. In the vertical excitation spectra of the isolated isoalloxazines the T_3 state is situated energetically between the S_1 and S_2 state. (For further discussion see Section 3.1.3.) The following triplet state (T_4) is dominated by the ($n_{O2} \rightarrow \pi^*_L$)transition. In difference to the corresponding state in the singlet manifold, the multi-reference character is much less pronounced.

As our calculations show, the low-lying excitation energies for IA, MIA, and LF are very similar. In the following we therefore, if not stated otherwise, only discuss MIA.

3.1.2. Excited state geometries and adiabatic transition energies of MIA

For the calculation of all excited states the C_s-symmetry constraint has been retained. The geometries are depicted in Fig. 2 and the electronic excitation energies calculated with DFT/MRCI at the respective geometries can be seen in Fig. 4. Numerical values of the adiabatic excitation energies are collected in Table 3.

Table 3
MIA: adiabatic singlet and triplet DFT/MRCI excitation energies ΔE_{adia} [eV], scaled zero-point vibrational energy corrections (ZPVE) [eV] of low-lying excited states

Geometry	ΔE_{adia}	PEH	ZPVE
S1	2.69	S_1	−0.08
S2	2.90	S_1	−0.07
S3	2.92	S_1	−0.13
S5	3.47 [a]	S_3	–
T1	2.06	T_1	−0.11
T2	2.58	T_2	−0.04
T3	2.79	T_2	−0.11
T4	2.89	T_2	–

[a] Adiabatic excitation energy at the T3 geometry (see text for explanation).

3.1.2.1. S1 and T1 electronic structures. We obtaina minimum nuclear structure for the ($\pi \rightarrow \pi^*$) excited S1 state in which the C(4a) —N(5) bond is elongated by 6.7 pm and the C(4) —C(4a) and C(4a) —C(10a) bonds are shortened by 4.9 pm and 3.8 pm, respectively. This finding is in good agreement with those of Ref. [13,12] and corresponds to the change of nonbonding character of the π_H orbital in that region to an antibonding (C(4a) —N(5)) and bonding (C(4) —C(4a), C(4a) —C(10a)) character in π_L. At the level of TDDFT (B3LYP), this structure only presents a saddle-point on the S_1 PEH. One imaginary frequency ($\bar{\nu}_1 = i150\,\text{cm}^{-1}$) is obtained. It corresponds to an A″-symmetric normal mode which can be described as a mixture of an *oop* deformation of the N(1) and O(2) atoms of the ring and a rotation of the 10-methyl group. We performed a calculation of the TDDFT and DFT/MRCI energies of the S_1 following the distortion along the imaginary A″ normal mode. While TDDFT exhibits an extremely shallow double minimum potential

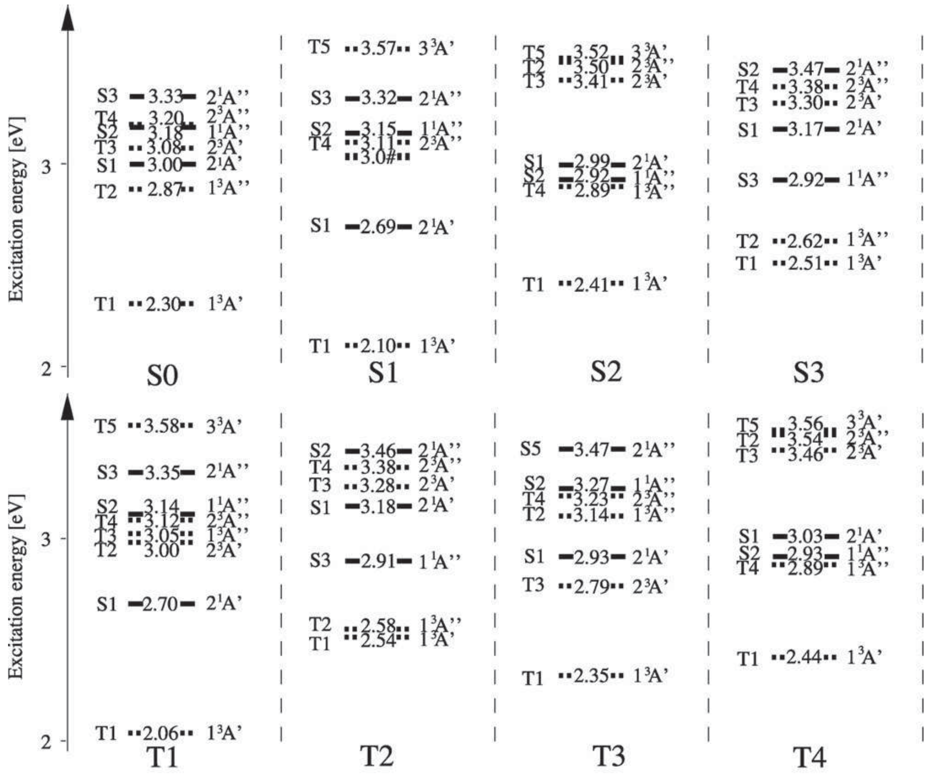

Excitation energies ot the triplet states from lowest to highest: 3.03 (1A",T2) and 3.04 (2A',T3)

Fig. 4. MIA: Electronic excitation energies (DFT/MRCI, [eV]) at various excited state geometries. For a better comparability, the electronic ground state energy at the S0 geometry has been chosen as the common origin.

well, DFT/MRCI clearly favors the C_s-symmetric structure. This phenomenon has been encountered before in psoralen, cytosine, and thiophene [43,40,41] and is considered an artifact of the TDDFT (B3LYP) method. This imaginary mode can also be observed in LF and IA.

From an energetic point of view, the relaxation effects on the S_1 state are moderate. Its adiabatic excitation energy amounts to 2.69 eV, corresponding to a stabilization by 0.34 eV. At the same time the electronic ground state is destabilized by 0.40 eV yielding a vertical emission energy of 2.28 eV. Due to the small energy difference, the rate of fluorescence to the ground state, calculated at the S_1 minimum, is rather low ($k_F \sim 5 \times 10^7\,s^{-1}$). The experimental rate of fluorescence of MIA in 2-methyltetrahydrofuran (77 K) [44] has been measured to be $k_F = 6.5 \times 10^7\,s^{-1}$ and is in excellent agreement with our calculated rate.

The excitation energies of the other low-lying singlet excited states are not much affected by the geometry relaxation. It is interesting to note that the second excited triplet state is blue-shifted to 3.03 eV at the S1 minimum and is thus located above the S_1, meaning that during the relaxation from the Franck–Condon (FC) region an intersection between the S_1 and T_2 PEH occurs. The crossing between singlet and triplet PEHs as observed here could serve as a funnel for the population of the triplet manifold (see Section 3.1.3).

The geometry of the T1 state is very similar to that of the S1 state. The widening of the C(4a) —N(5) and shortening of the C(4a) —C(10a) bond are more pronounced than at the S1 geometry. This similarity is also reflected in the adiabatic excitation energies. The adiabatic excitation energy of the T_1 state amounts to 2.06 eV in the gas phase.

3.1.2.2. S2 and T4 electronic structures. The computed structure for the (n → π*) excited S2 state is mainly influenced by the pronounced stretching of the C(2) —O(2) bond by 9.4 pm and the shortening of the N(1) —C(2) bond by 7.7 pm. This is in excellent accordance to the promotion of electron density from the n_{O2} orbital into the LUMO. Contrary to the ground state geometry the electron density of this *n* orbital is primarily localized at the O(2). Furthermore the C(4a) —N(5) bond is elongated by 6.6 pm and the C(4) —C(4a) and C(4a) —C(10a) bonds are shortened by 5.1 pm and 5.2 pm, respectively. At the level of TDDFT (B3LYP), this structure constitutes a minimum on the S_1 PEH. At this point of coordinate space the reverse ordering of the states is corroborated by the DFT/MRCI calculations. The S1 and S2 states are very close in energy ($\Delta E = 0.07$ eV) at this geometry, though. It is anticipated therefore that strong vibronic coupling may occur in the gas phase. According to the model by Lim [45] the proximity effect between a $^1(\pi \rightarrow \pi^*)$ and a $^1(n \rightarrow \pi^*)$ can lead to substantial radiationless decay of the $^1(\pi \rightarrow \pi^*)$ population by internal conversion to the ground state mediated by the $^1(n \rightarrow \pi^*)$ state. Experimentally the S2 state has never been observed, because of the low oscillator strength. The geometry of the T4 state, i.e., the triplet state corresponding to the S2 electronic structure, is very similar to the S2 geometry. It constitutes a minimum on the T_2 PEH, located energetically only slightly below the S2 minimum.

3.1.2.3. S3 and T2 electronic structure. We obtain a nuclear structure for the (n → π*) excited S3 state where the C(4) —C(4a) and C(5) —C(5a) bonds are shortened by 4.0 pm and 3.9 pm, respectively. At the TDDFT (B3LYP) level this structure is found to be a saddle point on the S_1 PEH. One imaginary frequency ($\tilde{\nu}_1 = i43$) is found. This corresponds to an A″-symmetric normal mode which can be described as a mixture of an *oop* deformation of the ring and a rotation of the 10-methyl group. A subsequent calculation of the DFT/MRCI and TDDFT (B3LYP) energies along the distortion of this imaginary normal mode shows the same picture as for the A″-symmetric imaginary normal mode at the S1 geometry, i.e., the *oop* deformation is an artifact of the TDDFT (B3LYP) treatment.

With regard to the energy, the relaxation effect on the optimized S3 state is stronger than for the S2 structure and yields an adiabatic excitation energy of 2.92 eV. As in TDDFT (B3LYP) this electronic state constitutes a local minimum on the S_1 PEH.

Again, the geometry and the excitation energy of the corresponding triplet state (T2) show no major difference. The optimized T2 state is red-shifted close to the T1 state at this geometry (difference around 0.04 eV) but the two states still retain the same order as at the ground state geometry.

3.1.2.4. S5 and T3 electronic structures. Due to root flipping the minimum nuclear arrangement of the (π → π*) S5 state could not be computed and only that of the corresponding triplet state is available. The computed minimum nuclear structure of the T3 state is characterized by the elongation of the C(4a) —N(5), C(6) —C(7), and C(8) —C(9) bonds by 7.0 pm, 5.5 pm, and 6.3 pm, respectively, and the shortage of the C(7) —C(8) bond by 4.2 pm. Looking at the π_{H-1} and π_L orbitals, the geometry shifts are in accordance to the change of character from bonding to antibonding for the three elongated bonds and vice versa for the shortened bond. The geometry relaxation leads to a stabilization by 0.33 eV and yields an adiabatic excitation energy of 2.79 eV. At the DFT/MRCI level this state exhibits a local minimum on the T_2 PEH. A calculation of the harmonic normal modes at TDDFT level yields a true minimum. The corresponding singlet state S5 is found to be on the S_3 PEH. Since it was not possible to optimize the S5 geometry, the adiabatic excitation energy of the S5 at the optimized T3 geometry is used. This is justified by the observation that for all other pairs of singlet and triplet states the adiabatic excitation energies at the two respective geometries are less than 0.05 eV apart.

3.1.3. Inter-system crossing

As mentioned in the introduction, the photochemical reaction of FMN with a nearby cysteine residue of the LOV domain takes place in an intermediate triplet state. It is accepted in the literature that this state is the first excited triplet state and that triplet formation happens very efficiently at a timescale of nanoseconds after absorption of a photon [46]. Inspection of Fig. 4 shows that, from an energetic point of view, the T1 and T2 are possible candidates for efficient ISC from S1 in the gas phase. As noted above, the energy gap between the S1 and T2 minima is small (0.11 eV). The energetic order of the T_2 and the S_1 PEHs even changes when proceeding from the S0 to the S1 geometry, resulting in an intersection between the two PEHs, which should be easily accessible from the Franck–Condon (FC) region. Since the two crossing PEHs are of (π → π*) and (n → π*) character, substantial spin–orbit coupling matrix elements between the two states can be expected, and an efficient population transfer to the triplet manifold might be possible.

A path between the S0 and the S1 geometry has been linearly interpolated for all three flavins. In Fig. 5 (top) the DFT/MRCI energies of low-lying states along that path in MIA can be seen. As expected, the crossing of the T_2 and the S_1 PEHs can be reached from the FC region without barrier. The excitation energy amounts to approximately 2.9 eV here. Spin–orbit coupling at the crossing point is substantial, with SOME values of 8.3(9.2) cm^{-1} and 1.9(2.7) cm^{-1} for the *x* and *y* components in MIA(IA), respectively. For LF similar results have been obtained. At CASPT2 level a homologous path has been found by Climent et al. for IA with SOME values between 2 cm^{-1} and 11 cm^{-1} [13].

The results of our evaluation of the rate constants $k_{ISC}(S \rightsquigarrow T)$ for singlet–triplet ISC in IA are summarized in Table 4. A more detailed

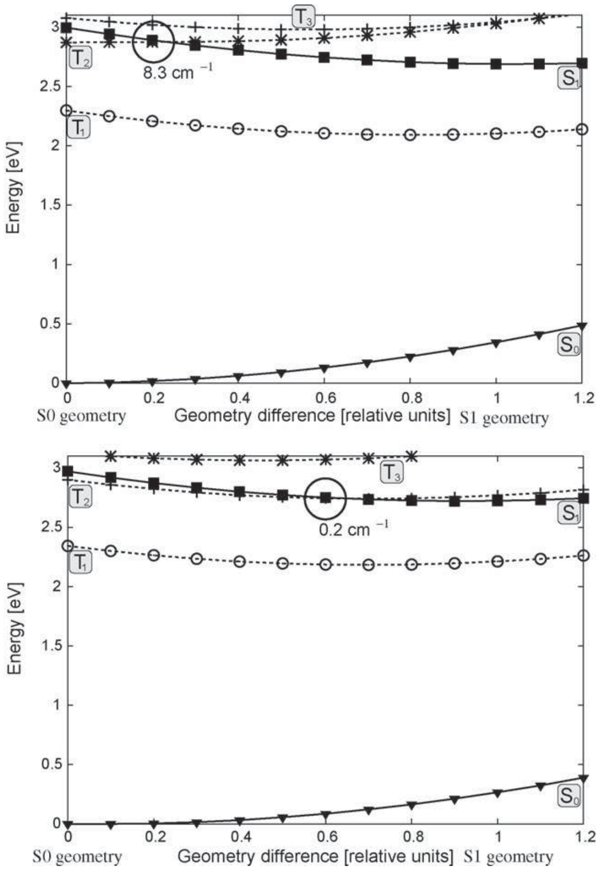

Fig. 5. MIA: DFT/MRCI energies of low-lying states along a linearly interpolated path between the S0 and the S1 geometry for the vacuum (top) and the COSMO environment (bottom). Singlet energy profiles are represented by solid lines, triplet profiles by dashed lines. Triangles symbolize the ground state, stars a ($n \rightarrow \pi^*$) state and circles, squares and plus signs ($\pi \rightarrow \pi^*$)states. For the crossing points the largest components of the spin–orbit coupling matrix elements $\langle T_2|H_{SO}|S_1\rangle$ are given.

overview about the calculations with further information about the parameters used, can be seen in the ESM (Table 2).

Let us first discuss the results of the Condon approximation, i.e., when only direct spin–orbit coupling is taken into account. In this case, only the ISC processes from the zero vibrational level of the S1 ($\pi \rightarrow \pi^*$) state to the vibrational states in the T2 ($n \rightarrow \pi^*$) potential well are fast. Due to the small energy gap between the S1 and T2 minima (which is further reduced due to the higher zero-point vibrational energy in the T2 state) the density of vibrational states in the final T2 potential well is small—far from the ideal situation of a quasi-continuum for which the Fermi Golden Rule was derived. The search interval η therefore had to be rather large. On the other hand, calculated relative energies are always afflicted with uncertainties. To study the sensitivity of the ISC rates with respect to the chosen value of the η parameter and the size of the energy gap, we carried out numerous test calculations the results of which are given in Tables 2 and 5 of the ESM. With the exception of the cases where only very few vibrational levels are found in the search interval, the calculated ISC rates k_{ISC} range between $\sim 1 \times 10^9$ s^{-1} and $\sim 2 \times 10^9$ s^{-1} for the $S_1 \rightsquigarrow T_{2x}$ channel. Due to the smaller electronic coupling matrix element (which enters quadratically) the corresponding $S_1 \rightsquigarrow T_{2y}$ ISC rate is calculated to be one order of magnitude smaller.

Table 4
IA: calculated rate constants k_{ISC} [s^{-1}] (right) for ($S_1 \rightsquigarrow T_n$) ISC channels (left) in the vacuum

Channel $i \rightsquigarrow f$	ΔE^{ad}	Direct SO, $\lvert\langle i\lvert\hat{H}_{SO}\rvert f\rangle\rvert_{q0}$	Rate, k_{ISC}
$S_1 \rightsquigarrow T_{1x}$	−0.65	–	3.1×10^6
$S_1 \rightsquigarrow T_{1y}$	−0.65	–	2.3×10^6
$S_1 \rightsquigarrow T_{1z}$	−0.65	0.9×10^{-2}	4.0×10^1
$S_1 \rightsquigarrow T_{2x}$	−0.11	13.7	$\sim 10^9$
$S_1 \rightsquigarrow T_{2y}$	−0.11	6.8	$\sim 10^8$
$S_1 \rightsquigarrow T_{2y}$	−0.11	–	–

Remaining columns: adiabatic electronic energy difference ΔE^{ad} [eV], direct SOME $\lvert\langle i\lvert\hat{H}_{SO}\rvert f\rangle\rvert_{q0}$ [cm^{-1}].

Table 5
MIA: vertical (**v**) and adiabatic (**a**) singlet and triplet DFT/MRCI excitation energies ΔE_{adia} [eV] in comparison with experimental data

Transition		ΔE_{adia}			Experiment		
		Vac.	AcN	H_2O	2MTHF [a]	AcN [b]	H_2O [c]
$S_0 \rightarrow S_1$	**v**	3.00	2.96	2.94	2.88	2.84	2.85
	a	2.69	–	–	2.70, 2.72	–	–
$S_0 \rightarrow S_5$	**v**	3.94	3.80	3.61	3.82	3.78	3.62
	a	3.47 [d]	–	–	3.53	–	–
$S_0 \rightarrow S_9$	**v**	4.86	4.86	4.90	–	4.65	4.70

AcN: acetonitrile, 2MTHF: 2-methyltetrahydrofuran.

[a] Absorption spectrum of 3,10-dimethylisoalloxazine in 2-methyltetrahydrofuran at 300 and 77 K, see Ref. [44].

[b] Absorption maximum in acetonitril, Ref. [11]

[c] Absorption maximum in water, Ref. [11]

[d] Adiabatic excitation energy at the T3 geometry (see text for explanation).

Tatchen et al. [35] and Perun et al. [47] recently observed that vibronic spin–orbit coupling remarkably enhances the ISC processes between two ($\pi \rightarrow \pi^*$) states. As a result of this Herzberg–Teller type interaction, the rates of the transitions $S_1(\pi{\rightarrow}\pi{*}) \rightsquigarrow T_{1x,1y}(\pi{\rightarrow}\pi{*})$ are increased from $\sim 10^{-2}$ s^{-1} to $\sim 10^6$ s^{-1}, but they cannot compete with the rates involving the respective T_2 levels.

Since the fastest process ($k_{\mathrm{ISC}} \sim 10^9$ s^{-1}) dominates the rate constant, we estimate the ISC from the $S_1(\pi{\rightarrow}\pi{*})$ state to the triplet manifold in the gas phase to take place at the timescale of nanoseconds, more than one magnitude faster than the spin-allowed radiative transition to the electronic ground state. This result indicates that after blue light absorption a significant part of excited state population could be transferred into the triplet manifold before the excited state population is depleted by fluorescence or internal conversion.

3.2. *Solvent effects*

As stated above we could not compare our calculated vacuum DFT/MRCI excitation energies with experimental gas phase data, but had to refer to measurements in solution (water and acetonitrile). As described in the introduction, the second visible band of isoalloxazines shows a pronounced solvatochromism. Since solvent effects have a substantial effect on the absorption spectra, they have been taken into account employing three models: (II) a continuum model using COSMO, (III) micro-hydration with four explicit water molecules (see Fig. 6) and (IV) a combination of both. In addition we have carried out COSMO calculations for a dielectric constant of $\epsilon = 36$ corresponding to acetonitrile (AcN).

3.2.1. *Vertical excitation energies in water*

The excitation energies of MIA in aqueous solution of the models II-IV are displayed and compared to those of the vacuum (I) in Fig. 7. In a simplified picture, the energetic stabilization or destabilization of the ground and excited states in polar solvents is connected to

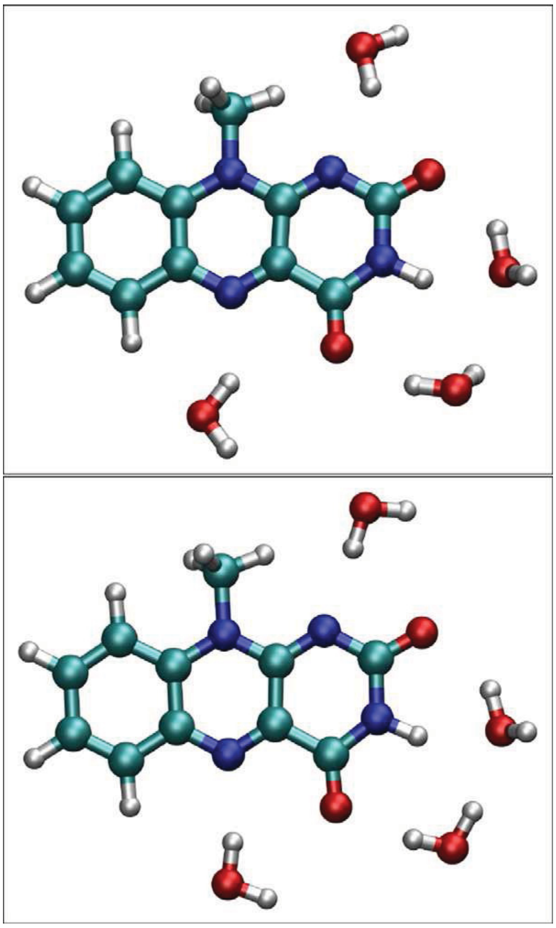

Fig. 6. MIA: Micro-hydrated cluster in the vacuum (top) and with COSMO (bottom).

their dipole moments and the extent of polarization they induce in the surrounding solvent. According to the dipole moments in Table 2, the effect on the excitation energies of the $(\pi_H \rightarrow \pi^*_L)$ and $(\pi_H \rightarrow \pi^*_{L+1})$ states should be small while the effect on the $(\pi_{H-1} \rightarrow \pi^*_L)$, and $(n \rightarrow \pi^*)$ states is expected to be strong.

In agreement with experimental trends and earlier quantum chemical investigations, [12,16] the excitation energies of the first and third visible transitions ($^1(\pi_H \rightarrow \pi^*_L)$ and $^1(\pi_H \rightarrow \pi^*_{L+1})$ states) are hardly affected by solvent effects, while the second visible transition ($^1(\pi_{H-1} \rightarrow \pi^*_L)$ state) is red-shifted by about 0.3 eV due to solvation in water. The vertical excitation energy obtained with our best solvation model (IV), 3.61 eV, agrees excellently with the experimental band maximum of 3.63 eV in neutral aqueous solution at room temperature [44]. It is seen that COSMO alone underestimates the solvent shift of that state. A comparison of the models (II) and (III) shows that a major part of the solvatochromism originates from hydrogen bonding. This finding is in accordance to the observation of Sikorska et al. [10] that the proticity of the solvents plays a more important role for the solvatochromism than the polarity. The corresponding triplet states ($^3(\pi_{H-1} \rightarrow \pi^*_L)$ and $^3(\pi_H \rightarrow \pi^*_L)$) show the same behavior as their singlet counterparts. The $^3(\pi_{H-1} \rightarrow \pi^*_L)$ state is red-shifted by up to 0.3 eV and lies, as soon as solvation is included, below the $^3(n_{N2} \rightarrow \pi^*_L)$ state. As will be seen in Section 3.2.2, these solvent shifts have a large impact on the ISC mechanism.

Within the manifold of $(n \rightarrow \pi^*)$states, the blue-shifts due to solvent effects are more pronounced for the $(n_{O2} \rightarrow \pi^*_L)$ states than for the $(n_{N2} \rightarrow \pi^*_L)$ states, which is also observed in Ref. [12]. Qualitatively this is easily understood. As shown in Fig. 6, the water molecules form strong hydrogen bonds with the oxygen acceptors. Because of the hydrogen bond interaction these lone-pair orbitals are stabilized. A promotion of one n_{O2} electron to the π^* orbital thus requires significantly more energy. As a result, solvation in water pushes the $(n_{O2} \rightarrow \pi^*_L)$ structure, which used to correspond to the S2 structure in the vacuum, energetically far above the S1 $^1(\pi_H \rightarrow \pi^*_L)$ structure and even above the $(n_{N2} \rightarrow \pi^*_L)$ structure. A participation of the S2 structure in the radiationless decay of the S1 state is therefore hindered. As for the $(\pi \rightarrow \pi^*)$ states, the prediction of solvent effects with COSMO underestimates the spectroscopic shift of the $(n \rightarrow \pi^*)$ states. In connection with the relaxation pathway the position of the $^3(n_{N2} \rightarrow \pi^*_L)$ state is of special interest. Due to the pronounced blue-shift for the models with conductor-like screening this state is no longer accessible from the S1 state. If only hydrogen bonding is involved, the $^3(n_{N2} \rightarrow \pi^*_L)$ state is almost degenerate to the $^1(\pi_H \rightarrow \pi^*_L)$ and $^3(\pi_{H-1} \rightarrow \pi^*_L)$ states. In protic systems with low polarity, such as proteins, it is possible that both triplet states could be involved in the ISC mechanism. A closer investigation of these systems is in progress and beyond the scope of this work.

3.2.2. Inter-system crossing in water

In order to estimate the impact of the solution on the relaxation pathway, DFT/MRCI calculations have been carried out with model (II) at the same geometries as in Section 3.1.3. In Fig. 5(bottom) the

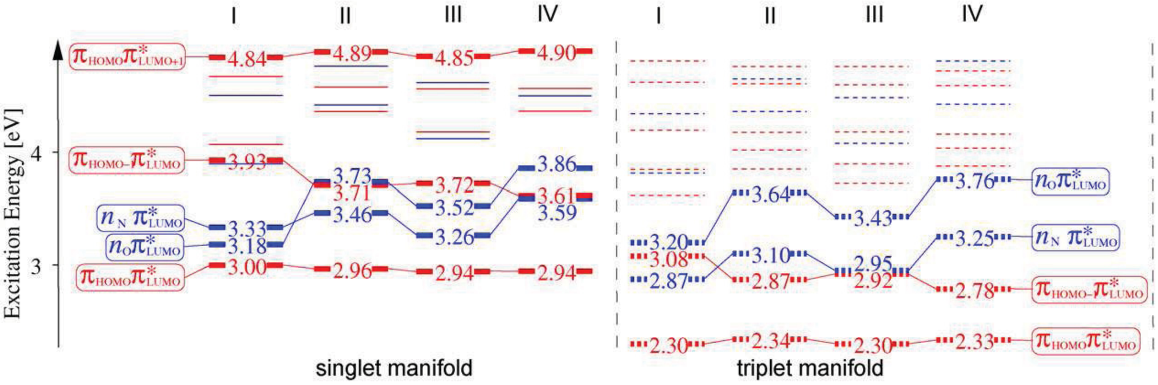

Fig. 7. MIA: Comparison of the vertical excitation energies for the vacuum (I), solvation with COSMO (II), micro-hydration with four explicit water molecules (III), and a combination of the latter (IV).

Table 6
IA: calculated rate constants k_{ISC} [s^{-1}] for ($S_1 \rightsquigarrow T_n$) ISC channels in aqueous solution

Channel $i \rightsquigarrow f$	ΔE^{ad}	Direct SO, $\lvert\langle i\lvert\hat{\mathrm{H}}_{\mathrm{SO}}\rvert f\rangle\rvert_{q0}$	Rate, k_{ISC}
$S_1 \rightsquigarrow T_{1x}$	−0.56	$< 10^{-3}$	3.6×10^5
$S_1 \rightsquigarrow T_{1y}$	−0.56	$< 10^{-3}$	2.8×10^5
$S_1 \rightsquigarrow T_{1z}$	−0.56	0.9×10^{-2}	1.1×10^2
$S_1 \rightsquigarrow T_{2x}$	−0.12	$< 10^{-3}$	$\sim 10^7$
$S_1 \rightsquigarrow T_{2y}$	−0.12	$< 10^{-3}$	$\sim 10^8$
$S_1 \rightsquigarrow T_{2y}$	−0.12	0.3×10^{-2}	1.1×10^1

For further information see 4.

DFT/MRCI energies of low-lying states along the path can be seen.

As noted above, the $^3(\mathrm{n}_{\mathrm{N2}} \rightarrow \pi^*_{\mathrm{L}})$ state is significantly blue-shifted and therefore energetically no longer accessible from low-lying vibrational levels of the S1 state. Due to the strong red-shift, the $^3(\pi_{\mathrm{H-1}} \rightarrow \pi^*_{\mathrm{L}})$ electronic structure (T3) represents the second excited triplet state (T_2) in aqueous solution. Near the S1 minimum, a crossing of the T_2 and the S_1 PEHs takes place without barrier at an excitation energy of about 2.75 eV. Direct spin–orbit coupling at the crossing point is very small. The values for all cartesian components of the SOME in IA are less than $10^{-3}\,\mathrm{cm}^{-1}$ and indicate a dramatically slower ISC rate than in the vacuum. The impact of vibronic spin–orbit coupling on the rate constant of isoalloxazines is huge.

As shown in Table 6, the rate constants of the $S_1 \rightsquigarrow T_1$ transitions increase from $\sim 10^2\ \mathrm{s}^{-1}$ to $\sim 10^5\ \mathrm{s}^{-1}$ when vibronic interactions are invoked. Nevertheless, they are much too slow to compete with the fluorescence ($k_{\mathrm{F}} \sim 5 \times 10^7\,\mathrm{s}^{-1}$). The calculated rates of the $S_1 \rightsquigarrow _{T2}$ intersystem crossing are more sensitive to the choice of computational parameters (number of coupling modes, size of the integration interval η, for details see Table 3 of the ESM) than of the $S_1 \rightsquigarrow T_1$ nonradiative transition. For the same reasons as discussed in Section 3.1.3, a search interval width of merely $0.1\,\mathrm{cm}^{-1}$ must be considered too small for potential wells lying so close in energy. It is interesting to observe that the rates of the $S_1 \rightsquigarrow T_2$ nonradiative transitions depend markedly on the number of coupling modes employed (see Table 3 of the ESM). In this case it is not sufficient to include the most strongly coupling modes. Astoundingly, but very comforting, the results are quite robust with respect to variations of the energy gap by a few hundred per centimeter, once a search interval of at least $10\,\mathrm{cm}^{-1}$ around the initial state is used in the calculations. With a sufficient number of vibrational states within the search interval and all coupling modes involved, the results converge towards k_{ISC} values of the order of $\sim 10^8\,\mathrm{s}^{-1}$. The experimental rate constants for FMN are $k_{\mathrm{ISC}} = 10^8\,\mathrm{s}^{-1}$ in water [4]. Although our theoretical results have to be judged with some reservation due to the fact that the excited state geometries were taken from the gas phase calculations and not relaxed in the presence of the solvent, the comparison with experiment shows that our values are in the right ballpark.

3.2.3. Excitation energies in acetonitrile and comparison with experiment

For acetonitrile solution only model II was employed at the vacuum ground state geometry. As for aqueous solution the excitation energy of the first visible transition ($^1(\pi_{\mathrm{H}} \rightarrow \pi^*_{\mathrm{L}})$state) is hardly affected by solvation in acetonitrile. For the 2A′ state the solvent shift amounts to merely 0.04 eV. Our computed vertical excitation energy of 2.96 eV fits well with the experimental band maximum of the absorption spectrum at 2.84 eV. Because of the small solvent shift of the vertical S0 → S1 excitation at the S0 geometry it appears to be save to neglect solvent effects when comparing energies of this electronic structure at other geometries, too. Our calculated gas phase value for the adiabatic S1 energy agrees very well with the experimental band origin of MIA in 2-methyltetrahydrofuran [44]. The vertical emission energy in the vacuum is calculated to be 2.35 eV which is in excellent agreement with experimental fluorescence maxima in acetonitrile and water at room temperature (2.33–2.38 eV) [11]. Due to the lower polarity of the solvent, the red-shift of the second visible transition ($^1(\pi_{\mathrm{H-1}} \rightarrow \pi^*_{\mathrm{L}})$state) is less pronounced than in water. The computed vertical excitation energy of 3.80 eV for the $3^1A'$ state agrees perfectly with the experimental band maximum of the absorption spectrum at 3.78 eV [11]. Our DFT/MRCI value of 3.47 eV shows good agreement with an experimental value of 3.53 eV [44] for the origin of the corresponding absorption band.

In the triplet manifold the order of the four lowest-lying states is retained with respect to the vacuum. In accord with the trends for the S1 state, the T1 state experiences only minor solvent effects. It is therefore not surprising that the experimental origin transition of the T1 phosphorescence at 2.14 eV [44] matches nearly perfectly with our calculated adiabatic T1 excitation energy of 2.06 eV in the vacuum. As their singlet counterparts, the two ($\mathrm{n} \rightarrow \pi^*$) states are blue-shifted whereas the $^3(\pi_{\mathrm{H-1}} \rightarrow \pi^*_{\mathrm{L}})$ state (T3) is red-shifted and becomes almost degenerate to the first excited singlet state.

4. Summary and conclusions

We have presented optimized ground-state geometries of isoalloxazine (IA), 10-methylisoalloxazine (MIA), and lumiflavin (LF). A comparison of the structure of MIA with experimental X-ray data reveals very good agreement of the structural parameters. The different states of methylation show only minor influence on the equilibrium geometries, mainly due to steric effects. Also the shape and energetic order of the frontier orbitals is very similar. A comparison of the DFT/MRCI absorption spectra of these three isoalloxazines shows that the vertical excitation energies are very much alike. This fact is in perfect agreement with experiment. To the best of our knowledge, experimental gas phase spectra in the visible and UV regions are not available so that a direct comparison with our calculated excitation energies of the isolated molecules is not possible at the present stage.

For the quantitative evaluation of inter-system crossing (ISC) rate constants, adiabatic excitation energies and vibrational frequencies of several low-lying singlet and triplet excited states have been determined. Our study shows that there are at least three minima on the first excited singlet potential energy hypersurface (PEH) corresponding to the $2^1A'$ (S_1), $1^1A''$ (S_2), and $2^1A''$ (S_3) states in the vertical spectrum.

Solvent effects have been taken into account for MIA with three different models for acetonitrile (COSMO) and water (COSMO, micro-hydration, and a combination of both). In accordance to earlier quantum chemical treatments, all three experimentally visible bands of the absorption spectrum of isoalloxazines could be assigned to ($\pi \rightarrow \pi^*$) transitions. Our calculated vertical excitation energies differ from the corresponding band maxima of the experimentally known absorption spectra by at most 0.2 eV. All models excellently reproduce the red-shift of the second visible $^1(\pi \rightarrow \pi^*)$ transition, observed in experiment and recent quantum mechanical studies. Solvent shifts of the triplet states have been presented in this work for the first time. They are particularly interesting with regard to ISC probabilities.

A linearly interpolated path has been constructed between the Franck–Condon region and the minimum geometry of the first excited $^1(\pi \rightarrow \pi^*)$ state which is responsible for the blue-light absorption. Along this path, DFT/MRCI energies have been calculated for the vacuum and aqueous solution (COSMO). On the basis of these calculations we suggest possible ISC channels. In both, vacuum and solution, we find a crossing between the S_1 and T_2 PEH along this reaction path. In agreement with earlier theoretical work by Climent et al. [13] a crossing between the $^1(\pi \rightarrow \pi^*)$ (S_1) and $^3(n \rightarrow \pi^*)$ (T_2) states is observed in the isolated flavins. Spin–orbit matrix elements (SOME) between the PEHs are substantial in that region. The minimum of the T_2 state is placed at a slightly lower energy than that of the S_1 state. The combination of favorable Franck–Condon factors between the initially populated S_1 and the T_2 state in the crossing region, substantial electronic spin–orbit coupling and a small energy gap raise the expectation of an efficient ISC. Quantitative ISC rate constants for nonradiative singlet–triplet transitions of flavins have been determined for the first time. We predict the transition to occur at the nanosecond timescale, with the individual rates being $k_{ISC} \sim 10^9\ s^{-1}$ and $k_{ISC} \sim 10^8\ s^{-1}$ for the $S_1 \rightsquigarrow T_{2x}$ and $S_1 \rightsquigarrow T_{2y}$ channels, respectively, in the vacuum. It may thus efficiently compete with or even quench the radiative decay of the S_1 state which is computed to take place at a rate of $k_F \sim 5 \times 10^7\ s^{-1}$. As a further channel for the nonradiative decay of the S_1 state our results suggest internal conversion to the ground state enhanced by the energetic proximity of the first $^1(n \rightarrow \pi^*)$ state.

In aqueous solution the $(n \rightarrow \pi^*)$ states are significantly blue-shifted so that the ISC channel described above for the isolated chromophore is no longer available. Instead, a crossing between the $^1(\pi \rightarrow \pi^*)(S_1)$ and $^3(\pi \rightarrow \pi^*)(T_2)$ states takes place. The SOME is much smaller in this case which at first glance hints at a much smaller ISC rate. However, vibronic spin–orbit coupling increases the latter to $k_{ISC} \sim 10^8\ s^{-1}$. Comparing this rate to the fluorescence rate $k_F \sim 5 \times 10^7\ s^{-1}$ we are lead to the conclusion that in water population transfer into the triplet manifold is still efficient after blue-light absorption, despite the fact that the $^3(n \rightarrow \pi^*)$ PEH cannot be reached. Internal conversion of the S_1 population is suppressed in aqueous solution due to the blue-shift of the lowest $^1(n \rightarrow \pi^*)$ state.

In this work, we propose a consistent model of the photophysical relaxation of flavin after blue-light absorption. In difference to earlier quantum chemical investigations, our work on the photophysics of flavins goes beyond the relaxation in the vacuum [13] or the impact of environmental effects on the vertical absorption spectrum [12,16]. In fact, for the first time the effect of aqueous solution on the relaxation pathway of flavins and ISC rate constants in both environments have been obtained.

What remains to be done is to investigate the photophysical relaxation of the flavin chromophore in the protein environment of the LOV domains. Work in that direction is currently undertaken.

Acknowledgment

Financial support by the Deutsche Forschungsgemeinschaft through SFB663/C1 is gratefully acknowledged.

Appendix A. Supplementary data

Supplementary data associated with this article can be found, in the online version, at doi:10.1016/j.jphotochem.2008.03.015.

References

[1] A. Losi, Photochem. Photobiol. 83 (2007) 1283–1300.
[2] W.R. Briggs, C.F. Beck, A.R. Cashmore, J.M. Christie, J. Hughes, J.A. Jarillo, T. Kagawa, H. Kanegae, E. Liscum, A. Nagatani, K. Okada, M. Salomon, W. Rüdiger, T. Sakai, M. Takano, M. Wada, J.C. Watson, Plant Cell 13 (2001) 993–997.
[3] M. Gomelsky, G. Klug, Trends Biochem. Sci. 10 (2002) 497–500.
[4] J.T.M. Kennis, S. Crosson, M. Gauden, I.H.M. van Stokkum, K. Moffat, R. van Grondelle, Biochemistry 42 (2003) 3385–3392.
[5] W. Holzer, A. Penzkofer, M. Fuhrmann, P. Hegemann, Photochem. Photobiol. 75 (2002) 479–487.
[6] W. Holzer, A. Penzkofer, P. Hegemann, Chem. Phys. 308 (2005) 79–91.
[7] T.E. Swartz, S.B. Corchnoy, J.M. Christie, J.W. Lewis, I. Szundi, W.R. Briggs, R.A. Bogomolni, J. Biol. Chem. 276 (2001) 36493–36500.
[8] M. Salomon, J.M. Christie, E. Knieb, U. Lempert, W.R. Briggs, Biochemistry 39 (2000) 9401–9410.
[9] M. Sung, T.A. Moore, P.-S. Song, J. Am. Chem. Soc. 94 (1972) 1730–1740.
[10] E. Sikorska, I.V. Khmelinskii, D.R. Worrall, J. Koput, M. Sikorski, J. Fluores. 14 (2004) 57–64.
[11] A.J.W.G. Visser, F. Müller, Hel. Chim. Acta 62 (1979) 593–608.
[12] J. Hasegawa, S. Bureekaew, H. Nakatsuji, J. Photochem. Photobiol. A 189 (2007) 205–210.
[13] T. Climent, R. González, M. Merchán, L. Serrano-Andrés, J. Phys. Chem. A 110 (2006) 13584–13590.
[14] E. Sikorska, I.V. Khmelinskii, J. Koput, J.L. Bourdelande, M. Sikorski, J. Mol. Struct. 697 (2004) 137–141.
[15] C. Neiss, P. Saalfrank, M. Parac, S. Grimme, J. Phys. Chem. A 107 (2003) 140–147.
[16] K. Zenichowski, M. Gothe, P. Saalfrank, J. Photochem. Photobiol. A 190 (2007) 290–300.
[17] R. Ahlrichs, M. Bär, H.-P. Baron, R. Bauernschmitt, S. Böcker, N. Crawford, P. Deglmann, M. Ehrig, K. Eichkorn, S. Elliott, F. Furche, F. Haase, M. Häser, C. Hättig, H. Horn, C. Huber, U. Huniar, M. Kattannek, A. Köhn, C. Kölmel, M. Kollwitz, K. May, P. Nava, C. Ochsenfeld, H. Öhm, H. Patzelt, D. Rappoport, O. Rubner, A. Schäfer, U. Schneider, M. Sierka, O. Treutler, B. Unterreiner, M. von Arnim, F. Weigend, P. Weis, H. Weiss, Turbomole (vers. 5.7), University of Karlsruhe (2004).
[18] A.D. Becke, J. Chem. Phys. 98 (1993) 5648–5652.
[19] P.J. Stephens, F.J. Devlin, C.F. Chabalowski, M.J. Frisch, J. Phys. Chem. 98 (1994) 11623–11627.
[20] R. Bauernschmitt, R. Ahlrichs, Chem. Phys. Lett. 256 (1996) 454–464.
[21] C. Kind, M. Reiher, J. Neugebauer, SNF Version 2.2.1: A Program Package for Numerical Frequency Analyses, Universität Erlangen, 1999–2002.
[22] A.P. Scott, L. Radom, J. Phys. Chem. 100 (1996) 16502–16513.
[23] S. Grimme, M. Waletzke, J. Chem. Phys. 111 (1999) 5645–5655.
[24] A.D. Becke, J. Chem. Phys. 98 (1993) 1372–1377.
[25] C. Lee, W. Yang, R.G. Parr, Phys. Rev. B 37 (1988) 785–789.
[26] M. Kleinschmidt, J. Tatchen, C.M. Marian, J. Comput. Chem. 23 (2002) 824–833.
[27] M. Kleinschmidt, C.M. Marian, Chem. Phys. 311 (2005) 71–79.
[28] B.A. Hess, C.M. Marian, U. Wahlgren, O. Gropen, Chem. Phys. Lett. 251 (1996) 365–371.
[29] B. Schimmelpfennig, Stockholms University, 1996.
[30] J. Tatchen, C.M. Marian, Chem. Phys. Lett. 313 (1999) 351–357.
[31] D. Danovich, C.M. Marian, T. Neuheuser, S.D. Peyerimhoff, S. Shaik, J. Phys. Chem. A 102 (1998) 5923–5936.
[32] A. Toniolo, M. Persico, J. Chem. Phys. 115 (2001) 1817–1827.
[33] A. Toniolo, M. Persico, J. Comput. Chem. 22 (2001) 968–975.
[34] B.R. Henry, W. Siebrand, vol. 1, John Wiley & Sons, London, 1973.
[35] J. Tatchen, N. Gilka, C.M. Marian, Phys. Chem. Chem. Phys. 9 (2007) 5209–5221.
[36] J. Tatchen, Distort, Universität Düsseldorf, 2005.
[37] A. Klamt, G. Schürmann, J. Chem. Soc., Perkin Trans. 2 (1993) 799–805.
[38] A. Schäfer, A. Klamt, D. Sattel, J. Lohrenz, F. Eckert, Phys. Chem. Chem. Phys. 2 (2000) 2187–2193.
[39] C. Reichardt, Solvents and Solvent Effects in Organic Chemistry, VCH, Weinheim, 1990.
[40] K. Tomić, J. Tatchen, C.M. Marian, J. Phys. Chem. A 109 (37) (2005) 8410–8418.
[41] S. Salzmann, M. Kleinschmidt, J. Tatchen, R. Weinkauf, C.M. Marian, Phys. Chem. Chem. Phys. 10 (2008) 380–392.
[42] M. Wang, C.J. Fritchie Jr., Acta Crystallogr. (1973) 2040–2045.
[43] J. Tatchen, C.M. Marian, Phys. Chem. Chem. Phys. 8 (2006) 2133–2144.
[44] J.K. Eweg, F. Müller, A. Visser, C. Veeger, D. Bebelaar, J. van Voorst, Photochem. Photobiol. 30 (1979) 463–471.
[45] E.C. Lim, J. Phys. Chem. 90 (1986) 6770–6777.
[46] A. Losi, E. Polverini, B. Quest, W. Gärtner, Biophys. J. 82 (2002) 2627–2634.
[47] S. Perun, J. Tatchen, C.M. Marian, ChemPhysChem 9 (2008) 282–292.

The Photophysics of Flavins: What Makes the Difference Between Gas Phase and Aqueous Solution?
(Electronic Supplementary Material)

Susanne Salzmann,[a] Jörg Tatchen,[a,b] Christel M. Marian[a,*]

[a] *Institute of Theoretical and Computational Chemistry, Heinrich Heine University Düsseldorf, Universitätsstr. 1, D-40225 Düsseldorf, Germany*

[b] *Chemical Physics Department, Weizmann Institute of Science, 76100 Rehovot, Israel*

---

[*] Corresponding author:
Email address: `Christel.Marian@uni-duesseldorf.de` (Christel M. Marian).
URL: `http://www.theochem.uni-duesseldorf.de` (Christel M. Marian).

1 Calculation of the intersystem crossing rate constants

In this appendix, we have assembled detailed information on the entities required for the evaluation of spin-forbidden nonradiative transition probabilities and on the sensitivity of the results with respect to technical parameters.

Table 1 lists harmonic frequencies of the 19 out-of-plane vibrations in the first excited $^1(\pi \rightarrow \pi^*)$ state (coupling modes for the $^1(\pi \rightarrow \pi^*) \rightsquigarrow ^3 (\pi \rightarrow \pi^*)$ vibronic spin-orbit interaction) and the derivatives of the spin-orbit coupling matrix elements with respect to distortions along their normal coordinates.

Information about the parameters chosen in the calculation of the rate constants for the nonradiative transitions from S_1 to the individual spin components of the T_1 and T_2 states and the dependence of the results on these parameters are contained in Table 2 (vacuum) and Table 3 (aqueous solution). A zero number of derivative coupling modes indicates direct spin-orbit coupling, nonzero numbers vibronic spin-orbit coupling.

As can be seen in Tables 2 and 3, the adiabatic energy difference between the S_1 and T_2 states is very small. It amounts to 905 cm^{-1} in the vacuum and 975 cm^{-1} in solution. The energy gap even decreases to 355 cm^{-1} in the vacuum and 966 cm^{-1} in solution when the respective vibrational ground levels are considered. In these cases, the vibrational density of states in the final state is surely much too low to assume that the final state levels form a continuum. For this reason the ISC rate constants have been calculated for several widths of the search interval η, in order to test their robustness (see Tables 2 and 3.) Due to the small energy difference between the ground vibrational levels in the vacuum, search intervals smaller than $\eta = 10$ cm^{-1} due not include final state vibrational levels and are thus not appropriate. For intervals that are wider, fairly stable results are obtained, i.e., the calculated ISC rates show the same order of magnitude. In aqueous solution the difference between the ground vibrational levels is a little bigger and final state vibrational levels can be populated also for smaller search interval widths.

Since the biggest uncertainty arises in the calculation of the excitation energies, also the sensitivity of the computed ISC rate constants with respect to the adiabatic electronic excitation energy and the search interval has been investigated. The results of these test calculations are shown in Tables 4 and 5. For a search interval width of $\eta = 0.1$ cm^{-1} large variations of the rate constants and the resulting number $\#v'$ of final state vibrational levels occurs. This value of η can therefore not be considered to yield reliable results in the present case. For $\eta = 1$ cm^{-1} this effect is much less dramatic and for $\eta = 10$ cm^{-1} the ISC rates are quite stable and show the same order of magnitude. Although from a strict point of view, the application of the interval search algorithm for the evaluation of the rate constants according to the Fermi Golden Rule is not justified under these circumstances, we still consider the resulting values for the ($S_1 \rightsquigarrow T_{2x,2y}$) channel in the vacuum and solution to represent at least rough estimates.

Table 1

IA: Harmonic frequencies ν_i [cm^{-1}] of the out-of-plane vibrational modes for the S_1 state. Derivatives of SOMEs [$-$icm^{-1}] with respect to the corresponding (dimensionless) normal coordinates at the equilibrium geometry q_0 of the S_1 state.

		vacuum		**cosmo**			
		$\frac{\partial\langle S_1\vert\hat{H}_{SO}\vert T_1\rangle}{\partial q_i}$		$\frac{\partial\langle S_1\vert\hat{H}_{SO}\vert T_1\rangle}{\partial q_i}$		$\frac{\partial\langle S_1\vert\hat{H}_{SO}\vert T_2\rangle}{\partial q_i}$	
mode	$\hat{\nu}_i$	(x)	(y)	(x)	(y)	(x)	(y)
1	50^a	-2.15	1.40	-0.53	0.65	-0.33	0.62
2	71	0.01	0.24	0.04	0.03	0.18	-0.08
3	82	-0.21	0.25	-0.02	0.06	0.07	-0.02
4	151	0.14	-0.40	0.02	-0.12	-0.25	-0.50
6	203	-0.33	0.29	0.06	0.04	0.12	-0.04
7	235	-0.55	0.78	-0.19	0.23	-0.04	0.24
8	319	0.19	0.12	-0.11	-0.01	-0.07	-0.02
12	423	0.30	-0.30	0.08	-0.11	-0.09	-0.10
13	478	0.05	0.10	0.02	-0.02	-0.05	0.09
15	523	-0.11	-0.62	-0.04	-0.06	0.16	-0.07
19	623	0.36	-0.15	0.21	-0.15	0.33	-0.22
20	636	0.03	0.47	-0.02	0.04	-0.21	0.29
22	695	-0.43	0.56	-0.14	0.22	-0.51	0.34
23	703	-0.00^b	0.12	0.06	-0.07	0.00	-0.15
25	724	0.28	0.01	0.04	0.02	0.25	-0.12
26	750	-0.04	0.08	0.13	0.02	0.23	0.10
28	841	-0.03	-0.13	-0.08	-0.00^b	-0.34	-0.05
30	908	0.26	-0.06	0.14	0.06	0.36	0.12
32	949	-0.06	0.07	0.04	-0.08	-0.27	-0.09

a: The TDDFT (B3LYP) PEH of the S_1 state exhibits a very flat double well shape along mode 1 with a slightly imaginary frequency (see text). The setting $\hat{\nu}_i$ represents an approximate harmonic model of the S1 state PEH along mode 1.

b: Absolute value of the derivative lower than 0.01 cm^{-1}

Table 2. IA: Calculated rate constants k_{ISC} [cm^{-1}] for ($S_1 \rightsquigarrow T_n$) ISC channels in the vacuum. Remaining columns: adiabatic electronic energy difference ΔE^{ad} [eV], direct SOME $|<i|\hat{H}_{SO}|f>|_{q0}$ [cm^{-1}], number $\#derivs$ of included derivatives w.r.t. *oop* modes in vibronic SO coupling, number $\#_{acc}$ of included accepting modes, width η [cm^{-1}] of search interval, resulting number $\#v'$ of final state vibrational levels within search interval.

parameters & and settings						**results**	
channel $i \rightsquigarrow f$	- ΔE^{ad}	direct SO $\|<i\|\hat{H}_{SO}\|f>\|_{q0}$	vib. SO $\#derivs$	acceptors $\#_{acc}$	interval η	levels $\#v'$	rate k_{ISC}
$S_1 \rightsquigarrow T_{1x}$	-0.65	-	8	41	0.1	39337	$1.5 \cdot 10^6$
$S_1 \rightsquigarrow T_{1x}$	-0.65	-	8	41	1	393236	$1.9 \cdot 10^6$
$S_1 \rightsquigarrow T_{1x}$	-0.65	-	8	41	10	3931222	$2.2 \cdot 10^6$
$S_1 \rightsquigarrow T_{1x}$	-0.65	-	18^a	41	0.1	691317	$0.8 \cdot 10^6$
$S_1 \rightsquigarrow T_{1x}$	-0.65	-	19	41	0.1	1287913	$3.1 \cdot 10^6$
$S_1 \rightsquigarrow T_{1y}$	-0.65	-	8	41	0.1	63138	$1.2 \cdot 10^6$
$S_1 \rightsquigarrow T_{1y}$	-0.65	-	8	41	1	633449	$1.6 \cdot 10^6$
$S_1 \rightsquigarrow T_{1y}$	-0.65	-	8	41	10	6344656	$2.3 \cdot 10^6$
$S_1 \rightsquigarrow T_{1y}$	-0.65	-	18^a	41	0.1	655306	$1.3 \cdot 10^6$
$S_1 \rightsquigarrow T_{1y}$	-0.65	-	19	41	0.1	1219629	$2.3 \cdot 10^6$
$S_1 \rightsquigarrow T_{1z}$	-0.65	$0.9 \cdot 10^{-2}$	0	41	1	25320	$4.0 \cdot 10^1$
$S_1 \rightsquigarrow T_{2x}$	-0.11	13.7	0	41	10	1	$1.7 \cdot 10^9$
$S_1 \rightsquigarrow T_{2x}$	-0.11	13.7	0	41	20	1	$0.9 \cdot 10^9$
$S_1 \rightsquigarrow T_{2x}$	-0.11	13.7	0	41	30	3	$5.3 \cdot 10^9$
$S_1 \rightsquigarrow T_{2x}$	-0.11	13.7	0	41	40	3	$4.0 \cdot 10^9$
$S_1 \rightsquigarrow T_{2x}$	-0.11	13.7	0	41	50	3	$3.3 \cdot 10^9$
$S_1 \rightsquigarrow T_{2x}$	-0.11	13.7	0	41	100	4	$1.9 \cdot 10^9$
$S_1 \rightsquigarrow T_{2x}$	-0.11	13.7	0	41	200	9	$2.6 \cdot 10^9$
$S_1 \rightsquigarrow T_{2y}$	-0.11	6.8	0	41	10	1	$4.5 \cdot 10^8$
$S_1 \rightsquigarrow T_{2y}$	-0.11	6.8	0	41	20	1	$2.2 \cdot 10^9$
$S_1 \rightsquigarrow T_{2y}$	-0.11	6.8	0	41	30	3	$1.3 \cdot 10^9$
$S_1 \rightsquigarrow T_{2y}$	-0.11	6.8	0	41	40	3	$9.9 \cdot 10^8$
$S_1 \rightsquigarrow T_{2y}$	-0.11	6.8	0	41	50	3	$7.7 \cdot 10^8$
$S_1 \rightsquigarrow T_{2y}$	-0.11	6.8	0	41	100	4	$4.9 \cdot 10^8$
$S_1 \rightsquigarrow T_{2y}$	-0.11	6.8	0	41	200	9	$6.6 \cdot 10^8$
$S_1 \rightsquigarrow T_{2z}$	-0.11	-	-	-	-	-	-

a: Here mode 1 is excluded.

Table 3. IA: Calculated rate constants k_{ISC} [s^{-1}] for ($S_1 \rightsquigarrow T_n$) ISC channels in aqueous solution. For further explanation and footnotes see Tab. 2

parameters & and settings						**results**	
channel		direct SO	vib. SO	acceptors	interval	levels	rate
$i \rightsquigarrow f$	ΔE^{ad}	$\mid < i \mid \hat{H}_{SO} \mid f > \mid_{q0}$	$\#derivs$	$\#_{acc}$	η	$\#v'$	k_{ISC}
$S_1 \rightsquigarrow T_{1x}$	-0.56	$< 10^{-3}$	8	41	0.1	42401	$0.9 \cdot 10^5$
$S_1 \rightsquigarrow T_{1x}$	-0.56	$< 10^{-3}$	8	41	1	423984	$1.4 \cdot 10^5$
$S_1 \rightsquigarrow T_{1x}$	-0.56	$< 10^{-3}$	8	41	10	4242084	$1.8 \cdot 10^5$
$S_1 \rightsquigarrow T_{1x}$	-0.56	$< 10^{-3}$	18^a	41	0.1	655306	$1.5 \cdot 10^5$
$S_1 \rightsquigarrow T_{1x}$	-0.56	$< 10^{-3}$	19	41	0.1	1219629	$3.0 \cdot 10^5$
$S_1 \rightsquigarrow T_{1y}$	-0.56	$< 10^{-3}$	8	41	0.1	54168	$1.7 \cdot 10^5$
$S_1 \rightsquigarrow T_{1y}$	-0.56	$< 10^{-3}$	8	41	1	543081	$2.1 \cdot 10^5$
$S_1 \rightsquigarrow T_{1y}$	-0.56	$< 10^{-3}$	8	41	10	5439360	$2.8 \cdot 10^5$
$S_1 \rightsquigarrow T_{1y}$	-0.56	$< 10^{-3}$	18^a	41	0.1	655306	$1.6 \cdot 10^5$
$S_1 \rightsquigarrow T_{1y}$	-0.56	$< 10^{-3}$	19	41	0.1	1219629	$3.7 \cdot 10^5$
$S_1 \rightsquigarrow T_{1z}$	-0.56	$0.9 \cdot 10^{-2}$	0	41	1	6687	$1.1 \cdot 10^2$
$S_1 \rightsquigarrow T_{2x}$	-0.12	$< 10^{-3}$	8	41	0.1	0	-
$S_1 \rightsquigarrow T_{2x}$	-0.12	$< 10^{-3}$	8	41	1	1	$4.1 \cdot 10^5$
$S_1 \rightsquigarrow T_{2x}$	-0.12	$< 10^{-3}$	8	41	10	11	$6.7 \cdot 10^7$
$S_1 \rightsquigarrow T_{2x}$	-0.12	$< 10^{-3}$	8	41	100	140	$2.5 \cdot 10^7$
$S_1 \rightsquigarrow T_{2x}$	-0.12	$< 10^{-3}$	18^a	41	0.1	1	$0.1 \cdot 10^8$
$S_1 \rightsquigarrow T_{2x}$	-0.12	$< 10^{-3}$	18^a	41	1	5	$0.1 \cdot 10^8$
$S_1 \rightsquigarrow T_{2x}$	-0.12	$< 10^{-3}$	18^a	41	10	86	$0.8 \cdot 10^8$
$S_1 \rightsquigarrow T_{2x}$	-0.12	$< 10^{-3}$	19	41	0.1	2	$0.3 \cdot 10^8$
$S_1 \rightsquigarrow T_{2x}$	-0.12	$< 10^{-3}$	19	41	1	12	$0.2 \cdot 10^8$
$S_1 \rightsquigarrow T_{2x}$	-0.12	$< 10^{-3}$	19	41	10	140	$0.9 \cdot 10^8$
$S_1 \rightsquigarrow T_{2y}$	-0.12	$< 10^{-3}$	8	41	0.1	1	$0.1 \cdot 10^7$
$S_1 \rightsquigarrow T_{2y}$	-0.12	$< 10^{-3}$	8	41	1	3	$0.1 \cdot 10^7$
$S_1 \rightsquigarrow T_{2y}$	-0.12	$< 10^{-3}$	8	41	10	19	$0.3 \cdot 10^8$
$S_1 \rightsquigarrow T_{2y}$	-0.12	$< 10^{-3}$	8	41	100	205	$0.2 \cdot 10^8$
$S_1 \rightsquigarrow T_{2y}$	-0.12	$< 10^{-3}$	18^a	41	0.1	1	$0.1 \cdot 10^7$
$S_1 \rightsquigarrow T_{2y}$	-0.12	$< 10^{-3}$	18^a	41	1	5	$0.2 \cdot 10^8$
$S_1 \rightsquigarrow T_{2y}$	-0.12	$< 10^{-3}$	18^a	41	10	86	$0.5 \cdot 10^8$
$S_1 \rightsquigarrow T_{2y}$	-0.12	$< 10^{-3}$	19	41	0.1	2	$0.2 \cdot 10^7$
$S_1 \rightsquigarrow T_{2y}$	-0.12	$< 10^{-3}$	19	41	1	12	$0.9 \cdot 10^8$
$S_1 \rightsquigarrow T_{2y}$	-0.12	$< 10^{-3}$	19	41	10	140	$0.8 \cdot 10^8$
$S_1 \rightsquigarrow T_{2z}$	-0.12	$0.3 \cdot 10^{-2}$	0	41	10	3	$1.1 \cdot 10^1$

a: Here mode 1 is excluded.

Table 4
IA: Investigation on the stability of the ISC rate constant k_{ISC} [10^9s^{-1}] for the (S$_1 \rightsquigarrow$T$_{2x}$) ISC channel in the vacuum, with respect to a shift of the adiabatic electronic energy difference ΔE^{ad} [cm^{-1}] and the search interval η [cm^{-1}]. Shifts [cm^{-1}] with respect to the calculated adiabatic electronic energy difference are shown in parentheses. In addition, the resulting number $\#v'$ of final state vibrational levels within the search interval is given. Only direct spin-orbit coupling was accounted for, and 41 accepting modes were used.

$(\mathbf{S}_1 \rightsquigarrow \mathbf{T}_{2x})$ **(vacuum)**											
	η	**10**		**20**		**30**		**50**		**100**	
ΔE^{ad}		$\#v'$	k_{ISC}	$\#v'$	k_{ISC}	$\#v'$	k_{ISC}	$\#v'$	k_{ISC}	$\#v'$	k_{ISC}
805	(-100)	0	**-**	0	**-**	0	**-**	0	**-**	2	**2.1**
855	(-50)	0	**-**	0	**-**	1	**2.8**	1	**1.7**	3	**1.7**
955	(+50)	1	**2.7**	1	**1.4**	2	**2.8**	3	**2.1**	5	**2.9**
1005	(+100)	0	**-**	0	**-**	0	**-**	2	**2.8**	7	**3.2**
1055	(+150)	0	**-**	2	**9.9**	3	**6.7**	4	**4.4**	8	**3.2**
1105	(+200)	1	**1.8**	2	**1.8**	3	**1.2**	6	**3.6**	9	**3.8**
1155	(+250)	2	**10.4**	3	**6.5**	3	**4.4**	5	**3.3**	12	**4.6**
1205	(+300)	2	**4.6**	2	**2.3**	4	**5.6**	6	**5.8**	15	**4.0**
1255	(+350)	1	**7.3**	4	**2.2**	7	**5.9**	10	**4.5**	17	**5.3**
1305	(+400)	1	**0.4**	3	**1.3**	6	**5.1**	11	**4.9**	21	**6.3**

Table 5
IA: Investigation on the stability of the ISC rate constant k_{ISC} [$10^8 \mathrm{s}^{-1}$] for the ($\mathrm{S}_1 \rightsquigarrow \mathrm{T}_{2x}$) and ($\mathrm{S}_1 \rightsquigarrow \mathrm{T}_{2y}$) ISC channels in aqueous solution, with respect to a shift of the adiabatic electronic energy difference ΔE^{ad} [cm^{-1}] and the search interval η [cm^{-1}]. Shifts [cm^{-1}] with respect to the calculated adiabatic electronic energy difference are shown in parentheses. In addition, the resulting number $\#v'$ of final state vibrational levels within the search interval is given. All 19 derivatives were included for the calculation of the vibronic spin-orbit coupling, and 41 accepting modes were used.

			(water)				
	η	**0.1**		**1.0**		**10**	
ΔE^{ad}		$\#v'$	k_{ISC}	$\#v'$	k_{ISC}	$\#v'$	k_{ISC}
			($\mathrm{S}_1 \rightsquigarrow \mathrm{T}_{2x}$)				
875	(-100)	2	**0.00009**	15	**0.03**	120	**0.5**
925	(-50)	1	**-**	14	**0.1**	129	**0.9**
1025	(+50)	3	**0.03**	19	**1.1**	186	**0.6**
1075	(+100)	4	**0.008**	36	**0.7**	292	**1.0**
1125	(+150)	6	**0.5**	36	**0.3**	347	**1.2**
1175	(+200)	2	**0.07**	26	**0.07**	370	**0.8**
1225	(+250)	8	**0.08**	50	**1.1**	490	**0.6**
1275	(+300)	6	**0.03**	75	**0.9**	685	**1.0**
1325	(+350)	12	**0.7**	80	**0.3**	848	**1.2**
1375	(+400)	5	**-**	78	**0.2**	900	**0.6**
			($\mathrm{S}_1 \rightsquigarrow \mathrm{T}_{2y}$)				
875	(-100)	2	**0.003**	15	**0.8**	120	**0.3**
925	(-50)	1	**-**	14	**0.4**	129	**0.7**
1025	(+50)	3	**0.005**	19	**0.3**	186	**0.4**
1075	(+100)	4	**0.009**	36	**1.8**	292	**0.6**
1125	(+150)	6	**0.3**	36	**0.2**	347	**0.8**
1175	(+200)	2	**0.002**	26	**0.3**	370	**0.7**
1225	(+250)	8	**0.04**	50	**0.4**	490	**0.8**
1275	(+300)	6	**0.02**	75	**0.5**	685	**0.9**
1325	(+350)	12	**0.2**	80	**0.8**	848	**1.0**
1375	(+400)	5	**-**	78	**3.8**	900	**1.1**

Paper II

Effects of protonation and deprotonation
on the excitation energies of lumiflavin

Susanne Salzmann and Christel M. Marian

Chem. Phys. Lett., **463** (2008) 400–404.

Chemical Physics Letters 463 (2008) 400–404

Contents lists available at ScienceDirect

Chemical Physics Letters

journal homepage: www.elsevier.com/locate/cplett

Effects of protonation and deprotonation on the excitation energies of lumiflavin ☆

Susanne Salzmann, Christel M. Marian *

Institute of Theoretical and Computational Chemistry, Heinrich Heine University Düsseldorf, Universitätsstr. 1, D-40225 Düsseldorf, Germany

A R T I C L E I N F O

Article history:
Received 27 June 2008
In final form 13 August 2008
Available online 15 August 2008

A B S T R A C T

Two protonated (N(1) and N(5) position) and a deprotonated (N(3) position) lumiflavin species have been investigated by means of the combined density functional/multi-reference configuration interaction method (DFT/MRCI). Vertical excitation energies are presented for the vacuum and for aqueous solution simulated with a conductor-like screening model. Additionally, protonation energies for the ground state and the first excited singlet and triplet states are presented. While in the ground state the N(1) position is favorably protonated, protonation in the excited states is preferred in N(5) position.

1. Introduction

In the last 15 years flavins, more precisely flavin mononucleotide (FMN) and flavin adenine dinucleotide (FAD), have gained interest due to their role as chromophores in blue-light photosensors. Until today, three different kinds of flavin-based photoreceptors are known, namely cryptochromes (cry), BLUF (blue light sensing using FAD) containing proteins and phototropins (phot). While the signaling mechanism in the latter two exhibits similarities, it is different in cryptochromes.

Phototropins comprise of two LOV (light, oxygen, and voltage) domains, LOV1 and LOV2, each binding FMN as a chromophore. In the absence of light the FMN is bound non-covalently to the protein backbone. Irradiation with blue light triggers a photocycle that leads to photobleaching. The primary step after blue-light absorption hereby involves a rapid decay of the excited singlet state to the lowest excited triplet state. From that state, an adduct-formation between the C(4a) atom of the flavin core and the S atom of a nearby cysteine residue takes place. In the resulting metastable thiol adduct, the isoalloxazine ring is protonated at N(5) position. In BLUF proteins, the formation of the signaling state occurs instead from the excited singlet state of the flavin chromophore. For the photocycle two amino acids (tyrosine and glutamine) are known to be crucial, when in proximity to the N(5) atom (for a detailed review on flavin-based blue-light photosensors see Ref. [1]).

The photophysical and photochemical behavior of flavins is dominated by the isoalloxazine (benzol[g]pteridine-2,4,(3H10H)-dione) core ring. To keep the calculations practicable, the ribyl chain of the natural chromophore has been replaced by a methyl group, which results in only minor changes in the vertical excitation spectra [2,3] and photophysical behavior [4]. For three (de)protonated lumiflavin species, shown in Fig. 1, vertical excitation spectra are presented and (if possible) compared with experiment. For the species LF1$^+$ and LF5$^+$ protonation energies for the ground state and the first excited singlet and triplet states are discussed.

2. Methods and computational details

Geometry optimizations of the ground state and low-lying electronically excited states of the (de)protonated flavins were carried out at the level of density functional theory (DFT) with the TURBOMOLE 5.7 [5] program package. For all calculations we employed the standard TZVP basis set from the TURBOMOLE library. The B3LYP functional [6,7] as implemented in TURBOMOLE 5.7 was used for optimizing the geometries. The cartesian coordinate system was chosen in a way that all atoms lie in the *xy* plane. For the optimization of the first electronically excited singlet state of the two protonated species time-dependent DFT [8,9] (TDDFT) was employed. The first electronically excited triplet state for the two protonated flavins was obtained with unrestricted DFT (UDFT). If possible, C_s symmetry constraints were imposed on the ground and excited state geometries of all molecules. To ensure that the resulting geometries correspond to true minima of the potential energy hypersurfaces (PEH), harmonic vibrational frequencies were calculated numerically with the program SNF [10].

Vertical electronic excitation energies, dipole transition matrix elements, and oscillator strengths were obtained from subsequent single-point calculations using the combined density functional theory/multi-reference configuration interaction (DFT/MRCI) method of Grimme and Waletzke [11]. This approach represents an effective means to obtain spin-restricted electronic spectra for organic systems with errors typically around 0.2 eV [12]. For the C_s-symmetric flavins, 10 roots for each of the two irreducible

---

☆ Supported by Deutsche Forschungsgemeinschaft through SFB663/C1.

* Corresponding author. Fax: +49 211 811366.
E-mail address: Christel.Marian@uni-duesseldorf.de (C.M. Marian).
URL: http://www.theochem.uni-duesseldorf.de (C.M. Marian).

0009-2614/$ - see front matter © 2008 Published by Elsevier B.V.
doi:10.1016/j.cplett.2008.08.050

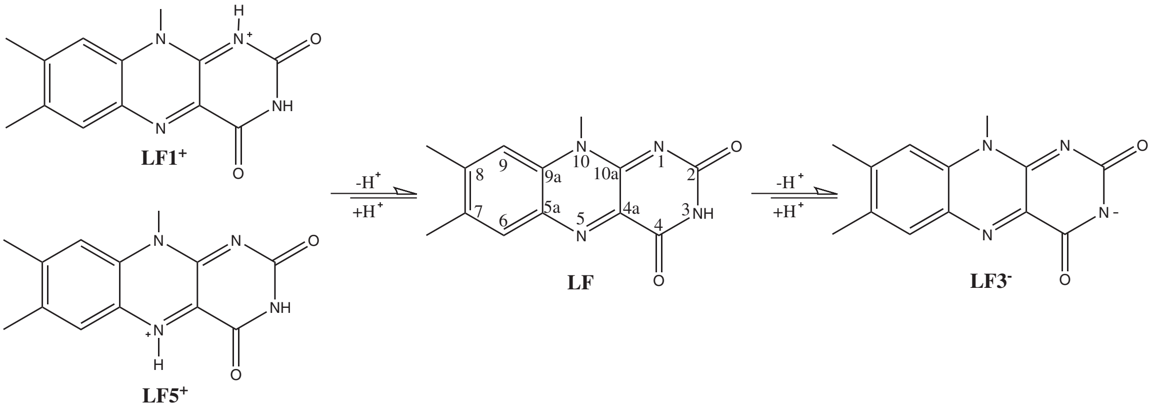

Fig. 1. (De)Protonated and neutral species of lumiflavin.

representations A' and A'' and for the asymmetric flavins 20 roots were calculated, both for the singlet and triplet manifolds.

To estimate spectral shifts due to electrostatic interaction in a polar solvent (water), we employed the conductor-like screening model (COSMO) which is implemented in the TURBOMOLE package [13,14]. A dielectric constant of $\epsilon = 78$ was chosen,[15] corresponding to water at ambient temperature.

3. Results and discussion

In this section the vertical excitation energies of the (de)protonated flavins as well as protonation energies for LF1$^+$ and LF5$^+$ are presented. A detailed investigation on the vertical absorption spectrum of neutral flavins and of lumiflavin in particular, can be found in previous work [16,17]. For LF3$^-$ and LF5$^+$ the ground and excited state nuclear arrangements were found to be C_s symmetric. (except for the first excited triplet state of LF5$^+$, where a slightly out-of-plane distorted minimum nuclear arrangement has been obtained.) For LF1$^+$ asymmetric structures, where the methyl group located at C10 is rotated by 90 degree, were found to be the minima on the ground and excited states potential energy hypersurfaces (PEH).

3.1. Vertical excitation energies

To our knowledge there are no experimental gas phase spectra on (ionic) flavins. Therefore our calculations have to be compared with measurements in (aqueous) solution (see Table 1). Earlier quantum chemical investigations as well as experiments on neutral lumiflavin have shown that the environment has a distinct influence on the position of the second absorption band [16–20]. In order to compare with experiment, calculations with COSMO have been performed to simulate water. The nomenclature used for the molecular orbitals (MOs) in Tables 2–4 is based on the order and shape of the MOs of 7,8-didemethyl-lumiflavin (see Fig. 3 of Ref. [16]) and does not necessarily present the given order for the ionic flavin species investigated here (see below).

Table 1
Experimental excitation energies (eV) in the energy range below 5 eV for a protonated and a deprotonated lumiflavin in comparison to the neutral compound. The absorption maxima are taken from Ref. [2]

Band	Neutral (FlH)[a]	Cation (FlH_2^+)[b]	Anion (FL^-)[c]
1	2.78	3.18	2.79
2	3.35		3.54
3	4.59	4.70	4.59

[a] Phosphate-buffer, pH 7.0.
[b] 6N HCl, pH 0.
[c] 2N NaOH, pH 13.

Table 2
LF1$^+$: vertical absorption energies ΔE (eV) and the oscillator strengths $f(L)$ at the ground state geometry

State		Electronic structure[a]	ΔE_{vacuum}	$f(L)$	ΔE_{COSMO}
S_0	1^1A	(0.95) ground state	0.00	–	0.00
S_1	2^1A	(0.55) $\pi_H \rightarrow \pi_L^*$ (0.28) $\pi_{H-1} \rightarrow \pi_L^*$	3.15	0.1031	3.12
S_2	3^1A	(0.55) $n_{O2} \rightarrow \pi_L^*$ (0.17) $n_N \rightarrow \pi_L^*$	3.27	0.0074	3.55
S_3	4^1A	(0.57) $\pi_{H-1} \rightarrow \pi_L^*$ (0.26) $\pi_H \rightarrow \pi_L^*$	3.34	0.4151	3.36
S_4	5^1A	(0.44) $n_N \rightarrow \pi_L^*$ (0.12) $n_{O2} \rightarrow \pi_L^*$ (0.11) $n_{O1} \rightarrow \pi_L^*$	3.52	0.0025	4.01
S_5	6^1A	(0.76) $\pi_{H-2} \rightarrow \pi_L^*$	4.29	0.0359	4.70
S_7	8^1A	(0.52) $\pi_{H-1} \rightarrow \pi_{L+1}^*$ (0.13) $\pi_H \rightarrow \pi_{L+2}^*$	4.82	0.6160	4.84
T_1	1^3A	(0.86) $\pi_H \rightarrow \pi_L^*$	2.50	–	2.51
T_2	2^3A	(0.83) $\pi_{H-1} \rightarrow \pi_L^*$	2.67	–	2.62
T_3	3^3A	(0.50) $n_N \rightarrow \pi_L^*$ (0.21) $n_{O2} \rightarrow \pi_L^*$	2.89	–	3.13

[a] Dominant configurations of the MRCI expansion of isolated LF1$^+$. For the COSMO calculation the electronic structure of the respective states is very similar to that of the vacuum.

Table 3
LF5$^+$: vertical absorption energies and oscillator strenghts at the ground state geometry

State		Electronic structure	ΔE_{vacuum}	$f(L)$	ΔE_{COSMO}
S_0	$1^1A'$	(0.93) ground state	0.00	–	0.00
S_1	$2^1A'$	(0.80) $\pi_H \rightarrow \pi_L^*$	2.07	0.1777	2.29
S_2	$1^1A''$	(0.75) $n_O \rightarrow \pi_L^*$	2.49	0.0001	3.41
S_3	$3^1A'$	(0.70) $\pi_{H-1} \rightarrow \pi_L^*$	2.89	0.2529	2.95
S_4	$2^1A''$	(0.80) $n_N \rightarrow \pi_L^*$	3.10	0.0003	3.58
S_5	$4^1A'$	(0.71) $\pi_{H-2} \rightarrow \pi_L^*$	3.30	0.0329	3.67
S_6	$3^1A''$	(0.73) $n_O \rightarrow \pi_L^*$	3.31	0.0001	4.00
S_7	$5^1A'$	(0.62) $\pi_{H-3} \rightarrow \pi_L^*$	3.53	0.0533	3.86
S_8	$6^1A'$	(0.31) $\pi_H \rightarrow \pi_{L+1}^*$ (0.21) $\pi_H \rightarrow \pi_{L+2}^*$	4.45	0.1800	4.59
S_{12}	$8^1A'$	(0.26) $\pi_H \rightarrow \pi_{L+1}^*$ (0.13) double exc.	4.84	0.5596	4.90
T_1	$1^3A'$	(0.86) $\pi_H \rightarrow \pi_L^*$	1.26	–	1.50
T_2	$2^3A'$	(0.85) $\pi_{H-1} \rightarrow \pi_L^*$	2.37	–	2.32
T_3	$1^3A''$	(0.77) $n_O \rightarrow \pi_L^*$	2.48	–	3.36

For more details see Table 2.

3.1.1. LF1$^+$

The vertical absorption energies of LF1$^+$ in vacuum and aqueous solution (COSMO) are shown in Table 2. In the energy range below

Table 4
$LF3^-$: vertical absorption energies and oscillator strengths at the ground state geometry

Vacuum[a]		COSMO		Vacuum	
State		Electr. structure	ΔE ($f(L)$)	Electr. structure	ΔE ($f(L)$)
S_0	$1^1A'$	(0.95) ground state	0.00 (–)	(0.95) ground state	0.00 (–)
S_5	$3^1A'$	(0.82) $\pi_H \rightarrow \pi_L^*$	2.91 (0.2842)	(0.81) $\pi_H \rightarrow \pi_L^*$	3.17 (0.3385)
S_1	$1^1A''$	(0.82) $n_N \rightarrow \pi_L^*$	3.02 (0.0012)	(0.80) $n_N \rightarrow \pi_L^*$	2.26 (0.0006)
S_3	$2^1A''$	(0.72) $n_{O2} \rightarrow \pi_L^*$	3.63 (0.0000)	(0.76) $n_{O2} \rightarrow \pi_L^*$	2.65 (0.0000)
S_2	$2^1A'$	(0.57) $\pi_{H-2} \rightarrow \pi_L^*$ (0.20) $\pi_{H-1} \rightarrow \pi_L^*$	3.67 (0.1448)	(0.80) $\pi_{H-2} \rightarrow \pi_L^*$	2.50 (0.0444)
S_9	$5^1A'$	(0.57) $\pi_{H-1} \rightarrow \pi_L^*$ (0.21) $\pi_{H-2} \rightarrow \pi_L^*$	3.87 (0.1881)	(0.29) $\pi_{H-1} \rightarrow \pi_L^*$ (0.26) $\pi_H \rightarrow \pi_{L+1}^*$ (0.13) $\pi_{H-2} \rightarrow \pi_{L+1}^*$	4.16 (0.0241)
S_4	$3^1A''$	(0.57) $n_{O1} \rightarrow \pi_L^*$	4.17 (0.0008)	(0.72) $n_{O1} \rightarrow \pi_L^*$	3.11 (0.0001)
S_{17}	$9^1A'$	(0.54) $\pi_{H-3} \rightarrow \pi_L^*$ (0.12) $\pi_{H-1} \rightarrow \pi_{L+1}^*$	4.61 (0.0184)	(0.35) $\pi_{H-3} \rightarrow \pi_L^*$ (0.27) $\pi_H \rightarrow \pi_{L+1}^*$	4.91 (0.4305)
S_{14}	$7^1A'$	(0.40) $\pi_H \rightarrow \pi_{L+2}^*$ (0.17) $\pi_H \rightarrow \pi_{L+1}^*$	4.77 (0.1382)	(0.63) $\pi_H \rightarrow \pi_{L+2}^*$	4.69 (0.0447)
S_{15}	$8^1A'$	(0.55) $\pi_H \rightarrow \pi_{L+1}^*$ (0.12) $\pi_H \rightarrow \pi_{L+2}^*$	4.96 (0.5324)	(0.28) $\pi_{H-1} \rightarrow \pi_L^*$ (0.19) $\pi_{H-3} \rightarrow \pi_L^*$ (0.16) $\pi_H \rightarrow \pi_{L+1}^*$	4.79 (0.4982)
T_3	$2^1A'$	(0.86) $\pi_H \rightarrow \pi_L^*$	2.24 (–)	(0.80) $\pi_H \rightarrow \pi_L^*$	2.29 (–)
T_2	$1^1A''$	(0.77) $n_N \rightarrow \pi_L^*$	2.90 (–)	(0.79) $n_N \rightarrow \pi_L^*$	2.10 (–)

For more details see Table 2.

[a] States are presented in the energetic order they have in the COSMO calculation. The reordering with respect to the vacuum conditions can be inferred from the S_n designation which refers to the ordering of states in the isolated molecule.

5 eV three states with substantial oscillator strength are found, namely S_1, S_3 and S_7. The first excited singlet state (S_1) is dominated by the linear combination of the ($\pi_H \rightarrow \pi_L^*$) and the ($\pi_{H-1} \rightarrow \pi_L^*$) excitations. Its vertical absorption energy is calculated to lie at 3.15 eV for the vacuum. The inverted combination of configurations is found for the S_3 state. The vertical excitation energy of this state in the vacuum is estimated to 3.34 eV. The third optically active state is the seventh excited singlet state S_7. It is dominated by the ($\pi_{H-1} \rightarrow \pi_{L+1}^*$) excitation and a little bit of the ($\pi_H \rightarrow \pi_{L+2}^*$) excitation. This state, energetically situated at 4.82 eV, exhibits the highest oscillator strength in the electronic excitation spectrum below 5 eV. In between those states, several transitions with small oscillator strength are found and mostly belong to ($n \rightarrow \pi*$) transitions. With the COSMO environment, the excitation energies of the three optically active bands are nearly unaffected. (The change in excitation energy is less than 0.05 eV.) Explicit inclusion of hydrogen bonding in the calculations, is expected to result in a red shift of the S_3 state [16,18] and possibly lessens the gap between the S_1 and the S_3 state. From that point, it appears plausible that the experimentally observed band around 3.18 eV can be assigned to both, the S_1 and the S_3 states whereas the S_7 state can be attributed to the band centered around 4.70 eV.

In the triplet manifold three states are located below the first excited singlet state. The first two excited triplet states are dominated by the ($\pi_H \rightarrow \pi_L^*$) and the ($\pi_H \rightarrow \pi_L^*$) excitations, respectively. Unlike the corresponding singlet states, no major configuration mixing takes place for the triplet states. Nevertheless, the two states are energetically close. As their singlet counterparts, their energetic position is nearly unaffected by the COSMO environment. The lowest singlet and triplet ($n \rightarrow \pi^*$) excited states experience blue shifts of the order of 0.2–0.3 eV in aqueous solution. The T_3 state therefore remains near-degenerate with the optically bright S_1 state and is expected to cause fast ISC [16,21].

3.1.2. $LF5^+$

For the vertical excitation energies of $LF5^+$ (see Table 3) no comparison with experimental absorption maxima is possible. Because of the lower proton affinity of the N(5) site in the electronic ground state (see below) this species is built to a minor extent only. In the excitation spectrum up to 5 eV four states with substantial oscillator strength are found (S_1, S_3, S_8, and S_{12}). The first excited singlet state (S_1) is dominated by the ($\pi_H \rightarrow \pi_L^*$) excitation. In the vacuum its vertical excitation energy amounts to merely 2.07 eV. In aqueous solution it is blue-shifted to 2.29 eV. The vertical excitation energy of the S_3 state is found at 2.89 eV (vacuum) and 2.95 eV (COSMO). In this state, the ($\pi_{H-1} \rightarrow \pi_L^*$) excitation prevails. The two higher-lying optically active states both exhibit a combination of the ($\pi_H \rightarrow \pi_{L+1}^*$) configuration with the ($\pi_H \rightarrow \pi_{L+2}^*$) configuration ($S_8$) and a double excitation (S_{12}), respectively. Energetically the two states are situated around 4.45 and 4.84 eV in the vacuum and 4.59 and 4.90 eV in aqueous solution. Only one excited triplet state is found below the first excited singlet state. It is dominated by the ($\pi_H \rightarrow \pi_L^*$) excitation. In aqueous solution this state is blue-shifted as its singlet counterpart. While in the absorption spectrum of $LF1^+$ the first and second optically bright states are shifted in a way that they appear as one band, in $LF5^+$ two individual bands with a larger gap than in neutral lumiflavin are expected.

Another substantial difference with respect to $LF1^+$ is the energy gap between the optically bright S_1 state (that is populated by blue light irradiation) and the lowest singlet and triplet ($n \rightarrow \pi^*$) excited states. In polar environments it is so large that non-radiative relaxation of S_1 via ISC will presumably play a secondary role in $LF5^+$. Protonation at the N(5) position of lumiflavin prior to electronic excitation will therefore prevent the efficient formation of an intermediate triplet state in photochemical reactions.

3.1.3. $LF3^-$

In difference to the protonated flavin species, the vertical excitation energies of the deprotonated lumiflavin (shown in Table 4) depend heavily on the environment. Experimentally three bands, centered around 2.79 eV, 3.54 eV, and 4.59 eV, are observed. For the calculations in the vacuum, no agreement with experiment can be found. As soon as solvent effects are taken into account, a substantial change in the ordering as well as in the electronic structure of the excited states is found. This comes along with a reordering of the occupied π orbitals. If not stated differently, the results obtained with the COSMO environment are discussed. The lowest-lying band observed in experiment can be assigned to the ($\pi_H \rightarrow \pi_L^*$) excitation. It is situated around 2.91 eV, 0.2 eV above the experimental value. Although it is common practice to identify the experimental band maxima with vertical excitation energies, it recently has been shown that for the first band of flavins this presumption does not hold [17]. In neutral LF the vertical absorption energy is found to be 0.2 eV higher than the band maximum, leading to the assumption that the same situation holds for the anionic species. In comparison to the vacuum, this transition is red shifted (0.26 eV), due to the destabilization of the π_H MO in aqueous solution. The second experimentally observed band can be assigned to the two linear combinations of the ($\pi_{H-1} \rightarrow \pi_L^*$) and the ($\pi_{H-2} \rightarrow \pi_L^*$) conformations. In aqueous solution the $\pi_{H\text{-}1}$ MO is destabilized, while the $\pi_{H\text{-}2}$ orbital is stabilized, resulting in a red shift of the first transition and a blue-shift of the second transition. Inclusion of hydrogen bonding possibly enhances this effect. Finally, the third absorption band observed, can be assigned to the two linear combinations of the ($\pi_H \rightarrow \pi_{L+1}^*$) and the ($\pi_H \rightarrow \pi_{L+2}^*$) conformations. It constitutes the most intensive band in the excitation spectrum below 5 eV.

In the triplet manifold two states are found below the lowest excited singlet state (S_5, the S_n designation in Table 4 refers to the ordering of states in the isolated molecule). The T_1 state is dominated by the ($\pi_H \rightarrow \pi_{L+1}^*$) excitation. The second excited triplet state is the lowest ($n \rightarrow \pi^*$) state. It is found near-degenerate with the optically bright S_5 state and is expected to cause fast ISC [16,21].

3.2. Protonation energies

For the two flavin species LF1$^+$ and LF5$^+$, protonation energies calculated in the vacuum for the ground and the first excited singlet and triplet state (S_1 and T_1) are given in Table 5. Experimental investigations [2] have shown that in the ground state protonation takes place at N(1) position. Our DFT/MRCI calculations reproduce this trend. In LF1$^+$ the ground state is 0.45 eV (43.6 kJ/mol) lower in energy than in LF5$^+$. The electronic structures of the S_1 and the T_1 state of lumiflavin are very similar, i.e., they are dominated by the ($\pi_H \rightarrow \pi_L^*$) transition. In both cases protonation is more favorable at N(5) position than at N(1) position. For the S_1 state the difference between the protonation energies in these positions amounts to 0.62 eV (60.3 kJ/mol) and it is even more pronounced in the T_1 state 0.79 eV (76.0 kJ/mol). Note that the preferential stabilization of the T_1 state of LF5$^+$ leads to a very small energy gap between the T_1 and S_0 states of that species (see Fig. 2). These trends can be qualitatively understood at the MO level (see Fig. 3 for the densities of the most important MOs of neutral LF). Most of the bonding interaction between H$^+$ and LF is contributed by the n_N orbital in which the electron density is almost equally distributed over the N(1) and N(5) positions. However, for the protonation energies also the π-electron densities at the N(1) and N(5) centers play an important role. In the electronic ground state, the π_H MO is doubly occupied. It exhibits substantial electron density at the N(1) atom whereas a node is observed at N(5). Protonation in the ground state thus occurs preferentially at N(1). Upon $\pi_H \rightarrow \pi_L^*$ excitation, electron density is transferred from N(1) to N(5) with the consequence that protonation is favored at N(5) in the S_1 and the T_1 states.

Table 5
Comparison of the total energies E_{tot} (a.u.) and respective protonation energies (eV) for the two protonated species in vacuum

		LF1$^+$	LF5$^+$	LF
S_0	E_{tot} (a.u.)	−872.271840	−872.255225	−871.897586
	ΔE (eV)	−10.18	−9.73	–
S_1	E_{tot} (a.u.)	−872.164977	−872.187942	−871.799649
	ΔE (eV)	−9.94	−10.57	–
T_1	E_{tot} (a.u.)	−872.187117	−872.216051	−871.822741
	ΔE (eV)	−9.92	−10.70	–

Data of the neutral lumiflavin is taken from previous work [16,17].

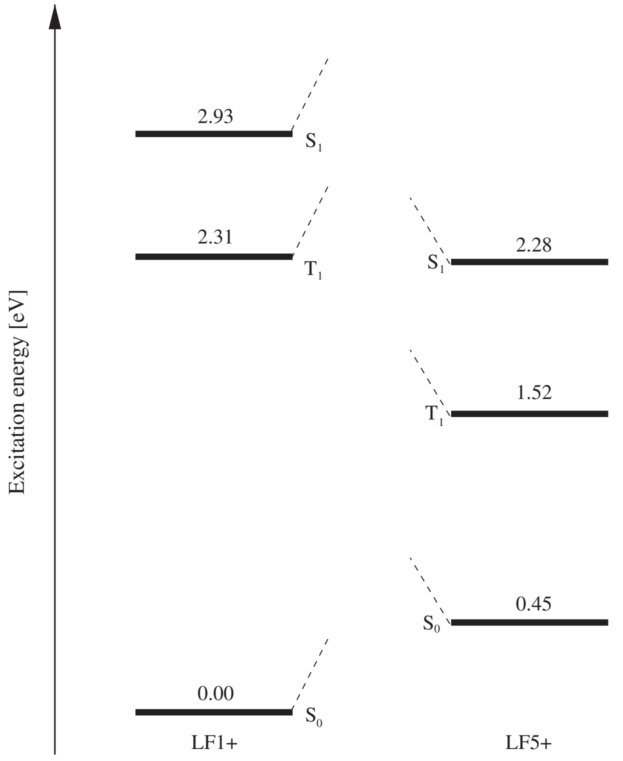

Fig. 2. Adiabatic energies (eV) of ground and excited states of the two protonated lumiflavin species. The energies are given with respect to the ground state energy of LF1$^+$.

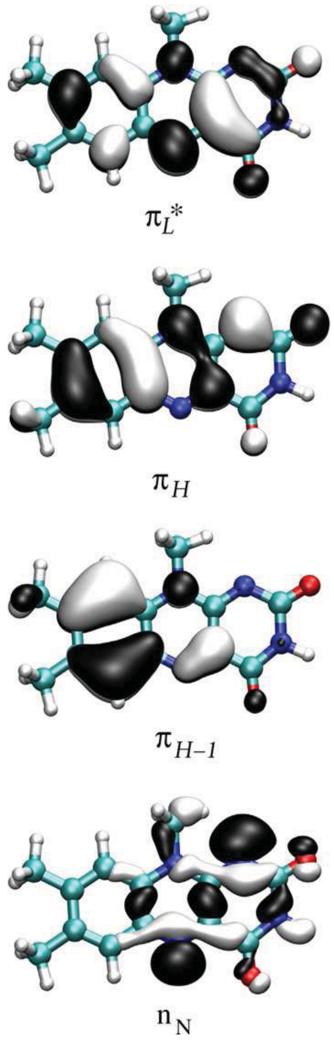

Fig. 3. Selected molecular orbitals of lumiflavin.

In the vacuum, protonation transfer from N(1) to N(5) position will not occur however, because of the high barrier for deprotonation. In polar protic solvents the migration should take place more easily on the excited potential energy surface but at least in the S_1 state it has to compete with fast deexcitation processes such as fluorescence for which we compute a rate $k_F \approx 1.6 \cdot 10^7$ s^{-1}. The T_1 state, on the other hand, may act as an energy sink. Here, concurrent deexcitation processes are expected to be much slower so that a change of the protonation site has a realistic chance to compete.

In the LOV domain, the proton is transferred from a nearby cyctein residue (CYS 57). QM/MM studies of a possible reaction path are under way. (Ref. Ramos et al. in progress) Earlier (U)DFT(B3LYP/6-31G**) [21] calculations show the same trends, predicting similar energy differences for the ground states (34.5 kJ/mol) and the first excited triplet states (79.6 kJ/mol) of $LF1^+$ and $LF5^+$.

4. Summary and conclusions

For the N(1) and N(5) protonated ($LF1^+$ and $LF5^+$) and the N(3) deprotonated ($LF3^-$) lumiflavin species, vertical DFT/MRCI excitation energies have been presented here for the first time. Comparison of the computed absorption energies of $LF1^+$ and $LF3^-$ with experimental results in water show good agreement. While for the anionic species, the position of the absorption maxima remains rather similar to the neutral LF, the cationic species $LF1^+$ shows a significantly different absorption spectrum. Here the first band is heavily blue-shifted while the second band experiences a red shift, resulting in an overlay of the two bands. For $LF5^+$, the experimentally yet unobserved species, we find a noticeable red shift of the first and second absorption bands with respect to neutral LF. Especially for $LF3^-$ our results show how important it is to involve solvent effects in order to reproduce experimental findings in water and to describe the photophysical behavior correctly.

For the two cationic species, $LF1^+$ and $LF5^+$, we presented protonation energies for the ground and first excited singlet and triplet states. In agreement with experiment [2] and earlier quantum chemical calculations [21], for the ground state protonation of the N(1) position is energetically more stable. In the first excited singlet and triplet states, this is different. Here the N(5) center is preferentially protonated. Particularly with regard to the biologically relevant flavin-based blue-light sensing BLUF and LOV domains, this finding is momentous since the N(5) atom is involved in their photochemical reactions after blue-light absorption. As mentioned in the Introduction, signaling happens in the LOV domain via an adduct formation of the C(4a) carbon atom of the isoalloxazine core of FMN and the sulfur atom of the nearby cysteine residue. The mechanism of that adduct formation is still under discussion [1,19,22,23]. One of the proposed reaction pathways comprises an initial proton transfer from cysteine to the N(5) atom. While this appears to be an energetically favorable reaction, our present results do not allow us to exclude the possibility of a radical mechanism.

In BLUF proteins (AppA) the signaling state ($BLUF_{Red}$) exhibits a slight red shift of the first (0.09 eV) and second (0.05 eV) absorption band [1]. The results of our calculations support the interpretation that the observed red shifts in $BLUF_{Red}$ is not due to a protonated flavin but rather to a reorganisation in the protein [1,24,25].

Acknowledgements

The authors would like to thank A. Losi (University of Parma) and W. Gärtner (MPI Mühlheim) for helpful discussions on the topic of LOV and BLUF domains.

References

[1] A. Losi, Photochem. Photobiol. 83 (2007) 1283.
[2] K.H. Dudley, A. Ehrenberg, P. Hemmerich, F. Müller, Helv. Chim. Acta 47 (1964) 1354.
[3] M. Sung, T.A. Moore, P.-S. Song, J. Am. Chem. Soc. 94 (1972) 1730.
[4] A. Bowd, P. Byrom, J.B. Hudson, J.H. Turnbull, Photochem. Photobiol. 8 (1968) 1.
[5] R. Ahlrichs et al., Turbomole (vers. 5.7).
[6] A.D. Becke, J. Chem. Phys. 98 (1993) 5648.
[7] P.J. Stephens, F.J. Devlin, C.F. Chabalowski, M.J. Frisch, J. Phys. Chem. 98 (1994) 11623.
[8] F. Furche, R. Ahlrichs, J. Chem. Phys. 117 (2002) 7433.
[9] R. Bauernschmitt, R. Ahlrichs, Chem. Phys. Lett. 256 (1996) 454.
[10] C. Kind, M. Reiher, J. Neugebauer, SNF Version 2.2.1: A Program Package for Numerical Frequency Analyses, Universität Erlangen, 1999–2002.
[11] S. Grimme, M. Waletzke, J. Chem. Phys. 111 (1999) 5645.
[12] M.R. Silva-Junior, M. Schreiber, W. Thiel, S.P.A. Sauer, J. Chem. Phys., in press.
[13] A. Klamt, G. Schüürmann, J. Chem. Soc., Perkin Trans. 2 (1993) 799.
[14] A. Schäfer, A. Klamt, D. Sattel, J.C.W. Lohrenz, F. Eckert, Phys. Chem. Chem. Phys. 2 (2000) 2187.
[15] C. Reichardt, Solvents and Solvent Effects in Organic Chemistry, VCH, Weinheim, 1990.
[16] S. Salzmann, J. Tatchen, C. Marian, J. Photochem. Photobiol. A 198 (2008) 221.
[17] S. Salzmann, C.M. Marian, M. Mansurova, W. Gärtner, in preparation.
[18] J. Hasegawa, S. Bureekaew, H. Nakatsuji, J. Photochem. Photobiol. A 189 (2007) 205.
[19] K. Zenichowski, M. Gothe, P. Saalfrank, J. Photochem. Photobiol. A 190 (2007) 290.
[20] E. Sikorska et al., J. Phys. Chem. A 108 (2004) 1501.
[21] R.M. Kowalczyk, E. Schleicher, R. Bittl, S. Weber, J. Am. Chem. Soc. 126 (2004) 11393.
[22] T. Domratcheva, R. Fedorov, I. Schlichting, J. Chem. Theory Comput. 2 (2006) 1565.
[23] M. Dittrich, P.L. Freddolino, K. Schulten, J. Phys. Chem. B 109 (2005) 13006.
[24] T. Domratcheva, B.L. Grigorenko, I. Schlichting, A.V. Nemukhin, Biophys. J. 94 (2008) 3872.
[25] A.L. Stelling, K.L. Ronayne, J. Nappa, P.J. Tonge, S.R. Meech, J. Am. Chem. Soc. 129 (2007) 15556.

Paper III

Photophysical properties of structurally and electronically modified flavin derivatives determined by spectroscopy and theoretical calculations

Susanne Salzmann, Víctor Martinez-Junza, Björn Zorn, Silvia Braslavsky,
Madina Mansurova, Christel M. Marian, and Wolfgang Gärtner

J. Phys. Chem. A, *submitted.*

Photophysical properties of structurally and electronically modified flavin derivatives determined by spectroscopy and theoretical calculations

---

Susanne Salzmann,[1] Víctor Martinez-Junza,[2] Björn Zorn,[2] Silvia E. Braslavsky,[2] Madina Mansurova,[2] Christel M. Marian*[1] and Wolfgang Gärtner*[2]

[1] Institute of Theoretical and Computational Chemistry, Heinrich Heine University, Düsseldorf, Universitätsstraße 1, Geb. 26.32, 40225 Düsseldorf, Germany

e-mail: Christel.Marian@uni-duesseldorf.de

[2] Max-Planck-Institute for Bioinorganic Chemistry

Postfach 1013 56, 45410 Mülheim an der Ruhr, Germany

e-mail: gaertner@mpi-muelheim.mpg.de

Keywords: Electronic structure calculations; Intersystem crossing rate constants; fluorescence decays; microsecond transient absorption; triplet state.

Abbreviations: 1DLF: 1-deazalumiflavin; 1DRF: 1-deazariboflavin; 5DLF: 5-deazalumiflavin; 5DRF: 5-deazariboflavin; COSMO: conductor-like screening model; DFT: density functional theory; DFT/MRCI: density functional theory/ multi-reference configuration interaction; DMLF: 7,8-di-demethyllumiflavin = 10-methylisoalloxazine; DMRF: 7,8-di-demethyl riboflavin; FAD: flavin-adenine-dinucleotide; FC: Franck-Condon; FMN: flavin mononucleotide; FWHM: full width at half maximum; IA: isoalloxazine; *ipr*RF: 8-isopropylriboflavin; ISC: intersystem crossing; LF: lumiflavin; MRSOCI: multi-reference spin-orbit coupling configuration interaction; PEH: potential energy hypersurface ; RF: riboflavin; SOMES: spin-orbit matrix elements; SPOCK: spin-orbit coupling kit; SI: Supporting Information; TDDFT: time-dependent density functional theory; TZVP: valence triple zeta with (1d/1p) polarization; UDFT: unrestricted density functional theory: ZPVE: zero point vibrational energy

Abstract

Four different riboflavin (RF) derivatives, two electronically modified compounds (1- and 5-deazariboflavin, 1DRF and 5DRF) and two sterically modified compounds (7,8-di-demethyl- and 8-isopropylriboflavin, DMRF and *ipr*RF), were subjected to a combination of time resolved measurements (absorption and fluorescence) and high-level quantum chemical investigations. Both alkyl modified flavins showed similar fluorescence properties as the parent compound, yet, 5DRF had a larger quantum yield of fluorescence (Φ_F = 0.52) than RF itself (Φ_F = 0.27). Interestingly, 1DRF did not show fluorescence at all under these steady state conditions. The triplet quantum yield was different for the modified flavins such that no triplet formation was found for 1DRF, whereas the other compounds all formed triplet states (Φ_{TR} for 5DRF: 0.64, and 0.50 and 0.23 for *ipr*RF and DMRF, respectively). The triplet states of the two alkyl-modified flavins decayed with similar time constants as the parent compound, whereas a shorter lifetime was measured for 5DRF (τ_{TR} = 15 µs, compared to τ_{TR} = 29 µs for RF). In the calculations, the flavin derivatives were modeled as lumiflavins, *i.e.*, without the ribityl chain. We conclude that for aqueous solutions of DMRF, *ipr*RF, and 5DRF intersystem crossing (ISC) takes place from the S_1 $^1(\pi\pi)$ to the T_2 $^3(\pi\pi)$ state by a vibronic spin-orbit coupling mechanism, a process common to most flavins, whereas ISC is slow in excited 1DRF due to the absence of a close-by triplet state.

Introduction

Flavins are widely found in nature as cofactors of many enzymes in which their versatile redox properties make them available for various roles.[1] In addition, there is an increasing interest in their photochemical properties since their discovery as chromophores in blue-light sensing photoreceptors.[2] Different light-induced reaction pathways of flavins (riboflavin RF, flavin mononucleotide FMN, and flavin-adenine-dinucleotide FAD, Fig. 1) in the various photosensory pigments have been detected (covalent bond formation, stable radical formation, hydrogen bond rearrangements and electron transfer reactions)[3] and, in fact, many research activities of both experimental and theoretical groups have been triggered by these discoveries.[4,5,6,7,8,9,10,11,12,13,14,15,16,17,18,19,20,21] However, in order to unravel those light-induced reactions (*e.g.*, the formation of the reactive triplet species of FMN in the light, oxygen, and voltage (LOV) domains of phototropin), a detailed knowledge of the electronic structure as well as the competing dissipation mechanisms is of particular importance.

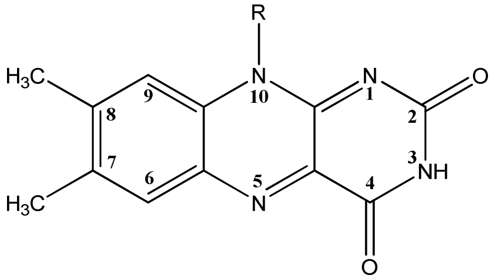

Figure 1. Chemical structure and labeling of flavins. R = CH_3 – lumiflavin; R = ribityl – riboflavin; R = ribityl-5’-phosphate – FMN, flavin mononucleotide; R = ribityl-(9-adenosyl)-pyrophosphate – FAD, flavin adenine dinucleotide.

We recently reported the improved chemical synthesis of two deaza-compounds (1- and 5-deazariboflavin, 1DRF and 5DRF) and two sterically modified compounds (7,8-di-demethyl- and 8-isopropylriboflavin, DMRF and *ipr*RF, for modifications see Fig. 1), in combination with the determination of their first absorption maxima and midpoint potentials.[22] With respect to their potential role as cofactors in photosensitive pigments, the energy dissipation processes of these flavin derivatives are of utter interest. We already could demonstrate that triplet generation in flavins follows different reaction mechanisms in gas phase and in solution.[9] With a combination of experiment and theory, the spectroscopic properties of these compounds are investigated in this report. Hereby, we take a special interest in the mechanism of the triplet state generation.

Experimental and computational details

Experimental setup

The chemical synthesis and electrochemical properties of flavin derivatives have recently been reported.[22] Fluorescence spectra of the water solutions of the flavin derivatives were recorded with a Cary Eclipse spectrometer (Varian, Palo Alto, USA) at an absorbance of A = 0.145 (DMRF, *ipr*RF), and of A = 0.0775 (5DRF) at their respective absorption maximum. The same solutions were used for determination of the fluorescence lifetimes in a FL920 spectrometer (Edinburgh Instruments, UK). Triplet quantum yields Φ_{Tr} of the flavin derivatives were determined by comparison to the known triplet quantum yield of RF. For the latter the literature value of $\Phi_{\mathrm{Tr}} = 0.6$ was used as reference.[37]

Transient absorbance changes after nanosecond-laser flash excitation were recorded using a LFP111 from Luzchem, Ontario, Canada and excitation with a Nd:YAG-driven tunable OPO laser (Nd:YAG, Innolas, Garching, Germany; OPO, GWU Lasertechnik, Erftstadt, Germany). The experiments were performed in the linear laser-energy dependence region of the transient absorbance changes. The flavin derivatives were dissolved in tridistilled water (A = 0.2), and the solutions were bubbled with nitrogen for 30 minutes prior to use. Samples were excited at λ = 422 nm (5DRF) and at λ = 432 nm (DMRF and *ipr*RF). For both wavelengths a riboflavin sample with matching absorbance was used as reference. Data analysis was performed with the Origin software.

Computational details

For the details of the geometry optimizations and the calculation of harmonic vibrational frequencies ((TD)DFT / TZVP) as well as the determination of excitation energies, dipole moments, and oscillator strengths of dipole-allowed transitions (DFT/MRCI / TZVP) we refer to earlier work.[9]

Theoretical radiative decay rates were obtained according to eq. 1

$$k_{rad} = \frac{4e^2}{3c^3\hbar^4}\left(E_i - E_f\right)^3 \left\langle f \middle| \vec{r} \middle| i \right\rangle^2 \qquad \textbf{(1)}$$

Expressing k_{rad} in units of s^{-1}, ΔE in cm^{-1} and μ_{el} = $\langle f|\vec{r}|i\rangle$ in atomic units (ea_0), the numerical pre-factor becomes $2.0261 \cdot 10^{-6}$. If $|i\rangle$ is chosen to be the wave function of the S_1 state, here determined at the DFT/MRCI level, and $\langle f|$ the corresponding ground state wave function, then k_{rad} represents the fluorescence rate k_F of the compound. Eq. (1) can also be used to evaluate the rates spin-forbidden radiative transitions. In this case, spin-orbit mixed wave functions of the initial and final states, obtained here via MRSOCI,[23] have to be employed. In the so-called high-temperature limit, which applies here, all fine-structure sublevels of the T_1 state are populated equally and their individual transition rates have to be averaged to yield the phosphorescence rate k_P.

Intensity distributions of the vibronic absorption transitions were determined in the FC approximation with the VIBES program developed in our laboratory.[24] Attending to efficiency reasons, not all modes were included. After careful testing, 30 modes with the largest displacements in the Duschinsky transformation were selected. For better comparison with the experimental data, the line spectra were broadened by Gaussian functions with constant full width at half maximum (FWHM) of 1000 cm^{-1}.

In the Condon approximation, electronic spin-orbit coupling matrix elements and vibrational overlaps are required for the theoretical determination of ISC rates. SOMES between the correlated DFT/MRCI wave functions were calculated using the SPOCK program developed in our laboratory.[25,26] The one-center mean-field approximation to the Breit-Pauli Hamiltonian was used for the description of the spin-orbit coupling, for reasons of efficiency. This nonempirical effective one-electron operator treats the expensive two-electron terms of the full Hamiltonian in a Fock-like manner[27,28] and has been shown to yield an accuracy better than 5 % of the full treatment.[29,30] Vibrational overlaps were determined employing the VIBES program.[24] Recent studies had shown, however, that a proper description of the nonradiative decay of the S_1 state of flavins in aqueous solution requires going beyond the Condon approximation.[9] To that end, the derivatives of the SOMES, necessary for evaluating the Herzberg-Teller type expansion of spin-orbit coupling around the $^1(\pi\pi^*)$ state minimum to first order, were calculated numerically by finite difference techniques as described.[31] Rate constants for the nonradiative decay of the S_1 state caused by vibronic spin-orbit coupling were also calculated using the VIBES program.[24] Herein, all totally symmetric and all out-of-plane (*oop*) vibrational modes were used as accepting and coupling modes, respectively. For more detailed information on the entities required for the evaluation of the ISC rate constants see the SI.

To estimate spectral shifts due to electrostatic interaction in polar solvents, we employed the COSMO which is implemented in the TURBOMOLE package.[32] The relative static permittivity (formerly called dielectric constant) of water at ambient temperature, $\varepsilon = 78$ was used. Due to technical reasons, C_1 symmetry had to be used for all calculations involving COSMO. For both singlet and triplet multiplicity 20 roots were computed. Since COSMO is not able to model hydrogen bonding, the effects of hydrogen bonding were mimicked by micro-hydration with four explicit water molecules as described in previous work.[9] UDFT was employed for the optimization of the first triplet state of this complex.

Results and Discussion

Absorption and Fluorescence Properties of Modified Flavins

Four RF derivatives were studied: 1DRF and 5DRF, showing an electronically modified structure, and the two sterically modified compounds, DMRF and *ipr*RF (for changes with respect to the structure of the parent compound, see Fig. 1). The modifications cause altered absorption maxima and molar absorption coefficients, as compared to riboflavin, in particular for the two deaza derivatives (Table 1). 1DRF showed a strong bathochromic shift of its absorption maximum (λ_{max} = 537 nm) and a reduced molar absorption coefficient (ε_{max} = 6800 M^{-1} cm^{-1}), the 5-deaza derivative showed a similar molar absorption coefficient as RF, but a significant hypsochromic shift of its absorption maximum (λ_{max} = 408 nm). The demethyl compound also showed a small hypsochromic shift in its absorption maximum (λ_{max} = 436 nm), whereas the absorption maximum of *ipr*RF was practically identical to that of the parent compound. Both alkyl-modified RF compounds had absorption coefficients identical to riboflavin.

No fluorescence was detected for 1DRF by steady-state measurements, in agreement with the known literature.[33] However, experiments using sub-ns pulses revealed a clearly detectable fluorescence for this compound in the short ps time range.[34] The other flavin derivatives showed a substantial fluorescence quantum yield (Table 1). Similar fluorescence quantum yields as those for riboflavin (Φ_F = 0.27)[35] were determined for the demethyl derivative and for *ipr*RF (Φ_{Fl} = 0.27), but a significantly larger quantum yield, Φ_{Fl} = 0.52, was found for the 5-deaza compound. The fluorescence decay time of the demethyl derivative (τ_{Fl} = 3.9 ns) was slightly shorter than that of RF (τ_{Fl} = 4.8 ns for RF), whereas the corresponding values for 5DRF (5 ns) and for *ipr*RF (4.7 ns) were in the same range as that of the parent compound RF.

Table 1 Spectroscopic properties of four structurally modified riboflavins and of the parent compound (RF).

	λ_{abs} (max)[a] /nm	ε_{max}[a] /$M^{-1}cm^{-1}$	λ_{em} (max) /nm	τ_{Fl} /ns	Φ_{Fl}
RF	450	12460	520	4.8	0.27
1DRF	537	6800	n.d.[b]	n.d.[b]	n.d.[b]
5DRF	400	12460	441	5.0	0.52
DMRF	436	12460	520	3.9	0.27
*ipr*RF	448	12460	520	4.7	0.27

[a] Taken from Ref. 22, Table 1.

[b] For a detailed investigation of the fluorescence properties of 1DRF see Ref. 34.

The data obtained for 5DRF can be compared to those reported by Isińska-Rak et al.[36] although their measurements for 5DRF were performed in acetonitrile and methanol, whereas we measured in water. Excellent agreement was found for RF (τ_{Fl} = 4.8 vs. 5.1 ns, Φ_{Fl} = 0.27 vs. 0.28), whereas the parameters for 5DRF determined here differ significantly from those cited above[36]: τ_{Fl} = 5.0 vs. 4.03 ns, and Φ_{Fl} = 0.52 vs. 0.11. This may be attributed to the different solvents used, but this behavior requires a more detailed comparative investigation.

Time-resolved absorption changes

Nanosecond laser flash excitation of the riboflavin derivatives caused transient absorption changes, except for 1DRF, which remained practically unchanged over the whole observation time. For the other three RF derivatives the absorption band underwent transient bleaching, concomitant with the formation of broad, structured absorption bands that extended far into the long wavelength range (Table 2). Riboflavin showed the formation of a broad absorption with maxima at 520 and ca. 700 nm with a quantum yield of 0.6 that decayed with a 29 µs lifetime. One should be aware that the reported quantum yields vary significantly from 0.4 up to 0.6.[37,38,39] These variations reported in the literature arise from varying experimental conditions, with the pH value of the solution being the most dominating factor changing the spectroscopic properties of flavins. The 5-deaza compound showed formation of a triplet band with a maximum around 500 nm (Figure 2). This species showed a slightly higher quantum yield (Φ_{Tr} = 0.64) and decayed faster than RF (τ_{Tr} = 14 µs). Smaller quantum yields were determined for the two alkyl modified compounds: Φ_{Tr} = 0.23 (decay time τ_{Tr} = 24 µs) for DMRF, and Φ_{Tr} = 0.50 (decay time τ_{Tr} = 27 µs) for *ipr*RF. The formation of broad, structured transient absorption bands was detected also for these compounds (only the spectra of 5DRF are shown here).

Table 2 Properties of flavin triplet states; λ_{max} and λ_{min} refer to the transient absorption maximum and minimum (bleaching) immediately after the ns laser pulse; τ_{Tr} is the triplet lifetime in aqueous solution under the degassing conditions used.

	τ_{Tr} /µs	λ_{max} /nm	λ_{min} /nm	Φ_{Tr}
RF	29	390,520, 700	450	0.60
1DRF[a]	-	-	-	-
5DRF	14	500	410	0.64
DMRF	24	380,510, 630	450	0.23
*ipr*RF	27	520, 700	460	0.50

[a] No triplet formation was observed for this compound.

Comparison with the recently reported[36] triplet parameters for 5DRF revealed again deviations: These authors measured a significantly longer triplet lifetime of 105 µs in contrast to the value of 14 µs found by us.

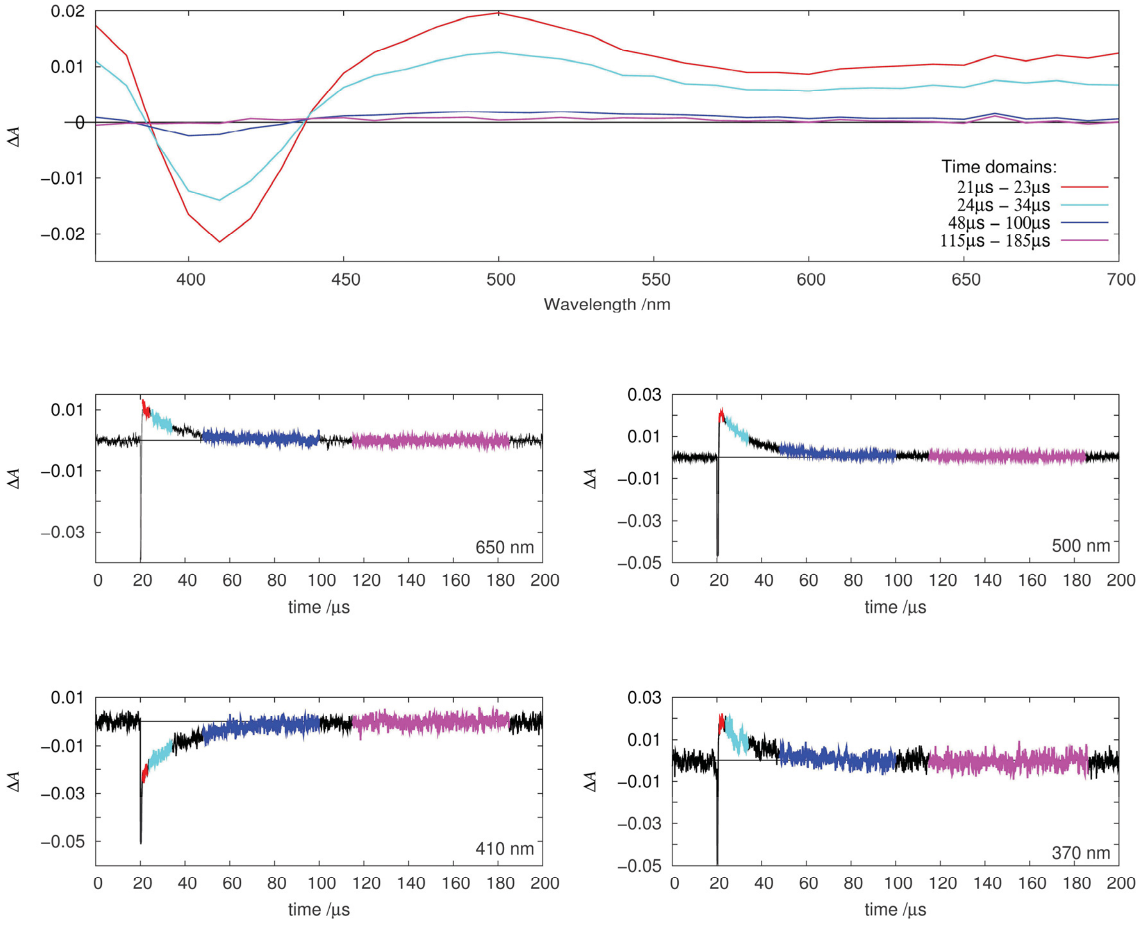

Figure 2 Transient absorption spectra of 5DRF for different time domains (uppermost panel) and kinetic traces at various wavelengths: 650 nm, 500 nm, 410 nm, and 370 nm. The color coding of the kinetic traces refers to the color coding of the transient spectra.

Calculated electronic absorption spectra

It has been shown earlier that the spectroscopic properties of RF and LF are nearly identical.[40,41,42] For this reason, the bulky ribityl chain was substituted by a methyl group in all calculations. Accordingly, the flavin compounds RF, DMRF, 1DRF, and 5DRF were modeled by LF, DMLF (=10-methylisoalloxazine, MIA, in Ref. 9), 1DLF, and 5DLF, respectively.

The ground and excited state geometries of LF and DMLF were taken from earlier work.[9] Except for the now present C-C bonds being longer than the original C-N-bonds, the exchange of the nitrogen atoms at positions 1 or 5 for a CH-group showed no major effect on the nuclear structure (for more information see SI). To facilitate the discussion, the minimum nuclear arrangement of the first excited singlet state is denoted $^1(\pi\pi)$ and the optimized geometry of the first triplet state is labeled $^3(\pi\pi)$.

LF and DMLF as models for RF and DMRF

The photophysical properties of the three flavin compounds IA, DMLF and LF in vacuum and in solution had been the topic of earlier work.[9] Thus, only a short abstract of the calculated vertical excitation spectra of LF and DMLF is given below. For a detailed comparison and discussion of our DFT/MRCI excitation energies of all three flavin compounds with experimental data and with earlier quantum chemical investigations see.[9]

Flavins show usually three absorption bands in the wavelength range longer than 250 nm. In previous quantum chemical studies they have all been assigned to $(\pi\rightarrow\pi^*)$ transitions.[9,10,11,12,13,14,15] The first band in the absorption spectrum corresponds to a transition from the ground state to the lowest-lying excited state of the singlet manifold (S_1) of LF and DMLF, and is dominated by the $(\pi_H\rightarrow\pi_L^*)$ (HOMO-LUMO) excitation. The position of that band is nearly unaffected by the surrounding solvent.[13,43] In contrast, the second visible band in the spectrum is known to exhibit a pronounced red shift in polar and protic solvents.[13,41,43] In the vacuum, this state corresponds to the fourth excited singlet state (S_4) and is mainly dominated by the $(\pi_{H-1}\rightarrow\pi_L^*)$ excitation. The most intensive of these three bands is found in the UV spectral region around 250 nm. It arises mainly from the $(\pi_H\rightarrow\pi_{L+1}^*)$ excitation.[9]

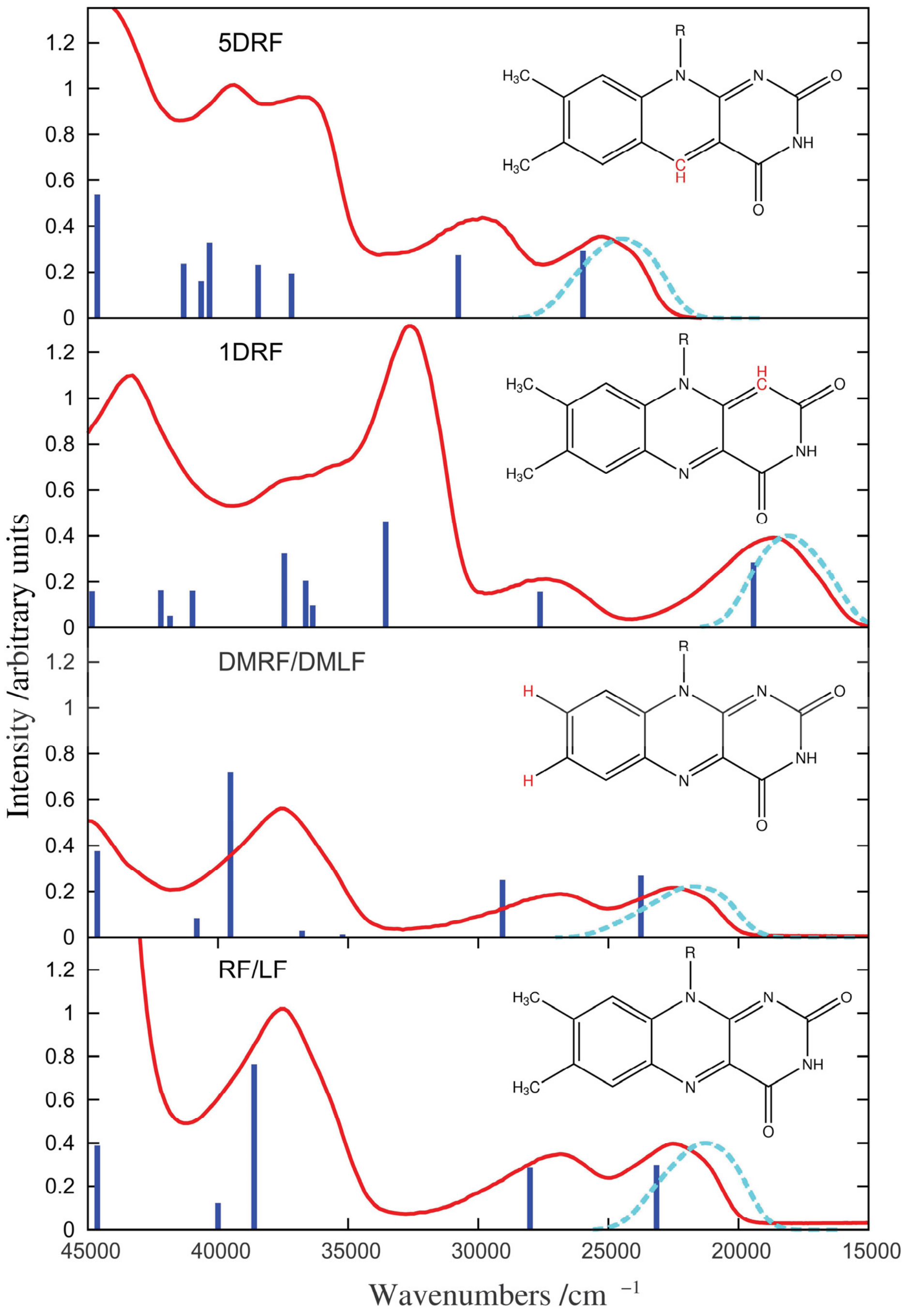

Figure 3 **LF, DMLF, 1DLF and 5DLF**: Comparison between experimental absorption spectra of the riboflavin derivatives (full lines) and DFT/MRCI vertical excitation energies and intensities of the lumiflavin derivatives (vertical lines) in water. In addition, simulated FC $S_0 \rightarrow S_1$ absorption bands (dashed line) are shown. For easier comparison with

experiment, the computed line spectrum (not shown) was broadened by Gaussian functions with FWHM = 1000 cm^{-1}.

Our calculations yield vertical excitation wavelengths of 432 nm for LF and 421 nm for DMLF for aqueous solution (referring to values in the gas phase of 422 nm and 409 nm, respectively). Although it is a common practice to identify the measured absorption maxima with vertical excitation energies, it has been shown that this approach is not always correct.[44,45,46] In cases, when the geometry shift is small, as for all flavins presented here, the vibrational wave functions do not necessarily have their maxima at the classical turning points,[46] and a displacement of the absorption maximum from the vertical excitation energy can occur (for more information see SI). The simulated FC $S_0 \rightarrow S_1$ absorption spectra of LF and DMLF are shown in Figure 3 together with the computed vertical excitation energies and the measured spectra of RF and DMRF. It is seen that the maxima of the simulated $S_0 \rightarrow S_1$ absorption bands are significantly red shifted with respect to the vertical excitation energies. A comparison with the measured peak positions and band shapes shows good agreement.

The second band, originating from the ($\pi_{H-1} \rightarrow \pi_L^*$) excitation shows a slightly lower oscillator strength than the first bright transition. With our best solvation model (COSMO + micro-hydration), we find a vertical excitation wavelength at 357 nm for LF and 343 nm for DMLF, respectively, in very good agreement with the measurements (375 nm for LF and 349 nm for DMLF). The energetic position of the third band is also well reproduced by the calculations. Furthermore, good qualitative agreement in the considered energy range is found between the computed and measured relative intensities of all optically bright transitions (Figure 3).

Low-lying nπ^* states that are involved in the photophysics of LF and DMLF in the gas phase, do not play a major role in the low-energy regime of these flavins in aqueous solution, where these states are blue-shifted by up to 0.7 eV. This does not exclude a participation of the ^{1}nπ^* states via vibronic coupling at elevated temperatures as described by Weigel et al.[47]

Table 3. Calculated vertical absorption wavelengths, λ/nm, for LF and DMLF in aqueous solution compared to experimental band maxima for RF and DMRF. The value of the calculated band maximum is given in parentheses. For more details, such as oscillator strengths and dipole moments, see the SI.

	Calculations (COSMO+μ-hyd.)			**Experiment**	
State[a]	transition (LF)	λ LF	λ DMLF[b]	λ RF	λ DMRF
S_0	ground state				
S_1	$\pi_H \rightarrow \pi_L$	432 (470)	421 (460)	450[c]	436[c]
S_4	$\pi_{H-1} \rightarrow \pi_L$	357	344	375	349
S_3	$n_{N2} \rightarrow \pi_L$ $n_{O2} \rightarrow \pi_L$	340	345	-	-
T_1	$\pi_H \rightarrow \pi_L$	555	532	-	-
T_3	$\pi_{H-1} \rightarrow \pi_L$	455	445	-	-
T_2	$n_{N2} \rightarrow \pi_L$ $n_{O2} \rightarrow \pi_L$ $n_{O1} \rightarrow \pi_L$	377	382	-	-

[a]: State ordering with respect to the vacuum calculation (see SI).

[b]: Vertical absorption energies taken from Ref. 9.

[c]: Absorption maxima in aqueous solution at ambient temperature taken from Ref. 22.

1DLF and 5DLF as models for 1DRF and 5DRF, respectively

The absorption spectra of both deaza derivatives, 1DLF and 5DLF, differ with respect to the parent compound such that 1DRF exhibits a strong bathochromic shift, whereas the absorption maximum of 5DRF is hypsochromically shifted (Table 1). Inspection of the optimized ground and excited state geometries reveals that structural changes are mostly restricted to the bonds adjacent to the substituted atoms (for more information see Figure S5 and S6 of the SI). Therefore, we can exclude purely geometrical effects as the origin of the altered spectroscopic properties. In order to shed some light on the spectroscopic shifts, the orbital energies of three decisive frontier π orbitals for all calculated compounds, the total energies of the two deaza flavins, 1DLF and 5DLF, and three MOs of LF are shown in Figure 4.

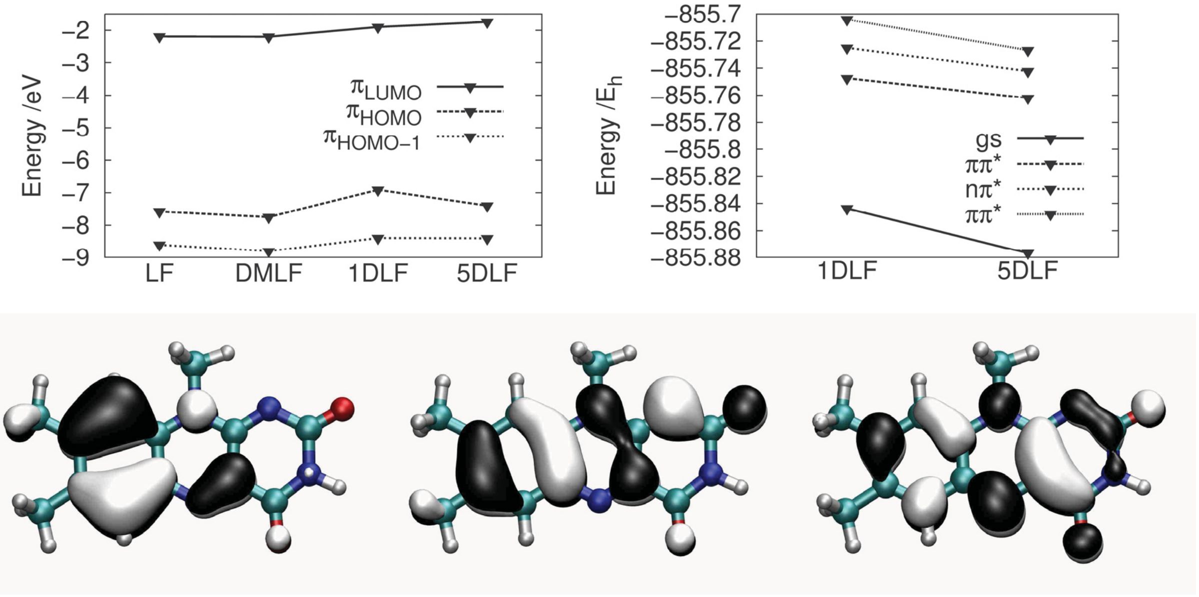

Figure 4 Left, top: Orbital energies of three frontier π orbitals for all calculated compounds in the vacuum. Right, top: Total energies of 1DLF in comparison to 5DLF. Bottom, left to right: π_{H-1} (HOMO-1), π_H (HOMO), and π_L^* (LUMO) of LF. The black and white coding describes the different phases (plus or minus) of the molecular orbital amplitudes.

In a simplified picture, the excitation energies depend on the differences between the orbital energies of the orbitals involved. As can be seen in Figure 4 (left), the orbital energies of 1DLF and 5DLF differ from those of the parent compound LF, which serves as reference in the following discussion. The π_H MO (HOMO) of 1DLF is destabilized, whereas for 5DLF no significant energy shift is found. the fact that the destabilization is more pronounced for the LUMO (π_L*) of 5DLF can be rationalized as follows. The charge distribution at the N(1) and N(5) positions is very different for the two MOs π_H and π_L*. The Coulomb attraction between the electrons and the nucleus is larger at the N center than at the C center. Therefore, exchange of an iminic nitrogen atom for a CH group causes a destabilization, if substantial electron density is found at the respective center. Hence, substitution at the N(1) position, influences the π_H MO, whereas the position of the π_L* MO is nearly unaffected. This results in a red-shift of the absorption. Substitution at the N(5) position, on the other hand, leads to a considerable destabilization of the π_L* MO, consequently causing a blue-shift of the absorption, since the π_H MO remains widely unaffected.

The vertical excitation wavelength of the first excited singlet state of 1DLF in the gas phase is red shifted by about 50 nm to 473 nm with respect to the parent compound. As in LF, this state is dominated by the $\pi_H \rightarrow \pi_L^*$ (HOMO-LUMO) transition. Polarity and effects of hydrogen bonding of the solvent accumulate an additional red-shift. We find a vertical excitation energy of 515 nm with our best solvent model, The band maximum in aqueous solution, as estimated from the simulated FC spectrum, is located at 553 nm, in good agreement with the experiment (537 nm for 1DRF). The position of the second optically bright band is unaffected by the replacement of the N(1) atom by a CH group. However, its oscillator strength is drastically smaller than that of LF. Similar to the parent compound, it is red-shifted by almost 0.4 eV in water. According to our calculations, more than one electronic transition contributes to the third band, which exhibits a pronounced shoulder at its short-wavelength side and is the strongest band in the considered energy regime.

Table 4. Vertical singlet and triplet DFT/MRCI excitation wavelength, λ /nm, for 1DLF at the ground state geometry in the vacuum and in aqueous solution. The value in parenthesis is the calculated band maximum. In addition to the dominant excitations, oscillator strengths f(r) and dipole moments, μ/Debye, are given. For more details see the SI. Experimental values refer to 1DRF.

	Vacuum	**COSMO+μ-hyd.**	**Experiment**

							1DRF
	State	transition	λ	f(r)	μ	λ	λ
S_0	$1^1A'$	ground state			9.1		
S_1	$2^1A'$	$\pi_H \rightarrow \pi_L$	473 (505)	0.276	11.3	515 (553)	537[a]
S_2	$1^1A''$	$n_O \rightarrow \pi_L$	374	0.001	3.6	320	-
S_3	$2^1A''$	$n_{ON2} \rightarrow \pi_L$ $n_{ON1} \rightarrow \pi_L$	346	0.003	7.9	329	-
S_4	$3^1A'$	$\pi_{H-1} \rightarrow \pi_L$	326	0.060	12.9	362	368
T_1	$1^3A'$	$\pi_H \rightarrow \pi_L$	660	-	9.6	693	-
T_2	$2^3A'$	$n_O \rightarrow \pi_L$ $n_{ON2} \rightarrow \pi_L$	399	-	5.2	368	-
T_3	$1^3A''$	$\pi_{H-1} \rightarrow \pi_L$ $\pi_H \rightarrow \pi_{L+1}$	399	-	12.3	447	-

[a]: Absorption maxima in aqueous solution at ambient temperature taken from Ref. 22.

The energetic positions of the dark $n\pi^*$ states in 1DLF are rather unaffected by water. Due to the substantial red-shift of the $^1(\pi\pi^*)$ (S_1) band, the $^1(n\pi^*)$ states are located more than 0.6 eV above that band in the vacuum. In water, the energy gap is even larger than 1 eV, excluding that the $^1(n\pi^*)$ states contribute to the photophysics of the first absorption band.

Table 5. Vertical singlet and triplet DFT/MRCI excitation wavelength, λ /nm, for 5DLF at the ground state geometry in vacuum and aqueous solution. The value in parenthesis is the calculated band maximum. In addition to the dominant excitations, oscillator strengths *f*(r) and dipole moments, μ/Debye, are given. For more details see the SI. Experimental values refer to 5DRF.

	vacuum					**COSMO+μ-hyd.**	**Experiment 5DRF**
	State	transitions	λ	*f*(r)	μ	λ	λ
S_0	$1^1A'$	ground state			9.8		
S_1	$2^1A'$	$\pi_H \rightarrow \pi_L$	397 (422)	0.324	9.5	385 (408)	400^a
S_2	$1^1A''$	$n_{O2} \rightarrow \pi_L$	339	0.000	1.3		-
S_3	$3^1A'$	$\pi_{H-1} \rightarrow \pi_L$ $\pi_H \rightarrow \pi_{L+1}$	304	0.151	13.2	325	335
T_1	$1^3A'$	$\pi_H \rightarrow \pi_L$	488	-	7.9	454	-
T_2	$2^3A'$	$\pi_{H-1} \rightarrow \pi_L$	389	-	12.7	414	-
T_3	$1^3A''$	$n_{O2} \rightarrow \pi_L$	347	-	1.7	320	-

[a]: Absorption maxima in aqueous solution at ambient temperature taken from Ref. 22.

The two lowest-lying absorption bands of 5DLF are blue shifted with respect to those for the parent compound LF. However, unlike for 1DLF, the energetic position of the first absorption band ($\pi_H \rightarrow \pi_L^*$) (HOMO-LUMO) is not very sensitive to the environment. Whereas the vertical excitation wavelength is calculated in vacuum to be 397 nm, it is found at 385 nm in aqueous solution. The band maximum in water is estimated at 408 nm, close to the experimental value of 400 nm (Figure 3). An excitation energy of 304 nm in the gas phase and 325 nm in aqueous solution is determined for the second band. Five energetically close-lying electronic transitions with significant oscillator strengths are made responsible for the strange shape of the third absorption band in the experimental spectrum of 5DRF. Similar to the parent compounds, good qualitative agreement between the calculated and measured relative intensities of the first three absorption bands of the deaza derivatives is observed.

Even in vacuum, the experimentally not observable $^1(n\rightarrow\pi^*)$ transitions are blue-shifted by at least 0.5 eV with respect to the parent compound, in agreement with earlier TDDFT investigations of 5DRF.[36]

Calculated fluorescence rate constants

Adiabatic excitation energies and radiative decay rate constants for the $^1(\pi\pi)$ state minimum nuclear arrangements are listed in Table 6. As found in earlier work,[9] the adiabatic excitation energies of the first $^1(\pi\pi)$ states of LF and DMLF are very similar. The onset of the absorption is somewhat blue-shifted for the $^1(\pi\pi)$ state of DMLF with respect to LF, in agreement with the experimental findings.

Table 6. Adiabatic excitation wavelengths, λ/nm, and radiative rate constants, k/s^{-1}, of the lowest-lying singlet state. ZPVE-corrected values are given in parentheses. The experimental fluorescence rates are obtained from τ_{Fl} and Φ_{Fl} (Table 1) via $k_F = \Phi_{Fl}/\tau_{Fl}$.

	vacuum		EXP.
	$E_{adia}(S_1)$	k_F	k_F
LF[a]	456 (489)	$6\cdot10^7$	$5.6\cdot10^7$
DMLF[a]	461 (475)	$5\cdot10^7$	$3.8\cdot10^7$
1DLF	543 (556)	$2\cdot10^7$	-
5DLF	432(449)	$7\cdot10^7$	$10\cdot10^7$

[a]: Excitation energies and fluorescence rate constants taken from Ref. 9.

As anticipated from the vertical excitation energies, the adiabatic excitation energies of 1DLF are red shifted with respect to the parent compound, whereas a blue shift is observed for 5DLF. Our model does not allow determining the solvent shift for emission in the same satisfying manner as for absorption. However, since the LF and DMLF transition energies show almost no solvent shifts, we expect the fluorescence rates in water to remain unchanged with respect to the gas phase.

The solvent causes a hypsochromic shift in the emission of 5DLF. Since the fluorescence rate constant is proportional to the cube of the emission energy, we expect the rate to increase in water. Concurrent with this trend, our calculated fluorescence rate constants show an excellent overall agreement with the experimental findings for RF, RMRF, and 5DRF. As pointed out above, 1DRF behaved differently and showed a fluorescence decay in the picoseconds time range.[34]

Triplet generation

As already stated in the Introduction, the light-induced reactions in the flavin-binding, blue-light photosensors comprise different reaction mechanisms of the flavin chromophores. The signaling reactions range from covalent bond formation (via a reactive triplet transient) to stable radical formation, hydrogen bond rearrangements, and electron transfer reactions. Clearly, the dissipation mechanisms that depopulate the primarily excited singlet state of the flavin cofactor strongly depend on the environmental surroundings.

In all flavin derivatives studied in this work, the lowest-lying excited triplet state (T_1) is dominated by the $\pi_H \rightarrow \pi_L^*$ (HOMO-LUMO) transition. In LF and DMLF its energetic position is mostly solvent independent. For the ordering of the second and third excited triplet states, which are energetically close to the S_1 state, the environment plays a decisive role. In the vacuum, the $^3n\pi^*$ state is situated below S_1 and the second $^3\pi\pi^*$ state is situated above (see Table 3). This order reverses in aqueous solution which is momentous for the ISC mechanism (see below). Similar to the singlet case, the lowest-lying excited triplet state of 1DLF is red-shifted by solvent effects (see Table 4). Contrary to LF, there is no second triplet state situated below the S_1 state in the vertical spectrum of 1DLF, neither in the vacuum nor in solution. Hence, only the T_1 state can contribute to the depopulation of the S_1 state via ISC. Considering 5DLF, the first excited triplet state in the FC region shows a similar blue-shift as its singlet counterpart. In the vacuum there is no other triplet state found below the S_1 state. However, the second $^3(\pi\pi^*)$ state is energetically close. In aqueous solution, this state is located below the S_1 state and possibly participates in the dissipation of that state.

In previous work we have shown that, due to the above mentioned sensitivity of several low-lying excited triplet states to the environment, the triplet generation in flavins follows different mechanisms for gas phase and aqueous solutions.[9] Back then, due to efficiency reasons, the ISC rate constants were only calculated for the smallest compound (IA in Ref. 9), because the number and the frequencies of the normal modes are of importance for the computational expense of the vibrational overlaps. The introduction of three methyl groups increases the number of normal modes by 27. Moreover, the torsional frequencies are very low. In combination with a large energy gap, the calculations become impracticable due to the immense number of vibrational levels in the final state. Rates for the ($S_1 \rightarrow T_1$) channel in LF were therefore evaluated employing a smaller integration interval and restrictions with respect to the excitation level of vibrational quanta (see SI for more information).

In order to estimate the ISC rate constants in water, the solvent shift of the electronic states has to be taken into account for the calculations of the SOME (derivatives) and the adiabatic electronic energy differences. Although with COSMO the charge distribution of the molecule that polarizes the surrounding solvent is taken into account properly only for the absorption energies, this is the only practicable way to introduce the solvent-induced shifts into the calculations of the SOME derivatives. The COSMO model has been employed also for the calculations of adiabatic electronic energy differences. Extensive tests (see SI, Table S13, Table S17, and Table S21) have shown that, by varying ΔE in a range of 1100 cm^{-1}, the order of magnitude of the ISC rate constant for the ($S_1 \rightarrow T_2$) channels remains stable. Our calculated ISC rate constants for vacuum and solution are found in Table 7.

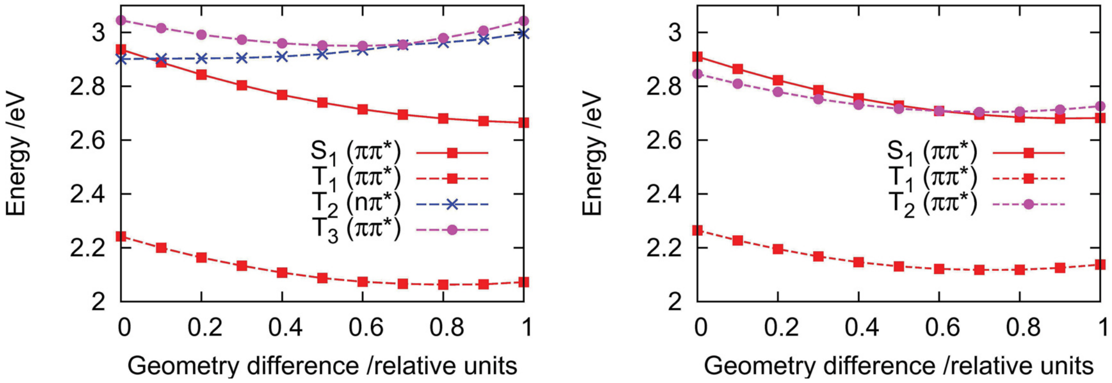

Figure 5 DFT/MRCI energies of low-lying states of LF along a linearly interpolated path between the ground state geometry (0) and the $^1(\pi\pi^*)$ geometry (1) for the vacuum (left) and aqueous solution (COSMO, right). For the energy profiles of DMLF, which are nearly identical, see Ref. 9, Figure 5.

LF and DMLF

We obtain a crossing between the S_1 and T_2 potential energy hypersurfaces along the reaction path connecting the FC region and the $^1(\pi\pi)$ minimum for LF and DMLF. This is the case both for vacuum and for aqueous solution. In the vacuum (Figure 5, left) the crossing is observed between the $^1(\pi\pi^*)$ (S_1) and the $^3(n\pi^*)$ (T_2) states. Spin-orbit coupling of the PEHs is substantial in that region. In agreement with El Sayed's rule, the direct ISC rate constants are found to be large (Table 7). Since the fastest process dominates the rate constant, we estimate that in the gas phase the ISC from the $S_1(\pi\pi^*)$ state to the triplet manifold takes place in nanoseconds for LF, and in about 100 picoseconds in DMLF. This ISC channel is no longer available in aqueous solution, due to the significant blue-shift of the $n\pi^*$ states. Instead, a crossing between the $^1(\pi\pi^*)$ (S_1) and the $^3(\pi\pi^*)$ (T_2) states takes place (Figure 5, right). However, spin-orbit matrix elements between the two states are negligible and, as a result, direct ISC is found to be very inefficient. Although this is in agreement with the widely used rules of thumb, it does not explain the substantial experimental ISC rate constants (k_{ISC} = 10^8 s^{-1}, Ref. 48) for RF in water. Only when vibronic spin-orbit coupling is taken into account, the rate constants reach values between ~10^7 s^{-1} and ~10^8 s^{-1} for the $S_1 \rightarrow T_{2x}$ and $S_1 \rightarrow T_{2y}$ channels of both compounds (Tables S13 and S17). Qualitatively this phenomenon can be interpreted as an intensity borrowing from the much faster $(\pi\pi^*)\rightarrow(n\pi^*)$ process.

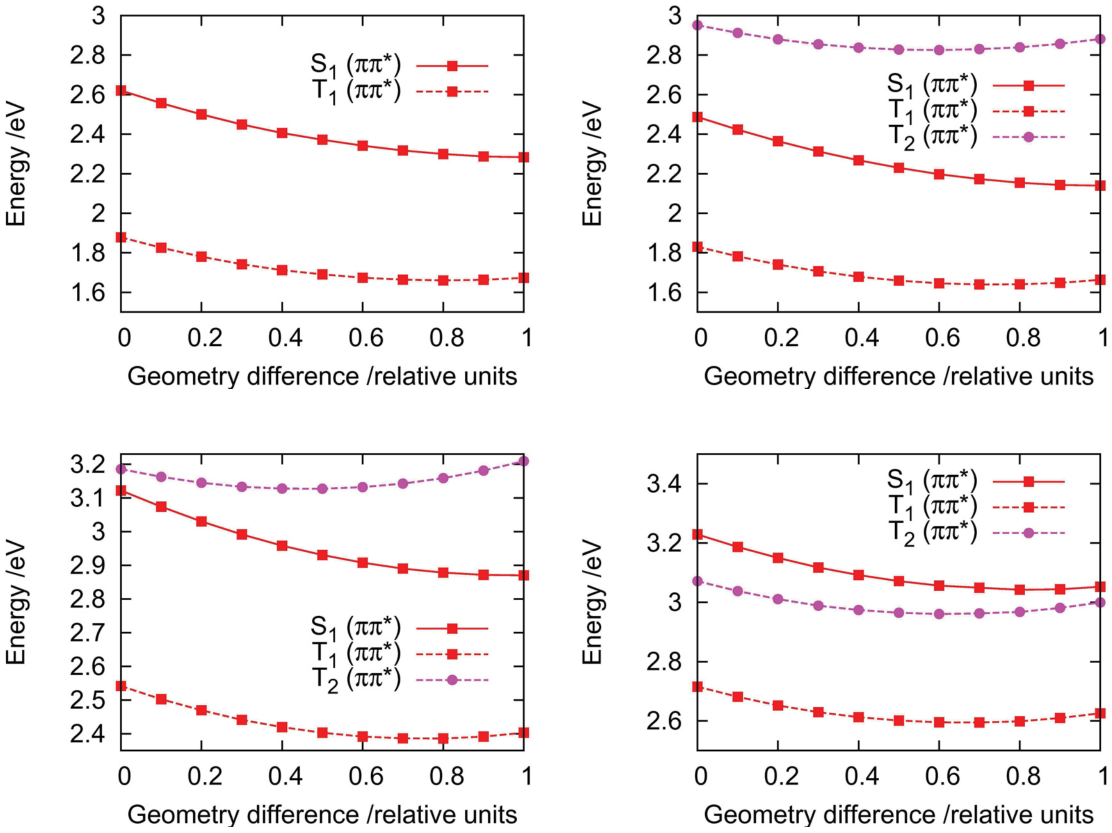

Figure 6 DFT/MRCI energies of low-lying states along a linearly interpolated path between the ground state geometry (0) and the $^1(\pi\pi^*)$ geometry (1) for 1DLF (top) and 5DLF (bottom) in the vacuum (left) and aqueous solution (COSMO, right).

1DLF and 5DLF

The DFT/MRCI energy profiles of 1DLF along the reaction path between the FC region and the $^1(\pi\pi)$ minimum are shown in Figure 6 (top). As already seen for the vertical excitation energies (FC region), there is no triplet state in close proximity to the first excited singlet state, independent of the environment. With the ISC initiating from the $^1(\pi\pi)$ (S_1) state, only the $^3(\pi\pi)$ (T_1) state can be populated. Vibronic spin-orbit coupling enhances the

ISC rate constant to ~10^5 s^{-1} in the gas phase and ~10^6 s^{-1} in aqueous solution (see Table S19 for details). Nevertheless, ISC appears to be much too slow in 1DLF to be able to compete with IC or fluorescence decay.

Table 7 Integrated rate constants k_{ISC}/s^{-1} for the intersystem crossing from the zero vibrational level of the first electronically excited singlet state (S_1) to all triplet vibrational levels (electronic states T_1 and T_2) located in a small energy interval of width 2η around the initial state. For detailed information on the procedure and the choice of parameters see SI.

	vacuum		**cosmo**	
	k_{ISC} ($S_1 \rightarrow T_1$)	k_{ISC} ($S_1 \rightarrow T_2$)	k_{ISC} ($S_1 \rightarrow T_1$)	k_{ISC} ($S_1 \rightarrow T_2$)
LF	~10^5-10^6	~10^9	~$3 \cdot 10^6$	~10^8
DMLF	~$1.6 \cdot 10^7$	~10^{10}	~$1 \cdot 10^7$	~10^7-10^8
1DLF	~$2 \cdot 10^6$	-	~$1 \cdot 10^6$	-
5DLF	~$2 \cdot 10^6$	-	~$7 \cdot 10^5$	~10^7-10^8

No crossing between the S_1 and T_2 PEH is observed along the reaction path between the FC region and the $^1(\pi\pi)$ minimum for 5DLF, in the isolated chromophore or in aqueous solution (Figure 6, bottom). In the vacuum, the minimum of the $^3(\pi\pi^*)$ T_2 state is situated closely above that of the S_1 state. With the ISC initiating from the $^1(\pi\pi)$ (S_1) state, only the $^3(\pi\pi^*)$ T_1 state can be populated. Vibronic spin-orbit coupling enhances the ISC rate constant to ~10^5 s^{-1}. In aqueous solution, however, the ordering of the $^1(\pi\pi^*)$ S_1 and the $^3(\pi\pi^*)$ T_2 states is altered. Although we do not observe a crossing between the $^1(\pi\pi^*)$ (S_1) and the $^3(\pi\pi^*)$ (T_2) states here, the minimum of the latter state should be energetically accessible from the initial state (S_1). When vibronic spin-orbit coupling is taken into account, our calculations predict the rate constant of ISC to range between ~10^7 s^{-1} and 10^8 s^{-1} for the $S_1 \rightarrow T_{2x}$ and $S_1 \rightarrow T_{2y}$ channels, respectively. For details see Table S22.

Depopulation of the $^1(\pi\pi^*)$ state

Processes in water and comparison with experiment

Summarizing, the calculations yield fluorescence rates and ISC rates of comparable magnitude for LF. The phosphorescence rate (see SI) is significantly smaller. Hence, it is not necessary to take this process into consideration. These findings are in qualitative agreement with our experimental quantum yields Φ_F (0.27) and Φ_{Tr} (0.60) for RF. For a more quantitative comparison of the quantum yields, further processes such as the non-radiative depopulation of the S_1 state by internal conversion need to be taken into account. For the demethylated compounds (DMLF and DMRF, respectively) we find fluorescence rates of similar magnitude as for the parent compounds. However, our calculations cannot explain the significantly lower triplet quantum yield Φ_{Tr} = 0.23, for DMRF. The fluorescence decay is found to be somewhat faster for 5DLF than for the parent compound. Therefore, fluorescence should gain importance with respect to the ISC process, as is qualitatively reflected in the ratio of our experimental quantum yields Φ_F (0.52) and Φ_{Tr} (0.64). These values add up to more than 1.0, but errors between 10 and 15 % should be considered. In 1DRF an ultrafast fluorescence decay was observed.[34] The mechanism of the quenching process is not known at present and needs further clarification.

Processes in the gas phase

For LF and DMLF our calculations find the nonradiative depletion more than one order of magnitude faster than the spin-allowed radiative transition to the electronic ground state. Our results suggest that internal conversion to the ground state enhanced by the energetic proximity of the first $^1(n\pi^*)$ state is an additional competing channel. On this basis we predict that for isolated LF (RF) and DMLF (DMRF) fluorescence should not be observable. Due to the lack of a second accessible triplet state, the ISC rate in excited 5DLF is found to be more than one order of magnitude smaller than in the parent compound. Furthermore, $^1(n\pi^*)$ states should not participate actively in the nonradiative decay of the S_1 state. Accordingly, deactivation via fluorescence should prevail for 5DLF (5DRF) in the gas phase. ISC cannot compete with the spin-allowed radiative transition to the electronic ground state in excited 1DLF. Additionally, $^1(n\pi^*)$ states are not accessible. Thus, triplet generation in 1DLF should be negligible and radiative decay via fluorescence should be substantial.

Triplet-Triplet Absorption

It has been found earlier that triplet-triplet absorption spectra of LF calculated in the gas phase cannot be compared to measurements in aqueous solution.[14] Since the triplet-triplet excitation energies significantly depend on the surrounding environment, we employ our full solvent model (COSMO + μ-hydr.), although, as described above, the treatment of solvent effects with COSMO for non-FC excitations is not ideal. The resulting line spectra of the vertical triplet-triplet excitation energies are displayed and compared to our experimental data in Figure 7.

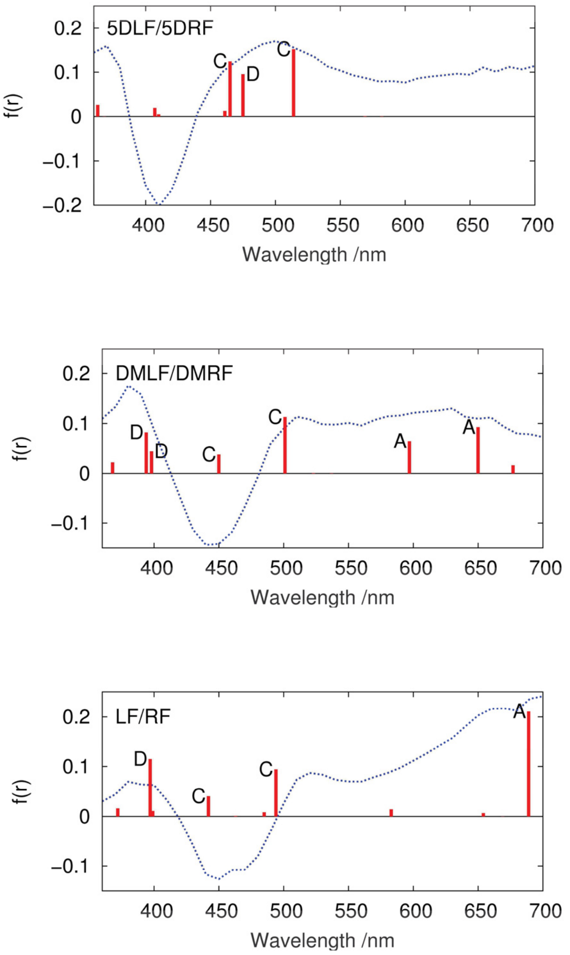

Figure 7 Comparison of the experimental and calculated (COSMO + μ-hydr.) triplet-triplet absorption spectra of the parent compound and the demethyl and 5-deaza derivatives. Only states with an oscillator strength f(r) greater than 0.01 are shown. For the definition of the labels A, C, and D see Table 8.

When we compare the calculated line spectra with our experimental data, we have to keep in mind that the reciprocal wavelength scale is very sensitive in the low energy regime. The typical DFT/MRCI error bars of ± 0.2 eV[49] translate to ± 20 nm (around 360 nm) up to ± 90 nm (around 700 nm). The majority of the excited triplet states show substantial multi-configuration character. However, we could find three different electronic transitions (labeled A, C, D in the following, see Table 8) for all investigated flavins that contribute with significant intensity to the transient spectra. In addition, two different electronic excitations (labeled b, see Table 8) with minor intensity are found.

Table 8 LF: Assignment of the vertical triplet-triplet excitation wavelengths λ /nm to the electronic structure. The electronic excitations are given with respect to the open-shell triplet ground state. Intensities are indicated in parentheses.

transitions		λ			
label	**excitation**	**LF**	**DMLF**	**1DLF**	**5DLF**
A	$\pi_{H-3}\rightarrow\pi_H$	689 (vs)	650,597 (s),(s)	690,601 (s),(s)	752 (s)
b	$\pi_{H-2}\rightarrow\pi_H$ $\pi_L\rightarrow\pi_{L+1}$	583 (w)	677 (w)	506 (m[a])	879 (w)
C	$\pi_{H-4}\rightarrow\pi_H$ $\pi_L\rightarrow\pi_{L+2}$	494,442 (s),(m)	501,450 (s),(m)	448 (s)	514,465 (vs),(s)
D	$\pi_L\rightarrow\pi_{L+3}$	397 (s)	398,394 (m),(s)	397 (vs)	475 (s)

[a]: Small contributions of C-type and D-Type configuration increase the intensity

We find four $T_1\rightarrow T_n$ excitations with substantial oscillator strength for the parent compound (LF) within the detection range of the experiment. The lowest-lying transition with high intensity is dominated by the ($\pi_{H-3}\rightarrow\pi_H$) excitation (A-type) and is assigned to the experimental maximum at 700 nm (see Table 2). In good agreement with the experiment, this transition shows the highest oscillator strength in the detection range. The second and third optically bright states are attributed to linear combinations of the ($\pi_{H-4}\rightarrow\pi_H$) and ($\pi_L\rightarrow\pi_{L+2}$) configurations (C-type) with minor contributions of double excitations. The lower-lying state are assigned to the experimental maximum at 520 nm. Unfortunately, this transition is partially overlaid by the absorbance minimum caused by the bleaching. Its oscillator strength is roughly half of that of the A-type transition. This is reflected by the experiment. The higher-lying C-type state is completely obscured by the absorbance minimum. In fact, it was shown by Swartz et al. [50] that the triplet absorption of FMN in water solution in this spectral region is only slightly less intense than at 600 - 700 nm, supporting our theoretical findings. The fourth bright state is dominated by the ($\pi_L \rightarrow \pi_{L+3}$) excitation (D-type). Its transition wavelength compares well with the maximum around 390 nm in our experiment. A linear combination of the ($\pi_{H-2} \rightarrow \pi_H$) and ($\pi_L \rightarrow \pi_{L+1}$) configurations (b-type) is found in between the A-type and the low-lying C-type state. This dark state is isolated from the optically bright in LF, whereas this order changes in the other compounds.

The absorption spectrum of DMLF/DMRF is different from that of the parent compound. The lowest-lying maximum (630 nm) of the transient spectrum exhibits reduced intensity and a blue-shift. Two excited states with substantial oscillator strength are found in this wavelength region. They arise from linear combinations of A-type and b-type electronic states causing a distribution of the A-type transition probability among two bands. Inspection of the shape of the π_{H-3} MO gives an explanation for the blue shift of the A-type states. This particular MO shows substantial electron density at the C(7)-C(8) bond. Apparently, the removal of methyl groups from the two carbon atoms C7 and C8 strengthens this bond. Hence, the π_{H-3} MO is stabilized and promotion of one electron out of this MO is energetically less favorable. The energetic locations and intensities of the C-type peaks in DMLF and LF are similar. The longer wavelength transition can be assigned to the transient absorption maximum at 510 nm, whereas the other one is found again in the region of the bleach peak. Linear combination with double excitations causes the D-type configuration to distribute the intensity among two nearly degenerated transitions.

Similar to the corresponding parent compound these transitions contribute to the shortest wavelength maximum in the observation range.

The excited state with A-type electronic structure is red-shifted in 5DLF with respect to the parent compound. Our calculations predict the transition to be located at 752 nm, outside the experimental detection range. Admixture with b-type configurations does not occur in this compound because of a substantial red shift of the corresponding transition (see Table 8). Close to the experimental maximum, at 500 nm, three excited states with C and D-type structure are found that all contribute intensity in that spectral region.

Conclusion

Structural and electronic changes that were introduced into riboflavin by chemical synthesis (the 1- and 5-deaza-derivatives and the 7,8-di-demethyl and 8-isopropyl riboflavins) cause significant changes in the photophysical and photochemical properties of these compounds. Especially the deaza compounds exhibit strongly changed absorbances (a hypsochromic shift for 5DRF and a bathochromic absorption for 1DRF). They also have different fluorescence properties: no steady state fluorescence could be measured for 1DRF (and only ultrafast measurements revealed a fluorescence for this compound!), whereas 5DRF showed a significantly enhanced fluorescence yield. Also the triplet formation and decay processes are different from those of the parent RF. The DMRF derivative showed a much smaller triplet yield, whereas the triplet yields of *ipr*RF and RF were quite similar. The most interesting result is surely the absence of a triplet formation pathway for 1DRF, a finding that is excellently explained by the calculations.

The absorption properties of the parent compound and the derivatives are reflected in a convincing manner by our quantum chemical calculations on the lumiflavins. The results show that two aspects should be considered when the calculated values are compared to the experimental band maxima of the compounds in solution. First, the vertical excitation energy is blue shifted with respect to the band maximum and second, solvent shifts play a decisive role in the energetic position of the absorption bands of the two deaza compounds. With our best solvent model (COSMO and μ-hydration with four water molecules) the calculated absorption maxima fit remarkably well the experimental values.

We predict that fast (spin-forbidden) nonradiative processes quench the fluorescence of excited LF and DMLF in the gas phase. Our calculations show that ISC cannot compete with deactivation via fluorescence in 1DLF and 5DLF. Whereas we expect substantial fluorescence from excited 5DLF, we cannot exclude the involvement of ultrafast spin-allowed nonradiative processes in 1DLF.

Intersystem crossing takes place from the S_1 $^1(\pi\pi)$ to the T_2 $^3(\pi\pi)$ state by a vibronic spin-orbit coupling mechanism in aqueous solutions of RF, DMRF, *ipr*RF, and 5DRF. The rate for triplet formation from the S_1 state is small in excited 1DLF due to the absence of a close-by triplet state. Accordingly, no triplet state formation is observed for that riboflavin derivative.

Acknowledgements

This work was supported by the SFB663, TP B3 and TP C1. We thank the referees for valuable comments.

References

---

(1) Silva, E., Edwards, A.M., Eds. *Flavins Photochemistry and Photobiology;* RSC Publishing: Cambridge, England, 2006.

(2) Briggs, W.R.; Christie, J. M. *Trends Plant Sc.* **2002**, *7*, 204-210.

(3) Losi, A., Flavin-based photoreceptors in bacteria. In *Flavin photochemistry and photobiology*, IV ed.; Silva, E., Edwards, A. M., Eds.; Elsevier: Amsterdam, The Netherlands, 2006; pp. 223-269.

(4) Losi, A. *Photochem. Photobiol*. **2007**, *83*, 1283-1300.

(5) Edmondson, D.E.; Ghisla, S. Flavoenzyme Structure and Function. In *Methods in Molecular Biology*, vol. 131 (Flavoprotein Protocols); S.K. Chapman, G.A. Reid Eds.; Humana Press Inc., Totowa, NJ; **1999**, pp. 157-179.

(6) Scola-Nagelschneider, G.; Hemmerich, P. *Eur. J. Biochem*. **1976**, *66*, 567-577.

(7) Kasai, S.; Fritz, B.J.; Matsui, K. *Bull. Chem. Soc. Jpn*. **1987**, *60*, 3041-3042.

(8) Murthy, Y.V.S.N.; Massey, V. *J. Biol. Chem.* **1998**, *273,* 8975-8982.

(9) Salzmann, S.; Tatchen, J.; Marian, C.M. *J. Photochem. Photobiol. A* **2008**, *198*, 221-231.

(10) Hasegawa, J.; Bureekaew, S.; Nakatsuji, H. *J. Photochem. Photobiol. A* **2007**, *189*, 205-210.

(11) Climent, T.; González, R.; Merchán, M.; Serrano-Andrés, L. *J. Phys. Chem. A* **2006**, *110*, 13584-13590.

(12) Sikorska, E.; Khmelinskii, I.V.; Koput, J.; Bourdelande, J.L.; Sikorski, M. *J. Mol. Struct*. **2004**, *697*, 137-141.

(13) Sikorska, E.; Khmelinskii, I.V.; Worrall, D.R.; Koput, J.; Sikorski, M. *J. Fluores.* **2004**, *14*, 57-64.

(14) Neiss, C.; Saalfrank, P.; Parac, M.; Grimme, S. *J. Phys. Chem. A* **2003**, *107*, 140-147.

(15) Zenichowski, K.; Gothe, M.; Saalfrank, P. *J. Photochem. Photobiol. A* **2007**, *190*, 290-300.

---

(16) Domratcheva, T.; Fedorov, R.; Schlichting, I. *J. Chem. Theory Comput.* **2006**, *2*, 1565-1574.

(17) Dittrich, M.; Freddolino, P.L.; Schulten, K. *J. Phys. Chem. B* **2005**, *109*, 13006-13013.

(18) Domratcheva, T.; Grigorenko, B.L.; Schlichting, I.; Nemukhin, A.V. *Biophys. J.* **2008**, *94*, 3872-3879.

(19) Götze, J.; Saalfrank, P. *J. Photochem. Photobiol. B* **2009**, *94*, 87-95.

(20) Sadeghian, K.; Bocola, M.; Schütz, M. *J. Am. Chem. Soc.* **2008**, *130*, 12501-12513.

(21) Silva-Junior, M.R.; Salzmann, S., Marian, C.M., Thiel, W. *unpublished results.*

(22) Mansurova, M.; Koay, M.S.; Gärtner, W. *Eur. J. Org. Chem.*, **2008**, 5401-5406.

(23) Kleinschmidt, M.; Tatchen, J.; Marian, C.M. *J. Chem. Phys.*, **2006**, *124*, 124101.

(24) Tatchen, J. VIBES, Universität Düsseldorf, 2005.

(25) Kleinschmidt, M.; Tatchen, J.; Marian, C.M. *J. Comput. Chem.* **2002**, *23*, 824-833.

(26) Kleinschmidt, M.; Marian, C.M. *Chem. Phys.* **2005**, *311*, 71-79.

(27) Hess, B. A.; Marian, C.M.; Wahlgren, U.; Gropen, O. *Chem. Phys. Lett.* **1996**, *251*, 365-371.

(28) Schimmelpfennig, B. AMFI, Stockholms University, 1996.

(29) Tatchen, J.; Marian, C.M. Chem. *Phys. Lett.* **1999**, *313*, 351-357.

(30) Danovich, D.; Marian, C.M.; Neuheuser, T.; Peyerimhoff, S.D.; Shaik, S. *J. Phys. Chem. A* **1998**, *102*, 5923-5936.

(31) Tatchen, J.; Gilka, N.; Marian, C.M. *Phys. Chem. Chem. Phys.* **2007**, *9*, 5209-5221.

(32) Ahlrichs, R.; Bär, M.; Baron, H.-P.; Bauernschmitt, R.; Böcker, S.; Crawford, N.; Deglmann, P.; Ehrig, M.; Eichkorn, K.; Elliott, S.; Furche, F.; Haase, F.; Häser, M.; Hättig, C.; Hellweg, A.; Horn, H.; Huber, C.; Huniar, U.; Kattannek, M.; Köhn, A.; Kölmel, C.; Kollwitz, M.; May, K.; Nava, P.; Ochsenfeld, C.; Öhm, H.; Patzelt, H.; Rappoport, D.; Rubner, O.; Schäfer, A.; Schneider, U.; Sierka, M.; Treutler, O.; Unterreiner, B.; von Arnim, M.; Weigend, F.; Weis, P.; Weiss, H.; TURBOMOLE V510, University of Karlsruhe, 2008.

(33) Spencer, R.; Fisher, J.; Walsh, C. *Biochemistry* **1977**, *16*, 3586-3594.

(34) Slavov, C.; Mansurova, M.; Holzwarth, A.R.; Gärtner, W. *Photochem. Photobiol. submitted.*

(35) Drössler, P.; Holzer, W.; Penzkofer, A.; Hegemann, P. *Chemical Physics* **2003**, *286*, 409-420.

(36) Insińska-Rak, M.; Sikorska, E.; Bourdelande, J.L.; Khmelinskii, I. V.; Prukała, W.; Dobek, K.; Karolczak, J.; Machado, I.F.; Ferreira, L.F.V.; Komasa, A.; Worrall, D.R.; Sikorski, M.; *J. Mol. Struct*. **2006**, *783*, 184-190.

(37) Crovetto, L., Martinez-Junza, V., Braslavsky, S.E. *Photochem. Photobiol.* **2006**, *82*, 281-290.

(38) Chacon, J.N.; McLearie, J.; Sinclair, R.S.; *Photochem. Photobiol.* **1988**, *47*, 647-656.

(39) Grodowski, M.S.; Veyret, B.; Weiss, K. *Photochem. Photobiol.* **1977**, *26*, 341-352.

(40) Dudley, K.H.; Ehrenberg, A.; Hemmerich, P.; Müller, F. *Helv. Chim. Acta* **1964**, *47*, 1354-1383.

(41) Sung, M.; Moore, T.A.; Song, P.-S. *J. Am. Chem. Soc.* **1972**, *94*, 1730-1740.

(42) Bowd, A.; Byrom, P.; Hudson, J. B.; Turnbull, J. H. *Photochem. Photobiol.* **1968**, *8*, 1-10.

(43) Visser, A.J.W.G.; Müller, F. *Helv. Chim. Acta* **1979**, *62*, 593-608.

(44) Bomble, Y.J.; Sattelmeyer, K.W.; Stanton, J. F.; Gauss, J. *J. Chem. Phys.* **2004**, *121*, 5236-5240.

(45) Davidson, E.R.; Jarzęcki, A. A. *Chem. Phys. Lett.* **1998**, *285*, 155-159.

(46) Cederbaum, L.S.; Domcke, W. *J. Chem. Phys.* **1976**, *64*, 603-611.

(47) Weigel, A.; Dobryakov, A. L.; Veiga, M.; Pèrez Lustres, J. L. *J. Phys. Chem. A*, **2008**, *112*, 12054-12065)

(48) Kennis, J.T.M.; Crosson, S.; Gauden, M.; van Stokkum, I.H.M.; Moffat, K.; van Grondelle, R. *Biochemistry* **2003**, *42*, 3385- 3392.

(49) Silva-Junior, M. R.; Schreiber, M.; Thiel, W. *J. Chem. Phys.* **2008**, *129*, 1-14.

(50) Swartz, T. E., Carchnoy, S. B., Christie, J. M., Lewis, J. W., Szundi, I., Biggs, W. R., Bogomolni, R. A. *J. Biol. Chem.* **2001**, *276*, 36493-36500.

Photophysical properties of structurally and electronically modified flavin derivatives determined by spectroscopy and theoretical calculations

Supporting Information (SI)

Susanne Salzmann, Víctor Martinez-Junza, Björn Zorn, Silvia E. Braslavsky, Madina Mansurova, Christel M. Marian, and Wolfgang Gärtner

Molecular orbitals and vertical absorption energies in vacuum and different solvent models.

In this part of the appendix, we give more elaborate information on the vertical excitation energies for the calculations in the vacuum and with the different solvation models, for the four flavin compounds lumiflavin (LF), 7,8-di-demethyllumiflavin (=10-methylisoalloxazine, DMLF), 1-deazalumiflavin (1DLF), and 5-deazalumiflavin (5DLF).

In addition to the vertical excitation energies that are listed in Table S1-3, the frontier molecular orbitals (MOs), as obtained from the vacuum calculation, of LF, 1DLF, and 5DLF are shown in Figure S1-3. The information for DMLF (vacuum and aqueous solution) and for LF (vacuum only) has been taken from earlier work.[i] Since the shape and energetic ordering of the frontier MOs of DMLF are nearly identical to those of LF, no MOs are displayed for this compound. (They can be found in Ref. [i], Figure 3.)

For the C_s symmetric ground-state geometry of 1DLF one *out-of-plane (oop)* normal mode with an imaginary frequency was found in the DFT(B3-LYP) optimizations. A similar behavior has been observed earlier for excited state minima in other organic chromophores and shown to be an artifact of the DFT(B3LYP) method.[i,ii,iii,iv] We therefore employ the C_s symmetric structure.

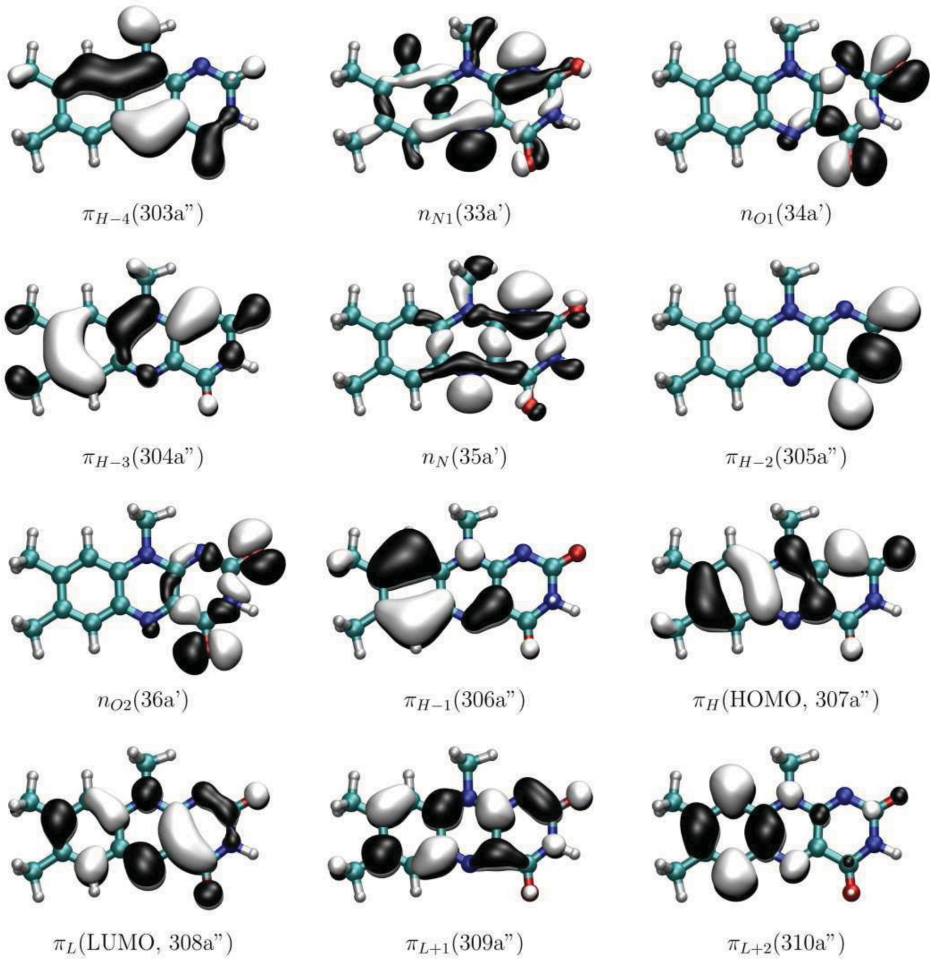

π_{H-4}(303a") n_{N1}(33a') n_{O1}(34a')

π_{H-3}(304a") n_{N}(35a') π_{H-2}(305a")

n_{O2}(36a') π_{H-1}(306a") π_{H}(HOMO, 307a")

π_{L}(LUMO, 308a") π_{L+1}(309a") π_{L+2}(310a")

Figure S1 LF: Frontier Orbitals in the vacuum at the ground state geometry.

Table S1 LF,DMLF: Vertical singlet and triplet excitation energies/ wavelengths ΔE [eV/ nm] at the ground state geometry in the vacuum in comparison to aqueous solution (COSMO and COSMO+μ-hydration (for details see text)). For DMLF only the excitation energies of the best solvation model (COSMO+μ-hydration) are given. In addition to the dominant excitations, c^2-values, oscillator strengths f(r) and dipole moments μ [Debye] are listed.

	vacuum					COSMO	COSMO+μ-hyd.	
	State	electr. structure	ΔE LF	f(r)	μ	ΔE LF	ΔE LF	ΔE DMLF
S_0	1^1A'	(0.95) gs			9.6			
S_1	2^1A'	(0.83) $\pi_H \rightarrow \pi_L$	2.94/ 422	0.322	11.1	2.90/ 428	2.87/ 432	2.94/ 421
S_2	1^1A"	(0.44) $n_{O2} \rightarrow \pi_L$ (0.33) $n_{N2} \rightarrow \pi_L$	3.21/ 386	0.002	5.3	3.77/ 329	3.88/ 319	3.86/ 321
S_3	2^1A"	(0.42) $n_{N2} \rightarrow \pi_L$ (0.26) $n_{O2} \rightarrow \pi_L$	3.35/ 370	0.001	5.2	3.49/ 355	3.64/ 340	3.59/ 345
S_4	3^1A'	(0.76) $\pi_{H-1} \rightarrow \pi_L$	3.84/ 323	0.208	15.3	3.58/ 329	3.47/ 357	3.61/ 344
T_1	1^3A'	(0.86) $\pi_H \rightarrow \pi_L$	2.24/ 553	-	7.8	2.26/ 550	2.23/ 555	2.33/ 532
T_2	2^3A'	(0.60) $n_{N2} \rightarrow \pi_L$ (0.12) $n_{O2} \rightarrow \pi_L$ (0.11) $n_{O1} \rightarrow \pi_L$	2.90/ 427	-	8.4	3.13/ 396	3.29/ 377	3.25/ 382
T_3	1^3A"	(0.77) $\pi_{H-1} \rightarrow \pi_L$	3.05/ 407	-	14.0	2.82/ 440	2.73/ 455	2.78/ 445

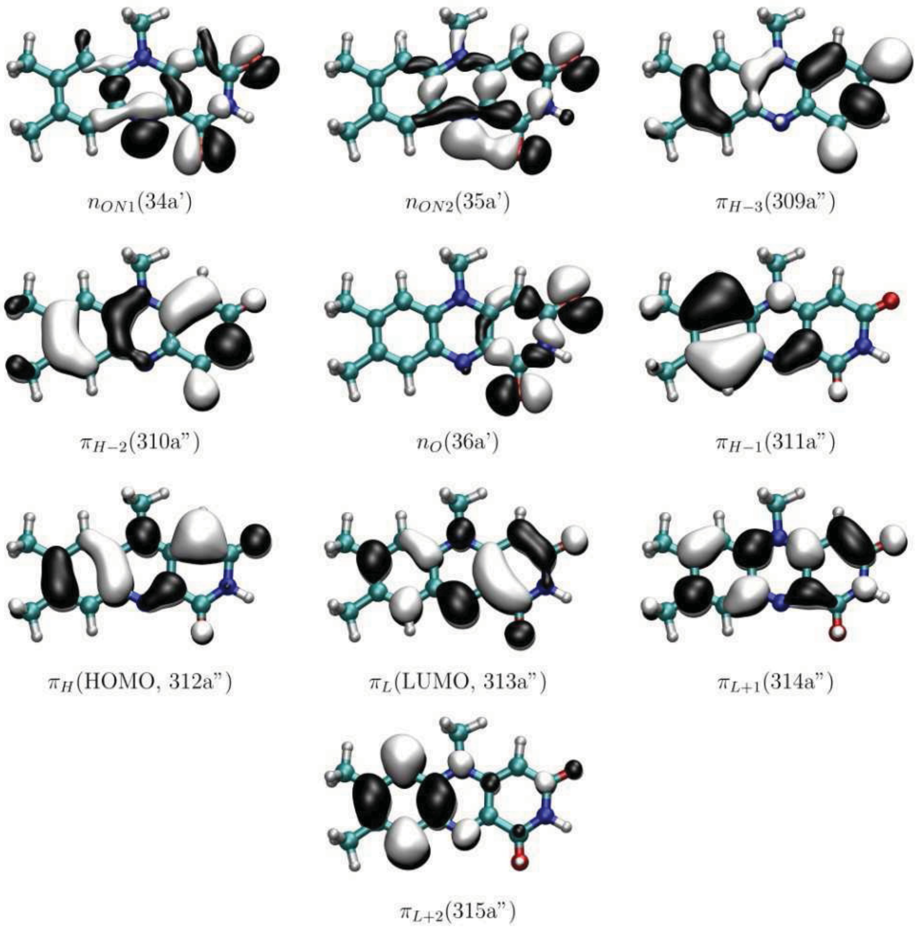

n_{ON1}(34a') n_{ON2}(35a') π_{H-3}(309a")

π_{H-2}(310a") n_{O}(36a') π_{H-1}(311a")

π_{H}(HOMO, 312a") π_{L}(LUMO, 313a") π_{L+1}(314a")

π_{L+2}(315a")

Figure S2 1DLF: Frontier Orbitals in the vacuum at the ground state geometry

Table S2 1DLF: Vertical singlet and triplet DFT/MRCI excitation energies/ wavelengths ΔE [eV/ nm] at the ground state geometry in the vacuum in comparison to aqueous solution (COSMO,μ-hydration and both). In addition to the dominant excitations, c^2-values, oscillator strengths f(r) and dipole moments μ [Debye] are given.

	vacuum					**COSMO**	**μ-hydr.**	**COSMO+μ-hyd.**
	State	electr. structure	ΔE	f(r)	μ	ΔE	ΔE	ΔE
S_0	$1^1A'$	(0.94) gs			9.1			
S_1	$2^1A'$	(0.82) $\pi_H \rightarrow \pi_L$	2.62/ 473	0.276	11.3	2.44/ 509	2.49/ 498	2.41/ 515
S_2	$1^1A''$	(0.69) $n_O \rightarrow \pi_L$	3.23/ 374	0.001	3.6	3.60/ 345	3.44/ 360	3.88/ 320
S_3	$2^1A''$	(0.49) $n_{ON2} \rightarrow \pi_L$ (0.30) $n_{ON1} \rightarrow \pi_L$	3.58/ 346	0.003	7.9	3.76/ 330	3.66/ 339	3.76/ 329
S_4	$3^1A'$	(0.61) $\pi_{H-1} \rightarrow \pi_L$	3.80/ 326	0.060	12.9	3.59/ 345	3.58/ 346	3.42/ 362
T_1	$1^3A'$	(0.86) $\pi_H \rightarrow \pi_L$	1.88/ 660	-	9.6	1.80/ 688	1.81/ 685	1.79/ 693
T_2	$2^3A'$	(0.47) $n_O \rightarrow \pi_L$ (0.25) $n_{ON2} \rightarrow \pi_L$	3.10/ 399	-	5.2	3.35/ 370	3.20/ 388	3.37/ 368
T_3	$1^3A''$	(0.58) $\pi_{H-1} \rightarrow \pi_L$ (0.17) $\pi_H \rightarrow \pi_{L+1}$	3.11/ 399	-	12.3	2.91/ 426	2.94/ 421	2.77/ 447

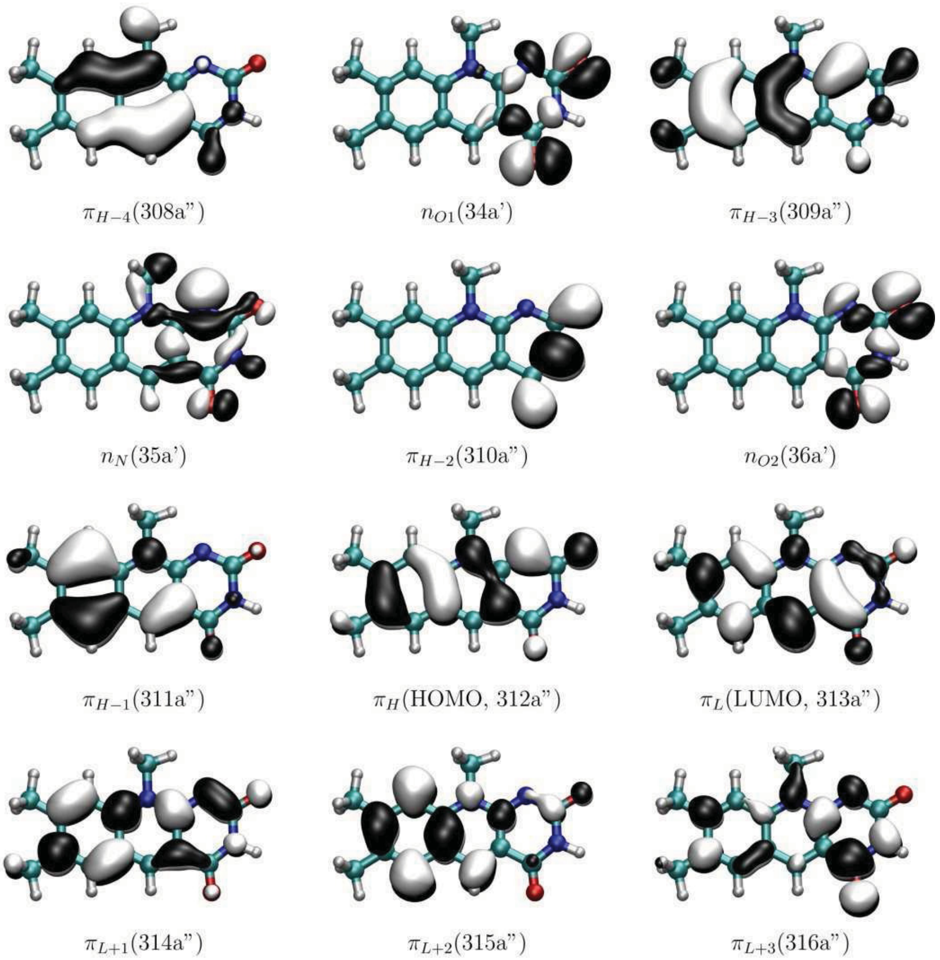

π_{H-4}(308a") n_{O1}(34a') π_{H-3}(309a")

n_N(35a') π_{H-2}(310a") n_{O2}(36a')

π_{H-1}(311a") π_H(HOMO, 312a") π_L(LUMO, 313a")

π_{L+1}(314a") π_{L+2}(315a") π_{L+3}(316a")

Figure S3 5DLF: Frontier orbitals in the vacuum at the optimized ground state geometry.

Table S3 5DLF: Vertical singlet and triplet DFT/MRCI excitation energies/ wavelengths ΔE [eV/ nm] at the ground state geometry in the vacuum in comparison to aqueous solution (COSMO,μ-hydration and both). In addition to the dominant excitations, c^2-values, oscillator strengths f(r) and dipole moments μ [Debye] are given.

	vacuum					**COSMO**	**μ-hyd.**	**COSMO+μ-hyd.**
	State	electr. structure	ΔE	f(r)	μ	ΔE	ΔE	ΔE
S_0	1^1A'	(0.95) ground state		0	9.8			
S_1	2^1A'	(0.83) $\pi_H \rightarrow \pi_L$	3.12/ 397	0.324	9.5	3.22/ 385	3.17/391	3.22/ 385
S_2	1^1A"	(0.67) $n_{O2} \rightarrow \pi_L$	3.66/ 339	0.000	1.3	4.18/ 297	4.15/299	4.46/ 278
S_3	3^1A'	(0.71) $\pi_{H-1} \rightarrow \pi_L$ (0.10) $\pi_H \rightarrow \pi_{L+1}$	4.08/ 304	0.151	13.2	3.92/ 316	3.98/312	3.82/ 325
T_1	1^3A'	(0.85) $\pi_H \rightarrow \pi_L$	2.54/ 488	-	7.9	2.71/ 457	2.68/463	2.73/ 454
T_2	2^3A'	(0.76) $\pi_{H-1} \rightarrow \pi_L$	3.18/ 389	-	12.7	3.05/ 407	3.10/400	2.99/ 414
T_3	1^3A"	(0.64) $n_{O2} \rightarrow \pi_L$	3.58/ 347	-	1.7	4.08/ 304	3.82/325	3.87/ 320

Comparison of the ground state and $^1(\pi\pi^*)$ state geometries of LF, 1DLF and 5DLF

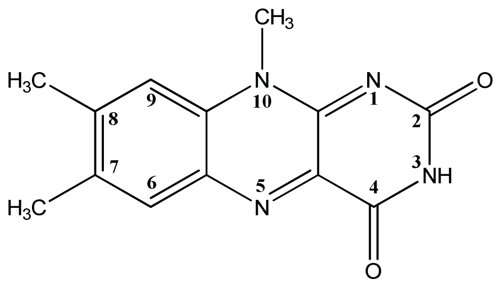

Figure S4 Chemical structure and labeling of lumiflavin.

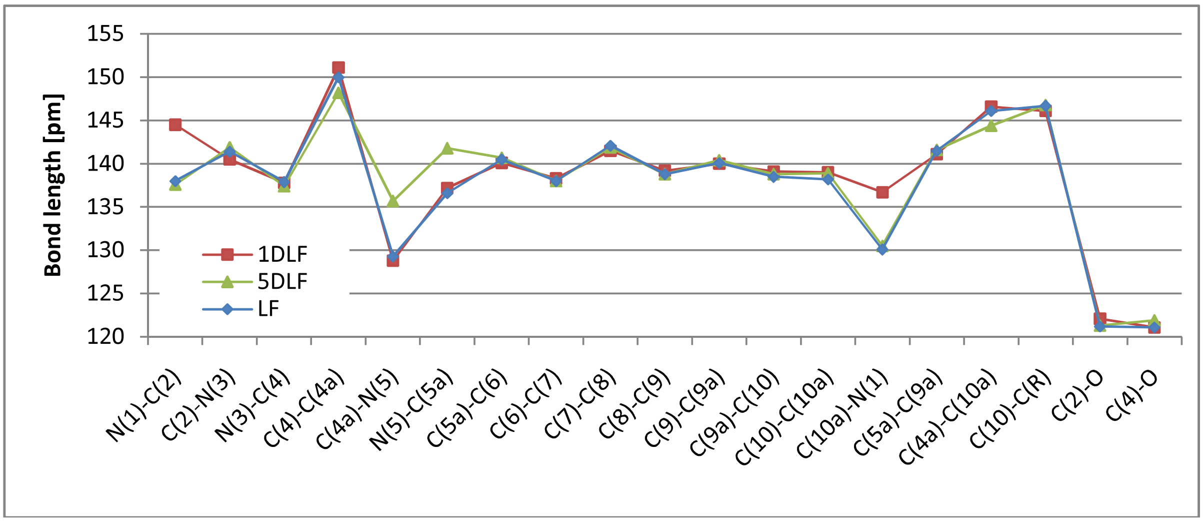

Figure S5 Comparison of selected ground state geometry bond lengths [pm] of 1DLF, 5DLF, and LF in the vacuum.

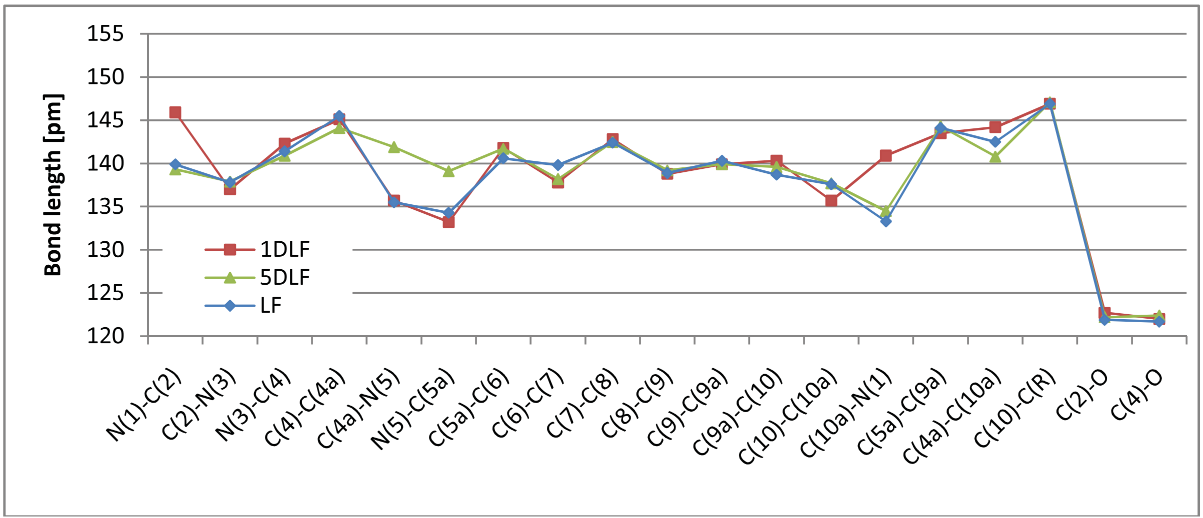

Figure S6 Comparison of selected $^1(\pi\pi^*)$ geometry bond lengths [pm] of 1DLF, 5DLF, and LF in the vacuum.

The bond lengths [pm] at the $^3(\pi\pi^*)$ geometry (not shown) are very similar to the respective values at the $^1(\pi\pi^*)$ geometry.

Vibronic absorption spectra of LF, DMLF, 1DLF, and 5DLF

It is a common practice to identify the experimental band maxima with vertical excitation energies. Nevertheless, it has been shown that this presumption does not always hold.[v,vi,vii] If the change in the geometry from the ground state to the excited state is small, the vibrational wave functions do not have their maxima at the classical turning points.[vii] For isoalloxazine, DMLF, and LF it is evident that most quantum chemical investigations find the vertical absorption energy approximately 0.2 eV above the experimental band maximum.[i,viii,ix,x,xi,xii,xiii] Since the position of the first absorption band is mostly unaffected by the surrounding environment,[xiv,xv] solvent effects can be excluded as a reason for this deviation. In order to shed light on the underlying reasons and validate the theoretically determined excited state geometries, vibrational intensity distributions of the $S_0 \rightarrow S_1$ transition were computed. Due to limitations in the program and regarding the size of the molecule, even with the restriction to 30 modes (see Computational details of the main paper), an energy range of only 4000 cm^{-1} above the first transition was considered.

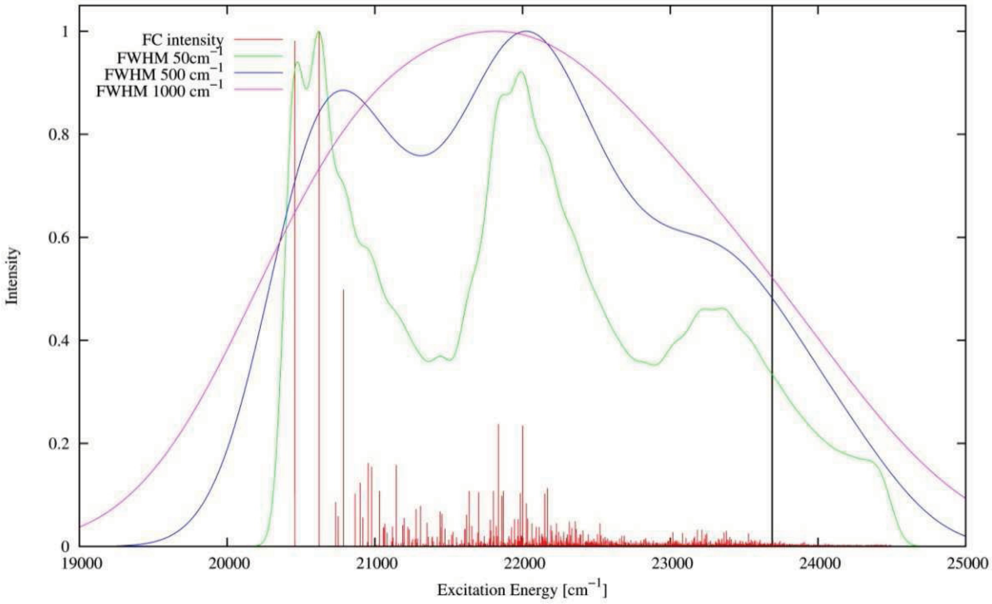

Figure S7 LF: Simulated Franck-Condon $S_0 \rightarrow S_1$ absorption spectra for the gas phase.

In order to compare with the experimental spectra in solution, the line spectrum was broadened with Gaussian functions. Figure S7 shows how the choice of the full width at half maximum (FWHM) of the Gaussian functions influences the shape of the obtained band. The origin transition and the second transition are by far the strongest single lines in the spectrum (FC integrals 0.0434 and 0.0443). As soon as the line spectrum is convoluted with Gaussian functions, the intensities of the enormous number of states with tiny FC integrals at higher energies accumulate. With growing FWHM of the Gaussian functions this effect is intensified and the relative intensity of the origin transition and the second transition decrease. With a FWHM of 500 cm^{-1} the obtained band appears very similar to that of FMN in the LOV domain[xvi,xvii] and with a FWHM of 1000 cm^{-1} all vibronic structure has disappeared. The latter bands are used for our comparison to the flavin derivatives in water. For all compounds, the line spectrum and the shape of the simulated $S_0 \rightarrow S_1$ absorption band in the gas phase are compared with experimentally obtained absorption bands in water in Figure S8. For none of the four flavins the calculated band maximum and the vertical excitation energy coincide. In all cases, the band maximum is red shifted with respect to the vertical excitation energy by 0.1 eV - 0.2 eV. While for LF and DMLF the calculated absorption bands agree very well with the experimental bands, for the two deazaflavins deviations of 1000 cm^{-1} to 1500 cm^{-1} are observed, which originate from sensitivity of that band towards the environment. Unfortunately, due to technical reasons, it is not possible to obtain the adiabatic excitation energies for any solvent model including COSMO. The calculation of (singlet and triplet) excitation energies with the DFT/MRCI program always employs the singlet ground state Kohn-Sham orbitals. Therefore, the DFT/MRCI calculation can only comprise the charge distribution for the (singlet) electronic ground state. While for the calculation of the vertical singlet absorption energies this is correct, it is not meaningful for the calculation of the adiabatic absorption energies. As a workaround, we applied the very solvent shifts for the calculated absorption band that were obtained for the vertical excitation energies. As soon as solvent effects are taken into account (See Figure 3 of the main article) our calculated absorption bands are consistently found somewhat too low, which is characteristic for the DFT/MRCI.[xviii]

Calculation of the radiative fluorescence and phosphorescence rate constants

Table S4 Calculated fluorescence and phosphorescence rates for all compounds in the gas phase. For the fluorescence, the vertical emission energies $\Delta E(S_0 \leftarrow S_1)$ [cm^{-1}], the dipole transition matrix elements μ_{el} $(S_0 \leftarrow S_1)$ [E_h] and the resulting radiative rate constants k_F [s^{-1}] and lifetimes τ_F [ns] are given. For the phosphorescence, the vertical emission energies $\Delta E(S_0 \leftarrow T_{1,\zeta})$ [cm^{-1}], the dipole transition matrix elements $|\mu_{el}(S_0 \leftarrow T_{1,\zeta})|$ [a.u.] and the resulting radiative rate constants $k_{P,\zeta}$ [s^{-1}], lifetimes $\tau_{P,\zeta}$ [ns] of the three triplet sublevels, and the high-temperature lifetimes τ_{ht} [ns] are listed. Since the excitation energy of the three sublevels of the triplet state is identical within the numerical accuracy, it is shown only once.

	Fluorescence $(S_0 \leftarrow S_1)$				Phosphorescence $(S_0 \leftarrow T_1)$				
	Δ**E**$(S_0 \leftarrow S_1)$	μ_{el} $(S_0 \leftarrow S_1)$	k_F	τ_F	Δ**E**$(S_0 \leftarrow T_1)$	$\lvert\mu_{el}(S_0 \leftarrow T_{1,\zeta})\rvert$	$k_{P,\zeta}$	$\tau_{P,\zeta}$	τ_{ht}
LF	19057.9	2.023	$5.7 \cdot 10^{7}$	17.4	14156.4	0.0000023	$3.0 \cdot 10^{-5}$	32887.1	13.4[a]
						0.0000970	$5.4 \cdot 10^{-2}$	18.5	
						0.0001093	$1.7 \cdot 10^{-1}$	5.7	
DMLF	18916.0	1.889	$4.9 \cdot 10^{7}$	20.4	14066.1	0.0000023	$3.0 \cdot 10^{-5}$	33524.5	17.5
						0.0001742	$1.7 \cdot 10^{-1}$	5.8	
						0.0000023	$3.0 \cdot 10^{-5}$	33524.5	
1DLF	15222.7	1.855	$2.5 \cdot 10^{7}$	40.6	9597.0	0.0000666	$7.9 \cdot 10^{-3}$	125.9	43.4
						0.0000021	$7.9 \cdot 10^{-6}$	126617.6	
						0.0000703	$8.9 \cdot 10^{-3}$	113.0	
5DLF	20521.1	1.968	$6.8 \cdot 10^{7}$	14.8	16894.1	0.0000046	$2.1 \cdot 10^{-4}$	4837.5	8.8
						0.0000860	$7.2 \cdot 10^{-2}$	13.8	
						0.0001652	$2.7 \cdot 10^{-1}$	3.8	

[a]: Experimental phosphorescence lifetimes at 77K in solvent matrix range from 0.1 to 0.2 s.[xix]

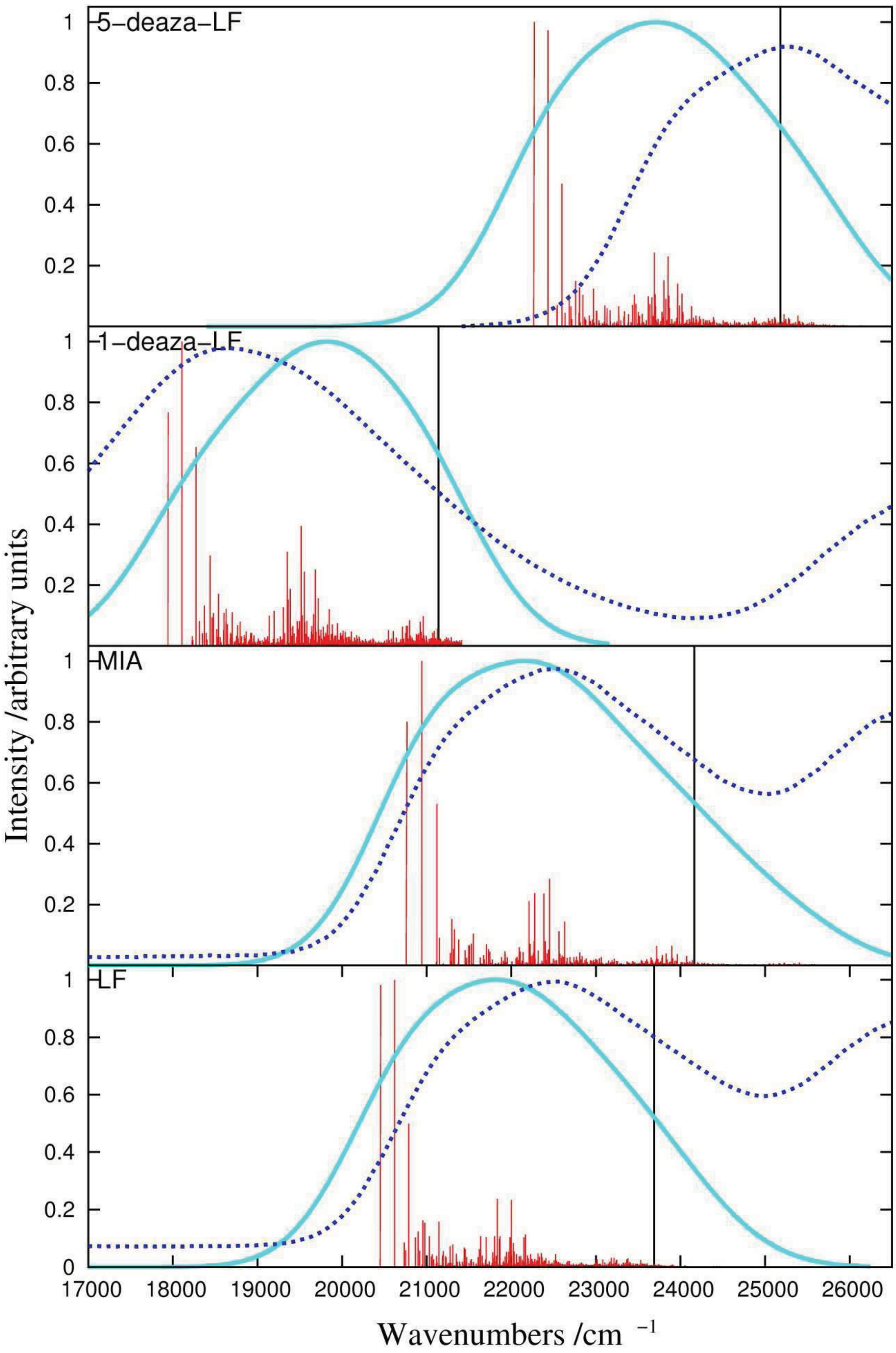

Figure S8 LF, DMLF, 1DLF and 5DLF: Simulated Franck-Condon $S_0 \rightarrow S_1$ absorption spectra for the gas phase. For easier comparison with experiment (dashed line), the computed line spectrum was broadened by Gaussian functions with FWHM=1000 cm^{-1} (solid line). The vertical line represents our respective vertical DFT/MRCI excitation energy.

Calculation of the intersystem crossing rate constants

In this part of the appendix, we have assembled detailed information on the entities required for the evaluation of spin-forbidden non-radiative transition probabilities and on the sensitivity of the results with respect to technical parameters.

Table S5 – S8 list harmonic frequencies of the *out-of plane* (*oop*) vibrations in the first excited $^1(\pi\rightarrow\pi^*)$ state (coupling modes for the $^1(\pi\rightarrow\pi^*)\rightsquigarrow{}^3(\pi\rightarrow\pi^*)$ vibronic spin-orbit interaction) an the derivatives of the spin-orbit coupling matrix elements with respect to distortions along their normal coordinates for the four flavin compounds.

According to Toniolo and Persico,[xx,xxi] it is possible to approximate the Fermi Golden Rule expression for the ISC rate constants k_{ISC} by a summation over rates of transitions from the initial level $|i,\mathrm{v}=0\rangle$ to individual final vibronic levels $|f,\mathrm{v}'\rangle$ in an energy interval of width 2η around the energy $E_{i,\mathrm{v}=0}$. Here, the vectors v and v' represent sets of vibrational quantum numbers in all normal modes of the initial (i) and final (f) electronic state, respectively. If we denote the coupling matrix elements driving the radiationless transition by $H^{SO}_{\mathrm{v}=0,\mathrm{v}'}$ the rate constant is obtained as

$$k_{\mathrm{ISC}}(i \rightsquigarrow f) = \frac{2\pi}{\hbar\eta} \sum_{|E_{f,\mathrm{v}'}-E_{i,\mathrm{v}=0}|<\eta} \left|H^{\mathrm{SO}}_{\mathrm{v}=0,\mathrm{v}'}\right|^2 \qquad (1)$$

$H^{SO}_{\mathrm{v}=0,\mathrm{v}'}$ can be expanded in a Taylor series in the variables $\{q_\kappa\}$, the normal coordinates, around some reference point $\mathbf{q}_0$ which we have chosen to coincide with the minimum of the S1 state.

$$H^{SO}_{\mathrm{v}=0,\mathrm{v}'} = \left\langle i\middle|\widehat{\mathcal{H}}_{SO}\middle|f\right\rangle\Big|_{\mathbf{q}_0} \langle \mathrm{v}=0|\mathrm{v}'\rangle + \sum_\kappa \left(\frac{\partial}{\partial q_\kappa}\left\langle i\middle|\widehat{\mathcal{H}}_{SO}\middle|f\right\rangle\right)\Big|_{\mathbf{q}_0} \langle \mathbf{v}=0|q_\kappa|\mathbf{v}'\rangle + O(|\mathbf{q}|^2) \qquad (2)$$

The first term on the right-hand side of Eq. (2) is a purely electronic matrix element multiplied by Franck-Condon factors and is denominated direct spin–orbit coupling in the following, whereas the term in the second line of Eq. (2) represents the first-order derivative coupling and is named vibronic spin–orbit coupling.

The first-order derivatives of the SOMEs were calculated numerically by finite difference techniques, more precisely, by means of the symmetrized two-point formula:

$$\frac{\partial}{\partial q_\kappa}\left\langle i\middle|\widehat{\mathcal{H}}_{SO}\middle|f\right\rangle\Big|_{\mathbf{q}_0} \approx \frac{\langle i|\widehat{\mathcal{H}}_{SO}|f\rangle|_{\mathbf{q}_0+\epsilon e_\kappa} - \langle i|\widehat{\mathcal{H}}_{SO}|f\rangle|_{\mathbf{q}_0-\epsilon e_\kappa}}{2\epsilon}\,. \qquad (3)$$

Here, e_κ denotes the unit vector pointing into the direction of the normal mode with index κ in the nuclear configuration space. (For more details see Ref. xxii.)Thus, single-point DFT/MRCI and subsequent SPOCK runs have to be carried out at two distorted molecular geometries $\mathbf{q}_0 \pm \epsilon e_\kappa$ for each normal mode. For obtaining the derivatives employed in the final computations of the ISC rate constants, the displacement increment ϵ is set to a numerical value of 0.1 (referring to dimensionless normal mode coordinates $\mathbf{q}_\kappa$). In order to minimize the errors induced by numerical noise, we always take both the reference space and the CI space from a preceding DFT/MRCI single-point calculation without symmetry constraints at the reference geometry q_0. The molecular orbitals employed in the single-point CI calculations are reoptimized for the distorted geometries, of course.

Since the *oop* distortion exhibits a symmetric potential well, we do not expect a deviation between the SOME at two distorted molecular geometries $\mathbf{q}_0 \pm \epsilon e_\kappa$. For our calculations in the vacuum this is fulfilled. There, in most cases, we find the difference between the two SOME to be less that 0.00001 cm^{-1}. For our calculations of the SOME derivatives in aqueous solution with COSMO, however, larger deviations between the two SOMEs of up to 0.003 cm^{-1} turn up. At the two distorted molecular geometries even the SCF total energies and the eigenvalues of the KS orbitals differ by approximately 10^{-6} E_H. (The convergence criteria for the SCF calculation was chosen to 10^{-7} E_H for the energy and the density.) This can be explained by the fact that the cavity construction for the COSMO calculation uses coordinates that are slightly distorted. Although it would be desirable to obtain the derivatives of the SOME with COSMO with a higher precision, the induced errors do not change the order of magnitude of the resulting ISC rate constant, only its prefactor. This is shown for DMLF in Table S 5.

Table S5 DMLF: Analysis of the stability of the rate constants k_{ISC} [s^{-1}] for ($S_1 \rightarrow T_{1x}$) ISC channel in water (COSMO) with respect to the used derivatives.

	k_{ISC}		
	η=0.001	η=0.01	η=0.1
$\frac{\partial}{\partial q_k}\langle i\vert\hat{\mathcal{H}}_{SO}\vert f\rangle\vert_{\mathbf{q}_0+\epsilon e_\kappa}$	$4.62\cdot10^6$	$5.63\cdot10^6$	$6.22\cdot10^6$
$\frac{\partial}{\partial q_k}\langle i\vert\hat{\mathcal{H}}_{SO}\vert f\rangle\Big\vert_{\mathbf{q}_0}$	$4.75\cdot10^6$	$6.65\cdot10^6$	$7.79\cdot10^6$
$\frac{\partial}{\partial q_k}\langle i\vert\hat{\mathcal{H}}_{SO}\vert f\rangle\Big\vert_{\mathbf{q}_0-\epsilon e_\kappa}$	$4.69\cdot10^6$	$6.98\cdot10^6$	$9.00\cdot10^6$

Table S6 DMLF: Harmonic frequencies ν_i [cm^{-1}] of the out-of-plane vibrational modes for the S_1 state. Derivatives of SOMEs [cm^{-1}] with respect to the corresponding (dimensionless) normal coordinates at the equilibrium geometry q_0 of the S_1 state.

		vacuum		**COSMO**			
		$\frac{\partial\langle S_1\vert H_{SO}\vert T_1\rangle}{\partial q_i}$		$\frac{\partial\langle S_1\vert H_{SO}\vert T_1\rangle}{\partial q_i}$		$\frac{\partial\langle S_1\vert H_{SO}\vert T_2\rangle}{\partial q_i}$	
mode	ν_i	(x)	(y)	(x)	(y)	(x)	(y)
1	50^{a}	-2.43	0.50	-1.07	0.91	-0.85	1.02
2	57	0.02	0.25	0.05	0.07	0.15	-0.07
3	67	0.34	-0.41	0.17	-0.15	0.09	-0.09
4	117	0.10	-0.19	-0.09	0.14	0.17	0.21
5	139	0.57	-1.03	0.11	-0.06	-0.05	-0.44
7	224	-0.02	0.33	-0.04	0.17	0.26	0.24
8	227	0.23	-0.35	0.15	-0.21	0.17	-0.29
9	272	0.59	-0.29	0.32	-0.23	0.15	-0.11
12	360	-0.14	-0.50	-0.04	-0.05	0.20	-0.14
14	429	-0.34	-0.31	-0.16	0.14	0.23	0.05
16	478	-0.08	0.04	-0.05	0.06	-0.04	-0.03
19	537	-0.02	-0.99	-0.19	0.15	-0.08	0.20
22	625	0.52	-0.29	0.27	-0.17	0.36	-0.17
24	636	0.09	-1.06	-0.04	-0.18	0.26	-0.46
25	699	0.11	0.10	0.00^{b}	0.05	0.12	-0.06
27	722	-0.34	0.14	-0.07	-0.12	-0.27	0.00^{a}
28	740	-0.08	0.10	-0.14	0.11	-0.35	0.11
31	840	0.07	0.19	0.05	0.00^{a}	0.35	-0.03
33	907	-0.27	0.23	-0.14	-0.02	-0.37	-0.06
34	949	-0.08	0.26	0.00^{a}	-0.09	-0.28	-0.12
41	1142	-0.16	0.29	-0.04	0.09	-0.17	0.15
55	1500	-0.09	-0.13	-0.10	0.04	-0.23	0.04
63	3113	-0.04	0.10	-0.01	0.00^{a}	-0.05	0.03

a: The TDDFT (B3LYP) PEH of the S_1 state exhibits a very flat double well shape along mode 1 with a slightly imaginary frequency (ν_1=i150 cm^{-1}). The setting ν_i represents an approximate harmonic model of the S_1 state PEH along mode 1.

b: Absolute value of the derivative lower than 0.01 cm^{-1}.

Table S7 LF: Harmonic frequencies ν_i [cm^{-1}] of the out-of-plane vibrational modes for the S_1 state. Derivatives of SOMEs [cm^{-1}] with respect to the corresponding (dimensionless) normal coordinates at the equilibrium geometry q_0 of the S_1 state.

		vacuum		**COSMO**			
		$\frac{\partial\langle S_1\|H_{SO}\|T_1\rangle}{\partial q_i}$		$\frac{\partial\langle S_1\|H_{SO}\|T_1\rangle}{\partial q_i}$		$\frac{\partial\langle S_1\|H_{SO}\|T_2\rangle}{\partial q_i}$	
mode	ν_i	(x)	(y)	(x)	(y)	(x)	(y)
1	47[a]	1.98[a]	-1.42	0.89	-0.40	0.98	-0.61
2	47	-0.02	0.20	0.03	0.06	0.05	-0.03
3	62	-0.65	0.60	-0.33	0.17	-0.28	0.17
4	95	0.24	-0.24	0.15	-0.05	0.17	0.06
5	122	-0.03	0.01	0.02	0.00[a]	-0.02	-0.02
6	142	0.23	-0.03	0.29	0.00[a]	0.12	-0.34
7	154	0.17	-0.20	0.12	-0.08	0.00[a]	-0.29
9	180	-0.02	-0.07	-0.05	-0.04	-0.07	-0.06
10	197	0.27	-0.27	-0.11	0.11	-0.04	0.21
11	216	0.02	0.21	0.00[a]	-0.04	-0.25	-0.16
13	292	0.48	-0.17	-0.22	0.07	-0.09	-0.09
15	309	-0.02	0.06	-0.03	-0.11	0.13	-0.20
18	383	-0.38	0.22	-0.14	0.05	-0.11	0.04
20	440	-0.37	-0.20	-0.01	0.09	0.03	0.14
23	494	-0.11	0.06	-0.01	0.04	-0.30	0.23
25	545	-0.30	0.17	-0.10	0.06	0.05	0.01
29	632	-0.08	0.07	-0.05	-0.11	0.31	-0.35
30	635	-0.34	-0.13	0.26	0.09	0.34	0.21
32	702	-0.11	0.04	0.08	-0.05	0.08	-0.20
34	733	0.19	0.15	-0.22	-0.08	-0.22	0.12
37	836	0.20	-0.03	0.12	-0.03	0.48	-0.01
39	866	0.15	-0.05	-0.14	0.05	-0.03	0.07
43	1034	0.00[a]	0.07	0.05	-0.02	0.14	-0.04
45	1045	-0.04	0.08	-0.03	-0.03	-0.11	-0.03
48	1143	0.11	-0.07	-0.03	0.05	-0.15	0.09
65	1474	-0.01	0.10	-0.01	0.00[a]	0.00[a]	0.00[a]
66	1489	0.00[a]	-0.05	0.03	0.00[a]	-0.08	0.00[a]
69	1502	-0.09	0.07	0.09	0.01	0.22	0.00[a]
79	3060	-0.03	0.04	0.02	-0.01	-0.03	0.00[a]
80	3063	0.00[a]	0.10	0.00[a]	0.01	0.03	0.00[a]
81	3107	0.05	0.08	0.03	0.00[a]	0.05	-0.02

a: The TDDFT (B3LYP) PEH of the S_1 state exhibits a very flat double well shape along mode 1 with a slightly imaginary frequency ($\nu_1 = i47$ cm^{-1}). The setting ν_i represents an approximate harmonic model of the S_1 state PEH along mode 1.

b: Absolute value of the derivative lower than 0.01 cm^{-1}.

Table S8 1DLF: Harmonic frequencies ν_i [cm^{-1}] of the out-of-plane vibrational modes for the S$_1$ state. Derivatives of SOMEs [cm^{-1}] with respect to the corresponding (dimensionless) normal coordinates at the equilibrium geometry q_0 of the S$_1$ state.

		vacuum		**COSMO**	
		$\frac{\partial\langle S_1\vert H_{SO}\vert T_1\rangle}{\partial q_i}$		$\frac{\partial\langle S_1\vert H_{SO}\vert T_1\rangle}{\partial q_i}$	
mode	ν_i	(x)	(y)	(x)	(y)
1	44	-0.22	0.20	-0.08	0.09
2	58	0.02	0.06	-0.03	0.01
3	92	-0.23	0.15	-0.10	0.05
4	123	0.37	-0.26	0.17	-0.08
5	143	-0.11	0.10	-0.03	0.07
6	153	-0.05	0.02	-0.07	0.00[a]
8	170	0.12	-0.11	0.08	0.05
9	183	0.17	-0.19	0.08	-0.10
10	209	0.18	-0.13	0.14	-0.05
11	227	0.20	-0.17	0.12	-0.10
14	310	0.11	0.03	0.07	0.08
16	332	0.32	-0.15	0.22	-0.09
18	390	-0.13	0.05	-0.03	-0.04
21	448	-0.06	0.07	0.02	0.02
24	527	0.16	-0.05	0.08	0.05
26	546	-0.02	0.16	0.00[a]	0.07
27	570	0.00[a]	0.20	-0.05	0.07
30	636	-0.02	-0.10	-0.02	-0.13
31	650	-0.10	0.19	-0.05	0.14
33	704	0.10	-0.13	0.05	-0.11
35	744	0.19	-0.24	0.07	-0.12
38	847	-0.09	0.05	-0.05	0.03
40	870	0.08	0.04	0.09	0.00[a]
45	1046	-0.03	-0.00[a]	-0.02	0.00[a]
46	1053	0.00[a]	-0.04	-0.02	0.01
48	1137	-0.04	0.11	0.00[a]	0.04
67	1481	0.00[a]	0.05	0.02	0.01
68	1490	0.03	-0.00[a]	0.00[a]	0.00[a]
69	1496	0.01	0.03	0.02	0.00[a]
80	3059	-0.01	-0.01	0.00[a]	0.00[a]
82	3073	-0.00[a]	-0.00[a]	0.00[a]	0.00[a]
84	3121	0.03	-0.02	0.03	0.00[a]

a: Absolute value of the derivative lower than 0.01 cm^{-1}.

Table S9 5DLF: Harmonic frequencies ν_i [cm^{-1}] of the out-of-plane vibrational modes for the S_1 state. Derivatives of SOMEs [cm^{-1}] with respect to the corresponding (dimensionless) normal coordinates at the equilibrium geometry q_0 of the S_1 state.

		vacuum		COSMO			
		$\frac{\partial\langle S_1\vert H_{SO}\vert T_1\rangle}{\partial q_i}$		$\frac{\partial\langle S_1\vert H_{SO}\vert T_1\rangle}{\partial q_i}$		$\frac{\partial\langle S_1\vert H_{SO}\vert T_2\rangle}{\partial q_i}$	
mode	ν_i	(x)	(y)	(x)	(y)	(x)	(y)
1	47	-0.11	0.06	-0.09	0.00[a]	0.07	0.13
2	58	0.32	-0.25	-0.13	0.11	0.11	-0.21
3	76	0.52	-0.58	-0.22	0.25	0.08	-0.43
4	108	0.30	-0.38	-0.15	0.19	-0.12	-0.11
5	132	0.00[a]	0.01	0.14	0.02	-0.01	0.05
6	144	0.02	-0.11	0.10	0.11	-0.06	0.00[a]
8	166	-0.11	0.12	0.15	0.09	-0.19	0.32
9	189	0.05	-0.06	-0.02	0.05	-0.02	-0.02
10	195	0.10	-0.23	-0.05	0.07	0.07	-0.24
11	238	0.04	0.11	0.00[a]	-0.03	0.22	0.10
14	300	0.04	0.22	-0.02	-0.13	0.00[a]	0.27
15	304	0.13	-0.12	-0.06	0.09	-0.23	0.04
18	385	0.16	-0.03	-0.10	0.00[a]	-0.13	0.13
21	448	0.20	-0.05	-0.06	0.07	-0.12	-0.05
25	555	-0.13	0.10	0.07	-0.16	0.29	0.11
26	575	-0.42	0.21	0.12	-0.19	-0.20	0.28
28	613	-0.04	-0.22	0.09	0.05	0.52	-0.46
29	623	0.09	0.02	-0.15	-0.09	0.32	0.04
32	710	0.00[a]	-0.10	0.09	0.18	-0.22	-0.26
34	738	0.04	0.12	-0.07	-0.06	0.07	-0.10
36	788	-0.14	0.11	0.08	0.00[a]	-0.07	0.07
38	844	-0.16	0.10	0.08	0.00[a]	-0.25	-0.03
39	856	0.00[a]	-0.02	0.00[a]	-0.03	0.11	0.03
45	1039	-0.02	0.03	0.00[a]	-0.02	0.10	0.03
46	1049	-0.03	-0.02	-0.02	0.01	-0.08	-0.03
49	1145	-0.03	0.06	-0.05	0.04	-0.21	0.03
66	1474	0.00[a]	0.00[a]	0.01	0.00[a]	0.00[a]	0.00[a]
68	1489	0.00[a]	0.00[a]	0.00[a]	0.00[a]	-0.04	0.01
70	1504	0.05	-0.03	-0.03	0.03	0.06	-0.04
81	3053	0.00[a]	-0.01	0.00[a]	-0.02	0.02	0.01
82	3068	-0.02	-0.00[a]	-0.02	0.00[a]	0.00[a]	0.00[a]
84	3109	0.03	0.12	-0.02	-0.04	0.12	0.03

a: Absolute value of the derivative lower than 0.01 cm^{-1}.

Table S10 DMLF: Calculated rate constants k_{ISC} [s^{-1}] for ($S_1 \rightarrow T_n$) ISC channels in the vacuum.

Channel	**parameters & settings**						**results**	
channel ($i \rightarrow f$)	energy ΔE^{ad}	direct SO $\lvert\langle T_1 \lvert H_{SO} \rvert S_1\rangle\rvert q_0$	vib. SO #derivs	acceptors #acc	interval η	quanta #lq	level #v'	rate k_{ISC}
$S_1 \rightarrow T_{1x}$	5045	-	23	46	0.001	1	5969	$6.3\cdot10^{5}$
$S_1 \rightarrow T_{1x}$	5045	-	23	46	0.001	3	23126	$1.2\cdot10^{6}$
$S_1 \rightarrow T_{1x}$	5045	-	23	46	0.001	5	27312	$1.2\cdot10^{6}$
$S_1 \rightarrow T_{1x}$	5045	-	23	46	0.001	7	28293	$1.2\cdot10^{6}$
$S_1 \rightarrow T_{1x}$	5045	-	23	46	0.001	9	28558	$1.2\cdot10^{6}$
$S_1 \rightarrow T_{1x}$	5045	-	23	46	0.001	11	28619	$1.2\cdot10^{6}$
$S_1 \rightarrow T_{1x}$	5045	-	23	46	0.001	-	28639	$1.2\cdot10^{6}$
$S_1 \rightarrow T_{1x}$	5045	-	23	46	0.01	1	60707	$2.7\cdot10^{6}$
$S_1 \rightarrow T_{1x}$	5045	-	23	46	0.01	3	233947	$5.0\cdot10^{6}$
$S_1 \rightarrow T_{1x}$	5045	-	23	46	0.01	5	276664	$5.1\cdot10^{6}$
$S_1 \rightarrow T_{1x}$	5045	-	23	46	0.01	7	286528	$5.1\cdot10^{6}$
$S_1 \rightarrow T_{1x}$	5045	-	23	46	0.01	9	289108	$5.1\cdot10^{6}$
$S_1 \rightarrow T_{1x}$	5045	-	23	46	0.01	11	289809	$5.1\cdot10^{6}$
$S_1 \rightarrow T_{1x}$	5045	-	23	46	0.01	-	290036	$5.1\cdot10^{6}$
$S_1 \rightarrow T_{1x}$	5045	-	23	46	0.1	1	606590	$5.0\cdot10^{6}$
$S_1 \rightarrow T_{1x}$	5045	-	23	46	0.1	3	2342120	$8.8\cdot10^{6}$
$S_1 \rightarrow T_{1x}$	5045	-	23	46	0.1	5	2769551	$8.9\cdot10^{6}$
$S_1 \rightarrow T_{1x}$	5045	-	23	46	0.1	7	2868180	$8.9\cdot10^{6}$
$S_1 \rightarrow T_{1x}$	5045	-	23	46	0.1	9	2894072	$8.9\cdot10^{6}$
$S_1 \rightarrow T_{1x}$	5045	-	23	46	0.1	11	2901237	$8.9\cdot10^{6}$
$S_1 \rightarrow T_{1x}$	5045	-	23	46	0.1	-	2903708	$8.9\cdot10^{6}$
$S_1 \rightarrow T_{1y}$	5045	-	23	46	0.001	1	5969	$3.3\cdot10^{5}$
$S_1 \rightarrow T_{1y}$	5045	-	23	46	0.001	3	23126	$1.4\cdot10^{6}$
$S_1 \rightarrow T_{1y}$	5045	-	23	46	0.001	5	27312	$1.4\cdot10^{6}$
$S_1 \rightarrow T_{1y}$	5045	-	23	46	0.001	7	28293	$1.4\cdot10^{6}$
$S_1 \rightarrow T_{1y}$	5045	-	23	46	0.001	9	28558	$1.4\cdot10^{6}$
$S_1 \rightarrow T_{1y}$	5045	-	23	46	0.001	11	28619	$1.4\cdot10^{6}$
$S_1 \rightarrow T_{1y}$	5045	-	23	46	0.001	-	28639	$1.4\cdot10^{6}$
$S_1 \rightarrow T_{1y}$	5045	-	23	46	0.01	1	60707	$3.6\cdot10^{6}$
$S_1 \rightarrow T_{1y}$	5045	-	23	46	0.01	3	233947	$4.7\cdot10^{6}$
$S_1 \rightarrow T_{1y}$	5045	-	23	46	0.01	5	276664	$4.7\cdot10^{6}$
$S_1 \rightarrow T_{1y}$	5045	-	23	46	0.01	7	286528	$4.7\cdot10^{6}$
$S_1 \rightarrow T_{1y}$	5045	-	23	46	0.01	9	289108	$4.7\cdot10^{6}$
$S_1 \rightarrow T_{1y}$	5045	-	23	46	0.01	11	289809	$4.7\cdot10^{6}$
$S_1 \rightarrow T_{1y}$	5045	-	23	46	0.01	-	290036	$4.7\cdot10^{6}$
$S_1 \rightarrow T_{1y}$	5045	-	23	46	0.1	1	606590	$4.5\cdot10^{6}$
$S_1 \rightarrow T_{1y}$	5045	-	23	46	0.1	3	2342120	$7.8\cdot10^{6}$
$S_1 \rightarrow T_{1y}$	5045	-	23	46	0.1	5	2769551	$7.8\cdot10^{6}$
$S_1 \rightarrow T_{1y}$	5045	-	23	46	0.1	7	2868180	$7.8\cdot10^{6}$
$S_1 \rightarrow T_{1y}$	5045	-	23	46	0.1	9	2894072	$7.8\cdot10^{6}$
$S_1 \rightarrow T_{1y}$	5045	-	23	46	0.1	11	2901237	$7.8\cdot10^{6}$
$S_1 \rightarrow T_{1y}$	5045	-	23	46	0.1	-	2903708	$7.8\cdot10^{6}$
$S_1 \rightarrow T_{1z}$	5045	0.01012	-	46	0.01	-	352	1.2
$S_1 \rightarrow T_{1z}$	5045	0.01012	-	46	0.1	-	3711	$9.1\cdot10^{1}$
$S_1 \rightarrow T_{1z}$	5045	0.01012	-	46	1.0	-	36775	$1.5\cdot10^{2}$
$S_1 \rightarrow T_{2x}$	899	8.72779		46	See Table S11 for further information			$\sim10^{9}$
$S_1 \rightarrow T_{2y}$	899	0.31495		46				$\sim10^{6}$
$S_1 \rightarrow T_{2z}$	899	-	-	-	-	-	-	-

Table S11 DMLF: Analysis of the stability of the rate constants k_{ISC} [s^{-1}] for ($S_1 \rightarrow T_{2x}$) ISC channel in the vacuum with respect to the adiabatic energy ΔE^{ad} [cm^{-1}] and the width of the search interval η [cm^{-1}].

	η=1		**η=10**		**η=50**		**η=100**	
ΔE^{ad}	# states	k_{ISC}	# states	k_{ISC}	# states	k_{ISC}	# states	k_{ISC}
799	-	-	3	$3.0\cdot10^{9}$	13	$4.3\cdot10^{9}$	27	$6.8\cdot10^{9}$
899	1	$6.2\cdot10^{10}$	1	$6.2\cdot10^{9}$	20	$2.0\cdot10^{9}$	5	$1.4\cdot10^{9}$
999	1	$2.0\cdot10^{9}$	10	$2.8\cdot10^{9}$	31	$1.9\cdot10^{10}$	61	$1.1\cdot10^{10}$
1099	2	$3.3\cdot10^{9}$	10	$1.9\cdot10^{10}$	42	$6.3\cdot10^{9}$	87	$1.6\cdot10^{10}$
1199	1	$5.9\cdot10^{8}$	15	$3.8\cdot10^{10}$	63	$2.1\cdot10^{10}$	126	$1.3\cdot10^{10}$
1899	16	$5.4\cdot10^{9}$	121	$4.2\cdot10^{9}$	648	$3.6\cdot10^{9}$	1298	$3.6\cdot10^{9}$

Table S12 DMLF: Calculated rate constants k_{ISC} [s^{-1}] for ($S_1 \rightarrow T_n$) ISC channels in water (COSMO).

Channel	**parameters & settings**						**results**	
channel (i→f)	energy ΔE^{ad}	direct SO $\vert\langle T_1\vert H_{SO}\vert S_1\rangle\vert_{q_0}$	vib. SO #derivs	acceptors #acc	interval η	quanta #lq	level #v'	rate k_{ISC}
$S_1 \rightarrow T_{1x}$	3973	$< 10^{-3}$	23	46	0.001	1	502	$4.6\cdot10^{6}$
$S_1 \rightarrow T_{1x}$	3973	$< 10^{-3}$	23	46	0.001	3	1419	$4.7\cdot10^{6}$
$S_1 \rightarrow T_{1x}$	3973	$< 10^{-3}$	23	46	0.001	5	1584	$4.7\cdot10^{6}$
$S_1 \rightarrow T_{1x}$	3973	$< 10^{-3}$	23	46	0.001	-	1624	$4.7\cdot10^{6}$
$S_1 \rightarrow T_{1x}$	3973	$< 10^{-3}$	23	46	0.01	1	5024	$5.9\cdot10^{6}$
$S_1 \rightarrow T_{1x}$	3973	$< 10^{-3}$	23	46	0.01	3	13903	$6.6\cdot10^{6}$
$S_1 \rightarrow T_{1x}$	3973	$< 10^{-3}$	23	46	0.01	5	15527	$6.6\cdot10^{6}$
$S_1 \rightarrow T_{1x}$	3973	$< 10^{-3}$	23	46	0.01	-	15975	$6.6\cdot10^{6}$
$S_1 \rightarrow T_{1x}$	3973	$< 10^{-3}$	23	46	0.1	1	49392	$7.2\cdot10^{6}$
$S_1 \rightarrow T_{1x}$	3973	$< 10^{-3}$	23	46	0.1	3	138755	$7.8\cdot10^{6}$
$S_1 \rightarrow T_{1x}$	3973	$< 10^{-3}$	23	46	0.1	5	155742	$7.8\cdot10^{6}$
$S_1 \rightarrow T_{1x}$	3973	$< 10^{-3}$	23	46	0.1	-	160147	$7.8\cdot10^{6}$
$S_1 \rightarrow T_{1y}$	3973	$< 10^{-3}$	23	46	0.001	1	502	$2.6\cdot10^{6}$
$S_1 \rightarrow T_{1y}$	3973	$< 10^{-3}$	23	46	0.001	3	1419	$2.8\cdot10^{6}$
$S_1 \rightarrow T_{1y}$	3973	$< 10^{-3}$	23	46	0.001	5	1584	$2.8\cdot10^{6}$
$S_1 \rightarrow T_{1y}$	3973	$< 10^{-3}$	23	46	0.001	-	1624	$2.8\cdot10^{6}$
$S_1 \rightarrow T_{1y}$	3973	$< 10^{-3}$	23	46	0.01	1	5024	$4.4\cdot10^{6}$
$S_1 \rightarrow T_{1y}$	3973	$< 10^{-3}$	23	46	0.01	3	13903	$4.7\cdot10^{6}$
$S_1 \rightarrow T_{1y}$	3973	$< 10^{-3}$	23	46	0.01	5	15527	$4.8\cdot10^{6}$
$S_1 \rightarrow T_{1y}$	3973	$< 10^{-3}$	23	46	0.001	-	15975	$4.8\cdot10^{6}$
$S_1 \rightarrow T_{1y}$	3973	$< 10^{-3}$	23	46	0.1	1	49392	$3.7\cdot10^{6}$
$S_1 \rightarrow T_{1y}$	3973	$< 10^{-3}$	23	46	0.1	3	138755	$4.2\cdot10^{6}$
$S_1 \rightarrow T_{1y}$	3973	$< 10^{-3}$	23	46	0.1	5	155742	$4.4\cdot10^{6}$
$S_1 \rightarrow T_{1y}$	3973	$< 10^{-3}$	23	46	0.001	-	160147	$4.4\cdot10^{6}$
$S_1 \rightarrow T_{1z}$	3973	0.00987	-	46	0.01	-	36	$2.6\cdot10^{1}$
$S_1 \rightarrow T_{1z}$	3973	0.00987	-	46	0.1	-	335	$7.7\cdot10^{1}$
$S_1 \rightarrow T_{1z}$	3973	0.00987	-	46	1.0	-	3353	$1.2\cdot10^{3}$
$S_1 \rightarrow T_{2x}$	508	$< 10^{-3}$	23	46	See Table S13 for further information			~10^{7}-10^{8}
$S_1 \rightarrow T_{2y}$	508	$< 10^{-3}$	23	46				~10^{7}-10^{8}
$S_1 \rightarrow T_{1z}$	508	0.00102	-	46	10	-	-	-
$S_1 \rightarrow T_{1z}$	508	0.00102	-	46	100	-	8	$2.2\cdot10^{2}$
$S_1 \rightarrow T_{2z}$	508	0.00102	-	46	1000	-	466	$1.3\cdot10^{2}$

Table S13 DMLF: Analysis of the stability of the rate constants k_{ISC} [s^{-1}] for ($S_1 \rightarrow T_{2x,y}$) ISC channel in aqueous solution with respect to the adiabatic energy ΔE^{ad} [cm^{-1}] and the width of the search interval η [cm^{-1}].

	1=10		**η=10**		**η=100**	
ΔE^{ad}	# states	k_{ISC}	# states	k_{ISC}	# states	k_{ISC}
($S_1 \rightarrow T_{2x}$)						
408	2	$1.2 \cdot 10^7$	13	$6.2 \cdot 10^7$	115	$3.9 \cdot 10^7$
508	5	$4.8 \cdot 10^8$	26	$1.3 \cdot 10^8$	229	$5.9 \cdot 10^7$
608	2	$1.3 \cdot 10^7$	42	$4.2 \cdot 10^7$	427	$9.4 \cdot 10^7$
708	4	$3.3 \cdot 10^7$	71	$1.4 \cdot 10^8$	780	$1.7 \cdot 10^8$
1008	35	$3.6 \cdot 10^6$	385	$6.7 \cdot 10^7$	3989	$1.0 \cdot 10^8$
1508	391	$7.2 \cdot 10^7$	4058	$1.1 \cdot 10^8$	41558	$1.4 \cdot 10^8$
($S_1 \rightarrow T_{2y}$)						
408	2	$2.1 \cdot 10^6$	13	$1.5 \cdot 10^8$	115	$5.6 \cdot 10^7$
508	5	$3.5 \cdot 10^8$	26	$3.8 \cdot 10^7$	229	$7.8 \cdot 10^7$
608	2	$2.2 \cdot 10^7$	42	$3.9 \cdot 10^7$	427	$1.1 \cdot 10^8$
708	4	$3.4 \cdot 10^8$	71	$1.0 \cdot 10^8$	780	$1.2 \cdot 10^8$
1008	35	$2.5 \cdot 10^6$	385	$8.7 \cdot 10^7$	3989	$1.1 \cdot 10^8$
1508	391	$3.7 \cdot 10^7$	4058	$2.1 \cdot 10^8$	41558	$1.3 \cdot 10^8$

The calculation of the ISC crossing rate constants with the inclusion of vibronic spin-orbit coupling is very laborious. The calculation time hereby depends on various factors, including the number of vibrational degrees of freedom included. For all calculations, the complete set of in-plane and *oop* vibrations was used as accepting and coupling modes, respectively. For DMLF, it is still possible to calculate the rate constants for the $S_1 \rightarrow T_{1x,y}$ ISC channels without further restrictions. For the bigger flavins this is problematic.[1] The VIBES program allows to restrict the amount of quanta for the excitations in the vibrational levels of the final state. Table S10 shows the ISC rate constants k_{ISC} [s^{-1}] for the ($S_1 \rightarrow T_{1x,y}$) channels in the vacuum for a different number of quanta in the vibrational levels of the final state. It is evident, that the ISC rate constant typically is converged for 3 quanta.

---

[1] The calculation of the ISC rate constant for the ($S_1 \rightarrow T_{1x}$) channel with an maximum of one quantum per vibrational level and an interval width of η=0.001 cm^{-1} took ~1.5 h for DMLF, ~282.5 h for LF, ~10.5 h for 1DLF, and 2 h for 5DLF.

Table S14 LF: Calculated rate constants k_{ISC} [s^{-1}] for ($S_1 \rightarrow T_n$) ISC channels in the vacuum.

Channel	**parameters & settings**						**results**	
channel ($i \rightarrow f$)	energy ΔE^{ad}	direct SO $\lvert\langle T_1 \lvert H_{SO} \rvert S_1 \rangle\rvert_{q_0}$	vib. SO #derivs	acceptors #acc	interval η	quanta #lq	level #v'	rate k_{ISC}
$S_1 \rightarrow T_{1x}$	5069	-	31	56	0.0001	1	14777	$9.2 \cdot 10^4$
$S_1 \rightarrow T_{1x}$	5069	-	31	56	0.0001	3	71718	$2.9 \cdot 10^5$
$S_1 \rightarrow T_{1x}$	5069	-	31	56	0.0001	5	88877	$2.9 \cdot 10^5$
$S_1 \rightarrow T_{1x}$	5069	-	31	56	0.0001	-	95324	$2.9 \cdot 10^5$
$S_1 \rightarrow T_{1x}$	5069	-	31	56	0.001	1	147348	$3.9 \cdot 10^5$
$S_1 \rightarrow T_{1y}$	5069	-	31	56	0.0001	1	14777	$1.0 \cdot 10^5$
$S_1 \rightarrow T_{1y}$	5069	-	31	56	0.0001	3	71718	$1.7 \cdot 10^5$
$S_1 \rightarrow T_{1y}$	5069	-	31	56	0.0001	5	88877	$1.7 \cdot 10^5$
$S_1 \rightarrow T_{1y}$	5069	-	31	56	0.0001	-	95324	$1.7 \cdot 10^5$
$S_1 \rightarrow T_{1y}$	5069	-	31	56	0.001	1	147348	$2.2 \cdot 10^5$
$S_1 \rightarrow T_{1z}$	5069	0.07004	-	56	0.01	-	2797	$4.4 \cdot 10^2$
$S_1 \rightarrow T_{1z}$	5069	0.07004	-	56	0.1	-	27886	$3.4 \cdot 10^3$
$S_1 \rightarrow T_{1z}$	5069	0.07004	-	56	1	-	280430	$5.9 \cdot 10^3$
$S_1 \rightarrow T_{2x}$	482	6.79006	-	56	See Table S15 for further information.			$\sim 10^9$
$S_1 \rightarrow T_{2y}$	482	0.4373	-	56				$\sim 10^6$
$S_1 \rightarrow T_{2z}$	482	-	-	-	-	-	-	-

Table S15 LF: Analysis of the stability of the rate constants k_{ISC} [s^{-1}] for ($S_1 \rightarrow T_{2x}$) ISC channel in the vacuum with respect to the adiabatic energy ΔE^{ad} [cm^{-1}] and the width of the search interval η [cm^{-1}].

	η=10		**η=50**		**η=100**	
ΔE^{ad}	# states	k_{ISC}	# states	k_{ISC}	# states	k_{ISC}
482	0	-	1	$1.5 \cdot 10^9$	1	$0.7 \cdot 10^9$
582	0	-	1	$0.5 \cdot 10^9$	1	$0.3 \cdot 10^9$
682	0	-	2	$0.8 \cdot 10^9$	5	$1.0 \cdot 10^9$
782	1	$1.3 \cdot 10^9$	3	$0.9 \cdot 10^9$	8	$1.0 \cdot 10^9$
882	2	$3.2 \cdot 10^9$	7	$1.6 \cdot 10^9$	12	$1.4 \cdot 10^9$
982	2	$1.8 \cdot 10^9$	10	$1.2 \cdot 10^9$	24	$2.1 \cdot 10^9$

Table S16 LF: Calculated rate constants k_{ISC} [s^{-1}] for ($S_1 \rightarrow T_n$) ISC channels in water (COSMO).

Channel	**parameters & settings**						**results**	
channel (i→f)	energy ΔE^{ad}	direct SO $\lvert\langle T_1 \lvert H_{SO} \rvert S_1\rangle\rvert q_0$	vib. SO #derivs	acceptors #acc	interval η	quanta #lq	level #v'	rate k_{ISC}
$S_1 \rightarrow T_{1x}$	4639	$< 10^{-3}$	31	56	0.001	1	51002	$5.2 \cdot 10^6$
$S_1 \rightarrow T_{1x}$	4639	$< 10^{-3}$	31	56	0.001	3	213746	$5.2 \cdot 10^6$
$S_1 \rightarrow T_{1x}$	4639	$< 10^{-3}$	31	56	0.001	5	258068	$5.2 \cdot 10^6$
$S_1 \rightarrow T_{1x}$	4639	$< 10^{-3}$	31	56	0.001	-	273681	$5.2 \cdot 10^6$
$S_1 \rightarrow T_{1x}$	4639	$< 10^{-3}$	31	56	0.01	1	508686	$1.5 \cdot 10^6$
$S_1 \rightarrow T_{1x}$	4639	$< 10^{-3}$	31	56	0.01	3	2135104	$3.2 \cdot 10^6$
$S_1 \rightarrow T_{1x}$	4639	$< 10^{-3}$	31	56	0.01	5	2579122	$3.2 \cdot 10^6$
$S_1 \rightarrow T_{1x}$	4639	$< 10^{-3}$	31	56	0.1	1	5088246	$1.9 \cdot 10^6$
$S_1 \rightarrow T_{1y}$	4639	$< 10^{-3}$	31	56	0.001	1	51002	$4.7 \cdot 10^5$
$S_1 \rightarrow T_{1y}$	4639	$< 10^{-3}$	31	56	0.001	3	213746	$4.8 \cdot 10^5$
$S_1 \rightarrow T_{1y}$	4639	$< 10^{-3}$	31	56	0.001	5	258068	$4.8 \cdot 10^5$
$S_1 \rightarrow T_{1y}$	4639	$< 10^{-3}$	31	56	0.001	-	273681	$4.8 \cdot 10^5$
$S_1 \rightarrow T_{1y}$	4639	$< 10^{-3}$	31	56	0.01	1	508686	$2.2 \cdot 10^5$
$S_1 \rightarrow T_{1y}$	4639	$< 10^{-3}$	31	56	0.01	3	2135104	$2.6 \cdot 10^5$
$S_1 \rightarrow T_{1y}$	4639	$< 10^{-3}$	31	56	0.01	5	2579122	$2.6 \cdot 10^5$
$S_1 \rightarrow T_{1y}$	4639	$< 10^{-3}$	31	56	0.1	1	5088246	$4.5 \cdot 10^5$
$S_1 \rightarrow T_{1z}$	4639	0.01282	-	56	0.01	-	972	$3.6 \cdot 10^1$
$S_1 \rightarrow T_{1z}$	4639	0.01282	-	56	0.1	-	9783	$9.4 \cdot 10^1$
$S_1 \rightarrow T_{1z}$	4639	0.01282	-	56	1.0	-	99824	$1.2 \cdot 10^2$
$S_1 \rightarrow T_{2x}$	917	$< 10^{-3}$	31	56	See Table S17 for further information.			$\sim 10^8$
$S_1 \rightarrow T_{2y}$	917	$< 10^{-3}$	31	56				$\sim 10^7$
$S_1 \rightarrow T_{2z}$	917	0.00275	-	56	0.01	-	1	$3.4 \cdot 10^1$
$S_1 \rightarrow T_{2z}$	917	0.00275	-	56	0.1	-	12	$1.5 \cdot 10^2$
$S_1 \rightarrow T_{2z}$	917	0.00275	-	56	1.0	-	123	$8.3 \cdot 10^2$

Table S17 LF: Analysis of the stability of the rate constants k_{ISC} [s^{-1}] for the ($S_1 \rightarrow T_{2x}$) and ($S_1 \rightarrow T_{2y}$) ISC channels in aqueous solution (COSMO) with respect to the adiabatic energy ΔE^{ad} [cm^{-1}] and the width of the search interval η [cm^{-1}].

	η=1		**η=10**		**η=100**	
ΔE^{ad}	# states	k_{ISC}	# states	k_{ISC}	# states	k_{ISC}
($S_1 \rightarrow T_{2x}$)						
817	149	$3.0 \cdot 10^7$	1687	$1.1 \cdot 10^8$	17364	$1.0 \cdot 10^8$
917	283	$5.3 \cdot 10^7$	3009	$1.1 \cdot 10^8$	31743	$1.1 \cdot 10^8$
1017	577	$1.3 \cdot 10^8$	5259	$1.5 \cdot 10^8$	56419	$1.3 \cdot 10^8$
1117	883	$3.3 \cdot 10^7$	9464	$1.7 \cdot 10^8$	97662	$1.2 \cdot 10^8$
1217	1577	$6.0 \cdot 10^7$	16034	$9.3 \cdot 10^7$	166392	$1.3 \cdot 10^8$
1917	44356	$1.2 \cdot 10^8$	438970	$1.4 \cdot 10^8$	4528879	$1.6 \cdot 10^8$
($S_1 \rightarrow T_{2y}$)						
817	149	$2.6 \cdot 10^7$	1687	$6.7 \cdot 10^7$	17364	$6.1 \cdot 10^7$
917	283	$1.7 \cdot 10^7$	3009	$9.9 \cdot 10^7$	31743	$7.0 \cdot 10^7$
1017	577	$1.6 \cdot 10^8$	5259	$7.1 \cdot 10^7$	56419	$7.4 \cdot 10^7$
1117	883	$3.4 \cdot 10^7$	9464	$9.0 \cdot 10^7$	97662	$6.9 \cdot 10^7$
1217	1577	$5.4 \cdot 10^7$	16034	$6.5 \cdot 10^7$	166392	$7.4 \cdot 10^7$
1917	44356	$8.5 \cdot 10^7$	438970	$8.9 \cdot 10^7$	4528879	$9.1 \cdot 10^7$

Table S18 1DLF: Calculated rate constants k_{ISC} [s^{-1}] for ($S_1 \to T_n$) ISC channels in the vacuum.

Channel	**parameters & settings**						**results**	
channel (i→f)	energy ΔE^{ad}	direct SO $\|\langle T_1\|H_{SO}\|S_1\rangle\|q_0$	vib. SO #derivs	acceptors #acc	interval η	quanta #lq	level #v'	rate k_{ISC}
$S_1 \to T_{1x}$	5324	-	32	58	0.001	1	20364	$1.3 \cdot 10^5$
$S_1 \to T_{1x}$	5324	-	32	58	0.001	3	63950	$2.7 \cdot 10^5$
$S_1 \to T_{1x}$	5324	-	32	58	0.001	5	80354	$2.7 \cdot 10^5$
$S_1 \to T_{1x}$	5324	-	32	58	0.001	-	90774	$2.7 \cdot 10^5$
$S_1 \to T_{1x}$	5324	-	32	58	0.01	1	205147	$2.0 \cdot 10^5$
$S_1 \to T_{1x}$	5324	-	32	58	0.01	3	642177	$3.1 \cdot 10^5$
$S_1 \to T_{1x}$	5324	-	32	58	0.01	5	805319	$3.1 \cdot 10^5$
$S_1 \to T_{1x}$	5324	-	32	58	0.1	1	2052523	$7.9 \cdot 10^5$
$S_1 \to T_{1y}$	5324	-	32	58	0.001	1	20364	$1.3 \cdot 10^5$
$S_1 \to T_{1y}$	5324	-	32	58	0.001	3	63950	$3.0 \cdot 10^5$
$S_1 \to T_{1y}$	5324	-	32	58	0.001	5	80354	$3.0 \cdot 10^5$
$S_1 \to T_{1y}$	5324	-	32	58	0.001	-	90774	$3.0 \cdot 10^5$
$S_1 \to T_{1y}$	5324	-	32	58	0.01	1	205147	$2.1 \cdot 10^6$
$S_1 \to T_{1y}$	5324	-	32	58	0.01	3	642177	$2.2 \cdot 10^6$
$S_1 \to T_{1y}$	5324	-	32	58	0.01	5	805319	$2.2 \cdot 10^6$
$S_1 \to T_{1y}$	5324	-	32	58	0.1	1	2052523	$6.7 \cdot 10^5$
$S_1 \to T_{1z}$	5324	0.00439	-	58	0.01	-	10795	$2.4 \cdot 10^1$
$S_1 \to T_{1z}$	5324	0.00439	-	58	0.1	-	109623	$4.4 \cdot 10^1$
$S_1 \to T_{1z}$	5324	0.00439	-	58	1.0	-	1101240	$3.8 \cdot 10^1$

Table S19 1DLF: Calculated rate constatnts k_{ISC} [s^{-1}] for ($S_1 \rightarrow T_n$) ISC channels in water (COSMO).

Channel	**parameters & settings**						**results**	
channel (i→f)	energy ΔE^{ad}	direct SO $\lvert\langle T_1 \lvert H_{SO} \rvert S_1\rangle\rvert q_0$	vib. SO #derivs	acceptors #acc	interval η	quanta #lq	level #v'	rate k_{ISC}
$S_1 \rightarrow T_{1x}$	4065	$< 10^{-3}$	32	58	0.001	1	1376	$2.6 \cdot 10^5$
$S_1 \rightarrow T_{1x}$	4065	$< 10^{-3}$	32	58	0.001	3	3460	$2.7 \cdot 10^5$
$S_1 \rightarrow T_{1x}$	4065	$< 10^{-3}$	32	58	0.001	5	4121	$2.7 \cdot 10^5$
$S_1 \rightarrow T_{1x}$	4065	$< 10^{-3}$	32	58	0.001	-	4511	$2.7 \cdot 10^5$
$S_1 \rightarrow T_{1x}$	4065	$< 10^{-3}$	32	58	0.01	1	13977	$3.0 \cdot 10^5$
$S_1 \rightarrow T_{1x}$	4065	$< 10^{-3}$	32	58	0.01	3	34883	$1.2 \cdot 10^6$
$S_1 \rightarrow T_{1x}$	4065	$< 10^{-3}$	32	58	0.01	5	41471	$1.2 \cdot 10^6$
$S_1 \rightarrow T_{1x}$	4065	$< 10^{-3}$	32	58	0.1	1	140491	$6.6 \cdot 10^5$
$S_1 \rightarrow T_{1x}$	4065	$< 10^{-3}$	32	58	0.1	3	346827	$8.0 \cdot 10^5$
$S_1 \rightarrow T_{1x}$	4065	$< 10^{-3}$	32	58	0.1	5	411997	$8.0 \cdot 10^5$
$S_1 \rightarrow T_{1y}$	4065	$< 10^{-3}$	32	58	0.001	1	1376	$1.0 \cdot 10^5$
$S_1 \rightarrow T_{1y}$	4065	$< 10^{-3}$	32	58	0.001	3	3460	$1.1 \cdot 10^5$
$S_1 \rightarrow T_{1y}$	4065	$< 10^{-3}$	32	58	0.001	5	4121	$1.1 \cdot 10^5$
$S_1 \rightarrow T_{1y}$	4065	$< 10^{-3}$	32	58	0.001	-	4511	$1.1 \cdot 10^5$
$S_1 \rightarrow T_{1y}$	4065	$< 10^{-3}$	32	58	0.01	1	13977	$2.7 \cdot 10^5$
$S_1 \rightarrow T_{1y}$	4065	$< 10^{-3}$	32	58	0.01	3	34883	$4.0 \cdot 10^5$
$S_1 \rightarrow T_{1y}$	4065	$< 10^{-3}$	32	58	0.01	5	41471	$4.0 \cdot 10^5$
$S_1 \rightarrow T_{1y}$	4065	$< 10^{-3}$	32	58	0.1	1	140491	$6.0 \cdot 10^5$
$S_1 \rightarrow T_{1y}$	4065	$< 10^{-3}$	32	58	0.1	3	346827	$6.8 \cdot 10^5$
$S_1 \rightarrow T_{1y}$	4065	$< 10^{-3}$	32	58	0.1	5	411997	$6.8 \cdot 10^5$
$S_1 \rightarrow T_{1z}$	4065	0.00313	-	58	0.01	-	517	1.0
$S_1 \rightarrow T_{1z}$	4065	0.00313	-	58	0.1	-	5195	$3.8 \cdot 10^1$
$S_1 \rightarrow T_{1z}$	4065	0.00313	-	58	1.0	-	54084	$4.4 \cdot 10^1$

Table S20 5DLF: Calculated rate constants k_{ISC} [s^{-1}] for ($S_1 \rightarrow T_n$) ISC channels in the vacuum.

channel	**parameters & settings**						**results**	
channel (i→f)	energy ΔE^{ad}	direct SO $\|\langle T_1\|H_{SO}\|S_1\rangle\|q_0$	vib. SO #derives	acceptors #acc	interval η	quanta #lq	level #v'	rate k_{ISC}
$S_1 \rightarrow T_{1x}$	4070	$< 10^{-3}$	32	58	0.001	1	5593	$4.5 \cdot 10^4$
$S_1 \rightarrow T_{1x}$	4070	$< 10^{-3}$	32	58	0.001	3	16199	$5.0 \cdot 10^4$
$S_1 \rightarrow T_{1x}$	4070	$< 10^{-3}$	32	58	0.001	5	18995	$5.0 \cdot 10^4$
$S_1 \rightarrow T_{1x}$	4070	$< 10^{-3}$	32	58	0.001	-	20187	$5.0 \cdot 10^4$
$S_1 \rightarrow T_{1x}$	4070	$< 10^{-3}$	32	58	0.01	1	55794	$2.0 \cdot 10^5$
$S_1 \rightarrow T_{1x}$	4070	$< 10^{-3}$	32	58	0.01	3	161930	$2.2 \cdot 10^5$
$S_1 \rightarrow T_{1x}$	4070	$< 10^{-3}$	32	58	0.01	5	189544	$2.2 \cdot 10^5$
$S_1 \rightarrow T_{1x}$	4070	$< 10^{-3}$	32	58	0.1	1	557393	$9.5 \cdot 10^5$
$S_1 \rightarrow T_{1x}$	4070	$< 10^{-3}$	32	58	0.1	3	1626181	$1.5 \cdot 10^6$
$S_1 \rightarrow T_{1x}$	4070	$< 10^{-3}$	32	58	0.1	5	1903213	$1.5 \cdot 10^6$
$S_1 \rightarrow T_{1y}$	4070	$< 10^{-3}$	32	58	0.001	1	5593	$5.4 \cdot 10^4$
$S_1 \rightarrow T_{1y}$	4070	$< 10^{-3}$	32	58	0.001	3	16199	$6.4 \cdot 10^4$
$S_1 \rightarrow T_{1y}$	4070	$< 10^{-3}$	32	58	0.001	5	18995	$6.4 \cdot 10^4$
$S_1 \rightarrow T_{1y}$	4070	$< 10^{-3}$	32	58	0.001	-	20187	$6.4 \cdot 10^4$
$S_1 \rightarrow T_{1y}$	4070	$< 10^{-3}$	32	58	0.01	1	55794	$4.0 \cdot 10^5$
$S_1 \rightarrow T_{1y}$	4070	$< 10^{-3}$	32	58	0.01	3	161930	$4.1 \cdot 10^5$
$S_1 \rightarrow T_{1y}$	4070	$< 10^{-3}$	32	58	0.01	5	189544	$4.1 \cdot 10^5$
$S_1 \rightarrow T_{1y}$	4070	$< 10^{-3}$	32	58	0.1	1	557393	$4.1 \cdot 10^5$
$S_1 \rightarrow T_{1y}$	4070	$< 10^{-3}$	32	58	0.1	3	1626181	$5.5 \cdot 10^5$
$S_1 \rightarrow T_{1y}$	4070	$< 10^{-3}$	32	58	0.1	5	1903213	$5.5 \cdot 10^5$
$S_1 \rightarrow T_{1z}$	4070	0.01176	-	58	0.01	-	393	$5.3 \cdot 10^2$
$S_1 \rightarrow T_{1z}$	4070	0.01176	-	58	0.1	-	3470	$1.5 \cdot 10^2$
$S_1 \rightarrow T_{1z}$	4070	0.01176	-	58	1.0	-	35442	$1.6 \cdot 10^2$

Table S21 5DLF: Calculated rate constants k_{ISC} [s^{-1}] for ($S_1 \rightarrow T_n$) ISC channels in aqueous solution.

channel	**parameters & settings**						**results**	
channel ($i \rightarrow f$)	energy ΔE^{ad}	direct SO $\vert\langle T_1\vert H_{SO}\vert S_1\rangle\vert q_0$	vib. SO #derives	acceptors #acc	interval η	quanta #lq	level #v'	rate k_{ISC}
$S_1 \rightarrow T_{1x}$	3682	$< 10^{-3}$	32	58	0.001	1	5593	$1.4\cdot10^{4}$
$S_1 \rightarrow T_{1x}$	3682	$< 10^{-3}$	32	58	0.001	3	16199	$1.7\cdot10^{4}$
$S_1 \rightarrow T_{1x}$	3682	$< 10^{-3}$	32	58	0.001	5	18995	$1.7\cdot10^{4}$
$S_1 \rightarrow T_{1x}$	3682	$< 10^{-3}$	32	58	0.001	-	20187	$1.7\cdot10^{4}$
$S_1 \rightarrow T_{1x}$	3682	$< 10^{-3}$	32	58	0.01	1	55794	$9.5\cdot10^{4}$
$S_1 \rightarrow T_{1x}$	3682	$< 10^{-3}$	32	58	0.01	3	161930	$1.0\cdot10^{5}$
$S_1 \rightarrow T_{1x}$	3682	$< 10^{-3}$	32	58	0.01	5	189544	$1.0\cdot10^{5}$
$S_1 \rightarrow T_{1x}$	3682	$< 10^{-3}$	32	58	0.1	1	557393	$2.1\cdot10^{5}$
$S_1 \rightarrow T_{1x}$	3682	$< 10^{-3}$	32	58	0.1	3	1626181	$2.9\cdot10^{5}$
$S_1 \rightarrow T_{1x}$	3682	$< 10^{-3}$	32	58	0.1	5	19033213	$2.9\cdot10^{5}$
$S_1 \rightarrow T_{1y}$	3682	$< 10^{-3}$	32	58	0.001	1	5593	$1.4\cdot10^{4}$
$S_1 \rightarrow T_{1y}$	3682	$< 10^{-3}$	32	58	0.001	3	16199	$1.4\cdot10^{4}$
$S_1 \rightarrow T_{1y}$	3682	$< 10^{-3}$	32	58	0.001	5	18995	$1.4\cdot10^{4}$
$S_1 \rightarrow T_{1y}$	3682	$< 10^{-3}$	32	58	0.001	-	20187	$1.4\cdot10^{4}$
$S_1 \rightarrow T_{1y}$	3682	$< 10^{-3}$	32	58	0.01	1	55794	$1.1\cdot10^{5}$
$S_1 \rightarrow T_{1y}$	3682	$< 10^{-3}$	32	58	0.01	3	161930	$1.1\cdot10^{5}$
$S_1 \rightarrow T_{1y}$	3682	$< 10^{-3}$	32	58	0.01	5	189544	$1.1\cdot10^{5}$
$S_1 \rightarrow T_{1y}$	3682	$< 10^{-3}$	32	58	0.1	1	557393	$2.5\cdot10^{5}$
$S_1 \rightarrow T_{1y}$	3682	$< 10^{-3}$	32	58	0.1	3	1626181	$3.7\cdot10^{5}$
$S_1 \rightarrow T_{1y}$	3682	$< 10^{-3}$	32	58	0.1	5	19033213	$3.7\cdot10^{5}$
$S_1 \rightarrow T_{1z}$	3682	0.00316	-	58	0.01	-	138	0.8
$S_1 \rightarrow T_{1z}$	3682	0.00316	-	58	0.1	-	1295	$2.1\cdot10^{2}$
$S_1 \rightarrow T_{1z}$	3682	0.00316	-	58	1	-	12751	$6.0\cdot10^{1}$
$S_1 \rightarrow T_{2x}$	852	$< 10^{-3}$	32	58	For further details see Table S22.			$\sim10^{7}$-10^{8}
$S_1 \rightarrow T_{2y}$	852	$< 10^{-3}$	32	58				$\sim10^{7}$-10^{8}
$S_1 \rightarrow T_{2z}$	852	0.00878	-	58	1	-	1	$1.1\cdot10^{1}$
$S_1 \rightarrow T_{2z}$	852	0.00878	-	58	10	-	13	$5.6\cdot10^{3}$
$S_1 \rightarrow T_{2z}$	852	0.00878	-	58	100	-	107	$9.1\cdot10^{3}$

Table S22 5DLF: Analysis of the stability of the rate constants k_{ISC} [s^{-1}] for ($S_1 \rightarrow T_{2x}$) ISC channel in aqueous solution with respect to the adiabatic energy ΔE^{ad} [cm^{-1}] and the width of the search interval η [cm^{-1}].

	η=1		**η=10**		**η=100**	
ΔE^{ad}	# states	k_{ISC}	# states	k_{ISC}	# states	k_{ISC}
($S_1 \rightarrow T_{2x}$)						
752	102	$0.7\cdot10^{7}$	1037	$3.3\cdot10^{7}$	11027	$6.2\cdot10^{7}$
852	188	$1.2\cdot10^{7}$	1925	$1.1\cdot10^{8}$	20384	$7.6\cdot10^{7}$
952	348	$9.1\cdot10^{7}$	3453	$8.7\cdot10^{7}$	36672	$7.8\cdot10^{7}$
1052	596	$4.8\cdot10^{7}$	6109	$6.2\cdot10^{7}$	64391	$7.6\cdot10^{7}$
1152	1065	$3.9\cdot10^{7}$	10585	$4.4\cdot10^{7}$	110754	$8.4\cdot10^{7}$
1852	31091	$2.0\cdot10^{7}$	312705	$7.3\cdot10^{7}$	3223323	$9.5\cdot10^{7}$
($S_1 \rightarrow T_{2y}$)						
752	102	$0.8\cdot10^{7}$	1037	$4.3\cdot10^{7}$	11027	$8.2\cdot10^{7}$
852	188	$0.5\cdot10^{7}$	1925	$5.1\cdot10^{7}$	20384	$7.3\cdot10^{7}$
952	348	$8.8\cdot10^{7}$	3453	$5.8\cdot10^{7}$	36672	$7.3\cdot10^{7}$
1052	596	$2.0\cdot10^{8}$	6109	$7.5\cdot10^{7}$	64391	$7.1\cdot10^{7}$
1152	1065	$4.8\cdot10^{7}$	10585	$6.4\cdot10^{7}$	110754	$6.5\cdot10^{7}$
1852	31091	$3.2\cdot10^{7}$	312705	$1.2\cdot10^{8}$	3223323	$9.7\cdot10^{7}$

---

[i] S. Salzmann, J. Tatchen, C.M. Marian, J. Photochem. Photobiol. A **198** (2008) 221.

[ii] K. Tomić, J. Tatchen, C.M. Marian, J. Phys. Chem. A **109** (37) (2005) 8410–84

[iii] S. Salzmann, M. Kleinschmidt, J. Tatchen, R.Weinkauf, C.M. Marian, Phys. Chem. Chem. Phys. **10** (2008) 380–392.

[iv] J. Tatchen, C.M. Marian, Phys. Chem. Chem. Phys. **8** (2006) 2133–2144.

[v] Y.J. Bomble, K.W. Sattelmeyer, J.F. Stanton, J. Gauss, J. Chem. Phys. **121** (2004) 5236-5240.

[vi] E.R. Davidson, A.A. Jarzęcki, Chem. Phys. Lett. **285** (1998) 155-159.

[vii] L.S. Cederbaum, W. Domcke, J. Chem. Phys. **64** (1976) 603-611.

[viii] J. Hasegawa, S. Bureekaew, H. Nakatsuji, J. Photochem. Photobiol. A **189** (2007) 205–210.

[ix] T. Climent, R. González, M. Merchán, L. Serrano-Andrés, J. Phys. Chem. A **110** (2006) 13584–13590.

[x] E. Sikorska, I.V. Khmelinskii, J. Koput, J.L. Bourdelande, M. Sikorski, J. Mol. Struct. **697** (2004) 137–141.

[xi] E. Sikorska, I.V. Khmelinskii, D.R. Worrall, J. Koput, M. Sikorski, J. Fluores. **14** (2004) 57–64.

[xii] C. Neiss, P. Saalfrank, M. Parac, S. Grimme, J. Phys. Chem. A **107** (2003) 140–147.

[xiii] K. Zenichowski, M. Gothe, P. Saalfrank, J. Photochem. Photobiol. A **190** (2007) 290–300.

[xiv] E. Sikorska, I.V. Khmelinskii, D.R. Worrall, J. Koput, M. Sikorski, J. Fluoresc. **14** (2004) 57–64.

[xv] A.J.W.G. Visser, F. Müller, Helv. Chim. Acta **62** (1979) 593–608.

[xvi] J.T.M. Kennis, S. Crosson, M. Gauden, I.H.M. van Stokkum, K. Moffat, R. van Grondelle, Biochemistry **42** (2003) 3385–3392.

[xvii] M. Salomon, J.M. Christie, E. Knieb, U. Lempert, W.R. Briggs, Biochemistry **39** (2000) 9401–9410.

[xviii] M.R. Silva-Junior, M. Schreiber, W. Thiel, J. Chem. Phys. **129** (2008) 1-14.

[xix] W.E. Kurtin, P.-S. Song, Photochem. Photobiol. **9** (1969) 127.

[xx] A. Tonilo, M. Persico, J. Chem. Phys. **115** (2001) 1817.

[xxi] A. Tonilo, M. Persico, J. Comput. Chem. **22** (2001) 968.

[xxii] J. Tatchen, N. Gilka, C.M. Marian, Phys. Chem. Chem. Phys. **9** (2007) 5209.

Paper IV

The photophysics of alloxazines:
A quantum chemical investigation in vacuum and solution

Susanne Salzmann and Christel M. Marian

Photochem. Photobiol. Sc., *submitted.*

The photophysics of alloxazine: A quantum chemical investigation in vacuum and solution

Susanne Salzmann and Christel M. Marian
Institute of Theoretical and Computational Chemistry,
Heinrich Heine University Düsseldorf,
Universitätsstr. 1, D-40225 Düsseldorf, Germany[*]

(Dated: June 12, 2009)

Abstract

(Time-dependent) Kohn-Sham density functional theory and a combined density functional/multi-reference configuration interaction method (DFT/MRCI) were employed to explore the ground and low-lying electronically excited states of alloxazine, a flavin related molecule. Spin-orbit coupling was taken into account using an efficient, nonempirical mean-field Hamiltonian. Intersystem crossing (ISC) rate constants for $S \rightsquigarrow T$ transitions were computed, employing both direct and vibronic spin-orbit coupling. Solvent effects were mimicked by a conductor like screening model and micro-hydration with up to six explicit water molecules.

Multiple minima were found on the first excited singlet (S_1) potential energy hypersurface (PEH) with electronic structures $^1(n\pi^*)$ and $^1(\pi\pi^*)$, corresponding to the dark 1 ^1A" (S_1) state and the nearly degenerate, optically bright 2 $^1A'$ (S_2) state in the vertical absorption spectrum, respectively. In the vacuum the minimum of the $^1(n\pi^*)$ electronic structure is clearly found below that of the $^1(\pi\pi^*)$ electronic structure. Population transfer from $^1(\pi\pi^*)$ to $^1(n\pi^*)$ may proceed along an almost barrierless pathway. Hence, in the vacuum, internal conversion (IC) between the 2 $^1A'$ and the 1 ^1A" state is expected to be ultrafast and fluorescence should be quenched completely. The depletion of the $^1(n\pi^*)$ state is anticipated to occur via competing IC and direct ISC processes. In aqueous solution this changes, due to the blue shift of the $^1(n\pi^*)$ state and the red shift of the $^1(\pi\pi^*)$ state. However, the minimum of the $^1(n\pi^*)$ state still is expected to be found on the S_1 PEH. For vibrationally relaxed alloxazines pronounced fluorescence and ISC by a vibronic spin-orbit coupling mechanism is expected. At elevated temperatures or excess energy of the excitation laser, the $^1(n\pi^*)$ state is anticipated to participate in the deactivation process and to partially quench the fluorescence.

---

*Electronic address: `Christel.Marian@uni-duesseldorf.de`; URL: `http://www.theochem.uni-duesseldorf.de`

I. INTRODUCTION

The early interest in alloxazines and lumichromes (7,8-dimethyl-alloxazines) that started in the 1960s, resulted from the observed phototautomerism between the alloxazinic and isoalloxazinic forms (see Figure 1) of those compounds in pyridine or acetic acid solutions. [1–8] Although, in the ground state, the alloxazinic form is more stable than its respective isoalloxazinic isomer, the latter is of much greater biological relevance. [9–11] It has not been until the last ten years that alloxazines have found increased interest in a more physiological context. [12]

While isoalloxazines are commonly known as chromophores of blue-light photo-receptors, alloxazines exhibit the first and second absorption band in the ultra violet A (UVA) region. Experimentally the first absorption band of alloxazine (AL) and lumichrome (LC) is located around 3.2-3.3 eV and shows no significant dependence on the environment. This is different for the second absorption band. With increasing polarity and proticity of the solvent a red shift of that band is observed. [13, 14] For LC in water this shift results even in a merge of the first and second absorption bands. [15] (A detailed compilation of experimental spectroscopic data of AL and LC in various solvents can be found in Table S1 in the Electronic Supplementary Information (ESI).)

A major difference between alloxazines and the corresponding isoalloxazines is the fluorescence quantum yield Φ_F. While flavins are known for their intense fluorescence (Φ_F=0.30 for lumiflavin in water [15, 16]), alloxazines show a significantly lower fluorescence quantum yield (Φ_F <0.1 for AL and LC in various solvents, see ESI Table S1.). Earlier theoretical investigations have shown the major difference between AL and isoalloxazine (IA) to be the energetic ordering of the lowest excited $^1(\pi\pi^*)$ and $^1(n\pi^*)$ states. [13, 17–20] For flavins, the first excited singlet state (S_1) in the Franck-Condon (FC) region is found to be of $(\pi\pi^*)$ character in all solvents. [17, 21–28] In theoretical work on isolated AL and LC, the optically dark $^1(n\pi^*)$ state is found to be below or degenerate with the optically bright $^1(\pi\pi^*)$ state, presumably leading to a substantial radiationless decay of the $^1(\pi\pi^*)$ population to the electronic ground state. [13, 17–20] Weigel *et al.* [29] found indications for a participation of the $^1(n\pi^*)$ state in the dissipation of the $^1(\pi\pi^*)$ state of isoalloxazines in water at higher temperatures or high excess excitation energies, too.

So far, quantum chemical investigations of alloxazines have been restricted to the singlet states at the FC point. [13, 17] Only little is known about the position of the triplet states, possible energy dissipation pathways, or environmental effects. In this work the absorption spectra of AL and LC have been investigated in gas phase and solution with different solvation models. For AL minimum nuclear arrangements of low-lying electronically excited states and relaxation pathways of these states have been studied, taking spin-orbit coupling into account. Radiative and nonradiative rate constants have been computed *in vacuo* and the changes in aqueous solution are discussed qualitatively. On the basis of these results a relaxation scheme of electronically excited alloxazines in different environments is proposed.

II. METHODS AND COMPUTATIONAL DETAILS

All geometry optimizations were carried out at the level of (time dependent) density functional theory ((TD)DFT/B3LYP/TZVP) using the TURBOMOLE 5.10 [30] program package. C_s symmetry constraints were imposed on the ground- and excited-state nuclear arrangements of all molecules. The Cartesian coordinate system was chosen in a way that the xy plane coincides with the molecular plane. To ensure that the resulting geometries correspond to true minima of the potential energy hypersurface (PEH), harmonic vibrational frequencies were calculated numerically with the program SNF. [31] Zero-point vibrational energy corrections (ZPVE) were scaled by a factor of 0.9614 as recommended for the B3LYP functional. [32]

Vertical electronic excitation energies, dipole (transition) moments, and oscillator strengths were obtained from subsequent single-point calculations using the combined density functional theory / multi-reference configuration interaction (DFT/MRCI) method of Grimme and Waletzke. [33] For all geometries we calculated ten roots for each of the two irreducible representations A' and A" of the C_s symmetry both for the singlet and triplet manifolds.

The intensity distributions of the vibronic absorption and emission transitions were determined in the FC approximation using the VIBES program. [34] For AL, 41 symmetric A' and 19 asymmetric A" modes exist. All 41 symmetric modes were included into the calculation of the FC spectra. The FC distributions of the spectra were obtained by computing transitions between the lowest vibrational level in the initial state and vibrational levels in an energy range of ≈ 6000 cm^{-1} in the final state. Therefore, hot bands do not occur in the simulated absorption spectra. To keep the calculations practicable, a limit of 10 quanta per mode was set for the excitation of the final state modes. For the generation of the line spectra, all FC factors were gathered into bins on a grid with interval width $d = 2$ cm^{-1}. For better comparison with the experimental spectra in the condensed phase, the line spectra were broadened by Gaussian functions with full width at half maximum (FWHM) of 50 cm^{-1}, 500 cm^{-1}, or 1000 cm^{-1} with the program PLOTTER. [35] It has been discussed before, how the choice of the FWHM of the Gaussian function influences the shape of the resulting band. [27]

For the computation of the spin-orbit coupling matrix elements (SOMEs) between the correlated DFT/MRCI wavefunctions we used the spin-orbit coupling kit (SPOCK) [36, 37] developed in our laboratory. For reasons of efficiency, the one-center mean-field approximation to the Breit-Pauli Hamiltonian was used for the description of the spin-orbit coupling. This nonempirical effective one-electron operator treats the expensive two-electron terms of the full Breit-Pauli Hamiltonian in a Fock-like manner. [38, 39]

Rate constants for inter-system crossing from the S$_1$ state to the three sublevels of the T$_1$, T$_2$, and T$_3$ state, respectively, were calculated using the VIBES program. [34] According to El-Sayed's rule, SOMEs between $(\pi\pi^*)$ and $(n\pi^*)$ states are in general much larger than SOMEs between two $(\pi\pi^*)$ states.[40] Thus, the Condon approximation (also dubbed direct spin-orbit coupling in the following) will yield ISC rate constants that are typically slow for El-Sayed forbidden processes. As recent studies in our laboratory have shown, vibronic coupling enhances the ISC rate constants between two $(\pi\pi^*)$ states. [26, 27, 41, 42] Therefore, a Herzberg-Teller type expansion was carried out around the $^1(\pi\pi^*)$ state minimum, taking into account the first-order derivatives of the spin-orbit interaction with respect to *out-of-plane (oop)* normal mode coordinates (so called vibronic spin-orbit coupling). When the molecular geometry is distorted in this way, $(\pi\pi^*)$ and $(n\pi^*)$ states are able to interact and become mixed. The first-order derivatives of the SOMEs were calculated numerically by finite difference techniques as described in Ref. [41]. (For further details on the choice of computational parameters such as the width of the search integral see the ESI.)

To estimate spectral shifts due to electrostatic interaction in polar solvents we employed the conductor-like screening model (COSMO) which is implemented in the TURBOMOLE package. [43, 44] Dielectric constants of $\epsilon = 78$ and $\epsilon = 36$ were chosen,[45] corresponding to water and acetonitrile (AcN), respectively, at ambient temperatures. When COSMO was applied, the MRCI expansion was built up from the one-particle basis of COSMO optimized Kohn-Sham orbitals. Because of technical reasons, C_1 symmetry had to be used for all calculations involving COSMO and DFT/MRCI. For both singlet and triplet multiplicity 20 roots were computed.

III. RESULTS AND DISCUSSION

In this section the minimum nuclear arrangements of the ground state of AL and LC as well as the lowest-lying excited states of AL and the corresponding electronic spectra are presented. The energetic order of the states is sensitive to the nuclear geometry and typically more than one minimum is found on a particular potential energy hypersurface (PEH). This situation is known for various molecules. [26, 46–48] Here, the vertical order of the excited states does not correspond to their adiabatic order. To aid the discussion, the low-lying excited ($\pi\pi^*$) states are denoted according to their predominant electronic structure, e.g. $^1(\pi_H\pi_L^*)$, $^3(\pi_H\pi_L^*)$, $^3(\pi_{H-1}\pi_L^*)$, and the lowest-lying ($n\pi^*$) state of each multiplicity is referred to as $^1(n\pi^*)$ and $^3(n\pi^*)$, respectively.

A. Vertical excitation spectra of alloxazine and lumichrome

To our knowledge, there is no experimental gas-phase data available for AL or LC. Therefore, we have to compare to spectra measured in condensed phase. Inspection of experimental results (Table S1, ESI) shows that especially the position of the second absorption band depends on the surrounding environment. [13, 14] However, not only optically bright states are influenced by solution. Rather, solvent shifts of dark transient states have a substantial effect on the excited state energy dissipation. [26] For this reason, in addition to the gas-phase calculations, solvent effects have been taken into account employing three models: (II) a continuum model using COSMO, (III) micro-hydration with 4-6 explicit water molecules (see Fig. 4) and (IV) a combination of both.

1. Gas phase

The most important structural parameters of the ground-state equilibrium geometry of AL can be found in Figure 2. Direct comparison with those of IA (see Ref. [26], Table 1) shows that for most bonds the change in bond length is less than 2 pm. As the two chemical structures in Figure 1 already indicate, the tautomerization changes the bond characters such that the N(10)-C(10a) bond of AL is found to be 5.8 pm shorter and the C(10a)-N(1) bond 8.6 pm longer than in IA. The structural parameters for LC are very similar to those of AL. The only difference between the two compounds worth to be mentioned is an elongation of the C(7)-C(8) bond. As for flavins, this observation can mainly be attributed to the two sterically challenging methyl groups. [26]

An overview of the vertical DFT/MRCI energies is given in Table I. To aid the discussion, the shapes and ordering of relevant molecular frontier orbitals of AL are depicted in Figure 3. Those orbitals show a close similarity to the respective molecular orbitals (MOs) of the isomeric flavins. (See Ref. [26], Figure 3). The biggest difference can be observed for the n-orbitals. While in isoalloxazines the relevant frontier orbitals are mainly combinations of either lone pairs belonging to the two oxygen or the two imide nitrogen atoms, in AL all four mentioned lone pairs contribute to the two MOs, n_{N-O} and n_{N+O}. For LC the shape of the molecular orbitals is very similar to those shown here.

Apart from semi-empirical calculations, [18–20] only few quantum chemical investigations have been carried out on ALs. The TDDFT (B3LYP/6-31G*) studies of the vertical excitation energies of AL and LC in the gas phase by Sikorska et *al.* yield results very similar to ours. [13, 17]

In AL, the first excited singlet state (S_1) is found to be of $^1(n\pi^*)$ character (Table I). Merely 0.06 eV above the S_1 state, a second excited singlet state with $^1(\pi\pi^*)$ electronic structure is found. In LC the two states are nearly degenerate with their respective vertical excitation energies only 0.03 eV apart. However, their energetic ordering is changed. For both compounds, the $^1(n\pi^*)$ state is dominated by the $n_{N+O} \rightarrow \pi_L$ excitation and its dipole transition probability is found to be 25 times smaller than that of the $^1(\pi\pi^*)$ state, where the $\pi_H \rightarrow \pi_L$ excitation prevails. The third excited singlet state (S_3) is of $^1(n\pi^*)$ character. It is dominated by the optically dark linear combination of the $n_{N-O} \rightarrow \pi_L$ and $n_O \rightarrow \pi_L$ excitations. The next singlet state in the vertical absorption spectrum (S_4) is found to have significant absorption probability with an oscillator strength comparable to that of the S_2 state. Its electronic structure is dominated by the $\pi_{H-1} \rightarrow \pi_L$ configuration.

In the triplet manifold we find three states below the S_1 state. The first and third excited triplet states (T_1 and T_3) are both $^3(\pi\pi^*)$ transitions, whereas the T_2 state is of $^3(n\pi^*)$ character. The former states are dominated by a linear combination of the $\pi_H \rightarrow \pi_L$ and $\pi_{H-1} \rightarrow \pi_L$ configurations and in the latter state a linear combination of the $n_{N+O} \rightarrow \pi_L$ and the $n_{N-O} \rightarrow \pi_L$ excitations prevails. In the gas phase, the vertical excitation energy of these three state is well below the lowest-lying optically bright singlet state for AL and LC, respectively. The T_4 state, another $^3(n\pi^*)$ transition, is located well above the lowest-lying optically bright singlet state and therefore it is not of interest for relaxation processes out of the latter state.

2. Spectroscopic shifts in water

The excitation energies of AL in aqueous solution of the models II-IV are displayed and compared to those of the vacuum (I) in Figure 4. In our previous work on flavins, we used four water molecules to simulate the effects of hydrogen bonding between the chromophore and aqueous solution. For AL, due to the lack of the methyl group at the N(10) center, four water molecules do not seem to be sufficient to mimic that interaction. Therefore, we subsequently added up to two further water molecules in the vicinity of the heteroatoms of the chromophore and optimized the respective interaction geometries. (The complex nuclear arrangements are displayed in Figure 1 of the ESI.) As Figure 4 shows, the addition of explicit water molecules has a noticeable impact on the excitation energies, i.e. a substantial part of the solvatochromism originates from hydrogen bonding. Furthermore, it is seen that COSMO (model II) or microhydration (model III) alone underestimate the solvent shifts. This behavior is known and has been encountered before for flavins. [26, 27] Unless stated otherwise, only our best solvent model (model IV with 6 explicit water molecules) has been employed for comparison with experiment.

When compared with gas phase results, all low-lying excited states of AL show substantial shifts in aqueous solution. The first optically bright transition ($^1(\pi_H\pi_L^*)$ state) is red shifted by about 0.15 eV due to solvation in water. This finding is different to the situation in flavins, as the position of the first absorption band in these compounds is nearly independent of the surrounding solvent. The experimental band maxima of AL and LC in aqueous solution are found at 3.27 eV (AL, [49]) and 3.22 eV (LC, [13]), respectively, in excellent agreement with our calculated values (Table II). For the second visible transition ($^1(\pi_{H-1}\pi^*_L)$ state) the red shift is more pronounced. For AL, our model estimates the vertical excitation energy to 3.81 eV in good accordance with the experimental band maximum in aqueous solution (3.76 eV, [49]). A similar agreement is observed in LC where our vertical excitation energy of 3.66 eV compares well with an experimental band maximum of 3.51 eV. [13] For the two low-lying $^3(\pi\pi^*)$ states, solvation lessens the multi-reference character, and adjusts the electronic structure more to their singlet counterparts. Accordingly these states show similar solvent shifts as compared to the respective singlet states.

For the lowest-lying $^1(n\pi^*)$ state, a blue shift up to 0.28 eV is found. With a vertical excitation energy of 3.67 eV in AL and 3.72 eV in LC, solvation in water pushes the $^1(n\pi^*)$ structure, which used to be located on the S_1 PEH in the vacuum, energetically far above the $^1(\pi_H\pi^*_L)$ structure. A participation of the $^1(n\pi^*)$ structure in the radiationless decay of this $^1(\pi\pi^*)$ state is therefore hindered. (For a more detailed discussion see Section III C 2.) In AL the vertical excitation energy of the lowest-lying $^3(n\pi^*)$ state is found at 3.32 eV, degenerate with that of the optically bright $^1(\pi_H\pi^*_L)$ state.

3. Spectroscopic shifts in acetonitrile

For AcN solution only model II was employed at the respective ground state geometry. The vertical excitation energies for AL and LC in AcN are also given in Table II. As for aqueous solution the excitation energies of all low-lying excited states are affected by solvation in AcN. Our computed vertical excitation energies of 3.39 eV and 3.32 eV in AL and LC fit well with the experimental band maximum of the absorption spectrum at 3.33 eV [12] and 3.26 eV, [12] respectively. The same is true for the second absorption band, where our calculated values agree nicely with the experimental data. Moreover, also the shift between AcN and aqueous solution is satisfactorily reproduced, which gives additional confidence to our results. The optically dark $^1(n\pi^*)$ state is located at 3.56 eV in AL and 3.60 eV in LC. While in AL the energy gap to the optically bright $^1(\pi_H\pi^*_L)$ state is less than 0.2 eV, for LC it is found to be about 0.3 eV. As we will see later, the energetic position of that dark $^1(n\pi^*)$ state has an influence on the competing de-excitation processes.

B. Excited state geometries and adiabatic transition energies of alloxazine

As the results in the last section have shown, the electronic excitation energies of AL and LC are very similar. Therefore, we do not expect any qualitative changes for the excited state geometries and adiabatic transition energies of LC as compared to AL. Since the two additional methyl groups of LC increase the computational cost noticeably, this and the following sections have been restrained to AL.

a. *($n\pi^*$) electronic structures* We obtain a minimum nuclear arrangement for the $^1(n\pi^*)$ structure of isolated AL (Figure 2) where the C(5a)-C(9a) bond is elongated by 5.6 pm and the C(4)-C(4a) and C(5)-C(5a) bonds are shortened by 4.0 pm and 4.3 pm, respectively. The changes of most other bond lengths is between 1 pm and 2.5 pm. This finding is consistent with an excitation of one electron from the n_{N+O} orbital into the π_L* orbital. With regard to the energy, the relaxation effect on the optimized $^1(n\pi^*)$ structure is moderate and yields an adiabatic excitation energy of 3.21 eV. At the same time, the ground state is destabilized by 0.44 eV, resulting in a vertical emission energy of 2.77 eV. Due to the small dipole transition probability and the rather small energy difference, the rate of fluorescence to the ground state, calculated at the $^1(n\pi^*)$ minimum, is very low ($k_F = 4.6 \cdot 10^4$ s^{-1}). Hence, for the $^1(n\pi^*)$ state, non-radiative energy dissipation to the ground state is considered to be by far more efficient. At the $^1(n\pi^*)$ geometry the energetic ordering of the two electronic structures $^3(\pi_H\pi^*_L)$ and $^3(n\pi^*)$ is inverted with respect to the FC region (Figure 5). Furthermore, it can be noted that the third excited triplet state is blue shifted such that it comes to lie above the S$_1$ PEH. Therefore, we anticipate an intersection between the S$_1$ and T$_3$ PEHs occurring on the relaxation path between the FC region and the $^1(n\pi^*)$ minimum. (See section III C 1).

For the $^3(n\pi^*)$ state, the nuclear arrangement is quite similar to that of the $^1(n\pi^*)$ state. However, at the level of TDDFT (B3LYP), this structure is found to constitute a second-order saddle point on the T$_1$ PEH. Two imaginary frequencies ($\bar{\nu}_1 = i585.90cm^{-1}$ and $\bar{\nu}_2 = i111.91cm^{-1}$) are obtained which correspond to A” symmetric normal modes and hence can be described as *oop* deformations of the AL ring system. However, subsequent calculations of the DFT/MRCI energies of the T$_1$ PEH following the distortion along each imaginary modes, clearly favor the C$_s$ symmetric structure. This phenomenon has been encountered before in various organic heterocycles, including flavins, [26] and is considered an artifact of the TDDFT (B3LYP) method. The adiabatic excitation energy of the optimized $^3(n\pi^*)$ structure amounts to 2.82 eV in the gas phase. It is remarkable that the DFT/MRCI energy of the S_1 state is slightly lower at the $^3(n\pi^*)$ geometry than at the optimized $^1(n\pi^*)$ geometry. This shows that the S_1 PEH is very flat in this area of coordinate space. In the gas phase this structure represents the global minimum on the S_1 PEH.

b. $(\pi_H\pi_L^*)$ *electronic structures* For the $^1(\pi_H\pi_L^*)$ structure we obtain a minimum nuclear arrangement in which the C(4a)-N(5) and C(6)-C(7) bonds are elongated by 3.9 pm and 5.3 pm, respectively, and the C(4)-C(4a) bond is shortened by 4.1 pm (Figure 2). This finding reflects the change of character in the corresponding frontier orbitals from bonding to antibonding for the C(6)-C(7) bond, weakly antibonding to strongly antibonding for the C(4a)-N(5) bond, and from nonbonding to bonding for the C(4)-C(4a) bond. Since this geometry distortion of the nuclear frame is unfavorable for the $^1(n\pi^*)$ electronic structure, a reversal of the energetic ordering of the $^1(n\pi^*)$ and $^1(\pi\pi^*)$ structures with respect to the FC region is observed. At the level of TDDFT (B3LYP), this structure only represents a saddle point. One imaginary frequency ($\bar{\nu}_1 = i279.27cm^{-1}$) is obtained for an *oop* deformation. Again, the saddle point disappears at the DFT/MRCI level following the distortion along the imaginary A" mode. The adiabatic excitation energy of the $^1(\pi_H\pi_L^*)$ structure amounts to 3.27 eV. In the gas phase and apolar solvents, the minimum of the $^1(n\pi^*)$ structure is thus located energetically below this $^1(\pi\pi^*)$ minimum. We therefore anticipate strong vibronic coupling between the $^1(n\pi^*)$ and $^1(\pi\pi^*)$ potential wells and a concomitant fast IC under these conditions. Fluorescence to the electronic ground state, obtained at this second S_1 minimum, is calculated to occur at 2.96 eV with a natural rate of $k_F = 3.3 \cdot 10^7\text{s}^{-1}$ ($\tau_F = 30$ ns). Experimentally, the maximum of the fluorescence emission for AL ranges between 2.85 eV in 1,4-dioxane and 2.79 eV in AcN and the radiative decay rate of this state was found to range between $k_F = 1.8 - 12 \cdot 10^7\text{s}^{-1}$, [12, 13, 16, 17, 50] which is in good agreement with our calculated values. It is noteworthy that the $^3(n\pi^*)$ and $^3(\pi_{H-1}\pi_L^*)$ electronic structures are near-degenerate with the $^1(\pi_H\pi_L^*)$ at the respective $^1(\pi\pi^*)$ minimum. From qualitative arguments the singlet-triplet crossing is expected to have a high probability in isolated AL at this point in coordinate space.

For the $^3(\pi_H\pi_L^*)$ structure, we obtain a nuclear arrangement that noticeably differs from that of the $^1(\pi_H\pi_L^*)$ structure. This is consistent with the slightly altered electronic structure of the $^3(\pi_H\pi_L^*)$ state. While in the singlet case the $\pi_H \rightarrow \pi_L$ excitation prevails, the $^3(\pi_H\pi_L^*)$

electronic structure is dominated by the linear combination of the $\pi_H \rightarrow \pi_L$ and $\pi_{H-1} \rightarrow \pi_L$ configurations. The adiabatic excitation energy of the $^3(\pi_H\pi_L^*)$ minimum amounts to 2.43 eV, thus representing the global minimum on the T_1 PEH.

c. $^3(\pi_{H-1}\pi_L^*)$ *electronic structure* For the $^3(\pi_{H-1}\pi_L^*)$ structure optimization yields a nuclear arrangement that, at the level of TDDFT (B3LYP), is found to be a saddle point on the T_2 PEH. One imaginary frequency ($\bar{\nu}_1 = i290.46cm^{-1}$) is obtained, which corresponds to a A" symmetric normal mode. At the level of DFT/MRCI this $^3(\pi\pi^*)$ electronic structure represents a minimum on the T_1 PEH instead. Its adiabatic excitation energy amounts to 2.88 eV. At this nuclear geometry the $^3(\pi_H\pi_L^*)$ electronic structure is located 0.06 eV above $^3(\pi_{H-1}\pi_L^*)$. Due to the small energy gap between the $^3(\pi\pi^*)$ states and their inverted energetic order, a crossing between these two states that transfers population of the $^3(\pi_{H_1}\pi_L^*)$ to the $^3(\pi_H\pi_L^*)$ should be nearby.

1. *Simulated Franck-Condon absorption spectra of alloxazine*

When comparing quantum chemical calculations with experiment it is common practice to identify the experimental band maxima with vertical excitation energies. Nevertheless it has been shown that this presumption does not always hold. [51–53] If the change in the geometry from the ground state to the excited state is small, the vibrational wave functions do not have their maxima at the classical turning points. [53] Hence, the experimental band maxima do not coincide with the vertical excitation energies. Recently, we could show that this is the case for lumiflavin and three of its derivatives. [27] In these compounds the band maxima are calculated approximately 0.2 eV below the corresponding vertical excitation energies. To shed light on this phenomenon and to validate the theoretically determined excited state geometries, vibrational intensity distributions of the $(gs) \rightarrow^1 (\pi_H\pi_L^*)$ and $(gs) \leftarrow^1 (\pi_H\pi_L^*)$ transitions in AL were computed *in vacuo*.

Inspection of Figure 6 shows that, dependent of the chosen FWHM, the $(gs) \rightarrow^1 (\pi_H\pi_L^*)$ absorption exhibits some structure. With a FWHM of 500 cm^{-1} the shape of our simulated $(gs) \rightarrow^1 (\pi_H\pi_L^*)$ absorption band is very similar to the experimental band shape in ethanol at 77K.[20] The band maximum is located at 3.31 eV, 0.16 eV below the vertical excitation energy. Comparison of that value with the experimental band maxima in apolar solvents like 1,4-dioxane shows perfect agreement. [12] For the $(gs) \leftarrow^1 (\pi_H\pi_L^*)$ emission band (Figure 7) the difference between the vertical emission energy (2.97 eV) and the band maximum (2.91 eV) is not as pronounced.

With our current methods it was not possible to determine the solvent shift of the onset of the absorption band in water. As a workaround, the effect of the solvent shift on the vertical excitation energy (see Table II) was used to estimate the band maximum in aqueous solution. A comparison with experimental data of AL in water and AcN shows good agreement with our estimated $(gs) \rightarrow^1 (\pi_H\pi_L^*)$ band maxima.

C. Nonradiative relaxation processes of alloxazine

Experimental data (Table S1, ESI) shows that in AL and LC only a minor part of the excited state population decays via fluorescence. This behavior, which is essentially different to that of flavins, is widely attributed to the energetic position of the lowest-lying $^1(n\pi^*)$ state. [13, 17–20] While in the gas phase, this state is almost degenerate with the optically bright $^1(\pi_H\pi_L^*)$ state solvent effects expand the gap between those two states. (See Table II.) Therefore, it can be anticipated that different relaxation channels are responsible for the energy dissipation in vacuum and aqueous solution. To shed some light on possible relaxation mechanisms we constructed linearly interplolated paths from the FC region to the $^1(n\pi^*)$ and $^1(\pi_H\pi_L^*)$ minima, respectively (see Figure 8), and additionally one connecting the $^1(n\pi^*)$ and $^1(\pi_H\pi_L^*)$ minima (see Figure 9).

1. *Relaxation in the gas phase*

a. Internal conversion As pointed out in section III B, the $^1(n\pi^*)$ and the $^1(\pi_H\pi_L^*)$ excited states are almost degenerate in the energetic range of the first absorption band. Of the two states, only the $^1(\pi_H\pi_L^*)$ structure is connected to the electronic ground state by a considerable dipole transition probability. Nevertheless, the proximity of the two excited states impacts on the photophysical behavior in gas phase. From Figure 8 (top) it is obvious that a crossing between the $^1(n\pi^*)$ and the $^1(\pi_H\pi_L^*)$ states happens close to the FC region. A further crossing is found along a linearly interpolated path between the two excited state minima (see Figure 9). This point on the conical intersection seam is located less than 0.07 eV above the $^1(\pi_H\pi_L^*)$ minimum. (Due to the linear interpolation this value is an upper limit for the barrier height.) With such a small barrier, zero-point motion alone should be sufficient to couple the $^1(n\pi^*)$ and $^1(\pi_H\pi_L^*)$ states. Although we cannot present rate constants for internal conversion, this process is expected to be ultrafast.

b. Intersystem crossing Since it can be anticipated that the $^1(n\pi^*)$ state borrows population from the electronically bright $^1(\pi_H\pi_L^*)$ state (see above), both electronic states may serve as initial states for ISC. Inspection of Figure 8 (top) shows that, from an energetic point of view, the $^3(\pi_H\pi_L^*)$, $^3(n\pi^*)$, and $^3(\pi_{H-1}\pi_L^*)$ are possible candidates for efficient ISC from $^1(n\pi^*)$ as well as $^1(\pi_H\pi_L^*)$.

The results of our evaluation of the rate constants $k_{ISC}(\mathrm{S} \rightsquigarrow \mathrm{T})$ for singlet-triplet ISC in AL in the vacuum are summarized in Table IV. A more detailed overview about the calculations with further information about the parameters used, can be seen in the ESI (Table 3 and 4). At the $^1(\pi_H\pi_L^*)$ minimum nuclear arrangement, the S_1 PEH is energetically very close to the almost degenerate T_2 and T_3 PEHs. The crossing of all three PEHs is nearby, as can be seen in Figure 8 (top). In case of direct spin-orbit coupling, only the ISC processes from the zeroth vibrational level of the $^1(\pi_H\pi_L^*)$ state to the vibrational states in the $^3(n\pi^*)$ potential well are fast ($\sim 10^9$ s^{-1}). The direct ISC rate for the $^1(\pi_H\pi_L^*) \rightsquigarrow^3 (\pi_{H-1}\pi_L^*)$ channel cannot compete as long as planar nuclear arrangements are considered. Herzberg-Teller interaction yields strong mixing of the nearly degenerate $^3(n\pi^*)$ and the $^3(\pi_{H-1}\pi_L^*)$ structures, leading to a tremendous increase of the SOMEs along the *oop* distortions. As a result, the rates of the transition $(\pi_H\pi_L^*) \rightsquigarrow^3 (\pi_{H-1}\pi_L^*)_{x,y}$ are increased to $\sim 10^{11}$ s^{-1}. With such fast transitions, perturbation theory, as used in the present work, is at its limits and a dynamic treatment would be more favorable.

At the $^1(n\pi^*)$ geometry, the order of the electronic states has changed noticeably with respect to the FC region. This results in a crossing between the S_1 and T_3 PEHs along the FC-$^1(n\pi^*)$ relaxation pathway. Furthermore, at the $^1(n\pi^*)$ minimum the S_1 and the T_2 PEHs are rather close (difference in energy less than 0.2 eV) and it is obvious from Figure 8 (top, left) that a crossing between the states with $^1(n\pi^*)$ and $^3(\pi_H\pi_L^*)$ character is nearby. Since, in both cases, the interaction occurs between an $(n\pi^*)$ state and a $(\pi\pi^*)$ state, substantial spin-orbit coupling matrix elements are found. The ISC rates for the $^1(n\pi^*) \rightsquigarrow^3 (\pi_H\pi_L^*)$ and $^1(n\pi^*) \rightsquigarrow^3 (\pi_{H-1}\pi_L^*)$ channels are of the order of $\sim 10^9$ s^{-1}$- \sim 10^{10}$ s^{-1}. Vibronic spin-orbit coupling enhances the ISC rate between the two $(n\pi^*)$ states, too, but the obtained rates cannot compete with those of the El Sayed-allowed processes.

2. *Relaxation processes in water*

For aqueous solution, adiabatic excitation energies have been obtained by applying the spectroscopic shifts obtained with our best solvent model for the vertical excitation energies. In the same way we acquired the energetic position of the low-lying excited state PEHs along the linearly interpolated paths presented in Figure 8 (bottom) and Figure 9 (bottom).

a. Internal conversion Our results in Table III as well as Figure 8 (bottom) and Figure 9 (bottom) indicate that, despite their solvents shifts, the $^1(n\pi^*)$ and $^1(\pi_H\pi_L^*)$ potential wells both constitute minima on the S_1 PEH. In the same manner as for isolated AL, we can estimate that the height of the barrier between the $^1(\pi_H\pi_L^*)$ and the $^1(n\pi^*)$ minimum does not exceed 0.3 eV with respect to the $^1(\pi_H\pi_L^*)$ minimum and that its top is located roughly 0.1 eV above the FC point. Due to interaction with the surrounding solvent molecules a transition between the two minima should be possible. This finding is in line with recent work on the photophysics of lumiflavin in water. Weigel *et al.* presented evidence for the participation of a $^1(n\pi^*)$-like state in the deexcitation processes on an ultrafast timescale by means of femtosecond pump-supercontinuum probe spectroscopy. [29]

b. Intersystem crossing In order to estimate the ISC rate constants in water, the solvent shift of the electronic states have to be taken into account for the calculations of the SOME (derivatives) and the adiabatic electronic excitation energy differences. Although the COSMO model is applicable strictly only for the absorption energies and does not comprise the whole interaction with water, this is the only practicable way to introduce the solvent induced shifts into the calculations of the SOME derivatives. The results of our evaluation of the rate constants $k_{ISC}(\mathrm{S} \rightsquigarrow \mathrm{T})$ for singlet-triplet ISC in AL in aqueous solution are summarized in Table V. (For more details see ESI Table S5 and S6.)

The inclusion of solvent effects via COSMO has a negligible influence on the SOMEs between the S_1 and T_1 PEHs. ISC rate constants for the $^1(n\pi^*) \rightsquigarrow ^3 (\pi_H\pi_L^*)_x$ and $^1(n\pi^*) \rightsquigarrow ^3 (\pi_H\pi_L^*)_y$ channels are calculated to $\sim 10^{10}$ s^{-1} and $\sim 10^8$ s^{-1}, respectively. Comparison to our results in the vacuum encourages the conclusion that the increase of the energy gap due to solvent effects has no major impact on the ISC rate constants.

Considering direct spin-orbit coupling at the $^1(\pi_H\pi_L^*)$ minimum, substantial SOMEs are only obtained between the S_1 and the T_3 PEHs. Since the adiabatic electronic excitation energy difference between the corresponding minima is very small, the density of vibrational states in the final state at the energy of the initial state is zero — far from the ideal situation of a quasi-continuum for which the Fermi Golden Rule was derived. One may assume, however, that thermal population of the excited vibrational levels yields ISC rate constants of a similar order of magnitude as in vacuum. For the $^1(\pi_H\pi_L^*) \rightsquigarrow^3 (\pi_{H-1}\pi_L^*)$ channels vibronic spin-orbit coupling enhances the ISC rate to $\sim 10^7$ s^{-1} and $\sim 10^8$ s^{-1}.

IV. SUMMARY AND CONCLUSIONS

We have presented vertical excitation energies of AL and LC in gas phase and solution. Solvent effects have been taken into account by three different models for AcN (COSMO) and water (COSMO, micro-hydration, and a combination of both). In the vacuum we find, in agreement with earlier quantum chemical calculations, that the lowest-lying $^1(n\pi^*)$ and $^1(\pi\pi^*)$ states are nearly degenerate. Effects of aqueous solution cause a seperation of the two states by 0.3-0.5 eV, depending on the molecule. In addition, our calculations show that all low-lying excited states are sensitive to the surrounding environment. With regard to experimental absorption data in AcN and water, our calculated vertical absorption properties show a convincing agreement with respect to solvent shifts and excitation energies.

For the quantitative evaluation of ISC rate constants, adiabatic excitation energies and vibrational frequencies of several low-lying singlet and triplet excited states of AL have been determined. Our major results are sketched in Figure 10. The present study shows that there are at least two different minima on the first excited singlet PEH corresponding to the $^1(n\pi^*)$ electronic structure and the $^1(\pi_H\pi_L^*)$ structure. In the vacuum the $^1(n\pi^*)$ minimum is located 0.1 eV below the $^1(\pi_H\pi_L^*)$ minimum. Population of the dark $^1(n\pi^*)$ state from the optically bright $^1(\pi_H\pi_L^*)$ state is found to occur along an almost barrierless pathway and we anticipate the IC rate to be ultrafast. Unfortunately, experimental information on the spectroscopical behavior of AL in the gas phase is not available. Our theoretical results indicate that after light absorption the $^1(\pi_H\pi_L^*)$-$^1(n\pi^*)$ IC process quenches fluorescence completely and transfers the $^1(\pi_H\pi_L^*)$ state population to the $^1(n\pi^*)$ state, from where ISC and internal conversion to a vibrationally hot ground state compete.

In aqueous solution the energetic order of the $^1(n\pi^*)$ and $^1(\pi_H\pi_L^*)$ states reverses. Our calculations estimate the energy gap to 0.3 eV in AL. Nevertheless, we predict the $^1(n\pi^*)$ electronic structure to remain a minimum on the S$_1$ PEH. In aqueous solution the quantum yield of fluorescence is predicted to depend on the temperature and the excitation wavelengths. At low excitation energies, our calculations predict fluorescence rates and ISC rates of comparable magnitude, and fluorescence should be observable. At elevated temperatures, or high excess energy of the pump laser additional ISC channels and IC to the $^1(n\pi^*)$ state are expected to weaken the spin-allowed radiative transition to the electronic ground state, as observed in experiment. [12, 13, 16, 17, 50]

V. ACKNOWLEDGMENTS

Financial support by the Deutsche Forschungsgemeinschaft through SFB663/C1 is gratefully acknowledged.

---

[1] J. Koziol, Absorption spectra of riboflavin, lumiflavin, and lumichrome in organic solvents, *J. Experimentia*, 1965, **21**, 189–190.

[2] J. Koziol, Studies on Flavins in organic solvents-I*. Spectral characteristics of riboflavin, riboflavin tetrabutyrate and lumichrome, *Photochem. Photobiol.*, 1966, **5**, 41–54.

[3] J. Koziol, Fluorometric analyses of riboflavin and its coenzymes, *Methods Enzymol.*, 1971, **18**, 253–285.

[4] P.-S. Song, M. Sun, A. Koziolowa and J. Koziol, Spectroscopic characterization of poly(alanylglycylglycine), *J. Am. Chem. Soc.*, 1974, **96**, 4319–4323.

[5] R. D. Fugate and P.-S. Song, Lifetime study of phototautomerism of alloxazine and lumichromes, *Photochem. Photobiol.*, 1976, **24**, 479–481.

[6] J. D. Choi, R. D. Fugate and P.-S. Song, Nanosecond time-resolved fluorescence of phototautomeric lumichrome, *J. Am. Chem. Soc.*, 1980, **102**, 5293–5297.

[7] E. Sikorska, I. Khmelinskii, M. Hoffmann, I. F. Machado, L. F. V. Ferreira, K. Dobek, J. Karolczak, A. Krawczyk, M. Insińska-Rak and M. Sikorska, Ground- and excited-state double proton transfer in lumichrome/acetic acid system: Theoretical and experimental approach, *J. Phys. Chem. A*, 2005, **109**, 11707–11714.

[8] E. Sikorska, H. Szymusiak, A. Koziolowa, J. Spanget-Larsen and M. Sikorski, Spectroscopy and photophysics of alloxazines studied in their ground and first excited singlet states, *J. Photochem. Photobiol. A.*, 2003, **158**, 45–53.

[9] P. F. Heelis, The photophysical and photochemical properties of flavins (isoalloxazines), *Chem. Soc. Rev.*, 1982, **11**, 15–39.

[10] V. Massey, The chemical and biological versatility of riboflavin, *Biochem. Soc. Trans.*, 2000, **28**, 283–296.

[11] A. Losi, Flavin-based blue-light photosensors: A photobiophysics update, *Photochem. Photobiol.*, 2007, **83**, 1283–1300.

[12] M. Sikorski, D. Prukala, M. Insińska-Rak, I. Khmelinskii, D. R. Worrall, S. L. Williams, J. Hernando, J. L. Bourdelande, J. Koputa and E. Sikorska, Spectroscopy and photophysics of dimethyl-substituted alloxazines, *J. Photochem. Photobiol. A*, 2008, **200**, 148–160.

[13] E. Sikorska, I. V. Khmelinskii, W. Prukala, S. L. Williams, M. Patel, D. R. Worrall, J. L.

Bourdelande, J. Koput and M. Sikorski, Spectroscopy and photophysics of lumiflavins and lumichromes, *J. Phys. Chem. A*, 2004, **108**, 1501–1508.

[14] E. Sikorska, I. V. Khemlinskii, D. R. Worrall, S. L. Williams, R. Gonzalez-Moreno, J. L. Bourdelande, J. Koput and M. Sikorski, Photophysics of 1-methyllumichrome, *J. Photochem. Photobiol. A*, 2004, **162**, 193–201.

[15] M. Sikorski, E. Sikorski, A. Koziolowa, R. G. Moreneo, J. L. Bourdelande, R. P. Steer and F. Wilkinson, Photophysical properties of lumichromes in water, *J. Photochem. Photobiol. B*, 2001, **60**, 114–119.

[16] M. S. Grodowski, B. Veyret and K. Weiss, Photochemistry of flavins. II. Photophysical properties of alloxazines and isoalloxazines, *Photochem. Photobiol.*, 1977, **26**, 341–352.

[17] E. Sikorska, I. V. Khmelinskii, D. R. Worrall, J. Koput and M. Sikorski, Spectroscopy and photophysics of iso- and alloxazines: Experimental and theoretical study, *J. Fluores.*, 2004, **14**, 57–64.

[18] J. Komasa, J. Rychlewski and J. Koziol, Electronic structure of alloxazine and its methyl derivatives, *J. Mol. Struct. (Theochem)*, 1988, **170**, 205–212.

[19] H. Szymusiak, J. Komarski and J. Koziol, An INDO/S MO study of alloxazine and its monomethyl derivatives, *J. Chem. Soc. Perkin Trans.*, 1990, **2**, 229–236.

[20] M. Sung, T. A. Moore and P.-S. Song, Molecular luminescence studies of flavines. I. Excited states of flavins, *J. Am. Chem. Soc.*, 1972, **94**, 1730–1740.

[21] T. Climent, R. González, M. Merchán and L. Serrano-Andrés, Theoretical insight into the spectroscopy and photochemistry of isoalloxazine, the flavin core ring, *J. Phys. Chem. A*, 2006, **110**, 13584–13590.

[22] J. Hasegawa, S. Bureekaew and H. Nakatsuji, SAC-CI theoretical study on the excited states of lumiflavin: Structure, excitation spectrum, and solvation effect, *J. Photochem. Photobiol. A*, 2007, **189**, 205–210.

[23] E. Sikorska, I. V. Khmelinskii, J. Koput, J. L. Bourdelande and M. Sikorski, Electronic structure of isoalloxazines in their ground and excited states, *J. Mol. Struct.*, 2004, **697**, 137–141.

[24] C. Neiss, P. Saalfrank, M. Parac and S. Grimme, Quantum chemical calculation of excited states of flavin-related molecules, *J. Phys. Chem. A*, 2003, **107**, 140–147.

[25] K. Zenichowski, M. Gothe and P. Saalfrank, Exciting flavins: Absorption spectra and spin-orbit coupling in light-oxygen-voltage (LOV) domains, *J. Photochem. Photobiol. A*, 2007, **190**,

290–300.

[26] S. Salzmann, J. Tatchen and C. M. Marian, The photophysics of flavins: What makes the difference between gas phase and aqueous solution?, *J. Photochem. Photobiol. A*, 2008, **198**, 221–231.

[27] S. Salzmann, V. Martinez-Junza, B. Zorn, S. E. Braslavsky, M. Mansurova, C. M. Marian and W. Gärtner, Photophysical properties of structurally and electronically modified flavin derivatives determined by spectroscopy and theoretical calculations, *J. Phys. Chem. A*.

[28] J. Götze and P. Saalfrank, Serine in BLUF domains displays spectral importance in computational models, *J. Photochem. Photobiol. B*, 2009, **94**, 87–95.

[29] A. Weigel, A. L. Dobryakov, M. Veiga and J. L. P. Lustres, Photoinduced Processes in Riboflavin: Superposition of $\pi\pi^*$-$n\pi^*$ states by vibronic coupling, transfer of vibrational coherence, and population dynamics under solvent control, *J. Phys. Chem. A*, 2008, **112**, 12054–12065.

[30] R. Ahlrichs, M. Bär, H.-P. Baron, R. Bauernschmitt, S. Böcker, N. Crawford, P. Deglmann, M. Ehrig, K. Eichkorn, S. Elliott, F. Furche, F. Haase, M. Häser, C. Hättig, H. Horn, C. Huber, U. Huniar, M. Kattannek, A. Köhn, C. Kölmel, M. Kollwitz, K. May, P. Nava, C. Ochsenfeld, H. Öhm, H. Patzelt, D. Rappoport, O. Rubner, A. Schäfer, U. Schneider, M. Sierka, O. Treutler, B. Unterreiner, M. von Arnim, F. Weigend, P. Weis and H. Weiss, *TURBOMOLE (Vers. 5.10)*, Universität Karlsruhe, 2008.

[31] C. Kind, M. Reiher and J. Neugebauer, SNF *Version 2.2.1: A Program Package for Numerical Frequency Analyses*, Universität Erlangen, 1999-2002.

[32] A. P. Scott and L. Radom, Harmonic Vibrational Frequencies: An evaluation of Hartree-Fock, Møller-Plesset, Quadratic Configuration Interaction, Density Functional Theory, and Semiempirical Scale Factors, *J. Phys. Chem.*, 1996, **100**, 16502–16513.

[33] S. Grimme and M. Waletzke, A combination of Kohn-Sham density functional theory and multi-reference configuration interaction methods, *J. Chem. Phys.*, 1999, **111**, 5645–5655.

[34] J. Tatchen, VIBES, Universität Düsseldorf, 2005.

[35] M. Dierksen, PLOTTER *Verison 0.3*, Westfälische Wilhelms-Universität Münster, 2002.

[36] M. Kleinschmidt, J. Tatchen and C. M. Marian, Spin-orbit coupling of DFT/MRCI wavefunctions: Method, test calculations, and application to thiophene, *J. Comput. Chem.*, 2002, **23**, 824–833.

[37] M. Kleinschmidt and C. M. Marian, Efficient generation of matrix elements for one-electron spin-orbit operators, *Chem. Phys.*, 2005, **311**, 71–79.

[38] B. A. Hess, C. M. Marian, U. Wahlgren and O. Gropen, A mean-field spin-orbit method applicable to correlated wavefunctions, *Chem. Phys. Lett.*, 1996, **251**, 365–371.

[39] B. Schimmelpfennig, *AMFI*, 1996, Stockholms University.

[40] M. A. El-Sayed, The radiationless processes involving change of multiplicity in the diazenes, *J. Chem. Phys.*, 1962, **36**, 573–574.

[41] J. Tatchen, N. Gilka and C. M. Marian, Intersystem crossing driven by vibronic spin-orbit coupling: A case study on psoralen, *Phys. Chem. Chem. Phys.*, 2007, **9**, 5209–5221.

[42] S. Perun, J. Tatchen and C. M. Marian, Singlet and triplet excited states and intersystem crossing in free-base porphyrin: TDDFT and DFT/MRCI study, *ChemPhysChem*, 2008, **9**, 282–292.

[43] A. Klamt and G. Schüürmann, COSMO: A new approach to dielectric screening in solvents with explicit expressions for the screening energy and its gradient, *J. Chem. Soc., Perkin Trans.*, 1993, **2**, 799–805.

[44] A. Schäfer, A. Klamt, D. Sattel, J. Lohrenz and F. Eckert, COSMO Implementation in TURBOMOLE: Extension of an efficient quantum chemical code towards liquid systems, *Phys. Chem. Chem. Phys.*, 2000, **2**, 2187–2193.

[45] C. Reichardt, *Solvent effects in organic chemistry*, VCH Weinheim, 1990.

[46] K. Tomić, J. Tatchen and C. M. Marian, Quantum chemical investigation of the electronic spectra of the keto, enol, and keto-imine tautomers of cytosine, *J. Phys. Chem.*, 2005, **A 109 (37)**, 8410–8418.

[47] S.Salzmann, M. Kleinschmidt, J. Tatchen, R. Weinkauf and C. M. Marian, Excited states of thiophene: Ring opening as deactivation mechanism, *Phys. Chem. Chem. Phys.*, 2008, **10**, 380.

[48] N. Gavrilov, S. Salzmann and C. M. Marian, Deactivation via ring opening: A quantum chemical study of the excited states of furan and comparison to thiophene, *Chem. Phys*, 2008, **349**, 269–277.

[49] R. H. Dekker, B. N. Srinivasan, J. R. Huber and K. Weiss, Photochemistry of flavins-I. Conventional and laser flash photolysis study of alloxazine, *Photochem. Photobiol.*, 1973, **18**, 457–466.

[50] M. Sikorski, E. Sikorska, D. R. Worrall and F. Wilkinson, Efficiency of singlet oxygen generation by alloxazines and isoalloxazines, *J. Chem. Soc. Faraday Trans.*, 1998, **94**, 2347–2353.

[51] Y. J. Bomble, K. W. Sattelmeyer, J. F. Stanton and J. Gauss, On the vertical excitation energy of cyclopentadiene, *J. Chem. Phys.*, 2004, **121**, 5236–5240.

[52] E. R. Davidson and A. A. Jarzecki, Zero point corrections to vertical excitation energies, *Chem. Phys. Lett.*, 1998, **285**, 155–159.

[53] L. S. Cederbaum and W. Domcke, A many-body approach to the vibrational structure in molecular electronic spectra. I. Theory, *J. Chem. Phys.*, 1976, **64**, 603–611.

TABLE I: Vertical singlet and triplet excitation energies ΔE [eV] in comparison with recent quantum chemical calculations. In addition oscillator strengths $f(r)$ and dipole moments μ [Debye] are given.

	Alloxazine (AL)					**Lumichrome (LC)**			
State	**(c^2) electronic structure**	$\Delta\mathbf{E}_{DFT/MRCI}$	$\Delta\mathbf{E}_{other}$	μ	$f(L)$	$\Delta\mathbf{E}_{DFT/MRCI}$	$\Delta\mathbf{E}_{other}$	μ	$f(L)$
S_0 1^1A'	(0.95)*ground state*	0.00		4.87	0	0.00		6.21	0
S_1 1^1A"	(0.72) $n_{N+O} \rightarrow \pi_L$	3.41	3.3^a	4.54	0.0054	3.44	3.42^b	5.87	0.00536
S_2 2^1A'	(0.78) $\pi_H \rightarrow \pi_L$	3.47	3.5^a	6.69	0.1353	3.41	3.45^b	8.35	0.14532
S_3 2^1A"	(0.47) $n_{N-O} \rightarrow \pi_L$ + (13.3) $n_O \rightarrow \pi_L$	3.86		1.70	0.0000	3.89	3.96^b	2.17	0.00001
S_4 3^1A'	(0.76) $\pi_{H-1} \rightarrow \pi_L$	4.02	4.0^a	9.92	0.1488	3.91	3.93^b	11.86	0.18709
S_5 3^1A"	(0.58) $n_N \rightarrow \pi_L$	4.76		5.59	0.0001	4.78		6.68	0.00009
T_1 1^3A'	(0.68) $\pi_H \rightarrow \pi_L$ + (14.8) $\pi_{H-1} \rightarrow \pi_L$	2.77	-	7.71	-	2.76	-	9.13	-
T_2 1^3A"	(0.66) $n_{N+O} \rightarrow \pi_L$ + (14.3) $n_{N-O} \rightarrow \pi_L$	3.04	-	4.76	-	3.07	-	6.06	-
T_3 2^3A'	(0.70) $\pi_{H-1} \rightarrow \pi_L$ − (18.2) $\pi_H \rightarrow \pi_L$	3.11	-	5.65	-	3.02	-	7.87	-

a: TDDFT(B3LYP/6-31G*), see Ref. [17].

b: TDDFT(B3LYP/6-31G*), see Ref. [13].

TABLE II: Vertical (**v**) singlet DFT/MRCI excitation energies ΔE [eV] of AL and LC in gas phase, AcN and water in comparison to experimental data. In addition, estimates of the absorption maxima (**m**) are given for the first absorption band.

			$\Delta E_{DFT/MRCI}$						Experiment			
		electronic	**AL**			**LC**			**AL**		**LC**	
Transition		structure	vac.	AcN	H_2O	vac.	AcN	H_2O	AcN	H_2O	AcN	H_2O
$S_0 \rightarrow S_1$	**v**	$^1(n\pi^*)$	3.41	3.56	3.67	3.44	3.60	3.72	-	-	-	-
$S_0 \rightarrow S_2$	**v**	$^1(\pi_H\pi_L^*)$	3.47	3.39	3.32	3.41	3.32	3.23	3.33^a	3.27^b	3.26^a	3.22^c
$S_0 \rightarrow S_2$	**m**	$^1(\pi_H\pi_L^*)$	3.31	3.23	3.16	-	-	-	3.33^a	3.27^b	3.26^a	3.22^c
$S_0 \rightarrow S_4$	**v**	$^1(\pi_{H-1}\pi_L^*)$	4.02	3.90	3.81	3.91	3.76	3.66	3.87^a	3.76^b	3.71^a	3.51^c
	v	$^3(\pi_H\pi_L^*)$	2.77	2.69	2.64	2.76	2.66	2.59	-	-	-	-
	v	$^3(n\pi^*)$	3.04	3.20	3.32	3.02	3.23	3.37	-	-	-	-
	v	$^3(\pi_{H-1}\pi_L^*)$	3.11	3.03	2.96	3.07	2.91	2.83	-	-	-	-

a : Absorption maxima, Ref. [17, 50].

b : Absorption maxima read from Ref. [49], Figure 1.

c : Absorption maxima, Ref. [13].

TABLE III: AL: Adiabatic singlet and triplet DFT/MRCI excitation energies ΔE^{ad} [eV], and scaled zero-point vibrational energy corrections (ZPVE) [eV] of low-lying excited states in the gas phase. Additionally, estimates for the adiabatic excitation energies in aqueous solution $\Delta E^{ad}(\mathrm{H_2O})$ [eV] are given.

Geometry	ΔE^{ad}	PEH	ZPVE	$\Delta E^{ad}(\mathrm{H_2O})$
$^1(n\pi^*)$	3.21,3.16^a	S_1	-0.16	3.47,3.42^a
$^1(\pi_H\pi_L^*)$	3.27	S_1	-0.16	3.12
$^3(\pi_H\pi_L^*)$	2.43	T_1	-0.17	2.30
$^3(n\pi^*)$	2.82	T_1	-0.18	3.11
$^3(\pi_{H-1}\pi_L^*)$	2.88	T_1	-0.05	2.78

a :Adiabatic excitation energy at the $^3(n\pi^*)$ geometry. (See text for explanation.)

TABLE IV: IA: Calculated rate constants k_{ISC} [s^{-1}] for ($S \rightsquigarrow T$) ISC channels in the vacuum. Remaining columns: adiabatic electronic energy difference ΔE^{ad} [eV], direct SOME $| < i|\hat{H}_{SO}|f > |_{q0}$ [cm^{-1}]. Since the ordering of the electronic states is sensitive to the nuclear structure, the electronic structure of the triplet states is given for the determination of the ISC channel.

	$^1(n\pi^*)$			$^1(\pi_H\pi_L^*)$		
$i \rightsquigarrow f$	ΔE^{ad}	$\mid < i\mid\hat{H}_{SO}\mid f > \mid_{q0}$	k_{ISC}	ΔE^{ad}	$\mid < i\mid\hat{H}_{SO}\mid f > \mid_{q0}$	k_{ISC}
$S \rightsquigarrow^3 (\pi_H\pi_L^*)_x$	0.77	11.7	$\sim 10^9 - 10^{10}$	0.84	-	$\sim 10^6$
$S \rightsquigarrow^3 (\pi_H\pi_L^*)_y$	0.77	-4.3	$\sim 10^8 - 10^9$	0.84	-	$\sim 10^5$
$S \rightsquigarrow^3 (\pi_H\pi_L^*)_z$	0.77	-	-	0.84	0.7×10^{-2}	$\sim 10^1$
$S \rightsquigarrow^3 (n\pi^*)_x$	0.42	-	$\sim 10^8$	0.45	3.4	$\sim 10^9$
$S \rightsquigarrow^3 (n\pi^*)_y$	0.42	-	$\sim 10^7$	0.45	3.6	$\sim 10^9$
$S \rightsquigarrow^3 (n\pi^*)_z$	0.42	1.9×10^{-1}	$\sim 10^5$	0.45	-	-
$S \rightsquigarrow^3 (\pi_{H-1}\pi_L^*)_x$	0.33	1.5	$\sim 10^8$	0.40	-	$\sim 10^{11}$
$S \rightsquigarrow^3 (\pi_{H-1}\pi_L^*)_y$	0.33	9.6	$\sim 10^{10}$	0.40	-	$\sim 10^{11}$
$S \rightsquigarrow^3 (\pi_{H-1}\pi_L^*)_z$	0.33	-	-	0.40	$< 10^{-3}$	$\sim 10^{-1}$

TABLE V: IA: Calculated rate constants k_{ISC} [s^{-1}] for ($S \rightsquigarrow T$) ISC channels in aqueous solution. For more details see Table IV.

	$^1(n\pi^*)$			$^1(\pi_H\pi_L^*)$		
$i \rightsquigarrow f$	ΔE^{ad}	$\|<i\|\hat{H}_{SO}\|f>\|_{q0}$	k_{ISC}	ΔE^{ad}	$\|<i\|\hat{H}_{SO}\|f>\|_{q0}$	k_{ISC}
$S \rightsquigarrow^3 (\pi_H\pi_L^*)_x$	1.12	11.1	$\sim 10^{10}$	0.82	-	$\sim 10^5$
$S \rightsquigarrow^3 (\pi_H\pi_L^*)_y$	1.12	-4.8	$\sim 10^8$	0.82	-	$\sim 10^5$
$S \rightsquigarrow^3 (\pi_H\pi_L^*)_z$	1.12	-	-	0.82	0.7×10^{-2}	$\sim 10^1$
$S \rightsquigarrow^3 (n\pi^*)_x$	0.31	-	$\sim 10^8$	0.01	4.1	-
$S \rightsquigarrow^3 (n\pi^*)_y$	0.31	-	$\sim 10^7 - 10^8$	0.01	3.3	-
$S \rightsquigarrow^3 (n\pi^*)_z$	0.31	1.6×10^{-1}	$\sim 10^4$	0.01	-	-
$S \rightsquigarrow^3 (\pi_{H-1}\pi_L^*)_x$	0.64	-3.7	$\sim 10^9$	0.34	-	$\sim 10^8$
$S \rightsquigarrow^3 (\pi_{H-1}\pi_L^*)_y$	0.64	-2.4	$\sim 10^8 - 10^9$	0.34	-	$\sim 10^7$
$S \rightsquigarrow^3 (\pi_{H-1}\pi_L^*)_z$	0.64	-	-	0.34	0.110^{-2}	$\sim 10^1$

Fig. 1 Chemical structure and labeling of alloxazine (benzo-[*g*]pteridine-2,4(1H,3H)-dione, **AL**, left) and isoalloxazine (benzo-[*g*]pteridine-2,4(3H,10H)-dione, **IA**, right). Lumichrome (**LC**) is 7,8-dimethylalloxazine and flavins are 7,8-dimethyl substituted isoalloxazines.

Fig. 2 (TD)DFT (B3LYP,TZVP) equilibrium structures of the ground and excited states of AL. All bond lengths are given in pm.

Fig. 3 AL: Frontier orbitals at the optimized ground-state (S0) geometry. (Iso-value=0.3)

Fig. 4 AL: Comparison of the vertical excitation energies for the vacuum (I), solvation with COSMO (II), micro-hydration with 4-6 explicit water molecules (III), and a combination of models II and III (IV). Singlet energy profiles are represented by solid lines, triplet profiles by dashed lines.

Fig. 5 Electronic excitation energies (DFT/MRCI, [eV]) at various excited state geometries. Singlet energy profiles are represented by solid lines, triplet profiles by dashed lines.

Fig. 6 AL: Simulated Franck-Condon $(gs) \rightarrow^1 (\pi_H \pi_L^*)$ absorption spectra. The computed line spectrum was broadened by Gaussian functions with different FWHM. The vertical line represents our respective vertical DFT/MRCI excitation energy.

Fig. 7 AL: Simulated Franck-Condon $(gs) \leftarrow^1 (\pi_H \pi_L^*)$ emission spectrum. The computed line spectrum was broadened by Gaussian functions with different FWHM. The vertical line represents our vertical DFT/MRCI excitation energy.

Fig. 8 AL: DFT/MRCI energies of low-lying states along a linearly interpolated path between the S0 and the $^1(n\pi^*)$ geometry (left) and S0 and the $^1(\pi_H \pi_L^*)$ geometry (right) for the vacuum (top) and aqueous solution (bottom). Singlet energy profiles are represented by solid lines, triplet profiles by dashed lines. Stars symbolize the $(n\pi_L^*)$ state, squares the $(\pi_H \pi_L^*)$ state and circles the $(\pi_{H-1} \pi_L^*)$ state.

Fig. 9 AL: DFT/MRCI energies of low-lying excited states of alloxazine in the gas phase along a linearly interpolated path between the $^1(n\pi^*)$ (left) and the $^1(\pi_H \pi_L^*)$

geometry (right) for the vacuum (top) and aqueous solution (bottom). Singlet energy profiles are represented by solid lines, triplet profiles by dashed lines. Stars symbolize the ($n\pi^*_L$) state, squares the ($\pi_H\pi^*_L$) state, and circles the ($\pi_{H-1}\pi^*_L$) state.

Fig. 10 Schematic representation of the relaxation channels in alloxazine in vacuum (left) and aqueous solution (right). Only relevant processes are depicted. All rates are given in [s^{-1}]. Curly arrows represent processes that are activated by temperature. Note that non-radiative transitions are isoenergetic, leading from the initial state to vibrationally hot levels of the final state. For the sake of clarity, this has been neglected and the processes represented by dashed and dotted vertical lines. For lumichrome a qualitatively similar picture is expected.

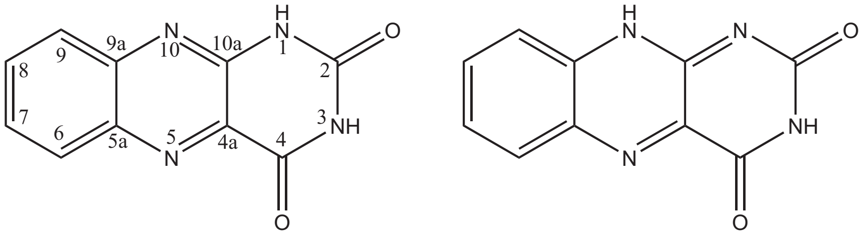

FIG. 1: Chemical structure and labeling of alloxazine (benzo-[*g*]pteridine-2,4(1H,3H)-dione, **AL**, left) and isoalloxazine (benzo-[*g*]pteridine-2,4(3H,10H)-dione, **IA**, right). Lumichrome (**LC**) is 7,8-dimethylalloxazine and flavins are 7,8-dimethyl substituted isoalloxazines.

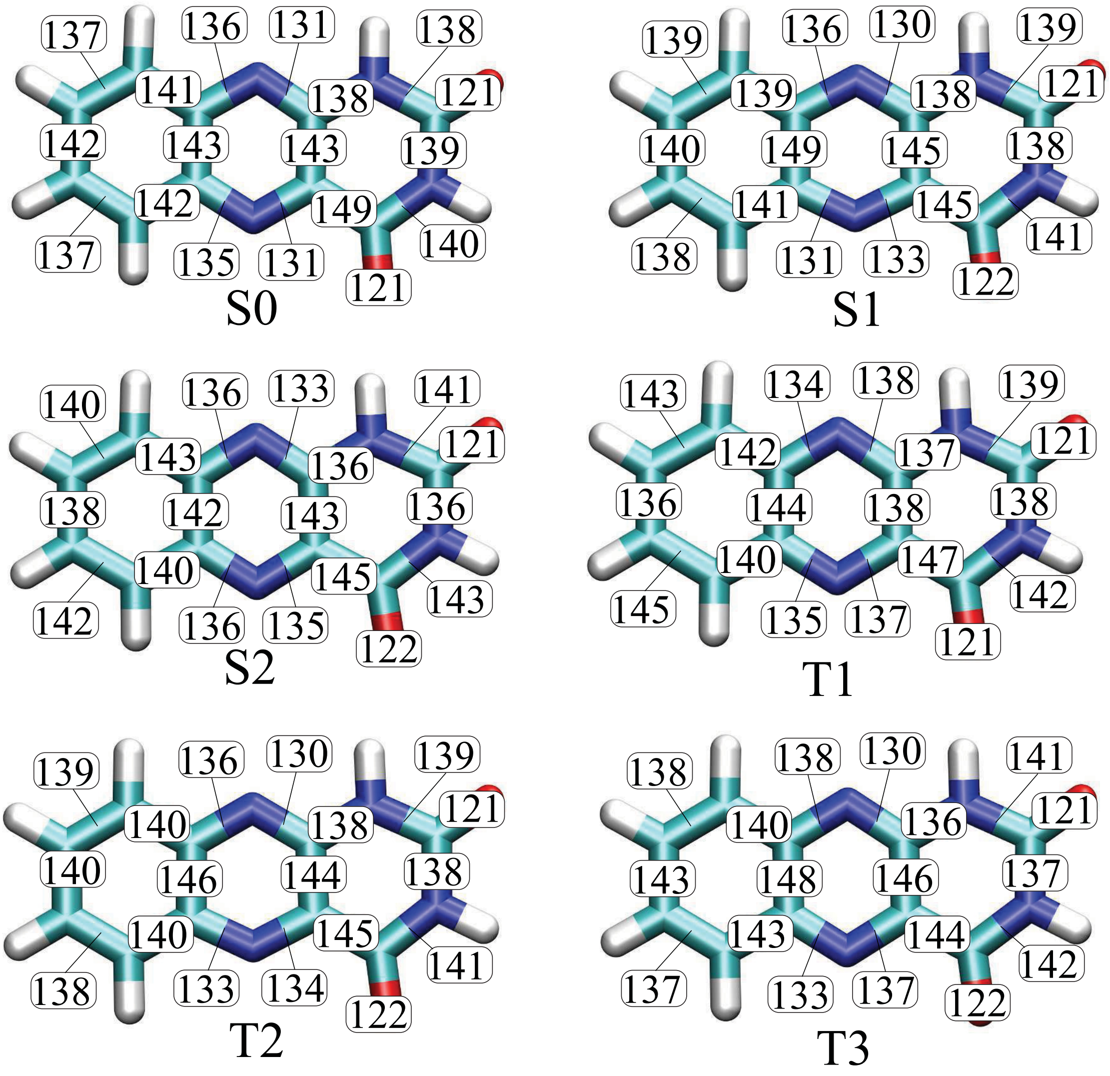

FIG. 2: (TD)DFT (B3LYP,TZVP) equilibrium structures of the ground and excited states of AL. All bond lengths are given in pm.

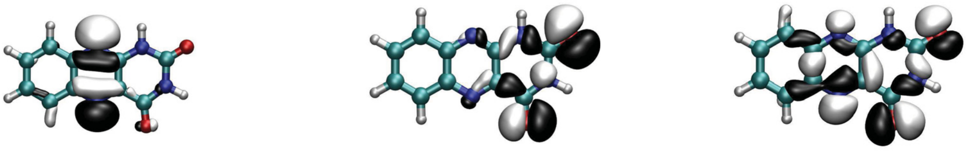

(a) n_N(27 a') (b) n_O(28 a') (c) n_{N-O}(29 a')

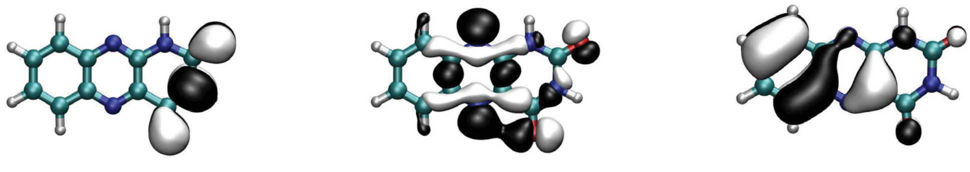

(d) π_{H-2}(245 a") (e) n_{N+O}(30 a') (f) π_{H-1}(246 a")

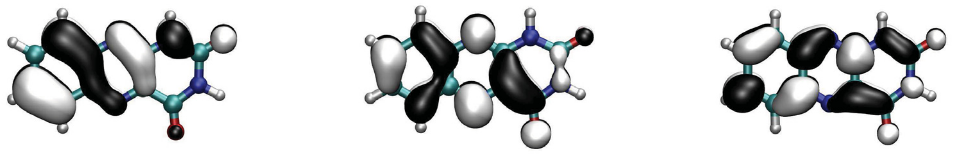

(g) π_H(247 a") (h) π_L(248 a") (i) π_{L+1}(249 a")

FIG. 3: AL: Frontier orbitals at the optimized ground-state (S0) geometry. (Isovalue=0.3)

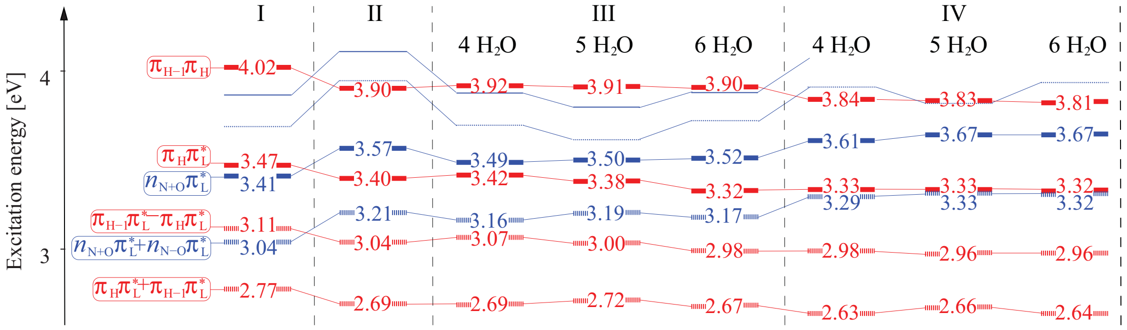

FIG. 4: AL: Comparison of the vertical excitation energies for the vacuum (I), solvation with COSMO (II), micro-hydration with 4-6 explicit water molecules (III), and a combination of models II and III (IV). Singlet energy profiles are represented by solid lines, triplet profiles by dashed lines.

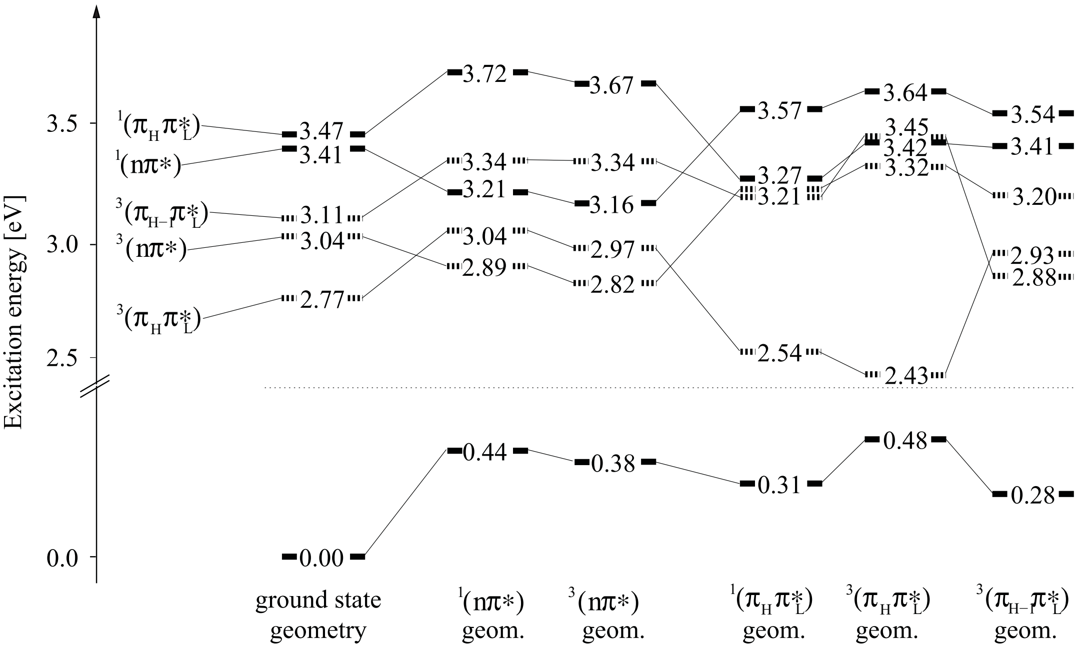

FIG. 5: Electronic excitation energies (DFT/MRCI, [eV]) at various excited state geometries. Singlet energy profiles are represented by solid lines, triplet profiles by dashed lines.

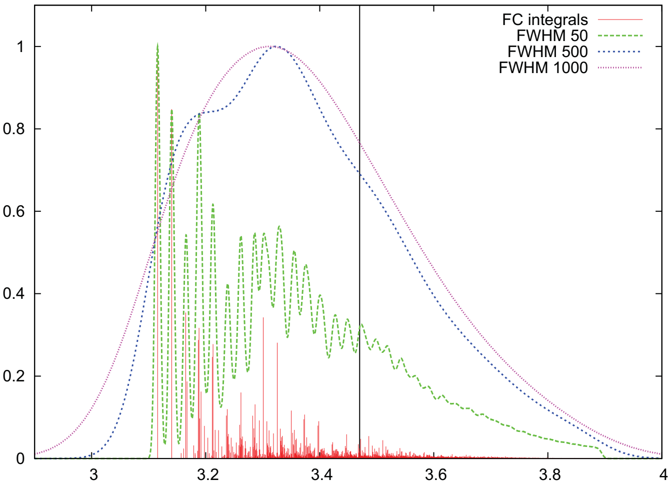

FIG. 6: AL: Simulated Franck-Condon $(gs) \to^1 (\pi_H \pi_L^*)$ absorption spectra. The computed line spectrum was broadened by Gaussian functions with different FWHM. The vertical line represents our vertical DFT/MRCI excitation energy.

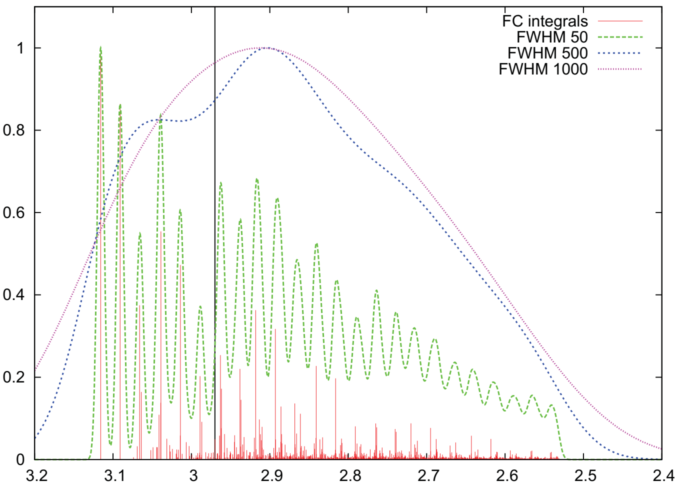

FIG. 7: AL: Simulated Franck-Condon $(gs) \leftarrow^1 (\pi_H \pi_L^*)$ emission spectrum. The computed line spectrum was broadened by Gaussian functions with different FWHM. The vertical line represents our respective vertical DFT/MRCI excitation energy.

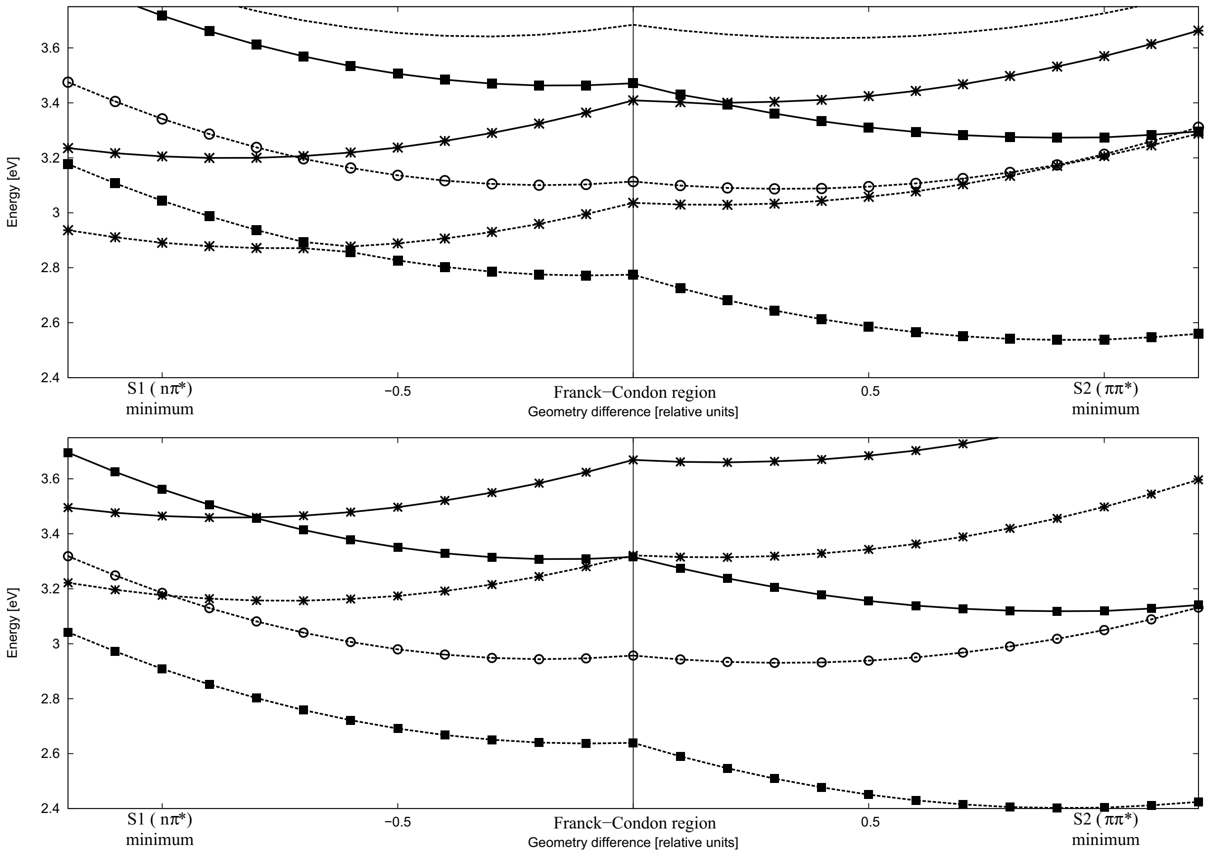

FIG. 8: AL: DFT/MRCI energies of low-lying states along a linearly interpolated path between the S0 and the $^1(n\pi^*)$ geometry (left) and S0 and the $^1(\pi_H\pi_L^*)$ geometry (right) for the vacuum (top) and aqueous solution (bottom). Singlet energy profiles are represented by solid lines, triplet profiles by dashed lines. Stars symbolize the $(n\pi_L^*)$ state, squares the $(\pi_H\pi_L^*)$ state and circles the $(\pi_{H-1}\pi_L^*)$ state.

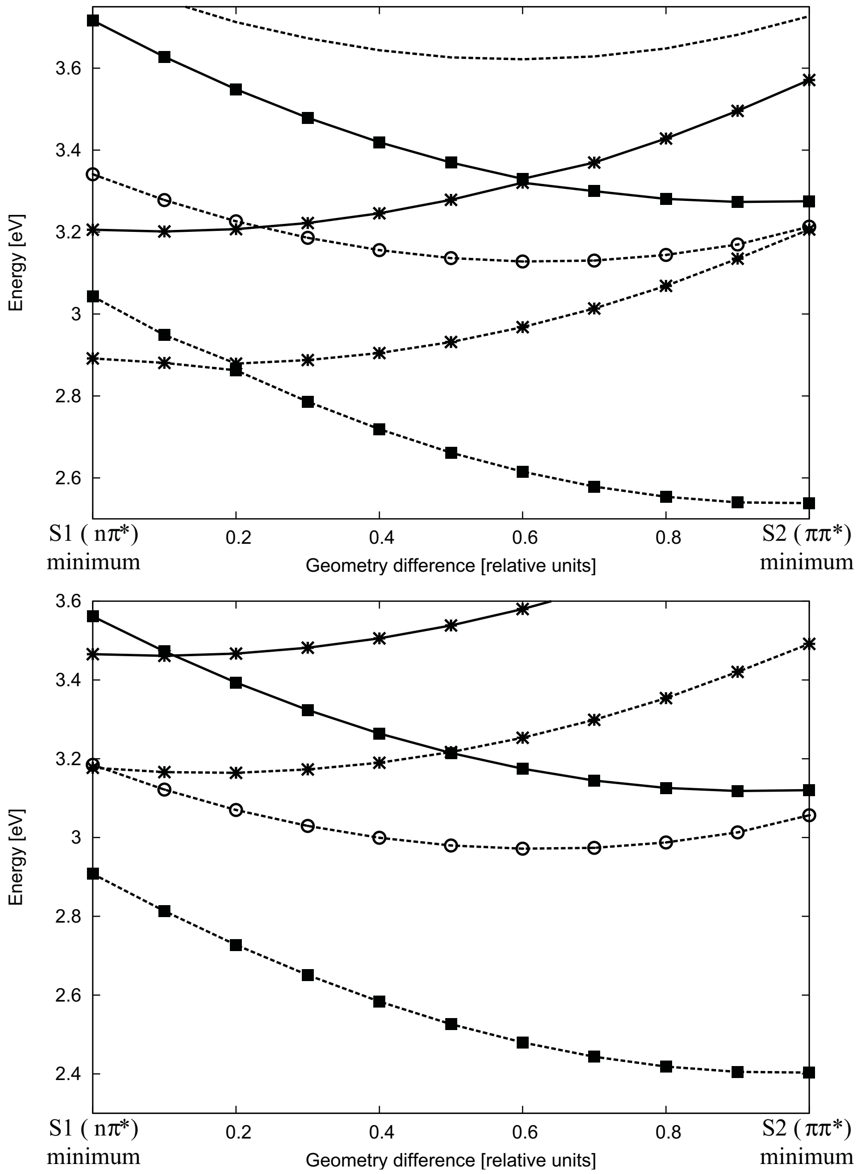

FIG. 9: AL: DFT/MRCI energies of low-lying excited states of alloxazine in the gas phase along a linearly interpolated path between the $^1(n\pi^*)$ (left) and the $^1(\pi_H\pi_L^*)$ geometry (right) for the vacuum (top) and aqueous solution (bottom). Singlet energy profiles are represented by solid lines, triplet profiles by dashed lines. Stars symbolize the $(n\pi_L^*)$ state, squares the $(\pi_H\pi_L^*)$ state, and circles the $(\pi_{H-1}\pi_L^*)$ state.

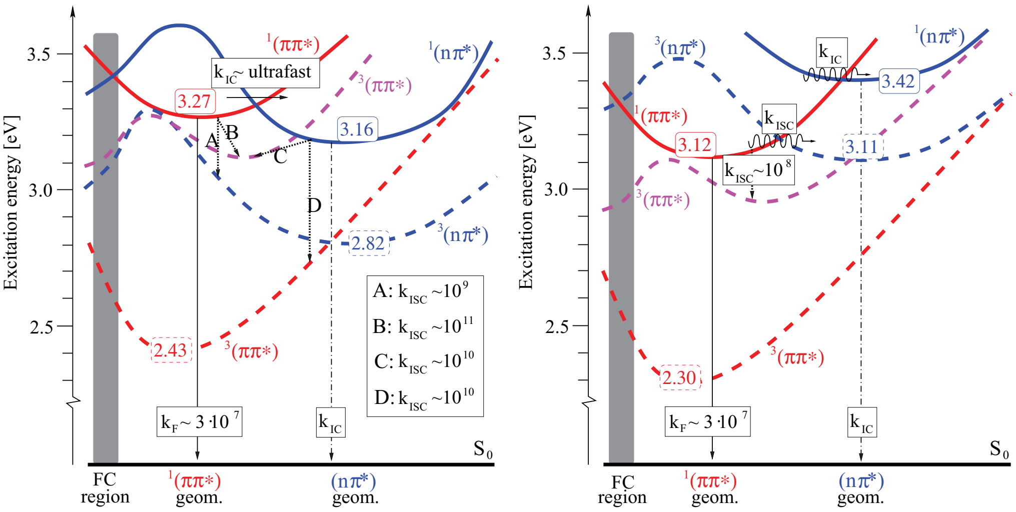

FIG. 10: Schematic representation of the relaxation channels in alloxazine in vacuum (left) and aqueous solution (right). Only relevant processes are depicted. All rates are given in [s^{-1}]. Curly arrows represent processes that are activated by temperature. Note that non-radiative transitions are isoenergetic, leading from the initial state to vibrationally hot levels of the final state. For the sake of clarity, this has been neglected and the processes represented by dashed and dotted vertical lines. For lumichrome a qualitatively similar picture is expected.

Graphical Abstract

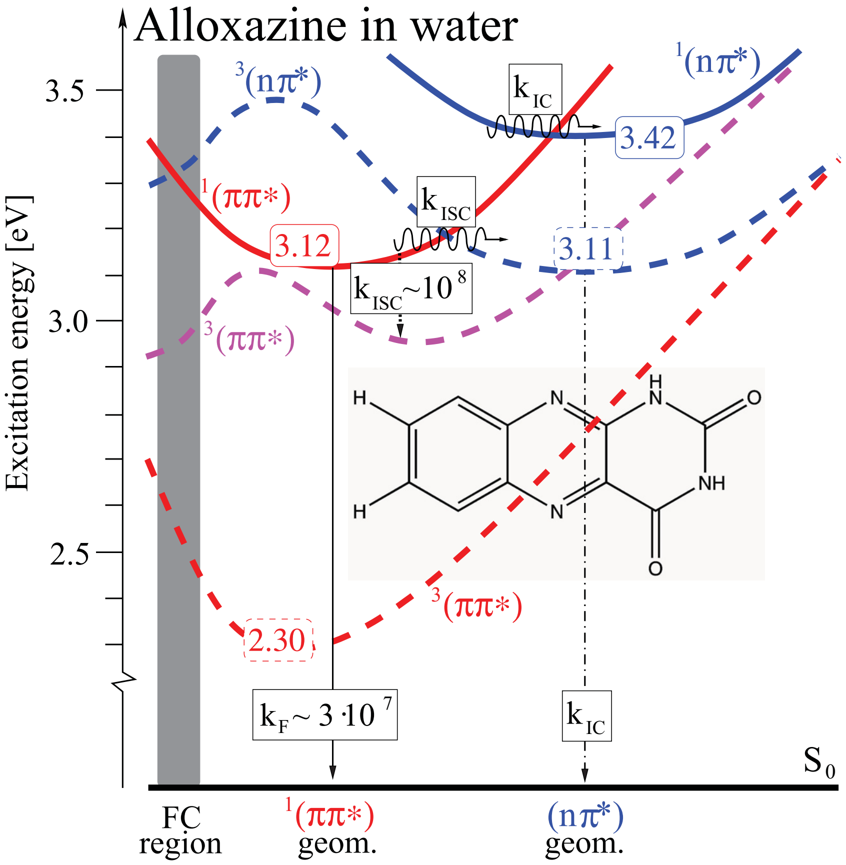

We show that the decay mechanism of the optically bright $^1(\pi_H\pi^*_L)$ state of alloxazine depends strongly on the polarity and hydrogen-bonding ability of the solvent. For gas phase and nonpolar solvents we predict complete quenching of the fluorescence whereas in aqueous solution a competition between fluorescence and intersystem crossing to the T_2 and T_3 states is found.

The photophysics of alloxazine: A quantum chemical investigation in vacuum and solution

Electronic Supplementary Information

Susanne Salzmann and Christel M. Marian
Institute of Theoretical and Computational Chemistry,
Heinrich Heine University Düsseldorf,
Universitätsstr. 1, D-40225 Düsseldorf, Germany[*]

(Dated: June 12, 2009)

---

[*]Electronic address: `Christel.Marian@uni-duesseldorf.de`; URL: `http://www.theochem.uni-duesseldorf.de`

I. EXPERIMENTAL DATA

(See Table I)

II. OPTIMIZED GEOMETRIES OF ALLOXAZINE WATER COMPLEXES

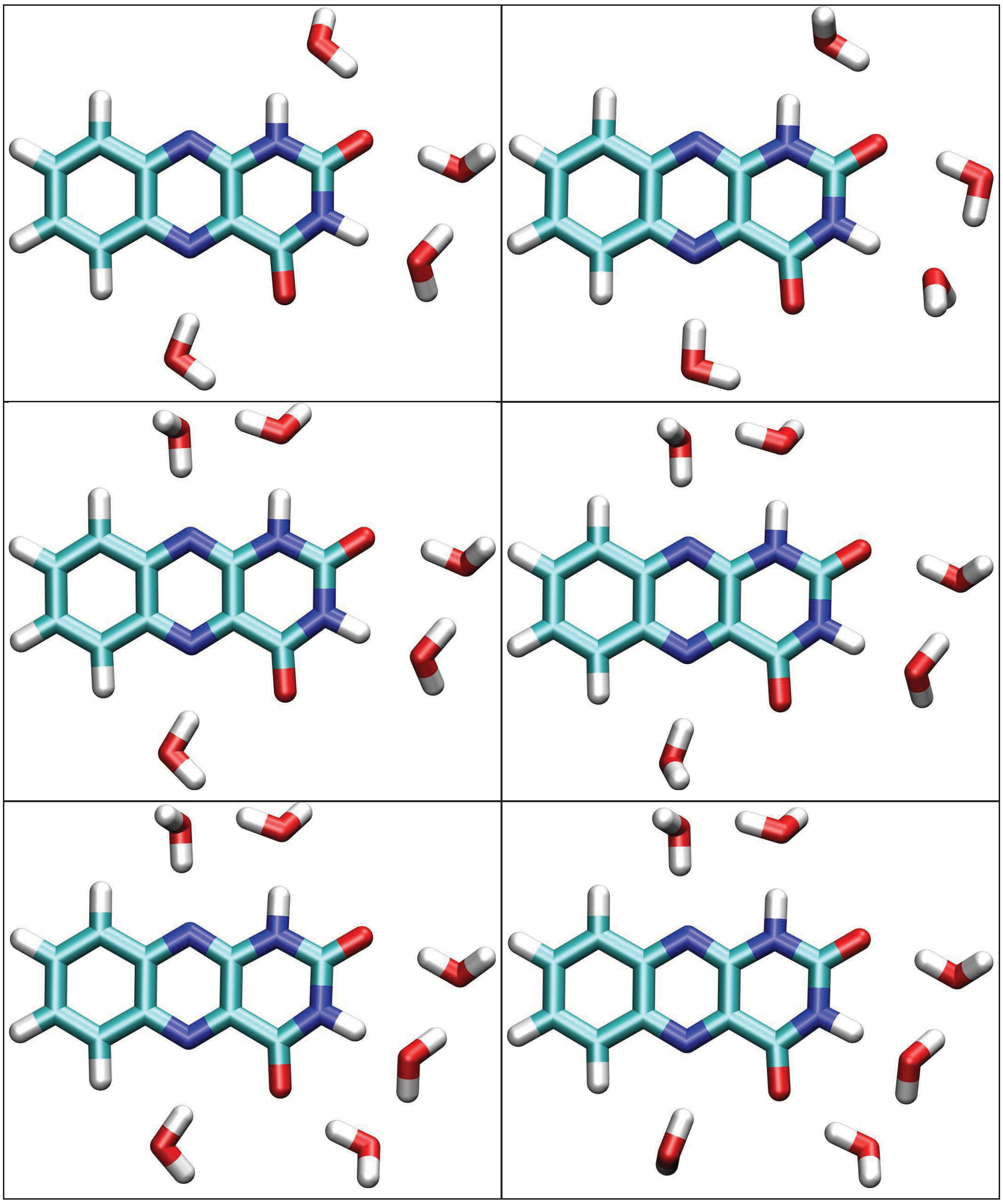

FIG. 1: AL: Optimized geometries of alloxazine water complexes. Left: micro-hydration, right: micro-hydration and COSMO.

TABLE I: Experimental spectroscopic data of alloxazine and lumichrome in various solvents. (Dx: 1,4-dioxane, DCE: 1,2-dichloroethane, AcN: acetonitrile, EtOH: ethanol, and MeOH: methanol.) In addition to the maxima of the first (λ_1) and second (λ_2) absorption bands and the fluorescence emission band (λ_F) [eV], fluorescence Φ_F and intersystem crossing Φ_{ISC} quantum yields, and fluorescence rate constants k_F [10^7 s^{-1}] are shown. (For comparison: lumiflavin in neutral aqueous solution Φ_{ISC}=0.67 and Φ_F=0.29[1])

	AL						**LC**					
	Dx	DCE	AcN	EtOH	MeOH	H_2O	Dx	DCE	AcN	EtOH	MeOH	H_2O
ϵ	2.21	10.37	35.94	24.55	32.66	78.30	2.21	10.37	35.94	24.55	32.66	78.30
protic	-	-	-	+	+	+	-	-	-	+	+	+
λ_1	3.33^a	3.32^a	3.33^b	$3.30^{c,d}$	3.30^f	3.27^g	3.27^h	3.25^h	3.26^b	3.24^d	3.23^h	3.22^h
λ_2	3.89^a	3.85^a	3.87^b	3.84^c,3.86^d	3.86^f	3.76^g	3.73^h	3.60^h	3.71^b	3.69^d	3.66^h	3.51^h
λ_F	2.85^a	2.86^a	2.87^b	2.79^d	-	-	2.79^h	2.81^h	2.84^b	2.74^d	2.74^h	2.59^h
Φ_F	-	0.023^a	0.009^b	$0.033^{e,i}$,$0.068^{e,j}$	-	$0.048^{k,m}$,$0.033^{k,n}$	0.027^h	0.026^h	0.028^b	$0.067^{e,i}$,$0.139^{e,j}$,0.036^k	0.032^h	0.088^h,$0.055^{k,m}$,$0.034^{k,n}$
Φ_{ISC}	-	-	0.36^l	-	-	$0.45^{k,m}$,$0.31^{k,n}$	-	-	0.73^l	0.61^k	-	$0.71^{k,m}$,$0.44^{k,n}$
k_F	-	12^a	2.6^b	-	1.8^a	$3.3^{k,n}$	6.0^h	4.3^h	4.3^h	4.2^k	3.0^h	3.2^h,$3.3^{k,n}$

a : Ref. [2].

b : Ref. [3, 4].

c : Read from Ref. [5], Figure 9.

d : Ref. [6].

e : Ref. [5].

f : Ref. [7].

g : Read from Ref. [8], Figure 1.

h : Ref. [9].

i : 298 K.

j : 77 K.

k : Ref. [1].

l : Quantum yield of singlet oxygen formation, Ref. [3].

m : Estimates for pH 6.

n : At pH 2.

III. CALCULATION OF THE INTERSYSTEM CROSSING RATE CONSTANTS

In this appendix, we have assembled detailed information on the entities required for the evaluation of spin-forbidden nonradiative transition probabilities and on the sensitivity of the results with respect to technical parameters.

According to Toniolo and Persico [10, 11], it is possible to approximate the Fermi Golden Rule expression for the ISC rate constants k_{ISC} by a summation over rates of transition from the initial level $|i, \mathbf{v} = \mathbf{0}\rangle$ to individual final vibronic levels $|f, \mathbf{v}'\rangle$ in an energy interval of width 2η around the energy $E_{i,\mathbf{v}=\mathbf{0}}$. Here, the vectors $\mathbf{v}$ and $\mathbf{v}'$ represent sets of vibrational quantum numbers in all normal modes of the initial (i) and final (f) electronic state, respectively. If we denote the coupling matrix elements driving the radiationless transition by $H^{SO}_{\mathbf{v}=\mathbf{0},\mathbf{v}'}$, the rate constant is obtained as

$$k_{ISC}\left(i \rightsquigarrow f\right) = \frac{2\pi}{\hbar\eta} \sum_{\left|E_{f,v'} - E_{i,\mathbf{v}=\mathbf{0}}\right| < \eta} \left|H^{SO}_{\mathbf{v}=\mathbf{0},\mathbf{v}'}\right|^2 \quad . \tag{1}$$

$H^{SO}_{\mathbf{v}=\mathbf{0},\mathbf{v}'}$ can be expanded in a Taylor series in the variables $\{q_\kappa\}$, the normal coordinates, around some reference point $\mathbf{q}_0$ [12] which we have chosen to coincide with the minimum of the S_1 state.

$$\begin{aligned} H^{SO}_{\mathbf{v}=\mathbf{0},\mathbf{v}'} &= \left\langle i \left| \hat{\mathcal{H}}_{\mathrm{SO}} \right| f \right\rangle \Big|_{\mathbf{q}_0=\mathbf{0}} \langle \mathbf{v} = \mathbf{0} | \mathbf{v}' \rangle \\ &+ \sum_\kappa \left(\frac{\partial}{\partial q_\kappa} \langle i | \hat{\mathcal{H}}_{\mathrm{SO}} | f \rangle \right) \Bigg|_{\mathbf{q}_0=\mathbf{0}} \langle \mathbf{v} = \mathbf{0} | q_\kappa | \mathbf{v}' \rangle \\ &+ O\left(|\mathbf{q}|^2\right) \end{aligned} \tag{2}$$

The first term on the right-hand side of equation (2) is a purely electronic matrix element and is denominated direct spin-orbit coupling in the following, whereas the term in the second line of equation (2) represents the first-order derivative coupling and is named vibronic spin-orbit coupling.

Tables II and III lists harmonic frequencies of the 19 out-of-plane vibrations in the first excited $^1(\pi \rightarrow \pi^*)$ and $^1(n \rightarrow \pi^*)$ states (coupling modes for the vibronic spin-orbit interaction) and the derivatives of the spin-orbit coupling matrix elements with respect to distortions along their normal coordinates.

The first-order derivatives of the SOMEs were calculated numerically by finite difference techniques, more precisely, by means of the symmetrized two-point formula:

$$\frac{\partial}{\partial q_\kappa} \left\langle i \left| \hat{\mathcal{H}}_{\mathrm{SO}} \right| f \right\rangle \Big|_{\mathbf{q}_0} \approx \frac{\left\langle i \left| \hat{\mathcal{H}}_{\mathrm{SO}} \right| f \right\rangle \Big|_{\mathbf{q}_0 + \epsilon \mathbf{e}_\kappa} - \left\langle i \left| \hat{\mathcal{H}}_{\mathrm{SO}} \right| f \right\rangle \Big|_{\mathbf{q}_0 - \epsilon \mathbf{e}_\kappa}}{2\epsilon} \tag{3}$$

Here, $\mathbf{e}_\kappa$ denotes the unit vector pointing into the direction of the normal mode v_κ. (For more details see Ref. [13].) Thus, single-point DFT/MRCI and subsequent Spock runs have to be carried out at two distorted molecular geometries $\mathbf{q}_0 \pm \epsilon \mathbf{e}_\kappa$ for each normal mode. For obtaining the derivatives employed in the final computations of the ISC rate constants, the displacement increment ϵ is set to a numerical value of 0.1 (referring to dimensionless normal mode coordinates $\mathbf{q}_\kappa$). In order to minimize the errors induced by numerical noise, the CI space from a preceding DFT/MRCI run without symmetry constraints at the reference geometry $\mathbf{q}_0$ is used in all calulations. The molecular orbitals employed in the single-point CI calculations are reoptimized for the distorted geometries, of course.

Since the oop distortion exhibits a symmetric potential well, we do not expect a deviation between the SOME at two distorted molecular geometries $\mathbf{q}_0 \pm \epsilon \mathbf{e}_\kappa$. For our calculations in the vacuum this is fulfilled. There, in most cases, we find the difference between the two SOME to be less that 0.00001 cm-1. For our calculations of the SOME derivatives in aqueous solution with COSMO, however, larger deviations between the two SOMEs turn up. This has been reported before and can be explained by the fact that the cavity construction for the COSMO calculation uses coordinates that are slightly distorted.[14] Although it would be desirable to obtain the derivatives of the SOME with COSMO with a higher precision, the induced errors do not change the order of magnitude of the resulting ISC rate constant, only its prefactor, as shown in Ref. [14] (Supplementary Information, Table 5).

Information about the parameters chosen in the calculation of the rate constants for the nonradiative transitions from $^1(n\pi^*)$ and $^1(\pi_H\pi_L^*)$ to the individual spin components of the $^3(\pi_H\pi_L^*)$, $^3(n\pi^*)$ and $^3(\pi_{H-1}\pi_L^*)$ states and the dependence of the results on these parameters are contained in Table IV to Table VII. A zero number of derivative coupling modes indicates direct spin-orbit coupling, nonzero numbers vibronic spin-orbit coupling.

TABLE II: AL: Harmonic frequencies ν_i [cm^{-1}] of the out-of-plane vibrational modes for the $^1(n\pi^*)$ and $^1(\pi_H\pi_L^*)$ states in the gas phase. Derivatives of SOMEs [$-i$cm^{-1}] with respect to the (dimensionless) normal coordinates at the corresponding equilibrium geometry q_0.

		$^1(n\pi^*)$				$^1(\pi_H\pi_L^*)$			
		$\frac{\partial<^1(n\pi^*)\vert\hat{H}_{SO}\vert^3(n\pi^*)>}{\partial q_i}$				$\frac{\partial<^1(\pi_H\pi_L^*)\vert\hat{H}_{SO}\vert^3(\pi_H\pi_L^*)>}{\partial q_i}$		$\frac{\partial<^1(\pi_H\pi_L^*)\vert\hat{H}_{SO}\vert^3(\pi_{H-1}\pi_L^*)>}{\partial q_i}$	
mode	$\hat{\nu}_i$	(x)	(y)	mode	$\hat{\nu}_i$	(x)	(y)	(x)	(y)
1	72.15	-0.35	0.18	1	50[a]	3.54	-1.22	-24.38	21.84
2	75.27	2.54	-0.31	2	67.92	-0.42	0.34	-31.48	33.06
3	137.73	-2.20	1.47	3	77.74	-0.10	-0.01	-26.78	28.06
4	151.84	-0.62	0.39	4	127.31	-0.54	-0.04	25.49	-25.87
6	180.98	4.69	-1.61	5	144.41	0.29	-0.07	27.41	-28.93
7	207.66	4.82	-1.95	7	223.02	-0.42	0.21	24.34	-24.94
8	330.88	-2.19	0.62	8	268.73	1.63	-1.00	-25.59	25.65
11	415.08	4.55	-1.05	10	337.94	0.81	-0.49	-24.23	24.63
13	477.36	0.19	0.20	12	405.52	1.33	-0.78	-25.01	25.29
14	498.66	-0.72	0.50	14	488.15	-0.51	0.27	24.12	-24.88
18	543.65	0.72	0.12	19	593.50	-0.38	0.16	24.47	-25.40
19	578.99	3.90	-1.15	20	642.08	1.09	-0.75	23.63	-25.40
21	612.81	0.07	0.27	21	651.09	0.41	-0.05	-24.53	25.37
23	661.55	-0.92	0.57	23	672.55	0.41	-0.23	-24.68	25.56
25	733.38	-0.38	-0.21	25	709.68	0.95	-0.66	-24.31	25.15
27	743.02	0.14	0.57	26	740.68	-0.15	-0.00[b]	25.22	-26.21
28	768.35	5.06	-1.60	28	779.01	0.67	-0.45	24.64	-25.89
30	886.27	1.29	-0.56	30	900.97	-0.13	0.18	21.12	-22.17
32	930.61	-0.91	0.29	32	916.89	-0.24	0.09	23.60	-24.37

a: The TDDFT (B3LYP) PEH exhibits a very flat double well shape along mode 1 with a slightly imaginary frequency (see text). The setting $\hat{\nu}_i$ represents an approximate harmonic model of the $^1(\pi_H\pi_L^*)$ state PEH along mode 1. Such an imaginary frequency in the initial state, where only $v = 0$ plays a role, does not change the vibrational density of states.

b: Absolute value of the derivative lower than 0.01 cm^{-1}

TABLE III: AL: Harmonic frequencies ν_i [cm^{-1}] of the out-of-plane vibrational modes for the $^1(n\pi^*)$ and $^1(\pi_H\pi_L^*)$ states in aqueous solution. Derivatives of SOMEs [$-i$cm^{-1}] with respect to the (dimensionless) normal coordinates at the corresponding equilibrium geometry q_0.

		$^1(n\pi^*)$				$^1(\pi_H\pi_L^*)$			
		$\frac{\partial<^1(n\pi^*)\vert\hat{H}_{SO}\vert^3(n\pi^*)>}{\partial q_i}$				$\frac{\partial<^1(\pi_H\pi_L^*)\vert\hat{H}_{SO}\vert^3(\pi_H\pi_L^*)>}{\partial q_i}$		$\frac{\partial<^1(\pi_H\pi_L^*)\vert\hat{H}_{SO}\vert^3(\pi_{H-1}\pi_L^*)>}{\partial q_i}$	
mode	$\hat{\nu}_i$	(x)	(y)	mode	$\hat{\nu}_i$	(x)	(y)	(x)	(y)
1	72.15	0.73	-0.00[b]	1	50[a]	1.24	-0.41	1.13	-0.20
2	75.27	1.70	-1.26	2	67.92	-0.20	0.21	-0.10	0.03
3	137.73	-5.96	2.22	3	77.74	-0.11	0.00	0.03	-0.02
4	151.84	-0.60	0.56	4	127.31	-0.27	-0.10	-0.47	-0.15
6	180.98	5.91	-2.98	5	144.41	0.15	-0.09	-0.05	0.11
7	207.66	11.84	-4.10	7	223.02	-0.21	0.12	-0.62	0.24
8	330.88	-2.59	1.33	8	268.73	0.89	-0.62	1.31	-0.62
11	415.08	0.92	-2.19	10	337.94	0.51	-0.34	0.92	-0.50
13	477.36	1.98	-0.74	12	405.52	0.60	-0.43	1.15	-0.71
14	498.66	-0.72	0.12	14	488.15	-0.29	0.17	-0.74	0.49
18	543.65	1.86	-0.59	19	593.50	-0.15	0.01	-0.40	0.26
19	578.99	3.13	-2.05	20	642.08	0.57	-0.43	0.14	0.24
21	612.81	-1.17	0.43	21	651.09	0.23	0.01	0.69	-0.52
23	661.55	-0.04	0.72	23	672.55	0.25	-0.17	0.45	-0.31
25	733.38	-0.56	0.06	25	709.68	0.54	-0.47	0.43	-0.40
27	743.02	-1.42	0.30	26	740.68	-0.07	0.00	-0.17	0.14
28	768.35	8.87	-4.27	28	779.01	0.52	-0.38	-0.50	0.29
30	886.27	3.00	-1.31	30	900.97	-0.12	0.09	-0.07	0.12
32	930.61	-1.93	0.82	32	916.89	-0.02	-0.03	-0.41	0.16

a: The TDDFT (B3LYP) PEH exhibits a very flat double well shape along mode 1 with a slightly imaginary frequency (see text). The setting $\hat{\nu}_i$ represents an approximate harmonic model of the $^1(\pi_H\pi_L^*)$ state PEH along mode 1. Such an imaginary frequency in the initial state, where only $v = 0$ plays a role, does not change the vibrational density of states.

b: Absolute value of the derivative lower than 0.01 cm^{-1}

TABLE IV: AL: Calculated rate constants k_{ISC} [s^{-1}] for (S $\rightsquigarrow$ T) ISC channels of the $^1(n\pi^*)$ state in the vacuum. Remaining columns: adiabatic electronic energy difference ΔE^{ad} [eV], direct SOME $| < i|\hat{H}_{SO}|f > |_{q0}$ [cm^{-1}], number $\#derivs$ of included derivatives w.r.t. *oop* modes in vibronic SO coupling, number $\#_{acc}$ of included accepting modes, width η [cm^{-1}] of search interval, resulting number $\#v'$ of final state vibrational levels within search interval.

		parameters & and settings				**results**	
channel	-	direct SO	vib. SO	acceptors	interval	levels	rate
$i \rightsquigarrow f$	ΔE^{ad}	$\vert < i\vert\hat{H}_{SO}\vert f > \vert_{q0}$	$\#derivs$	$\#_{acc}$	η	$\#v'$	k_{ISC}
$^1(n\pi^*) \rightsquigarrow {}^3(\pi_H\pi^*_L)_x$	6222	11.67	-	41	0.0001	20	$4.7 \cdot 10^9$
$^1(n\pi^*) \rightsquigarrow {}^3(\pi_H\pi^*_L)_x$	6222	11.67	-	41	0.001	183	$2.1 \cdot 10^9$
$^1(n\pi^*) \rightsquigarrow {}^3(\pi_H\pi^*_L)_x$	6222	11.67	-	41	0.01	1902	$1.6 \cdot 10^9$
$^1(n\pi^*) \rightsquigarrow {}^3(\pi_H\pi^*_L)_x$	6222	11.67	-	41	0.1	19481	$1.2 \cdot 10^{10}$
$^1(n\pi^*) \rightsquigarrow {}^3(\pi_H\pi^*_L)_x$	6222	11.67	-	41	1	194900	$1.3 \cdot 10^{10}$
$^1(n\pi^*) \rightsquigarrow {}^3(\pi_H\pi^*_L)_y$	6222	-4.28	-	41	0.0001	20	$6.4 \cdot 10^8$
$^1(n\pi^*) \rightsquigarrow {}^3(\pi_H\pi^*_L)_y$	6222	-4.28	-	41	0.001	183	$2.9 \cdot 10^8$
$^1(n\pi^*) \rightsquigarrow {}^3(\pi_H\pi^*_L)_y$	6222	-4.28	-	41	0.01	1902	$2.1 \cdot 10^8$
$^1(n\pi^*) \rightsquigarrow {}^3(\pi_H\pi^*_L)_y$	6222	-4.28	-	41	0.1	19481	$1.7 \cdot 10^9$
$^1(n\pi^*) \rightsquigarrow {}^3(\pi_H\pi^*_L)_y$	6222	-4.28	-	41	1	194900	$1.8 \cdot 10^9$
$^1(n\pi^*) \rightsquigarrow {}^3(\pi_H\pi^*_L)_z$	6222	-	-	-	-	-	-
$^1(n\pi^*) \rightsquigarrow {}^3(n\pi^*)_x$	3422	-	19	41	0.001	200	$3.1 \cdot 10^4$
$^1(n\pi^*) \rightsquigarrow {}^3(n\pi^*)_x$	3422	-	19	41	0.01	2103	$2.6 \cdot 10^8$
$^1(n\pi^*) \rightsquigarrow {}^3(n\pi^*)_x$	3422	-	19	41	0.1	20984	$3.9 \cdot 10^8$
$^1(n\pi^*) \rightsquigarrow {}^3(n\pi^*)_x$	3422	-	19	41	1	211340	$4.0 \cdot 10^7$
$^1(n\pi^*) \rightsquigarrow {}^3(n\pi^*)_y$	3422	-	19	41	0.001	200	$2.8 \cdot 10^4$
$^1(n\pi^*) \rightsquigarrow {}^3(n\pi^*)_y$	3422	-	19	41	0.01	2103	$2.8 \cdot 10^7$
$^1(n\pi^*) \rightsquigarrow {}^3(n\pi^*)_y$	3422	-	19	41	0.1	20984	$8.8 \cdot 10^6$
$^1(n\pi^*) \rightsquigarrow {}^3(n\pi^*)_y$	3422	-	19	41	1	211340	$5.7 \cdot 10^6$
$^1(n\pi^*) \rightsquigarrow {}^3(n\pi^*)_z$	3422	-0.19	-	41	0.01	5	$2.1 \cdot 10^4$
$^1(n\pi^*) \rightsquigarrow {}^3(n\pi^*)_z$	3422	-0.19	-	41	0.1	53	$8.9 \cdot 10^4$
$^1(n\pi^*) \rightsquigarrow {}^3(n\pi^*)_z$	3422	-0.19	-	41	1	562	$9.5 \cdot 10^4$
$^1(n\pi^*) \rightsquigarrow {}^3(\pi_{H-1}\pi^*_L)_x$	2634	1.48	-	41	1	4	$3.2 \cdot 10^8$
$^1(n\pi^*) \rightsquigarrow {}^3(\pi_{H-1}\pi^*_L)_x$	2634	1.48	-	41	10	37	$2.1 \cdot 10^8$
$^1(n\pi^*) \rightsquigarrow {}^3(\pi_{H-1}\pi^*_L)_x$	2634	1.48	-	41	100	420	$2.7 \cdot 10^8$
$^1(n\pi^*) \rightsquigarrow {}^3(\pi_{H-1}\pi^*_L)_y$	2634	9.56	-	41	1	4	$1.3 \cdot 10^{10}$
$^1(n\pi^*) \rightsquigarrow {}^3(\pi_{H-1}\pi^*_L)_y$	2634	9.56	-	41	10	37	$8.8 \cdot 10^9$
$^1(n\pi^*) \rightsquigarrow {}^3(\pi_{H-1}\pi^*_L)_y$	2634	9.56	-	41	100	420	$1.1 \cdot 10^{10}$
$^1(n\pi^*) \rightsquigarrow {}^3(\pi_{H-1}\pi^*_L)_z$	2634	-	-	-	-	-	-

TABLE V: AL: Calculated rate constants k_{ISC} [s^{-1}] for (S $\rightsquigarrow$ T) ISC channels of the $^1(\pi_H\pi_L^*)$ state in the vacuum. Remaining columns: adiabatic electronic energy difference ΔE^{ad} [eV], direct SOME $| < i|\hat{H}_{SO}|f > |_{q0}$ [cm^{-1}], number $\#derivs$ of included derivatives w.r.t. *oop* modes in vibronic SO coupling, number $\#_{acc}$ of included accepting modes, width η [cm^{-1}] of search interval, resulting number $\#v'$ of final state vibrational levels within search interval.

	parameters & and settings					**results**	
channel	-	direct SO	vib. SO	acceptors	interval	levels	rate
$i \rightsquigarrow f$	ΔE^{ad}	$\| < i\|\hat{H}_{SO}\|f > \|_{q0}$	$\#derivs$	$\#_{acc}$	η	$\#v'$	k_{ISC}
$^1(\pi_H\pi_L^*)\rightsquigarrow\ ^3(\pi_H\pi_L^*)_x$	6776	-	19	41	0.0001	1769	$3.8 \cdot 10^5$
$^1(\pi_H\pi_L^*)\rightsquigarrow\ ^3(\pi_H\pi_L^*)_x$	6776	-	19	41	0.001	17994	$1.1 \cdot 10^6$
$^1(\pi_H\pi_L^*)\rightsquigarrow\ ^3(\pi_H\pi_L^*)_x$	6776	-	19	41	0.01	178603	$2.8 \cdot 10^6$
$^1(\pi_H\pi_L^*)\rightsquigarrow\ ^3(\pi_H\pi_L^*)_y$	6776	-	19	41	0.0001	1769	$8.4 \cdot 10^4$
$^1(\pi_H\pi_L^*)\rightsquigarrow\ ^3(\pi_H\pi_L^*)_y$	6776	-	19	41	0.001	17994	$2.6 \cdot 10^5$
$^1(\pi_H\pi_L^*)\rightsquigarrow\ ^3(\pi_H\pi_L^*)_y$	6776	-	19	41	0.01	178603	$5.5 \cdot 10^5$
$^1(\pi_H\pi_L^*)\rightsquigarrow\ ^3(\pi_H\pi_L^*)_z$	6776	-0.01	-	41	0.01	5305	9.8
$^1(\pi_H\pi_L^*)\rightsquigarrow\ ^3(\pi_H\pi_L^*)_z$	6776	-0.01	-	41	0.1	53152	$1.8 \cdot 10^1$
$^1(\pi_H\pi_L^*)\rightsquigarrow\ ^3(\pi_H\pi_L^*)_z$	6776	-0.01	-	41	1	531576	$4.3 \cdot 10^1$
$^1(\pi_H\pi_L^*)\rightsquigarrow\ ^3(n\pi^*)_x$	3646	-3.43	-	41	0.001	1	$2.7 \cdot 10^6$
$^1(\pi_H\pi_L^*)\rightsquigarrow\ ^3(n\pi^*)_x$	3646	-3.43	-	41	0.01	9	$7.5 \cdot 10^7$
$^1(\pi_H\pi_L^*)\rightsquigarrow\ ^3(n\pi^*)_x$	3646	-3.43	-	41	0.1	83	$2.4 \cdot 10^9$
$^1(\pi_H\pi_L^*)\rightsquigarrow\ ^3(n\pi^*)_x$	3646	-3.43	-	41	1	992	$8.7 \cdot 10^8$
$^1(\pi_H\pi_L^*)\rightsquigarrow\ ^3(n\pi^*)_y$	3646	3.59	-	41	0.001	1	$3.0 \cdot 10^6$
$^1(\pi_H\pi_L^*)\rightsquigarrow\ ^3(n\pi^*)_y$	3646	3.59	-	41	0.01	9	$8.2 \cdot 10^7$
$^1(\pi_H\pi_L^*)\rightsquigarrow\ ^3(n\pi^*)_y$	3646	3.59	-	41	0.1	83	$2.6 \cdot 10^9$
$^1(\pi_H\pi_L^*)\rightsquigarrow\ ^3(n\pi^*)_y$	3646	3.59	-	41	1	992	$9.6 \cdot 10^8$
$^1(\pi_H\pi_L^*)\rightsquigarrow\ ^3(n\pi^*)_z$	3646	-	-	-	-	-	-
$^1(\pi_H\pi_L^*)\rightsquigarrow\ ^3(\pi_{H-1}\pi_L^*)_x$	3188	-	19	41	0.01	12	$1.4 \cdot 10^9$
$^1(\pi_H\pi_L^*)\rightsquigarrow\ ^3(\pi_{H-1}\pi_L^*)_x$	3188	-	19	41	0.1	96	$4.0 \cdot 10^9$
$^1(\pi_H\pi_L^*)\rightsquigarrow\ ^3(\pi_{H-1}\pi_L^*)_x$	3188	-	19	41	1	1045	$9.0 \cdot 10^{10}$
$^1(\pi_H\pi_L^*)\rightsquigarrow\ ^3(\pi_{H-1}\pi_L^*)_x$	3188	-	19	41	10	10395	$3.2 \cdot 10^{11}$
$^1(\pi_H\pi_L^*)\rightsquigarrow\ ^3(\pi_{H-1}\pi_L^*)_x$	3188	-	19	41	100	106107	$2.6 \cdot 10^{11}$
$^1(\pi_H\pi_L^*)\rightsquigarrow\ ^3(\pi_{H-1}\pi_L^*)_y$	3188	-	19	41	0.01	12	$1.6 \cdot 10^9$
$^1(\pi_H\pi_L^*)\rightsquigarrow\ ^3(\pi_{H-1}\pi_L^*)_y$	3188	-	19	41	0.1	96	$5.2 \cdot 10^9$
$^1(\pi_H\pi_L^*)\rightsquigarrow\ ^3(\pi_{H-1}\pi_L^*)_y$	3188	-	19	41	1	1045	$9.7 \cdot 10^{10}$
$^1(\pi_H\pi_L^*)\rightsquigarrow\ ^3(\pi_{H-1}\pi_L^*)_y$	3188	-	19	41	10	10395	$3.5 \cdot 10^{11}$
$^1(\pi_H\pi_L^*)\rightsquigarrow\ ^3(\pi_{H-1}\pi_L^*)_y$	3188	-	19	41	100	106107	$2.8 \cdot 10^{11}$
$^1(\pi_H\pi_L^*)\rightsquigarrow\ ^3(\pi_{H-1}\pi_L^*)_z$	3188	<0.01	-	41	1	22	$2.0 \cdot 10^{-1}$
$^1(\pi_H\pi_L^*)\rightsquigarrow\ ^3(\pi_{H-1}\pi_L^*)_z$	3188	<0.01	-	41	10	206	$3.3 \cdot 10^{-1}$
$^1(\pi_H\pi_L^*)\rightsquigarrow\ ^3(\pi_{H-1}\pi_L^*)_z$	3188	<0.01	-	41	100	2107	$4.0 \cdot 10^{-1}$

TABLE VI: AL: Calculated rate constants k_{ISC} [s^{-1}] for (S $\rightsquigarrow$ Tn) ISC channels of the $^1(n\pi^*)$ state in aqueous solution. Remaining columns: adiabatic electronic energy difference ΔE^{ad} [eV], direct SOME $| < i|\hat{H}_{SO}|f > |_{q0}$ [cm^{-1}], number *#derivs* of included derivatives w.r.t. *oop* modes in vibronic SO coupling, number $\#_{acc}$ of included accepting modes, width η [cm^{-1}] of search interval, resulting number $\#v'$ of final state vibrational levels within search interval.

		parameters & and settings				**results**	
channel	-	direct SO	vib. SO	acceptors	interval	levels	rate
$i \rightsquigarrow f$	ΔE^{ad}	$\| < i\|\hat{H}_{SO}\|f > \|_{q0}$	$\#derivs$	$\#_{acc}$	η	$\#v'$	k_{ISC}
$^1(n\pi^*) \rightsquigarrow {}^3(\pi_H\pi_L^*)_x$	9047	11.06	-	41	0.0001	2104	$7.7 \cdot 10^8$
$^1(n\pi^*) \rightsquigarrow {}^3(\pi_H\pi_L^*)_x$	9047	11.06	-	41	0.001	21800	$7.1 \cdot 10^9$
$^1(n\pi^*) \rightsquigarrow {}^3(\pi_H\pi_L^*)_x$	9047	11.06	-	41	0.01	220317	$9.6 \cdot 10^9$
$^1(n\pi^*) \rightsquigarrow {}^3(\pi_H\pi_L^*)_x$	9047	11.06	-	41	0.1	2202844	$1.0 \cdot 10^{10}$
$^1(n\pi^*) \rightsquigarrow {}^3(\pi_H\pi_L^*)_y$	9047	-4.76	-	41	0.0001	2104	$1.0 \cdot 10^7$
$^1(n\pi^*) \rightsquigarrow {}^3(\pi_H\pi_L^*)_y$	9047	-4.76	-	41	0.001	21800	$9.5 \cdot 10^7$
$^1(n\pi^*) \rightsquigarrow {}^3(\pi_H\pi_L^*)_y$	9047	-4.76	-	41	0.01	220317	$1.3 \cdot 10^8$
$^1(n\pi^*) \rightsquigarrow {}^3(\pi_H\pi_L^*)_y$	9047	-4.76	-	41	0.1	2202844	$1.4 \cdot 10^8$
$^1(n\pi^*) \rightsquigarrow {}^3(\pi_H\pi_L^*)_z$	9047	-	-	-	-	-	-
$^1(n\pi^*) \rightsquigarrow {}^3(n\pi^*)_x$	2525	-	19	41	0.001	14	$1.8 \cdot 10^7$
$^1(n\pi^*) \rightsquigarrow {}^3(n\pi^*)_x$	2525	-	19	41	0.01	126	$2.3 \cdot 10^9$
$^1(n\pi^*) \rightsquigarrow {}^3(n\pi^*)_x$	2525	-	19	41	0.1	1381	$3.5 \cdot 10^8$
$^1(n\pi^*) \rightsquigarrow {}^3(n\pi^*)_x$	2525	-	19	41	1	13747	$3.8 \cdot 10^8$
$^1(n\pi^*) \rightsquigarrow {}^3(n\pi^*)_y$	2525	-	19	41	0.001	14	$1.1 \cdot 10^5$
$^1(n\pi^*) \rightsquigarrow {}^3(n\pi^*)_y$	2525	-	19	41	0.01	126	$4.2 \cdot 10^8$
$^1(n\pi^*) \rightsquigarrow {}^3(n\pi^*)_y$	2525	-	19	41	0.1	1381	$5.4 \cdot 10^7$
$^1(n\pi^*) \rightsquigarrow {}^3(n\pi^*)_y$	2525	-	19	41	1	13747	$8.3 \cdot 10^7$
$^1(n\pi^*) \rightsquigarrow {}^3(n\pi^*)_z$	2525	-0.16	-	41	0.1	8	$3.7 \cdot 10^1$
$^1(n\pi^*) \rightsquigarrow {}^3(n\pi^*)_z$	2525	-0.16	-	41	1	65	$6.6 \cdot 10^4$
$^1(n\pi^*) \rightsquigarrow {}^3(n\pi^*)_z$	2525	-0.16	-	41	10	595	$6.5 \cdot 10^4$
$^1(n\pi^*) \rightsquigarrow {}^3(\pi_{H-1}\pi_L^*)_x$	5194	-3.71	-	41	0.1	264	$3.0 \cdot 10^9$
$^1(n\pi^*) \rightsquigarrow {}^3(\pi_{H-1}\pi_L^*)_x$	5194	-3.71	-	41	1	2624	$1.3 \cdot 10^9$
$^1(n\pi^*) \rightsquigarrow {}^3(\pi_{H-1}\pi_L^*)_x$	5194	-3.71	-	41	10	25807	$1.7 \cdot 10^9$
$^1(n\pi^*) \rightsquigarrow {}^3(\pi_{H-1}\pi_L^*)_y$	5194	-2.38	-	41	0.1	264	$1.3 \cdot 10^9$
$^1(n\pi^*) \rightsquigarrow {}^3(\pi_{H-1}\pi_L^*)_y$	5194	-2.38	-	41	1	2624	$7.0 \cdot 10^8$
$^1(n\pi^*) \rightsquigarrow {}^3(\pi_{H-1}\pi_L^*)_y$	5194	-2.38	-	41	10	25807	$5.4 \cdot 10^8$
$^1(n\pi^*) \rightsquigarrow {}^3(\pi_{H-1}\pi_L^*)_z$	5194	-	-	-	-	-	-

TABLE VII: AL: Calculated rate constants k_{ISC} [s^{-1}] for (S $\rightsquigarrow$ Tn) ISC channels of the $^1(\pi_H\pi^*_L)$ state in aqueous solution. Remaining columns: adiabatic electronic energy difference ΔE^{ad} [eV], direct SOME $| < i|\hat{H}_{SO}|f > |_{q0}$ [cm^{-1}], number $\#derivs$ of included derivatives w.r.t. *oop* modes in vibronic SO coupling, number $\#_{acc}$ of included accepting modes, width η [cm^{-1}] of search interval, resulting number $\#v'$ of final state vibrational levels within search interval.

	parameters & and settings					**results**	
channel	-	direct SO	vib. SO	acceptors	interval	levels	rate
$i \rightsquigarrow f$	ΔE^{ad}	$\vert < i\vert\hat{H}_{SO}\vert f > \vert_{q0}$	$\#derivs$	$\#_{acc}$	η	$\#v'$	k_{ISC}
$^1(\pi_H\pi^*_L)\rightsquigarrow {}^3(\pi_H\pi^*_L)_x$	6615	-	19	41	0.0001	1355	$1.3 \cdot 10^5$
$^1(\pi_H\pi^*_L)\rightsquigarrow {}^3(\pi_H\pi^*_L)_x$	6615	-	19	41	0.001	13316	$2.4 \cdot 10^5$
$^1(\pi_H\pi^*_L)\rightsquigarrow {}^3(\pi_H\pi^*_L)_x$	6615	-	19	41	0.01	133013	$5.7 \cdot 10^5$
$^1(\pi_H\pi^*_L)\rightsquigarrow {}^3(\pi_H\pi^*_L)_y$	6615	-	19	41	0.0001	1355	$8.0 \cdot 10^4$
$^1(\pi_H\pi^*_L)\rightsquigarrow {}^3(\pi_H\pi^*_L)_y$	6615	-	19	41	0.001	13316	$9.4 \cdot 10^4$
$^1(\pi_H\pi^*_L)\rightsquigarrow {}^3(\pi_H\pi^*_L)_y$	6615	-	19	41	0.01	133013	$1.4 \cdot 10^5$
$^1(\pi_H\pi^*_L)\rightsquigarrow {}^3(\pi_H\pi^*_L)_z$	6615	-0.01	-	41	0.01	4019	7.8
$^1(\pi_H\pi^*_L)\rightsquigarrow {}^3(\pi_H\pi^*_L)_z$	6615	-0.01	-	41	0.1	40084	$5.7 \cdot 10^1$
$^1(\pi_H\pi^*_L)\rightsquigarrow {}^3(\pi_H\pi^*_L)_z$	6615	-0.01	-	41	1	399325	$6.9 \cdot 10^1$
$^1(\pi_H\pi^*_L)\rightsquigarrow {}^3(\pi_{H-1}\pi^*_L)_x$	2762	-	19	41	0.1	17	$6.3 \cdot 10^5$
$^1(\pi_H\pi^*_L)\rightsquigarrow {}^3(\pi_{H-1}\pi^*_L)_x$	2762	-	19	41	1	257	$9.5 \cdot 10^7$
$^1(\pi_H\pi^*_L)\rightsquigarrow {}^3(\pi_{H-1}\pi^*_L)_x$	2762	-	19	41	10	2569	$1.1 \cdot 10^8$
$^1(\pi_H\pi^*_L)\rightsquigarrow {}^3(\pi_{H-1}\pi^*_L)_x$	2762	-	19	41	100	26325	$9.5 \cdot 10^7$
$^1(\pi_H\pi^*_L)\rightsquigarrow {}^3(\pi_{H-1}\pi^*_L)_y$	2762	-	19	41	0.1	17	$3.4 \cdot 10^5$
$^1(\pi_H\pi^*_L)\rightsquigarrow {}^3(\pi_{H-1}\pi^*_L)_y$	2762	-	19	41	1	257	$6.4 \cdot 10^6$
$^1(\pi_H\pi^*_L)\rightsquigarrow {}^3(\pi_{H-1}\pi^*_L)_y$	2762	-	19	41	10	2569	$3.1 \cdot 10^7$
$^1(\pi_H\pi^*_L)\rightsquigarrow {}^3(\pi_{H-1}\pi^*_L)_y$	2762	-	19	41	100	26325	$2.9 \cdot 10^7$
$^1(\pi_H\pi^*_L)\rightsquigarrow {}^3(\pi_{H-1}\pi^*_L)_z$	2762	<0.01	-	41	1	3	$6.9 \cdot 10^1$
$^1(\pi_H\pi^*_L)\rightsquigarrow {}^3(\pi_{H-1}\pi^*_L)_z$	2762	<0.01	-	41	10	51	$2.6 \cdot 10^1$
$^1(\pi_H\pi^*_L)\rightsquigarrow {}^3(\pi_{H-1}\pi^*_L)_z$	2762	<0.01	-	41	100	627	$5.5 \cdot 10^1$

---

[1] M. S. Grodowski, B. Veyret and K. Weiss, *Photochem. Photobiol.*, 1977, **26**, 341.

[2] M. Sikorski and D. Prukala and M. Insińska-Rak and I. Khmelinskii and D. R. Worrall and S. L. Williams and J. Hernando and J. L. Bourdelande and J. Koputa and E. Sikorska, *J. Photochem. Photobiol. A*, 2008, **200**, 148.

[3] M. Sikorski, E. Sikorska, D. R. Worrall and F. Wilkinson, *J. Chem. Soc. Faraday Trans.*, 1998, **94**, 2347.

[4] E. Sikorska, I. V. Khmelinskii, D. R. Worrall, J. Koput and M. Sikorski, *J. Fluores.*, 2004, **14**, 57.

[5] M. Sung, T. A. Moore and P.-S. Song, *J. Am. Chem. Soc.*, 1972, **94**, 1730.

[6] M. Sikorski, E. Sikorska, F. Wilkinson and R. P. Steer, *Can. J Chem.*, 1999, **77**, 472.

[7] J. Komasa, J. Rychlewski and J. Koziol, *J. Mol. Struct. (Theochem)*, 1988, **170**, 205.

[8] R. H. Dekker, B. N. Srinivasan, J. R. Huber and K. Weiss, *Photochem. Photobiol.*, 1973, **18**, 457.

[9] E. Sikorska, I. V. Khmelinskii, W. Prukala, S. L. Williams, M. Patel, D. R. Worrall, J. L. Bourdelande, J. Koput and M. Sikorski, *J. Phys. Chem. A*, 2004, **108**, 1501.

[10] A. Toniolo and M. Persico, *J. Chem. Phys.*, 2001, **115**, 1817.

[11] A. Toniolo and M. Persico, *J. Comput. Chem.*, 2001, **22**, 968.

[12] B. R. Henry and W. Siebrand, *Organic Molecular Photophysics*, John Wiley & Sons, London, 1973, vol. 1, pp. 153.

[13] J. Tatchen, N. Gilka and C. M. Marian, *Phys. Chem. Chem. Phys.*, 2007, **9**, 5209.

[14] S. Salzmann, V. Martinez-Junza, B. Zorn, S. E. Braslavsky, M. Mansurova, C. M. Marian and W. Gärtner, *J. Phys. Chem. A*, 2009, **submitted**.

Paper V

Influence of the LOV domain on low-lying excited states of flavin: A combined quantum-mechanics / molecular-mechanics investigation

Susanne Salzmann, Mario R. Silva-Junior, Walter Thiel, and Christel M. Marian

J. Phys. Chem. B, *submitted.*

Influence of the LOV domain on low-lying excited states of flavin: A combined quantum-mechanics / molecular-mechanics investigation

Susanne Salzmann,[†] Mario R. Silva-Junior,[‡] Walter Thiel,[‡] and Christel M. Marian[*,†]

Institute of Theoretical and Computational Chemistry, Heinrich Heine University Düsseldorf,
Universitätsstr. 1, D-40225 Düsseldorf, Germany, and Max-Plack-Institut für Kohlenforschung,
Kaiser-Wilhelm-Platz 1, 45470 Mülheim an der Ruhr, Germany

E-mail: Christel.Marian@uni-duesseldorf.de

Abstract

The ground and low-lying excited states of flavin mononucleotide (FMN) in the light, oxygen, and voltage sensitive (LOV) domain of the blue-light photosensor YtvA of *Bacillus subtilis* have been studied by means of combined quantum-mechanical / molecular-mechanical (QM/MM) methods. The FMN cofactor (without the side chain) was treated with density functional theory (DFT) for the geometry optimizations and a combination of DFT and multi-reference configuration interaction (MRCI) for the determination of the excitation energies, while the protein environment was represented by the CHARMM force field. In addition, several important amino acid side chains, including the reactive cysteine residue, were included in the QM region in order to probe their influence on the spectral properties of the cofactor in

---

[†] Heinrich-Heine Universität Düsseldorf
[‡] Max-Plack-Institut für Kohlenforschung

two protein conformations. Spin-orbit coupling has been taken into account employing an efficient, non-empirical spin-orbit mean-field Hamiltonian.

Our results reveal that the protein environment of YtvA-LOV induces spectral shifts for the $(\pi\pi^*)$ states that are similar to those in aqueous solution. In contrast, the blue shifts of the $(n\pi^*)$ states are smaller in the protein environment, enabling a participation of these states in the decay processes of the optically bright S_1 state. Increased spin-orbit coupling between the initially populated S_1 state and the T_1 and T_2 states is found in YtvA-LOV as compared to free lumiflavine in water. The enhanced singlet-triplet coupling is brought about partially by configuration interaction with $(n\pi^*)$ states at the slightly out-of-plane distorted minimum geometry. In addition, an external heavy-atom effect is observed when the sulfur atom of the nearby cysteine residue is included in the QM region, in line with experimental findings.

Introduction

In recent years flavins, in the form of flavin mononucleotide (FMN) and flavin adenine dinucleotide (FAD), have received growing attention especially due to their decisive role in blue light-mediated signal transduction in plants and bacteria.[1] Until today, three different kinds of flavin-based photoreceptor families are known, namely cryptochromes (cry), BLUF (Blue Light sensing Using FAD) containing proteins, and phototropins (phot).[1] The latter are plasma membrane-associated proteins which are primary photoreceptors for the mediation of phototropic plant movement. Two light, oxygen and voltage-sensitive (LOV) domains are present in each phot protein. In the dark-adapted state of the LOV domains FMN is bound noncovalently as cofactor. Upon absorption of blue light, the LOV domain undergoes a photocycle that leads to photobleaching (see Figure 1). The primary step after light absorption hereby involves a rapid decay of the excited singlet state to the lowest excited triplet state via an intersystem crossing (ISC) mechanism. In a second step a metastable covalent adduct of a nearby cysteine residue and the isoalloxazine framework of the chromophore is generated resulting in a structural signal that affects autophosphorylation.

FMN can be divided into two parts: (A) the isoalloxazine (benzol[*g*]pteridine-2,4(3H,10H)-

dione) core ring and (B) the ribophosphyl chain (see Figure 2). Since the photophysical and photochemical behavior of flavins is dominated by the isoalloxazine core, the experimental absorption and emission spectra of FMN, riboflavin (RF), and lumiflavin (LF) are very similar.[2,3] In the energy regime up to 5 eV (500 - 250 nm) the absorption spectrum of neutral, oxidized isoalloxazines exhibits three bands. While the first and third absorption bands are nearly unaffected by the environment, the second absorption band shows pronounced solvatochromism. Experiments have shown that the influence of the solvent polarity on the solvent-induced red shift of this band is rather low and that the ability of the solvent to form hydrogen bonds plays a more decisive role.[4,5] As our recent work demonstrates,[6,7] not only the ordering of low-lying potential energy hypersurfaces, but also the mechanism of triplet generation depends on the environment. In vacuum ISC proceeds from the S_1 $^1(\pi\pi^*)$ to the T_2 $^3(n\pi^*)$ state via a direct spin-orbit coupling (SOC) mechanism. In aqueous solution this ISC channel is energetically not accessible due to the blue shift of the $^3(n\pi^*)$ state. The high triplet quantum yield observed in experiment[8] cannot be explained by direct SOC. Instead, ISC between S_1 $^1(\pi\pi^*)$ and T_2 $^3(\pi\pi^*)$ is enhanced by a vibronic SOC mechanism, a process common to various other organic chromophores.[9,10]

Experimental data shows that the FMN binding pocket is highly conserved in the wild type amino acid (AA) sequences of LOV domains from various organisms.[1,11,12] Figure 3 (left) depicts the X-ray structure of the FMN binding site in the LOV domain of the bacterial photosensor YtvA, from *Bacillus subtilis*, a flavoprotein strictly related to the plant blue-light receptors in phototropins,[13] which positively regulates the general stress transcription factor and is activated by blue light absorption.[14–16] In accordance to the polar and nonpolar moieties of the isoalloxazine (IA) core ring, the binding pocket can be divided into polar and nonpolar regions. The benzene part of the cofactor is embedded into a nonpolar region, mainly built up from LEU, ILE and VAL. The heteroatoms of the pteridine moiety are coordinated by four highly conserved polar AAs, GLN66, ASN94, ASN104, and GLN123, respectively. Since, as mentioned above, a major part of the solvent shift of flavins has been attributed to the ability of the solvent to build up a hydrogen-bonding network around the heteroatom moiety of flavin,[4,5] a significant influence of these four

AAs on the energetic order of the low-lying singlet and triplet states in LOV domains, and hence the photophysics, is anticipated. With regard to the ISC mechanism, the influence of CYS62 is of interest, too. The presence of this cysteine residue has been made responsible for a shortening of the excited singlet state lifetime and an enhanced ISC rate in LOV-bound FMN as compared to FMN in solution or cysteine-less mutants, due to a heavy-atom effect of the sulfur atom near the flavin isoalloazine ring.[17] In the X-ray structures of YtvA-LOV and the phot1-LOV1 of the algae *Chlamydomonas reinhardtii (Cr)* (PDB codes 2PR5 and 1N9L, respectively), two positions are found for the sulfur atom of the reactive residue CYS62 (see Figure 3, left), with a probability of 70% for conformation A (confA) and 30% for conformation B (confB), respectively.[11,18] This finding, of course, raises the question whether the two cysteine conformations affect the photophysics in a different manner.

To our knowledge, only three quantum chemical investigations of flavin in the LOV domain exist.[19–21] All these studies employ the phot1 LOV1 domain of *Chlamydomonas reinhardtii* (PDB codes 1N9L and 1N9N)[18] and the main focus lies on the adduct formation mechanism. Among these, only Zenichowski et *al.*[19] conducted calculations on the absorption properties of LF in phot1-LOV1. However, this investigation was restricted to the vertical excitation energies at the nuclear arrangements of the dark-adapted X-ray structure (PDB code 1N9L)[18] and the LOV domain was modeled as LF with the functional groups of seven AAs of the LOV binding pocket.[19]

In this work, the ground and low-lying excited states of FMN in the LOV domain of the blue-light photosensor YtvA of *Bacillus subtilis* are investigated using combined quantum-mechanical / molecular-mechanical (QM/MM) methods.[22,23] Our earlier work on guanine has shown that this approach is an effective means for the description of solvent effects on absorption spectra.[24] In addition to the FMN cofactor (modeled as LF), several important AA side chains, including GLN66, ASN94, ASN104, and GLN123 as well as the reactive residue CYS62, were accounted for quantum mechanically, in order to probe the influence of the particular choice of QM region on ground state geometries and vertical excitation energies. At the minimum nuclear arrangements of the primarily excited S_1 state, spin-orbit coupling was determined, taking the cofactor and the two conformations of CYS62 into account. On the basis of these calculations as well as comparison to earlier work on flavins in vacuum and solution,[6,7] we discuss the events that take place immediately after blue-light absorption.

Methods and computational details

Setup and choice of QM regions

The initial geometry was based on an X-ray structure (PDB code 2PR5).[11] The unit cell of the crystal structure is built up of two nearly identical monomers. The differences are mainly in the loops between the structural units and can result from the different contact partners in the asymmetric unit cell. These differences are not relevant for our purposes since the vertical and adiabatic excitation energies of the flavin cofactor will only be influenced by the AA side chains in the binding pocket close to the cofactor, and not by distant loops. Therefore, it was considered sufficient to use only the core LOV domain of monomer A for our investigation. On the other hand, the two orientations of CYS62 observed in the X-ray structure (confA and confB, see Figure 3, left) are expected to affect the spectroscopic properties of the nearby cofactor, and hence both were considered in the present work. The simulated system comprised the LOV domain, consisting of 101 amino acids, 240 crystallographic water molecules, and the FMN cofactor, solvated in a 35 Å water sphere. The detailed setup procedure at the MM level is described in detail in Supporting Information (SI). Here we only note that the needed force-field parameters for the FMN cofactor were taken from the literature,[25] with some adjustment of partial MM charges (see SI). During system setup, all (non-hydrogen) atoms of protein and cofactor were frozen to preserve the X-ray structure, and only hydrogen atoms and water molecules were allowed to move during these initial MM relaxation steps.

Since the optically active part of the LOV domains is the IA core of FMN, the smallest QM region denoted by QM-1 in the following (see Figure 4) merely consists of LF. In this case, there is only one covalent bond between the QM and the MM parts, which was saturated by a hydrogen link atom. The cofactor was cut at the sugar chain between the first and second carbon center counted from the isoaloxazine ring (see Figure 2). Since the residue CSY62 and the four polar side chains of GLN66, ASN94, ASN104, and GLN123 are expected to impact on the photophysics of the cofactor, the functional groups of these residues are taken into account in the more extended QM regions QM-2 to QM-4 (see Figure 4). QM-2 includes all atoms of GLN66, ASN94, ASN104, and GLN123 that can contribute to the hydrogen-bonding network. QM-3 and QM-4 differ from QM-1 and QM-2, respectively, by an additional methanethiol that models CYS62. To account for possible effects arising from the different sulfur positions of CYS62, calculations were performed both for confA and confB.

QM/MM calculations

The QM/MM calculations were done with the ChemShell package.[26] Two different QM methods were employed (see below). The MM part was described by the CHARMM/TIP3P[27,28] force field, run through the DL_POLY code[29] in ChemShell. The electrostatic interaction between QM and MM atoms was taken into account by including all MM point charges in the one-electron part of the QM Hamiltonian. The boundary region was treated via a link atom approach with the charge-shift scheme.[26,30]

All QM/MM geometry optimizations were carried out using (time dependent) density functional theory ((TD)DFT/B3LYP/TZVP) and the TURBOMOLE 5.10[31] program package. They employed the HDLC optimizer[32] in ChemShell. The optimized region consisted of the QM region and all MM residues with a distance of less than 9 Å from FMN. The ground-state geometry was optimized for all possible combinations of QM region (QM-1 to QM-4) and conformation (confA, confB). For the excited states, nuclear arrangements were determined for the QM-1 model only, for the following reason. It is well known that TDDFT with standard functionals does not describe the energetic position and the long-range behavior of charge transfer (CT) states correctly.[33] In our case, low-lying CT states are found at the TDDFT/B3LYP level for QM regions that extend beyond LF, i.e., for QM-2 to QM-4 which include neighboring residues. They result from the excitation of one electron from an occupied orbital of one of these residues to an unoccupied orbital of flavin. However, DFT/MRCI calculations (see below) show these low-lying CT states to be TDDFT/B3LYP artifacts, and therefore we refrained from excited-state TDDFT-based geometry optimizations for systems with QM regions QM-2 to QM-4.

Vertical electronic excitation energies, dipole (transition) moments, and oscillator strengths were obtained from subsequent single-point QM/MM calculations using the combined density functional theory / multi-reference configuration interaction (DFT/MRCI) method of Grimme and Waletzke.[34] Earlier QM calculations on thiophene had resulted in a marked stabilization of low-lying excited valence states upon augmentation of the basis set with a diffuse p function on sulfur (exponent 0.009988).[35] Therefore, using the QM-3 model in both conformations, we performed benchmark calculations on the vertical excitation energies with different basis sets on sulfur (TZVP, TZVPP, and TZVPP+R, see Ref.[35] for details) and a TZVP basis on all other atoms. The results were found to depend only marginally on the choice of basis set. Therefore, we adopted the TZVP basis set for all atoms in the present study. After careful calibration the number of roots determined in the MRCI calculations on the singlet (triplet) manifold was chosen to be 5 (7) for QM-1 and QM-2, and 6 (8) for QM-3 and QM-4, respectively.

As a further test, harmonic vibrational frequencies of only the QM-1 region were calculated numerically at the QM/MM optimized geometries of the ground and excited states, using the NumForce script from the TURBOMOLE 5.10[31] program package (with energies and gradients computed at the QM level with inclusion of MM charges). As expected, these calculations at non-stationary points produce several (4-5) imaginary frequencies (see SI for details). Some of these are due to the external constraints during QM/MM geometry optimization which transform the translational and rotational motions of free LF to very low-frequency librations with respect to the protein cage; in the test calculations, these librations may be found at small imaginary frequencies since the QM/MM interactions are only partly taken into account (electrostatics). For similar reasons, the torsion of the methyl group at the C(8) center has a small imaginary frequency in the S_1 and T_2 states. Moreover, one imaginary mode is found around $\nu_1 \approx i260\mathrm{cm}^{-1}$, corresponding to a rotation of the methyl group at the N(10) center. This imaginary frequency arises as the methyl group is forced into its position by the link atom. In order to check the influence of rotations of the C(8) and N(10) methyl groups on the vertical excitation energies we performed constrained minimum energy path optimizations of the electronic ground state of free LF along these two reaction coordinates. Subsequent DFT/MRCI calculation along these paths reveal that the rotational barriers are small (around 0.06 eV) and that the vertical excitation energies vary by less than 0.05 eV (i.e., by far less than the typical error bar of the DFT/MRCI method[34,36]). In summary, we conclude from these tests that the optimized geometries indeed represent minima with regard to all essential internal coordinates and that the presence of "soft" imaginary modes for librations and methyl rotations does not significantly affect the calculated spectra.

Spin-orbit matrix elements (SOMEs) between the correlated DFT/MRCI wavefunctions were computed using the spin-orbit coupling kit (SPOCK).[37,38] For reasons of efficiency, the one-center mean-field approximation to the Breit-Pauli Hamiltonian was applied for the description of the spin-orbit coupling. This nonempirical effective one-electron operator treats the expensive two-electron terms of the full Breit-Pauli Hamiltonian in a Fock-like manner.[39,40]

Results and discussion

Ground-state geometries and vertical excitation energies

The minimum nuclear arrangements of LF in YtvA-LOV were determined for all four QM regions (see Figure 4) in combination with each of the two CYS62 conformations. For a given QM region, the optimized ground-state bond lengths for confA and confB differ in most instances by at most 0.1 - 0.2 pm. Therefore, only the results for confA are displayed in Table 1 (see SI for the complete list of optimized ground-state bond lengths of LF). In order to evaluate structural changes caused by surrounding AA residues, results for LF in vacuum and aqueous solution, taken from previous work,[6,7] are included in Table 1. Due to the protein environment, the chromophoric ring system deviates slightly from planarity, with the relevant dihedral angles being distorted by less than 3 degrees. As a general trend, the equilibrium bond distances of LF in YtvA-LOV are closer to the results in water than to those in the isolated molecule. The structural changes are more pronounced for the pteridine moiety, as the lone-pair orbitals of the N(1), O(2), O(4), and N(5) centers form strong hydrogen bonds with the surrounding AA residues or water molecules. Both carbonyl bonds are lengthened by these hydrogen-bonding interactions. For example, the C(2)-O bond is stretched by 2.1 pm in our water model (see Ref. [6,7] for details), and by 2.2-2.3 pm in YtvA-LOV when the hydrogen-bonding residues GLN66, ASN94, ASN104, and GLN123 are explicitly treated in the QM region (QM-2, QM-4); the elongation is smaller (1.5-1.6 pm) when these residues are handled at the MM level.

When comparing the vertical excitation energies, we see significant differences not only between the various QM regions, but also between the two conformations considered (confA, confB). Illustrative results for DFT/MRCI excitation energies are compiled in Table 2. Again, results for LF in vacuum and aqueous solution[6,7] are included for comparison (see SI for a complete list of vertical excitation energies for all combinations of QM region and conformation). To aid the discussion, the molecular orbitals (MOs) of QM-1/confA are displayed in Figure 5. For QM-1 and QM-2 there are no significant differences between the MOs of confA and confB, while the addition of methanethiol (QM-3 and QM-4) has some effect (see below).

In accordance with our previous findings for vacuum and aqueous solution, the lowest-lying singlet state (S_1) corresponds to the optically bright ($\pi_H \rightarrow \pi_L^*$) transition. Depending on the combination of QM region and conformation, its vertical excitation energy ranges between 2.77 eV and 2.86 eV, in excellent agreement with the experimental absorption maximum at 2.76 eV. However, as we have shown recently for isolated LF and related molecules, vertical excitation energies and band maxima do not coincide.[7] In these compounds the calculated band maxima are located 0.1-0.2 eV below the corresponding vertical excitation energies. Similar shifts are expected here, in line with the general experience that DFT/MRCI tends to underestimate vertical excitation energies by around 0.2 eV.[36]

Similar vertical excitation energies are found for the second and third excited singlet state (S_2

and S_3). These two states are located between 0.4 eV and 0.6 eV above the blue-light activated S_1 state. In confA the S_2 state is mainly dominated by the optically bright $(\pi_{H-1} \rightarrow \pi_L^*)$ transition, while in the S_3 state the $(n_N \rightarrow \pi_L^*)$ excitation prevails. For mere LF (QM-1) these two excited states are almost degenerate. Extension of the QM region such that the cysteine is included (QM-3, QM-4) yields a preferential red shift of the $(\pi\pi^*)$ excited S_2 state in confA, lifting the degeneracy with the S_3 state. In confB the S_2 and S_3 states are degenerate, even causing a mixture of the $(\pi\pi^*)$ and $(n\pi^*)$ electronic character for QM-3 and QM-4. As Figure 6 illustrates for QM-3, a lone-pair orbital (p_S) at the sulfur center of CYS62 mixes with the π_{H-1} MO of the cofactor. Since in the latter MO the electron density is mainly located at the benzene moiety of LF, the pronounced red shift of S_2 in QM-3 and QM-4 of confA can be attributed to the interaction between the p_S and π_{H-1} orbitals. This finding is in line with recent fluorescence line narrowing experiments that identify a weak electronic interaction between the flavin and the thiol group of the conserved cysteine.[17] Comparison with DFT/MRCI results for the S_2 state of LF in vacuum and water shows that the environmental influence of the binding pocket of YtvA-LOV closely resembles the situation in aqueous solution, with a pronounced red shift in both media (see Table 2). This is also in line with experimental studies which locate the maximum of the second absorption band around 3.3 eV in YtvA and water,[4,7,13,41,42] in good agreement with our DFT/MRCI results.

According to our recent work, the low-lying $^1(n\pi^*)$ states are blue-shifted in water with respect to the gas phase by about 0.3 eV for the $^1(n_N \rightarrow \pi_L^*)$ state and 0.7 eV for the $^1(n_O \rightarrow \pi_L^*)$ state.[7] In YtvA-LOV, the latter state (S_4) shows a similar solvent shift (by about 0.7 in QM-1 and 0.5 in QM-4) while the energetic position of the former state (S_3) is less affected by the protein environment (by about 0.1 eV in QM-1, almost no shift in QM-4). The four polar AA side chains of YtvA-LOV and the explicit water molecules of our previously used solvent model[7] coordinate the carbonyl groups of the pteridine moiety in a similar manner (see Figure 3). As a substantial part of the solvent shift of the $(n_O \rightarrow \pi_L^*)$ states arises from hydrogen bonding,[6] we find comparable vertical excitation energies for these states in protein and water. In variance to this behavior, the blue shift of the $(n_N \rightarrow \pi_L^*)$ states has been shown to originate from the polarity of the solvent.[6] Hence, little solvent shift of this state is to be expected in YtvA-LOV which agrees with the results of our best model (QM-4).

Contrary to an earlier TDDFT study of phot1-LOV1 by Zenichowski et *al.*,[19] we do not find low-energy CT excitations below or slightly above the optically bright S_1 state at the DFT/MRCI level. However, we do identify one CT state which corresponds to the excitation of an electron from a sulfur lone-pair (see Figure 6) into the LUMO of LF. In the singlet and triplet manifold this state is situated well above the S_1 state (by 0.8 eV in confA and 1 eV in confB), and thus it does not contribute to the S_1 photophysics studied presently.

At the FC point, two excited triplet states, T_1 and T_2, are found below the S_1 state, with $(\pi_H \rightarrow \pi_L^*)$ and $(\pi_{H-1} \rightarrow \pi_L^*)$ electronic structures, respectively. The energetic position of the T_1 state is nearly unaffected by the environment and ranges between 2.15 eV and 2.21 eV. Compared to vacuum, the T_2 state is red-shifted in water (by about 0.3 eV) and YtvA-LOV (by about 0.3-0.5 eV). As in the case of its singlet counterpart (S_2), the red shift of the T_2 state is more pronounced in QM-3 and QM-4 of confA and can be attributed to the interaction between the p_S and π_{H-1} orbitals (see Figure 6). Slightly above the S_1 state a third excited triplet state is found in YtvA-LOV, corresponding to the $(n_N \rightarrow \pi_L^*)$ transition. Like its singlet counterpart, this state shows little solvent shift (by about 0.2 eV in QM-1 and less than 0.1 eV in QM-4) in the protein as compared to vacuum results. As we shall see later, the energetic position of the T_2 and T_3 states will be of significance for the deexcitation of the S_1 state.

Minima of low-lying excited states and adiabatic excitation energies

We optimized the nuclear arrangements of the first excited singlet state and the two lowest-lying triplet states in both conformations (confA and confB) using the smallest QM region (QM-1). As in the case of the ground state, the structural parameters of confA and confB differ only slightly. Therefore, Figure 7 shows the structural changes of the excited states relative to the ground state only for confA (see SI for the complete list of optimized bond lengths of LF). In addition, the respective structural changes relative to LF in vacuum are given for comparison.[6,7] Adiabatic excitation energies are collected in Table 3 together with results of previous theoretical work and experiment.[6,7,21,43] The values, addressed as best estimates in that table, are obtained by adding the differences between our QM-1 and QM-4 results in the FC region to the adiabatic energies, as obtained within the QM-1 model.

The S_1 and T_1 states are both dominated by the ($\pi_H \rightarrow \pi_L^*$) excitation. In a simple picture, the structural changes in the excited-state nuclear arrangements, relative to those of the ground state, reflect the changes in character between the two frontier orbitals. Inspection of Figure 5 and Figure 7 shows, for example, that the elongations of the C(4a)-N(5), C(6)-C(7), and C(10)-C(10a) bonds compare well with a change of character in the corresponding frontier orbitals at these bonds from bonding to antibonding. For the T_2 state, we obtain a minimum nuclear arrangement where the C(7)-C(8) is shortened and the C(4a)-N(5) and C(8)-C(9) bonds are significantly elongated. Again, this finding is consistent with an excitation from the π_{H-1} orbital into the π_L^* orbital.

The computed adiabatic excitation energies are quite similar for confA and confB. It is remarkable that the adiabatic excitation energies of the S_1 and T_1 states are comparable for YtvA-LOV and vacuum, which is in line with the observed solvent independence of the $S_0 \rightarrow S_1$ absorption band. Comparison to experimental data shows convincing agreement (see Table 3), as zero-point vibrational corrections are expected to yield a small red shift on the adiabatic excitation energy. The vertical DFT/MRCI emission energy is 2.36 eV for confA and 2.39 eV for confB, while the experimental fluorescence spectrum exhibits a peak around 2.49 eV and a shoulder around 2.37 eV.[13] We determined the fluorescence rate constant to be 4×10^7 s^{-1} for both conformations, which is very similar to our results for LF in vacuum (5×10^7 s^{-1}). Measurements show heterogeneities in the fluorescence lifetimes, which have been related to alternative protein conformations or the presence of protein dimers.[43] Using the relation $k_F = \frac{\tau_F}{\Phi_F}$ the experimental fluorescence rate constant can be ascertained to 6×10^7 s^{-1}, in good qualitative agreement to our findings.

For the T_1 state our adiabatic DFT/MRCI excitation energy accords fine with experimental photocalorimetric results.[43] A slightly higher value was obtained in QM/MM calculations on Cr-LOV where restricted open-shell Hartree-Fock (ROHF) was used for describing the quantum mechanical part.[21] In contrast to S_1 and T_1, the T_2 state exhibits a significant dependence of the adiabatic excitation energy on the environment. While the adiabatic excitation energy is 2.77 eV in vacuum, the protein environment of YtvA-LOV yields a stabilization by 0.3 eV which is in line with the red shift of the vertical excitation energy of this state. As for aqueous solution, the minimum of this state is found below that of the S_1 state, which will be important with regard to the ISC mechanism (see below).[6,7]

Attempts to obtain the $^{1,3}(n_N \rightarrow \pi_L^*)$ minima were not successful due to continued root flipping in the TDDFT optimization. Compared to our gas phase results little influence of YtvA-LOV is found on the excitation energy of these states at the FC point when the best model (QM-4) is employed. We will therefore use the adiabatic excitation energies, obtained for the isolated chromophore ($^1(n_N \rightarrow \pi_L^*)$ 2.95 eV, $^3(n_N \rightarrow \pi_L^*)$ 2.61 eV), as rough estimates for the location of the corresponding minima in YtvA-LOV.

Intersystem crossing

According to El-Sayed's rule,[44] SOMEs between $(\pi\pi^*)$ and $(n\pi^*)$ states are in general much larger than SOMEs between two $(\pi\pi^*)$ states. Thus, when only direct spin-orbit coupling is considered (Condon approximation), ISC rate constants are much lower for $(\pi\pi^*) \rightsquigarrow (\pi\pi^*)$ processes than for $(\pi\pi^*) \rightsquigarrow (n\pi^*)$ processes. However, recent studies have shown that vibronic spin-orbit coupling enhances the ISC rate constants between two $(\pi\pi^*)$ states in various chromophores.[6,7,9,10] In case of vibronic spin-orbit coupling, out-of-plane distortions along the vibrational normal modes cause an interaction and thus a mixing of $(\pi\pi^*)$ and $(n\pi^*)$ states and thus an increase of the interaction. Qualitatively, the resulting enhancement of the ISC rate constants between two $(\pi\pi^*)$ states can be seen as an intensity borrowing from the much faster $(\pi\pi^*) \rightsquigarrow (n\pi^*)/(n\pi^*) \rightsquigarrow (\pi\pi^*)$ processes. However, the extent of mixing between the $(\pi\pi^*)$ and $(n\pi^*)$ states depends on the energy gap between those states:[45] Typically, the smaller the gap between $(\pi\pi^*)$ and $(n\pi^*)$ states, the larger the enhancement of the ISC process.

Within the manifold of triplet states, the energetic order of the low-lying electronic states in

YtvA-LOV is akin to our results in aqueous solution. As discussed above, two excited triplet states, T_1 and T_2, are situated below the blue-light absorbing S_1 state in the vertical absorption spectrum. When these states are relaxed to their equilibrium nuclear arrangements, their minima are found to lie about 0.6 eV and 0.2 eV, respectively, below the S_1 minimum. The lowest-lying $^3(n_N \rightarrow \pi^*)$ state is located slightly above S_1 in the vertical excitation spectrum. Our rough estimate of the adiabatic excitation energy of that state (see above) indicates that its minimum could be near degenerate with the S_1 minimum in YtvA-LOV or lie even slightly below. Although the vibrational density of states (VDOS) in the $^3(n_N \rightarrow \pi^*)$ potential well will be low at the energy of the relaxed S_1 state, a participation of the $^3(n_N \rightarrow \pi^*)$ state in the decay of S_1 via a direct spin-orbit coupling ISC mechanism is likely. Under physiological conditions vibrationally hot levels of the initial singlet state will be populated where the VDOS in the final state is higher and the transition occurs more easily.

As already discussed in the computational section, the environmental constraints transform translation and rotation of free LF into low-energy librations. As the determination of vibrational overlaps between initial and final state depends on the separation of molecular translation and rotation from vibrational degrees of freedom, we refrain from calculating the ISC rate constants in YtvA-LOV explicitly. However, we can give a qualitative picture of the situation in YtvA-LOV as we have determined the influence of the protein environment on spin-orbit coupling between low-lying states. Table 4 compiles SOMEs between the S_1 state and the T_1, T_2, and T_3 states, respectively. In addition, results for free LF in aqueous solution (modeled with COSMO) and vacuum are presented to aid the discussion. To estimate the influence of CYS62 on the SOMEs, single-point calculations for our best model (QM-4) have been performed at the QM-1 geometries.

SOMEs between the S_1 and T_1 states and between the S_1 and T_2 states are calculated to be very small, as these states are all dominated by $(\pi \rightarrow \pi^*)$ excitations. As mentioned above, due to the protein environment the chromophoric ring system does not retain planarity. In this context we note that the slight out-of-plane distortion is more pronounced for confB than for confA, which increases the admixture of $(n\pi^*)$ character into the electronic structure of initial and final states. As a result, the SOMEs for QM-1 between the S_1 and the T_2 state are found noticeably increased for confB, as compared to the results for confA or *planar* LF in water. Considering the rather small energy gap between the T_2 state and the $^3(n\pi^*)$ state this hints to a substantial enhancement of the ISC rate constants due to vibronic spin-orbit coupling. Between the S_1 and T_3 states, SOMEs are found to decrease when vacuum, QM-1, and QM-4 are compared. This finding is reflected in the electronic structure of the final state. While in the vacuum this state is a pure $(n\pi^*)$ state with an overall contribution of 80 % for the $(n_N \rightarrow \pi_L^*)$ excitations, in YtvA-LOV $(\pi \rightarrow \pi^*)$ and other excitations are mixed into the electronic structure and the amount of $(n_N \rightarrow \pi_L^*)$ excitations decreases in QM-1 and even further in QM-4. When the sulfur atom of CYS62 is included in the QM region, SOMEs between the S_1 and T_1 states and between the S_1 and T_2 states are substantially increased. This evidence for an external heavy-atom effect is in line with experimental findings. Compared to FMN in solution and cysteine-less mutants, a shortening of the S_1 lifetime by a factor of 2-3 [8,46,47] and a weak electronic interaction between the flavin and the thiol group of the conserved cysteine [17] is observed for *wild type* LOV domains.

Even without explicitly calculating ISC rate constants, we thus propose that $^1(\pi\pi^*) \rightsquigarrow ^3(\pi\pi^*)$ processes play an important role for the ISC mechanism in YtvA-LOV, enhanced by vibronic spin-orbit coupling and an external heavy-atom effect. Variations in the isoalloxazine sulfur distance, as induced by thermal vibrations, could even increase the latter effect. As a proper description of the thermal fluctuations in the excited state would necessitate dynamics simulations including non-adiabatic and spin-orbit coupling, we cannot provide definitive results at present. However, we do see large SOMEs involving radical sulfur species during the bond formation process. [48]

Summary and Conclusions

In this work we have explored the ground and low-lying excited states of FMN in the LOV domain of the blue-light photosensor YtvA of *Bacillus subtilis* by means of combined quantum-mechanical / molecular-mechanical (QM/MM) methods. For many of the properties investigated, the polar hydrogen-bonding environments in YtvA-LOV and in aqueous solution induce similar changes with respect to nonpolar environments. One example is the considerable red shift of the second band ($\pi_{H-1} \rightarrow \pi_L^*$) in the experimental absorption spectrum of YtvA which can be reproduced by our calculations. The conformation of the cysteine residue CYS62 exhibits some influence on the computed position of the second absorption band, especially if the cysteine side chain is included in the QM region. The electronic interaction between the π_{H-1} MO of the isoalloxazine core and the p_S lone-pair on sulfur is particularly pronounced for confA. Treating the four polar active-site AA side chains at the QM or MM level has only a minor effect on the vertical DFT/MRCI excitation energies. In contrast, when using TDDFT/B3LYP, the S_1 state can be described realistically only with the QM-1 region, since it acquires charge transfer character upon incorporation of these active-site residues into the QM region (QM-2, QM-4).

Within the manifold of triplet states, the energetic order of low-lying electronic states in YtvA-LOV is akin to our results in aqueous solution. We find two excited triplet states, T_1 and T_2, below the blue-light absorbing S_1 state. As they are both dominated by $(\pi \rightarrow \pi^*)$ excitations, spin-orbit coupling between S_1/T_1 and S_1/T_2 is small. The lowest-lying $^3(n\pi^*)$ state is located around 0.2 eV above S_1 in the Franck-Condon region. However, when we compare our best model (QM-4) with the findings in gas phase, we see little influence of YtvA-LOV on the energetic position of this state. Therefore, under physiological conditions, the $^1(\pi\pi^*) \rightsquigarrow ^3(n\pi^*)$ channel is assumed to be accessible in YtvA-LOV. In addition, we do expect that $(\pi\pi^*) \rightsquigarrow (\pi\pi^*)$ processes play an important role for ISC in YtvA-LOV, as they are enhanced via vibronic spin-orbit coupling and external heavy-atom effect.

Acknowledgement

Financial support by the Deutsche Forschungsgemeinschaft through SFB663/C1 and SFB663/C4 is gratefully acknowledged. S.S. would like to thank W. Gärtner (MPI Mülheim) for helpful discussions on the topic of LOV domains.

Supporting Information Available

Extended information on ground-state and excited-state nuclear arrangements, low-frequency vibrational normal modes and excitation energies is found in the Supporting Information. This material is available free of charge via the Internet at `http://pubs.acs.org`.

References

(1) Losi, A. *Photochem. Photobiol.* **2007**, *83*, 1283–1300.

(2) Bowd, A.; Byrom, P.; Hudson, J. B.; Turnbull, J. H. *Photochem. Photobiol.* **1968**, *8*, 1–10.

(3) Sung, M.; Moore, T. A.; Song, P.-S. *J. Am. Chem. Soc.* **1972**, *94*, 1730–1740.

(4) Sikorska, E.; Khmelinskii, I. V.; Prukala, W.; Williams, S. L.; Patel, M.; Worrall, D. R.; Bourdelande, J. L.; Koput, J.; Sikorski, M. *J. Phys. Chem. A* **2004**, *108*, 1501–1508.

(5) Weigel, A.; Dobryakov, A. L.; Veiga, M.; Lustres, J. L. P. *J. Phys. Chem* **2008**, *112*, 12054–12065.

(6) Salzmann, S.; Tatchen, J.; Marian, C. M. *J. Photochem. Photobiol. A* **2008**, *198*, 221–231.

(7) Salzmann, S.; Martinez-Junza, V.; Zorn, B.; Braslavsky, S. E.; Mansurova, M.; Marian, C. M.; Gärtner, W. *J. Phys. Chem. A, submitted*.

(8) Kennis, J. T. M.; Crosson, S.; Gauden, M.; van Stokkum, I. H. M.; Moffat, K.; van Grondelle, R. *Biochem.* **2003**, *42*, 3387–3392.

(9) Tatchen, J.; Gilka, N.; Marian, C. M. *Phys. Chem. Chem. Phys.* **2007**, *9*, 5209–5221.

(10) Perun, S.; Tatchen, J.; Marian, C. M. *ChemPhysChem* **2008**, *9*, 282–292.

(11) Möglich, A.; Moffat, K. *J. Mol. Biol.* **2007**, *373*, 112–126.

(12) Nakasako, M.; Zikihara, K.; Matsuoka, D.; Katsura, H.; Tokutomi, S. *J. Mol. Biol.* **2008**, *381*, 718–733.

(13) Losi, A.; Polverini, E.; Quest, B.; Gärtner, W. *Biophys. J.* **2002**, *82*, 2627–2634.

(14) Akbar, S.; Gaidenko, T. A.; Kang, C. M.; O'Reilly, M.; Dervine, M. K.; Price, C. W. *J. Bacteriol.* **2001**, *183*, 1329–1338.

(15) Gaidenko, T. A.; Kim, T. J.; Weigel, A. L.; Brody, M. S.; Price, C. M. *J. Bacteriol.* **2006**, *188*, 6387–6395.

(16) Avila-Perez, M.; Hellingwerf, K. J.; Kort, R. *J. Bacteriol.* **2006**, *188*, 6411–6414.

(17) Alexandre, M. T. A.; Grondelle, R.; Hellingwerf, K. J.; Robert, B.; Kennis, J. T. M. *Phys. Chem. Chem. Phys.* **2008**, *10*, 6693–6702.

(18) Fedorov, R.; Schlichting, I.; Hartmann, E.; Domratcheva, T.; Fuhrmann, M.; Hegemann, P. *Biophys. J.* **2003**, *84*, 2474–2482.

(19) Zenichowski, K.; Gothe, M.; Saalfrank, P. *J. Photochem. Photobiol. A* **2007**, *190*, 290–300.

(20) Domratcheva, T.; Fedorov, R.; Schlichting, I. *J. Chem. Theory Comput.* **2006**, *2*, 1565–1574.

(21) Dittrich, M.; Freddolino, P. L.; Schulten, K. *J. Phys. Chem. B* **2005**, *109*, 13006–13013.

(22) Senn, H. M.; Thiel, W. *Top. Curr. Chem.* **2007**, *268*, 173–290.

(23) Senn, H. M.; Thiel, W. *Angew. Chem. Int. Ed.* **2009**, *48*, 1198–1229.

(24) Parac, M.; Doerr, M.; Marian, C. M.; Thiel, W. *J. Comp. Chem.* **2009**, DOI: 10.1002/jcc.21233.

(25) Luo, G. B.; Andricioaei, I.; Xie, X. S.; Karplus, M. *J. Phys. Chem. B* **2006**, *110*, 9363–9367.

(26) Sherwood, P. et al. *J. Mol. Struct. (THEOCHEM)* **2003**, *632*, 1–28.

(27) Jorgensen, L. W.; Chandrasekhar, J.; Madura, J. D.; Impey, R. W.; Klein, M. L. *J. Chem. Phys.* **1983**, *79*, 926–935.

(28) Brooks, B. R.; Bruccoleri, R. E.; Olafson, B. D.; States, D. J.; Swaminathan, S.; Karplus, M. *J. Comp. Chem.* **1983**, *4*, 187–217.

(29) Smith, W.; Forester, T. R. *J. Mol. Graph.* **1996**, *14*, 136–141.

(30) de Vries, A. H.; Sherwood, P.; Collins, S. J.; Rigby, A. M.; Rigutto, M.; Kramer, G. J. *J. Phys. Chem. B* **1999**, *103*, 6133–6141.

(31) Ahlrichs, R. et al. *TURBOMOLE (Vers. 5.7)*, Universität Karlsruhe, 2004.

(32) Billeter, S. R.; Turner, A. J.; Thiel, W. *Phys. Chem. Chem. Phys.* **2000**, *2*, 2177–2186.

(33) Dreuw, A.; Weisman, J. L.; Head-Gordon, M. *J. Chem. Phys.* **2003**, *119*, 2943–2946.

(34) Grimme, S.; Waletzke, M. *J. Chem. Phys.* **1999**, *111*, 5645–5655.

(35) Salzmann, S.; Kleinschmidt, M.; Tatchen, J.; Weinkauf, R.; Marian, C. M. *Phys. Chem. Chem. Phys.* **2008**, *10*, 380–392.

(36) Silva-Junior, M. R.; Schreiber, M.; Sauer, S. P. A.; Thiel, W. *J. Chem. Phys.* **2008**, *128*, 104103/1–14.

(37) Kleinschmidt, M.; Tatchen, J.; Marian, C. M. *J. Comput. Chem.* **2002**, *23*, 824–833.

(38) Kleinschmidt, M.; Marian, C. M. *Chem. Phys.* **2005**, *311*, 71–79.

(39) Hess, B. A.; Marian, C. M.; Wahlgren, U.; Gropen, O. *Chem. Phys. Lett.* **1996**, *251*, 365–371.

(40) Schimmelpfennig, B. 1996, Stockholm University.

(41) Heelis, P. F. *Chem. Soc. Rev.* **1982**, *11*, 15–39.

(42) Visser, A. J. W. G.; Müller, F. *Hel. Chim. Acta* **1979**, *62*, 593–608.

(43) Losi, A.; Quest, B.; Gärtner, W. *Photochem. Photobiol. Sci.* **2003**, *2*, 759–766.

(44) El-Sayed, M. A. *J. Chem. Phys.* **1962**, *36*, 573–574.

(45) Lim, E. C. *J. Phys. Chem.* **1986**, *90*, 6770–6777.

(46) Holzer, W.; Penzkofer, A.; Fuhrmann, M.; Hegemann, P. *Photochem. Photobiol.* **2002**, *75*, 479–487.

(47) Schuttrigkeit, T. A.; Kompa, C. K.; Salomon, S.; Rudiger, W.; Michel-Beyerle, M. E. *Chem. Phys.* **2003**, *294*, 501–508.

(48) Silva-Junior, M. R.; Salzmann, S.; Marian, C. M.; Thiel, W. *in preparation*.

Table 1: Selected ground-state bond lengths [pm] of LF in four different QM regions of confA compared with earlier results in vacuum and aqueous solution.[6,7] Atomic labels are displayed in Figure 2.

	LF		**LOV-confA**			
	vac.	H_2O	QM-1	QM-2	QM-3	QM-4
N_1-C_2	138.0	135.8	136.4	136.0	136.3	136.1
C_2-N_3	141.4	140.0	140.9	140.4	141.1	140.4
N_3-C_4	137.9	136.2	137.0	136.9	136.8	136.9
C_4-C_{4a}	150.0	148.4	148.3	148.1	148.0	148.1
C_{4a}-N_5	129.3	130.2	130.1	130.2	130.1	130.2
N_5-C_{5a}	136.6	135.3	135.1	135.0	134.9	134.9
C_{5a}-C_6	140.5	141.0	140.8	140.9	140.9	140.9
C_6-C_7	138.0	137.3	137.1	137.0	137.0	137.0
C_7-C_8	142.1	142.9	142.7	142.8	142.7	142.7
C_8-C_9	138.8	138.5	138.7	138.6	138.7	138.7
C_9-C_{9a}	140.1	140.0	139.9	139.8	139.9	139.8
C_{9a}-N_{10}	138.5	138.3	139.5	139.2	139.3	139.3
N_{10}-C_{10a}	138.2	136.6	137.4	137.1	137.3	137.1
C_{10a}-N_1	130.1	132.2	131.6	131.8	131.7	131.8
C_{5a}-C_{9a}	141.5	141.8	142.2	142.3	142.2	142.2
C_{4a}-C_{10a}	146.1	144.7	145.0	144.6	144.8	144.5
C_2-O	121.2	123.3	122.7	123.5	122.6	123.4
C_4-O	121.1	122.6	122.1	122.5	122.4	122.5

Table 2: Selected vertical singlet and triplet excitation energies ΔE [eV] for different QM regions of confA and confB in comparison to experimental absorption maxima and the results for LF in vacuum and aqueous solution. Also given are the dominant excitations and the oscillator strengths $f(r)$ of optically bright states.

		ΔE($f(r)$)						
	electronic	**confA**		**confB**		**LF**		**YtvA**
	structure	**QM-1**	**QM-4**	**QM-1**	**QM-4**	**vac.**[a]	**H_2O**[b]	**Exp.**[c]
S_1	$\pi_H \rightarrow \pi_L^*$	2.84 (0.2804)	2.77 (0.2438)	2.86 (0.2935)	2.83 (0.2880)	2.94 (0.3220)	2.87 (0.2986)	2.76
S_2	$\pi_{H-1} \rightarrow \pi_L^*$	3.40 (0.2926)	3.14 (0.2470)	3.46 (0.2701)	3.37[d] (0.1928)	3.84 (0.2078)	3.47 (0.2879)	3.31
S_3	$n_N \rightarrow \pi_L^*$	3.46	3.34	3.47	3.31[d] (0.0833)	3.35	3.64	
CT	$p_S \rightarrow \pi_L^*$		3.57		3.83			
S_4	$n_O \rightarrow \pi_L^*$	3.87	3.71	3.87	3.70	3.21	3.88	
T_1	$\pi_H \rightarrow \pi_L^*$	2.19	2.15	2.21	2.20	2.24	2.23	-
T_2	$\pi_{H-1} \rightarrow \pi_L^*$	2.68	2.53	2.73	2.63	3.05	2.73	-
T_3	$n_N \rightarrow \pi_L^*$	3.08	2.99	3.08	2.96	2.90	3.29	-

[a] Taken from Ref.[6]

[b] Taken from Ref.[7]

[c] Absorption maxima of FMN in the LOV domain of YtvA, Ref.[13]

[d] The $\pi_{H-1} \rightarrow \pi_L^*$ and $n_N \rightarrow \pi_L^*$ excitations mix.

Table 3: Adiabatic singlet and triplet DFT/MRCI excitation energies ΔE_a [eV] for confA and confB of YtvA-LOV (QM-1 model) in comparison to LF in *vacuo* and experimental 0-0 transitions.

	ΔE_a			Best estimate[a]			ΔE_{0-0}
State	vac.[b]	confA	confB	conf A	conf B	Theo.	Exp.
S_1 $\pi\pi^*$	2.67	2.67	2.67	2.60	2.64		2.56[c]
T_1 $\pi\pi^*$	2.04	2.06	2.07	2.02	2.06	2.20[d]	2.05[e]
T_2 $\pi\pi^*$	2.77	2.44	2.47	2.29	2.37		
T_3 $n\pi^*$	2.61	–	–				

[a] See text.

[b] Taken from Ref.[6]

[c] Absorption and fluorescence spectra from Ref.[13]

[d] Cr-LOV, QM/MM calculations using ROHF/6-31G(2d,2p) for the inner region, Ref.[21]

[e] Photocalorimetric study of YtvA-LOV, Ref.[43]

Table 4: Comparison of SOMEs [cm^{-1}] between the S_1 state and the T_1 and T_2 states in YtvA-LOV and aqueous solution. The results for QM-4 are obtained as single-point calculations at the respective QM-1 geometries.

	confA		**confB**		**H_2O^a**	**vacuum^a**
	QM-1	QM-4	QM-1	QM-4	LF	LF
$\sum_{i=x,y,z} \lvert\langle S_1 \lvert \hat{H}_{SO_i} \rvert T_1\rangle\rvert^2$	0.16	0.64	0.20	0.42	0.01	0.01
$\sum_{i=x,y,z} \lvert\langle S_1 \lvert \hat{H}_{SO_i} \rvert T_2\rangle\rvert^2$	0.07	1.62	0.23	0.65	<0.01	–
$\sum_{i=x,y,z} \lvert\langle S_1 \lvert \hat{H}_{SO_i} \rvert T_3\rangle\rvert^2$	6.15	4.57	6.86	3.99	–	8.26

[a] Taken from Ref.[6]

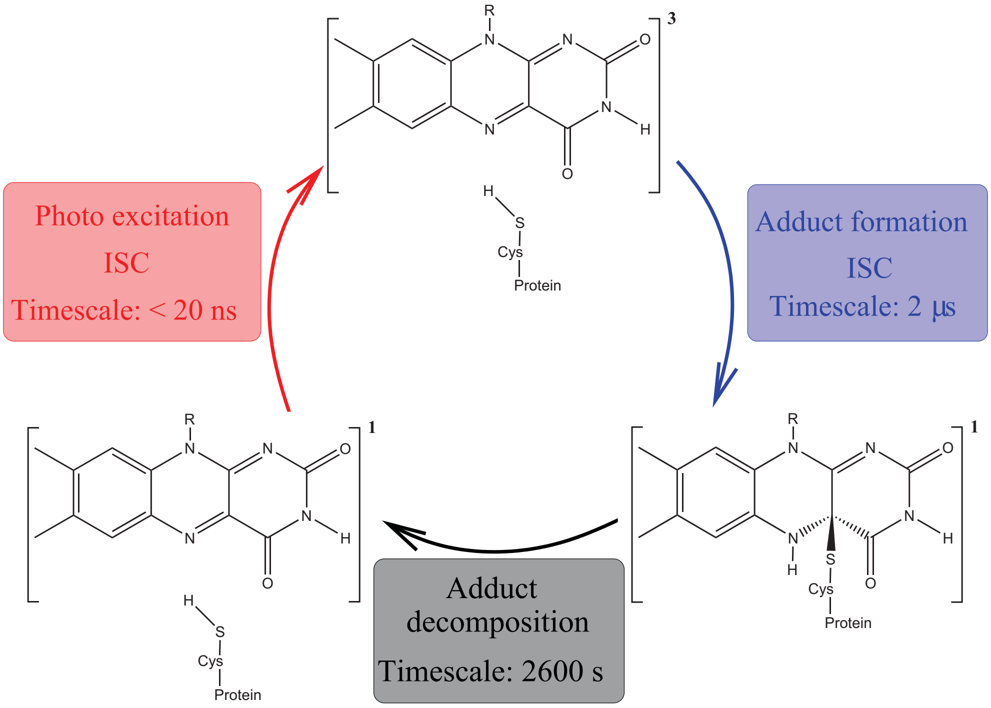

Figure 1: Photocycle of the LOV domains. In the darkness, the chromophore FMN (see Figure Figure 2) is bound noncovalently in the LOV domain (LOV-447). Upon photo-excitation, the lowest-lying triplet state (LOV-660) is formed via intersystem crossing (ISC). Accompanied by a second ISC an adduct (LOV-390) between the chromophore and a nearby cysteine is formed. LOV-390 usually decomposes on the timescale of minutes and the photocycle can start again. The kinetic data refers to the protein YtvA from *B. subtilis*.[13]

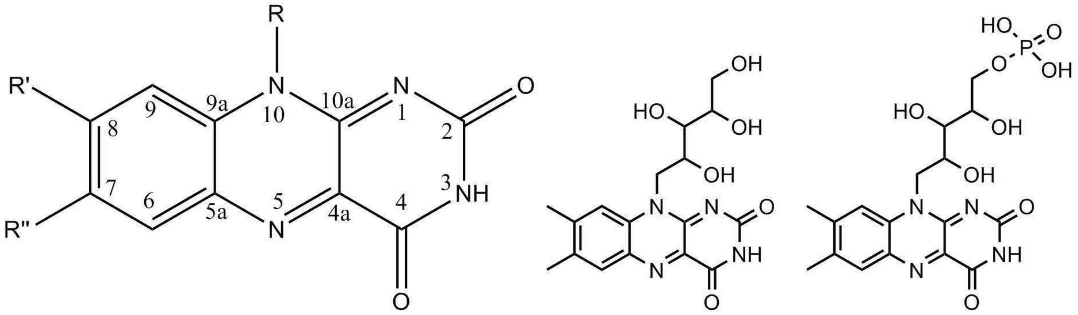

Figure 2: Left: Structure and IUPAC labeling of flavins (R=R’=R”=H: Isoalloxazin (IA); R=R’=R”=Me: Lumiflavin (LF)). Right: Two biologically relevant flavins, riboflavin (RF, vitamin B_2) and flavin mononucleotide (FMN).

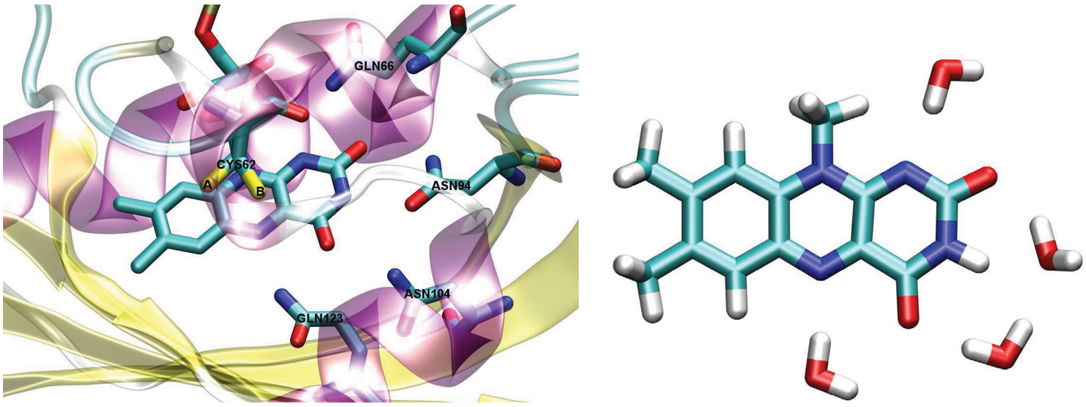

Figure 3: Left: View into the binding pocket of FMN in the LOV domain of the photosensor YtvA of *Bacillus subtilis (Bs)* (PDB code 2PR5).[11] Shown are the two conformers of the cysteine residue and the four polar AAs that coordinate the pteridine moiety. Right: Coordination of the heteroatoms of LF with four explicit water molecules.

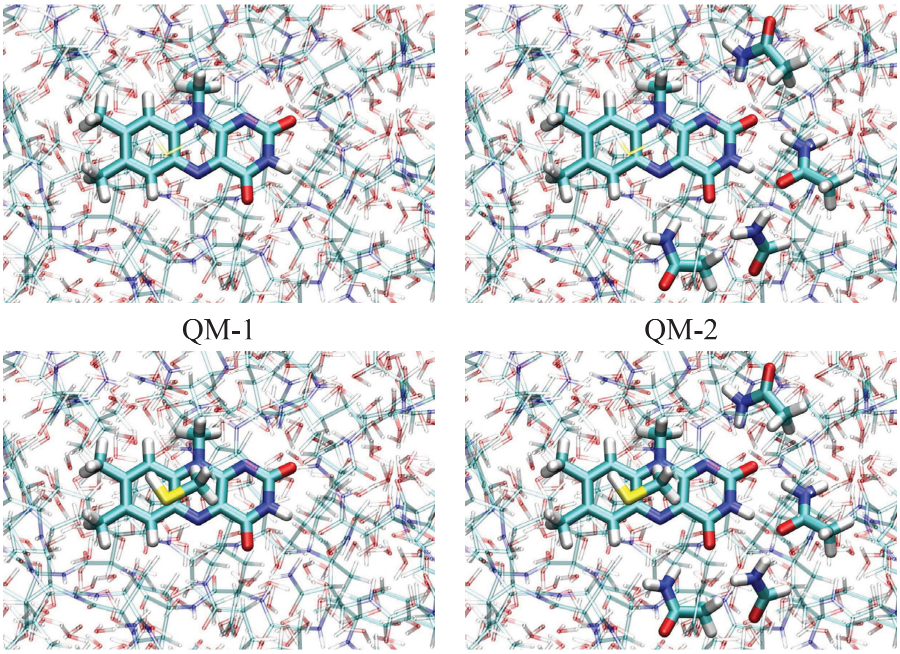
QM-1 QM-2

QM-3 QM-4

Figure 4: Illustration of various QM regions (thick, solid bonds and atoms represent the QM region and thin, transparent bonds the MM region) employed in the ground-state QM/MM geometry optimizations and the evaluation of the excited-state energies (see text).

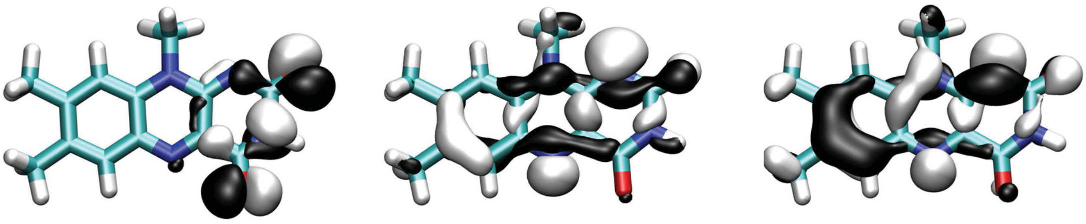

n_O (43a) n_N/π (45a) π/n_N (46a)

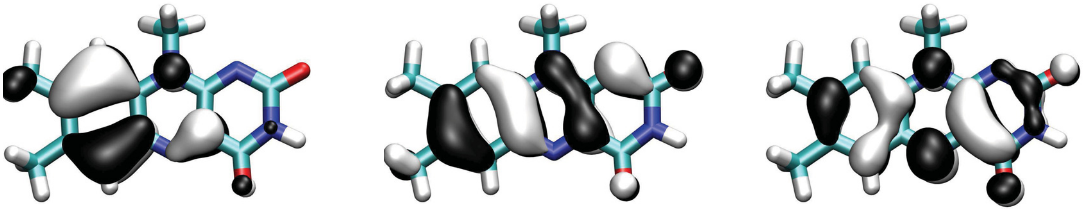

π_{H-1} (47a) π_H (HOMO, 48a) π_L^* (LUMO, 49a)

Figure 5: Frontier orbitals (QM-1/confA) at the ground-state geometry.

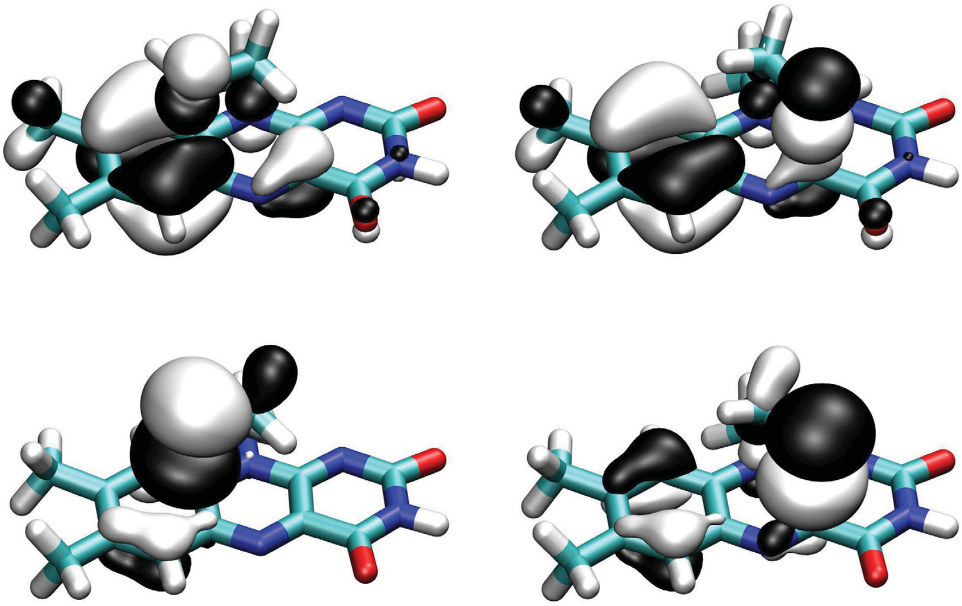

Figure 6: Admixture between the p_S and π_{H-1} MOs for QM-3 of confA (left) and confB (right).

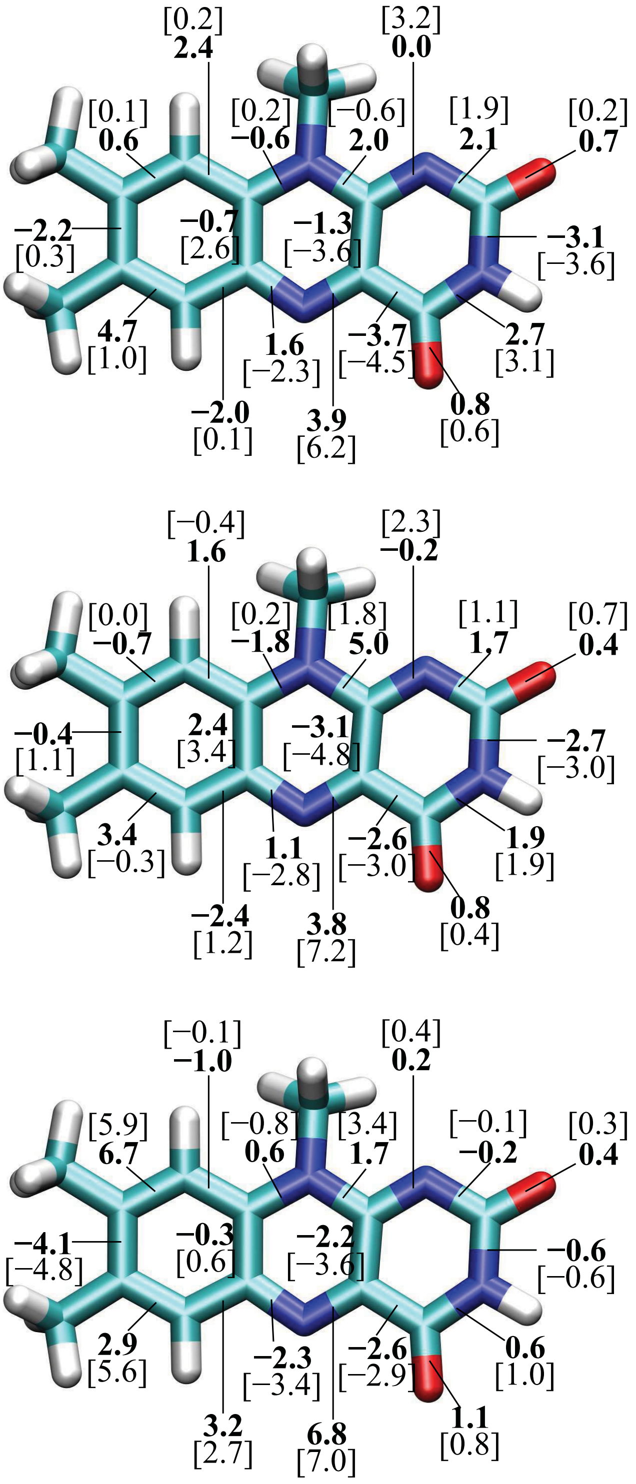

Figure 7: Structural changes [pm] for the nuclear arrangements of excited states in YtvA-LOV (confA) with respect to the ground-state geometries. Top: S_1 $\pi\pi^*$, middle: T_1 $\pi\pi^*$, and bottom: T_2 $\pi\pi^*$. For comparison the respective vacuum bond lengths[6,7] are displayed in square brackets.

Influence of the LOV domain on low-lying excited states of flavin: A combined quantum-mechanics / molecular-mechanics investigation

Supporting Information

Susanne Salzmann,[†] Mario R. Silva-Junior,[‡] Walter Thiel,[‡] and Christel M. Marian[*,†]

Institute of Theoretical and Computational Chemistry, Heinrich Heine University Düsseldorf, Universitätsstr. 1, D-40225 Düsseldorf, Germany, and Max-Plack-Institut für Kohlenforschung, Kaiser-Wilhelm-Platz 1, 45470 Mülheim an der Ruhr, Germany

E-mail: Christel.Marian@uni-duesseldorf.de

Preparation of the system The initial geometry was based on an X-ray structure (PDB code 2PR5).[1] For this investigation, only the core LOV domain (residue 25-126) was considered in our calculations. One monomer from the crystallographic dimer was used with its FMN cofactor, which corresponds to the A chain of the PDB structure. 240 associated crystal water molecules (chain A) were included in the model. Apart from CYS62 there are four different residues with alternate atom positions, namely THR54, LYS60, THR100 and ASN107, all located outside the FMN binding pocket. Upon visible inspection of their environment, conformation B was chosen for LYS60 due to favorable hydrogen bonds with crystal water w874 and w908, and conformation

---

[†] Heinrich-Heine Universität Düsseldorf
[‡] Max-Plack-Institut für Kohlenforschung

A was taken for the remaining residues. Protein hydrogen positions were built with CHARMM.[2] The assignments of the protonation state of ionizable groups were cross-checked with the empirical pK_a prediction program propKa.[3] On the basis of this evaluation, the only histidine residue (HIS69) was protonated due to favorable hydrogen bonding with w851 and w852. Note that this residue is found to be outside the binding pocket. The system was neutralized with 9 sodium ions and solvated in a 35 Å water sphere. The force-field parameters for the FMN cofactor were adapted from published FAD parameters.[4] The charges of the phosphate atoms (PB, O3A, O3B) in the ribityl chain were manually adjusted with the constraint that the total charge of the FMN cofactor remains -2. The resulting values given in Figure 1 are comparable to MM charges adopted in other recent studies.[5,6] Minor variations in the chosen force-field parameters for FMN are not expected to be critical for our purposes, since a full MM description of the cofactor is used only during the setup phase; in the QM/MM calculations, the crucial chromophore part of the cofactor is always included in the QM region. During system setup, all (non-hydrogen) atoms of protein and cofactor were frozen to preserve the X-ray structure, and only hydrogen atoms and water molecules were allowed to move during the various minimization steps (1000 steps of steepest descent (SD) minimization followed by 1000 steps of adopted basis Newton-Raphson (abNR) minimization). In order to retain the two CYS62 conformations, we refrained from performing MM molecular dynamics simulations.

```
RESI FMN  -2.000       !
GROUP                  !                                            GROUP
ATOM O3A  O2L    -0.90 !           O1B                              ATOM NX1  NX1  -0.89
ATOM PB   P       1.10 !           |                                ATOM HX1  HX1   0.43
ATOM O1B  O2L    -0.90 !      O3B-PB-O3A                            ATOM CX1  CX1   0.82
ATOM O2B  O2L    -0.90 !       |   |                                ATOM OX1  OX1  -0.61
ATOM O3B  OSL    -0.40 !       |   O2B                              ATOM CX2  CX2   0.24
GROUP                  ! HS51-CS5-HS52                              ATOM CX3  CX3   0.37
ATOM CS1  CT2     0.21 !       |                                    ATOM NX2  NX2  -0.81
ATOM HS11 HA      0.09 ! HS41-CS4-OS4-HS42                          ATOM CX4  CX4   1.09
ATOM HS12 HA      0.09 !       |                                    ATOM OX2  OX2  -0.66
ATOM CS2  CT1     0.17 ! HS31-CS3-OS3-HS32                          ATOM NY1  NY1  -0.60
ATOM HS21 HA      0.09 !       |                                    ATOM CY1  CY1   0.60
ATOM OS2  OH1    -0.66 ! HS21-CS2-OS2-HS22                          ATOM CY2  CY2  -0.30
ATOM HS22 H       0.43 !       |                                    ATOM NY2  NY2   0.20
ATOM CS3  CT1     0.17 ! HS11-CS1-HS12                              ATOM CZ1  CZ1  -0.46
ATOM HS31 HA      0.09 !        \                                   ATOM HZ1  HZ1   0.24
ATOM OS3  OH1    -0.66 !         \                                  ATOM CZ2  CZ2   0.19
ATOM HS32 H       0.43 !          \                                 ATOM CZ5  CT3  -0.44
ATOM CS4  CT1     0.17 !           \                                ATOM HZ51 HA    0.09
ATOM HS41 HA      0.09 !            \                               ATOM HZ52 HA    0.09
ATOM OS4  OH1    -0.66 !             \                              ATOM HZ53 HA    0.09
ATOM HS42 H       0.43 !              \        HZ4 HZ61 HZ62        ATOM CZ3  CZ3   0.18
ATOM CS5  CT2     0.22 !               \       |    |  /            ATOM CZ6  CT3  -0.48
ATOM HS51 HA      0.09 !  OX2   NX2     NY2   CZ4   CZ6--HZ63       ATOM HZ61 HA    0.09
ATOM HS52 HA      0.09 !   \\  /   \   /   \ /   \\ /               ATOM HZ62 HA    0.09
                       !    CX4     CX3    CY2   CZ3   HZ53         ATOM HZ63 HA    0.09
                       !     |       |     ||     |    |            ATOM CZ4  CZ4  -0.28
                       !    NX1     CX2    CY1   CZ2---CZ5--HZ52    ATOM HZ4  HZ4   0.19
                       !    /  \   /   \  // \   //    |
                       !  HX1   CX1     NY1   CZ1      HZ51
                       !        ||             |
                       !        OX1           HZ1
```

Figure 1: CHARMM charges for flavin mononucleotide (FMN) adapted from FAD parameters by Luo et al.[4]

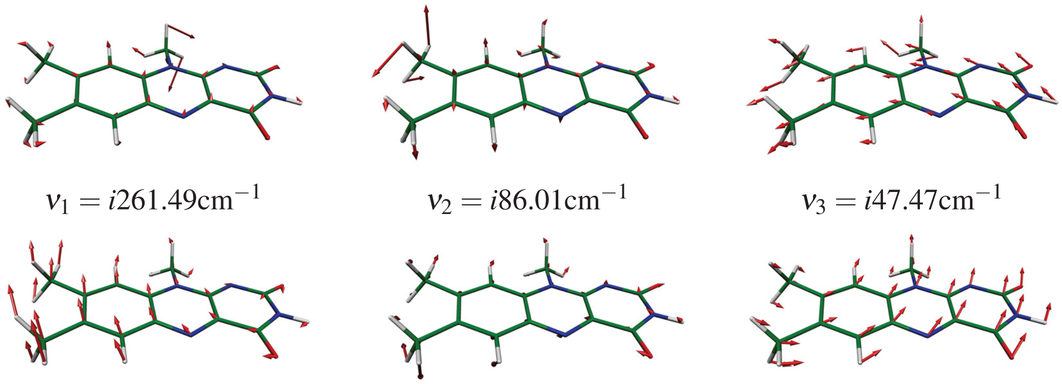

$\nu_1 = i261.49\text{cm}^{-1}$ $\nu_2 = i86.01\text{cm}^{-1}$ $\nu_3 = i47.47\text{cm}^{-1}$

$\nu_4 = i27.01\text{cm}^{-1}$ $\nu_5 = 11.17\text{cm}^{-1}$ $\nu_6 = 33.05\text{cm}^{-1}$

Figure 2: Distortions along low-energy vibrational normal modes at the S_1 geometry. For the nuclear arrangements of the other states a qualitatively similar picture is found.

Table 1: Selected ground-state bond lengths [pm] of LF for the four QM regions in confA and confB, respectively. Atomic labels are displayed in Figure 2 of the main paper.

	LOV (Konf. A)				**LOV (Konf. B)**			
	QM-1	QM-2	QM-3	QM-4	QM-1	QM-2	QM-3	QM-4
N_1-C_2	136.4	136.0	136.3	136.1	136.2	135.9	136.2	135.9
C_2-N_3	140.9	140.4	141.1	140.4	141.0	140.3	140.9	140.2
N_3-C_4	137.0	136.9	136.8	136.9	136.9	136.9	137.0	137.0
C_4-C_{4a}	148.3	148.1	148.0	148.1	148.2	148.3	148.2	148.3
C_{4a}-N_5	130.1	130.2	130.1	130.2	130.1	130.2	130.0	130.1
N_5-C_{5a}	135.1	135.0	134.9	134.9	135.2	135.2	135.2	135.2
C_{5a}-C_6	140.8	140.9	140.9	140.9	140.9	140.9	141.0	141.0
C_6-C_7	137.1	137.0	137.0	137.0	137.2	137.2	137.2	137.2
C_7-C_8	142.7	142.8	142.7	142.7	142.8	142.8	142.8	142.8
C_8-C_9	138.7	138.6	138.7	138.7	138.4	138.5	138.5	138.5
C_9-C_{9a}	139.9	139.8	139.9	139.8	139.9	139.9	139.9	139.9
C_{9a}-N_{10}	139.5	139.2	139.3	139.3	138.9	138.9	139.0	138.9
N_{10}-C_{10a}	137.4	137.1	137.3	137.1	137.2	137.0	137.3	137.0
C_{10a}-N_1	131.6	131.8	131.7	131.8	131.5	131.7	131.6	131.7
C_{5a}-C_{9a}	142.2	142.3	142.2	142.2	142.1	142.1	142.1	142.1
C_{4a}-C_{10a}	145.0	144.6	144.8	144.5	144.8	144.5	144.9	144.6
C_2-O	122.7	123.5	122.6	123.4	122.7	123.4	122.7	123.4
C_4-O	122.1	122.5	122.4	122.5	122.3	122.4	122.2	122.3

Table 2: Selected excited-state bond lengths [pm] of LF for region QM-1 in confA and confB, respectively. The data of LF in vacuum is taken from.[7] Atomic labels are displayed in Figure 2 of the main paper.

	$^1(\pi\pi^*)$ **S**$_1$			$^3(\pi\pi^*)$ **T**$_1$			$^3(\pi\pi^*)$ **T**$_2$		
	LF	**confA**	**confB**	**LF**	**confA**	**confB**	**LF**	**confA**	**confB**
N_1-C_2	139.9	138.5	138.7	139.1	138.1	138.1	137.9	136.2	136.1
C_2-N_3	137.8	137.8	137.6	138.4	138.2	138.0	140.8	140.3	140.4
N_3-C_4	141.4	139.7	139.9	139.8	138.9	139.1	138.9	137.6	137.7
C_4-C_{4a}	145.5	144.6	144.5	147.0	145.7	145.6	147.1	145.7	145.7
C_{4a}-N_5	135.5	134.0	134.1	136.5	133.9	134.0	136.3	136.9	136.9
N_5-C_{5a}	134.3	136.7	136.5	133.8	136.2	136.2	133.2	132.8	132.8
C_{5a}-C_6	140.6	138.8	138.9	141.7	138.4	138.6	143.2	144.0	144.1
C_6-C_7	139.0	141.8	141.6	137.7	140.5	140.3	143.6	140.0	140.4
C_7-C_8	142.4	140.5	140.6	143.2	142.3	142.4	137.3	138.6	138.5
C_8-C_9	138.9	139.3	139.1	138.8	138.0	137.9	144.7	145.4	145.2
C_9-C_{9a}	140.3	142.3	142.0	139.7	141.5	141.3	140.0	138.9	139.0
C_{9a}-N_{10}	138.7	138.9	138.7	138.7	137.7	137.6	137.7	140.1	139.6
N_{10}-C_{10a}	137.6	139.4	139.0	140.0	142.4	141.9	141.6	139.1	139.0
C_{10a}-N_1	133.3	131.6	131.7	132.4	131.4	131.4	130.5	131.8	131.8
C_{5a}-C_{9a}	144.1	141.5	141.8	144.9	144.6	144.6	142.1	141.9	142.0
C_{4a}-C_{10a}	142.5	143.7	143.5	141.3	141.9	141.7	142.5	142.8	142.6
C_2-O	121.9	122.9	123.0	121.9	123.1	123.1	121.5	123.1	123.1
C_4-O	121.7	122.9	123.1	121.5	122.9	122.8	121.9	123.2	123.1

Table 3: confA:Vertical singlet excitation energies ΔE [eV] for different QM regions. In addition to the dominant excitations, oscillator strengths $f(r)$ of optically bright states are given.

	electronic structure	**ΔE($f(r)$)**			
		QM-1	**QM-2**	**QM-3**	**QM-4**
S_0	*ground state*	0.00	0.00	0.00	0.00
S_1	$\pi_H \rightarrow \pi_L^*$	2.84	2.79	2.82	2.77
		(0.2804)	(0.2974)	(0.2321)	(0.2438)
S_2	$\pi_{H-1} \rightarrow \pi_L^*$	3.40	3.31	3.21	3.14
		(0.2926)	(0.2500)	(0.2367)	(0.2470)
S_3	$n_N \rightarrow \pi_L^*$	3.46	3.35	3.45	3.34
CT	$p_S \rightarrow \pi_L^*$			3.65	3.57
S_4	$n_O \rightarrow \pi_L^*$	3.87	3.71	3.89	3.71

Table 4: confB:Vertical singlet excitation energies ΔE [eV] for different QM regions. In addition to the dominant excitations, oscillator strengths $f(r)$ of optically bright states are given.

	electronic structure	**ΔE($f(r)$)**			
		QM-1	**QM-2**	**QM-3**	**QM-4**
S_0	*ground state*	0.00	0.00	0.00	0.00
S_1	$\pi_H \rightarrow \pi_L^*$	2.86	2.82	2.85	2.83
		(0.2935)	(0.3089)	(0.2718)	(0.2880)
S_2	$\pi_{H-1} \rightarrow \pi_L^*$	3.46	3.38	3.39[a]	3.37[a]
		(0.2701)	(0.2892)	(0.2253)	(0.1928)
S_3	$n_N \rightarrow \pi_L^*$	3.47	3.34	3.45[a]	3.31[a]
				(0.0422)	(0.0833)
S_4	$n_O \rightarrow \pi_L^*$	3.87	3.69	3.88	3.70
CT	$p_S \rightarrow \pi_L^*$			3.92	3.83

[a] The $\pi_{H-1} \rightarrow \pi_L^*$ and $n_N \rightarrow \pi_L^*$ excitations mix.

References

(1) Möglich, A.; Moffat, K. *J. Mol. Biol.* **2007**, *373*, 112–126.

(2) Jorgensen, L. W.; Chandrasekhar, J.; Madura, J. D.; Impey, R. W.; Klein, M. L. *J. Chem. Phys.* **1983**, *79*, 926–935.

(3) Li, H.; Robertson, A. D.; Jensen, H. J. *Proteins: Struct. Funct. Bioinf.* **2005**, *61*, 704–721.

(4) Luo, G. B.; Andricioaei, I.; Xie, X. S.; Karplus, M. *J. Phys. Chem. B* **2006**, *110*, 9363–9367.

(5) Freddolino, P. L.; Dittrich, M.; Schulten, K. *Biophys. J.* **2006**, *91*, 3630–3639.

(6) Sadeghian, K.; Bocola, M.; Schütz, M. *J. Am. Chem. Soc.* **2008**, *130*, 12501–12513.

(7) Salzmann, S.; Tatchen, J.; Marian, C. M. *J. Photochem. Photobiol. A* **2008**, *198*, 221–231.

Paper VI

Excited states of thiophene:
Ring opening as deactivation mechanism

Susanne Salzmann, Martin Kleinschmidt, Jörg Tatchen,
Rainer Weinkauf, and Christel M. Marian

Phys. Chem. Chem. Phys., **10** (2008) 380–392.

Excited states of thiophene: ring opening as deactivation mechanism†

Susanne Salzmann,[a] Martin Kleinschmidt,[a] Jörg Tatchen,[a] Rainer Weinkauf[b] and Christel M. Marian*[a]

Received 9th July 2007, Accepted 10th September 2007
First published as an Advance Article on the web 28th September 2007
DOI: 10.1039/b710380h

(Time-dependent) Kohn–Sham density functional theory and a combined density functional/multi-reference configuration interaction method (DFT/MRCI) were employed to explore the ground and low-lying electronically excited states of thiophene. Spin–orbit coupling was taken into account using an efficient, nonempirical mean-field Hamiltonian. Phosphorescence lifetimes were calculated by means of SPOCK.CI, a selecting direct multi-reference spin–orbit configuration interaction program. Throughout this paper, we use the following nomenclature: S1, S2,· · ·, T1, T2,· · ·, denominate electronic structures in their energetic order at the ground state minimum geometry, whereas S_1, S_2,· · ·, T_1, T_2,· · ·, refers to the actual order of electronic states at a given nuclear geometry. Multiple minima were found on the first excited singlet (S_1) potential energy hypersurface with electronic structures S1 ($\pi_{HOMO-1} \rightarrow \pi^*_{LUMO} + \pi_{HOMO} \rightarrow \pi^*_{LUMO+1}$), S2 ($\pi_{HOMO} \rightarrow \pi^*_{LUMO}$), and S3 ($\pi_{HOMO} \rightarrow \sigma^*$) corresponding to the 2 $^1A_1$ (S_1), 1 $^1B_2$ (S_2), and 1 $^1B_1$ (S_3) states in the vertical absorption spectrum, respectively. The S1 and S2 minimum geometries show out-of-plane deformations of the ring. The S3 electronic structure yields the global minimum on the S_1 surface with an adiabatic excitation energy of merely 3.81 eV. It exhibits an asymmetric planar nuclear arrangement with one significantly elongated C–S bond. A constrained minimum energy path calculation connecting the S1 and S3 minima suggests that even low-lying vibrational levels of the S1 potential well can access the global minimum of the S_1 surface. Nonradiative decay of the electronically excited singlet population to the electronic ground state *via* a close-by conical intersection will be fast. According to our work, this ring opening mechanism is most likely responsible for the lack of fluorescence in thiophene and the ultrafast decay of the S1 vibrational levels, as observed in time-resolved pump–probe femtosecond multiphoton ionization experiments. An alternative relaxation pathway leads from the S1 minimum *via* vibronic coupling to the S2 potential well followed by fast inter-system crossing to the T_2 state. For an estimate of individual rate constants a quantum dynamical treatment will be required. The global minimum of the T_1 surface has a chair-like nuclear conformation and corresponds to the T1 (1 $^3B_2$, $\pi_{HOMO} \rightarrow \pi^*_{LUMO}$) electronic structure. Phosphorescence is weak here with a calculated radiative lifetime of 0.59 s. For the second potential well on the T_1 surface with T3 (1 $^3B_1$, $\pi_{HOMO} \rightarrow \sigma^*$) electronic structure, nonradiative processes are predicted to dominate the triplet decay.

1. Introduction

This work was motivated by the observation of the ultrafast decay of low-lying vibrational levels of the first excited singlet state (2 $^1A_1$) of thiophene by time-resolved pump–probe femtosecond multiphoton ionization spectroscopy[1] and the desire to understand the underlying mechanisms. After population of the zeroth vibrational level of the optically bright S_1 state by one-photon absorption (238.4 nm), the time-evolution of the excited state was probed by ionizing the molecules with a second laser (276.2 nm) and measuring the energy of the photoelectrons. Details of the experimental procedure and its results can be found in an accompanying paper by Weinkauf *et al.*[2] These authors found a decay time of 80 ± 10 fs for the photoexcited S_1 state, in agreement with the previous observation of broad A–X absorption bands and the lack of fluorescence.[3–5]

By experimental means alone it has not been possible to unravel the identity of the fast deactivation mechanism. Two triplet states, 1 $^3B_2$ and 1 $^3A_1$, are known to be situated energetically below the S_1 state.[6–8] In α-oligothiophenes, inter-system crossing (ISC) rates increase with decreasing the chain length *n*, *i.e.*, the triplet quantum yield Φ_T is largest for $n = 2$ ($\Phi_T = 0.99$).[9–12] On these grounds, the femtosecond decay of the S_1 population in thiophene was tentatively attributed to a fast ISC.[1]

In the last decade, thiophene has been the object of many different quantum chemical investigations,[4,8,13–16] but they

---

[a] *Institute of Theoretical and Computational Chemistry, Heinrich Heine University Düsseldorf, Universitätsstr. 1, D-40225 Düsseldorf, Germany. E-mail: Christel.Marian@uni-duesseldorf.de*
[b] *Institute of Physical Chemistry, Heinrich Heine University Düsseldorf, Universitätsstr. 1, D-40225 Düsseldorf, Germany*

† The HTML version of this article has been enhanced with colour images.

have not been able to provide a comprehensive picture of its photophysics so far. In particular, singlet–triplet coupling remained obscure. A first quantum chemical investigation including spin–orbit interaction between the S_1 state and close-by triplet states carried out in our laboratory[15] was rather disappointing in this respect. Spin–orbit coupling between the S_1 and T_2 states is symmetry forbidden at the S_0 equilibrium geometry and it remains small ($< 1\ \mathrm{cm}^{-1}$) even for sizeable out-of-plane distortions of the sulfur atom. Spin–orbit interaction between the S_1 and T_1 states is symmetry allowed but is too small to explain an ISC on the femtosecond time scale. Large spin–orbit coupling matrix elements (SOMEs) were observed for states involving a $\pi \rightarrow \sigma^*$ excitation but these states are situated significantly above the S_1 state in the vertical absorption region.

To unravel the mechanisms underlying the ultrafast decay of the S_1 state of thiophene, we extend our previous theoretical investigation[15] and explore the properties of low-lying singlet and triplet potential energy hypersurfaces (PEHs). In the present study, we determine the minimum nuclear arrangements in various electronically excited states of thiophene. Additional calculations of constrained minimum energy paths (CMEPs) connecting those stationary points provide information on relaxation pathways. SOMEs at singlet–triplet intersections allow us to estimate the efficiency of ISCs.

2. Methods and computational details

The electronic ground state geometry was optimized at the level of density functional theory (DFT) using the B3LYP functional[17,18] as implemented in the TURBOMOLE 5.6[19] program package. For the optimization of the electronically excited singlet and triplet state geometries time dependent DFT[20] (TDDFT) was employed. Due to triplet instabilities we applied unrestricted DFT (UDFT) in some cases. C_{2v} symmetry constraints were imposed on the ground state geometry of thiophene. The Cartesian coordinate system was chosen in a way that all atoms lie in the yz-plane. For the determination of the electronically excited states the symmetry constraint was loosened to C_s, preserving either the xz- or the yz-mirror planes. To ensure that the resulting geometries correspond to true minima of the PEH, harmonic vibrational frequencies were calculated numerically with the program SNF.[21] Zero-point vibrational energy corrections (ZPVE) were scaled by a factor of 0.9614 as recommended for the B3LYP functional.[22]

In the calculations we employed three different basis sets: the standard TZVP and TZVPP basis sets from the TURBOMOLE library as well as a so-called TZVPP + R basis set, where 1s1p1d diffuse Gaussian Rydberg functions with origin at sulfur were added. The exponents of 0.011253, 0.009988, and 0.014204, respectively, were taken from the Rydberg basis for thiophene as given in ref 23. They were also employed in our preceding study on thiophene.[15]

Vertical electronic excitation energies, dipole (transition) matrix elements, and oscillator strengths were obtained from subsequent single-point calculations using the combined density functional theory/multi-reference configuration interaction (DFT/MRCI) method of Grimme and Waletzke.[24] This approach represents an effective means to obtain spin-restricted electronic spectra for organic systems with errors typically less than 0.2 eV. The principle idea is to include major parts of dynamic electron correlation by DFT whereas static electron correlation effects are taken into account by short MRCI expansions. This MRCI expansion is built up in a one-particle basis of Kohn–Sham orbitals employing the BHLYP functional.[25,26] For effectivity reasons and to avoid double-counting of the dynamic correlation, virtual orbitals with energies above 2 E_H were discarded in the DFT/MRCI calculations. The eight 1s electrons of carbon and the ten 1s, 2s and 2p electrons of sulfur constituted the frozen core. The remaining 26 valence electrons were correlated. For the ground state geometry we calculated five roots per irreducible representation of the C_{2v} symmetry, both for the singlet and triplet manifolds, while at the lower C_s symmetry points ten roots for each of the two irreducible representations A′ and A″ were determined.

To check the validity of the (TD)DFT and DFT/MRCI approaches, a few high-level *ab initio* CASPT2 geometry optimizations and single-point calculations were carried out using the MOLPRO program package.[27,28] For technical reasons, the TZVP basis had to be employed in these cases. The underlying complete active space comprised 8 electrons distributed over 3σ and 5π type orbitals. The selection of this active space was motivated by its ability to describe the opening of the thiophene ring. Further details will be given in connection with the discussion of the results.

For the computation of the SOMEs between the correlated DFT/MRCI wavefunctions we used the spin–orbit coupling kit (SPOCK)[15,29] developed in our laboratory. For reasons of efficiency, the one-center mean-field approximation to the Breit-Pauli Hamiltonian is used for the description of the spin–orbit coupling. This nonempirical effective one-electron operator treats the expensive two-electron terms of the full Breit-Pauli Hamiltonian in a Fock-like manner.[30] The spin–orbit mixed wavefunctions required for the calculation of the (complex-valued) electric dipole transition moment vectors μ_{el} were obtained *via* multi-reference spin–orbit configuration interaction (MRSOCI).[31] The probability $\Gamma_{1,\zeta}$ of the spin-forbidden radiative transition from the three triplet sublevels is then given by

$$\Gamma_{1,\zeta} = \frac{4e^2}{3c^3\hbar^4}\,\Delta E^3_{\mathrm{S}_0\leftarrow\mathrm{T}_{1,\zeta}}\,|\mu_{\mathrm{el}}(\mathrm{S}_0 \leftarrow \mathrm{T}_{1,\zeta})|^2 \qquad (2.1)$$

wherein $\mathrm{T}_{1,\zeta}$ represents one of the three spin–orbit coupled sublevels and $\Delta E_{\mathrm{S}0\leftarrow\mathrm{T}_{1,\zeta}}$ its vertical emission energy.[32] Whether transitions from the three triplet sublevels can be observed individually or not, depends on the size of the fine-structure splitting and on the temperature. In the so-called high-temperature limit, all fine-structure sublevels are populated equally and their individual transition probabilities have to be averaged then.

3. Results and discussion

A. Optimized geometries and electronic spectra

In this section, the nuclear arrangements of the ground state as well as the lowest-lying excited states of thiophene and the

Table 1 Selected ground-state geometry parameters for three different AO basis sets in comparison with experimental data. Atomic labels are explained in Fig. 1. Estimated experimental uncertainties are given in brackets

	TZVP	TZVPP	TZVPP + R	Experiment[41]
r(S–C(1))/Å	1.740	1.726	1.725	1.7140(20)
r(C(1)–C(2))/Å	1.362	1.364	1.364	1.3696(50)
r(C(2)–C(2′))/Å	1.427	1.424	1.424	1.4232(30)
θ(C(1′)–S–C(1))/°	91.2	91.7	91.7	92.2(2)
θ(S–C(1)–C(2))/°	111.6	111.5	111.4	111.5(2)
θ(C(1)–C(2)–C(2′))/°	112.9	112.7	112.7	112.5(2)

corresponding vertical electronic excitation energies are presented. The energetic order of the states is sensitive to the nuclear geometry and typically more than one minimum is found on a particular PEH. This situation is quite common for molecules which show an ultrafast decay of the excited states, such as thiophene. Here, the vertical order of the excited states does not correspond to their adiabatic order. To avoid confusion, we use two different nomenclatures to designate pure multiplicity states: S1, S2,· · ·, T1, T2, · · · denominate *electronic structures* in their energetic order at the ground state minimum geometry. The nomenclature $S_1, S_2, \cdots, T_1, T_2, \cdots$ refers to the actual order of *electronic states* at a given nuclear geometry. At the ground state equilibrium geometry, the two nomenclatures are identical, of course. A third type of designation will be used to label spin–orbit-mixed wavefunctions. It will be explained in section 3.3.

1. Ground state geometry and vertical transition energies. The electronic ground state of thiophene has C_{2v} symmetry. The geometric parameters obtained for the three basis sets are displayed in Table 1. Atomic labels are explained in Fig. 1. Comparison with the experimental data shows that the TZVP basis set is insufficient for a proper description of the nuclear geometry whereas the values of the TZVPP and TZVPP + R basis set yield satisfactory results. The C–C bond lengths are reproduced well in all three basis sets and lie within the experimental error bars in case of the TZVPP and TZVPP + R basis. In contrast, the TZVP basis set predicts a C–S bond distance that is about 2.5 pm too long. The addition of the second set of polarization functions (TZVPP basis set) improves the description of the C–S bond significantly while the augmentation of the basis set by Rydberg functions has no major effect on the geometry. A similar observation is made regarding the bond angles. The S–C–C/C–C–C angles are well reproduced in all three basis sets. The poorer description of the C–S–C angle is, of course, directly related to the difficulties met for the C–S bonds.

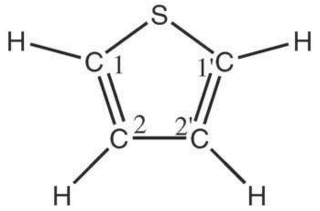

Fig. 1 Chemical structure and atom labeling of thiophene.

The mediocre performance of the TZVP basis in describing the C–S bond length is not specific for the DFT calculations. While the CASPT2 optimized C–C bond lengths (r(C(1)–C(2)) = 1.359 Å and r(C(2)–C(3)) = 1.420 Å) are in excellent agreement with experimental values, the C–S bond distance resulting from the CASPT2 optimization (r(S–C(1)) = 1.766 Å) deviates from the experimental value of 1.714 Å by more than 5 pm.

The excitation energies computed with three different AO basis sets at the respective ground state geometries show some interesting differences (Fig. 2). While the addition of a second set of polarization functions had a marked influence on the C–S bond length, its effect on the excitation energies is minor: the excitation energies change by at most 0.05 eV. The largest difference between the two basis sets is the appearance of an additional $^3A_1$ state below 6 eV in the TZVPP basis set. When diffuse functions are added to the TZVPP basis, we do not only observe the appearance of further Rydberg states in the energy regime below 6 eV. Rather unexpectedly, also the low-lying valence states are red shifted by about 0.2 to 0.3 eV. Our first guess was that the additional d function (exponent 0.014204) enhances the representation of the 3d orbital of sulfur. The latter

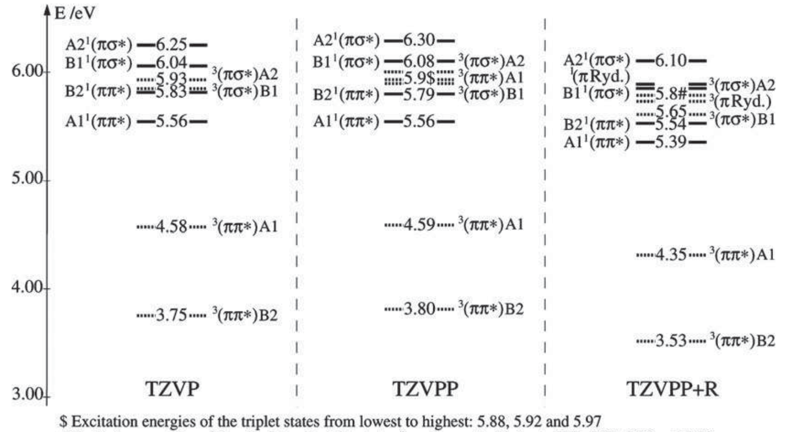

$ Excitation energies of the triplet states from lowest to highest: 5.88, 5.92 and 5.97
# Excitation energies of the singlet and triplet states from lowest to highest: 5.77, 5.80, 5.86 and 5.88

Fig. 2 Vertical transition energies (DFT/MRCI) of the lowest electronic states at the ground state geometries of three different AO basis sets.

Table 2 Vertical singlet and triplet excitation energies ΔE of thiophene (TZVPP + R basis) in comparison with experimental band maxima. In addition, dominant excitations with corresponding c^2 values, differential r^2 expectation values Δr^2 [bohr^2], oscillator strengths $f(r)$ and dipole moments μ [Debye] are given

State		Electronic structure	ΔE DFT/MRCI/eV	Exp. band maximum	Δr_2	$f(r)$	μ
S_0	1^1A_1	S0 (0.984) ground state	0.00	0.00	0.0	0.0000	0.59
S_1	2^1A_1	S1 (0.771) $\pi_2 \rightarrow \pi_4$*, (0.125) $\pi_3 \rightarrow \pi_5^*$	5.39	5.43[a], 5.26[b]	2.4	0.1142	0.36
S_2	1^1B_2	S2 (0.909) $\pi_3 \rightarrow \pi_4^*$	5.54	5.52[c], 5.61[a], 5.64[b]	2.4	0.1121	0.53
S_3	1^1B_1	S3 (0.480) $\pi_3 \rightarrow \sigma^*$, (0.439) $\pi_3 \rightarrow$ Ryd.	5.86	—	25.3	0.0040	5.69
S_4	1^1A_2	S4 (0.913) $\pi_3 \rightarrow$ Ryd.	5.88	—	56.7	0.0000	1.89
S_5	2^1A_2	S5 (0.547) $\pi_2 \rightarrow \sigma^*$, (0.286) $\pi_2 \rightarrow$ Ryd.	6.10	—	19.6	0.0000	4.85
⋮	⋮		⋮		⋮	⋮	
T_1	1^3B_2	T1 (0.942) $\pi_3 \rightarrow \pi_4^*$	3.53	3.75[d], 3.74[ae]	−1.1	—	1.36
T_2	1^3A_1	T2 (0.897) $\pi_2 \rightarrow \pi_4^*$, (0.065) $\pi_3 \rightarrow \pi_5^*$	4.35	4.62[ade]	1.3	—	0.78
T_3	1^3B_1	T3 (0.549) $\pi_3 \rightarrow \sigma^*$, (0.375) $\pi_3 \rightarrow$ Ryd.	5.65	—	18.7	—	5.52
T_4	1^3A_2	T4 (0.743) $\pi_3 \rightarrow$ Ryd., (0.115) $\pi_2 \rightarrow \sigma^*$	5.77	—	47.2	—	0.79
T_5	2^3A_2	T5 (0.497) $\pi_2 \rightarrow \sigma^*$, (0.426) $\pi_2 \rightarrow$ Ryd.	5.80	—	21.6	—	3.22
⋮	⋮		⋮		⋮	⋮	
T_{19}	5^3B_2	T19 (0.653) $\sigma \rightarrow \sigma^*$, (0.223) $\pi_2 \rightarrow$ Ryd.	7.76	—	8.5	—	1.82
⋮	⋮		⋮		⋮	⋮	

[a] Electron energy loss spectroscopy.[7,8] [b] Magnetic circular dichroism.[35] [c] Absorption.[4] [d] Electron impact.[36] [e] Electron energy loss spectroscopy.[4]

is known to participate actively in the bonding of hypervalent sulfur[33] and might be important in the excited states, too. However, additional test calculations showed that the considerable red shift is brought about mainly by the diffuse p function (exponent 0.009988). Could the stabilization of the excited states be possibly explained by an improved description of polar configurations? A test-wise augmentation of the TZVPP basis by a p orbital with an exponent of 0.0351 (from Dunning's aug-cc-pVTZ basis for the sulfur anion[34]) hardly showed any effect. It thus seems that a diffuse p function is essential for an appropriate description of the low-lying valence states despite the fact that the r^2 expectation values of their electronic charge distributions are inconspicuous (Table 2). The phenomenon remains unexplained so far. Summarizing, the geometry data (Table 1) as well as the excitation energies (Fig. 2) have shown that the description of thiophene in the TZVPP + R basis set is superior to that in the TZVP and TZVPP basis sets. In the following, we therefore only present the data obtained from the calculations employing the TZVPP + R basis set.

A detailed comparison of vertical excitation energies of thiophene with the results of recent quantum chemical calculations[4,13,14] has been provided by Kleinschmidt *et al.*[15] who performed comparable DFT/MRCI calculations. As their results differ only marginally from the vertical excitation spectrum computed here, we refrain from repeating this discussion. An overview of the excited-state properties obtained in the present study and their leading electronic configurations at the ground-state equilibrium geometry is given in Table 2. The occupied π_2 orbital (HOMO−1) and the virtual π_4^* orbital (LUMO) are of b_1 symmetry. Both have substantial amplitudes at the sulfur center where the a_2 symmetric π_3 (HOMO) and π_5^* (LUMO + 1) orbitals have nodal planes. The σ^* orbital is of b_2 symmetry and exhibits contributions from sulfur 3d and diffuse functions. Plots of these molecular orbitals are depicted in Fig. 1–3 of ref. 15. The following brief characterization of the low-lying excited states of thiophene is meant to ease the subsequent discussion of the results at excited-state minimum geometries.

In the singlet manifold, the lowest-lying excited state does not correspond to the HOMO–LUMO transition but is a linear combination of the two excitations $\pi_2 \rightarrow \pi_4^*$ and $\pi_3 \rightarrow \pi_5^*$ in A_1 symmetry. Our computed excitation energy of 5.39 eV for the 2 $^1A_1$ state is in excellent agreement with the experimental absorption maximum of electron energy loss spectroscopy at 5.43 eV[7] and magnetic circular dichroism at 5.26 eV.[35] It should be noted, however, that the identification of band maxima with calculated vertical absorption energies is questionable in the presence of strong vibronic coupling as encountered here. A more meaningful comparison is possible on the basis of adiabatic transition energies (see section 3.1.2). The S_2 (1 $^1B_2$) state is dominated by the $\pi_3 \rightarrow \pi_4^*$ (HOMO–LUMO) transition. Energetically, it is located at 5.54 eV, in excellent accord with the experimental absorption maxima at 5.52 eV,[4] 5.61 eV,[7] and 5.64 eV.[35] The S_0–S_1 (X–A) and S_0–S_2 (X–B) transitions exhibit medium size oscillator strengths. The small Δr^2 values with respect to the ground state electronic charge distribution show that the S1 and S2 electronic structures can be classified as valence states. This stands in contrast to the next higher states which possess noticeably larger Δr^2 values. The S_3 (1 $^1B_1$) state has major contributions from both a ($\pi \rightarrow \sigma^*$) and a ($\pi \rightarrow$ Ryd.) configuration. Higher energetic states are of no importance for the following discussion and are therefore not considered here.

Two triplet states are situated below the first excited singlet state at the ground state equilibrium geometry. In contrast to the situation in the singlet manifold, the $\pi_3 \rightarrow \pi_4^*$ (HOMO–LUMO) excitation is the prevailing configuration in the T_1 (1 $^3B_2$) state. Vertically, this state is located at 3.53 eV, somewhat lower than the experimental absorption maximum of electron impact at 3.75 eV[36] and electron energy loss spectroscopy at 3.74 eV.[4] The T_2 (1 $^3A_1$) state is dominated by the $\pi_2 \rightarrow \pi_4^*$ excitation with minor contributions from the $\pi_3 \rightarrow \pi_5^*$ configuration. Its multi-reference character is not as pronounced as in the corresponding singlet case. Its computed vertical excitation energy of 4.35 eV is considerably lower than the experimental band maximum at 4.62 eV (see, however, section 3.1.2). As in the singlet manifold, the

Table 3 Selected parameters from the optimized excited state geometries of thiophene

Symmetry	S1 $C_s(xz)$	S2 $C_s(xz)$	S3 $C_s(yz)$	T1 $C_s(xz)$	T2 $C_s(xz)$	T3 $C_s(yz)$
r(S–C(1))/Å	1.799	1.756	2.693	1.779	1.780	2.820
r(S–C(1′))/Å	1.799	1.756	1.662	1.779	1.780	1.665
r(C(1)–C(2))/Å	1.394	1.444	1.340	1.463	1.398	1.344
r(C(1′)–C(2′))/Å	1.394	1.444	1.404	1.463	1.398	1.400
r(C(2)–C(2′))/Å	1.436	1.369	1.422	1.344	1.443	1.418
θ(C(1′)–S–C(1))/°	92.7	92.6	77.8	89.5	93.2	76.9
θ(S–C(1)–C(2))/°	99.8	111.5	95.2	111.1	105.6	91.4
θ(C(1)–C(2)–C(2′))/°	114.7	111.2	120.1	113.4	114.2	122.7
θ(C(2)–C(2′)–C(1′))/°	114.7	111.2	122.6	113.4	114.2	124.2
θ(C(2′)–C(1′)–S)/°	99.8	111.5	124.4	111.1	105.6	124.8
δ(S–C(1)–C(2)–C(2′))/°	27.4	19.2	0.0	8.7	17.9	0.0

two lowest-lying triplet states show very small Δr^2 values. In the T_3 ($1\ ^3B_1$) state the amplitude of the ($\pi \rightarrow \sigma^*$) configuration is larger than in its singlet counterpart but the contributions from Rydberg excitations are not negligible.

2. Excited state geometries and adiabatic transition energies. In this section, we present the computed geometries and excitation energies of the three lowest-lying excited states from both the singlet and the triplet manifolds. In case of the S1, S2, T1, and T2 geometries, the *xz* mirror plane was found to be preserved while a buckling of the molecular ring took place. The S3 and T3 electronic structures preserve the *yz* mirror plane (molecular plane) but a ring opening was observed. The most important geometry parameters of the optimized excited state structures are listed in Table 3. The nuclear arrangements are depicted in Fig. 3. Fig. 4 gives an overview of the energetic location of the lowest singlet and triplet states at these points. Adiabatic excitation energies are presented in Table 4 together with experimental band origins.

a. S1 and T2 geometries. The minimum nuclear arrangement of the ($\pi_2 \rightarrow \pi_4^* + \pi_3 \rightarrow \pi_5^*$) S1 electronic structure is displayed in Fig. 3a. In contrast to the ground state geometry, the S1 geometry shows a noticeable out-of-plane distortion of the sulfur atom (δ = 27.4°). All bonds in the ring are elongated, with the strongest effect found for the C–S bonds. At the level of TDDFT (B3LYP), this structure is not a minimum but represents a saddle point. One imaginary frequency ($\bar{\nu} = i207$ cm^{-1}) is obtained for an A″ symmetric normal mode which corresponds to a deformation of the five-membered ring. A subsequent geometry optimization without symmetry constraints located a true minimum which is red shifted with respect to the saddle point by merely 242 cm^{-1} (0.03 eV). The symmetry breaking, however, turns out to be an artifact of the TDDFT method. DFT/MRCI calculations favor the C_s symmetric structure clearly by about 725 cm^{-1} (0.09 eV) over the slightly asymmetric TDDFT minimum structure (see Fig. 5). Similar observations have been made for other heterocycles such as cytosine[37] and psoralen.[38] TDDFT(B3LYP) potential energy surfaces of these compounds tend to be too flat. In the following we therefore employed the C_s symmetric structure.

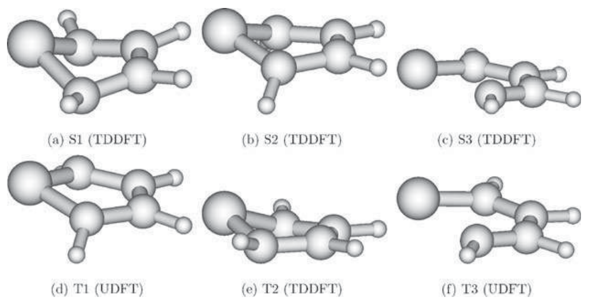

Fig. 3 Geometries of the three lowest-lying singlet and triplet excited states.

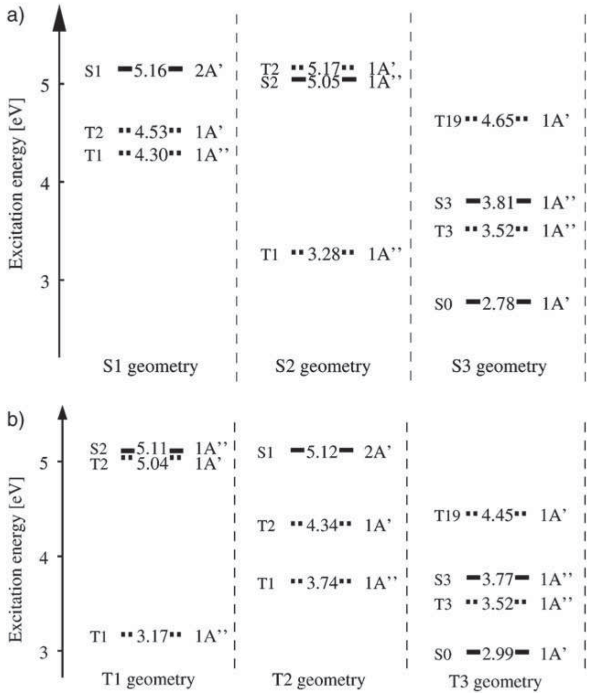

Fig. 4 Electronic excitation energies (DFT/MRCI) at various excited state geometries. For a better comparability, the electronic ground state energy at the S0 geometry has been chosen as the common origin.

The most important valence orbitals obtained at the S1 geometry are displayed in Fig. 6. Because of its node at the sulfur center, the π_3' orbital (Fig. 6a)—that used to be the HOMO at the S0 geometry—is less affected by the out-of-plane distortion of the ring than the π_2' orbital (Fig. 6b). At the S1 geometry, the energetic order of these two orbitals has

Table 4 Adiabatic singlet and triplet DFT/MRCI excitation energies ΔE_{adia}, scaled zero-point vibrational energy corrections (ZPVE), and dipole moments of excited states of thiophene (TZVPP + R basis set). Where available, experimental band origins are shown for comparison

Geometry	ΔE_{adia}/eV	PEH	ZPVE/eV	μ/D	Exp. 0–0 band
S1	5.16	S_1	−0.16	1.21	5.16[abc]
S2	5.05	S_1	−0.16	0.95	
S3	3.81	S_1	−0.11	2.44	
T1	3.17	T_1	−0.14	1.71	3.23[d], 3.15[e], 3.42[f]
T2	4.34	T_2	−0.10	1.49	4.38[dg]
T3	3.52	T_1	−0.12	2.45	

[a] Femtosecond multiphoton ionization spectra.[1] [b] Absorption.[4] [c] Absorption.[3] [d] Electron energy loss spectroscopy.[7,8] [e] Electron impact.[36] [f] Phosphorescence.[5] [g] Photoelectron spectroscopy.[39]

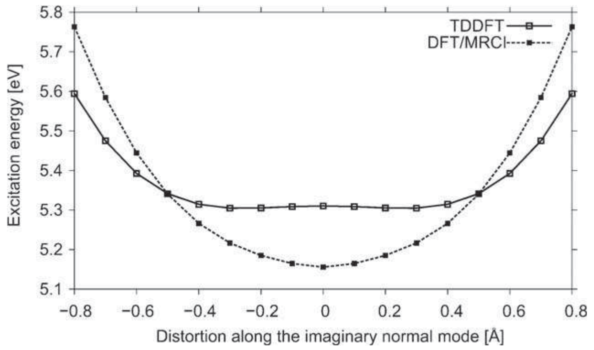

Fig. 5 Cut through the S_1 PEH at the S1 minimum. Zero distortion corresponds to the C_s symmetric geometry shown in Fig. 3a. The coordinate of the imaginary vibrational mode belongs to the a″ irreducible representation. Note that an imaginary frequency was obtained only in the TDDFT calculation.

therefore changed. The high-energetic $\sigma^{*\prime}$ orbital (Fig. 6d) is displayed here for later convenience.

From an energetic point of view, the relaxation effects on the S1 structure are moderate (0.23 eV). The calculated adiabatic excitation energy of 5.16 eV is in excellent agreement with the experimental value of 5.16 eV for the 0–0 transition as observed in femtosecond multiphoton ionization[1] and UV absorption spectra.[3,4] ZPVE corrections (also shown in Table 4) slightly worsen the perfect agreement. We did not include ZPVE corrections automatically because the vibrational frequencies of the excited state are evaluated at the TDDFT (B3LYP) level. Having seen that the excited state PEH is markedly too flat at this level of treatment—at least for some vibrational modes (see Fig. 5)—we believe the ZPVE corrections to be overestimated but of the correct sign. The vertical emission energy (3.38 eV) of the S1 is strongly red shifted with respect to absorption because the ground state energy has been raised significantly (1.78 eV) due to the unfavorable buckling of the five-membered ring. All other low-lying states experience blue shifts which are particularly strong for the ($\pi_3' \rightarrow \pi_4^{*\prime}$) excited states in A″ symmetry that correspond to the T_1 ($^3B_2$) and S_2 ($^1B_2$) states at the ground state geometry.

The minimum nuclear structure of the corresponding triplet (T2, Fig. 3e) is similar to the one of S1 but exhibits a significantly smaller out-of-plane distortion of the five-membered ring. At the level of TDDFT (B3LYP), the T2 structure is a true minimum on the T_2 PEH. The geometry relaxation shows almost no effect on the energy of the optimized state, *i.e.*, the PEH is very flat. The calculated adiabatic excitation energy of 4.34 eV is in excellent agreement with the experimental value of 4.38 eV for the origins of the electron energy loss spectrum[7,8] and photoelectron spectra.[39] The good agreement of the adiabatic excitation energies suggests that the considerable deviation of the computed vertical excitation energy at the ground state geometry from observed band maxima at 4.62 eV (see section 3.1.1) is not caused by errors in the computational procedure but has a different origin.

It is remarkable that the DFT/MRCI energy of the S_1 state is slightly lower at the T2 geometry than at the TDDFT optimized S1 geometry which shows two things: (1) The out-of-plane distortion of the S1 structure is overestimated at the TDDFT level. (2) The S_1 PEH is very flat with respect to buckling of the thiophene ring. It will therefore be very difficult to predict emission energies properly. As the thiophene ring is less buckled at the T2 geometry, the vertical emission energy of the S_1 state at this point (4.35 eV) differs considerably from its value at the S1 minimum geometry.

b. S2 and T1 geometries. Fig. 3b shows the calculated nuclear arrangement in the S2 minimum. It is chair-like with slight out-of-plane deformation of the C–S bonds and an out-of-plane distortion of the C(1)–H bonds in the opposite direction. The S2 electronic structure is characterized by a double bond between the two C(2)–C(2′) centers and a diradicaloidic electron distribution at the C(1) and C(1′) centers. Accordingly, the C–S bonds and the C(1)–C(2) bonds are elongated by 3 and 8 pm, respectively, while the C(2)–C(2′) bond is shortened by 5.5 pm with respect to the S0 geometry. At the level of TDDFT (B3LYP), this structure constitutes a true minimum on the S_1 (!) PEH, not on the S_2 PEH as might have been expected. The reverse ordering of states is corroborated by the DFT/MRCI calculations. The geometry relaxation leads to a red shift by almost 0.5 eV and yields an adiabatic excitation energy of 5.05 eV. Experimentally, the origin of the S2 (1^1B_2) state has never been observed because the Franck–Condon overlap with the ground state level is small and the S1 (2^1A_1) bands are located in the same energy regime. By virtue of the significant geometry distortion in the excited state, the S0–S2 band is wide and shows large Franck–Condon activity. The vertical emission energy of S2 is estimated to lie at approximately 3.3 eV, considerably lower than the vertical absorption energy.

The minimum geometry for the T1 structure can be seen in Fig. 3d. The geometry optimization resulted in a nuclear arrangement that shows large similarities with the S2

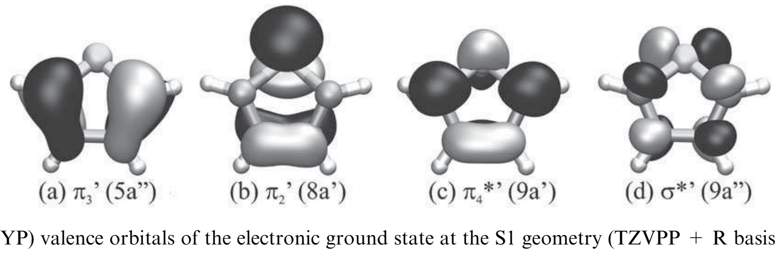

(a) π_3' (5a″) (b) π_2' (8a′) (c) $\pi_4^{*\prime}$ (9a′) (d) $\sigma^{*\prime}$ (9a″)

Fig. 6 Kohn–Sham (BHLYP) valence orbitals of the electronic ground state at the S1 geometry (TZVPP + R basis set). The orbitals appear in energetic order. In the S1 electronic structure, the 5a″ orbital is doubly occupied, the 8a′ and 9a′ orbitals are singly occupied, and the 9a″ orbital is vacant. Isolines are drawn at a value of 0.05.

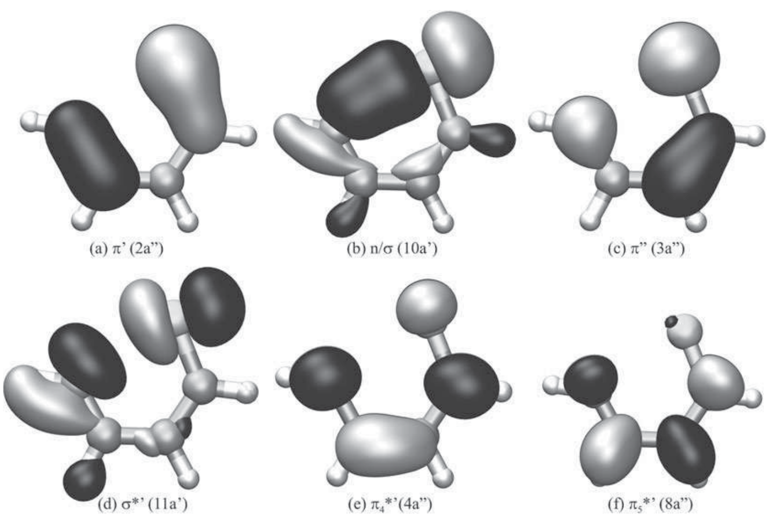

(a) π' (2a") (b) n/σ (10a') (c) π'' (3a")

(d) $\sigma^{*\prime}$ (11a') (e) $\pi_4^{*\prime}$(4a") (f) $\pi_5^{*\prime}$ (8a")

Fig. 7 Kohn–Sham (BHLYP) valence orbitals of the electronic ground state at the S3 geometry (TZVPP + R basis set). The presentation of the orbitals is in energetic order. In the S3 electronic structure, the 2a″ and 10a′ orbitals are doubly occupied, the 3a″ and 11a′ orbitals are singly occupied, and the 4a″ and 8a″ orbitals are vacant. Isolines are drawn at a value of 0.05. The orbital density distributions at the T3 geometry are similar.

geometry. However, as already observed for T2, the out-of-plane distortion of the T1 minimum structure is significantly smaller than in the singlet case. The bond length changes, on the other hand, are more pronounced for the T1 configuration. At the level of UDFT (B3LYP), this structure is a true minimum on the T_1 PEH. In the DFT/MRCI calculations, the geometry relaxation effects a red shift of 0.36 eV which yields the global minimum on the T_1 PEH. The adiabatic excitation energy of 3.17 eV is in excellent agreement with the experimental values of 3.15 eV of electron impact studies[36] and of 3.23 eV obtained by electron energy loss spectroscopy.[8] Becker *et al.*[5] report weak phosphorescence of monothiophene with a 0–0 band located near 3.42 eV, not only in disagreement with our results but also in contradiction to the lower adiabatic excitation energy observed in the electron energy loss spectra. The latter discrepancy has also been noticed by Haberkern *et al.*[8] who doubt the origin of the weak phosphorescence signal. For a more detailed discussion of this point we refer to section 3.3.

c. S3 and T3 geometries. The nuclear structure of the lowest-lying singlet ($\pi \rightarrow \sigma^*$) state is characterized by an opening of the five-membered ring (Fig. 3c). Compared to the ground state geometry, one of the C–S bonds is elongated by approximately 97 pm while the second is shortened by about 6 pm. The C(1)–C(2) bond is 2 pm shorter than at the S0 geometry, the C(1′)–C(2′) bond is elongated by 4 pm, while the C(2)–C(2′) bond length is essentially unchanged. The planar S3 nuclear arrangement can thus be interpreted as belonging to an open-chain conformation with C(1′)–S and C(1)–C(2) double bonds. According to the harmonic vibrational analysis, this structure represents another true minimum on the S_1(!) PEH. With regard to the energy, the relaxation effect on the optimized state is huge. The adiabatic excitation energy amounts to merely 3.81 eV which leads us to the conclusion that this is the global minimum on the S_1 PEH. The vertical emission energy is very low (1.03 eV), because the ring opening is very unfavorable for the ground state electronic structure. It can be assumed that a conical intersection takes place between the S_0 and the S_1 PEH with increasing degree of ring-opening (see also section 3.2). For later convenience, the most important valence orbitals obtained at the S3 geometry are displayed in Fig. 7.

For the S3 structure two types of CASPT2 calculations were carried out. The first type is based on CASSCF orbitals that were generated for a 1 : 1 mixture of ground state (A′) and excited state (A″) orbitals. This choice will be labelled PT2(mix). The second type uses excited state (A″) orbitals and is labelled PT2(single). As a first test, we computed the CASPT2 excitation energies at the TDDFT optimized S3 geometry. To our contentment, the CASPT2 single-point energies reproduce the DFT/MRCI excitation energies very well. The PT2(single) and PT2(mix) calculations yield energy gaps between the S_0 and S_1 states of 1.09 eV and 1.13 eV, respectively, with the S_1 state placed at energies of 3.97 and 3.99 eV, respectively, above the ground state minimum. Geometry optimization of the S3 electronic structure at the CASPT2 level results in minimum nuclear arrangements that lie significantly closer to the conical intersection between the S_0 and the S_1 PEH than the TDDFT structure. Using CASSCF orbitals specifically optimized for the upper state (PT(single)), we find the S–C(1) bond to be elongated to 3.109 Å. Also the S–C(1′) bond (r(S–C(1′)) = 1.744 Å) is markedly longer that the corresponding TDDFT value (see Table 3). Similar, but slightly less pronounced bond elongations (r(S–C(1)) = 3.057 Å, r(S–C(1′)) = 1.724 Å) are obtained in the PT2(mix) calculations. The large differences result, to a major extent, from the flatness of the S_1 PEH in this region of the coordinate space. This can be seen from a comparison of the excitation energies. The inadequacy of the TZVP basis set plays an underpart here. The adiabatic excitation energies of the S3 minimum at the respective levels of treatment amount to 3.80 eV (PT2(single)) and 3.84 eV (PT2(mix)). The corresponding energy gaps between the S_0 and S_1 PEHs have shrunk to 0.37 eV (PT2(single)) and 0.49 eV (PT2(mix)). DFT/MRCI calculations, carried out at the PT2(single) and PT2(mix) S3 minimum geometries, yield excitation energies (3.77 and 3.75 eV, respectively) and S_0–S_1 gaps (0.37 and 0.43 eV, respectively) in very good agreement with the CASPT2 energies.

The UDFT geometry optimization of the T3 structure leads to a minimum nuclear arrangement (Fig. 3c) similar to that of the S3 geometry but an even larger ring-opening angle. According to the vibrational analysis at the level of UDFT (B3LYP), this structure represents a second true minimum on the T_1(!) PEH. As in the corresponding singlet case, the geometry relaxation strongly affects the energy of this state that is lowered by 2.34 eV with respect to the vertical absorption region. The enormous destabilization of the electronic ground state configuration results in a vertical emission energy of only 0.53 eV. Again, it may be assumed that an intersection with the S_0 state is close-by.

B. Nonradiative decay

The fact that thiophene shows no fluorescence and the ultrafast depletion of the population in the S1 state indicate the presence of effective nonradiative relaxation processes. The multiple minima on the S_1 potential energy hypersurface (see section 3.1.2) suggest the existence of several intersections between the electronically excited singlet surfaces in addition to ISC with triplet states. In the following paragraph, we concentrate on the singlet PEHs. ISC from the S_1 to the triplet manifold is dealt with subsequently.

1. Singlet intersections

a. Coupling of the S_1 and S_2 PEHs. The S1 and S2 minimum structures (Fig. 3a and b and Table 3) can be converted into one another by an out-of-plane vibration of the C(1)–H and C(1′)–H bonds combined with deformation modes of the ring. As both structures have comparable minimum energies, we expect strong vibronic coupling between the vibrational levels in their respective A′ and A″ potential wells of the S_1 surface. A quantitative treatment of this coupling requires multidimensional quantum dynamics and is beyond the scope of the present work. Calculations of this type including four electronic states and 13 vibrational modes have recently been performed by Köppel *et al.*[16] The PEHs they have used for their quantum dynamical simulations exhibit somewhat higher electronic excitation energies than the ones found in the present study, but the dynamics should qualitatively be the same. Köppel *et al.* find an ultrafast bidirectional internal conversion, *i.e.*, the population fluctuates back and forth between the 2^1A_1 (S1) and 1^1B_2 (S2) states at the femtosecond time scale. The vibronic coupling of the S_1 and S_2 states alone does, however, not explain the observations by Lehr[1] and Weinkauf *et al.*[2] because an oscillating population of the S1 and S2 potential wells would be detected in the femtosecond ionization spectra which is not the case. Instead, the intermediate state—originally assigned by Lehr[1] to the T_2 state—decays with a time constant of 25 ± 10 fs. Thus, if the S2 structure turns out to be the intermediate state observed by Lehr[1] and Weinkauf *et al.*[2] a second channel is needed for an ultrafast depletion of the S2 population.

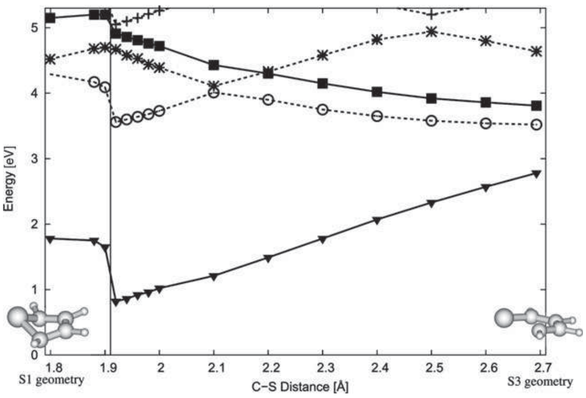

Fig. 8 DFT/MRCI energies of low-lying states along the S_1 CMEP between the S1 and the S3 minimum potential wells. Singlet energy profiles are represented by solid lines, triplet profiles by dashed lines. Triangles symbolize S_0, circles T_1, stars T_2, squares S_1, plus signs T_3. The vertical line indicates the change of electronic structure in the optimized S_1 state from $\pi \rightarrow \pi^*$(S1, left) to $\pi \rightarrow \sigma^*$ (S3, right).

b. Ring opening. According to our calculations, the dissociative $\pi \rightarrow \sigma^*$ S3 structure constitutes the global minimum on the S_1 PEH. A reaction path proceeding from the S1 minimum to the S3 potential well promises several crossings between the S_1 and triplet PEHs. To gain further information about this possible relaxation pathway, CMEP calculations were carried out. One of the C–S bonds was chosen as a reaction coordinate. Keeping the C(1)–S bond distance fixed, all other internal degrees of freedom of the first excited singlet state were optimized without symmetry constraints at the TDDFT (B3LYP) level. Single-point DFT/MRCI energies along this CMEP are shown in Fig. 8. To aid the discussion, the characters of the S_0, S_1, T_1, T_2, and T_3 wavefunctions along this reaction path are displayed in Table 5.

At the S1 minimum, the state corresponding to the S3 electronic structure is located at 6.27 eV, more than 1 eV above the S_1 state. Starting at the S1 minimum and following the reaction path to the S3 minimum, we were therefore surprised to find that the DFT/MRCI energy profile of the first excited singlet state shows only a very shallow barrier. It appears that small asymmetric C–S bond stretchings are sufficient to yield a substantial decrease of the S–C(1)–C(2)–C(2′) dihedral angle. The saddle-point is located about 0.04 eV above the S1 minimum at a C(1)–S bond length of approximately 1.90 Å where the S_1 wavefunction begins changing its character from S1 ($\pi \rightarrow \pi^*$) to S3 ($\pi \rightarrow \sigma^*$). At this point the thiophene ring is essentially planar. The wavefunction character remains mixed for the next 0.2 Å until at about 2.1 Å the S3 character clearly prevails. For larger C(1)–S distances, the S_1 PEH declines very smoothly and without any further barrier toward the S3 minimum. The quantitative evaluation of rate constants is beyond the scope of the present work. It requires the calculation of nonadiabatic coupling matrix elements as well as a quantum mechanical treatment of the excited state dynamics in many dimensions,

Table 5 Prevailing character of the wavefunctions of low-lying electronic states along the CMEP between the S1 and the S3 state potential wells

C(1)–S/Å	1.799	1.88–1.92	2.0	2.10–2.30	2.40	2.50–2.69
S_0	Ground state (gs)					
S_1	$(\pi_2' \rightarrow \pi_4^{*\prime})$		$(\pi'' \rightarrow \sigma^{*\prime})$, $(\pi'' \rightarrow \pi_4^{*\prime})$	$(\pi'' \rightarrow \sigma^{*\prime})$		
T_1	$(\pi_3' \rightarrow \pi_4^{*\prime})$	$(\pi_3' \rightarrow \pi_4^{*\prime})$, $(\pi_2' \rightarrow \pi_4^{*\prime})$	$(\pi'' \rightarrow \pi_4^{*\prime})$	$(\pi'' \rightarrow \sigma^{*\prime})$		
T_2	$(\pi_2' \rightarrow \pi_4^{*\prime})$	$(\pi_2' \rightarrow \pi_4^{*\prime})$, $(\pi_3' \rightarrow \pi_4^{*\prime})$	$(\pi'' \rightarrow \sigma^{*\prime})$	$(\pi \rightarrow \pi^{*})$		$(\sigma \rightarrow \sigma^{*\prime})$
T_3	$(\pi_2' \rightarrow \sigma^{*\prime}$, Ryd.)		$(\pi' \rightarrow \pi_4^{*\prime})$	$(\pi' \rightarrow \sigma^{*\prime})$	$(\sigma \rightarrow \sigma^{*\prime})$	$(\pi'' \rightarrow \pi_4^{*\prime})$

including at least the ring opening and the out-of-plane deformation modes. Nevertheless, it seems reasonable to assume that the nonradiative decay of the S1 population *via* this relaxation pathway occurs at the femtosecond timescale and is irreversible. The latter assumption is based on the observations that the potential energy release is large in the S3 well and that the S_1 state can undergo a conical intersection with the electronic ground state close to the S3 minimum (see below).

The energy profile of the S_0 state shows the consequence of two antagonistic effects: the decrease in the energy due to the flattening of the molecule on the one hand, the increase in the energy due to the dissociation of the ring on the other hand. The small energy gaps between the S_0 and S_1 PEHs at the S3 and T3 minimum geometries (see section 3.1.2) indicate the possibility of a conical intersection in case of a further widening of the ring. To obtain further information, CMEP calculations starting at the T3 geometry were performed. Due to technical reasons the calculations were carried out at UDFT (B3LYP) level optimizing the T_1 state. Again the C–S distance was chosen as reaction coordinate. In Fig. 9, single-point DFT/MRCI energies along this CMEP are displayed. The conical intersection of the S_1 and S_0 states occurs at a C(1)–S distance around 3.4 Å with an electronic energy of about 3.87 eV. This energy is only slightly higher than the minimum energy, *i.e.*, the S_1 PEH is very flat in this region of the coordinate space. The conical intersection can thus be easily accessed energetically on the excited state PEH. Conical intersections typically act like funnels transferring electronically excited states to the lower PEH on a femtosecond time scale.[40] It its interesting to note that optimization of the electronic ground state starting from the geometry at the conical intersection leads to a ring closure again. We have found no indication of a stable open-chain conformation in the ground state. Nonradiative decay of the first excited singlet state *via* the ring opening mechanism thus produces vibrationally hot thiophene molecules in the original ground state potential well.

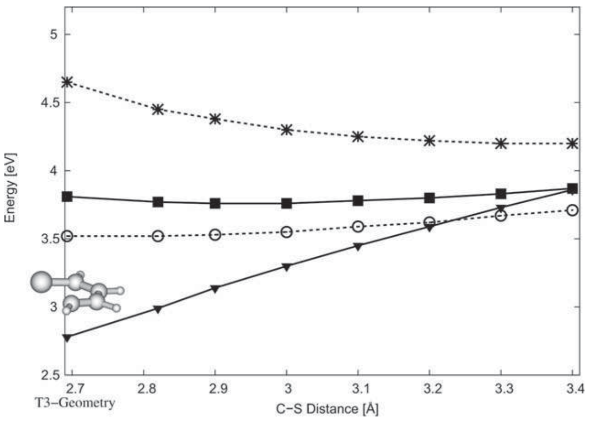

Fig. 9 DFT/MRCI energies of low-lying states along the T_1 CMEP between the T3 minimum and a conical intersection with the S_0 state. For labeling refer to Fig. 8.

2. Inter-system crossing. For an ISC to be effective, three prerequisites have to be fulfilled: (1) The singlet and triplet states involved should be close in energy, (2) their spin–orbit coupling should be reasonably strong, and (3) the density of vibrational levels should be high in the accepting state.

Essential quantities for understanding the triplet formation process after photoexcitation of thiophene are the electronic SOMEs connecting the S_1 PEH with the T_1, T_2, and T_3 surfaces. As already pointed out in our previous publication on the spin–orbit coupling in thiophene,[15] conditions (1) and (2) are not met for the low-lying excited states at the ground state equilibrium geometry. In general, large SOMEs can be expected if the two states are singly excited with respect to each other and if there is a significant probability for the electrons to be near the sulfur center (heavy-atom effect) in both orbitals involved. However, all SOMEs between the low-lying $\pi \rightarrow \pi^*$ excited singlet and triplet states are small as long as C_{2v} symmetry is preserved because one of the two π orbitals involved in the excitation has zero amplitude at the position of the sulfur atom. Large spin–orbit coupling matrix elements were observed for states involving a $\pi \rightarrow \sigma^*$ excitation but these states are situated significantly above the S_1 state at the S0 geometry. Proceeding from the ground state geometry to the minima of the excited states generally increases the size of the SOMEs (see Table 6).

a. Spin–orbit coupling between S2 and T2. It is interesting to note that the energy gap between the S_1 and T_2 PEHs is very small at the S2 and T1 minimum geometries (see schematic overview in Fig. 10). The reversed energetic order of states at

Table 6 Spin–orbit coupling matrix elements (SOME) [cm^{-1}] at the ground state geometry and all computed excited state geometries

SOME	S0	S1	S2	S3	T1	T2	T3
$\langle T_1\|\hat{\mathscr{H}}_{SO}(x)\|S_0\rangle$	—	—	—	—	—	—	—
$\langle T_1\|\hat{\mathscr{H}}_{SO}(y)\|S_0\rangle$	−0.17	6.12	17.96	115.07	−16.65	0.75	116.85
$\langle T_1\|\hat{\mathscr{H}}_{SO}(z)\|S_0\rangle$	—	5.90	3.50	46.24	−2.14	−1.72	45.00
$\langle T_2\|\hat{\mathscr{H}}_{SO}(x)\|S_0\rangle$	—	57.29	10.09	13.82	−0.61	−40.38	10.75
$\langle T_2\|\hat{\mathscr{H}}_{SO}(y)\|S_0\rangle$	—	—	—	—	—	—	—
$\langle T_2\|\hat{\mathscr{H}}_{SO}(z)\|S_0\rangle$	—	—	—	—	—	—	—
$\langle T_1\|\hat{\mathscr{H}}_{SO}(x)\|S_1\rangle$	—	—	4.63	0.08	7.74	—	0.18
$\langle T_1\|\hat{\mathscr{H}}_{SO}(y)\|S_1\rangle$	−0.36	−10.36	—	—	—	15.85	—
$\langle T_1\|\hat{\mathscr{H}}_{SO}(z)\|S_1\rangle$	—	−1.92	—	—	—	2.61	—
$\langle T_2\|\hat{\mathscr{H}}_{SO}(x)\|S_1\rangle$	—	−11.85	—	—	—	9.18	—
$\langle T_2\|\hat{\mathscr{H}}_{SO}(y)\|S_1\rangle$	—	—	33.53	−96.13	−29.98		108.31
$\langle T_2\|\hat{\mathscr{H}}_{SO}(z)\|S_1\rangle$	—	—	19.26	−46.56	−8.69		46.72
$\langle T_3\|\hat{\mathscr{H}}_{SO}(x)\|S_1\rangle$	—	—	−1.91	−0.14	−2.47	—	−0.25
$\langle T_3\|\hat{\mathscr{H}}_{SO}(y)\|S_1\rangle$	—	−43.50	—	—	—	47.44	—
$\langle T_3\|\hat{\mathscr{H}}_{SO}(z)\|S_1\rangle$	−2.02	−12.77	—	—	—	6.23	—

the two geometries indicates that an intersection of the S_1 and T_2 PEHs is close-by. The spin–orbit interaction between the S2 and T2 configurations dominating the S_1 and T_2 states, respectively, amounts to ≈ 30 cm^{-1}, strong enough to cause a substantial transfer of excited state population to the triplet manifold and possibly explain the very short lifetime of the intermediate state (25 ± 10 fs) observed by Lehr[1] and Weinkauf *et al.*[2] One should not forget, however, that the efficient S2–T2 ISC concurs with the ultrafast S2–S1 internal conversion which, in turn, has to compete with the irreversible S1–S3 internal conversion. Individual rate constants for these processes and branching ratios are therefore difficult to predict even qualitatively.

b. ISC along the ring-opening reaction coordinate. At the S1 minimum geometry, the S_1 and T_2 states have similar electronic structures. Their spin–orbit coupling is therefore moderate (≈ 10 cm^{-1}) here. The S_1 and T_3 states, on the other hand, are coupled by a $\pi_4^{*\prime} \rightarrow \sigma^{*\prime}$ single excitation. Both orbitals (Fig. 6) exhibit high electron density at sulfur and give rise to a sizable spin–orbit integral. However, the energy gap between S_1 and T_3 is too large to give rise to a notable interaction. The close proximity of the S_1, T_2, and T_3 PEHs in the interval between C(1)–S = 1.90 Å and 1.94 Å could lead to an ultrafast ISC, given that the spin–orbit interaction is sizable. At a C(1)–S distance of 2.2 Å another intersection between the T_2 and the S_1 PEHs can be located. We will therefore focus our discussion on these areas of the coordinate space.

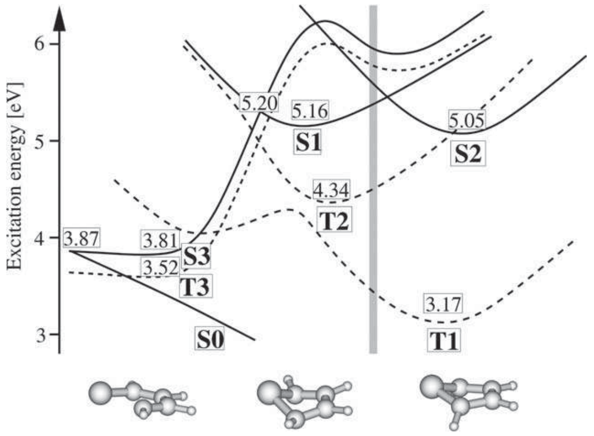

Fig. 10 Schematic overview over nonradiative relaxation pathways of photoexcited thiophene. The gray bar indicates the vertical absorption region.

At a C(1)–S bond distance of about 1.92 Å, T_2 undergoes an avoided curve crossing with T_3 and changes its electronic structure from a T2 type to a T3 type. By virtue of out-of-plane modes this avoided curve crossings could be turned into a conical intersection. At this value of the reaction coordinate, also an avoided crossing of the S_1 and S_2 PEHs is observed, accompanied by a rapid change of electronic character of the S_1 state from $\pi \rightarrow \pi^*$ to $\pi \rightarrow \sigma^*$. The electronic singlet–triplet interaction is rather strong (≈ 40 cm^{-1}) here. Whether the coupling will result in an efficient ISC is very difficult to anticipate because the transition probability will critically depend on the strength of the nonadiabatic interaction between the S1 and S3 structures and on the details of the dynamics, *e.g.* on the velocity of the wavepacket.

At a C(1)–S distance of 2.2 Å where the second intersection between the T_2 and the S_1 PEHs takes place, the T_2 wavefunction can be characterized by a $\pi'' \rightarrow \pi_4^{*\prime}$ electronic structure which is singly excited with respect to the $\pi'' \rightarrow \sigma^{*\prime}$ configuration that dominates the S_1 wavefunction here. The matrix element of the *y* component of the spin–orbit operator amounts to ≈ 50 cm^{-1} at this geometry. Again, the prerequisites (1)–(3) are fulfilled but the ISC probability will depend strongly of the details of the dynamics.

c. Nonradiative decay of the T_1 state. Getting an idea of the efficiency of a T_1–S_0 ISC regards the size of the direct SOMEs connecting the T_1 and S_0 states at the global minimum of the T_1 PEH (T1 geometry). These SOMEs are not vanishing (Table 6) but they are not large enough for an effective radiationless transition to occur between PEHs that are displaced by at least 2 eV at this point of the coordinate space. A rough estimate using the harmonic approximation yields an ISC rate for the T_1 state of the order of ≈ 1 s^{-1}.

This could be different for higher excited vibrational levels. At the open-chain T3 minimum nuclear arrangement which constitutes a local minimum on the T_1 PEH, very large SOMEs between the T_1 and S_0 states are observed (see Table 6). At this geometry, the T_1 state is characterized by a single excitation from the 3a″ to the 11a′ orbital. As may be seen in Fig. 7, both orbitals have large amplitudes at the sulfur center. As a consequence, SOMEs of the order of 100 cm^{-1} are obtained. The same is true for the intersection between the T_1 and S_0 states that occurs at a C–S distance around 3.2 Å with an electronic energy of about 3.60 eV (Fig. 9), only marginally higher than the local T3 minimum. The strong spin–orbit interaction between the T_1 and S_0 states ($\langle T_1|\hat{\mathscr{H}}_{SO}(y)|S_0\rangle = -122.42$ cm^{-1} and $\langle T_1|\hat{\mathscr{H}}_{SO}(z)|S_0\rangle = -43.91$ cm^{-1}) will lead to an efficient quenching of triplet population in this area of coordinate space.

Table 7 Phosphorescence of thiophene for both local minima on the T_1 potential surface. Listed are vertical excitation energies $\Delta E(S_0 \leftarrow T_{1,\zeta})$ [cm^{-1}], electric dipole transition moments $|\mu_{el}(S_0 \leftarrow T_{1,\zeta})|$ [ea_0], transition propabilities $\Gamma_{1,\zeta}$ [s^{-1}] and radiative lifetimes $\tau_{1,\zeta}$ [s] of the three sublevels $T_{1,\zeta}(\zeta = a, b, c)$ of the T_1 state. The direction of the electric dipole transition moment is given in parentheses

(a) Phosphorescence ($S_0 \leftarrow T_{1,\zeta}$) at the T1 geometry

MRSOCI

	$\Delta E_{S0} \leftarrow T_{1,\zeta}$	$\lvert\mu_{el}(S_0 \leftarrow T_{1,\zeta})\rvert$	$\Gamma_{1,\zeta}$	$\tau_{1,\zeta}$
$T_{1,a}$	16236.6	$1.56 \times 10^{-4}(x)$	0.21	4.76
$T_{1,b}$	16236.6	$2.25 \times 10^{-4}(y/z)$	0.44	2.27
$T_{1,c}$	16236.7	$7.12 \times 10^{-4}(y/z)$	4.40	0.23
	High-temperature limit		1.68	0.59

(b) Phosphorescence ($S_0 \leftarrow T_{1,\zeta}$) at the T3 geometry

MRSOCI

	$\Delta E_{S0} \leftarrow T_{1,\zeta}$	$\lvert\mu_{el}(S_0 \leftarrow T_{1,\zeta})\rvert$	$\Gamma_{1,\zeta}$	$\tau_{1,\zeta}$
$T_{1,a}$	4278.5	$1.24 \times 10^{-3}(x)$	0.25	4.07
$T_{1,b}$	4278.5	$0.90 \times 10^{-3}(y/z)$	0.13	7.76
$T_{1,c}$	4283.0	$10.2 \times 10^{-3}(y/z)$	16.43	0.06
	High-temperature limit		5.60	0.18

C. Phosphorescence

Weak phosphorescence was reported for thiophene with the maximum of the T_1 emission band positioned at 2.88 eV and a 0–0 band located near 3.42 eV.[5] The total triplet lifetime (radiative and nonradiative) was found to be of the order of 1 μs, approximately 100 times shorter than in bithiophene. The reason why phosphorescence is so weak could not be determined unambiguously by Becker *et al.*[5] They speculated that either the triplet quantum yield Φ_T of thiophene is unusually low compared to the oligothiophenes or that the T_1 state undergoes rapid nonradiative decay.

As indicated before we have found two local minima on the T_1 potential surface. Therefore we calculated the phosphorescence lifetimes for both geometries T1 and T3. For the designation of spin–orbit-mixed wavefunctions, we introduce a third nomenclature in this chapter. As spin–orbit interaction strengths lie well within the Russell–Saunders LS coupling regime, it makes sense to use approximate spin quantum numbers even for the mixed multiplicity states. While T_1 denominates the pure triplet state as obtained from a spin–orbit-free DFT/MRCI calculation, the nomenclature $T_{1,a}$ is used to dub a fine-structure sublevel of the spin–orbit-mixed T_1 wavefunction as resulting from a MRSOCI run. The results of the MRSOCI calculations are shown in Table 7.

At the T1 geometry, the fine-structure splitting of the triplet sublevels due to spin–orbit coupling is small. The $T_{1,a}$ and $T_{1,b}$ levels are nearly degenerate while the $T_{1,c}$ is situated about 0.1 cm^{-1} higher in energy. The zero-field splitting cannot be directly compared with experiment because of the missing dipolar spin–spin contributions in the calculations. The electric dipole transition moments $|\mu_{el}(S_0 \leftarrow T_{1,\zeta})|$ connecting the three triplet sublevels with the electronic ground state lie in the range of 10^{-4} ea_0. The transition from the $T_{1,a}$ sublevel is x polarized. Due to the low molecular symmetry the y and z polarizations of the phosphorescence are mixed. The probability of radiative transition from the three sublevels is small. In the high-temperature limit, the phosphorescence lifetime averages 0.59 s. A comparison with the total triplet lifetime measured by Becker *et al.*[5] is hampered by the fact that neither the quantum yields nor the nonradiative decay rates of the T_1 state are known. Concerning the triplet quantum yield, the most probable population of the T_1 state proceeds indirectly *via* various S_1–T_2 intersections (see section 3.2.2). A rough estimate of the radiationless decay rate at the T_1 minimum (section 3.2.2) yields a value of the same order of magnitude as the phosphorescence rate. Thus there is no indication for a fast decay of low-lying T_1 vibrational levels by intermolecular ISC. Concerning the energy, we expect the band origin to be located at about 3.0 eV and the maximum of the phosphorescence emission to occur around 2.0 eV. Even if solvent shifts are taken into account, it appears very unlikely that the maximum at 2.88 eV observed by Becker *et al.*[5] originates from the T1 minimum of the T_1 state of thiophene.

The fine-structure splitting of 4.5 cm^{-1} between the T_1 sublevels in the T3 potential well indicates that spin–orbit interaction is much stronger here than at the T1 geometry. Due to the large direct spin–orbit coupling, the probability for a radiative electronic transition from the $T_{1,c}$ sublevel to the ground state takes a value of 16 s^{-1}, yielding an average phosphorescence lifetime in the high-temperature limit of 0.18 s. However, Franck–Condon factors for the 0–0 transition are very small because of the large geometry shift so that we do not expect to observe the band origin. Furthermore, the T_1–S_0 energy gap amounts to only 0.53 eV at the T3 geometry so that a fast radiationless transition can be predicted. Moreover, the PEH of the T_1 state is very flat in this region of the coordinate space whereas the ground state potential energy increases strongly with growing C(1)–S distance. A small widening of the ring opening angle suffices to drive the system toward a conical intersection with the ground state (see section 3.2.2). Consequently, the occurrence of phosphorescence at the T3 geometry should be inhibited by fast radiationless depletion of the T_1 population.

4. Summary and conclusions

The aim of the present work was to explain the ultrafast decay of low-lying vibrational levels of the S_1 state of thiophene observed by time-resolved pump–probe femtosecond multiphoton ionization spectroscopy.[1,2] Photoexcitation of the 0–0 level of the A–X transition (2 $^1A_1$–1 $^1A_1$) results in the formation of a transient state on the femtosecond time scale (τ_1 = 80 ± 10 fs) that decays subsequently with a time constant of τ_2 = 25 ± 10 fs. In order to understand the underlying mechanisms we have explored electronically excited potential energy hypersurfaces and possible relaxation pathways. To this end, we have calculated minimum nuclear structures and transition energies of several low-lying excited singlet and triplet states and have determined singlet–triplet coupling strengths at minima and intersection points. Furthermore, a reaction path has been constructed that connects the primary excitation region with a conical intersection between the S_1 and S_0 states. (Recall that the labels $S_1, S_2, \cdots, T_1, T_2, \cdots$ refer to the actual order of electronic states at a given nuclear geometry whereas the labels S1, S2, $\cdots$, T1, T2, $\cdots$ denominate the electronic structures in their energetic order at the ground state minimum geometry.)

The results have been validated, at least for the low-lying $\pi \rightarrow \pi^*$ excited states, by comparing computed transition energies with available experimental spectra. Very good agreement is obtained for vertical and adiabatic transition energies, with errors typically less than 0.2 eV. We find three local minima on the S_1 PEH: S1 ($\pi_{\mathrm{HOMO}-1} \rightarrow \pi^*_{\mathrm{LUMO}} + \pi_{\mathrm{HOMO}} \rightarrow \pi^*_{\mathrm{LUMO}+1}$) with a boat-like nuclear arrangement and an adiabatic excitation energy of 5.16 eV which corresponds to the 2 $^1A_1$ state in the vertical absorption spectrum, S2 ($\pi_{\mathrm{HOMO}} \rightarrow \pi^*_{\mathrm{LUMO}}$) with a chair-like minimum at 5.05 eV that is derived from the 1 $^1B_2$ state in C_{2v} symmetry, and S3 ($\pi_{\mathrm{HOMO}} \rightarrow \sigma^*$) which exhibits an asymmetric planar structure with one significantly elongated C–S bond and correlates with the 1 $^1B_1$ mixed Rydberg-valence state in the vertical absorption region. To our surprise, the S3 structure represents the global minimum of the S_1 surface with an adiabatic excitation energy of 3.81 eV.

The lowest point on the T_1 PEH is found for the T1 ($\pi_{\mathrm{HOMO}} \rightarrow \pi^*_{\mathrm{LUMO}}$) structure with an adiabatic energy of 3.17 eV. Its geometry is similar to the S2 minimum but exhibits smaller out-of-plane distortions. The nuclear arrangement at the second minimum on the T_1 surface with T3 ($\pi_{\mathrm{HOMO}} \rightarrow \sigma^*$) electronic structure at 3.52 eV closely resembles the S3 geometry. The T2 structure ($\pi_{\mathrm{HOMO}-1} \rightarrow \pi^*_{\mathrm{LUMO}}$) has a less pronounced multi-configurational character than its singlet counterpart S1. Its minimum is situated on the second excited triplet PEH, 4.34 eV above the electronic ground state minimum.

We have detected two radiationless deactivation mechanisms involving transient singlet and triplet states which could possibly explain the ultrafast depletion of the initially excited S1 levels of thiophene. The relaxation pathways are sketched qualitatively in Fig. 10.

The first mechanism involves the intermediate opening of the thiophene ring at one of the C–S bonds. The reaction proceeds from the S1 minimum over a shallow saddle (barrier height 0.04 eV without zero-point corrections) to the global S3 minimum of the S_1 potential. In close proximity to the saddle point, the reaction path is intersected by the T_2 and T_3 potential energy surfaces. Spin–orbit coupling is strong here and could lead to an efficient inter-system crossing concurring with the nonadiabatic coupling of the S1 and S3 structures. From the S3 minimum a conical intersection of the S_1 and S_0 potential energy hypersurface is accessible at low cost (0.06 eV). Nonradiative decay of the S_1 population to the electronic ground state at this conical intersection and subsequent vibrational relaxation leads to a ring closure again and restores the C_{2v} structure of thiophene. A similar nonradiative pathway to the S_0 surface exists for triplet excited levels in the T3 potential well of the T_1 state.

The second mechanism is initiated by the transfer of S_1 population from the S1 minimum to the S2 potential well *via* strong vibronic coupling. The T_2 state intersects the S_1 potential energy surface close to the S2 minimum where an efficient inter-system crossing to the T2 structure can take place. Subsequent internal conversion within the triplet manifold should produce electronically excited thiophene in the T_1 state with high quantum yield. Whether the T1 or T3 potential wells will be reached will depend on the details of the nuclear dynamics. According to our studies, the levels in the T1 minimum of the T_1 state are long-lived and should give rise to detectable phosphorescence at low temperatures while fast nonradiative decay is expected for the T3 well.

From the data we have it is very difficult to discriminate between the two pathways. Possibly both are effective and even combinations are conceivable. One could imagine, for example, that the S_1 population oscillates once between the S1 and S2 potential wells before the irreversible transfer to the S3 minimum region takes place. From the lack of strong phosphorescence in experimental emission spectra of thiophene it appears unlikely, though, that the inter-system crossing between S_1 and T_2 can compete with the ring opening mechanism. A quantitative determination of rate constants and branching ratios of these processes requires extended multi-state quantum dynamical studies including many vibrational degrees of freedom. These are highly desirable but extremely difficult to carry out and are clearly beyond the scope of the present work.

Acknowledgements

Financial support by the Deutsche Forschungsgemeinschaft through projects Ma 1051/5-3 and SFB663 are gratefully acknowledged.

References

1 L. Lehr, *Zeitaufgelöste Photoelektronenspektroskopie an Molekülen und Molekülclustern*, PhD thesis, Technische Universität München, 2000.

2 R. Weinkauf, L. Lehr, E. W. Schlag, S. Salzmann and C. M. Marian, *Phys. Chem. Chem. Phys.*, 2007, accompanying paper, submitted.

3 G. Di Lonardo, G. Galloni, A. Trombetti and C. Zauli, *Chem. Soc., Faraday Trans. 2*, 1972, **68**, 2009.

4 M. H. Palmer, I. C. Walker and M. F. Guest, *Chem. Phys.*, 1999, **241**, 275.

5 R. S. Becker, J. S. de Melo, A. L. Maçanita and F. Elisei, *J. Phys. Chem.*, 1996, **100**, 18683.

6 S. Rentsch, J. P. Yang, W. Paa, E. Birckner, J. Schiedt and R. Weinkauf, *Phys. Chem. Chem. Phys.*, 1999, **1**, 1707.

7 K. R. Asmis, *Electron-Molecule Collisions: A Novel Instrument for Measuring Inelastic Differential Cross Sections at 180° Angle and Applications, Diss. Nr. 1142*, PhD thesis, Université de Fribourg, Switzerland, 1996.

8 H. Haberkern, K. R. Asmis and P. Swiderek, *Phys. Chem. Chem. Phys.*, 2003, **5**, 827–833.

9 H. C. Longuet-Higgins, *Trans. Faraday Soc.*, 1949, **45**, 173.

10 R. P. T. Lun, L. Bouscasse, E. J. Vincent and J. Metzger, *Bull. Soc. Chim. Fr.*, 1969, p. 1149.

11 W. Paa, J.-P. Yang and S. Rentsch, *Synth. Met.*, 2001, **119**, 525.

12 G. Buemi, F. Zuccarello and G. Romeo, *J. Mol. Struct. (THEOCHEM)*, 1983, **94**, 115.

13 L. Serrano-Andrés, M. Merchán, M. Fülscher and B. O. Roos, *Chem. Phys. Lett.*, 1993, **211**, 125.

14 J. Wan, M. Hada, M. Ehara and H. Nakatsuji, *J. Chem. Phys.*, 2001, **114**, 842.

15 M. Kleinschmidt, J. Tatchen and C. M. Marian, *J. Comput. Chem.*, 2002, **23**, 824.

16 H. Köppel, E. V. Gromov and A. B. Trofimov, *Chem. Phys.*, 2004, **304**, 35–49.

17 A. D. Becke, *J. Chem. Phys.*, 1993, **98**, 5648–5652.

18 P. J. Stephens, F. J. Devlin, C. F. Chabalowski and M. J. Frisch, *J. Phys. Chem.*, 1994, **98**, 11623–11627.

19 R. Ahlrichs, M. Bär, H.-P. Baron, R. Bauernschmitt, S. Böcker, P. Deglmann, M. Ehrig, K. Eichkorn, S. Elliott, F. Furche, F. Haase, M. Häser, C. Hättig, H. Horn, C. Huber, U. Huniar, M. Kattannek, A. Köhn, C. Kölmel, M. Kollwitz, K. May, C. Ochsenfeld, H. Öhm, A. Schäfer, U. Schneider, M. Sierka, O. Treutler, B. Unterreiner, M. von Arnim, F. Weigend and P. Weis and H. Weiss, Turbomole (vers. 5.6). Universität Karlsruhe, 2002.

20 R. Bauernschmitt and R. Ahlrichs, *Chem. Phys. Lett.*, 1996, **256**, 454–464.

21 C. Kind, M. Reiher and J. Neugebauer, SNF Version 2.2.1: A Program Package for Numerical Frequency Analyses, Universität Erlangen, 1999–2002.

22 A. P. Scott and L. Radom, *J. Phys. Chem.*, 1996, **100**, 16502.

23 Molcas on-line tutorial. Lund University, http://www.teokem.lu.se/molcas/tutor, 2002.

24 S. Grimme and M. Waletzke, *J. Chem. Phys.*, 1999, **111**, 5645.

25 A. D. Becke, *J. Chem. Phys.*, 1993, **98**, 1372–1377.

26 C. Lee, W. Yang and R. G. Parr, *Phys. Rev.*, 1988, **B 37**, 785.

27 P. Celani and H.-J. Werner, *J. Chem. Phys.*, 2003, **119**, 5044.

28 H.-J. Werner, P. J. Knowles, R. Lindh, F. R. Manby, M. Schtz, P. Celani, T. Korona, G. Rauhut, R. D. Amos, A. Bernhardsson, A. Berning, D. L. Cooper, M. J. O. Deegan, A. J. Dobbyn, F. Eckert, C. Hampel, G. Hetzer, A. W. Lloyd, S. J. McNicholas, W. Meyer, M. E. Mura, A. Nicklass, P. Palmieri, R. Pitzer, U. Schumann, H. Stoll, A. J. Stone, R. Tarroni and T. Thorsteinsson, Molpro, version 2006.1, a package of *ab initio* programs. http://www.molpro.net, 2006.

29 M. Kleinschmidt and C. M. Marian, *Chem. Phys.*, 2005, **311**, 71–79.

30 B. A. Hess, C. M. Marian, U. Wahlgren and O. Gropen, *Chem. Phys. Lett.*, 1996, **251**, 365.

31 M. Kleinschmidt, J. Tatchen and C. M. Marian, *J. Chem. Phys.*, 2006, **124**, 124101.

32 C. Marian, in *Reviews In Computational Chemistry*, ed. K. Lipkowitz and D. Boyd, Wiley-VCH, Weinheim, 2001, vol. 17, pp. 99–204.

33 A. Strömberg, U. Wahlgren, L. G. M. Pettersson and P. E. M. Siegbahn, *Chem. Phys.*, 1984, **89**, 323–328.

34 D. E. Woon and T. H. Dunning, Jr, *J. Chem. Phys.*, 1993, **98**, 1358–1371.

35 R. Håkansson, B. Nordén and E. N. Thulstrup, *Chem. Phys. Lett.*, 1977, **50**, 306.

36 W. M. Flicker, O. A. Mosher and A. Kuppermann, *Chem. Phys. Lett.*, 1976, **38**, 489.

37 K. Tomić, J. Tatchen and C. M. Marian, *J. Phys. Chem.*, 2005, **A 109**(37), 8410–8418.

38 J. Tatchen and C. M. Marian, *Phys. Chem. Chem. Phys.*, 2006, **8**, 2133–2144.

39 J. E. Chadwick and B. E. Kohler, *J. Chem. Phys.*, 1994, **98**, 3031.

40 W. Domcke, D. R. Yarkony and H. Köppel, *Conical Intersections Electronic Structure, Dynamics and Spectroscopy*, World Scientific, Singapore, 2004.

41 J. H. Callomon, E. Hirota, W. J. Lafferty, A. G. Maki and C. S. Pote, *LANDOLT-BORNSTEIN, Numerical Data and Functional Relations in Science and Technology, Vol. 7 of New Series, Group II: Atomic and Molecular Physics, Structure Data of Free Polyatomic Molecules*, Springer Verlag, 1976.

Paper VII

Ultrafast dynamics in thiophene investigated by femtosecond pump probe photoelectron spectroscopy and theory

Rainer Weinkauf, Leo Lehr, Edward W. Schlag,
Susanne Salzmann, and Christel M. Marian

Phys. Chem. Chem. Phys., **10** (2008) 393–404.

Ultrafast dynamics in thiophene investigated by femtosecond pump probe photoelectron spectroscopy and theory

R. Weinkauf,*[a] L. Lehr,†[b] E. W. Schlag,[b] S. Salzmann[c] and C. M. Marian[c]

Received 9th July 2007, Accepted 14th November 2007
First published as an Advance Article on the web 28th November 2007
DOI: 10.1039/b710381f

A hybrid of a time-of-flight mass spectrometer and a time-of-flight "magnetic-bottle type" photoelectron (PE) spectrometer is used for fs pump–probe investigations of the excited state dynamics of thiophene. A resonant two-photon ionization spectrum of the onset of the excited states has been recorded with a tunable UV laser of 190 fs pulse width. With the pump laser set to the first intense transition we find by UV probe ionization first a small time shift of the maxima in the PE spectrum and then a fast decay to a low constant intensity level. The fitted time constants are 80 ± 10 fs, and 25 ± 10 fs, respectively. Theoretical calculations show that upon geometry relaxation the electronic state order changes and conical intersections between excited states exist. We use the vertical state order S_1, S_2, S_3 to define the terms S1, S2, and S3 for the characterization of the electron configuration of these states. On the basis of our theoretical result we discuss the electronic state order in the UV spectra and identify in the photoelectron spectrum the origin of the first cation excited state D_1. The fast excited state dynamics agrees best with a vibrational dynamics in the photo-excited S1 (80 ± 10 fs) and an ultrafast decay *via* a conical intersection, presumably a ring opening to the S3 state (25 ± 10 fs). The subsequently observed weak constant signal is taken as an indication, that in the gas phase the ring-closure to S_0 is slower than 50 ps. An ultrafast equilibrium between S1 and S2 before ring opening is not supported by our data.

1. Introduction

Thiophene, C_4H_4S, is an aromatic heterocycle because the sulfur electron lone pair fully participates at the conjugated π system.[1] It is the monomer unit of α-oligothiophene polymers which have a high photostability, a high photoconductivity and promise to bridge the properties of plastics and semiconductors.[2,3] Remarkable is the fast intersystem crossing (ISC) in small α-oligothiophenes. For example, in bithiophene almost 100% of excited molecules undergo ICS.[4] This strongly deviates from the "normal behavior" found for most of molecular systems where the ratios of ISC to the internal conversion (IC) and fluorescence rates are small.[5] Because the S_1 states of other conjugated polymers are long-lived,[2,3] this effect seems to be correlated with the presence of the sulfur atoms.

Interestingly the S_1 lifetimes of α-oligothiophenes increase with the lengths of the oligomers: bithiophene 51 ps, terthiophene 135 ps, tetrathiophene 531 ps.[4,6,7] If this trend holds also for the extrapolation to the monomer unit thiophene one would expect an ultrafast decay in agreement with experimental observations (see below). In Fig. 1 the electronic energies of singlet and triplet states (adiabatic energies) of bi-, ter- and tetrathiophene as measured previously by anion photoelectron spectroscopy are plotted *versus* 1/*n*, with *n* as the number of thiophene units.[8] An empirical model predicts for thiophenes that in such a plot the electronic state energies lie on straight lines.[8] When extrapolating to *n* = 1 (see Fig. 1) also the T_2 state is predicted to be below S_1 in agreement with electron

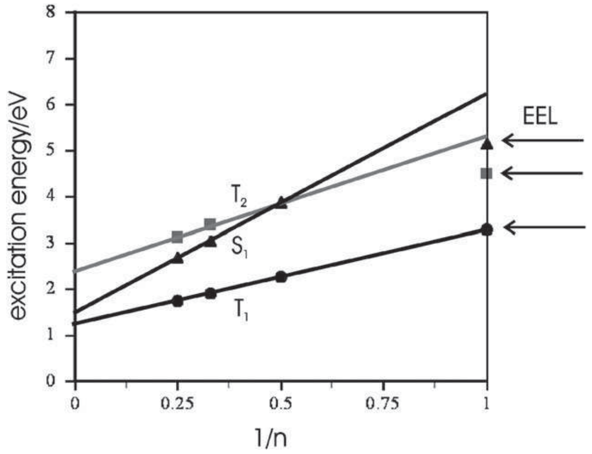

Fig. 1 The S_1, T_1 and T_2 energies in α-oligothiophenes plotted over 1/*n* (*n*: number of thiophene units) as determined by photodetachment photoelectron spectroscopy.[8] Note the extrapolation to *n* = 1 and the results from electron energy loss spectra.[12] In thiophene two triplet states are situated below S_1.

---

[a] *Institut für Physikalische Chemie und Elektrochemie, Heinrich-Heine-Universität Düsseldorf, Universitätsstraße 1, 40225 Düsseldorf, Germany. E-mail: weinkauf@uni-duesseldorf.de*
[b] *Institut für Physikalische und Theoretische Chemie der TU München, Lichtenbergstraße 4, 85747 Garching, Germany*
[c] *Institut für Theoretische Chemie, Heinrich-Heine-Universität Düsseldorf, Universitätsstraße 1, 40225 Düsseldorf, Germany*
† Present address: Accenture GmbH, Maximilianstrasse 35, D-80539 München, Germany.

energy loss spectra[9–13] and calculations.[13–16] For comparison the onset values of T_1, T_2 and S_1 as determined from the high-resolution electron energy loss spectra of ref. 12 are included in Fig. 1. Since ISC plays an important role in the photophysics of α-oligothiophenes an interesting question for thiophene is to what extent the T_2 state participates at the fast excited state dynamics.

The UV-spectrum of thiophene in gas phase has been studied by a lot of groups[13,17–39] and the assignments have been revised several times. All assignments agree that the low-lying intense transition at 41 595 cm^{-1} is the vibrational origin of S_1 and that the transitions at lower energies, despite their large intensity (up to 44% of the presumable origin peak[14]), are hot bands. To explain the high thermal population of the ground state vibrations, Varsányi *et al.*[35] attributed the hot bands to the two vibrations of lowest frequency. This assignment was in disagreement with Di Lonardo *et al.*[32] and Beiting *et al.*[36] who correlated the hot band transitions to thermal excitations of relatively high-energetic modes in the energy range 750 to 1100 cm^{-1}. For this assignment the relatively large intensity of the hot band transitions at or around room temperature can only be explained by their very favorable Franck–Condon-factors. It is important to note that surely this assignment of relatively strong bands to hot band transitions was influenced by the fact that the second excited singlet state was calculated to be vertically far above S_1 (3145 cm^{-1},[14] 2500 cm^{-1} [13]). Recent calculations of Köppel *et al.* in C_{2v} symmetry, however, show that the vertical S_1 to S_2 state difference may be smaller (1209 cm^{-1} [40]) or the states may even exchange their energetic position upon geometry relaxation.[16,40]

Beside positions and intensities the UV vapor absorption spectra of thiophene also provide energy widths. In the UV spectrum already the first strong transition is broad and the peak width increases further with increasing vibrational energy. If one would exclusively attribute the width of the first transition in ref. 33 to a fast decay, one would calculate a lifetime of about 100 ± 50 fs. Such an ultrashort lifetime is also supported by the lack of any fluorescence.[4] It may, however, be that the energy width in the UV spectrum is not only due to homogeneous broadening but also due to the rotational band contour or the limited resolution of the spectrometer. Hence the excited state lifetime could be considerably longer than that estimated from the energy width of the transition. This uncertainty was our motivation to investigate the excited state dynamics of isolated thiophene by fs pump–probe photoelectron spectroscopy in a supersonic expansion.

In fs pump–probe experiments on pure thiophene solution a lifetime of the S_1 state shorter than the laser pulse autocorrelation of 960 fs was found (laser pulse width: 650 fs).[41] In this experiment a weak strongly red-shifted emission at 430 nm (peak maximum) was attributed to the laser-induced T_1 phosphorescence emission. There is, however, such a large inconsistency of the T_1 lifetime measured in this paper (30 ps[41]) to the lifetime measured previously (1 μs[4]) that the assignment of the emission at 430 nm to the T_1 phosphorescence should be considered as questionable. Possibly high laser intensity necessary for the non-resonant two-photon S_0–S_1 pump excitation process used in this experiment may have caused artifacts. Although trying hard even in pure thiophene solution we could not find any fluorescence or phosphorescence and also triplet–triplet excited state absorption measurements failed. In conclusion, all optical experiments on thiophene support an ultrafast decay of its first excited states.

For thiophene the remaining open questions we address here are: (i) what the correct order of excited electronic states is; (ii) what the excited state lifetime in the isolated molecule is; and (iii) what the possible excited state decay mechanism is. In this work, we apply two-color UV–UV fs pump–probe photoelectron spectroscopy to investigate the excited state dynamics of thiophene. We interpret the experimental data on the basis of theoretical calculations, which are as far as needed included in this paper. The complete set of theoretical data is presented in an accompanying paper.[16] For reviews on fs time-resolved photoelectron spectroscopy see Lochbrunner *et al.*[42] and Hertel *et al.*[43]

2. Methods and techniques

2.1 Theoretical methods

The theoretical work performed up to now on thiophene is reviewed in great detail in the accompanying paper.[16] Note that all previous theoretical work on thiophene except the work published by Köppel and co-workers[40] is dealing with calculated vertical spectra. Köppel and co-workers calculated the vibronic coupling of the three lowest-lying excited singlet states, but still maintained the C_{2v} symmetry in the excited state, thus not fully allowing the molecule to react to the photoexcitation.[40] In the accompanying paper we perform excited state geometry relaxation without symmetry restrictions.[16]

In the theoretical part of the present paper we focus on vertical ionization energies at different excited state geometries to support the interpretation of the fs pump–probe PES. For comparison with the PE spectra, we also optimized the structures of the cation ground state (D_0) and first excited state (D_1) and determined their vibrational frequencies. All calculations were performed using the TURBOMOLE 5.7 program package.[44]

The TZVPP + Rydberg basis set, described in detail in ref. 15, was employed for calculating geometries and electronic energies. Vibrational frequencies were determined in the smaller TZVP basis and scaled by 0.9613. Ionization potentials were computed as the difference between density functional theory (DFT) energies of the neutral ground state using the B3LYP,[45,46] exchange and correlation functional and the results of corresponding unrestricted DFT (UDFT) calculations of the ionic species.

In the following we use the nomenclature S1, S2, *etc.* for the state order at the neutral ground state geometry. These labels are then also used at other geometries and can be understood as a nomenclature for the character of the electronic excitation (see Table 1).

2.2 Experimental methods and the experimental setup

In this paper we present fs one color resonant enhanced photoionization spectrum (R2PI spectrum) and two-color

Table 1 Calculated adiabatic excitation energies ΔE_a [eV] of various low-lying valence states in neutral thiophene as well as adiabatic IE_a and vertical ionization energies IE_v [in eV] with respect to the neutral excited state minimum. In addition, the IE values of the S1 state at the S_0 state geometry are listed. The difference $IE_v - IE_a$ is defined as ΔIE_{av} and is an indication of the geometry shift between neutral and cation states. The percentage of bifurcation for the ionic states has been estimated from the weight of the corresponding electron configuration in the neutral state and is given as value *b*

Neutral state		ΔE_a	State, configuration			IE_a	IE_v	ΔIE_{av}	*b*
S1at S_0 geometry			**D1**	$^2B_1$	$(3b_1)^{-1}$	3.73	3.83	0.10	77%
			D0	$^2A_2$	$(1a_2)^{-1}$	3.24	3.43	0.19	13%
S1	$14a' \rightarrow 15a'$	5.16	**D1**	$^2A'$	$(14^{\circ\prime})^{-1}$	3.96	5.13	1.17	84%
			D0	$^2A''$	$(8a'')^{-1}$	3.47	5.54	2.07	2%
S2	$8a'' \rightarrow 15a'$	5.05	**D1**	$^2A'$	$(14a')^{-1}$	4.07	6.11	2.04	<1%
			D0	$^2A''$	$(8a'')^{-1}$	3.58	4.51	0.93	89%
S3	$4a'' \rightarrow 19a'$	3.81	**D0/D1**	$^2A''$	$(4a'')^{-1}$	—	7.24	—	86%
T1	$8a'' \rightarrow 15a'$	3.17	**D1**	$^2A'$	$(14a')^{-1}$	5.95	7.55	1.60	<1%
			D0	$^2A''$	$(8a'')^{-1}$	5.46	6.08	0.62	95%
T2	$14a' \rightarrow 15a'$	4.34	**D1**	$^2A'$	$(14a')^{-1}$	4.78	5.38	0.60	84%
			D0	$^2A''$	$(8a'')^{-1}$	4.29	5.33	1.04	2%

pump probe photoelectron spectra (R(1 + 1′)PI-PES. The experimental setup is described elsewhere.[47] In short, the apparatus combines a linear time-of-flight mass spectrometer with a time-of-flight "magnetic bottle type" photoelectron spectrometer.[48–50] Its specificity is that both spectrometers use the same ion source, the same field-free drift region and the same multi-channel plate detector. The apparatus consists of three vacuum chambers. The inlet chamber which contains the inlet nozzle and a skimmer, the second chamber which hosts the ion source and the strong magnet of the magnetic bottle and the third chamber which contains the drift tube with a magnetic guiding field and the detector.

The nozzle has an orifice of 50 μm and can be heated up to 450 K. A continuous inlet was chosen in order to allow high laser repetition rates up to 1 kHz. The source chamber is pumped by a turbo molecular pump (1000 l s^{-1}) to achieve collision-free conditions. The supersonic expansion was skimmed 40 mm downstream with a heated skimmer of 1 mm diameter.

The second chamber contains the ion source, which is used simultaneously for the mass and the photoelectron spectrometers. The laser crosses the molecular jet perpendicularly in the middle of the first part of a two-stage ion source. For electron detection the ion source is set to zero field or to small acceleration or deceleration fields. By this the electron energy is shifted into the energy range for optimized electron energy resolution.[51] To increase electron collection efficiency a "magnetic bottle type" time-of-flight photoelectron spectrometer was used. The idea is to guide mostly all photoelectrons to the detector by an inhomogeneous magnetic field parallel to the flight axis. For electrons emitted anti-parallel, *i.e.* to the rear or to the front in the direction of the detector, a flight-time broadening occurs resulting in loss of kinetic energy resolution. Hence, for practical reasons a compromise has to be found between detection efficiency and energy resolution.

For ion detection after 1 or 2 μs the extraction plates are pulsed to a high voltage (1500 and 1000 V) to accelerate the ions to the detector. The two-field ion source is constructed in such a way that the space focus can be corrected to the second order.[52] The flight path was 50 cm providing a mass resolution of $m/\Delta m = 750$. Ions and electrons were detected on the same multi-channel plate detector. Ions or electrons enter the detector by a gold mesh. The first MCP surface is set to +200 V for electron and ion detection. Hence positive ions with energy of 1250 eV are still detected with reasonable detection efficiency.

As a result of our timing scheme first the electrons arrive and then the positive ions. All measurable photoelectrons reach the detector within the first 2 μs and therefore the photoelectron spectrum can be discriminated from even the fastest ion species in the mass spectrum. The signal was split with a 50 Ω, 6 dB power divider (SUHNER). The first 2 μs of the photoelectron spectrum were measured with a single particle counting system (Stanford Research SRS430) and the ion mass spectrum was recorded by an oscilloscope or gated integrators. The energy resolution of the photoelectron spectrometer depends on the overall kinetic energy and is, for example, 49 meV for 0.5 eV and 65 meV for 1 eV photoelectron kinetic energy. The photoelectron energies and intensities were calibrated by ionization of CH_3I and the two spin–orbit components of I.

The laser system used for the experiments is a commercially available femtosecond laser system consisting of an argon-ion pumped Ti:Sapphire oscillator (Coherent Mira Basic), a regenerative amplifier (Spectra Physics Superspitfire) pumped by an Nd:YLF Laser (Spectra Physics Supermerlin) followed by a multi-pass amplifier. The pulses of the fundamental of 790 nm have a pulse duration of about 80 fs and are afterwards frequency converted by a parametric generator (Light Conversion TOPAS), mixed and frequency doubled. The ultraviolet laser pulses are tunable between 230 and 280 nm and have typical energies of up to 20 μJ. We typically use 5 μJ for the pump (238.4 nm) and 10 μJ for the probe (276 nm) excitation. The pulse duration in the UV is 190 fs as measured directly in the supersonic expansion *via* non-resonant two-photon ionization of furan. Tunable wavelengths were obtained by keeping the Ti:Sapphire oscillator frequency constant and tilting the non-linear crystal of the parametric generator. Point-wise wavelength calibration is performed by a monochromator. All features of the OPA lasers and the mixing and doubling processes are computerized and optimized automatically.

3. Theoretical and experimental results and their comparison

In this chapter we compare excited state spectra as well as pump–probe and HeI photoelectron spectra with theoretical data.

3.1 The lowest excited states of thiophene and the interpretation of the UV spectrum

In the following we present a selection of excited state calculations, which are reported in more detail in the accompanying paper.[16] The theoretical data are used for comparison to previously published gas phase UV spectra and to our one-colour resonant two-photon ionization (R2PI) spectrum recorded with a fs laser in a supersonic expansion.

3.1.A Theory: excited state calculations, the order of states. The ordering of the electronic states of thiophene changes when the excited states are allowed to relax their geometry. In the following we use the nomenclature S1, S2, *etc.* for the vertical state order at the neutral ground state geometry and S_1, S_2, and so forth for the adiabatic state order. The labels S1, S2 and S3 are then better understood as a nomenclature for the character of the electronic states: S1 and S2 are π–π^* states ($14a' \rightarrow 15a'$ and $8a'' \rightarrow 15a'$) and S3 is a π–σ^* state ($4a'' \rightarrow 19a'$). When going from vertical to adiabatic geometries the S3 state becomes S_1, S1 becomes S_3 and S2 remains S_2. From this it follows that there are conical intersections between excited states, which are expected to be involved in the fast dynamics. The situation is shown as a sketch in Fig. 2. A vertical grey band indicates the Franck–Condon area from the S_0 ground state geometry. Note that the *x*-axis is schematic and is not a single coordinate. Note also that due to the conical intersections the local minima are minima on a single surface.

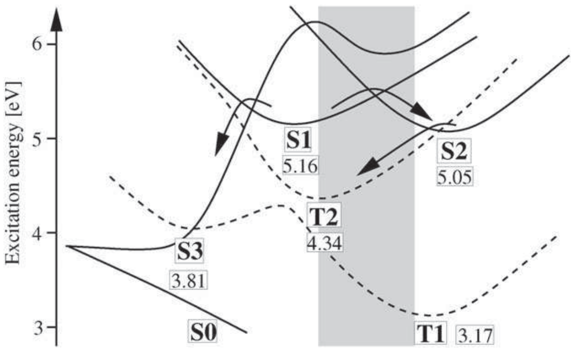

Fig. 2 Electronic state energies and qualitative potential energy surfaces of the first electronic excited states of thiophene. Note that the nomenclature S1, S2 ... stands for the electronic character of the electronic states. After photoexcitation to S1 the main relaxation pathways (i) and (ii) are indicated by arrows. Note that the energy of conical intersections is not explicitly known and that the motion through the intersection can even take place below the crossing. The S_0 Franck–Condon range is indicated by a vertical grey band. For further explanation see text.

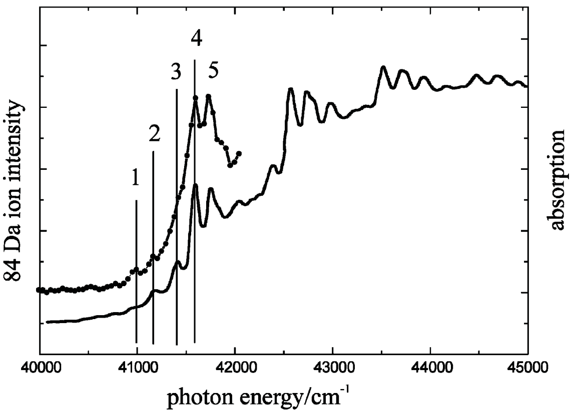

Fig. 3 One-colour fs R2PI spectrum of thiophene (upper trace) recorded in a supersonic expansion in comparison to the UV vapour absorption spectrum at room temperature (lower trace, taken from ref. 33). Note that despite the cooling in the supersonic expansion the intensities of peaks 1–3 are similar in both spectra. Because the adiabatic energy of S2 is predicted to lie below S1, transitions 1–3 may be due to S_0–S2 transitions. For further explanations see text.

The UV absorption spectrum of thiophene in the gas phase taken from ref. 33 is displayed in Fig. 3 (lower trace). It shows a high peak density on top of a broad unresolved hump. The high peak density can have several reasons:

(i) hot bands,

(ii) a superposition of the vibronic S_0–S1 and S_0–S2 transitions and

(iii) low frequency modes of a single or several excited states.

Ad (i): Assuming that the vibrational energies of the excited state are similar, previous vibrational assignments attributed even intense transitions to hot bands.[32] Measurements with different temperatures, however, showed that this is not the case.[33]

Ad (ii): To unravel the contribution of the excited states to the first part of the UV spectrum one also needs at least rough estimates of Franck–Condon factors. As stated above, S1 is below S2 in the vertical absorption spectrum, but adiabatically S1 is above S2. This means that the S1 geometry is closer to the S0 geometry than the S2 geometry. Unfortunately this geometry effect cannot be directly observed in the UV absorption spectrum because S1 and S2 bands can overlap. However, the character of the electronic excitations of T1 and S2 as well as T2 and S1 correspond to each other. The geometries of the corresponding states are therefore very similar in our calculations. Hence, the broad T1 spectrum and the relatively sharp T2 spectrum in ref. 12 support the above statement that the S0 to S1 geometry change is smaller than the S0 to S2 geometry change. On this new basis the gas phase UV absorption spectrum in Fig. 3 (lower spectrum)[33] is then tentatively explained by a soft onset of the S0–S2 transition (the S2 origin is calculated to be at 5.05 eV[16]), which is overlaid by the strong S0–S1 onset. The open question is at which energy the S2 state shifts into the S0 Franck–Condon range. On this basis the assignments of the first small bands in the UV spectrum of thiophene, classified up to now as hot bands, should be partly reconsidered and probably reinterpreted as S0–S2 cold band transitions. The strong transition No. 4 at 5.156 eV[13] is then still attributed to the origin transition of S1 (the S1 origin is calculated by us to lie at 5.16 eV[16]) and the intense transitions at higher energies to vibrations of S1 (see iii).

Ad (iii): We find low-frequency modes in the excited states of thiophene, which can explain the dense vibrational structure in the UV spectrum. Frequency calculations of the excited states in ref. 16 find large shifts to lower energies for bond stretching modes and out-of-plane modes. For example, the lowest-frequency mode in the non-planar S2 calculated by harmonic approximation has the energy of 166 cm^{-1} (TDDFT). Note, however, that this mode is an out-of-plane mode in a double well potential and should therefore in reality have even smaller energy. This example shows that in contrast to the neutral ground state (lowest-energetic mode 462 cm^{-1}) in the excited states there are low-energy modes. Although the equivalent frequency calculations for S1 are technically difficult[16] and have not been performed, one can assume that also in the non-planar S1 low-frequency vibrations exist, which could explain the strong transitions above transition No. 4. This is strongly supported by the fact that the fingerprint formed by peaks 4 and 5 is repeated several times at higher energies. Hence it seems as if exclusively the S1 state contributes to the strong transitions in the UV spectrum of thiophene as shown in Fig. 3 (solid line). This tentative interpretation is also supported by our fs R2PI spectrum recorded in a supersonic expansion (see next section).

3.1.B Experiment: Fs resonant two-photon ionization (R2PI). We had the following reasons to record fs R2PI spectra of thiophene:

(i) The wavelength calibration of fs UV lasers is complicated and we wanted to make sure that the pump laser is resonant with the thiophene transition.

(ii) The R2PI spectrum also could prove whether a resonant ionization scheme *via* excited states works and non-resonant contributions are weak.

(iii) A R2PI spectrum of thiophene cooled by a supersonic expansion might provide information on the interpretation of the first weak peaks as hot or cold bands.

For recording the R2PI spectra the fs laser wavelength was tuned and the parent cation signal recorded. In Fig. 3 the one-color fs R2PI spectrum of thiophene (upper trace) is compared to the absorption spectrum taken from ref. 33 (lower trace). With fs R2PI only the first part of the excited state spectrum around the origin was recorded because of the wavelength limitation of the doubling crystal. Due to the broad bandwidth of the fs laser the fs R2PI spectrum is broader than the absorption spectrum, but positions and structures of the first transitions are well reproduced. The small transitions 1–3 appear in both spectra at the same positions. Note that in the fs spectrum the third transition forms only a shoulder in the steep rise of transition No. 4. The similar intensities of peaks 1–3 in both spectra and the fact that we used a supersonic cooling in our fs experiment and that Di Lonardo *et al.*[32] used temperatures close to room temperature is an indication that transitions 1, 2 and probably 3 are cold bands of the S_0–S2 excitation as proposed in section 3.1.A. Peak 4 would then be assigned as before to the origin of the S_0–S1 transition. Although Varsányi *et al.*[33] and Beiting *et al.*[36] published UV spectra of thiophene at different temperatures and derived from their intensities the hot band character of bands 1, 2 and 3, there is still room for reinterpretations. Note especially that with increasing temperature the peak widths broaden and the presumable hot band transitions might "gain intensity" by an increasing overlap with the wings of the broad and intense peak No. 4, thus simulating a higher population.

The high intensity of peak 5 in our fs R2PI spectrum also supports that. Furthermore the low-frequency modes found in S2 show that this transition is due to a low-frequency mode in S1 and therefore a cold band. The width of the fs R2PI spectrum in Fig. 3 (upper spectrum) shows that with a fs pulse if the wavelength center of the fs laser is set to transition No. 4 a preferential excitation of the origin band 4 is possible, but that transitions 3 and 5 as well as other transitions hidden in the broad pedestal could be excited.

3.2 Energetics and geometry of the two lowest ionic states

In this chapter calculations of the vertical and adiabatic ionization energies of D_0 and D_1 are compared to the HeI and one-colour fs PE spectra presented in Fig. 4. The HeI spectrum is taken from Baker *et al.*[53]

3.2.A Theory: calculations on the two lowest ionic states and comparison to HeI PES. At fixed S_0 geometry, we obtain the first ionization energy for thiophene of 8.82 eV in good agreement with previous theoretical results.[13,54–56] Our results are compared with previous work in Table 2. The experimental values for the ionization onset are 8.80,[57] 8.85 eV,[58] 8.87 eV,[59–62] 8.90 eV,[63] 8.96.[64] In Fig. 4 our fs PE spectrum of thiophene at 50 fs pump–probe delay is compared to the HeI spectrum of ref. 57. The HeI spectrum shows a relatively sharp transition at the onset (peak position: 8.87 eV, width given by the PE resolution), which is attributed to the origin of the ground state D_0 ($^2A_2$) of the thiophene radical cation (this defines the experimental adiabatic IE to 8.87 eV). Some resolved vibrational features follow at higher energies, but

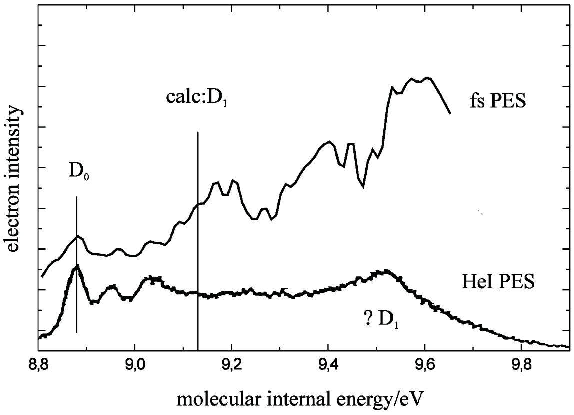

Fig. 4 Photoelectron spectra of thiophene: fs pump–probe R(1 + 1′)PI PES at 50 fs pump–probe delay (upper trace) and first part of the HeI spectrum taken from ref. 57. The first vibronic transitions of D_0 in the HeI spectrum are well reproduced in the fs PES. The broad peaks at higher energies in the fs PES do not match the D_0 state frequencies and are assigned to transitions to the D_1 state. For further explanation see text. The pump and probe wavelengths were 238.4 nm, and 276 nm, respectively.

Table 2 Calculated vertical IE_v [eV] and adiabatic ionization potentials IE_a [eV] of thiophene with respect to the electronic ground state minimum in comparison with literature values. (Experimental vertical ionization potentials: X^2A_2 = 8.87 eV, A^2B_1 = 9.52 eV[59])

Method	Ionic state			IE_v	IE_a	Ref.
DFT	$\mathbf{D_1}$	$^2B_1$	$(3b_1)^{-1}$	9.22	9.12	This work
	$\mathbf{D_0}$	$^2A_2$	$(1a_2)^{-1}$	8.82	8.63	
MRD-CI	$\mathbf{D_1}$	$^2B_1$	$(3b_1)^{-1}$	9.20		Palmer *et al.*[13]
	$\mathbf{D_0}$	$^2A_2$	$(1a_2)^{-1}$	8.93		
GF	$\mathbf{D_1}$	$^2B_1$	$(3b_1)^{-1}$	8.92		Palmer *et al.*[13]
	$\mathbf{D_0}$	$^2A_2$	$(1a_2)^{-1}$	8.82		
SAC-CI	$\mathbf{D_1}$	$^2B_1$	$(3b_1)^{-1}$	9.05		Wan *et al.*[54]
	$\mathbf{D_0}$	$^2A_2$	$(1a_2)^{-1}$	8.92		
OVGF	$\mathbf{D_1}$	$^2B_1$	$(3b_1)^{-1}$	9.07	8.93	Trofimov *et al.*[56]
	$\mathbf{D_0}$	$^2A_2$	$(1a_2)^{-1}$	8.65	8.42	

then the spectrum becomes unstructured. At 9.52 eV a broad hump is observed which was assigned to ionization to the first excited state D_1 ($^2B_1$) of the thiophene cation. Because the first transition to D_0 has the highest intensity the vertical and the adiabatic IE should be very similar. When relaxing the cation ground state geometry we calculate an adiabatic IE of 8.63 eV for D_0, just 0.19 eV below the vertical value. The comparison with the HeI spectrum shows that the error of the calculation of the adiabatic IE is −0.24 eV.

The second vertical IE of 9.22 eV, obtained at the (U)DFT level, agrees well with other theoretical values, but is about 0.30 eV lower than the broad hump in the HeI PES,[57] which was up to now attributed to the D_1 onset (Fig. 4, lower trace). The fact that the HeI D_1 spectrum is broad could, in principle, be due to a strong geometry shift of D_1 *versus* S_0 and/or a short lifetime. When relaxing D_1 a conical intersection with the D_0 state is reached in an in-plane asymmetric coordinate (b_2 symmetry) presumably close to the D_1 potential minimum at 9.12 eV, in agreement with earlier theoretical studies.[56] The presence of this intersection predicts a short lifetime of D_1 and a strong vibronic coupling between the D_0 and D_1 states. Especially the vibrational energy levels in D_0 which are close or isoenergetic to the D_1 levels should strongly couple to D_1 and also borrow transition intensity from there. This should lead to a broad and complex D_1 PE spectrum. The small difference between the adiabatic and the vertical IE of 0.1 eV shows that a geometry shift cannot account for the fact that D_1 is weak in the HeI PES.

3.2.B Experiment: the fs pump–probe PES at early pump–probe delay. The resonant two-color fs pump–probe PE spectrum (R(1 + 1′)PI PES) of thiophene at a pump–probe delay of 50 fs is presented in Fig. 4 above the HeI PES taken from ref. 57. The pump and probe wavelengths were 238.4 and 276 nm, respectively. At low internal molecular energies, the fs pump–probe PES reproduces the origin of the D_0 ($^2A_2$) state and the following two vibrational states of D_0 (compare Table 3). At higher ion energies intense and broad structures with increasing intensities are observed.

There are three possibilities for the assignment of the broad features at higher ion energies in the fs R(1 + 1′)PI PES:

(i) The transitions at higher ion energy are attributed to D_0 vibrations.

Table 3 Calculated vibrational frequencies ν of the D_0 ionic ground state of thiophene. All values have been scaled by 0.9613

Mode	Symmetry	ν/cm^{-1}
1	b_1	348
2	a_2	427
3	b_2	463
4	a_1	592
5	b_1	682
6	a_2	747
7	b_2	814
8	a_1	817
9	b_1	830
10	a_2	901
11	b_1	970
12	a_1	1034
13	a_1	1095
14	b_2	1204
15	a_1	1299
16	b_2	1324
17	a_1	1458
18	b_2	3094
19	a_1	3100
20	b_2	3103
21	a_1	3112

(ii) Electronic energy is lost for the photoionization due to an electronic inter-state relaxation.

(ii) The PES structures at higher energies involve transitions to the D_1 state.

Ad (i): The spacing between the D_0 origin and the first broad, strong feature is about 0.25–0.35 eV, *i.e.* approximately between 2000 and 2800 cm^{-1}. Calculations of the vibrational frequencies of D_0 (see Table 3) show that these transitions could only be attributed to combination bands and overtone vibrations. The exclusive and intense appearance of overtones and combination bands in any type of spectra is, however, very improbable in low-symmetry molecules. We therefore rule out this possibility.

Ad (ii): If the excited S1 state relaxes during the pulse width of the pump laser to a lower electronic state, the excitation from this vibrationally hot state yields transition energies, which are then given by the vibrations in the neutral excited state and the vibrations in the cation D_0 state. Because in the lower electronic state most of the vibrational energy is lost for ionization, the transitions to the cation should be shifted to lower electron energies. This should be a continuous energy shift in the time-resolved fs PES because of the present internal vibrational redistribution and assumed high vibrational density in the relaxed state. This is improbable because the PE spectrum at 0 fs or even at negative delays contains the same energetic features: they just appear and decay. Further reasons why point (ii) is implausible will be discussed in section 3.3.B.

Ad (iii): We strongly favour case (iii) because ionization from S1 strongly favours excitation to D_1 and the energetic position of the first broad structure (between 9.1 and 9.23 eV) would well agree with the calculated adiabatic IE of D_1 (9.12 eV). The fact that the PES spectrum is dense around the D_1 state origin is then explained by a strong vibronic D_0–D_1 coupling close to the conical intersection. The reason why the origin of D_1 is observed in R(1 + 1′)PI PES *via* S_1, but not in HeI spectroscopy is surely not given by the different Franck–Condon factors when exciting from S_0 or *via* S1 to the ion. It is, however, frequently observed in HeI PE spectroscopy that at the conical intersection the contour of the PE spectrum is distorted.

3.3 The excited state dynamics

3.3.A Experiment: the pump–probe PES. In Fig. 5 the contour plot of the fs pump–probe PE measurement is presented. The pump and the probe wavelengths used for ionization were 238.4 and 276 nm, respectively. The molecular internal energy (sum of pump and probe photon energy minus electron energy) is plotted *versus* the pump–probe delay. At pump–probe delay intervals of 25 fs full PE spectra have been recorded. In Fig. 5 the electron intensity is encoded into an equidistant color code (15 colors from green = low to red = high). Three vertical lines at different pump–probe delays are included to guide the eye. Two vertical lines mark the "low" (8.87 ± 0.01 eV) and "high" ion energies (9.55 ± 0.01 eV) for which cuts along the time axis are shown in Fig. 6.

In Fig. 5 and 6 at first glance it seems that with increasing pump–probe delay time the PE intensity builds-up and simply decays. Obviously the dynamics in the excited states of thiophene is faster than the pump and probe laser pulse widths of 190 fs. Due to that it is, in principle, difficult to find the small deviations from the laser pulse form. It is especially impossible to estimate rates directly from the curves without simulation, because at all pump–probe delays population build-up and decays are simultaneously active.

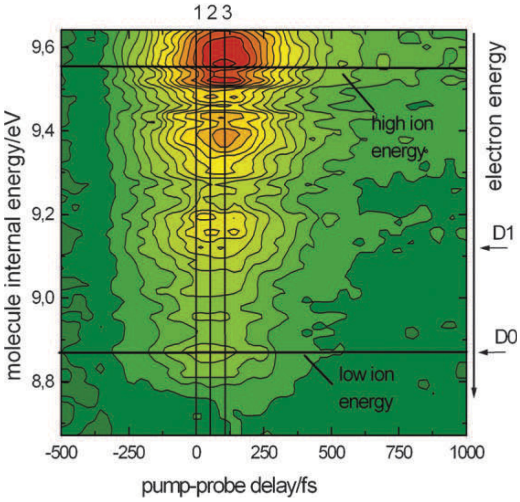

Fig. 5 Time-dependent fs two-color pump–probe R(1 + 1′)PI photoelectron spectrum of thiophene recorded *via* the presumable origin of S1. The following details are important: (i) The intensity maximum is, in general, delayed as expected for excitation through a resonance (see vertical line 1). (ii) There is a shift of the PE intensity maxima with the pump probe time when going from low to high ion energies (compare vertical lines 2 and 3). (iii) The decay of the PE signal at high ion energies is mostly given by the temporal shape of the pump laser and as ultrafast. (iv) A small pedestal remains, which is essentially constant for the time investigated. (v) Distinct peaks are observed along the energy axis, which simply appear and disappear with pump–probe delay. The pump and probe wavelengths were 238.4 and 276 nm, respectively. Note the two horizontal lines marking high and low ion energies (see Fig. 6) and the arrow marking the calculated D1 onset. For further explanations see text.

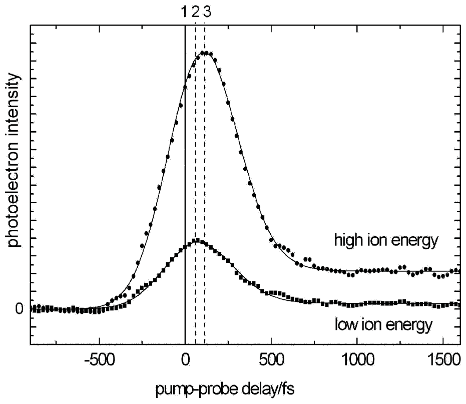

Fig. 6 Two cuts through the fs pump–probe photoelectron spectrum of Fig. 5 at two ion energies: (i) upper trace: pump–probe spectrum for the molecular energy of 9.55 ± 0.01 eV, and (ii) lower trace: pump–probe spectrum for a molecular energy of 8.87 ± 0.01 eV. Note the small time shift of the intensity maxima in the upper *versus* the lower spectrum. Note also the remaining signal at high ion energy and at long pump–probe delays. Both curves are used for the simulation of the excited state decay. For further explanations see text.

The following details can be found in the time resolved spectra of the excited state dynamics in thiophene (see Fig. 5 and 6):

(i) At pump–probe delay zero fs the signal still rises and the maximum intensity is reached at positive pump–probe delays, as expected for a pump–probe scheme through a resonant transition. This build-up dynamics is given by the S_0–S_1 absorption cross section and the laser intensity, which is time dependent. Therefore in the following discussion we do not refer to the pump build-up as a molecular dynamics.

(ii) At high ion energy (low-energy electrons) the maximum of the electron intensity is reached at longer pump–probe delay times than at low ion energy (high-energetic electrons). This temporal shift of the intensity maxima when going from low to high ion energies is about 60 fs (compare Fig. 6 upper and lower curves).

(iii) The temporal PE signal decay is comparable to the decrease of the Gaussian laser pulse intensity with time and is hence very fast.

(iv) At high ion energy a weak long-lived signal remains at longer pump–probe delays.

(v) Along the energy axis distinct peaks are observed which are especially helpful in finding a mechanism.

Several mathematical models can be set up to simulate the time-dependent PE spectra. We need, however, a model which is adapted to the photo-physics of thiophene. Hence in the following on the basis of the spectroscopic features we first search for a molecular mechanism and then set up a simulation which is based on the mechanism found.

3.3.B Theory and discussion: plausible decay pathways. In photoexcited thiophene several fast relaxation pathways are possible. The two most plausible pathways after S1 excitation are (see arrows in Fig. 2):

Relaxation pathway (i). A fast decay of S1 *via* a first conical intersection to S2, then a decay through a second intersection to T2 and from there a conventional internal conversion to T1.

Relaxation pathway (ii). A fast decay of S1 by a ring-opening to S3 possibly followed by a further relaxation back to the cyclic S_0 state. Also here all radiation-less transitions can occur through conical intersections.

Note that in both cases also an ultrafast equilibrium between S1 and S2 could be present, as predicted by Köppel *et al.*[40] An ultrafast oscillation between S1 and S2, which would take place in 10 fs,[40] surely could not be resolved by our limited time resolution. It would, however, lead to an average population in S1 and S2, which can be observed because S1 and S2 have different ionization preferences to the cation states D_0 and D_1 (see below).

Also, other decay pathways are possible which we do not consider in the following, because we believe that they are not explaining the ultrafast excited state decay of thiophene and therefore may only participate with a small percentage at the observed dynamics. For example, in relaxation pathway (ii) directly after relaxation to S3 some populations could go back to the cyclic T2 (see Fig. 2). Such an inter-system crossing (ISC) in a steep part of the S3 surface is, however, very improbable. Other routes involve already in the first relaxation step transitions to a triplet state which is not in accord with the ultrafast timescale found.

From our calculations of the excited state energies alone it is very difficult to decide along which pathway the system might decay. Whereas the relative accuracy of the excited state calculations causes only small errors (±0.1 eV), the bigger problem is that the potential energy surface crossings found might not be the lowest ones on the conical intersection seams and that even intersections might exist which we did not find. To overcome these problems one would need full quantum dynamic excited state calculations in C_1 symmetry, which are currently not feasible.

In the following we compare theory and experiment in order to find a plausible excited state decay mechanism. Such a comparison is complex since on the relaxation cascade through different electronic states the parameter set for the probe excitation changes considerably from state to state. The most important parameters are (a) the electronic transition moments, here the transition moments for the probe ionization to the ionic ground and first excited states, and (b) the corresponding Franck–Condon factors. (c) In addition, at each relaxation step a part of the electronic energy is converted to vibrational energy and thus the energy needed for ionization increases.

Whereas (a) and (b) can be addressed more or less directly by our calculations, point (c) is more difficult to treat. This is because the vibrational energy becoming available in the relaxation complicates the discussion of the Franck–Condon factors in (b). Our calculations cannot answer the question how in a state crossing through a conical intersection the electronic energy is distributed over the vibrational modes of the lower state. This is clearly a multidimensional problem in the normal mode manifold. For the interpretation of the PE spectra it would be important to know whether directly after the surface crossing the converted energy is mainly concentrated in coordinates in which the geometry shift between the excited state and the cation states is small or in coordinates in which this geometry shift is large. Because of the high vibrational density it is improbable that the reaction coordinate of the conical intersection is the coordinate with the largest geometry difference to the cation state.[16] This means that although we work in the gas phase and the energy has to stay in the molecule, the energy is mostly distributed over many normal modes, and we have a relatively small vibrational energy per mode. Hence in each electronic relaxation step electronic energy is lost for ionization.

Ionization from neutral electronic excited states (the probe process). In the following we present theoretical data for the probe ionization from the different neutral excited states to the two lowest cation states. We calculated electronic transition preferences as well as adiabatic and vertical ionization energies. The results are presented in Table 1. As for the neutral also we correlate the electronic character D0 with that of the cation D_0 state and the electronic character D1 with that of the D_1 state. The reason is that also the ionic states swap their energetic order upon geometry changes. For D0 the hole is in the $1a_2$ orbital (C_{2v} symmetry) or the corresponding 8 a″ orbital (C_s symmetry), for D1 ionization takes place from the $3b_1$ orbital (C_{2v} symmetry) or the corresponding 14a′ orbital (C_s symmetry).

In fs experiments in the gas phase one typically worries in the first place about the electronic energy which in electronic surface changes is converted to vibration. As our calculations, however, show the geometry relaxations of the electronically excited states of neutral thiophene lead to large increase of the energy required for vertical ionization. This means that after an electronic relaxation step the up-shift of the vertical IE can be larger than the energy converted to vibration. In some cases the neutral geometry shift caused by the dynamics may even lead to a reversal of the vertical order of the ionic states. This means that in the fs PE spectra peak positions and intensities can depend equally on vertical ionization energies as well as on the neutral electronic energy conversion.

The vertical ionization energies also contain qualitative information on Franck–Condon (FC) factors between the excited neutral state and the two cation states D0 and D1. For a better comparison to the experiment we calculated the difference ΔIE_{av} between the adiabatic IE and the vertical IE. ΔIE_{av} then corresponds to the vibrational energy at which the Franck–Condon factor becomes maximal and is therefore a measure for the neutral-to-cation geometry shift: a large ΔIE_{av} corresponds to a large geometry shift, a small ΔIE_{av} to a small geometry shift. The data are presented in Table 1 and visualized qualitatively in Fig. 7a and b. In Fig. 7a and b the order of the excited states S1, S2, S3, T2, and T1 are arranged (from left to right) in such a way that the two above-mentioned relaxation pathways (i) and (ii) are mimicked. Note that the dynamics is a multidimensional problem involving different reaction coordinates. It is therefore impossible to draw the decay pathway along a single reaction coordinate. Note also that the vibrational energy available after relaxation is

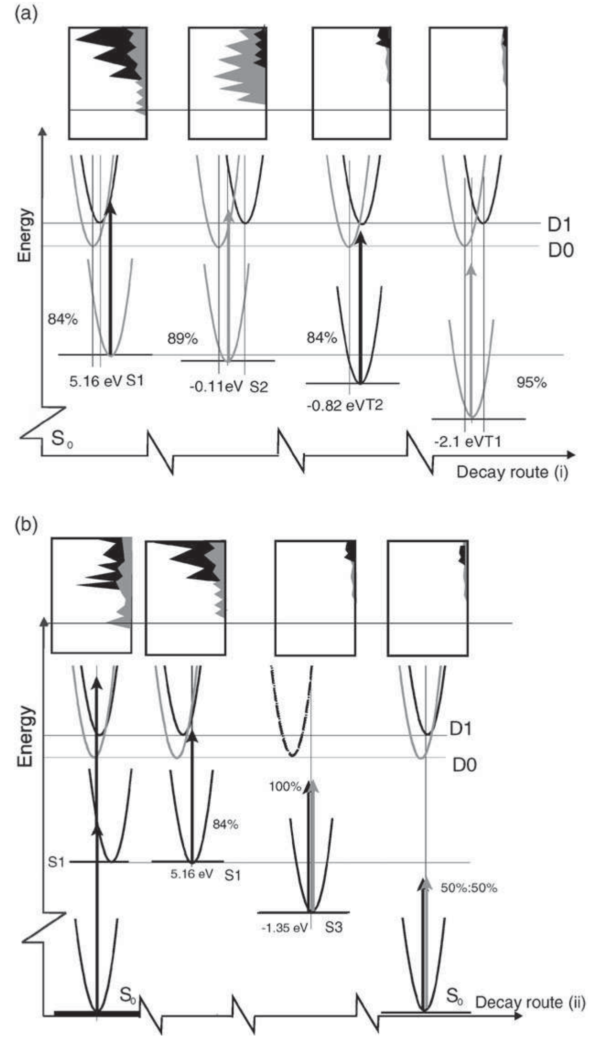

Fig. 7 The insets show energy schemes, qualitative geometry shifts and estimated PE spectra for the decay of the S1 state: from left to right (a) decay of S1 *via* route (i) and (b) *via* route (ii) (for explanation see text). The *x*-axis is interrupted to indicate that the reaction coordinates are fictive and different for each state. Note that although the experiment was performed in the gas phase the energy in one mode is less than the electronic energy converted to vibration. Section (b) contains the ionization *via* S1 at the S_0 geometry (first inset) and the S1 equilibrium geometry (second inset). The intensity changes between the PE spectra in the first and second inset in (b) (the PE spectra before and after the wave packet motion) explain the first part of the fs PES in Fig. 5. Note the electronic preferences for ionization: in most cases either ionization to D0 (gray arrows and peaks) or D1 (black arrows and peaks) is enhanced in the ionization. Note also that the vertical ionization energies undergo strong variations when going through different neutral states. We attribute the dynamics of photoexcited thiophene to the relaxation pathway (ii) as shown in (b). For further explanation see text.

presumably not present in one coordinate and therefore only to a small amount is available for ionization.

Ionization from S1. With our calculated vertical IE of 8.82 eV and the vertical S1 energy of 5.39 eV taken from the accompanying paper,[16] the vertical ionization energy from S1 ($2\ ^1A_1$) to the first ionic state D0 ($^2A_2$) at 0 delay time (this means still at the S_0 geometry) amounts to 3.43 eV. As known from section 3.2.A for ionization from S_0 ΔIE_{av} is 0.19 eV, which shows that S_0 and D0 have essentially the same geometry. For ionization *via* S1 we expect the cross section for ionization to D0 to be weak as the $1a_2 \rightarrow 2a_2$ excitation represents only a minor component (13%) of the multi-configurational S1 ($2\ ^1A_1$) state in the FC region of S_0. Ionization from the leading $3b_1 \rightarrow 4b_1$ electron configuration in S1 yields predominantly the first excited ion state D1 ($^2B_1$). As known from section 3.2 for ionization from S0 to D1 ΔIE_{av} is 0.1 eV, which in conclusion means that *via* S1 at pump–probe delay zero (at the S_0 geometry) a weak D0 but a strong D1 onsets are expected, in agreement with the fs R(1 + 1′)PE spectrum at 50 fs (see Fig. 3 and Fig. 7b first inset).

For ionization from the optimized S1 geometry (adiabatic S1 energy: 5.16 eV) to D0, the adiabatic IE is 3.47 eV and the vertical IE 5.45 eV, leading to $\Delta IE_{av} = 2.07$ eV. This means that the weak ionization channel to D0 would be spread over many vibrational excitations and especially the excitation to the D0 origin is very weak or missing (see Fig. 7b second inset, gray peaks). Note that at the structure of the S1 minimum the ionic states have a reversed order, *i.e.*, the D0 potential is situated energetically above the D1 surface (see Table 1). From the relaxed S1 the adiabatic IE of D1 is 3.96 eV and the vertical IE 5.13 eV. Hence, at the optimized S1 geometry ΔIE_{av} to D1 is 1.17 eV. In the part of the PES, which is accessible by our photon energy, this should lead to a distinct onset of the D1 state but also to vibronic bands with increasing intensities for increasing energies (see Fig. 7b, second inset, black peaks).

In conclusion, for the ionization route to D1 *via* S1 the ΔIE_{av} increases from 0.10 to 1.17 eV when the S1 state relaxes from the S_0 geometry to its optimum geometry. Hence a wave packet dynamics transferring the S1 state population from the S_0 geometry to the optimal S1 geometry would result in a time shift of the maximum electron intensity from low to high ion energies for the probe ionization. An even stronger energy shift effect with time is expected for the weak ionization to D0. The PE spectra for ionization *via* S1 at the S_0 and at the S1 geometry are qualitatively visualized in Fig. 7b (left two cases, gray: D0; black: D1). Note that the calculations visualized in Fig. 7b predicts for the wave packet dynamic in S1 a time shift of the intensity maxima between low and high ion energies as found in Fig. 5 and Fig. 6, lower and upper curves, respectively. Note that theory and Fig. 7b predict also a time shift between the intensity maxima at the energy of the D1 origin and the high ion energy, which is indeed found in the fs PES in Fig. 5 (compare positions of intensity maxima at the energy marked by the arrow "D1" and at the upper horizontal line).

The above agreements between theory and experiment strongly support the explanation of the time shift of the intensity maxima in the fs PES by a wave packet dynamics in S1.

It will be especially important for the simulation (see section 3.3.C) that theory and its visualization in Fig. 7 also predict that after the S1 wave packet motion the transition probability to the D0 origin vanishes, which means that the decay dynamics of the electron intensity at the D0 origin energy carries the information about the duration of the wave packet motion in S1. This wave packet dynamics is found in the lower experimental curve of Fig. 6.

Ionization from S2. In this section we want to clarify whether S2 participates in the excited state dynamics or not. At the S2 minimum structure (Fig. 7a, second inset) the optical excitation cross section favors strongly ionization to D0. For this ionization channel we calculate $IE_a = 3.58$ eV, $IE_v = 4.51$ eV and $\Delta IE_{av} = 0.93$ eV. For the weak D1 ionization channel we determine $IE_a = 4.07$ eV, $IE_v = 6.11$ eV and $\Delta IE_{av} = 2.04$ eV.

In the case of ionization from S2 we expect therefore relatively strong excitation to the origin and to vibrations of D0, but very weak ionization to D1. In addition, the latter would be smeared out over a large energy, which is mostly outside of our detection range due to the limited probe photon energy. In our fs $R(1 + 1')$PI PES, however, we find strong transitions which do not fit the D0 vibrations and which we attributed to transitions to D1 and coupled D0 combination bands (see section 3.3.B).

Especially the fact that in the experiment (Fig. 5) the electron intensity at the D0 origin transition energy (Fig. 6 lower curve) peaks earlier in pump–probe time then the electron intensity at the high-ion energy (Fig. 6 upper curve) is exactly opposite to what is expected for a S1-to-S2 dynamics (see Fig. 7a first two insets).

In case there would be an ultrafast oscillation between S1 and S2 or an equilibrium, we would at least see a time-averaged contribution of the two D0 and D1 ionization processes. This is clearly not observed also ruling out this possibility. Only in the very improbable case that the absolute ionization cross section S2–D0 would be considerably smaller than the ionization cross section S1–D1 we would not see the presence of a S2 population. In conclusion a participation of S2 is not supported by our experimental results and is unlikely.

At this stage we are able to explain the time-shift of the intensity maxima in the fs PES. We still have to explain the fast decay of the PE signal with time. For this in principle decays to T2 and S3 could account.

Ionization from T2 and T1. The decay of S1 to T2 directly or *via* S2 converts 0.82 eV of electronic energy to vibrations. Due to the limited pump photon energy, this electronic energy loss makes ionization from T2 in principle weak. In addition, from T2 preferentially the second ionic D1 state is addressed decreasing even further the ionization probability. For the T2 to D1 ionization the adiabatic IE is 4.78 eV, the vertical IE 5.38 eV and ΔIE_{av} is 0.60 eV. For the less favored T2 to D0 transition the adiabatic IE is 4.29 eV, the vertical IE 5.33 eV and ΔIE_{av} is 1.04 eV. Hence, due to the limited probe photon energy of 4.49 eV, ionization from T2 can only occur with small probability and mostly to D1. In order to match our fs PES the transition S2–T2 has to then be attributed to the ultrafast intensity decay. Well knowing that intersections between triplet and singlet states can enhance ISC we believe that it would be extremely implausible to assign this ultrafast time scale to the S2–T2 ISC.

In addition, T2 should quickly decay to T1. Although we did not find a conical intersection between T1 and T2, the internal conversion of T2 to T1 should be fast because of the small energy gap of 1.17 eV and the large geometry difference.[65] Because T1 is very low in energy (3.17 eV) ionization from T1 would be very unlikely. The nearly constant weak signal, which we find at high ion energies and at longer delays in the PE spectrum, has a lifetime larger than 50 ps, which we believe contradicts the expected fast T2–T1 dynamics.

In conclusion, our theoretical predictions for the relaxation pathway (i) (see Fig. 7a) in several points do not agree with the measured fs PES or lead to implausible assumptions. Especially the contribution of triplet states is ruled out. We therefore now concentrate on relaxation pathway (ii) *via* S3.

Ionization from S3. In relaxation pathway (ii) in Fig. 7b, after changing from S_0 to the relaxed S1 geometry (see Fig. 7b inset 1 and 2) S1 decays directly into S3 (inset 3) through a conical intersection. This pathway attributes the S1-to-S3 ring opening dynamics to the ultrafast decay dynamics in the fs PES. The decrease of the ionization intensity can be due to the fact that during the S1-to-S3 relaxation 1.35 eV is converted to vibrations and lost for ionization or due to a weak ionization cross section from the S3 in linear thiophene caused by the limited probe photon energy. The ionization from S3 (Fig. 7b, third inset) results in a mixture of D0 and D1 configurations since the asymmetric in-plane distortion (ring opening) mingles the $1a_2$ and $3b_1$ orbitals. The vertical excitation energy to the lowest-ionic state is shifted to such high energies (7.24 eV) that ionization becomes very improbable even with an internal vibrational energy of 1.35 eV. Since the non-cyclic thiophene is floppy and has high vibrational energy the transition probability to the cation is averaged over the wide potential of the chain-bending mode and thus explores areas of low energies for the cation which might still allow some small ionization probability.

Clearly because of a conical intersection of the S3 with the neutral ground state S_0 also a relaxation back to the ring structure would be possible. The question for this process is, however, to which extent the statistics of the large number of vibrational states in the linear structure is able to allow a fast recombination. After recombination to the cyclic structure ionization is practically excluded, because more than 4 eV of the electronic energy needed for ionization have to be bridged by vibrational energy or a two-photon excitation is necessary. If our interpretation that thiophene in S3 stays open is right, this would mean that the linear to cyclic recombination at high vibrational energy in the gas phase takes longer than our detection time, *i.e.* 50 ps.

In conclusion, the theoretical predictions for the relaxation pathway (ii) in Fig. 7b reproduce best the measured fs pump–probe $R(1+1')$PI PE spectrum. We do not find experimental evidence for an ultrafast equilibrium of S1 and S2 before the decay to S3.

3.3.C Simulation and time scales. Since we now have a plausible relaxation pathway we can set up a simulation model. The mechanism, which causes the time-dependent signals in Fig. 5 and 6 consists of a S1 population build-up during the pump laser pulse, a wave packet motion in S1, which brings population from the vertical geometry to the optimized S1 geometry and a fast decay to the S3. The time shift of the electron intensity maximum shows in Fig. 5 that decay to the S3 state happens in S1 from a structure different to S_0 but similar to the equilibrium structure of S1.

The PE signal at low ion energy with its maximum at about 50 fs pump–probe delay (Fig. 6 lower curve) is relatively easy to fit. It corresponds exclusively to the situation shown in the first inset of Fig. 7b and is interpreted as a laser-induced population build-up in S1 at the S_0 geometry and a decay by the wave packet motion. The build-up is given by the molecular transition moment and the laser intensity. The latter is time dependent and is assumed to follow a Gaussian time profile. It is therefore impossible to fit the build-up time by a single rate. If the S1 lifetime at the S_0 geometry would be infinitely long the maximum of the pump–probe signal would be reached exactly at the end of the pump laser pulse (at 190 fs). Because, however, the S1 population at the S_0 geometry decays by the wave packet dynamics with a time shorter than the laser pulse width, already the build-up process is affected by its decay, so that the maximum is reached at a shorter time.

The time dependence of the upper curve in Fig. 6 is more difficult to simulate because at high ion energies the PES contains two contributions: as calculations of the adiabatic and vertical IEs as visualized in Fig. 7b (left two insets) show, D0 and D1 can be excited by fs ionization form S1 at the S_0 geometry (see Fig. 7b first inset) and at the optimized S1 geometry (see Fig. 7b second inset). The S1 population before and after the wave packet motion can partly access the same cation states especially at high ion energies. Hence there is no a "yes" or "no" answer contained in the fs PES: the PES is at all times a superposition of ionization from S1 in the S_0 and the optimum S1structure. During the wave packet motion only the intensities at different ion energies change gradually with time, as observed in Fig. 5 and 6. Therefore at short pump–probe delays of the ionization process *via* S1 (which means mostly for molecules with a geometry close to the S_0 geometry) beside the origin transitions also D0 and D1 vibrations are populated. Hence the laser-induced fast build-up in S1 affects not only the fs PE spectrum at low ion energy (Fig. 6, lower curve), but also at high ion energies (Fig. 6, upper curve).

Since the wave packet motion moves population from a S_0-like structure to the optimized S1 structure, the decay of the signal at low ion energies in (Fig. 6, lower curve) contributes to the rise of the high-energetic signal (Fig. 6, upper curve). This means that the upper curve in Fig. 6 contains besides a first laser-induced build-up a second build-up dynamics caused by the wave packet motion. Hence we simulate the upper curve in Fig. 6 with two build-up rates whereby one is the decay rate of the signal in the lower curve in Fig. 6. The decay of the signal at high ion energies is finally exclusively attributed to the decay of S1 to S3.

It is necessary to understand that for the simulation both curves in Fig. 6 are used simultaneously and that the laser-induced build-up of the signal is not a molecular dynamics. Since our laser pulse widths are 190 fs the differential equations were solved numerically in 10 fs steps to allow for the temporal intensity change of the laser.

The simulation gives the following time scales: the S1 wave packet motion is simulated with 80 ± 10 fs. The decay part of the signal at high ion energy, which is attributed to the S1–S3 ring opening, is simulated with 25 ± 10 fs.

The mathematical accuracy of the fit is relatively high because the zero delay time was determined in parallel with the non-resonant ionization of furan (accuracy of the zero delay time below 25 fs). As mentioned above we justify our mechanism and the resulting simulation model by arguments which come from the PE spectra at different pump–probe times and theory. We admit that in case other mechanisms are assumed, also other simulation procedures could be chosen which would lead to quantitatively different results.

Since all time constants found lie within the laser pulse width a further inaccuracy might come from the problem that our simple model might not hold properly at the high laser intensities used. Nevertheless the real decay dynamics is expected to be ultrafast and not differ too much from the fitted time constants.

4. Conclusion

In this paper we presented measurements which show that the excited state decay of thiophene is ultrafast. Theory and experiment agree best for an excitation to the S1 state by the pump excitation, a fast wave packet dynamics in S1 (80 ± fs) which relaxes thiophene from the S0 geometry to the S1 equilibrium structure which is close to the conical intersection between S1 and S3 and an ultrafast decay *via* a conical intersection to S3 (25 ± 10 fs). The decay of S1 to the low-lying S3 opens the thiophene ring which simultaneously strongly reduces the photoionization probability. The remaining weak constant signal is attributed to an improbable ionization out of the linear structure. Its time independence is taken as an indication that the open-ring structure is entropically favoured and that recombination to the ring structure at the high energy present in the system in the gas phase is slower than our detection limit, here 50 ps. A participation of S2 at the dynamics is not observed, but cannot be fully excluded.

The complete S1–S2–S_0 cycle efficiently deactivates the electronic excitation energy, which could explain why the ring-opening is difficult to detect in solution experiments. The linear thiophene structure has been, however, postulated as reactive intermediate in photodissociation experiments in the gas phase.[66]

We cannot rule out alternative routes involving conical intersections with triplet states, but it does not seem to be reasonable that they account for such fast time scales. We also cannot rule out the involvement of other conical intersections not found in our calculations. Our ultrafast decay dynamics in thiophene also agrees qualitatively with our unpublished fluorescence, phosphorescence and excited state absorption measurements in solution, which provided no indications for long-lived excited states in thiophene. Especially, we tried to find T2 and T1 populations, but failed.

High-resolution UV spectra of cold thiophene molecules could yield further information concerning the order of electronic states of neutral thiophene, their vibrational structure (especially the nature of the hot band transitions) and their lifetime broadening. Pump–probe PE spectroscopy with shorter pulses over longer pump–probe delays and at different probe wavelength could provide a higher accuracy of the dynamics and possibly provide evidence of the dynamics of the ring closure.

A remarkable result of the calculations is that the vertical ionization energies at the relaxed geometries of the neutral excited states vary significantly from state to state. Hence, experimentally observed time-dependent shifts in PE spectra are sometimes better explained as shifts of the vertical ionization energies rather than as electronic relaxation in the neutral molecule, *i.e.*, conversion of electronic energy to vibrational energy in the neutral excited state manifold.

Acknowledgements

Financial support of the Deutsche Forschungsgemeinschaft, especially in the framework of the Sonderforschungsbereich 663, Heinrich-Heine University of Düsseldorf, is gratefully acknowledged.

References

1 *The chemistry of heterocyclic compounds, Vol. 3 and Vol. 44, Thiophene and its derivatives*, ed. A. Weissberger, E.C. Taylor and S. Gronowitz, Interscience, New York, 1952/1992.
2 *One Dimensional Metals*, ed. S. Roth, VCH Verlagsgesellschaft mbH, Weinheim, 1995.
3 *Handbook of conducting polymers*, ed. T. A. Skotheim, Marcel Dekker, New York, 1986, vol. 1 and 2.
4 R. S. Becker, J. Seixas de Melo, A. L. Macanita and F. Elisei, *J. Phys. Chem.*, 1996, **100**, 18683.
5 *Modern Molecular Photochemistry*, ed. N. J. Turro, University Science Books, Mill Valley, 1991.
6 H. Chosrovian, S. Rentsch, D. Grebner, D. U. Dahm and E. Birckner, *Synth. Met.*, 1993, **60**, 23.
7 S. Rentsch, D. V. Lap, M. Helbig and D. Grebner, *Exp. Tech. Phys.*, 1996, **42**, 47.
8 S. Rentsch, J. P. Yang, W. Paa, E. Birkner, J. Schiedt and R. Weinkauf, *Phys. Chem. Chem. Phys.*, 1999, **1**, 1707.
9 W. M. Flicker, O. A. Mosher and A. Kuppermann, *J. Chem. Phys.*, 1976, **64**, 1315.
10 W. M. Flicker, O. A. Mosher and A. Kuppermann, *Chem. Phys. Lett.*, 1976, **38**, 489.
11 E. H. van Veen, *Chem. Phys. Lett.*, 1976, **41**, 535.
12 K. R. Asmis, *PhD Thesis*, Universität Freiburg, Schweiz, 1996.
13 M. H. Palmer, I. C. Walker and M. F. Guest, *Chem. Phys.*, 1999, **241**, 275.
14 L. Serrano-Andrés, M. Merchán, M. Fülscher and B. O. Roos, *Chem. Phys. Lett.*, 1993, **211**, 125.
15 M. Kleinschmidt, J. Tatchen and C. M. Marian, *J. Chem. Phys.*, 2006, **124**, 124101.
16 Accompanying paper, S. Salzmann, M. Kleinschmidt, J. Tatchen, R. Weinkauf and C. M. Marian, *Phys. Chem. Chem. Phys.*, 2008, DOI: 10.1039/b710380h.
17 J. Pauer, *J. Chem. Soc., Abstr.*, 1897, **72**, 393.
18 J. Pauer, *Ann. Phys.*, 1897, **61**, 376.
19 W. N. Hartley and J. J. Dobbie, *J. Chem. Soc., Trans.*, 1898, **73**, 604.
20 J. E. Purvis, *J. Chem. Soc., Trans.*, 1910, **97**, 1648.
21 S. Menczel, *Z. Phys. Chem.*, 1927, **125**, 161.
22 J. Godart, *J. Chim. Phys. Phys.-Chim. Biol.*, 1937, **34**, 70.
23 H. Mohler, *Helv. Chim. Acta*, 1937, **20**, 1188.
24 G. Milazzo, *Gazz. Chim. Ital.*, 1938, **78**, 835.
25 W. C. Price and A. D. Walsh, *Proc. R. Soc. London, Ser. A*, 1941, **170**, 201.
26 W. C. Price and A. D. Walsh, *Quart. Rev. London*, 1943, **2**, 73.
27 M. R. Padhye and S. R. Desai, *Proc. Phys. Soc., London, Sect. A*, 1952, **65**, 298.
28 (*a*) G. Milazzo, *Gazz. Chim. Ital.*, 1948, **78**, 835; (*b*) G. Milazzo, *Gazz. Chim. Ital.*, 1953, **83**, 392.
29 J. J. Sicé, *J. Phys. Chem.*, 1960, **64**, 1572.
30 E. Jones and I. M. Moodie, *Tetrahedron*, 1965, **21**, 2413.
31 G. Horvát and Á. I. Kiss, *Spectrochim. Acta, Part A*, 1967, **23**, 921.
32 G. Di Lonardo, G. Galloni, A. Trombetti and C. Zauli, *J. Chem. Soc., Faraday Trans. 2*, 1972, **68**, 2009.
33 G. Varsányi, L. Hyulaszi, T. Veszpremi and T. Narisawa, *J. Chem. Soc., Perkin Trans. 2*, 1982, 761.
34 G. L. Bendalozzi, F. Bertinelli, P. Palmieri, A. Brillante and C. Taliani, *J. Chem. Phys.*, 1978, **69**, 5077.
35 G. Vasányi and T. Narisawa, *J. Chem. Soc., Perkin Trans. 2*, 1982, 761.
36 E. J. Beiting, K. J. Zeringue and R. E. Strickel, *Spectrochim. Acta, Part A*, 1985, **41**, 1413.
37 L. Nyulászy and T. Veszprémi, *Chem. Scr.*, 1986, **26**, 629.
38 L. Nyulászy and T. Veszprémi, *J. Mol. Struct.*, 1986, **140**, 253.
39 L. Nyulászy and T. Veszprémi, *Chem. Scr.*, 1988, **28**, 331.
40 H. Köppel, E. V. Gromov and A. B. Trofimov, *Chem. Phys.*, 2004, **304**, 35.
41 J. P. Yang, W. Paa and S. Rentsch, *Synth. Met.*, 1999, **101**, 624.
42 S. Lochbrunner, J. J. Larsen, J. P. Shaffer, M. Schmitt, T. Schultz, J. G. Underwood and A. Stolow, *J. Electron Spectrom. Relat. Phenom.*, 2000, **112**, 183.
43 I. V. Hertel and W. Radloff, *Rep. Prog. Phys.*, 2006, **69**, 1897.
44 R. Ahlrichs, M. Bär, H.-P. Baron, R. Bauernschmitt, S. Böcker, P. Deglmann, M. Ehring, K. Eichkorn, S. Elliott, F. Furche, F. Haase, M. Häser, C. Hättig, H. Horn, C. Huber, U. Huniar, M. Kattannek, A. Köhn, C. Kölmel, M. Kollwitz, K. May, C. Ochsenfeld, H. Öhm, A. Schäfer, U. Schneider, M. Sierka, O. Treutler, B. Unterreiner, M. von Arnim, F. Weigend, P. Weis and H. Weiss, TURBOMOLE 5.7 program package, 2004.
45 A. D. Becke, *J. Chem. Phys.*, 1993, **98**, 5648.
46 P. J. Stephens, F. J. Devlin, C. F. Chabalowski and M. J. Frisch, *J. Phys. Chem.*, 1994, **94**, 11623.
47 L. Lehr, R. Weinkauf and E. W. Schlag, *Int. J. Mass Spectrom.*, 2000, **203**, 191.
48 P. Kruit and F. H. Read, *J. Phys. E*, 1983, **16**, 313.
49 O. Cheshnovsky, S. H. Yang, C. L. Pettiette, M. J. Craycraft and R. E. Smalley, *Rev. Sci. Instrum.*, 1987, **58**, 2131.
50 H. Handschuh, G. Ganteför and W. Eberhardt, *Rev. Sci. Instrum.*, 1995, **66**, 3838.
51 R. Weinkauf and U. Boesl, *J. Chem. Phys.*, 1992, **98**, 4459.
52 R. Weinkauf, K. Walter, C. Weikhardt, U. Boesl and E. W. Schlag, *Z. Naturforsch.*, 1989, **44a**, 1219.
53 A. D. Baker, D. Betteridge, N. R. Kemp and R. E. Kirby, *Anal. Chem.*, 1970, **42**, 1064.
54 J. Wan, M. Hada, M. Ehara and H. Nakatsuji, *J. Chem. Phys.*, 2001, **114**, 842.
55 W. von Niessen, W. P. Kraemer and L. S. Cederbaum, *J. Electron Spectrosc. Relat. Phenom.*, 1976, **8**, 179.
56 A. B. Trofimov, H. Köppel and J. Schirmer, *J. Chem. Phys.*, 1998, **109**, 1025.
57 A. D. Baker, D. Betteridge, N. R. Kemp and R. E. Kirby, *Anal. Chem.*, 1970, **42**, 1064.
58 L. Klasnic, A. Sabljič, G. Kluge, J. Rieger and M. Scholz, *J. Chem. Soc., Perkin Trans. 2*, 1982, 539.
59 P. J. Derrik, L. Åsbrink, Q. Edquist, B.-Ö. Jonsson and E. Lindholm, *Int. J. Mass Spectrom. Ion Phys.*, 1971, **6**, 161.
60 J. W. Rabalais, L. O. Werme, T. Bergmark, L. Karlsson and K. Siegbahn, *Int. J. Mass Spectrom. Ion Phys.*, 1972, **9**, 185.
61 P. J. Derrik, L. Åsbink, O. Edquist and E. Lindholm, *Spectrochim. Acta, Part A*, 1971, **27**, 2525.
62 J. H. D. Eland, *Int. J. Mass Spectrom. Ion Phys.*, 1969, **2**, 471.
63 P. A. Clark, R. H. Gleiter and E. Heilbronner, *Tetrahedron*, 1973, **29**, 3085.
64 N. Kishimoto, H. Yamakado and K. Ohno, *J. Phys. Chem.*, 1996, **100**, 8204.
65 R. Englman and J. Jortner, *Mol. Phys.*, 1970, **18**, 145.
66 H. A. Wiebe and J. Heicklen, *Can. J. Chem.*, 1969, **47**, 2965.

Paper VIII

Deactivation via ring opening: A quantum chemical study of the excited states of furan and comparison to thiophene

Nemanja Gavrilov, Susanne Salzmann, and Christel M. Marian

Chem. Phys., **349** (2008) 269–277.

Available online at www.sciencedirect.com
ScienceDirect
Chemical Physics 349 (2008) 269–277
Chemical Physics
www.elsevier.com/locate/chemphys

Deactivation via ring opening: A quantum chemical study of the excited states of furan and comparison to thiophene

Nemanja Gavrilov [a,b], Susanne Salzmann [a], Christel M. Marian [a,*]

[a] *Institute of Theoretical and Computational Chemistry, Heinrich Heine University Düsseldorf, Universitätsstraße 1, Geb. 26.32, 40225 Düsseldorf, Germany*
[b] *Faculty of Chemistry, University of Belgrade, Studenski trg 12, P.O. Box 137, 11000 Belgrade, Serbia*

Received 29 November 2007; accepted 31 January 2008
Available online 9 February 2008

This work is dedicated to Hans Lischka on the occasion of his 65th birthday. His achievements in the development of advanced multiconfiguration interaction methods and their application to electronically excited molecules have greatly contributed to the understanding of photochemistry and photophysics.

Abstract

Minimum nuclear arrangements of the ground and low-lying excited electronic states of furan were obtained by means of (time dependent) Kohn–Sham density functional theory. A combined density functional/multi-reference configuration interaction method (DFT/MRCI) was employed to compute the spectral properties at these points.

Multiple minima were found on the first excited singlet (S_1) potential energy hypersurface with electronic structures S1, S2, S3 corresponding to the 1^1A_2 ($\pi \rightarrow$ 3s-Ryd), 1^1B_2 ($\pi \rightarrow \pi^*$), and 2^1A_1 ($\pi \rightarrow \pi^*$) states in the vertical absorption spectrum, respectively.

In analogy to recently published studies in thiophene [S. Salzmann, M. Kleinschmidt, J. Tatchen, R. Weinkauf, C.M. Marian, Phys. Chem. Chem. Phys. 10 (2008) 380] a deactivation mechanism for electronically excited furan was detected that involves the opening of the pentacyclic ring. We found a nearly barrierless relaxation pathway from the Franck–Condon region along a C–O bond-breaking coordinate. Hereby the initially excited $^1B_2\,(\pi \rightarrow \pi^*)$ state undergoes a conical intersection with a $^1B_1\,(\pi \rightarrow \sigma^*)$ state. The system can return to the electronic ground state through a second conical intersection of the $^1(\pi \rightarrow \sigma^*)$ state before the minimum of that B_1 state is reached.

Keywords: Electronic structure calculations; Heterocycles; Photochemistry; Quantum chemistry; Ring opening

1. Introduction

The vertical absorption spectra of the heterocyclic compounds pyrrole, furan, and thiophene have been well studied, both experimentally and theoretically [1–16]. Much less is known about the adiabatic excitation energies [17–21]. In addition to Rydberg excitations and triplet states, these systems possess low-lying valence singlet states, some of which are short-lived with lifetimes of the order of femtoseconds [22].

Some years ago, a relaxation pathway of photo-excited pyrrole was detected in which an N–H bond-breaking dissociative $^1(\pi \rightarrow \sigma^*_{NH})$ state undergoes conical intersections with the primarily excited $^1(\pi \rightarrow \pi^*)$ state as well as with the electronic ground state, thus leading to ultrafast decay of the excited state population [23]. Out-of-plane deformations of the pyrrole ring which couple the $^1(\pi \rightarrow \pi^*)$ and $^1(\pi \rightarrow \sigma^*_{NH})$ potential energy hypersurfaces, can also effectuate a direct conical intersection between the primarily excited $^1(\pi \rightarrow \pi^*)$ state and the electronic ground state [24]. Interestingly, Barbatti et al. [24] observed a significant elongation of one of the CN bonds at the latter conical intersection. While the decay mechanism involving the $^1(\pi \rightarrow \sigma^*_{NH})$ state is not available in furan and thiophene,

---

[*] Corresponding author. Fax: +49 211 81 13466.
E-mail address: christel.marian@uni-duesseldorf.de (C.M. Marian).

0301-0104/$ - see front matter © 2008 Elsevier B.V. All rights reserved.
doi:10.1016/j.chemphys.2008.01.060

out-plane-distortions combined with an asymmetric ring stretch represent a possible deactivation pathway of the latter molecules following photo-excitation of the first $^1(\pi \rightarrow \pi^*)$ state. Earlier theoretical work suggests that the low-lying singlet excited states of furan are strongly coupled by vibronic interactions [10–12]. A quantum chemical study carried out recently in our laboratory has shown that an alternative ultrafast relaxation pathway exists in thiophene that involves the opening of the pentacyclic ring [25]. In the present work it has been investigated whether the ring-opening mechanism plays a key role in photo-excited furan, too.

2. Theoretical section

Ground state geometries and harmonic vibrational frequencies of the furan molecule were determined at the restricted Kohn–Sham level (B3-LYP functional) [26–28] utilizing the Turbomole quantum chemistry program package [29]. The atomic orbital basis comprised TZVPP (valence triple zeta plus (2d1f, 2p1d) polarization) basis sets [30]. For the appropriate description of Rydberg states, it was augmented by a set of (2s, 2p, 2d) diffuse basis functions located on the oxygen atom with exponents taken from the work of Serrano-Andrés et al. [5]. For the four lowest-lying excited singlet and triplet states, geometry optimizations were carried out employing time-dependent density functional theory (TDDFT) [31], except for an open-chain $^3A''$ structure for which unrestricted density functional theory (UDFT) was used. Harmonic vibrational frequencies were evaluated numerically using the SNF package [32] and were scaled by 0.9613 as recommended for the B3-LYP functional [33].

At the optimized ground and excited state geometries, single-point calculations were carried out utilizing the combined density functional theory/multireference configuration interaction (DFT/MRCI) method [34]. Auxiliary basis functions for the resolution-of-the-identity approximation of two-electron integrals in the MRCI calculations were taken from the Turbomole library [35]. In the MRCI step, all valence electrons were correlated. In C_{2v} symmetry, five roots of singlet and triplet multiplicity, respectively, were determined simultaneously per irreducible representation. A linearly interpolated pathway connecting the Franck–Condon region (S_0 geometry) with the minimum of a planar open-chain $^3A''$ structure (DISS) was constructed using the DISTORT tool [36]. At these lower symmetry points (C_s symmetry), ten roots per irreducible representation were computed.

For being able to make a direct comparison with the photophysics of the sulfur homolog of furan, a similar pathway was constructed for thiophene. In the latter case, the path was extrapolated beyond the minimum of the $(\pi \rightarrow \sigma^*)$ excited state. Basis sets, minimum nuclear arrangements, and further computational parameters of the thiophene calculations have been described in detail in previous work [25].

3. Results and discussion

3.1. Optimized geometries and electronic spectra

In this section, the nuclear arrangements of the ground state as well as the lowest-lying excited states of furan and the corresponding vertical electronic spectra are presented. The energetic order of the states is sensitive to the nuclear geometry and typically more than one minimum is found on a particular potential energy hypersurface (PEH). This situation is quite common for molecules which show ultrafast decay of the excited states, such as furan. Here, the vertical order of the excited states does not correspond to their adiabatic order. To avoid confusion, we use two different nomenclatures: S1, S2,..., T1, T2,... denominate electronic structures in their energetic order at the ground state minimum geometry. The nomenclature $S_1, S_2, \ldots, T_1, T_2, \ldots$ refers to the actual order of electronic states at a given nuclear geometry. At the ground state equilibrium geometry, the two nomenclatures are identical, of course.

3.1.1. Ground state geometry and vertical excitation energies

The electronic ground state of furan has C_{2v} symmetry. The coordinate system was chosen in a way that the molecule lies in the (yz)-plane. The geometric parameters obtained from our calculations in comparison with experiment [37] and earlier quantum chemical investigations [10,15,38] are displayed in Table 1. Overall very good agreement is observed. The deviations of our calculated O–C and C–C bond lengths from the experimental values are smaller than 0.005 Å and less than 1° for the respective angles.

The vertical singlet and triplet excitation energies ΔE [eV] of furan in comparison with experimental band maxima and selected earlier quantum chemical investigations are displayed in Table 2. To aid the discussion relevant molecular frontier orbitals are shown in Fig. 2. For a recent collection of further theoretical results, see Ref. [14].

In the vertical absorption region, the 1^1A_2 ($\pi_3 \rightarrow$ 3s-Ryd) corresponds to the lowest excited singlet state, in agreement with experimental assignments [2] and earlier theoretical work [5,10,15]. The optically bright transition from the highest occupied molecular orbital (HOMO) to the lowest unoccupied molecular orbital (LUMO) $^1(\pi_3 \rightarrow \pi_4^*)$ yields the second excited singlet state (1^1B_2). Its $\langle r^2 \rangle$ expectation value indicates small contributions from Rydberg configurations. Our computed excitation energy of 6.00 eV compares excellently with measured band maxima of VUV absorption [3] and electron energy loss spectra [3,20] and earlier CASPT2 results [5]. Due to its small oscillator strength, the transition to the mixed $^1(\pi_3 \rightarrow \pi_5^*)$, $^1(\pi_2 \rightarrow \pi_4^*)$ state (2^1A_1) has not been identified experimentally. This is different in the heavier homolog thiophene where the corresponding 2^1A_1state constitutes the first excited singlet state in the Franck–Condon region and exhibits medium oscillator strength. Our computed

Table 1
Selected ground-state geometry parameters of furan together with experimental data and data of earlier quantum chemical investigations

Furan	This work	Exp.[a]	DFT[b]	CCSD[c]	MP2[d]	Thiophene	DFT[e]
r(O–C$_1$) [Å]	1.361	1.3622(2)	1.361	1.354	1.359	r(S-C$_1$) [Å]	1.725
r(C$_1$–C$_2$) [Å]	1.356	1.3610(3)	1.358	1.349	1.364	r(C$_1$–C$_2$) [Å]	1.364
r(C$_2$–C$_{2'}$) [Å]	1.432	1.4301(5)	1.435	1.433	1.426	r(C$_2$–C$_{2'}$) [Å]	1.424
θ(C$_1$–O – C$_{1'}$) [°]	106.9	106.56(2)	106.8	106.5	106.7	θ(C$_1$–S–C$_{1'}$) [°]	91.7
θ(O–C$_1$–C$_2$) [°]	110.4	110.65(2)	110.6	110.9	110.6	θ(S–C$_1$–C$_2$) [°]	111.4
θ(C$_1$–C$_2$–C$_{2'}$) [°]	106.2	106.07(2)	106.0	105.9	106.1	θ(C$_1$–C$_2$–C$_{2'}$) [°]	112.7

Atomic labels are explained in Fig. 1. For comparison also the most important ground state geometry parameters of thiophene are shown in the rightmost column.

[a] Ref. [37]. Estimated uncertainties are given in parentheses.
[b] Ref. [15]. DFT(B97-1)/TZVP+.
[c] Ref. [10]. CCSD/ cc-pVDZ+.
[d] Ref. [38]. MP2/ cc-pVTZ+.
[e] Ref. [25]. DFT(B3-LYP)/ TZVPP+R.

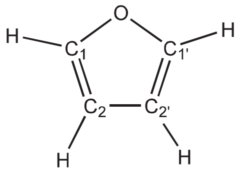

Fig. 1. Chemical structure and atom labeling of furan.

vertical DFT/MRCI excitation energy is very similar to the CASPT2 value of Serrano-Andrés [5]. The considerably higher excitation energies obtained at the CCSD [10], DFT [15] and SAC-CI [7] levels of theory stress the importance of multireference effects for these kind of states. We find the other linear combination of the $^1(\pi_3 \rightarrow \pi_5^*)$ and $^1(\pi_2 \rightarrow \pi_4^*)$ configurations (4^1A$_1$) which yields the most intense band in the VUV spectrum of furan at 8.06 eV, somewhat higher than the experimental band maximum. The fourth excited singlet state in our calculations is a $^1(\pi_3 \rightarrow$ 3p-Ryd) state of B$_1$ symmetry. In contrast, Palmer et al. [3] assigned the second Rydberg transition in their VUV spectrum at 6.47 eV to a $^1(\pi \rightarrow 3p_x$-Ryd) state of B$_2$ symmetry and identified the third Rydberg transition at 6.75 eV with the corresponding $^1(\pi \rightarrow 3p_y$-Ryd) state of B$_2$ symmetry while our results are supportive of the reversed ordering of the Rydberg series.

In the triplet manifold the first two states correspond to valence excitations. The vertical transition energy of the triplet coupled $(\pi_3 \rightarrow \pi_4^*)$ excitation (T$_1$ state, B$_2$ symmetry)

Table 2
Vertical singlet and triplet excitation energies ΔE [eV] of furan in comparison with experimental band maxima and selected earlier quantum chemical calculations

State	Electronic structure	ΔE			Δr^2	$f(r)$	μ
		This work	Exptl. band maximum	Other quantum chemical studies			
S$_0$ 1^1A$_1$ S0	(0.99) ground state	0.00			–	–	0.80
S$_1$ 1^1A$_2$ S1	(0.90) $\pi_3 \rightarrow$ s-Ryd	5.81	5.91[a]	6.01[f], 5.92[g], 5.97[h], 5.99[i]	41.1	–	0.13
S$_2$ 1^1B$_2$ S2	(0.75) $\pi_3 \rightarrow \pi_4^*$	6.00	6.04[b,c,d],6.06[e]	6.44[f], 6.04[g], 6.12[h], 6.40[i]	14.8	0.230	2.44
S$_3$ 2^1A$_1$ S3	(0.39) $\pi_3 \rightarrow \pi_5^*$ (0.31) $\pi_2 \rightarrow \pi_4^*$	6.25	–	6.72[f], 6.16[g], 6.69[h], 6.79[i]	3.3	0.000	1.25
S$_4$ 1^1B$_1$ S4	(0.89) $\pi_3 \rightarrow$ p-Ryd	6.30	6.75[c]	6.53[f], 6.46[g], 6.58[h], 6.45[i]	60.5	0.043	1.30
...							
S$_{15}$ 4^1A$_1$	(0.45) $\pi_3 \rightarrow \pi_5^*$ (0.45) $\pi_2 \rightarrow \pi_4^*$	8.06	7.80[c]	7.74[g], 8.34[i]	20.0	0.615	3.19
T$_1$ 1^3B$_2$ T1	(0.92) $\pi_3 \rightarrow \pi_4^*$	3.77	3.95[d], 3.99[b,e]	3.99[g], 4.39[i]	1.7	–	1.36
T$_2$ 1^3A$_1$ T2	(0.45) $\pi_2 \rightarrow \pi_4^*$ (0.44) $\pi_3 \rightarrow \pi_5^*$	4.99	5.22[d,e]	5.15[g], 5.63[i]	2.1	–	1.10
T$_3$ 1^3A$_2$ T3	(0.89) $\pi_3 \rightarrow$ s-Ryd	5.69	5.8[b]	5.86[g], 5.98[i]	40.1	–	0.08
T$_4$ 1^3B$_1$ T4	(0.87) $\pi_3 \rightarrow$ p-Ryd	6.20	6.7[b]	6.52[i]	58.7	–	1.28

In addition, dominant excitations with corresponding c^2 values, differential r^2 values Δr^2 [bohr^2], oscillator strengths $f(r)$ and dipole moments μ [Debye] are given.

[a] Resonantly enhanced multiphoton ionization, Ref. [2].
[b] Electron energy loss, Ref. [3].
[c] VUV absorption, Ref. [3].
[d] Electron energy loss, Ref. [19].
[e] Electron impact, Ref. [21].
[f] EOM-CCSD, Ref. [10].
[g] CASPT2, Ref. [5].
[h] DFT, Ref. [15].
[i] SAC/SAC-CI, Ref. [7].

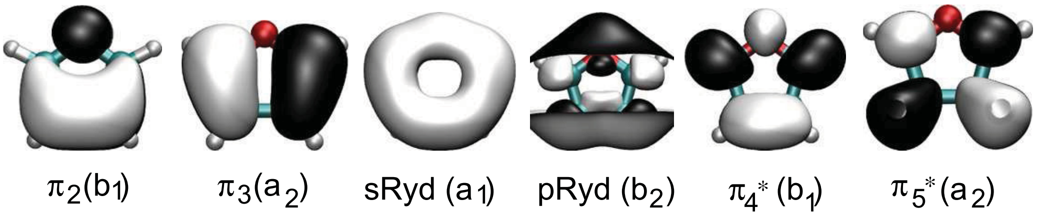

Fig. 2. Relevant molecular frontier orbitals of furan (B3LYP/TZVP) at the ground state geometry.

appears to be underestimated by about 0.2 eV by our method while the experimental value is reproduced very well by the CASPT2 results [5]. The same is true for the configuration-mixed T_2 state (1^3A_1). Among the Rydberg states, the excitation energy of the $^3(\pi_3 \rightarrow$ 3s-Ryd) state is reproduced well. For the triplet coupled ($\pi_3 \rightarrow$ 3p-Ryd) excitation of B_1 symmetry similar considerations hold as for the corresponding singlet state (see above).

3.1.2. Excited state geometries and adiabatic excitation energies

In this section, we present the relaxed geometries and excitation energies of the lowest-lying excited states from the singlet and triplet manifolds. If not stated otherwise, C_{2v} symmetry was retained during the excited state geometry optimization. For the optimization of the dissociated state (DISS) the molecular plane (C_s symmetry) was preserved. The most important geometry parameters of the optimized excited state structures are listed in Table 3. Table 4 gives an overview over the energetic location of the lowest singlet and triplet states at these points. Adiabatic excitation energies are presented in Table 5 together with experimental band origins.

3.1.2.1. S1 geometry. The geometry parameters of the ($\pi_3 \rightarrow$ 3s-Ryd) S1 electronic structure follow the expectations. Due to the bonding characteristics of the π_3 orbital (cp. Fig. 2), the C_1–C_2 ($C_{1'}$–$C_{2'}$) bond is elongated upon

Table 3
Selected parameters from the optimized excited state geometries of furan

Furan Symmetry	S1 C_{2v}	S2 C_{2v}	S3[a] C_{2v}	S3′[b] C_2	T1 C_{2v}	T2 C_{2v}	DISS $C_s(yz)$	Thiophene[c]	DISS $C_s(yz)$
$r(O–C_1)$	1.345	1.393	1.372	1.367	1.405	1.372	1.220	$r(S–C_1)$	1.665
$r(O–C_{1'})$	–	–	–	–	–	–	2.811	$r(S–C_{1'})$	2.820
$r(C_1–C_2)$	1.401	1.434	1.432	1.428	1.460	1.432	1.448	$r(C_1–C_2)$	1.400
$r(C_{1'}–C_{2'})$	–	–	–	–	–	–	1.350	$r(C_{1'}–C_{2'})$	1.344
$r(C_2–C_{2'})$	1.377	1.367	1.469	1.446	1.344	1.469	1.400	$r(C_2–C_{2'})$	1.418
$\theta(C_1–O–C_{1'})$	106.2	103.8	108.9	108.0	104.6	108.9	85.9	$\theta(C_1–S–C_{1'})$	76.9
$\theta(O–C_1–C_2)$	110.9	111.3	110.1	110.1	110.2	110.1	124.5	$\theta(S–C_1–C_2)$	124.8
$\theta(O–C_{1'}–C_{2'})$	–	–	–	–	–	–	80.7	$\theta(S–C_{1'}–C_{2'})$	91.4
$\theta(C_1–C_2–C_{2'})$	106.0	106.7	105.5	105.2	107.5	105.5	123.3	$\theta(C_1–C_2–C_{2'})$	124.2
$\theta(C_{1'}–C_{2'}–C_2)$	–	–	–	–	–	–	125.6	$\theta(C_{1'}–C_{2'}–C_{2'})$	122.7
$\theta(O–C_1–C_2–C_{2'})$	0.0	0.0	0.0	9.9	0.0	0.0	0.0	$\theta(S–C_1–C_2–C_{2'})$	0.0

For comparison also the geometry parameters of the planar open-chain $^3A''$ structure of thiophene are displayed.

[a] Saddle point.

[b] Minimum.

[c] Ref. [25] DFT(B3-LYP)/ TZVPP+R.

Table 4
Vertical excitation energies [eV] at various nuclear geometries

	S0 (C_{2v})		S1 (C_{2v})		S2 (C_{2v})		S3 (C_{2v}/C_s)		T1 (C_{2v})		T2 (C_{2v})		DISS (C_s)	
	ΔE		ΔE	@S0	ΔE	@S0	ΔE	@S0	ΔE	@S0	ΔE	@S0	ΔE	@S0
S_0	**0.00**	1^1A_1	0.17	S0	0.47	S0	0.39/0.52	S0	0.70	S0	0.46	S0	3.59	S4
S_1	5.81	1^1A_2	**5.66**	S1	**5.78**	S2	**5.85/5.79**	S3	5.89	S2	5.98	S3	4.22	S0
S_2	6.00	1^1B_2	5.75	S2	5.88	S1	5.95/5.91	S2	6.04	S1	6.11	S2	5.81	–
S_3	6.25	2^1A_1	6.10	S3	6.05	S3	6.00/6.13	S1	6.11	S3	6.17	S1	6.42	–
T_1	3.77	1^3B_2	3.41	T1	3.27	T1	3.52/3.53	T1	**3.31**	T1	3.73	T1	**3.13**	T4
T_2	4.99	1^3A_1	5.06	T2	5.15	T2	4.79/4.78	T2	5.39	T2	**4.78**	T2	4.81	–

For each stationary point, potential energies of the four lowest singlet (S_0–S_4) and two lowest triplet states (T_1, T_2) are displayed together with labels (S0–S4, T1–T4) designating the electronic structure of the state. Numbers printed in bold face indicate the DFT/ MRCI excitation energy of the electronic structure for which the geometry optimization was carried out.

Table 5
Adiabatic singlet and triplet DFT/MRCI excitation energies ΔE_{adia} [eV] of furan

Geometry[a]	ΔE_{adia}	PEH	Exp. 0–0	Earlier quantum chemical investigations
S1	5.66 (5.62)	S_1		5.84(5.79)[b], 5.83(5.80)[c]
S2	5.78 (5.61)[d]	S_1	5.70[e]	6.11(5.91)[b], 5.79[c]
S3/S3′	5.85/5.79[(*)]	S_1		6.36[b]
T1	3.27[(*)]	T_1	3.3[f]	–
T2	4.78(4.64)	T_2	4.98[g], 4.7[f]	–
DISS	3.13(2.96)	T_1		–
DISS	3.59	S_0		–

Values in parentheses include zero-point vibrational energy (ZPVE) corrections. Where available, experimental band origins are shown for comparison.

[a] Compare Table 3.

[b] EOM-CCSD, Ref. [10].

[c] TDDFT (B97-1), Ref. [15].

[d] Saddle point at TDDFT level (see text).

[e] Resonantly enhanced multiphoton ionization, Ref. [2].

[f] Electron impact, Ref. [21].

[g] Electron energy loss, Ref. [19].

[*] Not calculated.

promotion of one electron into a diffuse orbital while the C_2–$C_{2'}$ bond is shortened. The O–C_1 bond length remains nearly unchanged with respect to the ground state geometry. The same structural changes are observed in EOM-CCSD calculations [16] and TDDFT (B97-1/TZVP+) studies [15]. In agreement with our TDDFT (B3LYP) calculation, both investigations find the C_{2v}-symmetric structure to be a true minimum on the S_1 PEH. From an energetic point of view, the relaxation effects on the absorption spectrum remain small (0.15 eV).

3.1.2.2. *S2 and T1 geometries.* It turns out that our calculated C_{2v}-symmetric nuclear arrangement for the S2 state only presents a saddle point on the S_2 PEH at the level of TDDFT (B3LYP). One imaginary frequency ($=i171\ \mathrm{cm}^{-1}$) for a B_1 normal mode is obtained (see Table 6). A closer investigation of the TDDFT and DFT/MRCI excitation energies of that state following the distortion along the imaginary mode was performed. While TDDFT exhibits an extremely shallow double minimum potential well, DFT/MRCI clearly favors the C_{2v}-symmetric structure. This phenomenon has been encountered before in various organic molecules including thiophene [25,39,40] and is considered an artifact of the TDDFT (B3LYP) method. Also the TDDFT (B97-1/TZ2P+) study by Burcl et al. [15] predicts a C_s-symmetric out-of-plane (oop)-distortion of the molecule, not detected in EOM-CC2 [16] calculations. The latter method shows a C_s-symmetric

Table 6
Distortions of imaginary modes

S2	T1	
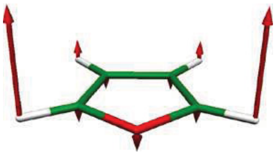	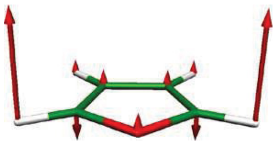	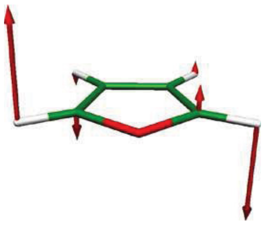
$i171\ \mathrm{cm}^{-1}$	$i446\ \mathrm{cm}^{-1}$	$i259\ \mathrm{cm}^{-1}$
1 A_2	1 A_2	1 B_1
−0.01[a] eV	−0.08[c] eV	−0.01 eV
+0.04[b] eV	+0.00[b] eV	+0.03 eV

S3			
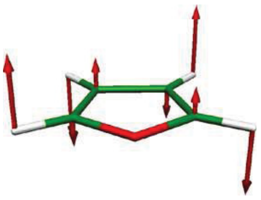	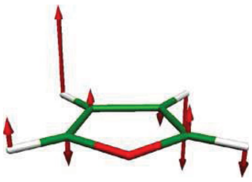	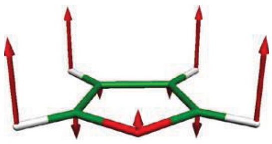	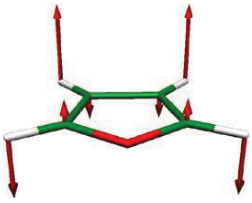
$i469\ \mathrm{cm}^{-1}$	$i397\ \mathrm{cm}^{-1}$	$i233\ \mathrm{cm}^{-1}$	$i90\ \mathrm{cm}^{-1}$
1 B_1	2 B_1	1 A_2	2 A_2
−0.02 eV	−0.03 eV	−0.01 eV	–
−0.02 eV	−0.05 eV	−0.02 eV	–

Given are from top to bottom, the frequency of the imaginary normal mode, the respective symmetry, the difference between the excitation energies ΔE of the C_{2v} and optimized distorted geometries at TDDFT(UDFT) and DFT/MRCI level.

[a] TDDFT energy.

[b] DFT/MRCI energy.

[c] UDFT energy.

in-plane-distortion of the molecule instead, corresponding to the elongation of one O–C bond. Although we do not find such an imaginary B_2-symmetric normal mode at TDDFT level, our results for the deactivation mechanism presented in the next section involve the opening of the pentacyclic ring. We preserve further discussion of that topic for later. In comparison to the ground state structural parameters, the C_1–C_2 ($C_{1'}$–$C_{2'}$) bond is elongated by 7.8 pm, the C_2–$C_{2'}$ bond is 6.5 pm shorter. This structural change is indicative of a double bond between the C_2 ($C_{2'}$) centers and a diradicaloidic electron distribution at the C_1 ($C_{1'}$) centers. The same trend is shown by EOM-CCSD calculations [10] and TDDFT (B97-1/TZVP+) [15] studies. A similar bond length change has been observed for the 1^1B_2 state in thiophene where it is accompanied by true out-of-plane-distortions, however [25]. With regard to the energy, the relaxation effect on the S2 electronic structure is moderate (0.22–0.25 eV). It is noticeable that at the S1 minimum the DFT/MRCI energy of the S2 state is actually 0.03 eV smaller than at the optimized S2 geometry, indicating that the minimum nuclear arrangements on the TDDFT and DFT/MRCI PEHs differ slightly. Furthermore, along the path connecting the S1 and S2 minima the energetic order of these electronic structures swaps. These facts suggest that the minimum of the S2 electronic state is very shallow along the O–C_1 and C_1–C_2 stretching coordinates and that substantial vibronic coupling may take place due to the energetic proximity of the involved states. The experimental determination of the origin of the 1^1B_2 state is problematic because of the high complexity of the band. Due to the significant geometry distortion in the excited state, the S0–S2 band is wide and featureless. Furthermore, the 1^1A_2 and 2^1A_1 states are in the same energetic range. Although their direct electric dipole transition moments to the electronic state are negligible, these states may contribute to the intricacy of that band due to intensity borrowing from the strong $1^1A_1 \rightarrow 1^1B_2$ electronic transition by means of vibronic coupling. Our calculated value for the adiabatic excitation energy is somewhat lower than those of EOM-CCSD (and CC) calculations but in the same ballpark as TDDFT studies.

The geometry optimization of the T1 structure resulted in a nuclear arrangement that shows large similarity with the S2 geometry. However the structural changes are more pronounced at the T1 minimum. Due to triplet instability, UDFT was used instead of TDDFT. At the level of UDFT (B3LYP), this C_{2v}-symmetric structure is a second-order saddle point on the T_1 PEH. One imaginary A_2 normal mode and one imaginary B_1 normal mode were obtained. (Details are found in Table 6.) For both normal modes subsequent geometry optimizations in reduced molecular point groups were carried out. In both cases UDFT favors the structure with lower symmetry while the DFT/MRCI method does not. Therefore both imaginary frequencies can be seen as an artifact of the UDFT(B3LYP) method. The relaxation effects on the T1 state energy (0.46 eV) are more pronounced than for the corresponding singlet state. The adiabatic DFT/MRCI excitation energy amounts to 3.31 eV. A comparison to the T1 energy at the S2 minimum shows another small red-shift. At that point the adiabatic T1 excitation energy is found to be 3.27 eV. Electron energy loss and electron impact studies [19,21] locate the beginning of the 1^3B_2 band at 3.3 eV which is in perfect agreement with our value.

3.1.2.3. S3 and T2 geometries. The C_{2v}-symmetric TDDFT optimized structure of the S3 state is found to be a saddle point on the S_5 PEH. The fact that the 2^1A_1 state corresponds to the fifth excited singlet state at the TDDFT level clearly reflects the inadequacy of this method to properly describe the intrinsically multiconfigurational character of its wavefunction. In contrast, the DFT/MRCI method places this point of the mixed $^1(\pi_3 \rightarrow \pi_5^*)$, $^1(\pi_2 \rightarrow \pi_4^*)$ S3 electronic structure on the S_1 PEH. We obtain four imaginary frequencies, corresponding to two A_2 and two B_1 normal modes. (More information can be found in Table 6.) The fourth imaginary mode ($i90\ \mathrm{cm}^{-1}$) is considered an artifact of the TDDFT(B3LYP) method. Subsequent geometry optimizations were carried out in lower symmetry point groups (C_s/C_2) with starting structures distorted along one of the three remaining imaginary modes. Three different stationary points have been found. In all three cases the TDDFT energy of the optimized state is slightly red-shifted (up to 0.03 eV) with respect to the C_{2v}-symmetric structure. The same qualitative picture emerges from the DFT/MRCI excitation energies at those structures, showing that at both levels of theory the respective PEH is very shallow. The C_2 symmetric nuclear arrangement (denoted as S3′) which is distorted along the second B_1 mode ($i397\ \mathrm{cm}^{-1}$) represents the most favorable structure at the DFT/MRCI level. For this reason, energies at this S3′ minimum are displayed in Tables 4 and 5 in addition to the values at the C_{2v}-symmetric saddle point. A similar situation has been encountered in a CCSD treatment by Gromov et al. [10] These authors find two stationary points for C_s symmetric structures (with mirror planes in the yz and xz planes) and a C_2 symmetric structure. Finally, also Christiansen et al. [16] reported a C_s symmetric structure the energy of which is red-shifted by 0.13 eV with respect to the C_{2v}-symmetric saddle point.

In comparison to the ground state all bonds of the C_{2v}-symmetric structure are elongated which is in agreement with earlier CCSD [10] studies. Especially the C_1–C_2 ($C_{1'}$–$C_{2'}$) bond loses its double bond character. Extending the comparison to the C_2-symmetric structure, the elongation of the C_1–C_2 ($C_{1'}$–$C_{2'}$) bond stays almost the same while for the other bonds the elongation is smaller. Furthermore the S3’ structure shows a twist of the ring by roughly 10° and a pronounced oop distortion of the C_2-hydrogen atoms. From an energetic point of view, the geometry relaxation effects on the optimized state are noticeable. The minimum has an adiabatic excitation energy of approximately 5.8 eV and thus lies about 0.4 eV lower than the vertical absorption energy.

The nuclear arrangement of the T2 state differs slightly from that of the corresponding singlet state S3. While the other bonds show no big difference, the C_2–$C_{2'}$ bond is elongated by almost 9 pm. The frequency analysis shows that this structure is a true minimum on the T_3 PEH at the level of TDDFT (B3LYP). The DFT/MRCI method places the respective electronic state on the T_2 PEH with an adiabatic excitation energy of 4.78 eV which is in about 0.2 eV lower than the designated 0–0 transition in experimental electron energy loss spectra [19,20].

3.1.2.4. DISS geometry. The dissociative $(\pi_3 \to \sigma^*)$ state (DISS) mentioned in the introduction is characterized by an opening of the five-membered ring. Compared to the ground state geometry, one of the C–O bonds is elongated by approximately 145 pm while the other C–O bond shrinks by 14 pm. The C_1–C_2 bond is 9.2 pm longer and the $C_{1'}$–$C_{2'}$ and C_2–$C_{2'}$ bonds are shorter by 0.6 and 3.2 pm, respectively. This planar nuclear arrangement can thus be interpreted as belonging to an open-chain conformation with a C–O and a $C_{1'}$–$C_{2'}$ double bond. It is very similar to the corresponding $^3A''$ structure of thiophene. The adiabatic excitation energy of the $^3(\pi_3 \to \sigma^*)$ state amounts to merely 3.13 eV which leads us to the conclusion that this could be the global minimum on the T_1 PEH. The adiabatic excitation energy of the corresponding singlet state is calculated to be 3.59 eV. It is noteworthy that the $^1(\pi_3 \to \sigma^*)$ state is situated 0.63 eV below the electronic ground state at this point of space, i.e., we expect a conical intersection to occur along the reaction coordinate. This topic is addressed in more detail in the following section.

3.2. Nonradiative decay

In Fig. 3, cuts through the PEHs of furan and thiophene along linearly interpolated paths (LIPs) between the respective Franck–Condon point (S0 geometry) and the open-ring structure (DISS geometry) are presented. On the abscissa, dimensionless coordinate differences are used where 0 stands the S0 geometry and 1 represents the DISS geometry. In terms of the most strongly varying coordinate, a step size of 0.1 corresponds to a change of the O–C_1 bond length by 14.5 pm in furan and of the S–C_1 bond length by 11 pm in thiophene. A geometry difference larger than 1 indicates a nuclear arrangement extrapolated beyond the DISS structure employing the same step sizes as for the LIP. Blow-ups of the higher-energy parts of the Franck–Condon regions (shown in the upper right corners) make it easier to follow the course of the potential energy curves through various intersections. In both molecules, the ring-opening mechanism involves $^1(\pi_3 \to \sigma^*)$ or $^3(\pi_3 \to \sigma^*)$ states. At the S0 geometry these states are located at very high energies. Upon asymmetric in-plane-distortion of the pentacyclic ring, the potential energies of these states steeply decrease. In furan and thiophene, nearly barrierless paths on the primarily excited $^1(\pi \to \pi^*)$ PEHs connect the Franck–Condon region and a conical intersection with the $^1(\pi_3 \to \sigma^*)$ state. In furan, the $^1(\pi_3 \to \pi_4{}^*)/^1(\pi_3 \to \sigma^*)$ crossing occurs at an energy of about 6.1 eV, i.e., roughly 0.1 eV above the Franck–Condon point on the $^1(\pi_3 \to \pi_4^*)$ PEH. Optimization of the conical intersection seam might even lead to the disappearance of the small barrier. At the conical intersection, the C_1–O bond is elongated with respect to its ground state equilibrium value by about 30 pm. In thiophene, elongation of the C_1–S bond by about 10 pm is sufficient to reach the $^1(\pi_3 \to \pi_5^*)$, $^1(\pi_2 \to \pi_4^*)/^1(\pi_3 \to \sigma^*)$ intersection which exhibits the same energy as the Franck–Condon point. Proceeding further along the reaction path effectuates a dramatic drop of the potential energy of the first excited singlet state and eventually leads to another conical intersection with the electronic ground state. Energetically the $^1(\pi_3 \to \sigma^*)$/S0 intersections are found at approximately 3.7 eV (furan) and 4.1 eV (thiophene). The ring-opening mechanism is thus believed to represent an efficient pathway for the nonradiative decay of the first excited $^1(\pi \to \pi^*)$ states that could explain the broad and diffuse structure of the low-energy VUV spectra of furan and thiophene.

One difference between the furan and thiophene pathways immediately catches the eye. In the furan case, the energy decrease of the $(\pi_3 \to \sigma^*)$ states (designated by circles in Fig. 3) is more pronounced and the conical intersection with the ground state occurs long before the minima of the $(\pi_3 \to \sigma^*)$ states are reached. In thiophene, one has to extrapolate the path beyond the minimum to encounter the $(\pi_3 \to \sigma^*)$/S0 intersection. Other differences are less obvious, but can be detected when inspecting the blow-ups. In furan, the primarily photo-excited state of the lowest band in the VUV spectrum is the $^1(\pi_3 \to \pi_4^*)$ (HOMO–LUMO) transition, represented by squares in Fig. 3. As discussed in detail above, the low-lying $^1(\pi_3 \to 3s)$ Rydberg state and the mixed $^1(\pi_3 \to \pi_5^*)$, $^1(\pi_2 \to \pi_4^*)$ valence state do not contribute directly to the absorption due to a lack of oscillator strength, but they may influence the spectral shape due to vibronic interaction with the optically bright state [10–12]. The appearance of resonances on the high-energy wing of the otherwise broad and structureless first VUV absorption band is in accord with our observation that the $^1(\pi_3 \to 3\text{p-Ryd})$ states are separated from the $^1(\pi \to \sigma^*)$ potential well by barriers. In thiophene, the two lowest singlet states have valence characters and exhibit out-of-plane distorted minimum geometries [25]. In the Franck–Condon region, the lowest $^1(\pi_3 \to \pi_5^*)$, $^1(\pi_2 \to \pi_4^*)$ transition and the slightly higher-lying $^1(\pi_3 \to \pi_4^*)$ transition have comparable dipole oscillator strength. As is apparent from Fig. 3, the conical intersections between these $^1(\pi \to \pi^*)$ states and the $^1(\pi \to \sigma^*)$ state occur much closer to the Franck–Condon region as in the furan case. For thiophene, the ultrafast decay of the S_1 origin was measured to take place on the femtosecond time scale [22]. To the best of our knowledge, corresponding femtosecond experiments on furan have not been carried out. From the purely qualitative arguments

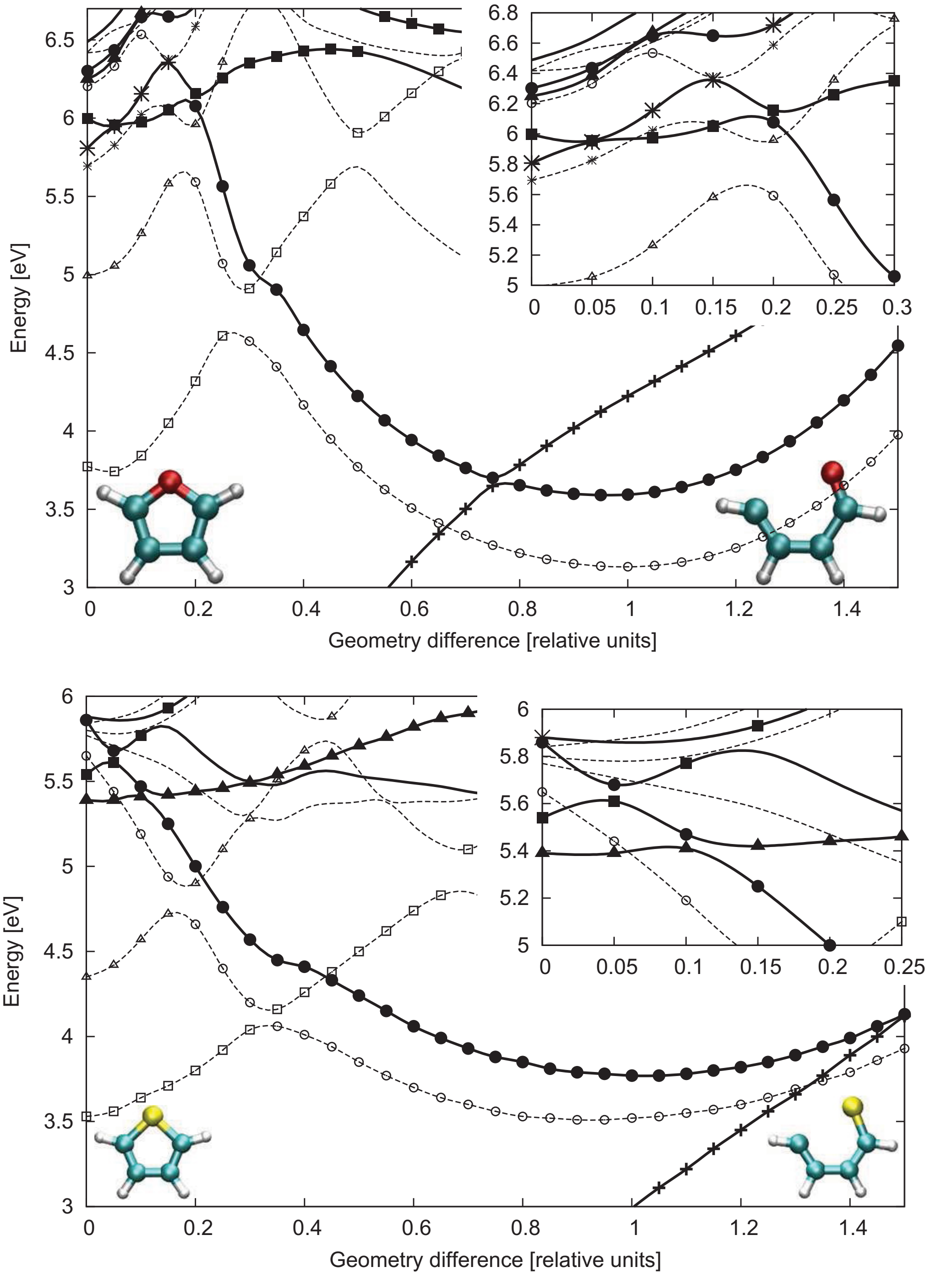

Fig. 3. Linearly interpolated path between the S0 and the DISS geometry in furan (top) and thiophene (bottom). Singlet energy profiles are represented by solid lines, triplet profiles by dashed lines. The electronic states are encoded with the following signs: plus signs symbolize the electronic ground state, boxes the $(\pi_3 \rightarrow \pi_4^*)$ state, triangles the mixed $(\pi_3 \rightarrow \pi_5^*/\pi_2 \rightarrow \pi_4^*)$ state, circles the dissociative $(\pi_3 \rightarrow \sigma^*)$ state and stars the lowest-lying Rydberg state.

brought forward in this section we would expect the decay process to be slightly slower than in thiophene.

4. Concluding remarks

A new deactivation mechanism of photo-excited furan based on the opening of the pentacyclic ring has been presented. The intermediate state connecting the primarily excited $^1(\pi_3 \rightarrow \pi_4^*)$ (HOMO–LUMO) state with the electronic ground state corresponds to a single excitation from the HOMO to a C–O anti-bonding MO, designated by $^1(\pi_3 \rightarrow \sigma^*)$ here. Along the reaction path two conical intersections occur, the first one close the Franck–Condon point, the second one before the minimum of the $^1(\pi_3 \rightarrow \sigma^*)$ state is reached. The deactivation mechanism is qualitatively similar to the ring-opening mechanism in the heavier furan homolog thiophene [25] although subtle differences exist between these two molecules with regard to the order of electronic states in the Franck–Condon region and their minimum nuclear arrangements. For thiophene, the decay of the S_1 (0–0) population was found to occur with a time constant of approximately 80 fs [22]. Due to the similarity of the deactivation mechanisms it can be assumed that photo-excited furan decays on the femtosecond time scale, too, explaining the diffuseness of the low-energy tail of its VUV spectrum.

For a more quantitative determination of the excited state lifetimes and a detailed understanding of the cascade of processes following the primary photo-excitation of furan wave-packet dynamics appears to be the method of choice. So far, quantum dynamical studies of photo-excited furan involved the $^1A_2$ ($\pi_3 \rightarrow$ 3s-Ryd), $^1B_2$ ($\pi_3 \rightarrow \pi_4^*$), $^1A_1$ ($\pi_3 \rightarrow \pi_5^*$), ($\pi_2 \rightarrow \pi_4^*$), and $^1B_1$ ($\pi_3 \rightarrow$ 3p-Ryd) excited states and a multitude of vibrational coupling modes [10–12], but did not take into account the $^1(\pi_3 \rightarrow \sigma^*)$ state. In light of our results, the inclusion of this state and the ring-opening coordinate appears to be mandatory. This would add further complexity to a multi-mode-multi-state quantum dynamics treatment and it is not clear whether an extension to additional states and modes could be accomplished with state-of-the-art methods at present. To obtain a semi-quantitative picture, an alternative approach might be on-the-fly surface-hopping dynamics in combination with MRCI electronic structure methods that has been presented recently by Hans Lischka and coworkers [41]. Although computationally demanding, this method has the advantage that potential energy hypersurfaces do not have to be pre-calculated and that the system can follow any path, the importance of which might not have been foreseen by the investigators.

Acknowledgements

N.G. gratefully acknowledges a visiting scholarship from the Serbian Ministry of Education and Sport. This work was supported by the German Research Council (DFG) within the framework of SFB 663/C1.

Appendix A. Supplementary material

Supplementary data associated with this article can be found, in the online version, at doi:10.1016/j.chemphys.2008.01.060.

References

[1] P.J. Derrick, L. Åsbrink, O. Edqvist, B.-Ö. Jonsson, E. Lindholm, Int. J. Mass Spectrom. Ion Phys. 6 (1971) 177.

[2] J.L. Roebber, D.P. Gerrity, R. Hemley, V. Vaida, Chem. Phys. Lett. 75 (1980) 104.

[3] M.H. Palmer, I.C. Walker, C.C. Ballard, M.F. Guest, Chem. Phys. 192 (1995) 111.

[4] M.H. Palmer, I.C. Walker, M.F. Guest, Chem. Phys. 241 (1999) 275.

[5] L. Serrano-Andrés, M. Merchán, I. Nebot-Gil, B.O. Roos, M. Fülscher, J. Am. Chem. Soc. 115 (1993) 6184.

[6] L. Serrano-Andrés, M. Merchán, M. Fülscher, B.O. Roos, Chem. Phys. Lett. 211 (1993) 125.

[7] J. Wan, M. Hada, M. Ehara, H. Nakasuji, J. Chem. Phys. 114 (2001) 842.

[8] M. Kleinschmidt, J. Tatchen, C.M. Marian, J. Comp. Chem. 23 (2002) 824.

[9] A.B. Trofimov, H. Köppel, J. Schirmer, J. Chem. Phys. 109 (1998) 1025.

[10] E.V. Gromov, A.B. Trofimov, N.M. Vitkovskaya, J. Schirmer, H. Köppel, J. Chem. Phys. 119 (2003) 737.

[11] H. Köppel, E.V. Gromov, A.B. Trofimov, Chem. Phys. 304 (2004) 35.

[12] E.V. Gromov, A.B. Trofimov, N.M. Vitkovskaya, H. Köppel, J. Schirmer, H.-D. Meyer, L.S. Cederbaum, J. Chem. Phys. 121 (2004) 4585.

[13] M. Pastore, C. Angeli, R. Cimiraglia, Chem. Phys. Lett. 422 (2006) 522.

[14] M. Pastore, C. Angeli, R. Cimiraglia, Chem. Phys. Lett. 426 (2006) 445.

[15] R. Burcl, R.D. Amos, N.C. Handy, Chem. Phys. Lett. 355 (2002) 8.

[16] O. Christiansen, P. Jørgensen, J. Am. Chem. Soc. 120 (1998) 3423.

[17] G. Di Lonardo, G. Galloni, A. Trombetti, C. Zauli, J. Chem. Soc., Faraday Trans. II 68 (1972) 2009.

[18] S. Rentsch, J.P. Yang, W. Paa, E. Birkner, J. Schiedt, R. Weinkauf, Phys. Chem. Chem. Phys. 1 (1999) 1707.

[19] K.R. Asmis, Dissertation, Université de Fribourg, Switzerland, 1996.

[20] H. Haberkern, K.R. Asmis, P. Swiderek, Phys. Chem. Chem. Phys. 5 (2003) 827.

[21] W.M. Flicker, O.A. Mosher, A. Kuppermann, Chem. Phys. Lett. 38 (1976) 489.

[22] R. Weinkauf, L. Lehr, E.W. Schlag, S. Salzmann, C.M. Marian, Phys. Chem. Chem. Phys. 10 (2008) 393.

[23] A.L. Sobolewski, W. Domcke, Chem. Phys. 259 (2000) 181.

[24] M. Barbatti, M. Vazdar, A.J.A. Aquino, M. Eckert-Maksić, H. Lischka, J. Chem. Phys. 125 (2006) 164323-1.

[25] S. Salzmann, M. Kleinschmidt, J. Tatchen, R. Weinkauf, C.M. Marian, Phys. Chem. Chem. Phys. 10 (2008) 380.

[26] C.T. Lee, W.T. Yang, R.G. Parr, Phys. Rev. B 37 (1988) 785.

[27] A.D. Becke, J. Chem. Phys. 98 (1993) 5648.

[28] P.J. Stephens, F.J. Devlin, C.F. Chabalowski, M.J. Frisch, J. Phys. Chem. 98 (1994) 11623.

[29] R. Ahlrichs et al., Tubomole 5.7, Universität Karlsruhe, Germany, 2004.

[30] A. Schäfer, C. Huber, R. Ahlrichs, J. Chem. Phys. 100 (1994) 5829.

[31] F. Furche, R. Ahlrichs, J. Chem. Phys. 117 (2002) 7433.

[32] J. Neugebauer, M. Reiher, C. Kind, B.A. Hess, J. Comp. Chem. 23 (2002) 895.

[33] A.P. Scott, L. Radom, J. Phys. Chem. 100 (1996) 16502.

[34] S. Grimme, M. Waletzke, J. Chem. Phys. 111 (1999) 5645.

[35] F. Weigend, M. Häser, H. Patzelt, R. Ahlrichs, Chem. Phys. Lett. 294 (1998) 143.

[36] J. Tatchen, Dissertation, Heinrich Heine Universität Düsseldorf, 2006.

[37] F. Mata, M.C. Martin, G.O. Sørensen, J. Mol. Struct. 48 (1978) 157.

[38] A. Mellouki, J. Liévin, M. Herman, Chem. Phys. 271 (2001) 239.

[39] J. Tatchen, C.M. Marian, Phys. Chem. Chem. Phys. 8 (2006) 2133.

[40] K. Tomić, J. Tatchen, C.M. Marian, J. Phys. Chem. A 109 (2005) 8410.

[41] M. Barbatti, G. Granucci, M. Persico, M. Ruckenbauer, M. Vazdar, M. Eckert-Maksić, H. Lischka, J. Photochem. Photobiol. A: Chem. 190 (2007) 228.

Deactivation via ring opening: A quantum chemical study of the excited states of furan and comparison to thiophene
(Electronic Supplementary Material)

Nemanja Gavrilov, Susanne Salzmann, and Christel M. Marian

Coordinates [bohr] of important stationary points.

S0

```
$coord
    0.00000000000000      0.00000000000000     -2.60583320687592      o
   -2.06663332586387      0.00000000000000     -1.07450370343632      c
   -1.35343588922665      0.00000000000000      1.38550699197015      c
    2.06663332586387      0.00000000000000     -1.07450370343632      c
    1.35343588922665      0.00000000000000      1.38550699197015      c
   -3.86949255523787      0.00000000000000     -2.01119723759309      h
   -2.58753485978006      0.00000000000000      3.00252461460178      h
    2.58753485978006      0.00000000000000      3.00252461460178      h
    3.86949255523787      0.00000000000000     -2.01119723759309      h
$end
```

S1

```
$coord
    0.00000000000000      0.00000000000000     -2.63328619551701      o
   -2.03191482960725      0.00000000000000     -1.10754099235158      c
   -1.30086244973915      0.00000000000000      1.43605889889342      c
    2.03191482960725      0.00000000000000     -1.10754099235158      c
    1.30086244973915      0.00000000000000      1.43605889889342      c
   -3.85632726893657      0.00000000000000     -2.01764338685487      h
   -2.57526316738808      0.00000000000000      3.02986585584657      h
    2.57526316738808      0.00000000000000      3.02986585584657      h
    3.85632726893657      0.00000000000000     -2.01764338685487      h
$end
```

S2

```
$coord
    0.00000000000000      0.00000000000000     -2.76546955219654      o
   -2.07198498270058      0.00000000000000     -1.14235702231658      c
   -1.29145032051110      0.00000000000000      1.45263193370954      c
    2.07198498270058      0.00000000000000     -1.14235702231658      c
    1.29145032051110      0.00000000000000      1.45263193370954      c
   -3.90343759773570      0.00000000000000     -2.02575552201674      h
   -2.56017321545806      0.00000000000000      3.04100098426679      h
    2.56017321545806      0.00000000000000      3.04100098426679      h
    3.90343759773570      0.00000000000000     -2.02575552201674      h
$end
```

S3

```
$coord
    0.00000000000000      0.00000000000000     -2.65994426188703      o
   -2.10944048801824      0.00000000000000     -1.15281140400150      c
   -1.38761093764590      0.00000000000000      1.45538375673539      c
    2.10944048801824      0.00000000000000     -1.15281140400150      c
    1.38761093764590      0.00000000000000      1.45538375673539      c
   -3.89925019617455      0.00000000000000     -2.10657211155664      h
   -2.63251366992147      0.00000000000000      3.05784548978174      h
    2.63251366992147      0.00000000000000      3.05784548978174      h
    3.89925019617455      0.00000000000000     -2.10657211155664      h
$end
```

S3’

```
$coord
    0.00000000000000      0.00000000000000     -2.16303986531716      o
   -2.09064020344072      0.01869743659877     -0.64480913189396      c
   -1.35646937398953     -0.16090308212250      1.94525061424641      c
    2.09064020344072     -0.01869743659878     -0.64480913189396      c
    1.35646937398953      0.16090308212250      1.94525061424641      c
   -3.90064762881911     -0.00120535223418     -1.57564147360841      h
   -2.57859308615750     -0.53147678672680      3.52662112026351      h
    2.57859308615750      0.53147678672680      3.52662112026351      h
    3.90064762881911      0.00120535223418     -1.57564147360841      h
$end
```

T1

```
$coord
    0.00000000000000      0.00000000000000     -2.80742667173535      o
   -2.10095754507722      0.00000000000000     -1.18405492582606      c
   -1.26954287222760      0.00000000000000      1.44733257711816      c
    2.10095754507722      0.00000000000000     -1.18405492582606      c
    1.26954287222760      0.00000000000000      1.44733257711816      c
   -3.93316346679090      0.00000000000000     -2.05845120857263      h
   -2.52122605561728      0.00000000000000      3.05328726877788      h
    2.52122605561728      0.00000000000000      3.05328726877788      h
    3.93316346679090      0.00000000000000     -2.05845120857263      h
$end
```

T2

```
$coord
    0.00000000000000      0.00000000000000     -2.68893182068523      o
   -2.09859698145498      0.00000000000000     -1.14044734497757      c
   -1.43399887682319      0.00000000000000      1.45943726078882      c
    2.09859698145498      0.00000000000000     -1.14044734497757      c
    1.43399887682319      0.00000000000000      1.45943726078882      c
   -3.88881790328473      0.00000000000000     -2.10062318153348      h
   -2.69655448413297      0.00000000000000      3.04718468138578      h
    2.69655448413297      0.00000000000000      3.04718468138578      h
    3.88881790328473      0.00000000000000     -2.10062318153348      h
$end
```

DISS

```
$coord
    1.57449907120488     -3.32839063725799      0.00000000000000      o
    1.25790215271922      1.12880300269893      0.00000000000000      c
   -1.38171979216117      1.31681479605308      0.00000000000000      c
   -3.00995733821961     -0.64660843439862      0.00000000000000      c
    2.59406185335315     -1.25990231502319      0.00000000000000      c
   -5.04356395213140     -0.80672913378155      0.00000000000000      h
   -2.17364954441914      3.22391771220687      0.00000000000000      h
    2.38017603178290      2.83972170024897      0.00000000000000      h
    4.67903212970050     -1.11918143485516      0.00000000000000      h
$end
```

Paper IX

UV excitation and radiationless deactivation of imidazole

Mario Barbatti, Hans Lischka, Susanne Salzmann, and Christel M. Marian

J. Chem. Phys., **130** (2009) 034305 (8 pages).

THE JOURNAL OF CHEMICAL PHYSICS **130**, 034305 (2009)

UV excitation and radiationless deactivation of imidazole

Mario Barbatti,[1,a)] Hans Lischka,[1,b)] Susanne Salzmann,[2] and Christel M. Marian[2,c)]
[1]*Institute for Theoretical Chemistry, University of Vienna, Währingerstrasse 17, A-1090 Vienna, Austria*
[2]*Institute of Theoretical and Computational Chemistry, Heinrich-Heine-University, Universitätsstrasse 1, D-40225 Düsseldorf, Germany*

(Received 11 November 2008; accepted 4 December 2008; published online 20 January 2009)

The vertical spectrum and the radiationless decay of imidazole have been investigated theoretically. Benchmark calculations were performed employing different methods and levels. Four different conical intersections were characterized and the reaction paths connecting the Franck–Condon region to them were computed. Two of the conical intersections show puckered structures while the other two show NH and ring dissociation patterns. The $\pi\pi^*/S_0$ N_1-puckered conical intersection is connected to the planar $\pi\sigma^*/S_0$ ring-opened conical intersection by a branch of the crossing seam. After excitation into the first $^1\pi\pi^*$ state, the internal conversion can occur either in this branch of crossing seam or along the NH-dissociation path. © *2009 American Institute of Physics*.
[DOI: 10.1063/1.3056197]

I. INTRODUCTION

Imidazole is the chromophore of important biological compounds such as histidine and histamine, both nonfluorescent species.[1] It is one of the chromophores of urocanic acid, a major UV absorber in the skin[2] that may be responsible for triggering photoaging[3] and UV-induced imunosupression.[4] The UV photoabsorption of imidazole should also contribute to the Soret band of vitamin B12 and analogous molecules[5] as well as to the photochemistry of purine nucleobases.[6–9] In spite of its importance, however, little attention has been dedicated to the theoretical characterization of its electronically excited states.[10–14]

Imidazole presents a broad and structureless absorption spectrum in condensed phase[15–19] with the first band centered at about 207 nm (5.99 eV) and the second at about 190 nm (6.53 eV). Two electronic states at 204 nm (6.09 eV) (Refs. 17 and 19) and 218 nm (5.69 eV) (Ref. 17) were identified in the 207 nm band by means of resonance Raman spectroscopy and assigned to $^1\pi\pi^*$ transitions. Very weak bands at 250 nm (4.96) and 265 nm (4.68 eV) were also reported[15,16] and were assigned either to transitions to the $^1\pi\sigma_{NH}{}^*(3s)$ state by Machado and Davidson[12] or to the two first A' triplet states by Serrano-Andrés *et al.*[13]

The vapor[20] spectrum of imidazole (see Fig. 1) has been recently measured in the range between 250 and 190 nm (4.96–6.53 eV). In addition to a broad band centered at about 206 nm and assigned to a $^1\pi\pi^*$ transition, there is also indication that another intense band should occur just below 190 nm. Two sharp peaks are observed at 198 nm (6.26 eV) and 194 nm (6.40 eV). The weak tail extending to long wavelengths (240 nm) has been assigned to the transition into the $^1\pi\sigma_{NH}{}^*(3s)$ state.[20] Different from the theoretical predictions,[13] the vapor spectrum shows that the center of the first band in gas phase remains basically unaffected when compared to condensed phases. The second band, however, undergoes strong variations in its position and relative intensity depending on the solvation conditions.[16]

Experimental investigations[20] of photoexcited imidazole by means of total kinetic energy release (TKER) spectroscopy have revealed that on one hand the excitation at long wavelengths (220 nm$<\lambda<$240 nm) results in fast H fragments produced on a time scale that is shorter than the parental rotational period. By analogy with pyrrole, Devine *et al.*[20] assigned this process to excitation followed by dissociation along the repulsive $^1\pi\sigma_{NH}{}^*(3s)$ state. On the other hand, at short wavelengths ($\lambda<$220 nm) a second component in the TKER spectra corresponding to slow H fragments becomes dominant. This feature is rationalized as a second dissociation process taking place from the vibrationally hot ground state of imidazole, which would be activated by internal conversion.

Although there are no specific theoretical investigations of conical intersections in imidazole, the analogy with related systems such as pyrrole[21,22] and adenine[6–8] assures that the $^1\pi\sigma_{NH}{}^*/S_0$ conical intersection should exist along the NH stretching reaction path.[23] In addition, our previous studies of other five-membered rings (pyrrole,[24,25] thiophene,[26,27] and furan[28]) and the results of Perun *et al.*[6] on adenine indicate that other conical intersections formed by ring opening and ring puckering should also exist in imidazole and eventually contribute to its internal conversion. Indirect evidence corroborating the hypothesis that ring deformations should be involved in the photodeactivation of imidazole comes from the experimental fact that the sterical hindering of imidazole by phenyl rings has the effect of producing highly efficient fluorescent materials.[29]

In the present work, we first investigate the vertical excitation spectrum of imidazole, providing benchmark results obtained with different theoretical methods and also providing new assignments of the experimental spectra. Second, we investigate the radiationless decay of imidazole by character-

---

[a)] Electronic mail: mario.barbatti@univie.ac.at.
[b)] Electronic mail: hans.lischka@univie.ac.at.
[c)] Electronic mail: christel.marian@uni-duesseldorf.de.

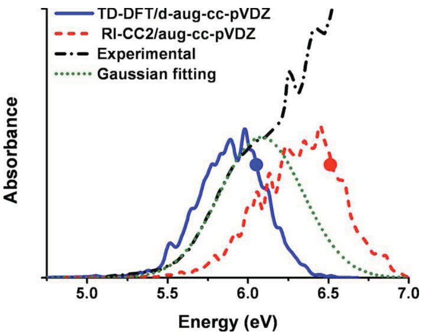

FIG. 1. (Color online) Simulations of the first band of the absorption spectrum of imidazole at TD-DFT/d-aug-cc-pVDZ and RI-CC2/aug-cc-pVDZ. The dots indicate the vertical excitation energy for each method. The experimental data are from Ref. 20. The Gaussian fitting corresponds to the peak centered at 6.08 eV, whose parameters are given in Table I.

izing different conical intersections and the deactivation paths connecting the Franck–Condon region to them. The aim is at highlighting the competition among the deactivation pathways and getting insights about the importance of each one depending on the excitation energy.

II. COMPUTATIONAL DETAILS

Complete active space self-consistent field (CASSCF) calculations were performed for imidazole in order to compute the extremes on the seam of conical intersections (MXS). The CAS space was composed by eight electrons in nine orbitals [CAS(8,9)]. The nine orbitals are the three π, the lone pair (n), three π^*, the $\sigma_{\mathrm{NH}}{}^*(3s)$, and one $\sigma_{\mathrm{CH}}{}^*$. Six states were used in the state averaging procedure (SA-6). This particular choice of active space was made aiming at setting a single theoretical level that allows for the calculation of reaction paths to all investigated conical intersections. The 6-31G* basis set[30] was used and the diffuse functions of the 6-31+G* basis set were added to the N_1 atom. This basis set will be denoted 6-31G*N_1+.

The optimizations were performed following the analytical gradient and nonadiabatic coupling procedures described in Refs. 31–35. The Cartesian coordinates of the ground state minimum and MXSs are available in the Supplementary Material.[36] Reaction paths were built by the method of linear interpolation of internal coordinates (LIICs) and the energies were plotted as a function of the mass-weighted distance (d_{MW}) between each point of the path and the minimum in the S_0 state. The structures of the puckered conical intersections were described in terms of the Cremer–Pople parameters (Q, ϕ).[37]

At the geometries along the linearly interpolated paths, single-point calculations were carried out utilizing the combined density functional theory/multireference configuration interaction (DFT/MRCI) method.[38] Auxiliary basis functions for the resolution-of-the-identity approximation of two-electron integrals in the MRCI calculations were taken from the TURBOMOLE library.[39,40] In the MRCI step, all valence electrons were correlated. The atomic orbital basis comprised the TZVPP [valence triple zeta plus $(2d1f,2p1d)$ polarization] basis set.[41] For the appropriate description of Rydberg states, this basis set was augmented by a set of $(1s,1p,1d)$ diffuse basis functions located on the N_1 atom with exponents taken from the work of Serrano-Andrés *et al.*[13] This basis set will be termed TZVPP+.

Vertical excitation energies and transition moments were additionally investigated using several different methods: the time-dependent density functional theory (TD-DFT) (Refs. 42 and 43) with the B3-LYP functional,[44] the resolution-of-identity coupled cluster to the second-order method (RI-CC2),[45–47] the complete active space self-consistent-field second-order perturbation theory in its multistate version (MS-CASPT2),[48] and the multireference configuration interaction (MRCI) method. The ground state geometry used in the vertical excitation investigations was optimized at DFT(B3-LYP)/aug-cc-pVTZ level.

The TD-DFT and RI-CC2 calculations were performed using the correlated (d)-aug-cc-pVXZ ($X=D,T$) (Ref. 49) basis sets. The MS-CASPT2 calculations were performed using the CAS(8,9) space afore mentioned and an IPEA shift[50] of 0.25. The 6-31+G* basis set was used. An additional set of s and p diffuse functions was added to the 6-31+G* in some calculations. They were obtained by dividing the exponent of the most diffuse functions of the 6-31+G* basis set by three. This basis set will be termed 6-31+2G*.

The MRCI calculations were performed including either single and double excitations (MR-CISD) or only single excitations (MR-CIS) from the reference space. The reference space was composed by six electrons and six orbitals [MRCI(6,6)], which includes all orbitals with CASSCF natural occupation between 0.1 and 1.9. The five core orbitals were kept frozen and the generalized interacting space restrictions[51] were employed in the MR-CISD. Higher-order excitations[32,52] were taken into account by means of the corrections proposed by Pople *et al.*[53] (+P) and by Langhoff and Davidson (+Q).[54] The 6-31+G* basis set was used.

Absorption spectrum simulations were performed by sampling the ground state geometries according to the Wigner distribution for the quantum harmonic oscillator and applying the Gaussian broadening approach described in Ref. 55. A broadening factor of 0.025 eV was employed. Five hundred points were employed in each simulation.

The TD-DFT and RI-CC2 calculations were performed with the TURBOMOLE program.[40] The MS-CASPT2 calculations were performed with the MOLCAS program.[56] The MRCI calculations and the CASSCF conical intersection optimizations were performed with the COLUMBUS program.[57–59] The spectrum simulations were performed with the NEWTON-X program.[55,60]

III. RESULTS AND DISCUSSION

A. Vertical excitation energies

Vertical excitation energies have been computed with several methods and levels. Energies, oscillator strengths, and state character for selected transitions are given in Table I. The CASPT2 results of Ref. 13 are given in this table as well. The complete set of currently computed vertical excitation energies and their assignments is given in the Tables SM1–SM5 of the Supplementary Material.[36] In order to

TABLE I. Selected vertical singlet excitation energies ΔE and oscillator strengths f of imidazole computed with different methods. The experimental entries correspond to the Gaussian fitting of the experimental spectrum of Ref. 20, where ΔE is the Gaussian center (eV) and f gives its area/width. The area was normalized to be 0.1 for the peak centered at 6.08 eV. Width is in eV.

		$\pi\sigma_{NH}^*(3s)$ (A'')		$\pi\sigma_{CH}^*$ (A'')		$n\sigma_{NH}^*(3s)$ (A')		$\pi\pi^*$ (A')	
Method	Basis set	ΔE (eV)	f	ΔE (eV)	f	ΔE (eV)	f	ΔE (eV)	f
TD-DFT	aug-cc-pVDZ	5.15	0.000	5.97	0.027	6.32	0.071	6.22	0.112
	aug-cc-pVTZ	5.15	0.000	5.95	0.025	6.31	0.046	6.18	0.127
	d-aug-cc-pVDZ	5.13	0.000	5.88	0.021	6.27	0.021	6.05	0.087
	d-aug-cc-pVTZ	5.14	0.000	5.89	0.021	6.29	0.020	6.05	0.090
RI-CC2	aug-cc-pVDZ	5.55	0.001	6.34	0.032	6.32	0.030	6.51	0.152
	aug-cc-pVTZ	5.69	0.000	6.47	0.029	6.43	0.027	6.51	0.147
	d-aug-cc-pVDZ	5.53	0.000	6.27	0.027	6.28	0.028	6.36	0.108
	d-aug-cc-pVTZ	5.69	0.000	6.41	0.034	6.44	0.026	6.46	0.124
DFT/MRCI	TZVPP+	5.44	0.001	6.25	0.034	6.94	0.041	6.11	0.187
MS-CASPT2	ANO-L-R[a]	5.71	0.000	6.38	0.000	7.10	0.018	6.72	0.126
	6-31+G*	5.82	0.000	6.69	0.014	6.83	0.036	6.72	0.107
	6-31+2G*	5.55	0.000	6.32	0.012	6.41	0.021	6.47	0.042
MR-CISD+P	6-31+G*	5.68	0.001	6.58	0.019	6.58	0.019	6.58	0.176
MRCIS(6,6)	6-31+G*	4.84	0.001	5.74	0.026	6.26	0.040	6.07	0.120
SA6-CAS(8,9)	6-31+G*	4.82	0.001	5.72	0.012	6.70	0.033	5.93	0.085
Expt.[b]				6.26	0.010/0.04	6.40	0.025/0.06	6.08 (6.25[c])	0.100/0.26

[a] Reference 13 (IPEA=0).
[b] Reference 20.
[c] Estimation of the experimental vertical excitation energy (see text).

compare the gas phase experimental spectrum of Ref. 20 with the theoretical data, we have fitted the spectrum with four Gaussian functions. The fitting parameters are given in Table I and Table II in the entry "Expt." The Gaussian areas were normalized as to have 0.100 (arbitrary units) for the Gaussian corresponding to the first $^1\pi\pi^*$ transition. This allows a more direct comparison to the calculated oscillator strengths.

All theoretical methods employed show that the $^1\pi\sigma_{NH}^*(3s)$ state is the lowest singlet excited state (Table I). It lies in the range of 5.1–5.8 eV depending on the theoretical level. The lowest energies for the $^1\pi\sigma_{NH}^*(3s)$ state are found with the TD-DFT level and the highest ones with CASPT2. The RI-CC2 and DFT/MRCI energies show intermediary values. Although it does not strictly correspond to a forbidden transition, the quasi-C_{2v} symmetry of imidazole (C_2 axis through NH bond) gives to this state a quasi-A_2 character explaining its almost zero intensity for the ground state minimum geometry. It is, however, possible that this transition contributes to the long wavelength tail of the spectrum via vibronic coupling.[20]

TABLE II. Excitation energies ΔE and oscillator strengths f of imidazole computed with different methods for the second $^1\pi\pi^*$ transition in imidazole. The experimental entry corresponds to the Gaussian fitting of the experimental spectrum of Ref. 20, where ΔE is the Gaussian center (eV) and f gives its area/width. The area was normalized as in Table I and width is in eV.

		$^1\pi\pi^*$ (A')	
Method	Basis set	ΔE (eV)	f
TD-DFT	aug-cc-pVDZ	6.89	0.044
	aug-cc-pVTZ[a]	6.86/6.92	0.029/0.033
	d-aug-cc-pVDZ	6.55	0.067
	d-aug-cc-pVTZ	6.53	0.066
RI-CC2	aug-cc-pVDZ	7.03	0.041
	aug-cc-pVTZ	6.99	0.032
	d-aug-cc-pVDZ	6.79	0.014
	d-aug-cc-pVTZ	7.12	0.068
DFT/MRCI	TZVPP+ [a]	6.58/6.78	0.032/0.028
MS-CASPT2	ANO-L-R[b]	7.15	0.143
Expt.[c]		6.59	0.075/0.09

[a] At this level the $^1\pi\pi^*$ transition splits in two neighboring components.
[b] Reference 13.
[c] Extrapolation of data from Ref. 20.

The first $^1\pi\pi^*$ state appears between 6.0 and 6.7 eV depending on the method (Table I), with TD-DFT and DFT/MRCI predicting the lowest transition energies and CASPT2 and RI-CC2 the highest energies. The energy of this state is quite dependent on the basis set diffuseness. At TD-DFT level, it is stabilized from 6.22 to 6.05 eV when the basis set is increased from aug-cc-pVDZ to d-aug-cc-pVDZ. The change from double-ζ to triple-ζ quality shows only a minor effect. Similarly, the RI-CC2 energy is stabilized from 6.51 to 6.36 eV by adding the diffuse functions to the aug-cc-pVDZ basis set. The same strong stabilization, however, is not observed when the diffuse functions are added to the triple-ζ basis.

At CASPT2 and MR-CISD levels the first $^1\pi\pi^*$ transition appears at relatively high energies. Curiously, the energy given by the CASSCF method is near the best TD-DFT value, which certainly results from a compensation of errors. Note that this situation is atypical for CASSCF calculations, which usually predicts excessively high $^1\pi\pi^*$ transition energies. Indeed, if the 6-31G*N$_1$+ basis set is used this is exactly what happens, indicating that the diffuse functions have a very strong stabilization effect within this method.

The transition energy for the first $^1\pi\pi^*$ state at CASPT2 is the same (6.72 eV) either with the 6-31+G* basis set or with the ANO-L plus a set of diffuse functions placed at the center of charge of the molecule (ANO-L-R), as used in Ref. 13. If an additional set of diffuse functions is used (6-31+2G*) the CASPT2 result is stabilized to 6.47 eV, a similar value as those obtained at the RI-CC2 level. Note that the ANO-L-R basis set contains strongly diffuse basis functions as the 6-31+2G* basis does. In the ANO-L-R, however, these diffuse functions are part of a contraction with other less diffuse functions, while they are uncontracted in the 6-31+2G* basis set.

The spectrum simulations for the first band are shown in Fig. 1 together with the experimental data[20] and the Gaussian fitting for this band. In relation to the band center, the vertical excitation into the first $^1\pi\pi^*$ state appears displaced to higher energies by 0.14 and 0.17 eV at TD-DFT and RI-CC2, respectively. Similar displacement has been observed in the case of the simulated spectrum of cyclopentadiene, too.[61] Supposing that the same factor applies to the experiments, the experimental vertical excitation energy should be at about 6.25 eV. The results in Table I show that while the DFT-based methods tend to predict the $^1\pi\pi^*$ vertical excitation energy below this value, the RI-CC2, CASPT2, and MR-CISD methods present just the opposite trend.

Two other states with nonzero oscillator strength appear close to the $^1\pi\pi^*$ state, the $^1\pi\sigma_{CH}{}^*$ and the $^1n\sigma_{NH}{}^*(3s)$ state (Table I). The $^1\pi\sigma_{CH}{}^*$ transition is at lower energies than the $^1\pi\pi^*$ transition for all methods except DFT/MRCI. The $^1n\sigma_{NH}{}^*(3s)$ transition energy on its turn is quite dependent on the employed method. For the TD-DFT and RI-CC2 methods it is in the 6.3–6.4 eV range. Note that, in contrast with the 6-31+G* basis set results, when the CASPT2 calculations are performed with the 6-31+2G* basis set there is a very good agreement between theory and the proposed assignments discussed in Sec. III B.

Besides the too high $^1\pi\pi^*$ transition energy, another indication that the CASPT2 method with the 6-31+G* and ANO-L-R basis sets is not adequately treating the transitions into the π^* orbitals is in the relatively strong oscillator strength (0.017 and 0.011, respectively) predicted to the first $^1n\pi^*$ transition (see Table SM4 of the Supplementary Material[36] and Ref. 13). In the approximate C_{2v} symmetry (C_2 axis passing through N_3 atom) the n and the π^* orbitals belong to the a_1 and a_2 representations, respectively, which means that this transition is approximately forbidden. Consistently, for all other methods for which the $^1n\pi^*$ was computed, including the CASPT2 using the 6-31+2G basis set, the oscillator strength is very nearly zero (Tables SM1 and SM2 of the Supplementary Material[36]).

The theoretical data for the second $^1\pi\pi^*$ transition are collected in Table II. The state character shown in Tables SM1–SM5[36] indicates a strong mixing with the $^1\pi 3p_x$ Rydberg transition for most of the employed levels. As occurred for the first band, the RI-CC2 and CASPT2 results predict too high energies to corroborate this assignment. The TD-DFT using doubly augmented basis sets and the DFT/MRCI results, on their turn, are in very good agreement with the experimental data, as discussed in Sec. III B.

B. Assignment of the absorption spectrum

Four states contribute to the low energy region of the imidazole absorption spectrum, two $^1\pi\pi^*$, the $^1\pi\sigma_{CH}{}^*$, and the $^1n\sigma_{NH}{}^*(3s)$ states. To facilitate the discussion in this section, we will take as the reference theoretical values the results obtained at TD-DFT/d-aug-cc-pVTZ (Table I) and our fitted values for the experimental spectrum of Ref. 20.

The first experimental band centered at 204 nm (6.08 eV) has been assigned to the first $^1\pi\pi^*$ transition,[20] whose vertical transition energy is 6.05 eV. The results of simulations of this first band at TD-DFT/d-aug-cc-pVDZ and RI-CC2/aug-cc-pVDZ corroborate this assignment (Fig. 1).

The fitting of the experimental data (Table II) with extrapolation of the region below 190 nm indicates that a second intense band should be centered at 6.59 eV (188 nm). This band can be assigned to the second $^1\pi\pi^*$ transition (6.53 eV). Both theoretical and experimental data indicate that the oscillator strength (Gaussian area in the experimental case) of the second band should be somewhat smaller than that of the first band. Nevertheless, the intensity of the second band is still higher, which implies that the wave packet excited into this second $^1\pi\pi^*$ state remains longer in the Franck–Condon region than when it is excited into the first $^1\pi\pi^*$ state.

The oscillator strength and transition energy (5.89 eV) of the $^1\pi\sigma_{CH}{}^*$ state is consistent with the sharp feature at 198 nm (6.26 eV) in the vapor absorption spectrum[20] and with the 218 nm (5.69 eV) peak in the water-solution spectrum.[18]

The $^1n\sigma_{NH}{}^*(3s)$ transition (6.29 eV) should be the origin of the sharp feature at 194 nm (6.40 eV) in the vapor spectrum. Due to the character of the singly occupied orbitals (n and $\sigma_{NH}{}^*$), the transition energy of this state should be strongly dependent on the pH and polarity of the solvent, which can explain the strong solvent effects experimentally observed in the region of the second band.[16] Thus, while the 187 nm (6.63 nm) peak observed in neutral and alkaline solutions[16] can be attributed to the $^1n\sigma_{NH}{}^*(3s)$ transition, this peak is vanished in strong acid solution[16] as a consequence of the protonation of the N_3 site.

C. Conical intersections

We have optimized and characterized four distinct extremes on the S_0/S_1 seam of conical intersections of imidazole. Their energies and main geometrical parameters are given in Table III. Their structures are shown in Fig. 2.

The lowest energy conical intersection presents a planar structure dissociated at the N_1C_2 bond. This kind of conical intersection has been previously identified in thiophene,[26,27] furan,[28] and also in the imidazole ring of adenine.[6] Close to the intersection the S_1 state has $^1\pi\sigma_{CN}{}^*$ character. The second lowest energy conical intersection occurs for NH stretching and, as usual for this kind of intersection,[21] the S_1 state has $^1\pi\sigma_{NH}{}^*$ character. Two ring-puckered conical intersections follow in energy and show $^1\pi\pi^*$ characters for the S_1 state. The first is puckered at the N_1 atom with an envelope

TABLE III. Energies and geometrical parameters of the ground state minimum and conical intersections. Q and ϕ are the Cremer–Pople parameters.

Geometry	State	E (eV) CASSCF[a]	E (eV) DFT/MRCI[b]	Q (Å)	ϕ (deg)	R_{12} (Å)	R_{24} (Å)	R_{NH} (Å)
Minimum S_0	$^1\pi\sigma_{NH}{}^*(3s)$	6.13	5.44	0.00	⋯ (Planar)	1.366	2.130	0.992
	$^1\pi\pi^*$	7.11	6.11					
MXS NC-dissociation	S_0/S_1	3.15	3.94[c]	0.00	⋯ (Planar)	2.990	2.425	1.005
MXS NH-dissociation	S_0/S_1	4.40	4.28[c]	0.00	⋯ (Planar)	1.345	2.125	1.608
MXS N-puckering (E_3)	S_0/S_1	6.16	6.02[c]	0.54	71.7 (E_3)	1.389	1.831	0.994
MXS NH-puckering (E_1)	S_0/S_1	5.04	5.29[c]	0.41	−0.1 (E_1)	1.888	2.229	1.007

[a] SA-6-CASSCF(8,9)/6-31G*N_1+.

[b] DFT/MRCI/TZVPP+.

[c] Average energy of the S_0 and S_1 states.

conformation (E_1). It has a close analog in pyrrole and likewise it presents a strong elongation of the N_1C_2 bond (see Table II). Finally, the fourth conical intersection is puckered at the N_3 atom (envelope E_3 conformation). The puckered conformation is such that a new bond is formed between atoms C_2 and C_4, similarly to what occurs in the puckered conical intersection of benzene.[62]

D. Reaction paths

The potential energy paths connecting the minimum in the ground state geometry to each conical intersection is given in Fig. 3. These paths were obtained by LIICs and are plotted as a function of the mass-weighted distance to the ground state minimum geometry. The small S_1/S_0 energy gaps at the position of the conical intersections (last point of each path) are due to the difference between the method used to compute the path, DFT/MRCI/TZVPP+, and that used to optimize the conical intersections, SA-6-CASSCF(8,9)/6-31G*N_1+. The paths recomputed for the same geometries at the SA-6-CASSCF(8,9) level are shown in Fig. SM1 of the Supplementary Material.[36]

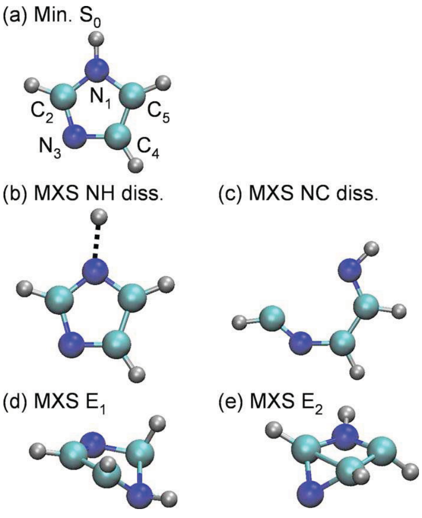

FIG. 2. (Color online) Geometry of the ground state minima (a) and of the S_0/S_1 conical intersections [(b)–(e)] in imidazole.

The conical intersection which requires the smallest deformation from the Franck–Condon region is the NH-stretched MXS (0.8 Å amu$^{1/2}$). It directly arises along the NH stretching path on the dissociative $^1\pi\sigma_{NH}{}^*$ surface and in the case of excitation into this state it is the only conical intersection that can be reached barrierlessly. It should certainly constitute the main funnel to the ground state for low energy excitations and the fast-H elimination experimentally observed[20] can be attributed to this pathway.

In the case of excitation into the first $^1\pi\pi^*$ state, the NH-stretched conical intersection is not directly accessible through the simple NH stretching mode. Figure 3 shows that other out-of-plane and in-plane distortions can lead to crossings between the S_2 and the S_1 states. In these cases, however, the dominance of the $\pi\sigma_{NH}{}^*$ channel is not assured anymore and other deactivation pathways may as well be activated.

The planar ring-opened conical intersection requires the strongest deformation from the Franck–Condon region. After excitation into the first $^1\pi\pi^*$ state, the S_1 ($^1\pi\pi^*$) path is flat until it crosses the $^1\pi\sigma_{CN}{}^*$ state that is stabilized by the N_1-C_2 bond stretching. After this crossing, the S_1 state shows a steep shape toward the intersection. Note that although the minimum on the crossing seam occurs at a dis-

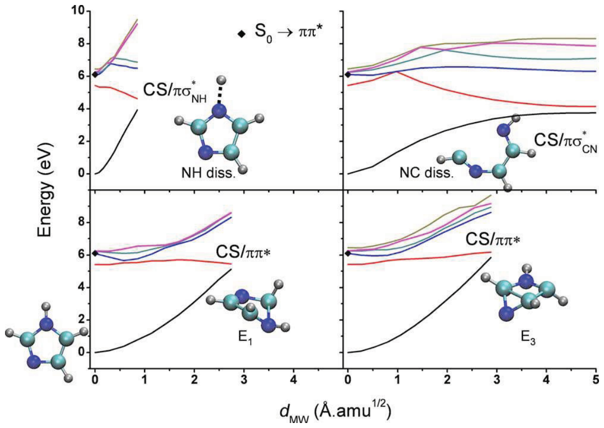

FIG. 3. (Color online) Reaction paths connecting the geometry of the ground state minimum to each S_0/S_1 conical intersection at DFT/MRCI/TZVPP+ level. CS: closed shell.

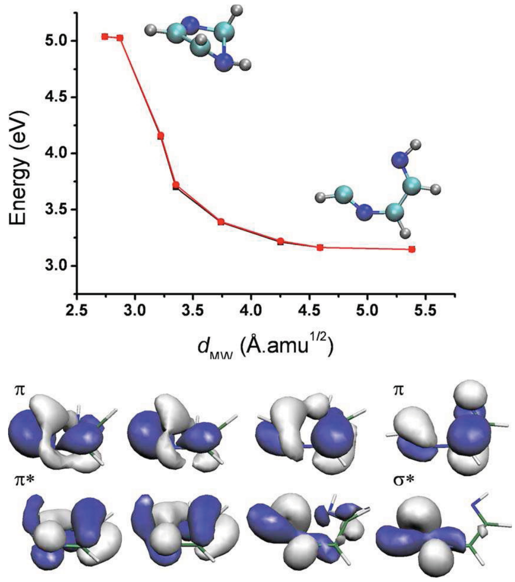

FIG. 4. (Color online) S_1 and S_0 energies along the branch of crossing seam connecting the planar ring-opened and the E_1-puckered conical intersections (top). Evolution of the singly occupied orbitals along the crossing seam (bottom).

tance of about 4.9 Å amu$^{1/2}$, planar ring-opened conical intersections with slightly higher energies can be reached along this path at distances as short as 3.4 Å amu$^{1/2}$. It is worth noting that dynamics simulations for adenine have shown internal conversion at this kind of conical intersection for a minor fraction of trajectories with large initial energy.[7]

The NH-puckered (E_1) and the N-puckered (E_3) conical intersections require distortions of, respectively, 2.7 and 2.9 Å amu$^{1/2}$. The Franck–Condon region is barrielessly connected to both. Also in both cases the S_1 state has the same $^1\pi\pi^*$ character as the first $^1\pi\pi^*$ excited state. In the case of the E_1 conical intersection, the π^* orbital has a component of the σ orbital involving atoms N_1 and C_2, while in the E_3 conical intersection it is mixed to a σ orbital linking C_2 and C_4. The fact that there is a diabatic connection between the $^1\pi\pi^*$ state and these conical intersections makes them candidates for explaining the formation of vibrationally excited imidazole inferred from the TKER results.[20] Nevertheless, their relatively high energy compared to the planar ring opened and to the NH-stretched conical intersections are factors acting against the deactivation through them.

Even though the E_1 and the planar ring-opened conical intersections have different electronic structures, the elongation of the N_1C_2 bond in the E_1 conical intersection raises the possibility that these two MXS may be connected by the same branch of crossing seam. In order to check this hypothesis, we have performed restricted conical intersection optimizations along the LIIC path connecting these two extremes on the crossing seam. The result is shown in Fig. 4 (top) and reveals that the E_1 conical intersection is not a minimum but probably a maximum on the crossing seam.

It is particularly interesting that this branch of crossing seam exists despite the different state characters of the E_1 and planar ring-opened conical intersections, $\pi\pi^*$ and $\pi\sigma_{CN}^*$, respectively. The inspection of the molecular orbitals along the seam shows, however, that there is no real diabatic transformation, but the singly occupied π^* orbital smoothly rotates to become the σ_{CN}^* orbital.

The existence of this branch of crossing seam has implications for the photochemistry of imidazole. As discussed above, while the E_3 conical intersection requires small deformations and high energies to be reached, the planar ring-opened conical intersection requires large deformations and low energies. Therefore, if photoexcited imidazole moves in this region of the excited state surface it should preferentially deactivate at middle points of this branch of crossing seam presenting intermediary distortions and energies.

The good agreement between the reaction paths computed at CASSCF level in Fig. SM1 of the Supplementary Material[36] and at DFT/MRCI level in Fig. 3 indicates that the CASSCF level can provide reliable surfaces for performing dynamics simulations in future work. All qualitative aspects of the paths—state ordering, barriers, and crossings—are the same for both methods. The main difference is that the excited state energies are, as expected, higher at CASSCF level than at DFT/MRCI level. Because this effect is stronger at the Franck–Condon region than at the conical intersections, the CASSCF surfaces are steeper than the DFT/MRCI surfaces, which can cause a reduction in the time scales of the dynamics. Nevertheless, since the selection of the reaction channels should be done close to the Franck–Condon region, this distortions should have minor influence on the selection of the pathways.

The CASSCF vertical excitation energies obtained when the 6-31+G* basis set is used for all atoms is in much better agreement with the correlated methods than the results with the diffuse functions restricted to the N_1 atom. Nevertheless, the single-point calculations computed with the 6-31+G* basis set along the reaction paths showed frequent exchange of orbitals between the active space and the doubly occupied and virtual spaces, with changes of the states included in the state averaging procedure. This instability makes the CASSCF(8,9)/6-31+G* level inadequate for dynamics simulations despite its very good performance at the ground state minimum geometry.

IV. CONCLUSIONS

The excited states of the imidazole chromophore have been investigated at several theoretical methods and levels, including TD-DFT, RI-CC2, DFT/MRCI, CASPT2, and MRCI. Vertical excitation energies were computed in order to characterize the first and second absorption bands of the gas phase spectrum. These bands are dominated by two $^1\pi\pi^*$ transitions with sharp features assigned to the $^1\pi\sigma_{CH}^*$ and the $^1n\sigma_{NH}^*(3s)$ Rydberg transitions. Strong solvent effect that have been experimentally detected[16] can be attributed to the presence of the $^1n\sigma_{NH}^*(3s)$ transition in the region between the two bands.

The ultrafast decay of imidazole has been investigated as well. Four different conical intersections have been identified and characterized. The reaction paths between the Franck–Condon region and these conical intersections have been determined at CASSCF and DFT/MRCI levels. Upon low excitation energies, the most favorable pathway is the NH stretching along the $^1\pi\sigma_{NH}^*$ repulsive state. Upon excitation into the lowest $^1\pi\pi^*$ state, all pathways are energetically accessible, including those along the $^1\pi\pi^*$ state and involving ring puckering.

A branch of crossing seam connecting the E_1-puckered conical intersection with $\pi\pi^*$/closed-shell character to the planar ring-open conical intersection with $^1\pi\sigma_{CN}^*$/closed-shell character has been mapped. The change in the electronic structure occurs smoothly along the seam by rotation of the singly occupied π^* orbital into a σ_{CN}^* orbital. The middle region of this crossing seam conjugating low energy and small geometric deformations should be more efficient for the radiationless decay than the two extremes.

It should be possible to experimentally check whether the deactivation occurs at this branch of crossing seam or not by monitoring photochemical products resulting from ring opening processes like in pyrrole.[24] Dynamics simulations for pyrrole[63] have shown that about a quarter of molecules deactivating at the puckered conical intersection undergoes such photochemical transformations. Due to the structural similarities, similar proportion can be expected for imidazole. Deactivation occurring at the E_3 puckered and at the NH dissociated conical intersection on their turn should correspond to photostable channels, which keep the ring integrity.

In this work, we have focused on the low energy excited states until the first and second $^1\pi\pi^*$ states. Nevertheless, the importance of deactivation channels involving ring deformation should increase at higher energy excitations. This is particularly relevant if we take into account that the first $^1\pi\pi^*$ state is not the optically strongest absorbing state. CASPT2 calculations by Serrano-Andrés *et al.*[13] predict the existence of another $^1\pi\pi^*$ state occurring at 8.51 eV, whose oscillator strength is almost five times larger that that for the first $^1\pi\pi^*$ state.

Since these conical intersections and reaction paths involve essentially the N_1, C_2, and N_3 atoms, the conclusions drawn here can also be extended to histidine, whose amino-acid chain connects either to C_4 or C_5 and should not interfere with the active sites in the conical intersection formation. Similar arguments hold for histidine derivatives, such as histamine, camosine, and urocanic acid.

ACKNOWLEDGMENTS

The authors want to thank L. Serrano-Andrés for providing the Rydberg functions used in the DFT/MRCI calculations. The authors also acknowledge the technical support and computer time at the Linux PC cluster Schrödinger III of the computer center of the University of Vienna. This work was supported by the Austrian Science Fund within the framework of the Special Research Program F16 (Advanced Light Sources) under Project No. P18411-N19, and by the German Research Council (DFG) within the framework of Contract No. SFB 663/C1.

[1] H. Du, R. C. A. Fuh, J. Z. Li, L. A. Corkan, and J. S. Lindsey, Photochem. Photobiol. **68**, 141 (1998).
[2] M. Norval, Prog. Biophys. Mol. Biol. **92**, 108 (2006).
[3] K. M. Hanson and J. D. Simon, Proc. Natl. Acad. Sci. U.S.A. **95**, 10576 (1998).
[4] E. C. De Fabo and F. P. Noonan, J. Exp. Med. **158**, 84 (1983).
[5] R. D. Fugate, C. A. Chin, and P. S. Song, Biochim. Biophys. Acta **421**, 1 (1976).
[6] S. Perun, A. L. Sobolewski, and W. Domcke, Chem. Phys. **313**, 107 (2005).
[7] M. Barbatti and H. Lischka, J. Am. Chem. Soc. **130**, 6831 (2008).
[8] C. M. Marian, J. Chem. Phys. **122**, 104314 (2005).
[9] C. M. Marian, M. Kleinschmidt, and J. Tatchen, Chem. Phys. **347**, 346 (2008).
[10] J. Del Bene and H. H. Jaffe, J. Chem. Phys. **48**, 4050 (1968).
[11] E. Bernarducci, P. K. Bharadwaj, K. Krogh-Jespersen, J. A. Potenza, and H. J. Schugar, J. Am. Chem. Soc. **105**, 3860 (1983).
[12] F. B. C. Machado and E. R. Davidson, J. Chem. Phys. **97**, 1881 (1992).
[13] L. Serrano-Andrés, M. P. Fulscher, B. O. Roos, and M. Merchán, J. Phys. Chem. **100**, 6484 (1996).
[14] L. Serrano-Andrés, M. P. Fülscher, and G. Karlström, Int. J. Quantum Chem. **65**, 167 (1997).
[15] E. A. Braude, Annu. Rep. Prog. Chem., Sect. C: Phys. Chem. **42**, 105 (1945).
[16] P. E. Grebow and T. M. Hooker, Biopolymers **14**, 871 (1975).
[17] T. G. Fawcett, E. E. Bernarducci, K. Krogh-Jespersen, and H. J. Schugar, J. Am. Chem. Soc. **102**, 2598 (1980).
[18] D. S. Caswell and T. G. Spiro, J. Am. Chem. Soc. **108**, 6470 (1986).
[19] S. A. Asher and J. L. Murtaugh, Appl. Spectrosc. **42**, 83 (1988).
[20] A. L. Devine, B. Cronin, M. G. D. Nix, and M. N. R. Ashfold, J. Chem. Phys. **125**, 184302 (2006).
[21] A. L. Sobolewski and W. Domcke, Chem. Phys. **259**, 181 (2000).
[22] V. Vallet, Z. G. Lan, S. Mahapatra, A. L. Sobolewski, and W. Domcke, Faraday Discuss. **127**, 283 (2004).
[23] M. N. R. Ashfold, B. Cronin, A. L. Devine, R. N. Dixon, and M. G. D. Nix, Science **312**, 1637 (2006).
[24] M. Barbatti, M. Vazdar, A. J. A. Aquino, M. Eckert-Maksic, and H. Lischka, J. Chem. Phys. **125**, 164323 (2006).
[25] M. Barbatti, B. Sellner, A. J. A. Aquino, and H. Lischka, in *Radiation Induced Molecular Phenomena in Nucleic Acid*, edited by M. K. Shukla and J. Leszczynski (Springer, Netherlands, 2008).
[26] S. Salzmann, M. Kleinschmidt, J. Tatchen, R. Weinkauf, and C. M. Marian, Phys. Chem. Chem. Phys. **10**, 380 (2008).
[27] R. Weinkauf, L. Lehr, E. W. Schlag, S. Salzmann, and C. M. Marian, Phys. Chem. Chem. Phys. **10**, 393 (2008).
[28] N. Gavrilov, S. Salzmann, and C. M. Marian, Chem. Phys. **349**, 269 (2008).
[29] S. Park, O. H. Kwon, S. Kim, S. Park, M. G. Choi, M. Cha, S. Y. Park, and D. J. Jang, J. Am. Chem. Soc. **127**, 10070 (2005).
[30] W. J. Hehre, R. Ditchfield, and J. A. Pople, J. Chem. Phys. **56**, 2257 (1972).
[31] R. Shepard, H. Lischka, P. G. Szalay, T. Kovar, and M. Ernzerhof, J. Chem. Phys. **96**, 2085 (1992).
[32] R. Shepard, in *Modern Electronic Structure Theory*, edited by D. R. Yarkony (World Scientific, Singapore, 1995), Vol. 1, p. 345.
[33] H. Lischka, M. Dallos, and R. Shepard, Mol. Phys. **100**, 1647 (2002).
[34] M. Dallos, H. Lischka, R. Shepard, D. R. Yarkony, and P. G. Szalay, J. Chem. Phys. **120**, 7330 (2004).
[35] H. Lischka, M. Dallos, P. G. Szalay, D. R. Yarkony, and R. Shepard, J. Chem. Phys. **120**, 7322 (2004).
[36] See EPAPS Document No. E-JCPSA6-130-039902 for the reaction paths calculated at CASSCF level, the complete tables of vertical excitation energies at several levels, and the Cartesian coordinates of all structures. For more information on EPAPS, see http://www.aip.org/pubservs/epaps.html.
[37] D. Cremer and J. A. Pople, J. Am. Chem. Soc. **97**, 1354 (1975).
[38] S. Grimme and M. Waletzke, J. Chem. Phys. **111**, 5645 (1999).
[39] F. Weigend, M. Häser, H. Patzelt, and R. Ahlrichs, Chem. Phys. Lett. **294**, 143 (1998).
[40] R. Ahlrichs, M. Bär, M. Häser, H. Horn, and C. Kölmel, Chem. Phys. Lett. **162**, 165 (1989).
[41] A. Schäfer, C. Huber, and R. Ahlrichs, J. Chem. Phys. **100**, 5829 (1994).
[42] R. Bauernschmitt and R. Ahlrichs, Chem. Phys. Lett. **256**, 454 (1996).
[43] F. Furche and R. Ahlrichs, J. Chem. Phys. **117**, 7433 (2002).

[44] A. D. Becke, J. Chem. Phys. **98**, 5648 (1993).
[45] O. Christiansen, H. Koch, and P. Jorgensen, Chem. Phys. Lett. **243**, 409 (1995).
[46] C. Hättig and F. Weigend, J. Chem. Phys. **113**, 5154 (2000).
[47] C. Hättig and A. Köhn, J. Chem. Phys. **117**, 6939 (2002).
[48] J. Finley, P. A. Malmqvist, B. O. Roos, and L. Serrano-Andrés, Chem. Phys. Lett. **288**, 299 (1998).
[49] T. H. Dunning, J. Chem. Phys. **90**, 1007 (1989).
[50] G. Ghigo, B. O. Roos, and P.-A. Malmqvist, Chem. Phys. Lett. **396**, 142 (2004).
[51] A. Bunge, J. Chem. Phys. **53**, 20 (1970).
[52] P. J. Bruna, S. D. Peyerimhoff, and R. J. Buenker, Chem. Phys. Lett. **72**, 278 (1980).
[53] J. A. Pople, R. Seeger, and R. Krishnan, Int. J. Quantum Chem. Synopsis **11**, 149 (1977).
[54] S. R. Langhoff and E. R. Davidson, Int. J. Quantum Chem. **8**, 61 (1974).
[55] M. Barbatti, G. Granucci, M. Persico, M. Ruckenbauer, M. Vazdar, M. Eckert-Maksic, and H. Lischka, J. Photochem. Photobiol., A **190**, 228 (2007).
[56] G. Karlström, R. Lindh, P. A. Malmqvist, B. O. Roos, U. Ryde, V. Veryazov, P. O. Widmark, M. Cossi, B. Schimmelpfennig, P. Neogrady, and L. Seijo, Comput. Mater. Sci. **28**, 222 (2003).
[57] H. Lischka, R. Shepard, F. B. Brown, and I. Shavitt, Int. J. Quantum Chem. **91**, 15 (1981).
[58] H. Lischka, R. Shepard, R. M. Pitzer, I. Shavitt, M. Dallos, T. Müller, P. G. Szalay, M. Seth, G. S. Kedziora, S. Yabushita, and Z. Y. Zhang, Phys. Chem. Chem. Phys. **3**, 664 (2001).
[59] H. Lischka, R. Shepard, I. Shavitt, R. M. Pitzer, M. Dallos, T. Mueller, P. G. Szalay, F. B. Brown, R. Ahlrichs, H. J. Boehm, A. Chang, D. C. Comeau, R. Gdanitz, H. Dachsel, C. Ehrhardt, M. Ernzerhof, P. Hoechtl, S. Irle, G. Kedziora, T. Kovar, V. Parasuk, M. J. M. Pepper, P. Scharf, H. Schiffer, M. Schindler, M. Schueler, M. Seth, E. A. Stahlberg, J.-G. Zhao, S. Yabushita, Z. Zhang, M. Barbatti, S. Matsika, M. Schuurmann, D. R. Yarkony, S. R. Brozell, E. V. Beck, and J.-P. Blaudeau, COLUMBUS, an ab initio electronic structure program, release 5.9.1, www.univie.ac.at/columbus, 2006.
[60] M. Barbatti, G. Granucci, H. Lischka, M. Ruckenbauer, and M. Persico, NEWTON-X, a package for Newtonian dynamics close to the crossing seam, version 0.14b, www.univie.ac.at/newtonx, 2007.
[61] Y. J. Bomble, K. W. Sattelmeyer, J. F. Stanton, and J. Gauss, J. Chem. Phys. **121**, 5236 (2004).
[62] I. J. Palmer, I. N. Ragazos, F. Bernardi, M. Olivucci, and M. A. Robb, J. Am. Chem. Soc. **115**, 673 (1993).
[63] B. Sellner, M. Barbatti, and H. Lischka (unpublished).

Supplementary Material

UV excitation and radiationless deactivation of imidazole

Mario Barbatti, Hans Lischka, Susanne Salzmann, Christel M. Marian

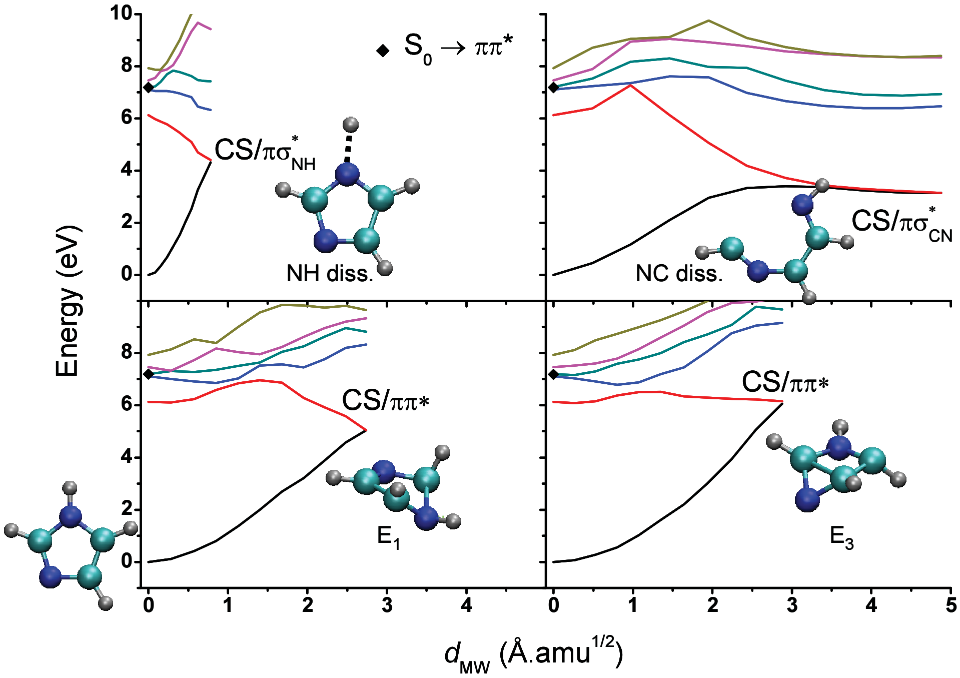

Fig. SM1 – Reaction paths connecting the geometry of the ground state minimum to each S_0/S_1 conical intersection at SA-6-CASSCF(8,9)/6-31G*N_1+ level. CS: closed shell.

Table SM1 - Vertical excitation energies, oscillator strengths and assignments at RI-CC2 level. S_0 energies in a.u.

	RI-CC2/aug-cc-pVDZ			RI-CC2/aug-cc-pVTZ			RI-CC2/d-aug-cc-pVDZ			RI-CC2/d-aug-cc-pVTZ		
	ΔE (eV)	*f*		ΔE (eV)	*f*		ΔE (eV)	*f*		ΔE (eV)	*f*	
S_0	-225.607390	-		-225.804371	-		-225.610171	-		-225.806293	-	
S_1	5.55	0.001	$\pi\sigma_{NH}*(3s)$	5.69	0.000	$\pi\sigma_{NH}*(3s)$	5.53	0.000	$\pi\sigma_{NH}*(3s)$	5.69	0.000	$\pi\sigma_{NH}*(3s)$
S_2	6.32	0.030	$n\sigma_{NH}*(3s)$	6.43	0.027	$n\sigma_{NH}*(3s)$	6.27	0.027	$\pi\sigma_{CH}*$	6.41	0.034	$\pi\sigma_{CH}*$
S_3	6.34	0.032	$\pi\sigma_{CH}*$	6.47	0.029	$\pi\sigma_{CH}*$	6.28	0.028	$n\sigma_{NH}*(3s)$	6.44	0.026	$n\sigma_{NH}*(3s)$
S_4	6.51	0.152	$\pi 3p_x/\pi\pi*$	6.51	0.147	$\pi 3p_x/\pi\pi*$	6.36	0.108	$\pi 3p_x/\pi\pi*$	6.46	0.124	$\pi 3p_x/\pi\pi*$
S_5	6.59	0.000	$\pi\sigma_{CH}*$	6.69	0.003	$n\pi*/\pi\sigma_{CH}*$	6.49	0.000	$\pi\sigma_{CH}*$	6.65	0.001	$\pi\sigma_{CH}*$
S_6	6.72	0.004	$\pi_{L-1}\sigma_{NH}*(3s)$	6.71	0.000	$\pi\sigma_{CH}*$	6.69	0.004	$\pi_{H-1}\sigma_{CH}*$	6.69	0.002	$n\pi*/n\pi_{L+1}*$
S_7	6.74	0.001	$n\pi*/n3p_x$	6.87	0.002	$\pi_{L-1}\sigma_{NH}*(3s)$	6.72	0.001	$n\pi*/n\pi_{L+1}*$	6.82	0.001	$\pi 3p_x/\pi\pi_{L+2}*$
S_8	7.03	0.041	$\pi\pi_{L+2}*/\pi_{H-1}\pi*$	6.99	0.032	$\pi 3p_x/\pi_{H-1}\pi*$	6.79	0.014	$\pi 3p_x/\pi\pi_{L+2}*$	6.87	0.002	$\pi_{H-1}\sigma_{CH}*$
S_9	7.15	0.004	$\pi 3s_{N3}$	7.25	0.006	$n\sigma_{CH}*$	6.92	0.001	πRyd(a')	7.08	0.001	πRyd(a')
S_{10}	7.30	0.000	$\pi\sigma_{CH}*$	7.26	0.004	$\pi 3s_{N3}$	7.02	0.002	πRyd(a')	7.12	0.068	$\pi\pi_{L+2}*$

Table SM2 - Vertical excitation energies, oscillator strengths and assignments at TD-DFT level. S_0 energies in a.u.

	TD-DFT(B3-LYP)/aug-cc-pVDZ			TDDFT/aug-cc-pVTZ			TD-DFT/d-aug-cc-pVDZ			TDDFT/d-aug-cc-pVTZ		
State	ΔE (eV)	*f*		ΔE (eV)	*f*		ΔE (eV)	*f*		ΔE (eV)	*f*	
S_0	-226.116615	-		-226.172243	-		-226.117680	-		-226.172515	-	
S_1	5.15	0.000	$\pi\sigma_{NH}*(3s)$	5.15	0.000	$\pi\sigma_{NH}*(3s)$	5.13	0.000	$\pi\sigma_{NH}*(3s)$	5.14	0.000	$\pi\sigma_{NH}*(3s)$
S_2	5.97	0.027	$\pi\sigma_{CH}*$	5.95	0.025	$\pi\sigma_{CH}*$	5.88	0.021	$\pi\sigma_{CH}*$	5.89	0.021	$\pi\sigma_{CH}*/\pi 3p_{yz}$
S_3	6.19	0.000	$\pi\sigma_{CH}*$	6.16	0.000	$\pi\sigma_{CH}*$	6.05	0.087	$\pi\pi*$	6.05	0.090	$\pi\pi*$
S_4	6.22	0.112	$\pi\pi*/n\sigma_{NH}*(3s)$	6.18	0.127	$\pi\pi*/\pi\pi_{L+1}*$	6.07	0.000	$\pi\sigma_{CH}*$	6.07	0.000	$\pi\sigma_{CH}*/\pi 3d$
S_5	6.32	0.071	$n\sigma_{NH}*(3s)/\pi\pi*$	6.31	0.046	$n\sigma_{NH}*(3s)$	6.27	0.021	$n\sigma_{NH}*(3s)$	6.29	0.020	$n\sigma_{NH}*(3s)$
S_6	6.41	0.003	$n\pi*$	6.40	0.003	$n\pi*$	6.40	0.002	$\pi 3p_{yz}/n\pi*$	6.39	0.002	$\pi\sigma_{CH}*/n\pi*$
S_7	6.53	0.002	$\pi_{H-1}\sigma_{NH}*(3s)$	6.54	0.001	$\pi_{L-1}\sigma_{NH}*(3s)$	6.40	0.001	$n\pi*/n\pi_{H+1}*$	6.39	0.001	$n\pi*/\pi\sigma_{CH}*$
S_8	6.70	0.003	$\pi\sigma_{CH}*$	6.66	0.003	$\pi\sigma_{CH}*$	6.49	0.000	$\pi_{H-2}3p_{yz}/\pi_{H-1}\sigma_{NH}*(3s)$	6.49	0.000	$\pi 3s_{N3}/\pi 3d$
S_9	6.89	0.044	$\pi\pi_{L+1}*/\pi_{L-1}\pi*$	6.86	0.029	$\pi\pi_{L+2}*/\pi_{L-1}\pi*$	6.51	0.001	$\pi_{H-1}\sigma_{NH}*(3s)/\pi 3p_{yz}$	6.53	0.000	$\pi_{H-1}\sigma_{NH}*(3s)/\pi 3p_{yz}$
S_{10}	7.03	0.000	$\pi 3s_{N3}$	6.92	0.033	$\pi\pi_{H+1}*/\pi\pi_{H+2}*$	6.55	0.067	$\pi\pi_{L-1}*$	6.53	0.066	$\pi\pi_{L+1}*$

Table SM3 - Vertical excitation energies, oscillator strengths and assignments at CASSCF and MRCI levels. S_0 energies in a.u.

	SA-6-CAS(8,9)/6-31+G*			MR-CIS(6,6)			MR-CISD(6,6)				
State	ΔE (eV)	*f*		ΔE (eV)	*f*		ΔE (eV)	ΔE (eV) +Q	ΔE (eV) +P	*f*	
S_0	-224.854148	-		-224.876728	-		-225.424704	-225.523210	-225.552191	-	
S_1	4.82	0.001	$\pi\sigma_{NH}$*(3s)	4.84	0.001	$\pi\sigma_{NH}$*(3s)	5.46	5.61	5.68	0.001	$\pi\sigma_{NH}$*(3s)
S_2	5.72	0.012	$\pi\sigma_{CH}$*	5.74	0.026	$\pi\sigma_{CH}$*	6.35	6.51	6.58	0.019	$\pi\sigma_{CH}$*
S_3	5.85	0.004	$\pi_{H-1}\sigma_{NH}$*(3s)	6.07	0.120	ππ*	6.67	6.62	6.58	0.176	ππ*
S_4	5.93	0.085	ππ*	6.25	0.002	$\pi_{H-1}\sigma_{NH}$*(3s)	6.98	6.99	6.97	0.000	$\pi_{H-1}\sigma_{NH}$*(3s)
S_5	6.70	0.033	$n\sigma_{NH}$*(3s)	6.26	0.040	$n\sigma_{NH}$*(3s)	7.37	7.18	7.04	0.037	$n\sigma_{NH}$*(3s)

Table SM4 - Vertical excitation energies, oscillator strengths and assignments at CASPT2 levels. S_0 energies in a.u.

CASPT2/SA-7-CAS(8,9)/6-31+G* [a]				CASPT2/SA-7-CAS(8,9)/6-31G+2G* [b]			
ΔE (eV)	*f*	ref. (%)[c]		ΔE (eV)	*f*	ref. (%)[c]	
-225.197101	-	85		-225.197250	-	86	
5.82	0.000	82	$\pi\sigma_{NH}$*(3s)	5.55	0.000	87	$\pi\sigma_{NH}$*(3s)
6.69	0.014	71	$\pi\sigma_{CH}$*	6.32	0.012	87	$\pi\sigma_{CH}$*
6.72	0.107	84	ππ*	6.41	0.021	87	$n\sigma_{NH}$*(3s)
6.75	0.017	80	nπ*	6.47	0.042	87	ππ*
6.83	0.036	54	$n\sigma_{NH}$*(3s)	6.67	0.002	86	$\pi_{H-1}\sigma_{NH}$*(3s)
6.98	0.002	84	$\pi_{H-1}\sigma_{NH}$*(3s)	6.99	0.007	86	nπ*

[a] IPEA = 0.25, shift = 0.0.

[b] IPEA = 0.25, shift = 0.1.

[c] Reference weigth.

Table SM5 - Vertical excitation energies, oscillator strengths and assignments at DFT/MRCI level. S_0 energies in a.u.

	DFT/MRCI/TZVPP+		
State	ΔE (eV)	*f*	
S_0	-226.171984	-	
S_1	5.44	0.001	$\pi\sigma_{NH}$*(3s)
S_2	6.11	0.187	$\pi\pi$*/$\pi 3p_x$
S_3	6.23	0.008	$\pi\sigma_{CH}$*/nπ*
S_4	6.25	0.034	$\pi\sigma_{CH}$*/nπ*
S_5	6.45	0.001	π-Ryd
S_6	6.58	0.032	$\pi 3p_x/\pi^*_{H-1}\pi_{L+1}^*$
S_7	6.78	0.028	$\pi 3p_x/\pi^*_{H-1}\pi_{L+1}^*$
S_8	6.85	0.001	$\pi_{H-1}\sigma_{NH}$*(3s)
S_9	6.94	0.041	nσ_{NH}*(3s)
S_{10}	6.96	0.001	π-Ryd

Cartesian coordinates (in Angstrom) of the optimized minima and conical intersections.

DFT(B3-LYP)/aug-cc-pVTZ

MIN S0

N	-0.014492	0.057140	1.149315
N	0.021062	0.685221	-0.968924
C	-0.008368	1.101093	0.273104
C	0.013281	-1.100642	0.405196
C	0.034865	-0.688056	-0.898154
H	-0.034230	0.119335	2.152045
H	-0.026123	2.128690	0.596049
H	0.014859	-2.075366	0.858593
H	0.059246	-1.296734	-1.785814

SA-6-CASSCF(8,9)/[N3,C,H:6-31G*;N1:6-31+G*]

MIN S0

N	-0.014493	0.056104	1.152765
N	0.021042	0.685323	-0.968536
C	-0.008189	1.095890	0.267630
C	0.013238	-1.100908	0.404176
C	0.034795	-0.687053	-0.896933
H	-0.034179	0.118737	2.142861
H	-0.025842	2.116464	0.585890
H	0.014770	-2.070423	0.851435
H	0.059332	-1.289597	-1.780166

MXS NC-dissociated

N	-0.022388	-0.426771	1.679757
N	0.027452	0.817928	-0.918260
C	0.002646	1.856664	-0.250789
C	0.010280	-1.121752	0.584098
C	0.035046	-0.524445	-0.706999
H	-0.035569	-1.030204	2.482960
H	0.000399	2.890748	-0.538900
H	0.020828	-2.203871	0.591429
H	0.061342	-1.133484	-1.587534

MXS NH-dissociated

N	-0.013186	0.051082	1.174101
N	0.021102	0.649329	-1.013718
C	-0.008577	1.064880	0.290646
C	0.013140	-1.060610	0.448593
C	0.034821	-0.665465	-0.941554
H	-0.054647	0.012072	2.781493
H	-0.022756	2.093361	0.578564
H	0.013194	-2.035703	0.889434
H	0.055388	-1.296304	-1.806292

MXS N-puckered

N	0.077802	0.032422	1.210039
N	0.679643	0.627212	-1.004107
C	-0.059569	0.960126	0.186098
C	0.006717	-1.162921	0.505043
C	-0.118724	-0.528639	-0.878709
H	-0.073178	0.173563	2.182204
H	-0.574702	1.894911	0.268610
H	0.742655	-1.933932	0.692691
H	-0.533844	-1.010859	-1.747184

MXS NH-puckered

N	0.395076	-0.169272	1.257784

N	0.037850	0.682202	-1.063508
C	-0.129633	1.297920	0.191007
C	-0.160766	-1.054405	0.439787
C	0.019390	-0.602560	-0.963664
H	0.039638	-0.185922	2.199355
H	-1.195259	1.437408	0.372754
H	-0.821218	-1.847068	0.742702
H	0.130444	-1.249302	-1.814016